Effects of Polyacrylamide Hydrogel on the Properties of Sand

by

David Stanley Graham

A thesis submitted to the Graduate Faculty of
Auburn University
in partial fulfillment of the
requirements for the Degree of
Master of Science

Auburn, Alabama
December 13, 2010

Keywords: liquefaction, polyacrylamide, hydrogel, Ottawa sand, triaxial testing

Approved by

David J. Elton, Chair, Professor of Civil Engineering
Ram B. Gupta, Philpott and West Point Stevens
Distinguished Professor of Chemical Engineering
J. Brian Anderson, Associate Professor of Civil Engineering

Abstract

A study on the effects of polyacrylamide hydrogel on the properties of Ottawa sand was conducted. Laboratory testing included stress-controlled cyclic triaxial tests, consolidated undrained triaxial compression tests, and one-dimensional consolidation tests. Experiments evaluating the effectiveness of electrical self-potential and capacitance measurement to detect polyacrylamide hydrogel in sand were conducted. A set of experiments to evaluate the shrinkage potential of polyacrylamide hydrogel treated sand due to dewatering were performed. Procedures for preparing frozen soil samples in the laboratory using both a freezer and liquid nitrogen are described. A new method of sample saturation using a syringe and hypodermic needle is also presented.

Treating sand with polyacrylamide hydrogel is a potential new method of soil liquefaction hazard mitigation, pore water modification. This study focuses on the effects of polyacrylamide hydrogel on the properties of Ottawa sand. Polyacrylamide Hydrogel was found to cause a slight increase in the magnitude of consolidation of Ottawa sand, reduce the shear strength of Ottawa sand, reduce dilation during shear, and increase the post liquefaction strength of Ottawa sand. Electrical self-potential and capacitance measurement successfully detected hydrogel in Ottawa sand in the laboratory. The shrinkage experiments indicate that volume change due to changes in water content may be of concern and require further investigation.

Acknowledgements

First, I would like to thank Dr. David Elton for his guidance on this project and for the many other things he has taught me. I would like to thank the rest of my thesis committee, Dr. Ram Gupta and Dr. Brian Anderson, for their input and support on this project. Several other people who have contributed significantly to this project are Mr. Mikkel Watts, Mr. Zane Hartzog, Ms. Melinda Hemingway, Dr. Loraine Wolf, and Dr. Richard Ray. Without these people this project would not have been possible.

I would also like to thank my wife, Mrs. Ruth Ann Graham, my parents, and my friends for their emotional support and love. I owe most of my success on this project to these people.

Finally, I would like to thank the Auburn University Department of Civil Engineering for providing me with an excellent education in the field of civil engineering. Specifically, I would like to thank Dr. Michael Stallings for his excellent leadership and vision for this department.

Table of Contents

List of Tables

List of Figures

Chapter 1: Introduction

1.1 Background

Soil liquefaction during earthquakes causes significant damage to structures that can result in human loss of life or injury, economic loss, and disruption of public services. The liquefaction-induced damage to the Port-au-Prince seaport following the January 2010 earthquake in Haiti is a prime example. Although methods exist to reduce a soil's susceptibility to liquefaction, most of these methods are not impractical or too costly for use under existing structures. At the very least, these methods often disrupt use of the structure. Many structures exist on potentially liquefiable sites. A new method of reducing liquefaction susceptibility, pore water modification, has the potential to provide a cost-effective solution to liquefaction hazard mitigation under existing structures without disrupting internal use of the building. Pore water modification involves the addition of a material that changes the physical properties in such a way that the effects of liquefaction are reduced.

1.2 Overview and Scope

Research was conducted to evaluate the potential of polyacrylamide hydrogel to modify soil pore water for the purpose of reducing liquefaction hazards and its effects on soil behavior under static conditions. Additional research on issues related to the instillation and verification of polyacrylamide hydrogel were also conducted. The testing included stress-controlled cyclic triaxial tests, static undrained consolidated triaxial tests, one-dimensional consolidation tests, geophysical detection experiments, and a shrinkage experiment.

Chapter 2: Literature Review

2.1 Liquefaction

2.1.1 Introduction

This chapter presents a literature review of the currently accepted understanding of soil liquefaction, methods of susceptibility analysis, and mitigation techniques. The term liquefaction was originally coined by Mogami and Kubo (1953). Since then, the term liquefaction has been used to describe several related phenomenon (Kramer 1996). Generally, liquefaction is defined as the transformation of a granular material from a solid to a liquefied state as a consequence of increased pore-water pressure and reduced effective stress (Marcuson 1978). The generation of excess pore pressure under undrained loading conditions is a hallmark of all liquefaction phenomena (Kramer 1996).

The catastrophic damage that can be caused by liquefaction was thrust into the spotlight of the geotechnical engineering community during a three-month period in 1964 when extensive liquefaction-related damage occurred during the Good Friday earthquake (M_w = 9.2) in Alaska and Niigata earthquake (M_s = 7.5) in Japan (Kramer 1996). Liquefaction-induced damage during these earthquakes included slope failures, bridge and foundation failures, and floatation of buried structures (Kramer 1996). Since these disasters, liquefaction has been studied extensively. Prevailing procedures of analysis and mitigation of liquefaction hazards have been slow to emerge.

2.1.2 Types of Liquefaction Failures

2.1.2.1 Loss of Strength

The strength of saturated fluid particle systems, including saturated soils, is dependent on the pore fluid pressure. Fluid pressure acts to force the particles apart, reducing the friction between particles and thus their ability to resist shear forces. The force of the pore fluid pushing the soil particles apart is counteracted by the weight of the surrounding soil pushing the particles together. Under static conditions, the pore fluid pressure is less than the stress caused by the weight of the surrounding soil particles. However during earthquakes, fast dynamic loading can cause the pore water pressures to increase to the point where they are equal to or higher than the normal stress. If the pore pressure is equal to or higher than the normal stress, the soil particles are no longer restrained from movement with respect to each other. At this point, the soil water system cannot resist shear forces and behaves as a liquid.

The idea that fluid pressure reduces the stress between soil particles is known as effective stress. The concept of effective stress is discussed in further detail in section 2.1.3.2 of this chapter. The key idea to note is that liquefaction occurs when the effective stress approaches zero. Liquefaction strength loss results in lateral spread, loss of bearing capacity, and flow failures.

Since liquefaction is the result of increased pore fluid pressure, it most often occurs in saturated soils. Specifically, loose saturated fine grained sands are the soil types most susceptible to liquefaction. During earthquake vibration or cyclic loading, the loose sand grains attempt to rearrange into a denser configuration, decreasing the pore volume. As a result, the pore water must either decrease in volume (drain) or increase in pressure. Because earthquake

vibrations cause the soil to densify quickly, the pore water does not have time to drain and must increase in pressure, causing a significant loss of strength known as liquefaction.

2.1.2.1.1 Loss of Bearing Capacity

When the soil supporting a structure liquefies and loses strength, large deformations can occur within the soil allowing the structure to settle and tip. Soils that typify the general subsurface conditions required for liquefaction-caused bearing failures are a layer of saturated, cohesionless soil (sand or silt) extending from near the ground surface to a depth approximately the width of the building (Hays 1981). Figures 2.5 and 2.9 show examples of bearing capacity failures.

2.1.2.1.2 Lateral Spread

Lateral spreads involve the lateral movement of large blocks of soil as a result of liquefaction in a subsurface layer. Movement takes place in response to the ground shaking generated by an earthquake. Lateral spreads generally develop on gentle slopes, most commonly between 0.3 and 3 degrees (Hays 1981). Horizontal movements on lateral spreads are commonly as much as 10 to 15 feet (Hays 1981). Where slopes are particularly favorable, and the duration of ground shaking is long, lateral movement may be as much as 100 to 150 feet. Lateral spreads usually break up internally, forming numerous fissures and scarps (Hays 1981). Figure 2.1, below, shows a lateral spread failure of a roadway after the 1989 Loma Prieta earthquake in California. Figures 2.3 and 2.6 show examples where lateral spread caused bridge piers to separate, literally removing the supports from under the bridge superstructure.

Bartlett and Youd (1995) developed empirical equations based on data collected from several U.S. and Japanese earthquakes to predict the horizontal displacement caused by lateral spread. Since the equations are empirical, they have limitations and cannot predict the amount of

displacement in all situations, but because lateral spread is the most common type of liquefaction-induced ground failure, the equations are a useful tool for estimating the resulting deformations, when used correctly.

Figure 2.1: Lateral spread roadway failure caused by the Oct. 17, 1989, Loma Prieta earthquake in California (NASA 2010)

2.1.2.1.3 Flow Failures

Flow failures, consisting of liquefied soil or blocks of intact material riding on a layer of liquefied soil, are the most catastrophic type of ground failure caused by liquefaction (Hays 1981). These failures commonly move several tens of feet and, if geometric conditions permit, several tens of miles (Hays 1981). Flows travel at velocities as great as many tens of miles per hour (Hays 1981). Flow failures usually form in loose saturated sands or silts on slopes greater than three degrees (Hays 1981). More information on flow liquefaction is presented in section 2.1.2.2.1.

2.1.2.2 Liquefaction-Related Phenomena

The term liquefaction is generally used to describe a variety of phenomena that involve loss of strength caused by the generation of excess pore pressure. While the generation of excess pore pressure is common to all liquefaction phenomena, the results of this process can be divided into two main categories: flow liquefaction and cyclic mobility (Kramer 1996).

2.1.2.2.1 Flow Liquefaction

Flow liquefaction produces the most dramatic effects of all the liquefaction-related phenomena, tremendous instabilities known as flow failures (Kramer 1996). Flow liquefaction can occur when the shear stress required for static equilibrium of a soil mass (the static shear stress) is greater than the shear strength of the soil in its liquefied state (Kramer 1996). Once triggered, the large deformations are driven by static shear stresses. The cyclic stresses may simply bring the soil to an unstable state at which its strength drops sufficiently to allow the static stresses to produce a flow failure (Kramer 1996). Flow liquefaction failures are characterized by the sudden nature of their origin, the speed with which they develop, and the large distance over which the liquefied materials often move (Kramer 1996). The Lower San Fernando Dam failure is an example of a flow liquefaction failure (see Figures 2.7 and 2.8).

2.1.2.2.2 Cyclic Mobility

Cyclic mobility is another liquefaction-related phenomenon that can also produce unacceptably large deformations as a result of earthquake shaking. In contrast to flow liquefaction, cyclic mobility occurs when the static shear stress is less than the shear strength of the liquefied soil (Kramer 1996). The deformations produced by cyclic mobility failures develop incrementally during earthquake shaking (Kramer 1996). Unlike flow liquefaction, the deformations produced by cyclic mobility are driven by both cyclic and static shear stresses

(Kramer 1996). The resulting deformations, known as lateral spreads, can occur on very gently sloping ground. Figures 2.3 and 2.4 show examples of cyclic mobility liquefaction failures.

A special case of cyclic mobility is level-ground liquefaction. Because static horizontal shear stresses that could drive lateral deformations do not exist, level-ground liquefaction can produce large, chaotic movement known as ground oscillation during earthquake shaking but produces little permanent lateral soil movement (Kramer 1996). Level ground liquefaction failures are caused by upward flow of water that occurs when seismically-induced excess pore pressures dissipate (Kramer 1996). Depending on the length of time required to reach hydraulic equilibrium, level-ground liquefaction failure may occur well after ground shaking has ceased (Kramer 1996). Level ground liquefaction is often characterized by excessive vertical settlement and consequent flooding of low-lying land and the development of sand boils (see Figure 2.2).

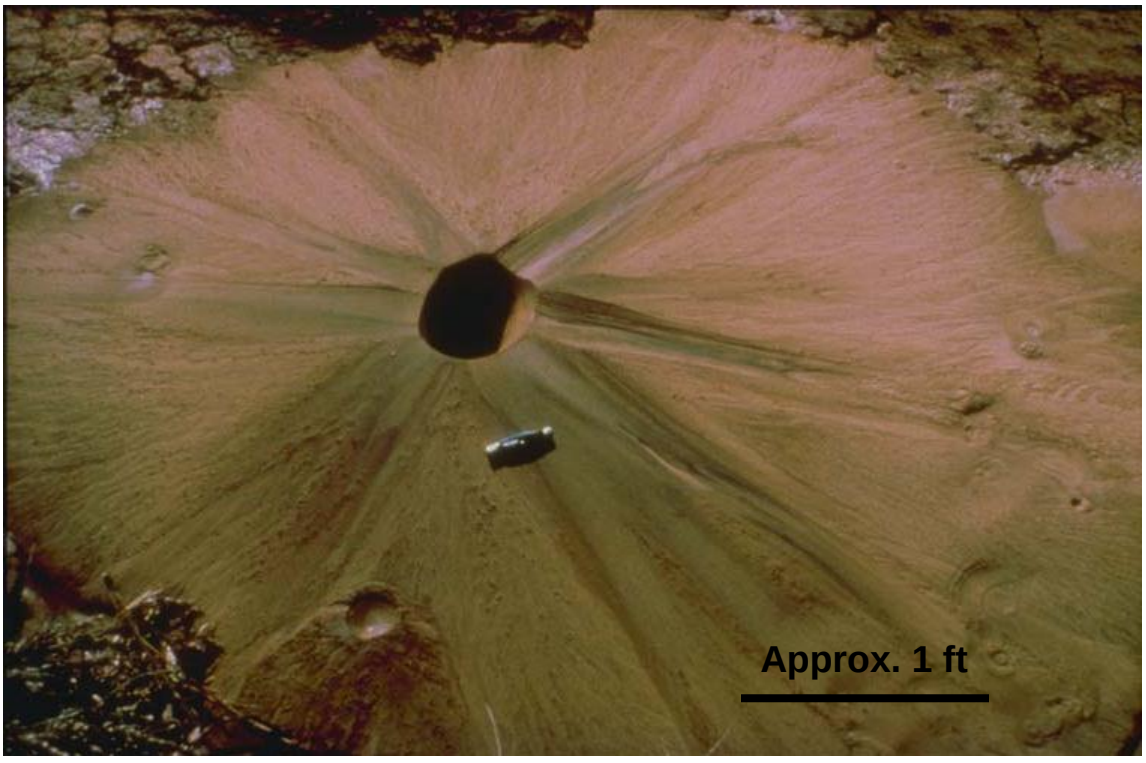

Figure 2.2: Example of a sand boil that developed after 1979 El Centro earthquake in California (WWU 2010)

2.1.2.3 Notable Liquefaction Events

2.1.2.3.1 "Good Friday" Earthquake, Alaska 1964

On March 27, 1964, a massive magnitude 9.2 earthquake occurred in Prince William Sound, Alaska: the largest earthquake in United States history, according to Stover and Cofman of the United States Geological Survey (USGS) (1993). Liquefaction in sand layers and in sand and silt seams in the clayey soils beneath Anchorage, Alaska, caused many of the destructive landslides that occurred during the earthquake (Seed 1968). This earthquake began to bring the issue of liquefaction and its effects to the attention of researchers. Figures 2.3 and 24 show some examples of the liquefaction-induced destruction in Alaska.

Figure 2.3: Damage to the "Million Dollar" railroad bridge due to lateral spread caused by the 1964 "Good Friday" earthquake (USGS 2006a)

Figure 2.4: Liquefaction-induced ground movement in Anchorage, Alaska, after the 1964 "Good Friday" earthquake (USGS 2006a)

2.1.2.3.2 Niigata, Japan 1964

On June 16, 1964, a magnitude 7.5 earthquake struck Japan, causing significant damage to the city of Niigata. The destruction was observed to be largely limited to buildings that were founded on top of loose, saturated soil deposits (Johnson 2000a). Figures 2.5 and 2.6 show some examples of the liquefaction-induced destruction in Niigata. Due to the large amount of liquefaction-induced damage and its close chronological proximity to the "Good Friday" earthquake, the Niigata earthquake confirmed liquefaction to be a major cause of damage during earthquakes worthy of research and investigation.

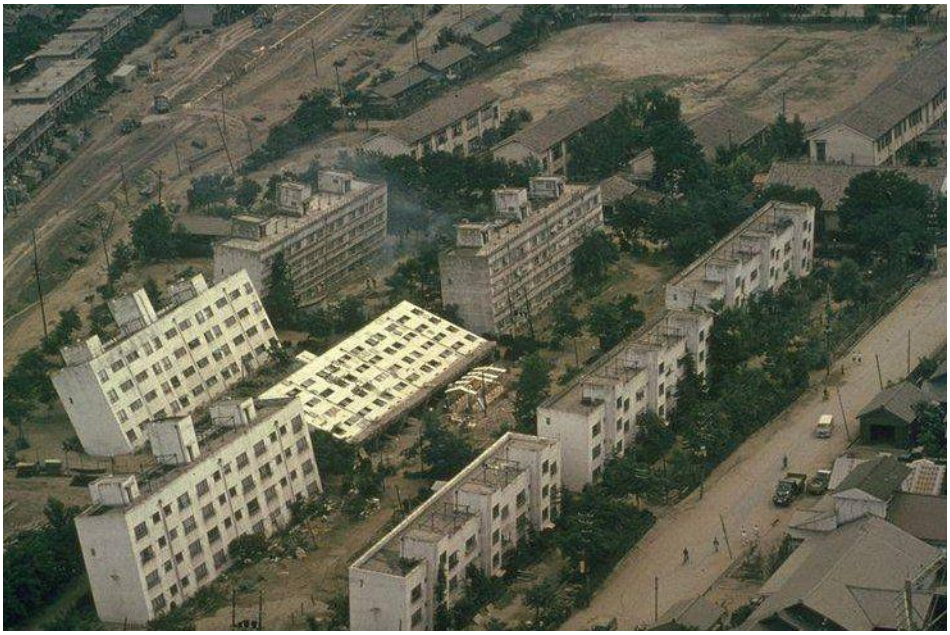

Figure 2.5: Liquefaction-induced bearing capacity failure of the Kawagishi-cho apartment buildings near the Shinano River after the 1964 Niigata earthquake (Johnson 2000a)

Figure 2.6: Shaw bridge failure caused by lateral spread of the foundation soils after the 1964 Niigata, Japan, earthquake (Johnson 2000a)

2.1.2.3.3 San Fernando Earthquake, California 1971

Also known as the Sylmar Earthquake, the San Fernando Earthquake was a magnitude 6.6 earthquake that struck a sparsely populated area of the San Gabriel Mountains, near San

Fernando, California. It lasted about 60 seconds and in that brief span of time, took 65 lives, injured more than 2,000, and caused property damage estimated at $505 million (Stover and Coffman 1993). Fortunately, a liquefaction-induced landslide that occurred on the upstream face of the Lower San Fernando Dam did not cause the dam to breach. Had the dam breached, 15 million tons of water would have inundated an area of the San Fernando Valley containing approximately 80,000 people (Page et al. 1996).

The earthen Lower San Fernando Dam, also known as the Lower Van Norman Dam, experienced a slope failure on its upstream slope. The slide was caused by the liquefaction of a loose alluvial sand deposit located under its foundation (See Figure 2.7). The slide carried away much of the crest and upstream concrete facing of the 2,100-foot-long dam (Page et al. 1996). As shown in Figure 2.8, only a narrow shattered wall of dirt remained to prevent the reservoir from flooding the valley below.

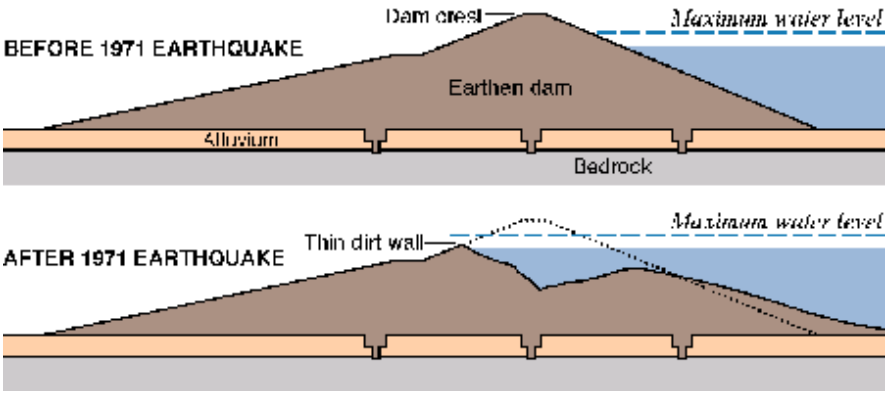

Figure 2.7: Schematic of the Lower San Fernando Dam before and after the 1971 San Fernando, California, earthquake (Page et al. 1996)

Figure 2.8: Aerial view of the Lower San Fernado Dam liquefaction-induced slope failure after the 1971 San Fernando, California, earthquake (USGS 2006b)

2.1.2.3.4 Loma Prieta Earthquake, California 1989

On October 17, 1989, a magnitude 7.1 earthquake occurred in the San Francisco Bay area of California. Extensive liquefaction-related deformations and sand boils were observed at the Moss Landing shoreline of Monterey Bay. The Moss Landing area was subsequently studied extensively. Case studies and damage overviews were published by Boulanger et al. (1997), Greene et al. (1991), and Tuttle et al. (1990).

2.1.2.3.5 Hyogo-Ken Nanbu Earthquake, Kobe, Japan 1995

On January, 17, 1995 a magnitude 6.9 earthquake occurred near Kobe, Japan. Extensive liquefaction-related damage was caused by the earthquake. The Kobe port, having been

constructed on two artificial islands made of relatively loose fill, and always water-saturated, suffered widespread liquefaction and settlement, and was incapacitated for two months (Louie 1996). Shipping was disrupted worldwide. Figures 2.9 and 2.10, below, show just some of the liquefaction-related damage that occurred near Kobe.

Figure 2.9: Partial bearing capacity failure of a building founded on liquefiable soil in Kobe, Japan, after the 1995 Hyogo-Ken Nanbu Earthquake (Louie 1996)

Figure 2.10: Liquefaction damage to man-made port islands in Kobe, Japan, after the 1995 Hyogo-Ken Nanbu Earthquake (Johnson 2000b)

2.1.3 Stresses within the Soil Mass that Govern Liquefaction Behavior

2.1.3.1 Total Vertical Stress

The weight, due to gravity, of the soil above a point in the subsurface induces vertical stress in the soil at that point. Loads, such as buildings, bearing on the soil mass above a point within that soil mass also induce vertical stress as that point. Sometimes these vertical forces are counteracted by a buoyant force caused by hydrostatic pressure. The vertical stress due to soil overburden and other surcharge loads without the effect of the buoyant force is known as total vertical stress, often referred to as just "total stress." David McCarthy also presents an overview of vertical stress in section 9.1 of his text (2002). Total vertical stress is a variable in the effective stress equation, which governs soil strength and, thus, liquefaction.

2.1.3.2 Effective Stress

Karl Terzaghi first published his theory of effective stress in 1925. He stated "All measurable effects of a change of stress [in a soil mass], such as compression, distortion and a change of shearing resistance are due exclusively to changes in effective stress." Effective stress is defined by the equation:

$$\bar{\sigma} = \sigma - u \qquad (2.1)$$

where $\bar{\sigma}$ is effective stress, σ is total stress, and u is neutral stress or pore fluid pressure. Holtz and Kovacs present an overview of the concept of effective stress in section 7.5 of their text (1981). Under normal static conditions, the pore fluid is water and the pore pressure is simply the hydrostatic pressure of that water at the point of interest.

2.1.3.3 Liquefaction and Effective Stress

Liquefaction occurs when the pore pressure is equal to or greater than the total vertical stress, mathematically yielding an effective stress less than or equal to zero. If the effective

stress is equal to zero, a cohesionless soil also has zero shear strength because shear strength is a function of effective stress governed by the equation:

$$\tau_f = \bar{\sigma} \tan(\bar{\phi}) \qquad (2.2)$$

where, τ_f is shear strength and $\bar{\phi}$ is the effective angle of internal friction. Materials that have no shear strength behave as a liquid, thus the term liquefaction.

Liquefaction occurs during earthquakes when the vibrations cause loose, cohesionless soil to densify. When a soil becomes denser, the pore volume is decreased. If drainage is unable to occur, the decrease in pore volume causes an increase in pore water pressure. If the pore water pressure builds to the point at which it is equal to the vertical stress, the effective stress becomes zero, the soil loses its strength, and it develops a liquefied state (Seed and Lee 1966).

2.1.2.4 Evaluation of Liquefaction Hazards

Liquefaction, both flow liquefaction and cyclic mobility, can cause significant damage that can be widespread or localized to a particular site. The high risk associated with liquefaction hazards warrants consideration in geotechnical investigation and design. Three questions should be addressed in evaluating liquefaction hazards (Kramer 1996):

1. Is the soil susceptible to liquefaction?
2. If the soil is susceptible, will liquefaction be triggered?
3. If liquefaction is triggered, will damage occur?

These questions address the most critical aspects of liquefaction hazard evaluation: susceptibility, initiation, and effects (Kramer 1996). All three of these considerations should be addressed for a proper evaluation of liquefaction hazards.

2.1.4.1 Soil Saturation

Because liquefaction is driven by excess pore pressure, soil is most susceptible to liquefaction when the pore space is filled with an incompressible fluid, like water, rather than a compressible fluid, like air. Full or near full saturation is typically considered necessary for liquefaction to occur. Because of this, liquefaction is most commonly observed near rivers, bays, and other bodies of water, where the groundwater table is close to the ground surface (Kramer 1996).

2.1.4.2 Liquefaction Susceptible Soil

Soil deposits that are susceptible to liquefaction are formed within a relatively narrow range of geological environments (Youd 1991). The depositional environment, hydrological environment, and age of a soil deposit all contribute to its liquefaction susceptibility (Youd and Hoose 1977). Soils deposited by humans can also be susceptible to liquefaction. Loose fills placed without compaction are especially susceptible to liquefaction. The stability of hydraulic fill dams and mine tailings piles, in which soil particles are loosely deposited by settling through water, remains an important contemporary seismic hazard (Kramer 1996).

In addition to the loose structure and the saturation conditions described in the previous section, the soil type also plays a role. For many years, liquefaction-related phenomena were thought to be limited to sands (Kramer 1996). However, Ishihara (1993) determined that coarse nonplastic silts with bulky particle shape are also susceptible to liquefaction. Clays and plastic silts are not susceptible to liquefaction because of the cohesive forces between the soil particles. Wang (1979) developed the so-called Chinese criteria, stating that silty soils must meet the

following requirements to be susceptible to liquefaction:

Fraction finer than 2.0e-4 in ≤ 15%

Liquid Limit ≤ 35%

Natural water content ≥ 0.9 LL

Liquidity index ≤ 0.75

Coarser-grained soils, like coarse sands and gravels, are also less susceptible to liquefaction because of their high permeability.

2.1.4.3 Earthquake Potential

Under field conditions, liquefaction occurs only when a potentially liquefiable site is subjected to certain loading conditions, typically caused by an earthquake. Therefore, part of evaluating liquefaction potential is evaluating the seismic potential. Predicting the magnitude, location, and time of occurrence of earthquakes is currently impossible. Two methods have traditionally been used to evaluate earthquake hazards: deterministic seismic hazard analysis (DSHA) and a probabilistic seismic hazard analysis (PSHA). DSHA is typically used for higher risk sites and sites supporting high risk structures. It is based on estimating a "design earthquake" that could occur based on the site location in relationship to known faults. PSHA uses statistical methods to determine design values based on a return period and historical data. More recently, the procedures of the International Building Code (IBC) have become common practice.

2.1.4.3.1 Deterministic Seismic Hazard Analysis (DSHA)

In the early years of geotechnical engineering, DSHA was the most common method of seismic hazard analysis. Today PSHA is more common, but DSHA is still used for sites with

poor subsurface conditions or sites with supporting high risk structures like dams or nuclear power plants.

DSHA involves determining a theoretical earthquake that could occur. A simple example of a deterministic statement of earthquake hazard could be: the earthquake hazard at site X is a peak ground acceleration of 0.5 g resulting from the occurrence of a magnitude 6.5 earthquake on fault Y at a distance of 10 miles (Rieter 1991). This analysis requires the specification of three basic elements: an earthquake source (fault Y), a controlling earthquake of specified size (magnitude 6.5) and a means of determining the hazard, which in this case is peak ground acceleration (0.5g), at the specified distance (10 miles) to the site (Rieter 1991). DSHA is useful in quantifying a worst-case scenario earthquake, which is why it is useful for structures for which failure has catastrophic consequences, but it provides no information on the likelihood of occurrence. Often, it is unlikely that the worst-case scenario earthquake will occur during the useful life of a structure. For this reason, designers most often use a probabilistic hazard analysis.

2.1.4.3.2 Probabilistic Seismic Hazard Analysis (PSHA)

From the early 1970's to the late 1990's, site specific PSHA replaced DSHA as the primary method of earthquake hazard analysis because it accounts for risk and uncertainties in the size, location, and rate of recurrence of earthquakes and in the variation of ground motion characteristics with earthquake size and location to be explicitly considered evaluation of seismic hazards (Kramer 1996). In contrast to the deterministic approach which makes use of discrete, single-valued events or models, probabilistic analysis allows the use of multi-valued or continuous events and models (Rieter 1991). An example of a deterministic statement of earthquake hazard could be: a peak ground acceleration of 0.5g with a 10% likelihood of

exceedance in 50 years. Both Kramer (1996) and Reiter (Rieter) present detailed explanations of how seismic risks and uncertainties should be addressed in their texts.

2.1.4.3.3 Seismic Hazard Analysis Procedures of the International Building Code (IBC) and ASCE 7

Since the first edition of the IBC in 2000, seismic hazards have been increasingly quantified using the IBC procedures. The seismic design procedures of the IBC (2006) are taken from ASCE 7 (2005), *Minimum Design Loads for Buildings and Other Structures*. Site-specific seismic hazard analysis using PSHA or DSHA is only required by the 2006 IBC and ASCE 7-05 for specific circumstances. Instead, seismic hazards are assessed based on spectral accelerations determined from maps developed by the National Earthquake Hazards Reduction Program (NEHRP) that are then modified based on the soil conditions of the site (seismic site classification). The NEHRP maps, which are republished in both the IBC (2006) and ASCE 7-05, are based on the USGS probabilistic hazard maps with additional modifications incorporating deterministic ground motions in selected areas and the application of engineering judgment (Leyendecker et al. 2000). Basically, these procedures are a combination PSHA and DSHA. An example problem using the IBC procedures is presented below.

In certain situations, including potentially liquefiable sites, the codes require that a site-specific analysis procedure be followed; however, with the exception of damped or seismically isolated structures subject to high seismic loads, the ground motions of the bedrock are still determined using the NEHRP maps. The difference is in how the overlying soil conditions are considered. Only for seismically isolated and/or damped structures with a mapped spectral acceleration for five percent damping and a one second period (S_1) greater than 0.6 g is a site-specific quantification of earthquake ground motion for the bedrock required.

Example 2.1: Determining Short and 1-Second Spectral Response Accelerations Using the IBC (2006)

Example site location: 15 miles northwest of Charleston, South Carolina

Step 1: Determine a Site Class (A through F) based on the soil properties in accordance with section 1613 of the IBC. Classification is based on shear wave velocities, SPT results, or shear strengths and defined by Table 1613.5.2.

IBC Table 1613.5.2

Site Class Definitions

Site Class	Soil Profile Name	AVERAGE PROPERTIES IN TOP 100 feet, SEE SECTION 1613.5.5		
		Soil shear wave velocity, $\overline{V}_s$, (ft/s)	**Standard penetration resistance, $\overline{N}$**	**Soil undrained shear strength, $\overline{S}_u$, (psf)**
A	Hard rock	$\overline{V}_s > 5{,}000$	N/A	N/A
B	Rock	$2{,}500 < \overline{V}_s \le 5{,}000$	N/A	N/A
C	Very dense soil and soft rock	$1{,}200 < \overline{V}_s \le 2{,}500$	$\overline{N} > 50$	$\overline{S}_u > 2{,}000$
D	Stiff soil profile	$600 \le V_s \le 1{,}200$	$15 \le \overline{N} \le 50$	$1{,}000 \le \overline{S}_u \le 2{,}000$
E	Soft soil profile	$\overline{V}_s < 600$	$\overline{N} < 15$	$\overline{S}_u < 1{,}000$
E	–	Any profile with more than 10 feet of soil having the following characteristics: 1. Plasticity index PI >20 2. Moisture content $w \ge 40\%$ 3. Undrained shear strength $\overline{S}_u$ <500 psf		
F	–	Any profile containing soil having one or more of the following characteristics: 1. Soils vulnerable to potential failure or collapse under seismic loading such as liquefiable soils, quick and highly sensitive clays, collapsible weakly cemented soils. 2. Peats and/or organic clays (H >10 feet of peat and/or highly organic clay where H = thickness of soil) 3. Very high plasticity clays (H >25 feet with plasticity index PI >75) 4. Very thick soft/medium stiff clays (H >120 feet)		

Site Class D (stiff soil) shall be used unless (1) sufficient data are known to justify another class, or (2) the jurisdictional authority determines Site Class E or F is

warranted. For this example it will be assumed that there is no reason Site Class D should not be used.

Step 2: Determine the *mapped acceleration parameters* (1) maximum considered earthquake (MCE) ground motion of 0.2-s spectral response acceleration (S_s), and (2) MCE ground motion of 1-s spectral response acceleration (S_1), from the maps in section 1613.5. The relevant maps for this problem are presented on the page 27 with the site location shown.

From the maps for the example site:

S_s = 200% of gravity = 2.00 g

S_1 = 50% of gravity = 0.50 g

Step 3: Determine the MCE spectral response acceleration for short periods (S_{MS}) and at 1 second (S_{M1}), adjusted for Site Class effects, using IBC Equations 16-37 and 16-38 respectively.

$$S_{MS} = F_a S_s \qquad \text{(IBC Equation 16-37)}$$

$$S_{M1} = F_a S_1 \qquad \text{(IBC Equation 16-38)}$$

where:

F_a = Site coefficient defined in Table 1613.5.3(1)

F_v = Site coefficient defined in Table 1613.5.3(2)

Table 1613.5.3(1)

Values of Site Coefficient F_a[a]

Site Class	MAPPED SPECTRAL RESPONSE ACCELERATION AT SHORT PERIOD				
	$S_S \leq 0.25$	$S_S = 0.5$	$S_S = 0.75$	$S_S = 1.00$	$S_S \geq 1.25$
A	0.8	0.8	0.8	0.8	0.8
B	1.0	1.0	1.0	1.0	1.0
C	1.2	1.2	1.1	1.0	1.0
D	1.6	1.4	1.2	1.1	1.0
E	2.5	1.7	1.2	0.9	0.9
F	Note b	Note b	Note b	Note b	Note b

a. Use straight-line interpolation for intermediate values of mapped spectral response acceleration at short period, S_s

b. Values shall be determined in accordance with Section 11.4.7 of ASCE 7

Table 1613.5.3(1)

Values of Site Coefficient F_v[a]

Site Class	MAPPED SPECTRAL RESPONSE ACCELERATION AT SHORT PERIOD				
	$S_1 \leq 0.1$	$S_1 = 0.2$	$S_1 = 0.3$	$S_1 = 0.4$	$S_1 \geq 0.5$
A	0.8	0.8	0.8	0.8	0.8
B	1.0	1.0	1.0	1.0	1.0
C	1.7	1.6	1.5	1.4	1.3
D	2.4	2.0	1.8	1.6	1.5
E	3.5	3.2	2.8	2.4	2.4
F	Note b	Note b	Note b	Note b	Note b

a. Use straight-line interpolation for intermediate values of mapped spectral response acceleration at short period, S_s

b. Values shall be determined in accordance with Section 11.4.7 of ASCE 7

For this example:

$$S_{MS} = F_a S_s = (1.0)(2.00\,\text{g}) = 2.00\,\text{g}$$

and

$$S_{M1} = F_a S_1 (0.75)(0.50\,\text{g}) = 0.75\,\text{g}$$

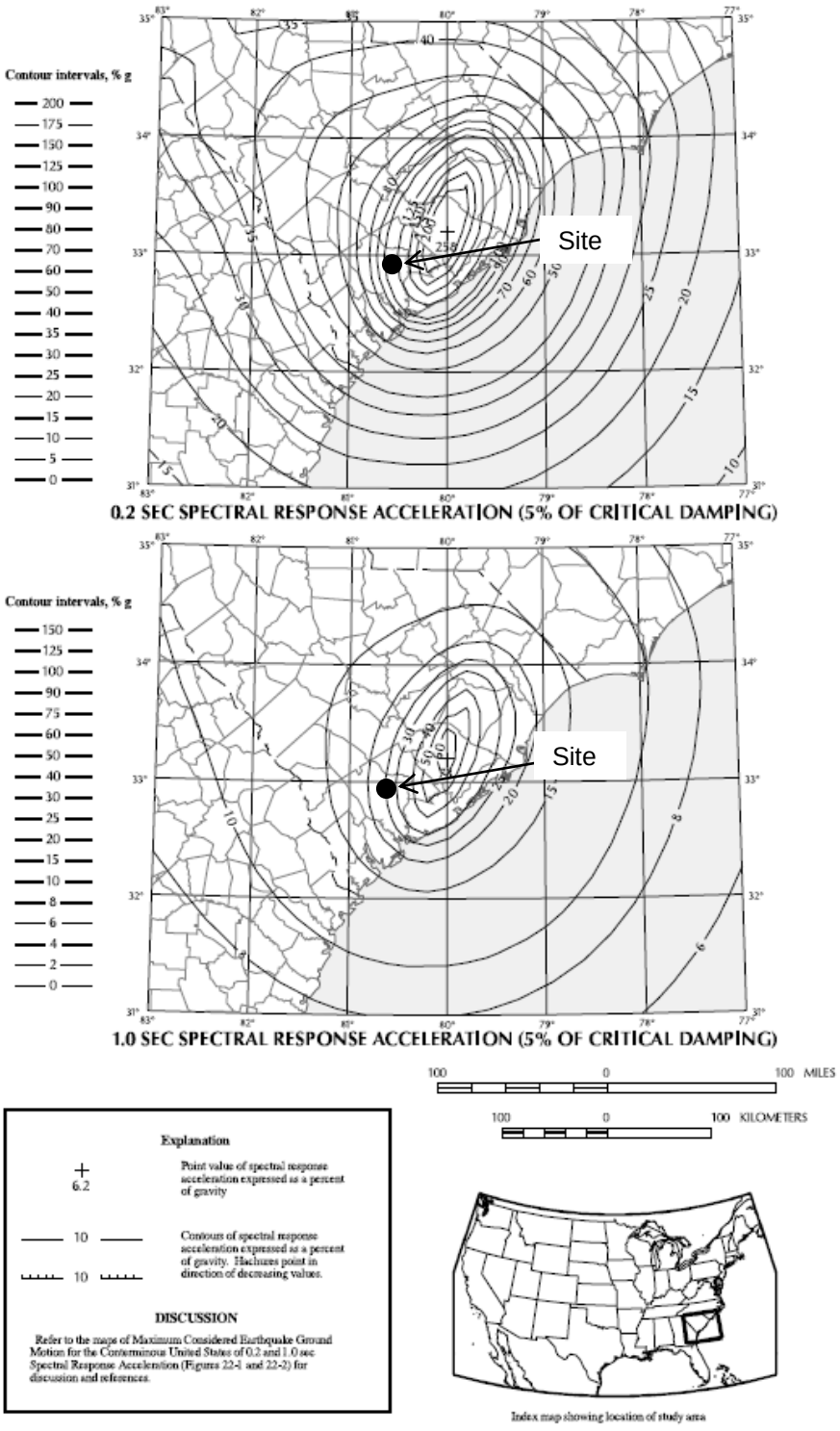

IBC Figure 1613.5(9) Maximum considered earthquake ground motion for region 4 of 0.2 and 1.0 sec spectral response acceleration (5% of critical damping), Site Class B

Step 5: Determine the design response acceleration parameter for short periods (S_{DS}) and for a 1-second period (S_{D1}) using Equations 16-39 and 16-40 respectively. The design response acceleration is two-thirds of the maximum considered acceleration:

$$S_{DS} = \frac{2}{3} S_{MS} \qquad \text{(IBC Equation 16-39)}$$

$$S_{D1} = \frac{2}{3} S_{M1} \qquad \text{(IBC Equation 16-40)}$$

These design spectral ordinates correspond to values with a 10-percent probability of exceedance within a 50-year period. Such an earthquake is sometimes described as a "500-year earthquake."

For this example:

$$S_{DS} = \frac{2}{3} S_{MS} = \left(\frac{2}{3}\right)(2.00\,\text{g}) = 1.33\,\text{g}$$

and

$$S_{D1} = \frac{2}{3} S_{M1} = \left(\frac{2}{3}\right)(0.75\,\text{g}) = 0.50\,\text{g}$$

The values of S_{DS} and S_{D1} can be used to determine the seismic design category or to create a design response spectrum curve.

Discussion: For liquefaction analysis, peak horizontal ground acceleration ($a_{\max}$), not spectral acceleration, is needed to perform the liquefaction analysis calculations. The IBC requires that $a_{\max}$ be determined using a site-specific analysis in accordance with Chapter 21 of ASCE 7-05 or it may be estimated as $S_{DS}/2.5$ in accordance with Section 1802.2.7 of the IBC.

2.1.2.5 Laboratory Evaluation of Liquefaction Susceptibility

If a soil is potentially susceptible to liquefaction, as described in section 2.1.4.2, its liquefaction susceptibility can be evaluated under laboratory conditions. In geotechnical practice, laboratory testing for liquefaction susceptibility is rare compared to more common field testing. However, laboratory testing is often used in liquefaction-related research. Most of the liquefaction laboratory tests consist of some scheme in which the soil is loaded cyclically. The cyclic loading is an attempt to replicate the effects of earthquake vibrations. Cyclic triaxial testing is the most common laboratory test for liquefaction susceptibility evaluation. Less common methods include cyclic simple shear, cyclic torsional shear, and shaking table devices.

2.1.5.1 Cyclic Triaxial Testing

Cyclic triaxial testing is based on, and is therefore very similar to, static triaxial testing. A cylindrical sample of soil is contained in a pressurized cell, separated from the confining fluid by a thin membrane. In any triaxial test, a stress difference between the radial direction and the vertical direction, known as the deviator stress, is applied to a soil sample while pore pressures and displacements (strains) are measured. For a cyclic triaxial test, the deviator stress is applied cyclically, either under stress-controlled conditions (typically by pneumatic or hydraulic loaders) or under strain-controlled conditions (by servohydraulic or mechanical loaders) (Kramer 1996). Typically the radial stress is held constant and the axial stress is cycled at a frequency of about 1 Hz (Kramer 1996). The ASTM D5311 (2004a) standard test method governs the procedure for stress controlled cyclic triaxial testing. There is not an ASTM specification for strain controlled cyclic triaxial testing. Figure 2.11 shows a schematic of a typical cyclic triaxial setup.

During a cyclic triaxial test, if the soil sample is liquefiable, the pore pressure (u) will increase to a value equal to that of the confining pressure (σ_3). When the pore pressure is equal

to the confining pressure, the effective stress (σ') is equal to zero. This is the point where liquefaction is typically considered to occur and is the criteria Seed and Lee (1966) used in their cyclic triaxial tests.

The number cycles until liquefaction (N_L) is another important piece of data produced by the cyclic triaxial test. Soils that exhibit more cycles before liquefaction are more resistant to liquefaction. When comparing cyclic triaxial data, it is important to understand that liquefaction resistance is not only a function of soil type, but also a function of soil density, effective confining pressure (σ_3'), peak cyclic deviator stress (σ_d), number of cycles of cyclic deviator stress (N), and overconsolidation ratio (OCR) (Das 1993). Since these variables can be different for different tests on the same soil, it is important to understand them and know their values when comparing cyclic triaxial data. More details about cyclic triaxial testing are presented in Kramer's (1996) text.

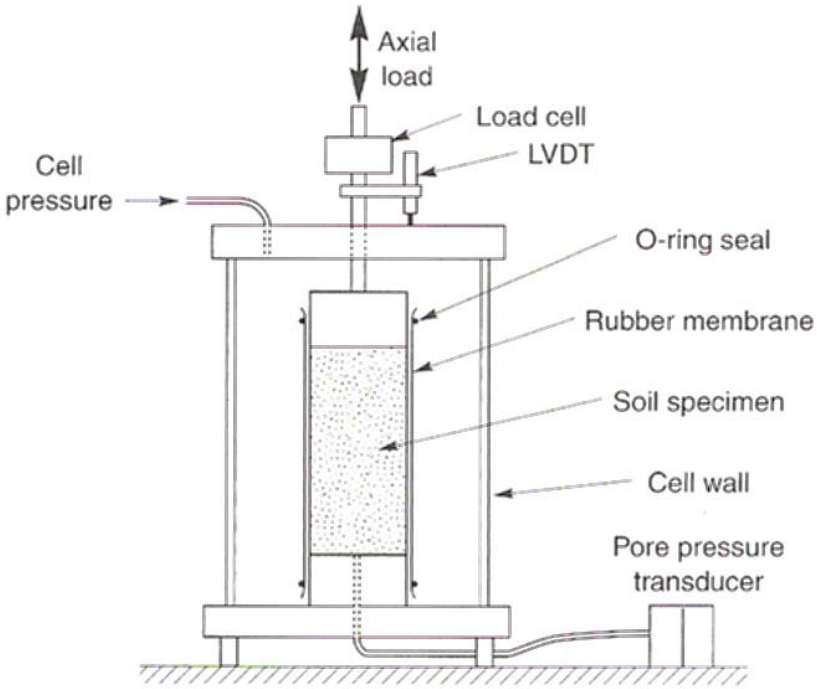

Figure 2.11 - Typical cyclic triaxial schematic (Kramer 1996)

2.1.5.2 Cyclic Simple Shear

Sometimes called cyclic direct simple shear, the simple shear device directly applies shear stress to the soil rather than indirectly as does the cyclic triaxial apparatus. In simple shear, a short cylindrical sample is restrained from lateral expansion, typically with a wire reinforced membrane or a system of stacked rings. When a vertical normal stress (σ_v) is applied to the sample, the resulting horizontal stress is equal to $K_o\sigma_{v,}$ where K_o is the coefficient of earth pressure at rest. The sample is sheared by applying a cyclic horizontal load to one end of the sample while restraining the other end of the sample from horizontal movement. A schematic of a cyclic simple shear device is presented in figure 2.12. The cyclic simple shear test is capable of reproducing earthquake stress condition more accurately than the cyclic triaxial test (Kramer 1996).

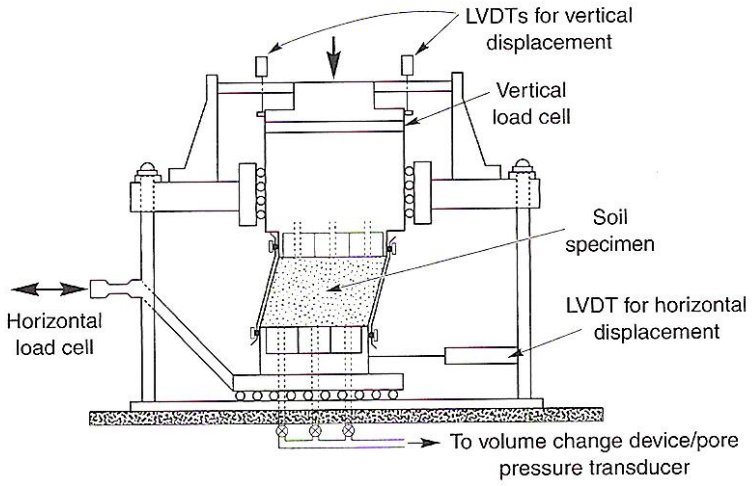

Figure 2.12 - Schematic of a cyclic simple shear device (Airey and Wood 1987)

2.1.5.3 Cyclic Torsional Shear

Many of the difficulties associated with the cyclic triaxial and cyclic simple shear tests can be avoided by loading a cylindrical soil specimen in torsion (Kramer 1996). Cyclic torsional shear

tests allow isotropic and anisotropic initial stress conditions and can impose cyclic shear stresses on horizontal planes with continuous rotation of principal stress axes (Kramer 1996). Ishihara and Li (1972) developed a test for solid cylindrical soil samples using cyclic torsional shear to evaluate liquefaction. Other researchers (Drenevich 1972; Ishibashi and Sherif 1974) developed tensional tests utilizing hollow cylindrical samples. Hollow samples have the advantage of less discontinuity of radial strain across the sample's cross-section. Figure 2.13 demonstrates how a torsional shear test on a hollow sample works. Torsional shear tests offer more control than other lab tests but the sample preparation is, especially for hollow samples, very difficult and the equipment is not commonly available.

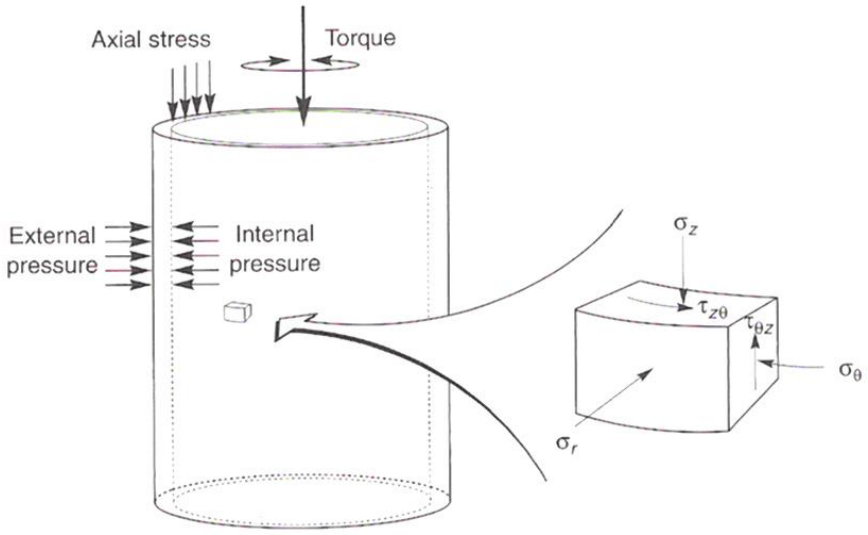

Figure 2.13: Hollow cylinder apparatus. The specimen is enclosed within internal and external membranes on which internal and external pressures can be applied independently. Application of cyclic torque induces cyclic shear stresses on horizontal planes (Kramer 1996).

2.1.5.4 Shaking Table

Unlike the tests described above where stress and boundary conditions are placed on a representative element of soil to test liquefaction, a shaking table test is a physical model test that

is basically a scaled down model of a field site. As the name implies, a shaking table is simply a device that can induce controlled movements to a model soil mass. Most shaking tables move horizontally in one direction, but shaking tables with multiple degrees of freedom have also been developed (Kramer 1996). Shaking tables can be large or small, include multiple soil layers and even model structures on the soil surface. Shaking tables also allow for a variety of instrumentation to be installed. The biggest drawback of shaking tables is the amount of effort required to set up a test and the limited thickness of soil that can be tested. Due to complexity and size, shaking tables are used almost exclusively for research purposes. A schematic of the shaking table test is presented in figure 2.14.

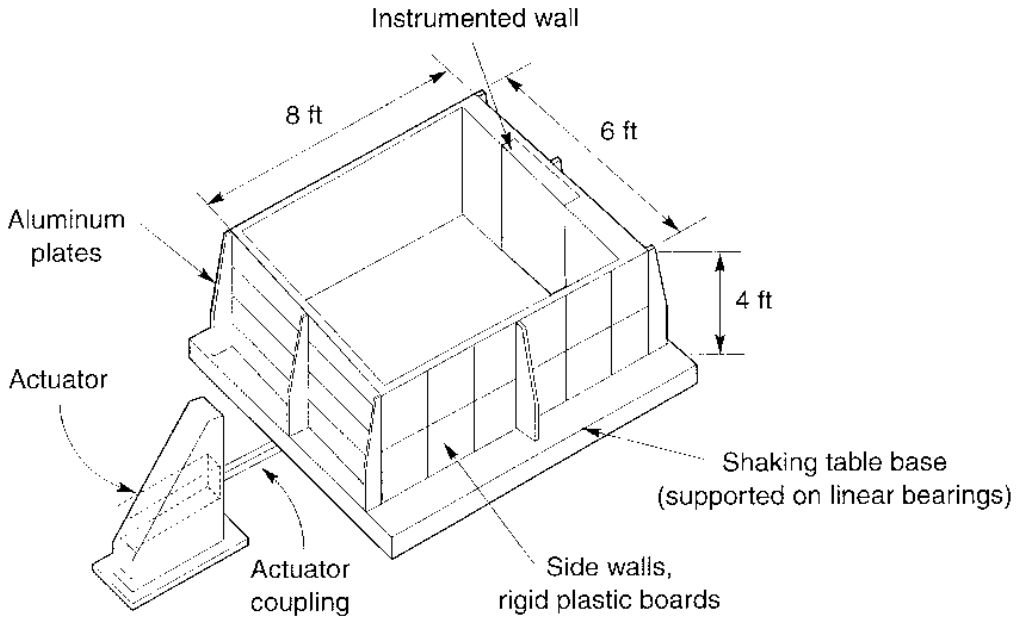

Figure 2.14: Example design of a shaking table with soil bin used for soil dynamics research (Kramer 1996)

2.1.2.6 Field (In-Situ) Evaluation of Liquefaction Susceptibility

In engineering practice, field testing procedures are the most common way to evaluate liquefaction susceptibility. Because Seed and Idriss (1971) developed the first practical

procedure for field evaluation based on the standard penetration test (SPT) and because the SPT is the most common geotechnical field test, methods based on Seed and Idriss' procedure and the SPT are by far the most common procedures used to evaluate soil liquefaction in the field. In recent years, as the cone penetration test (CPT) has gained more popularity, procedures have also been developed for the CPT. Shear wave velocity (V_s) testing is also a relatively common method of evaluating liquefaction susceptibility. The summary report from the 1996 and 1998 National Center for Earthquake Engineering Research (NCEER) workshops on evaluating liquefaction describes the procedures generally accepted and practiced for field evaluation of liquefaction susceptibility (Youd and Idriss 2001).

2.1.6.1 Evaluation Cyclic Stress Ratio (CSR)

In order to calculate or estimate the resistance of liquefaction, two variables will need to be calculated: CSR and cyclic resistance ratio (CRR). Ultimately, the factor of safety against liquefaction will be the ratio of CRR to CSR. The determination of CRR will vary based on the method of field testing; however, the CSR will be calculated the same way regardless of the field investigation method used.

Seed and Idriss (1971) formulated the following equation for CSR:

$$\text{CSR} = \left(\frac{\tau_{av}}{\bar{\sigma}_v}\right) = 0.65\left(\frac{a_{\max}}{g}\right)\left(\frac{\sigma_v}{\bar{\sigma}_v}\right) r_d \qquad (2.3)$$

where τ_{av} = average horizontal shear stress, $a_{\max}$ = peak horizontal acceleration at the ground surface, g = the acceleration of gravity, σ_v and $\bar{\sigma}_v$ are the total and effective vertical stresses, respectively, and r_d = stress reduction coefficient. The stress reduction coefficient accounts for flexibility of the soil profile. The NCEER committee (Youd and Idriss 2001) recommends using

equations developed Liao and Whitman (1986). The recommended equations, converted to U. S. customary units, are:

$$r_d = 1.0 - 0.002332z \quad \text{for } z \le 30\,\text{ft} \tag{2.4a}$$

$$r_d = 1.174 - 0.008138z \quad \text{for } 30\ \text{ft} < z \le 75\,\text{ft} \tag{2.4b}$$

where *z* is depth below the ground surface in feet where liquefaction is being evaluated.

2.1.6.2 Evaluation Using the Standard Penetration Test (SPT) ASTM D1586

The SPT is the most common in-situ test in geotechnical engineering. The information gained from SPT testing can be used for many types of analysis or property correlation besides liquefaction analysis. Since it is the most common test, SPT also has the largest database of historical data and case histories of any geotechnical test. As a result, empirical correlations can be made based on SPT blow count data. The SPT blow count (*N*) is the number of standard hammer blows required to drive the SPT split spoon sampler one foot into the soil. Details of the SPT are presented in most geotechnical textbooks including McCarthy's (2002).

The basic procedures for evaluating soil liquefaction based on the SPT were developed by Seed and Idriss (1971). Those procedures were modified, improved, and updated, primarily through landmark papers by Seed (1979), Seed and Idriss (1982), and Seed et al. (1985). Then, in 1985, Robert V. Whitman convened a workshop on behalf of the National Research Council (NRC), which produced a report (NRC 1985) that became the standard of practice for liquefaction assessment. In 1996, another workshop was convened by T. L. Youd and I. M. Idriss to update the 1985 report. The recommendations of the 1996 and subsequent 1998 workshops are presented in a report that was reprinted in the ASCE *Journal of Geotechnical and Geoenvironmental Engineering* in 2001 (Youd and Idriss). A brief overview of these procedures is present in the following sections.

2.1.6.2.1 SPT Evaluation of Cyclic Resistance Ratio (CRR)

Seed and Idriss (1982) originally developed correlations between corrected SPT blow count, $(N_1)_{60}$, and the CSR to cause liquefaction for a magnitude 7.5 earthquake. The CRR curves are based on case histories of sites in the U.S., Japan, and China. Visual inspection of the case study sites after earthquakes determined if a site had liquefied or not. The CSR for each site was estimated for each site, normalized to an magnitude 7.5 earthquake, and plotted against $(N_1)_{60.}$ Curves marking the CRR or the boundary between data points that did and did not liquefy were then developed. The chart, as modified by the NCEER workshops (Youd and Idriss 2001) is presented in Figure 2.15. It should be noted that the vertical axis is labeled both CSR and CRR. CRR is simply the minimum value of CSR at which liquefaction will occur for a soil having a specified $(N_1)_{60}$ and is represented by the curves. It should be noted that the plot is normalized for a magnitude 7.5 earthquake, thus CRR is actually the CRR for a magnitude 7.5 earthquake ($CRR_{7.5}$). $CRR_{7.5}$ will need to be modified for the design earthquake of interest. This modification of $CRR_{7.5}$ is discussed in section 2.1.6.5. NCEER (Youd and Idriss 2001) also presents the follow equation suggested by A. F. Rauch to approximate the clean-sand base curve:

$$CRR_{7.5} = \frac{1}{34 - (N_1)_{60}} + \frac{(N_1)_{60}}{135} + \frac{50}{\left[10 \cdot (N_1)_{60} + 45\right]^2} - \frac{1}{200} \qquad (2.5)$$

Equation 5 is valid for $(N_1)_{60} < 30$. The purpose of presenting this and other equations in addition to charts is to aid individuals who wish to use spreadsheets or other numerical analytical techniques to evaluate liquefaction hazards.

In the original development of the SPT liquefaction chart, Seed et al. (1985) noted an apparent increase of CRR with increased fines content. It is not clear if the apparent increase is due to an actual increase in liquefaction resistance or a decreased amount of penetration resistance (Youd and Idriss 2001). For this reason, Seed et al. (1985) developed CRR curves for

three different fines contents to allow designers to account for the apparent increase in CRR with increased fines content. An alternative method of quantifying the influence of fines is presented in the next section.

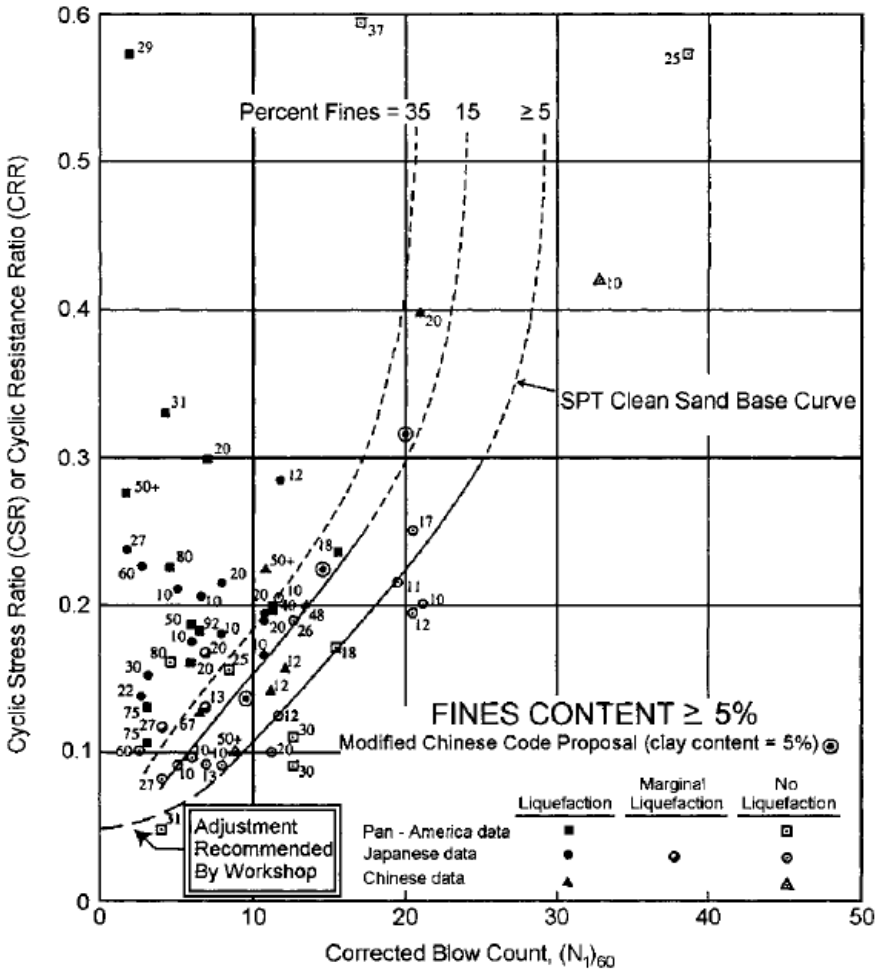

Figure 2.15: SPT curves for determining $CRR_{7.5}$ with data from liquefaction case histories (Youd and Idriss 2001)

2.1.6.2.1 Corrections for Fines Content

NCEER (Youd and Idriss 2001) present the following equations to correct $(N_1)_{60}$ for fines content (FC), allowing Equation 4 to be used for soils other than clean sands. Again, the equations are presented as an alternative to Figure 2.15 to facilitate the use of numerical analysis

methods. The following equations were developed by I. M. Idriss with the help of R. B. Seed for correction of $(N_1)_{60}$ to an equivalent clean sand value, termed $(N_1)_{60cs}$:

$$(N_1)_{60cs} = \alpha + \beta(N_1)_{60} \quad (2.6)$$

where α and β are determined by the equations:

$$\alpha = 0 \quad \text{for FC} \le 5\% \quad (2.7a)$$

$$\alpha = \exp\left[1.79 - \left(\frac{190}{\text{FC}^2}\right)\right] \quad \text{for } 5\% < \text{FC} < 35\% \quad (2.7b)$$

$$\alpha = 5.0 \quad \text{for FC} \ge 35\% \quad (2.7c)$$

$$\beta = 1.0 \quad \text{for FC} \le 5\% \quad (2.8a)$$

$$\beta = \left[0.99 + \frac{\text{FC}^{1.5}}{1000}\right] \quad \text{for } 5\% < \text{FC} < 35\% \quad (2.8b)$$

$$\beta = 1.2 \quad \text{for FC} \ge 35\% \quad (2.8c)$$

The back-calculated curve for 35% FC is virtually the same as the curve presented in Figure 2.14. The back-calculated curve for 15% curve plots to slightly to the right of the curve presented in Figure 2.15.

2.1.6.2.2 Other Corrections

Several factors in addition to fines content influence SPT test results. Other factors must be accounted for in order to accurately determine CRR. $(N_1)_{60}$ is the measured blow count, N, corrected for effective stress, hammer energy, borehole diameter, rod length, and the sampler type. $(N_1)_{60}$ is defined by the equation:

$$(N_1)_{60} = NC_N C_E C_B C_R C_S \quad (2.9)$$

where the correction coefficients are defined by Table 2.1. P_a in Table 2.1 is atmospheric pressure. A full discussion on the development of these correction factors is presented in the NCEER report (Youd and Idriss 2001).

Table 2.1: Corrections to SPT converted to U. S. customary units after Robertson and Wride (1998)

Factor	Equipment Variable	Term	Correction
Effective stress	–	C_N	$(P_a / \overline{\sigma}_v)^{9.5}$
Effective stress	–	C_N	$C_N \leq 1.7$
Energy ratio	Donut hammer	C_E	0.5 – 1.0
Energy ratio	Safety hammer	C_E	0.7 – 1.2
Energy ratio	Automatic-trip Donut type hammer	C_E	0.8 – 1.3
Borehole diameter	2.5 – 4.5 in	C_B	1.0
Borehole diameter	6 in	C_B	1.05
Borehole diameter	8 in	C_B	1.15
Rod Length	<10 ft	C_R	0.75
Rod length	10 – 13 ft	C_R	0.8
Rod length	13 – 20 ft	C_R	0.85
Rod length	20 – 33 ft	C_R	0.95
Rod length	33 – 100 ft	C_R	1.0
Sampling method	Standard sampler	C_S	1.0
Sampling method	Sampler without liners	C_S	1.1 – 1.3

2.1.6.3 Evaluation Using the Cone Penetration Test (CPT) ASTM D3441

The cone penetration test is the second most popular geotechnical field test, and is considered by many people to be a better tool because it yields a continuous profile of soil penetration resistance. The basic procedures for determining liquefaction resistance using the CPT are similar to that of the SPT. The CPT data is normalized and compared to a chart or equations to obtain CRR. Details about how the CPT is used to evaluate liquefaction are presented in the following subsection and in Youd and Idriss (2001). General details about the CPT can be found in most geotechnical textbooks including McCarthy (2002).

2.1.6.3.1 CPT Evaluation of CRR

Similar to the SPT, NCEER (Youd and Idriss 2001) present both a chart and set of equations to evaluate $CRR_{7.5}$ for clean sands. Robertson and Wride (1998) used data to create the chart and equations compiled from several case histories, including those by Stark and Olson (1995) and Suzuki et al. (1995). Their chart, as recommended by NCEER (Youd and Idriss 2001), is presented in Figure 2.16, and their equations, as recommended by NCEER, are:

$$\mathrm{CRR}_{7.5} = 0.833\left[\frac{(q_{c1N})_{cs}}{1000}\right] + 0.05 \qquad \text{for } (q_{c1N})_{cs} < 50 \tag{2.10}$$

$$\mathrm{CRR}_{7.5} = 93\left[\frac{(q_{c1N})_{cs}}{1000}\right]^3 + 0.08 \qquad \text{for } 50 \le (q_{c1N})_{cs} < 160 \tag{2.11}$$

where $(q_{c1N})_{cs}$ = the clean-sand cone penetration resistance normalized to one atmosphere of pressure. Just like the chart and equations for the SPT, the CRR is normalized to a magnitude 7.5 earthquake and will need to be modified according to the procedures presented in section 2.1.6.5.

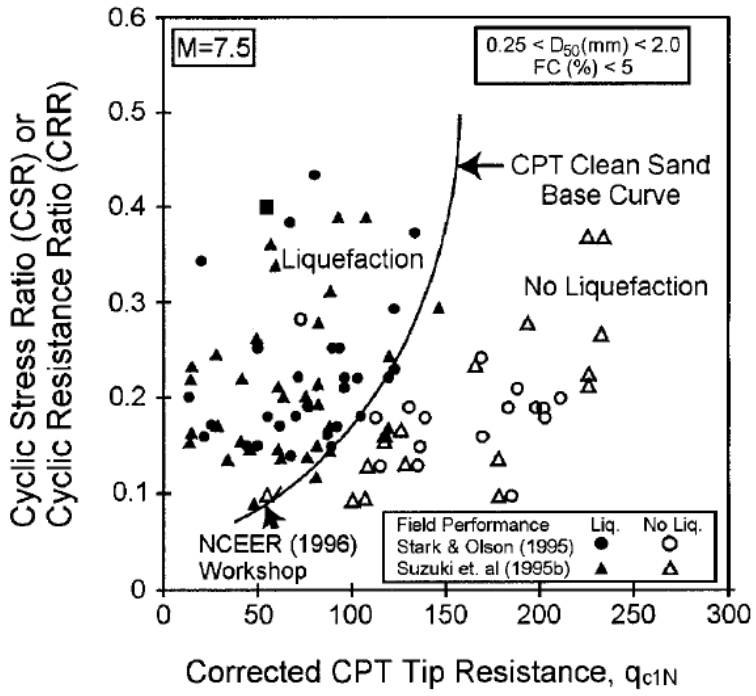

Figure 2.16: Curve recommended for calculation of CRR from CPT data with data from liquefaction case histories for M 7.5 earthquakes (Robertson and Wride 1998)

2.1.6.3.2 Normalization of Cone Penetration Resistance

The CPT procedure requires normalization of tip resistance using the equations:

$$q_{c1N} = C_Q\left(\frac{q_c}{P_a}\right) \tag{2.12}$$

where

$$C_Q = \left(\frac{P_a}{\overline{\sigma}_v}\right)^n \tag{2.13}$$

and where C_Q = the normalizing factor, q_c = the measured tip resistance, P_a = one atmosphere of pressure in the same units as the $\overline{\sigma}_v$ and q_c, n = exponent that varies with soil type, and q_{c1N} = the normalized tip resistance (Youd and Idriss 2001). At shallow depths C_Q becomes very large and should not be assigned a value greater than 1.7 for calculation of q_{c1N}.

The exponent *n* is 1.0 for clayey soils and 0.5 for clean sands (Olsen 1997). For silty soils, the value of *n* is between 0.5 and 1.0 (Olsen 1997). Since the CPT does not return a physical soil sample during testing, *n* is determined through an iterative process based on a value known as I_c. I_c is calculated from the equations:

$$I_c = \left[(3.47 - \log Q)^2 + (1.22 + \log F)^2\right]^{0.5} \tag{2.14}$$

where

$$Q = \left(\frac{q_c - \sigma_v}{P_a}\right)\left[\left(\frac{P_a}{\overline{\sigma}_v}\right)^n\right] \tag{2.15}$$

$$F = \left(\frac{f_s}{q_c - \sigma_v}\right) \times 100\% \tag{2.16}$$

and where f_s = cone sleeve resistance and *n* is the same exponent from equation 13 (Robertson and Wride 1998). Robertson and Wride (1998) and the NCEER report (Youd and Idriss 2001) suggest the following method for determining I_c and *n*:

1. Calculate I_c assuming $n = 1.0$
2. If $I_c > 2.6$, the soil is classified as clayey and is considered liquefiable.
3. If $I_c < 2.6$, the soil is most likely granular, and I_c should be recalculated with $n = 0.5$.
4. If the recalculated $I_c < 2.6$, then this recalculated I_c and $n = 0.5$ should be used in the analysis calculations.
5. If the recalculated I_c is > 2.6, the soil is likely to be very silty and possibly plastic, and I_c should be recalculated again with $n = 0.7$.
6. This recalculated I_c with $n = 0.7$ should be used in the analysis calculations.

Because these relationships are approximate and only correlations, it is recommended that some field samples be retrieved for laboratory verification. The field samples may be checked against

the criteria presented in section 2.1.4.2 or tested using one of the laboratory tests presented in section 2.1.5.

2.1.6.3.3 Correction for the Presence of Fines

As with the SPT, the CPT liquefaction correlations were developed for clean sands. Thus, a correction must be applied to the normalized tip resistance (q_{c1N}) to an equivalent clean-sand value, $(q_{c1N})_{cs}$. The NCEER report (Youd and Idriss 2001) recommends using Robertson and Wride's (1998) equations:

$$(q_{c1N})_{cs} = K_c q_{c1N} \tag{2.17}$$

Where

$$K_c = 1.0 \qquad \text{for } I_c \le 1.64 \tag{2.18a}$$

$$K_c = -0.403 I_c^4 + 5.581 I_c^3 - 21.63 I_c^2 + 33.75 I_c - 17.88 \qquad \text{for } I_c \le 1.64 \tag{2.18b}$$

and where I_c is determined as described in section 2.1.6.3.2.

2.1.6.4 Evaluation Using the Shear Wave Velocity (V_s)

Geophysical tests, including wave velocity tests, are growing in popularity as geotechnical field tests, especially for seismic related investigations. There are three main advantages of V_s over SPT and CPT: one, V_s measurements are possible at locations where the CPT or SPT may not be able to penetrate or where boring is not permitted or otherwise possible; two, V_s is a basic mechanical property of the soil, directly related to the small-strain shear modulus of the soil; and three, the small-strain shear modulus is a parameter required in

analytical procedures for estimating dynamic soil response and soil-structure interaction analyses (Youd and Idriss 2001). General information on wave velocity testing and determination can be found in Burger et al. (2005).

2.1.6.4.1 Evaluation of CRR Using the Shear Wave Velocity

The evaluation of CRR using V_s is very similar to that for the CPT and the SPT. V_s must first be corrected to a reference overburden stress. NCEER (Youd and Idriss 2001) recommends the following equation (Kayen et al. 1992; Robertson et al. 1992; Sykora 1987):

$$V_{s1} = V_s\left(\frac{P_a}{\overline{\sigma}_v}\right)^{0.25} \tag{2.19}$$

where V_{s1} = overburden stress corrected shear wave velocity, P_a = atmospheric pressure in the same units as $\overline{\sigma}_v$, and $\overline{\sigma}_v$ = effective stress at the depth of interest.

The NCEER (Youd and Idriss 2001) report recommends using the CRR–V_{s1} relationship developed by Andrus and Stokoe (2000). The graphical solution is presented in Figure 2.17. The corresponding equation is:

$$\mathrm{CRR}_{7.5} = 0.022\left(\frac{V_{s1}}{100}\right)^2 + 2.8\left(\frac{1}{V_{s1}^* - V_{s1}} - \frac{1}{V_{s1}^*}\right) \tag{2.20}$$

where V_{s1}^* = the limiting upper value of V_{s1} for liquefaction occurrence which varies linearly between 200 m/s for soils with a fines content of 35% to 215 m/s for soils with a fines content of 5% or less. As with the chart and equations for the SPT and CPT the CRR is normalized to a magnitude 7.5 earthquake and will need to be modified.

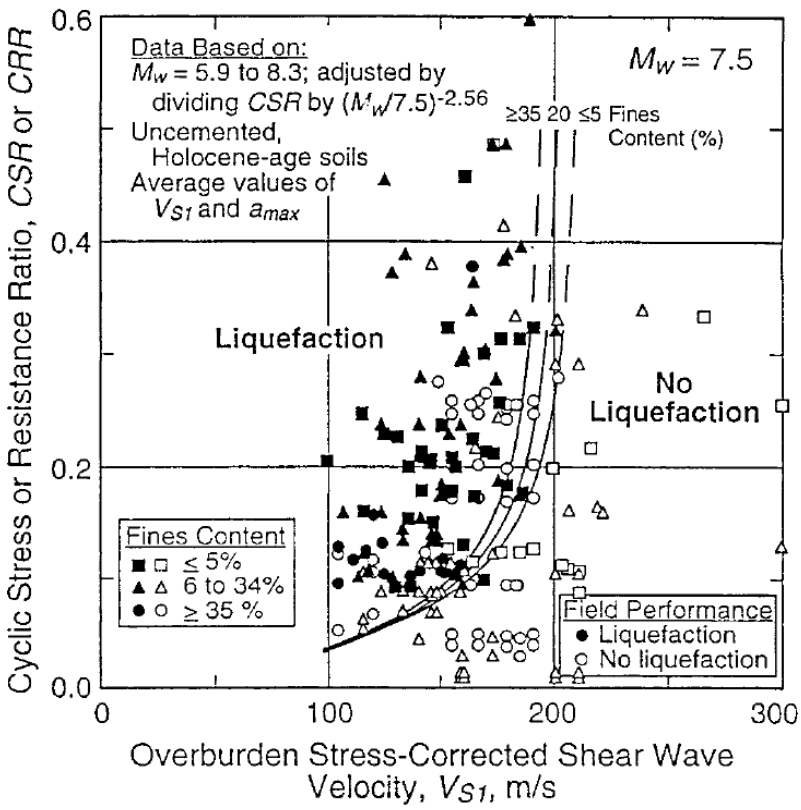

2.17: Liquefaction relationship recommended based on liquefaction data from compiled case histories for M 7.5 earthquakes (Andrus and Stokoe 2000)

2.1.6.5 Magnitude Scaling Factors (MSFs)

The CRR values determined from one of the three methods presented are only valid for magnitude 7.5 earthquakes. To adjust analysis for a larger or smaller earthquake, a MSF will need to be applied. The NCEER (Youd and Idriss 2001) report recommended MSFs defined by (Youd and Noble 1997):

$$\mathrm{MSF} = \frac{10^{2.24}}{\mathrm{M}_{\mathrm{w}}^{2.56}} \qquad (2.21)$$

where M_w is the moment magnitude of the design earthquake.

2.1.6.6 Calculating Factor of Safety (FS) against liquefaction

The most basic formulation of FS based on the NCEER (Youd and Idriss 2001) procedures is:

$$\mathrm{FS} = \left(\frac{\mathrm{CRR}_{7.5}}{\mathrm{CSR}} \right) \mathrm{MSF} \qquad (2.22)$$

where CSR = the cyclic stress ratio for the design earthquake, $\mathrm{CRR}_{7.5}$ = the cyclic resistance ratio for a magnitude 7.5 earthquake, and MSF = the magnitude scaling factor. Equation 22 can be modified to account for higher overburden stress and static stress conditions than those embodied in the case history data from which the simplified procedure was derived (Youd and Idriss 2001). In 1983, Seed introduced the correction factors K_σ and K_α to extrapolate equation 22 to different stress conditions. The modified version of equation 22 is simply:

$$\mathrm{FS} = \left(\frac{\mathrm{CRR}_{7.5}}{\mathrm{CSR}} \right) \mathrm{MSF} \cdot K_\sigma \cdot K_\alpha \qquad (2.23)$$

where K_σ = the correction factor for high overburden stress and K_α = the correction factor for sloping ground.

Laboratory and field data indicate that liquefaction resistance increases nonlinearly with increasing effective stress. The factor K_σ accounts for the nonlinearity for soil layers with overburden pressures higher than 21 lb/ft^2 (Seed 1983). Based on Seed's (1983) work, Hynes and Olsen (1999) compiled and analyzed and enlarged data set to develop an equation and chart for determining K_σ. The equation they derived is:

$$K_\sigma = \left(\frac{\bar{\sigma}_v}{P_a} \right)^{(f-1)} \qquad (2.24)$$

where $\bar{\sigma}_v$ = effective stress at the depth of interest, P_a = atmospheric pressure in the same units as $\bar{\sigma}_v$, and f is and function of the in-situ soil conditions, mainly relative density. The NCEER

(Youd and Idriss 2001) report recommend using values of f = 0.7 to 0.8 for relative densities (D_r) between 40 and 60% and values of f = 0.6 to 0.7 for D_r between 60 and 80%. The resulting relationships for K_σ based on different values of f are presented in Figure 2.18

Although both Seed (1983) and Harder and Boulanger (1997) have presented methods for evaluating K_α, the NCEER (Youd and Idriss 2001) report does not recommend use of K_α by anyone but specialists in geotechnical earthquake engineering due to the large variance in values of K_α.

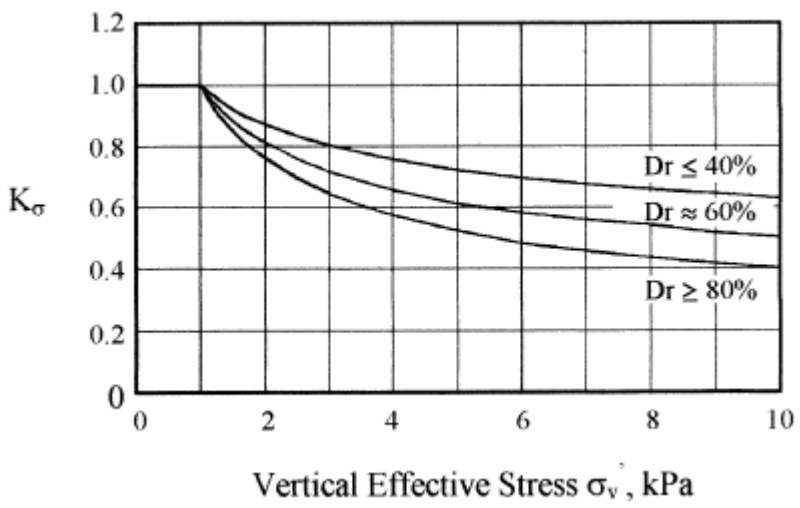

Figure 2.18: Recommended curves for estimating K_σ for engineering practice (Youd and Idriss 2001)

2.1.6.7 Influence of Age of Deposit

It has been noted that liquefaction resistance increases with age, both in real time and geologic time (Seed 1979; Youd and Hoose 1977; Youd and Perkins 1978). Seed (Seed 1979) observed as much as a 25% increase in liquefaction resistance between 100-day-old samples and freshly-prepared samples. In terms of geologic time, sediments that are less than a few thousand years old are generally much more susceptible to liquefaction than older Holocene sediments; Pleistocene sediments are even more resistant; and pre-Pleistocene sediments are generally

immune to liquefaction (Youd and Idriss 2001). Although this age dependent behavior is known, it is very difficult to quantify, and the factors that cause an increase in resistance to liquefaction are not well understood. Consequently, there is no analytical method for quantifying the effect of deposit age.

2.2 Ground Modification for Liquefaction Hazard Mitigation

2.2.1 Introduction

Once a liquefaction hazard has been identified, ground modification techniques can be used to mitigate the hazard. Ground modification alters the physical properties of the soil mass at the site, reducing or eliminating the risk of liquefaction during an earthquake. These techniques typically work in one of two ways: one, preventing the pore pressures from rising or, two, providing a drainage path to dissipate excess pore pressures that may be generated during an earthquake. The ground modification method that will work best at a particular site is a function of soil composition, thickness of the liquefiable layer, likely liquefaction failure mode, type of structure, construction considerations, etc. One of the biggest considerations is if the modification is to be performed before or after the structure is constructed. There are few viable options for ground modification mitigation post-construction.

2.2.2 Pre-Construction Ground Modification

Pre-construction ground modification typically consists of one of three techniques: densification, stabilization, or drainage. Sometimes a combination of two techniques is used. Densification and stabilization attempt to prevent the pore pressures from being generated. Drainage attempts to provide a "vent" to allow elevated pore pressures to bleed off. Densification is typically accomplished through some type of compaction or compaction

grouting; stabilization is typically accomplished through grouting or soil mixing; and drainage is typically accomplished through the installation of gravel or geosynthetic drains.

2.2.2.1 Compaction

Since liquefaction occurs when a loose soil attempts to densify, causing a decrease in void space and ultimately, an increase in pore pressure. Liquefaction can be prevented by densifying or compacting the soil so that the soil particles are already in a tightly packed configuration which will not have the tendency to densify during an earthquake.

Compaction techniques can be grouped into two general categories: kneading and vibratory. Kneading compaction is most effective on cohesive soils, while vibratory compaction is most effective on cohesionless soils like sands. Since liquefaction only occurs in soils with little to no cohesion, vibratory compaction techniques are the best compaction techniques to prevent liquefaction. Compaction grouting, a compaction method based on soil displacement rather than vibration or kneading, also works well on cohesionless soils.

Compaction techniques can also be categorized based on depth of influence, either shallow or deep. The soil must be densified at all depths where liquefaction may occur to be an effective mitigation technique. At sites where thick, natural deposits of potentially liquefiable soil exist, deep compaction techniques such as vibro-compaction, deep dynamic compaction, compaction grouting, and explosion compaction are appropriate. At sites where an embankment or fill is to be constructed from cohesionless soil, shallow compaction equipment such as rubber-tired rollers, vibratory rollers, impact rollers, tampers, and rammers are appropriate to compact the soil in thin lifts. Further details about these and other compaction techniques can be found in Hausmann (1990).

It has long been clear that densification reduces the risk of liquefaction. Hilf (1975) concludes that in order to reduce the risk of liquefaction to an acceptable level, it is advisable to densify the soil mass to a minimum relative density of 85% near the surface and at least 70% deeper within the soil mass.

2.2.2.2 Chemical, Permeation, and Jet Grouting

With the exception of compaction grouting, as discussed in the previous section, all forms of grouting attempt to prevent liquefaction by filling the void spaces with some form of grout that cements the soil particles together. Chemical, permeation, and jet grouting are three grouting methods commonly used to prevent liquefaction. In permeation grouting, highly fluidized Portland cement-based grout is injected into the soil at low pressures in an attempt to replace the pore water with grout without significantly fracturing the soil structure (Hausmann 1990). Chemical grouting works in a similar manner to permeation grouting except the grout is injected in the form of a two-part, usually sodium silicate-based, chemical grout (McMaster and Robinson 1996). Jet grouting is a relatively new technique developed since the 1960's (Welsh 1991) in which high-pressure jets of Portland cement grout are injected laterally into a borehole wall. The grout jet simultaneously excavates and mixes with the soil (Henn 1996). More details about grouting and grouting methods can be found in Hen (1996) or Hausmann (1990).

Grouting has some significant drawbacks that need to be considered prior to selecting it as means of soil improvement for preventing liquefaction. One concern is the reduction in permeability associated with grouting. The decrease in permeability reduces the drainage time and may lead to post-earthquake instability problems (NRC 1985). There is some general concern with the long-term stability of grouted soils over a period of repeated earthquake loadings, although there is little research on this subject due to the infrequent recurrence of

earthquakes. Grouting is rather expensive and it is difficult to fully verify where the grout is within the soil mass.

2.2.2.3 Vertical Drains and Stone Columns

Another approach to reducing liquefaction hazards is to provide a drainage path to relieve excess pore water pressures. Vertical gravel drains have been used as a liquefaction hazard mitigation method since the 1970's. Seed and Booker (1977) pioneered the basic design criteria for cylindrical vertical gravel drains based on Darcy's Law. Stone columns (essentially large diameter gravel drains) have also been successfully used to mitigate liquefaction hazards (Ashford et al. 2000; Mitchell et al. 1995). Stone columns, sometimes referred to as vibro-replacement or vibro-displacement, have the advantages of improving the strength and stiffness of the soil in addition to providing drainage. More recently, geosynthetic composite drains have also been employed to mitigate liquefaction hazards (Rollins et al. 2003).

2.2.3 Under-Building Ground Modification

The liquefaction potential of soils that support structures has only been a design consideration for approximately 40 years. Many older structures are founded on potentially liquefiable sites. Once a building is constructed, it is very difficult to modify the soil because the access is limited. Grouting and installation of drains has been performed beneath buildings; however, the difficulty and cost to perform such an operation is much greater than it would be prior to construction.

2.2.3.1 Grouting

Stabilizing potentially liquefiable soils under an existing structure in congested urban areas is difficult. In this situation, grouting may be the only option available to the engineer (Maher and Gucunski 1995). Based on a number of case studies, Andrus and Chung (1995)

conclude that compaction, jet, permeation, and chemical grouting are an effective and suitable means of liquefaction remediation ground improvement near existing structures. In most cases, post-construction grouting to prevent liquefaction requires drilling through the floor-slab and possibly the footings in order to inject grout where it is needed. Disruption of building usage during the grouting can be a large problem associated with post-construction grouting.

2.2.3.2 Vertical Drains

Not as common as grouting, drains can also be installed under existing structures. Similarly to grouting, drilling through the floor slab is required and disruption to building usage is a problem. Gravel drains have also been successfully used to mitigate liquefaction hazards around existing pile foundations (Harada et al. 2000).

2.2.4 Biological Soil Improvement

Research lead by Jason DeJong into microbial-induced calcite precipitation (MICP) for the purpose of soil improvement and ground modification has been performed (DeJong et al. 2006; DeJong et al. 2010; Martinez and DeJong 2009). MICP works by installing a microorganism, *Bacillus pasteurii*, in the soil where the microorganism causes the soil particles to be cemented together with calcium carbonate (calcite) precipitated from the ground water (DeJong et al. 2006). MICP has been shown to affect response of sand to undrained shear under laboratory conditions (DeJong et al. 2006). Neither laboratory nor field testing has been performed at this time (2010) to evaluate MICP's effectiveness at reducing the effects of liquefaction; however, the idea that MICP could be used to reduce the effects of liquefaction appears to be sound. DeJong et al. (2010) lists liquefaction prevention first on their list of envisioned applications. Because of the way MICP works, its application as a method to prevent

liquefaction under existing structures without disrupting the structure's use has the potential to be superior to the current methods described in section 2.2.3.

2.3 Pore Water Modification

2.3.1 Introduction

Another approach to preventing liquefaction is modifying the pore water rather than the soil structure. Theoretically, chemicals can be added to the pore water to change the pore water's physical behavior in such a way that cyclic loads do not cause pore pressure to build to a significant level, or the chemicals cause the soil-water system to disobey conventional effective stress governed strength behavior. Currently, pore water modification is not used in practice and is only the subject of research.

2.3.2 Pore Water Modification Using Bentonite

As indicated by the NCEER report (Youd and Idriss 2001), it has been established that the presence of fines, especially high plasticity fines, decreases a soil's susceptibility to liquefaction. It is also known that bentonite-water mixtures no longer behave as Newtonian fluids (Jones 1963). Base on these two principles, Haldavanekar et al. (2004) have performed research on the effectiveness of bentonite as means of preventing liquefaction under laboratory conditions. Cyclic triaxial tests showed that Ottawa sand specimens containing more than 5% of bentonite, by mass, are significantly less susceptible to liquefaction compared to the liquefaction susceptibility of clean Ottawa sand (Haldavanekar et al. 2004). Static triaxial tests and resonant column tests indicate a small decrease in strength and stiffness of Ottawa sand occurs with the addition of 5% bentonite (Haldavanekar et al. 2004). No field testing on the effectiveness of bentonite in preventing liquefaction has been performed. The biggest obstacle to implementing bentonite as a liquefaction prevention method in the field, especially under existing structures, is

finding a way to install the bentonite particles in the desired location without having them hydrate before they are in place.

2.4 Transport of Hydrogel Nanoparticles through Soil

2.4.1 Introduction

If hydrogel is to be successfully installed, it must be able to be transported through soil by means of natural or induced groundwater flow. Three main issues must be addressed in order for hydrogel particles to be transported through soil: size, coating, and particle interaction. Size has already been addressed. Particles have been produced small enough to fit between the sand voids. These particles are also small enough that they will stay in suspension during installation. The ability to coat the hydrogel particles with a material to prevent them from hydrating prematurely is being investigated. If this can be done it is possible that hydrogel may be transported through soil, but there are many other factors involved as well.

2.4.2 Studies on the Transport of Nanoparticles through Soil

Some resent studies on the transport of other similarly sized particles have been conducted, including: Cheng et al. (2005), Darlington et al. (2009), Fang et al. (2009), He et al. (2009), and Khodadoust et al. (2008). Mostly focused on either particles that could contaminate groundwater or could be used to remediate contaminated groundwater, like: aluminum, carbon-60, titanium dioxide, and cellulose coated iron, these studies used breakthrough column tests to evaluate the ability of the nanoparticles to pass through soil. The results of these studies indicated that the ability of nanoparticles to flow through soil is dependent on many factors including particle physical and chemical properties (Cheng et al. 2005; Darlington et al. 2009; He et al. 2009), soil physical and chemical properties (Darlington et al. 2009; Fang et al. 2009),

and pore water velocity (He et al. 2009). Published results of field studies of nanoparticle transport through soil were not found.

2.4.3 Discussion on the Transport of Hydrogel Nanoparticles through Soil

Based on the limited amount of information on the subject of nanoparticle transport through soil, it cannot be concluded at this time whether coated hydrogel nanoparticles can or cannot be easily transported through any type of soil. Without knowing what the coating material is impossible to know how the particles will interact with themselves, the soil, or the water. Until a coating material is selected, conclusions based other tests can only show that it is possible for some nanoparticles to be transported (Darlington et al. 2009; Fang et al. 2009; He et al. 2009; Khodadoust et al. 2008), and thus, because it is possible for some nanoparticles to be transported, it may be possible for coated hydrogel. Once a coating has been selected, experiments will be required to confirm whether or not it is possible.

2.5 Summary

Since then 1964 earthquakes in Niigata, Japan and Anchorage, Alaska, liquefaction has been extensively researched and observed. The causes of liquefaction are now fairly well understood in terms of effective stress principles and the tendency of loose sands to densify as a result of the vibrations caused by earthquakes. The magnitude and types of liquefaction related damage have also been observed and defined. Procedures to evaluate both the earthquake induced ground motions and the resulting liquefaction has been developed, and standards for these methods have been set. Several laboratory tests have also been developed to evaluate liquefaction potential under laboratory conditions. Ground modification methods have been proven as a means of reducing a site's susceptibility to liquefaction related damage.

Preventing liquefaction under existing buildings is difficult and no practical means of doing so without disrupting the use of the building has been implemented in the field. Further research is currently needed in this area. The research that is the subject of this paper attempts to address this need by pore water modification using a polyacrylamide hydrogel additive.

Chapter 3: Laboratory Testing Materials, Methods, and Procedures

3.1 Overview of Laboratory Tests

Laboratory tests have been performed on Ottawa sand to determine the effects of polyacrylamide hydrogel on the behavior of the soil. A variety of concentrations of hydrogel have been tested. Stress controlled cyclic triaxial tests performed by Dr. Richard Ray at The University of South Carolina were used to evaluate hydrogel's effectiveness at reducing a Ottawa sand's liquefaction susceptibility. Consolidated undrained (CU) triaxial tests were performed to evaluate hydrogel's effect on the strength of Ottawa sand. One-dimensional consolidation testing was performed to evaluate hydrogel's effect on the magnitude of consolidation of Ottawa sand. The cyclic and static triaxial testing and consolidation testing constituted the main scope of this project. Experiments were performed to evaluate the feasibility of geophysical methods for the field detection of hydrogel, an electrical self-potential experiment and a capacitance measurement experiment. Additionally, a qualitative test was performed to evaluate volume reduction due to dewatering of a hydrogel soil mixture. This chapter presents a summary of the testing procedures and equipment used. Detailed information about the testing equipment is in Appendix A.

3.2 Materials

3.2.1 Ottawa Sand

All of the tests and experiments were performed on Ottawa density sand. Ottawa sand was selected because it can be used to create relatively homogenous samples and because of its

precedent as a geotechnical research material. The grain size distribution of the Ottawa sand is presented in Figure 3.1.

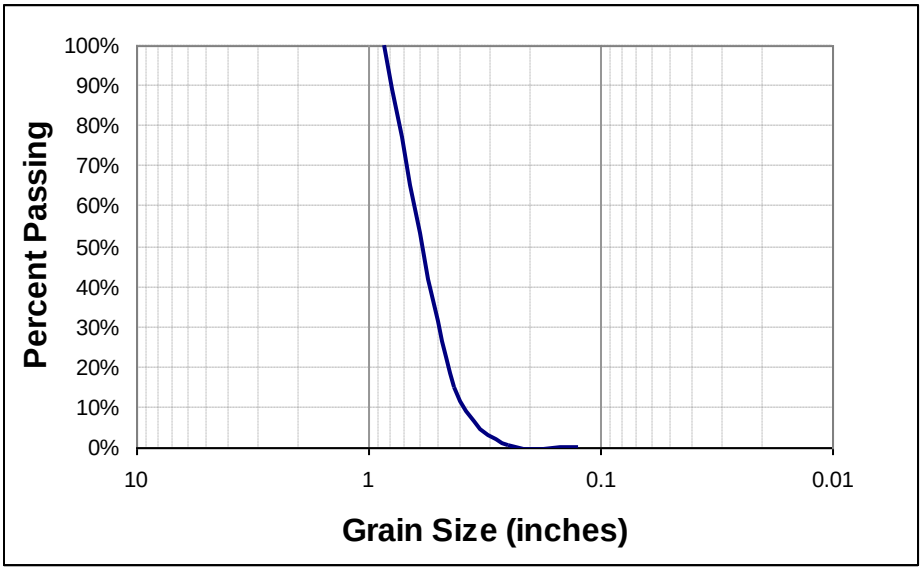

Figure 3.1: Grain size distribution of Ottawa sand

3.2.2 Polyacrylamide Hydrogel

Polyacrylamide hydrogel, generally referred to in this paper as hydrogel, is a commercially available water-absorbent polymer. The hydrogel used in most of the experiments presented in this paper is a ground powder ranging in size from $1.8x10^{-3}$ in to $3.0x10^{-3}$ in. Only two of the static CU triaxial tests were run using a different size of hydrogel. The hydrogel used for those tests was created in a lab using a polymerization process. The polymerized hydrogel particles ranged in size from $3x10^{-6}$ in to $1.4x10^{-5}$in, which is much smaller than the ground hydrogel particles.

3.2.3 Water

The water used to saturate the samples is dependent on the type of test being performed. Samples for both static and cyclic triaxial testing were prepared using deaired tap water that was

deaired with a Nold DeAerator™. Additional deaired tap water from the Nold DeAerator™ was also used during the static triaxial testing. The static triaxial tests were run using deaired water, but it is not know what deairing system Dr. Ray used to deair the water for the cyclic triaxial tests. Commercially purchased distilled water was used during the electrical self-potential and capacitance experiments to prevent false reading as a result of contaminants in the water. For all other test scenarios and sample saturation, plain tap water was used.

3.3 Sample Preparation for Consolidated Undrained Triaxial and Stress Controlled Cyclic Triaxial Testing

3.3.1 Equipment and Mold

Some special equipment is required for preparing frozen triaxial samples. This includes a mold and means of removing heat from the sample. Two methods of removing heat were used to freeze samples, freezing with cold air (a freezer) and freezing with liquid nitrogen.

The mold for shaping triaxial samples is a piece of 2.8-in diameter Shelby tube, 6-in tall, sealed on one end with a rubber membrane. The mold is placed into a frame designed to support the rubber membrane and hold a metal top plate (see Figure 3.2). The top plate has many holes drilled through it to allow water to flow out and for sample saturation using a hypodermic needle (see Figure 3.3). The purpose of the top plate is to resist the tendency of the sample to expand during freezing, which can cause it to crack.

Samples frozen using a freezer were frozen in a top-opening freezer set at -35°F. The mold and frame were placed on a foam rubber pad rather than directly on the freezer bottom. The pad reduces vibrations of the freezer compressor that could cause densification of the sample prior to freezing.

Samples frozen with liquid nitrogen were frozen in an open-top cylindrical polystyrene vessel in which the mold and frame are placed along with liquid nitrogen (see Figure 3.4). Another polystyrene container with a lid was used to transport liquid nitrogen from a compressed nitrogen cylinder to the lab.

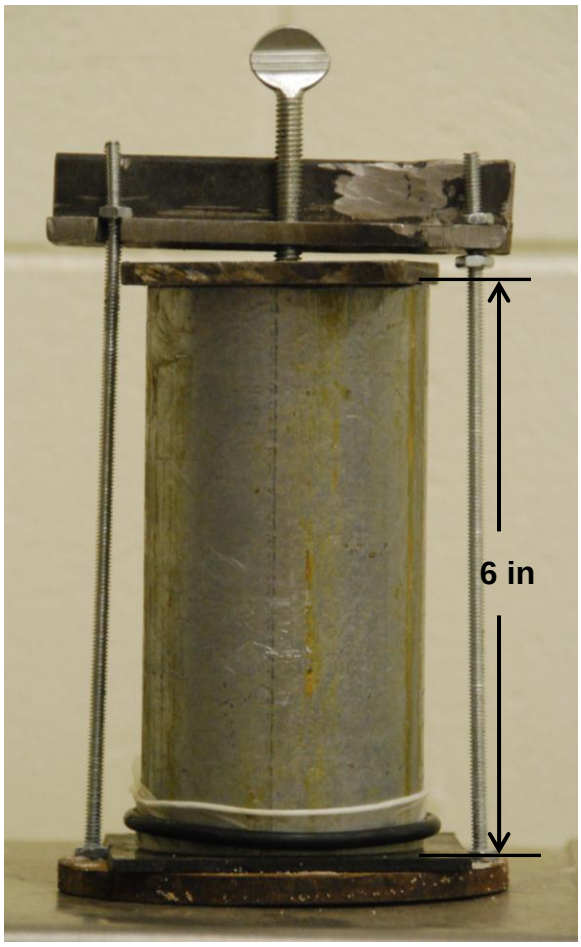

Figure 3.2: Mold in confining frame with top plate

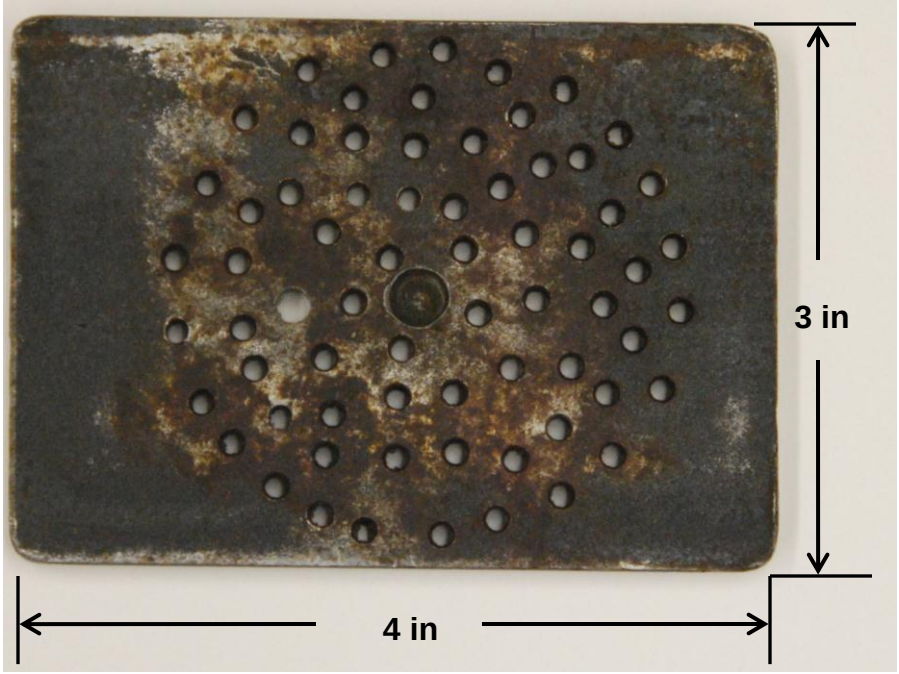

Figure 3.3: Top plate with holes

Figure 3.4:Polystyrene freezing vessel

3.3.2 Hydrogel/Sand Mixing Procedure

Samples containing hydrogel require the dry mixing of the Ottawa sand and hydrogel powder. The concentration of hydrogel in the sand is expressed in terms of a percentage of dry of mass hydrogel to dry mass of sand according to:

$$\%\text{concentration of hydrogel} = \left(\frac{\text{dry mass of hydrogel}}{\text{dry mass of sand}} \right) 100\% \qquad (3.25)$$

Dry sand was always prepared in batches of 300g. If more than 300g was needed, batches of 300g would be prepared and mixed with hydrogel then mixed together to create a large enough amount for the test being performed. For example, four beakers containing 300g of sand and the corresponding amount of hydrogel would be mixed individually and then combined to prepare an approximately 1000g triaxial sample. Once 300g of sand has been weighed in a beaker to an accuracy of +/-0.1g, the correct amount of hydrogel based on a back calculation of equation 1 corresponding to the desired concentration of hydrogel is massed to a precision of g +/-0.01g in a small aluminum cup. The hydrogel is then poured onto the top of the sand. The beaker is tilted to ≈45° and rotated by hand along its axis for five full rotations. This method was found by Shiver (2007) to produce the most uniform mixing.

3.3.3 Dry Funnel Deposition

The sand-hydrogel mixture was placed in the Shelby tube mold (Figure 3.2) using the dry funnel deposition method. The tip of a funnel is held about ½-in from the bottom of the mold. The sand-hydrogel mixture is placed in the top of the funnel and allowed to run out. As the level of the sand mixture rises, the funnel is also raised in order to maintain an approximately 1/2-in gap between the tip of the funnel and the top of the sand mixture. Once the top of the mold is reached, the sand level is struck even with the top of the mold. This method of deposition was

chosen because it is a dry method, yields relatively loose samples, and reduces segregation between the hydrogel and sand particles.

3.3.4 Saturating the Sample

The dry sand or dry sand-hydrogel mixture was saturated with deaired water prior to freezing. A 5-in syringe was used to inject the sample with the deaired water. The needle was carefully inserted through the holes in the top plate to the full length of the needle. Water was injected at a flow rate of no more than 0.2 fl oz/sec in order to prevent liquefaction at the needle tip. The needle was slowly withdrawn as water was injected. This process was repeated eight to ten times in order to saturate the sample entirely. Figure 3.5 shows the needle inserted through the top plate. Using this procedure, the sample is saturated from bottom to top over the entire cross-section of the sample. When a hydrogel sample is being prepared, the expanding hydrogel would cause the soil to become the very tightly packed in the mold making needle penetration and water injection more difficult.

This method of saturation was selected because it allows water to be injected at many locations inside the sample, saturating the sample in a relatively small amount of time. If the sample was saturated in the triaxial cell, permeating the water from bottom to top, it would take a very long time to saturate a sample due to the reduction in soil hydraulic conductivity caused by the presence of hydrogel.

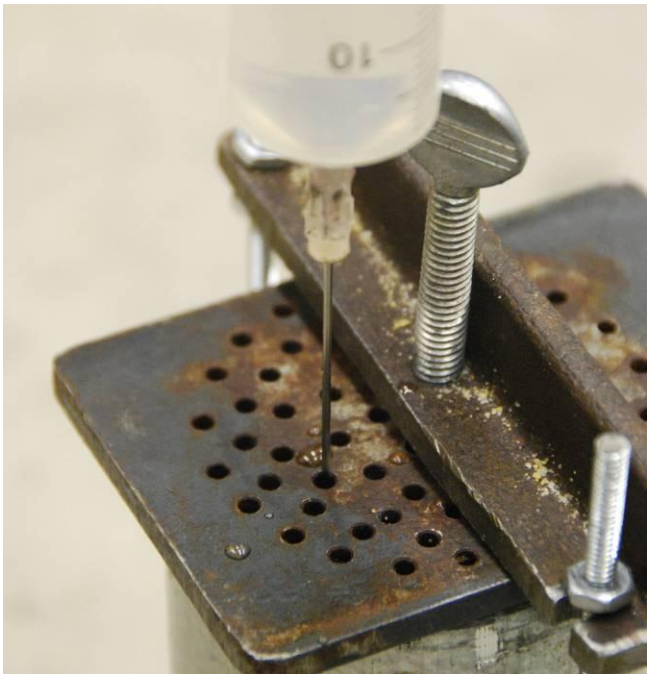

Figure 3.5: Needle inserted through holes in the top plate

3.3.5 Sample Freezing

Two methods of removing heat were used to freeze samples, freezing with cold air (a freezer) and freezing with liquid nitrogen. The purpose of using liquid nitrogen in lieu of the freezer was to reduce the amount of volume expansion during freezing.

3.3.5.1 Freezing with the Freezer

Samples frozen in the freezer were either carefully placed in the freezer after saturation or actually prepared in the freezer. In either case, the mold base was placed on a foam rubber mouse pad in the freezer to help absorb the vibrations of the freezer compressor, which could cause densification. Samples were allowed to freeze for at least eight hours. Examination of frozen samples has shown eight hours is sufficient time for the samples to freeze completely.

Freezing in a freezer cools the sample from the outside in, on all sides, including the top. As the pore water freezes, a drainage path is needed to expel water displaced by the expanding ice. Once the outside of the sample has frozen, the interior of the sample does not have a drainage path to expel the displaced water. As the water in the interior of the sample freezes, it can cause the sample to crack under tension (see Figure 3.6).

The top plate on the mold reduces the amount and severity of the tensile cracking. The top plate resists expansion. It is theorized that by resisting the expansion of the water, the tensile forces are reduced enough to prevent cracking until the ice is strong enough to resist the tensile forces internally.

The biggest disadvantage to the freezer method is that interior of the sample cannot be freely drained during freezing. Without drainage it is difficult to produce a frozen sample that doesn't exhibit a significant change in volume or some tensile cracking. Some of these issues are reduced or eliminated using the liquid nitrogen freezing method.

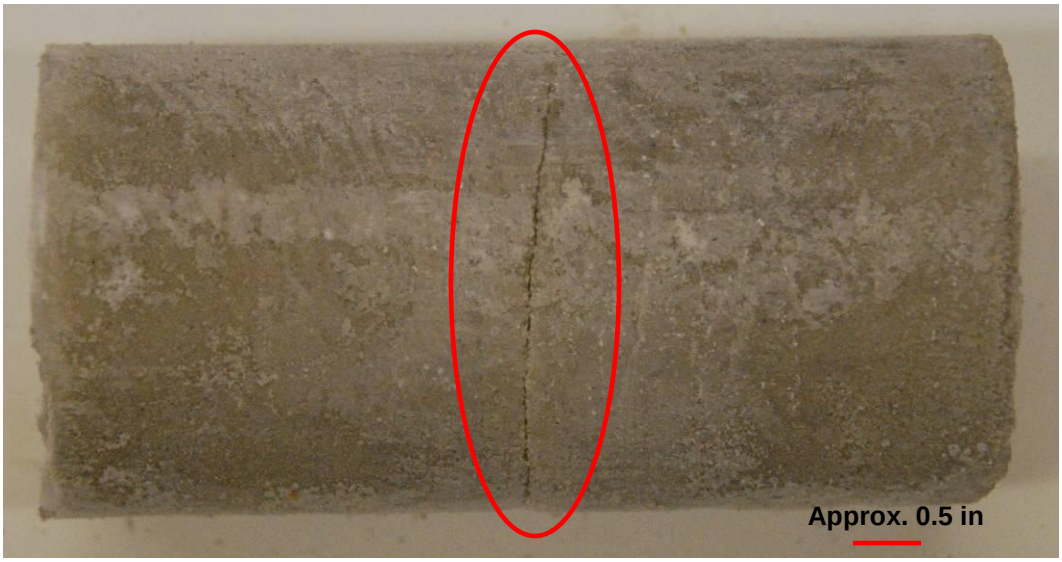

Figure 3.6: Sample with a tensile crack

3.3.5.2 Freezing with Liquid Nitrogen

Freezing samples with -321 °F liquid nitrogen provides a faster freezing time and freezes the sample from bottom-to-top as well as outside-to-inside with the exception of the top surface. Liquid nitrogen was poured at the rate of approximately one qt/min into a polystyrene freezing vessel containing the mold and sample without fully submerging the sample. For this pour rate, the level of liquid nitrogen rises around the sample at the rate of 3 in/min. As the nitrogen in the freezing vessel vaporized, additional liquid nitrogen was added to keep the sample nearly submerged. The freezing front moves from bottom-to-top and outside-to-inside. The moving freezing front allows the expanding ice to expel excess water out the top of the sample (see Figure 3.7). This free drainage almost fully eliminates the tensile cracking problems experienced with the freezer samples.

One sample was frozen with a temperature probe located in the center of the upper third of the sample to determine how much time is required to freeze a sample with liquid nitrogen. Ten minutes after liquid nitrogen was introduced, the internal temperature at the probe location was below -40 °F. Based on this test, the samples are considered to be fully frozen after 10 minutes of liquid nitrogen cooling.

It is also theorized that the quick freezing rate associated with the -321 °F liquid nitrogen may help reduce the amount of expansion during freezing. When water freezes under conventional temperature and pressure conditions, the water molecules arrange themselves in a crystalline structure with a lower density than that of liquid water at 32 °F. If liquid water is cooled at a sufficiently fast rate (1.8×10^7 °F/s) at atmospheric pressure, the molecules will be structurally arrested as a vitrified glass (Uhlmann 1972). The molecules of the liquid water do not have time to arrange into a crystalline structure. Because the molecules are frozen in place,

vitrified or “amorphous” ice does not exhibit a density that is discontinuous with that of liquid water. Details of this concept are described by Debenedetti (1996).

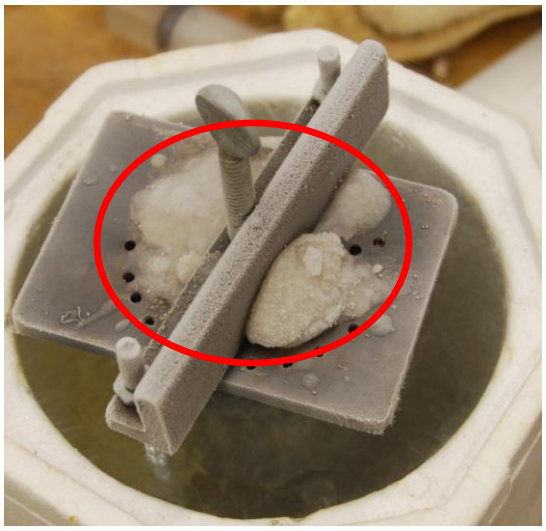

Figure 3.7: Ice forming on top of sample as a result of pore water expelled during freezing

3.3.6 Expansion During Freezing

Samples produced with both the freezer and liquid nitrogen freezing methods are affected by the expanding pore water during freezing. Samples frozen in the freezer generally exhibit more expansion than do the liquid nitrogen frozen samples. Freezer-frozen samples typically expand vertically about ¼-in, even with the confining top plate, while liquid nitrogen frozen samples typically expand vertically less than ⅛-in (see Figure 3.8).

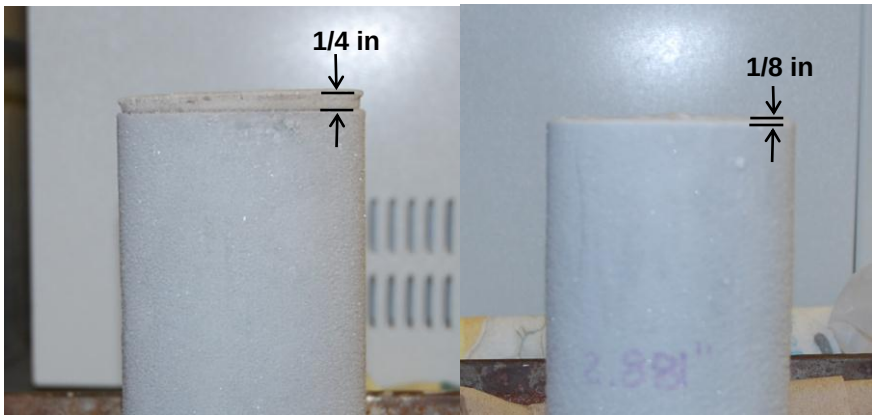

Figure 3.8: Difference in volume expansion of a freezer-frozen sample (left) and liquid nitrogen-frozen sample (right)

3.3.7 Sample Imperfections

Two common types of sample imperfections were often observed, tensile cracks and dry spots. Tensile cracking occurred in samples of all concentrations of hydrogel and was most prevalent in freezer-frozen samples. The cracking is a result of the expansion of the pore water as it freezes. Dry spots or incomplete saturation of a sample occurred mostly in samples of 0.25% hydrogel or more. Samples with significant imperfections were not tested for fear that the imperfections would influence the test results. Each of these types of imperfections is discussed in detail below.

3.3.7.1 Dry Spots

Some samples exhibited patches of unsaturated sand on their exterior. Dry sand could be seen sloughing off of the sample after extrusion. This issue is the result of isolated patches of incomplete saturation. These dry spots most commonly occurred on samples containing higher concentrations of hydrogel (> 0.25%). It is thought that the absorbency and low permeability of hydrogel prevented the water from saturating the dry spots. Saturating the sample with lower

flow rates from the syringe and more injections across the sample generally eliminated the problem in most samples. Only samples without or the most minor dry spots were tested.

3.3.7.2 Tensile Cracks

As shown in Figure 3.6, some samples exhibited tensile cracking caused by the expansion of pore water during freezing. Freezer-frozen samples more often exhibited transverse tensile cracking than the liquid nitrogen frozen samples, but the liquid nitrogen samples typically expelled more pore water during freezing, reducing the buildup of tensile stresses due to restricted expansion of the pore water. It appears that the freezer samples expand more than the liquid nitrogen frozen samples because the freezer method freezes the sample from the outside in, not allowing the expanding pore ice to displace excess pore water. Because the liquid nitrogen samples are more freely drained, they exhibit less expansion and thereby do not develop tensile forces strong enough to cause cracking. This theory is reinforced by the visible ice that forms on top of the sample as water exits samples during freezing. Additionally, the rate of freezing may reduce the amount of expansion of the water by causing some of the ice to vitrify rather than crystallize. The extent to which this effect reduces volume change is not quantified. Samples with tensile cracks were not tested in these experiments. These samples were not tested due to concerns of artificially low shear strengths due to possible weakened failure planes along the crack interface.

3.3.8 Removing the Sample from the Mold

Once the sample was frozen using one of the two methods described in Section 3.3.5, the mold was removed from the freezer, the top plate removed, and the mold allowed to warm slightly. The sample was then extracted from the mold using a standard hydraulic Shelby tube extruder. On occasion, samples particularly frozen to the inside of the mold were wrapped in a

damp rag to help warm the mold. Any imperfections, such as cracks or dry spots, were noted immediately after being extracted.

3.3.9 Sample Storage

Samples not immediately tested were wrapped in a layer of commercial plastic wrap and a layer of aluminum foil and placed into a plastic zip-top freezer bag to minimize sublimation of the pore ice. The wrapped and bagged sample was stored in the freezer at -35 °F until needed. Samples have successfully been stored up to a year in this manner with no evidence of sublimation.

3.4 Sample Setup in the Triaxial Cell

This section presents the basic setup procedure used for the CU triaxial tests. Detailed step-by-step procedures for the setup and running of a triaxial test are presented in Appendix C.

3.4.1. Basic Setup

Prior to performing a triaxial test, the extracted sample to be tested is removed from the freezer and placed on a balance to determine the wet mass. The height and diameter of the sample are directly measured using an electronic caliper. Five measurements are taken for height and diameter. The sample heights and diameters reported in this paper are the average of the five measurements of the frozen samples.

Once the mass, height, and diameter measurements have been recorded, the sample is placed in a new 0.025-in thick latex rubber membrane using a vacuum membrane stretcher. Four rubber O-rings are placed over the membrane near the center of the sample. The sample is returned to the freezer temporarily until it is installed in the triaxial cell.

Prior to the running a test, all the triaxial lines are flushed with deaired water. A saturated porous stone is placed on the bottom cap of the triaxial cell and then covered with a

saturated filter paper. Care is taken to make sure air bubbles are not trapped between the filter paper and the porous stone. The sample is then removed from the freezer and carefully placed on top of the base cap over the filter paper and porous stone. The membrane is secured to the bottom cap with two of the four O-rings. Then a saturated filter paper is placed on the top of the sample followed by a porous stone and the top cap. The top cap is secured with the remaining two O-rings. The lines to the top cap are connected and both the bottom and top caps are flushed with deaired water.

Once the sample has been sealed and flushed, a slight vacuum of 13 in of mercury (6 psi) is applied to the top and bottom of the sample to remove additional trapped air. The vacuum can also indicate whether there is a leak in the system by causing a continuous stream of bubbles to be seen in the panel board burettes. The vacuum pressure does not affect consolidation of the sample because the sample is still frozen.

At this point, the flushing process is complete and the chamber is assembled and filled with water. The vacuum is vented and a 2-psi effective confining pressure is applied to the sample. The sample is allowed to thaw as described in Section 3.4.2.

3.4.2. Sample Thawing

Once a sample is setup in the cell according to Section 3.4.1, it is allowed to thaw for three hours under a 2-psi effective confining pressure. Typically the 2-psi confining pressure is achieved by applying a 45-psi cell pressure and 43-psi back pressure. The three hour thaw time is considered sufficient based on a test sample that was allowed to thaw on the lab bench. During thawing, the back-pressure valves are left open, allowing for volume changes due to the thawing of the pore water, consolidation of the sample under the 2-psi confining pressure, water absorption of the hydrogel, or the driving of air into solution.

3.4.3. Sample Saturation

When running a CU triaxial test, it is important that the sample be very near 100% saturation in order to accurately measure pore pressure and calculate effective stress. This cannot be done if there is air in the system because air is compressible. Once a sample is thawed, it is tested for saturation. Saturation is checked by determining Skempton's B Coefficient (Holtz and Kovacs 1981). Skempton's B coefficient is defined as:

$$B = \frac{\Delta u}{\Delta \sigma} \tag{26}$$

where Δu = change in pore pressure and $\Delta \sigma$ = change in total stress. To perform this check in the laboratory, the back-pressure valves are shut and the cell pressure is raised 10.0 psi. Pore pressure measurements are taken before and after the cell pressure is raised. The measured change in pore pressure is then divided by 10.0 psi to determine the B coefficient. The closer the B coefficient is to 1.0, the closer to the sample is to 100%. Samples were only tested after a B value of 0.97 or greater was achieved. Based on the data presented by Black and Lee (1973), an Ottawa sand sample with a B value of 0.97 is over 99% saturated.

If the B value was less than 0.97 after the first check, the sample was flushed according to the procedure outlined in Section 3.4.4. After the sample was flushed, the B value was rechecked. If it was still too low, the back pressure and cell pressure were raised to help drive the air into solution. After the pressures were raised the sample was allowed to sit for at least an hour for the air to dissolve. The B value was then rechecked. If the B value was still too low, the pressures were raised again. If the pressures could not be raised further, the sample was allowed to saturate overnight before rechecking the B values. Only rarely were these measures required to achieve saturation.

3.4.4. Flushing the Sample

On rare occasions, if the B value was not high enough, water was permeated through the sample from bottom to top in order to flush out air in the sample. This was done by setting the back pressure on the bottom of the sample to 3 psi below the cell pressure while leaving the back pressure on the top of the sample set 2 psi below the cell pressure. The 1 psi pressure difference causes water to flow through the sample flushing out air bubbles trapped in the sample.

3.5 Consolidated Undrained Triaxial Testing

3.5.1 Triaxial Testing Equipment

Three main pieces of equipment are needed to run a triaxial test: a triaxial cell, a load frame, and a panel board. The triaxial cell used for this testing is Brainard-Kilman model S-510. The load frame used for this testing is a Brainard-Kilman model S-600 with an electronic control module. The panel board used is Durham Geo model S-500. Additional information about the equipment can be found in Appendix A.

3.5.2 Data Acquisition Equipment

To collect the data from a CU triaxial test with pore pressure measurements, at least three measurements need to be recorded: vertical displacement, load, and pore pressure. For testing presented in this paper, cell pressure and raw house air pressure were also recorded. These measurements were taken using sensors and an electronic data collection system. The sensors used were all sold under the company names of Boart Longyear, Brainard-Kilman, or Durham Geo, which are all different names for the company currently called Durham Geo. Two model E-124 pore pressure transducers, two model E-114 panel board pressure transducers, a model E-214 load cell, and a model E-312 linear displacement transducer were used during this testing. Data from the sensors was collected using an Optim Electronics Megadac model 3415AC data

collection unit, operated using TCS for windows software on an IBM laptop. Additional information about the data acquisition equipment and how to use it can be found in Appendices A and B.

3.5.3 Triaxial Consolidation

A triaxial test run on sand must be consolidated to an effective stress for the sample to have any strength since sand is cohesionless.

3.5.3.1 2-psi Consolidation

Initially, the CU triaxial tests were run at a 2-psi effective consolidation pressure. The reason for using this low consolidation pressure was to minimize densification of the samples due to consolidation, more accurately replicating loose sands that are the most susceptible to liquefaction. The 2-psi pressure difference between the cell and the back pressure was applied to the samples at the end of the initial triaxial setup, prior to thawing as described in Section 3.4.1. The samples were then allowed to consolidate as they thawed. Once a sufficient B value was reached, the test was run with the back-pressure valves closed (undrained).

3.5.3.2 15-psi Consolidation

After running several tests, it was decided that all further tests would be run at 15 psi effective consolidation pressure. The low 2-psi effective stresses meant that the stress paths and stress strain relationships before failure were only visible when plotted on a very small scale, making it difficult to discern differences between the stress strain behavior of samples with different amounts of hydrogel. Because 15 psi does not significantly increase the densification due to consolidation or the measurement of effective friction angle, consolidating samples to 15 psi solved the graphing problems without sacrificing the viability of the test. Samples consolidated to 15 psi were consolidated and thawed under 2 psi of effective stress and

consolidated to 15 psi just prior to the starting the test. The purpose of raising the effective consolidation pressure rather than initially setting the effective stress to 15 psi was to quantify the amount of difference in density between samples tested at 2 psi and 15 psi.

3.5.4 Strain Rate

It is important to strain the sample slowly enough that the pore pressures being measured at the ends of the sample are the same as the pore pressure at center of the sample. For sands, unless the test is run very fast, this is not an issue. Bishop and Henkel (Bishop and Henkel 1962) present equations to estimate the minimum strain rate at which a test should be run. For these tests, the load frame was set to run at the strain rate of 0.02 in/min (3.3%/min), a strain rate that is sufficiently slow based on Bishop and Henkel's equations.

3.5.5 Sample removal

Once a sample has been tested, it is dried to determine its dry mass. To do this, the cell is drained and disassembled, leaving the sample attached to the base. The sample is carefully deconstructed from the top down, and all the sand particles are washed into a metal pan using a squeeze bottle. Once all the material from the sample is in the pan, the pan is placed in a 200 °F oven for 24 hrs to dry. The dry sample is then weighed.

3.6 Stress Controlled Cyclic Triaxial Procedure

3.6.1 Basics of Cyclic Triaxial Testing

The procedures for a stress controlled cyclic triaxial test are governed by ASTM D5311. The initial setup of a cyclic triaxial test is virtually the same as that of a static triaxial test. The only difference between a static and a cyclic test is how the sample is loaded. In a stress controlled cyclic triaxial test, a set deviator stress is applied and released over a set a time. Then the same amount of stress is applied and released in the opposite direction over the same amount

of time. One sequence of going from zero deviator stress to positive deviator stress to negative deviator stress back zero deviator stress is called a cycle. The sample is loaded for several cycles until either liquefaction occurs or it is apparent that liquefaction will not occur. During a cyclic triaxial test, the pore pressure will typically increase. If it increases to a value equal to that of the confining pressure, the effective stress is equal to zero and liquefaction has occurred. More background information on cyclic triaxial testing is presented in Section 2.1.6.1.

3.6.2 Discussion of Testing Procedures Used by Dr. Ray

Testing generally followed ASTM D5311. Initial setup and thawing followed similar procedures to those used for the static triaxial testing. Samples were allowed to thaw in the chamber under the effective consolidation pressure used during testing (typically 15 psi or 20 psi). Thawing occurred with the backpressure valves open, giving the specimen access to free water at both ends, which compensates for the volume deficiency created when the pore ice melts. Specimens were loaded using a 1-Hz sinusoidal loading applied by a MTS computer controlled load frame. Load, pore pressure, and vertical displacement were recorded during testing. Tests were carried out to 200 cycles. Saturation was checked prior to testing. For all cases, the Skempton's B value was 0.87 or higher.

3.7 One-Dimensional Consolidation Testing

One-dimensional consolidation testing generally followed ASTM D2435. An overview of the procedures used is presented here. More detailed step-by-step procedures are presented in Appendix D.

3.7.1 Sample Preparation

Samples for consolidation testing were constructed using similar methods to those used to construct triaxial samples. Because consolidation samples are smaller in both diameter and

height than triaxial samples, a new mold was constructed using a brass consolidation confining ring (see Figure 3.9). A porous stone was placed in the bottom of the ring below a rubber membrane to create mold that is 0.5 in deep and 2.45 in in diameter. A confining frame used for the triaxial molds was shortened for use with the consolidation mold. The hydrogel/sand mixing, dry funneling, and sample saturation were all performed in the same manner as described in Sections 3.3.2 through 3.3.4. Sample imperfections such as cracking and dry spots were not an issue with the consolidation samples due to their small size. All of the consolidation samples were frozen in the same -35 °F freezer used for freezing and storing the triaxial samples. Samples were removed from the mold by slightly warming the outside of the ring mold in a room temperature water bath, then pushing the sample out by hand. Samples not tested immediately were stored in the freezer as described in Section 3.3.9.

Figure 3.9: Consolidation ring mold and shortened mold frame

3.7.2 Testing and Data Acquisition Equipment

The consolidation testing was performed using a Soil Test fixed ring consolidometer. Addition information about the consolidometer is in Appendix A. Displacement was measured and recorded using the Boart Longyear model E-312 displacement transducer. Data were recorded using the Optim Electronics, Megadac model 3415AC data collection unit, operated using TCS for windows software on an Dell laptop. Additional information about the data acquisition equipment and how to use it can be found in Appendices A and B.

3.7.3 Test Setup

First, the consolidometer ring is placed in the brass holding apparatus. A saturated porous stone is placed in the bottom of the ring. Then, a saturated filter paper is placed over the porous stone. The sample being tested is removed from the freezer, weighed, and measured for height and diameter. Height and diameter are measured in five locations with a digital caliper. The heights and diameters reported in this paper are the average of the five measurements. The sample is gently slid into the consolidation ring on top of the filter paper and porous stone. During this step, the edges of the sample may need to be slightly warmed with one's hands to aid in sliding it into the ring. A saturated filter paper and saturated porous stone are placed on top of the sample. This entire assembly is now placed under the loading piston of the consolidometer. It is very important that the piston is lined up with the consolidation ring so that the machine does not jam during testing. Any adjustments to the consolidometer need to be made while the sample is still frozen to prevent disturbance. The displacement transducer (LVDT) is attached to the cross bar on the holding apparatus with the end of the plunger resting on the crossbar that the piston is attached to. Finally, the loading arm is leveled. At this point, the sample is left to thaw for at least three hours. Once the sample has begun to thaw, it is important that the

consolidometer and table are not touched or bumped, as the sample could densify prior to the test.

3.7.4 Testing Procedures

Just prior to running the test, the Megadac is set to record the LVDT every second. Once the Megadac is recording, the first weight (1/16 ton/ft^2) is placed on the arm of the consolidometer. The arm is carefully leveled after the weight is applied. The LVDT readings are monitored and when consolidation appears to be complete, the next weight is added and the process is repeated. Weights are added is such a fashion that the stress on the sample is always doubled from the previous loading. The process is repeated until stress has reached 16 ton/ft^2. All the samples tested were loaded without an unload/reload cycle.

3.7.5 Sample Removal

Once a sample has been tested, it is dried to determine its dry mass. To do this, the entire ring and holding apparatus is removed from the consolidometer. The sample is carefully deconstructed from the top down, and all the sand particles are washed into a metal pan using a squeeze bottle. Once all the material from the sample has been washed into the pan, the pan is placed in a 200 °F oven for 24 hrs to dry. The dry sample is then weighed.

3.8 Electrical Self-Potential Experiments

Electrical self-potential or electrical spontaneous-potential is a geophysical subsurface investigation method in which the naturally existing potentials in a soil mass are measured. It has been used successfully in a variety of situations by scientists and engineers to perform such tasks as: detecting fractures in earth dams, tracking groundwater contamination plumes, monitoring soil bioremediation, and assessing geothermal fields (Naudet et al. 2003; Park et al. 2004; Rozycki et al. 2006; Yasukawa et al. 1993).

In electrical self-potential evaluations, no electrical charge is induced. Existing charges in the soil are measured. In the field, naturally occurring electrical potential stems from two sources: dynamic potential caused by the flow of water, other fluids, or heat and static potential caused by differences in the chemical composition of the subsurface. Three laboratory experiments were performed to evaluate the possibility of using electrical self-potential methods for the field detection of hydrogel. Because there was no flow of water in the laboratory model, the static potential differences caused by the hydrogel were easily isolated.

3.8.1 Equipment and Materials

The only specialized equipment required for self-potential measurements are the electrodes. Measurements were taken using a standard electrical multi-meter that is set to read DC millivolts (mV) within +/- 0.1 mV.

3.8.1.1 Electrode Construction

Conventional metal electrodes such as silver, nickel silver, or copper cannot be used to measure electrical self-potential due noise caused by polarization voltages. For this reason, non-polarizing electrodes must be used (Milsom 2003). If non-polarizing electrodes were not used, the noise level would be overshadowed by the small potential differences being measured. Silver chloride non-polarizing electrodes were constructed and used for the experiments presented in this paper.

The silver chloride electrodes consisted of an approximately ⅛-in inside diameter glass tube filled with a saturated potassium chloride salt solution. The glass rod is capped on one end with a rubber septum that holds a silver chloride plated silver wire immersed in a potassium chloride solution. The other end of the rod is capped with a Vycor® glass tip held in place by a heat shrink plastic. Vycor® glass is a special type of glass with microscopic fractures in it. The

fractures allow electrons to flow through the glass without allowing the solution inside the electrode to flow out or outside fluids to flow in. Figure 3.10 shows an electrode and its components.

The glass tubes for the electrodes with the Vycor® tips already attached were obtained from Dr. Loraine Wolf in the Auburn University Department of Geology and Geography. 0.5 mm silver wire was purchased from Fisher Scientific. The potassium chloride and rubber septums were purchased at the Auburn University Scientific Supply Store.

The first step to constructing the electrodes is to attach the Vycor® glass tip to the glass tube. This step was already completed. The next step is to make a saturated solution of distilled water and potassium chloride. This is done by adding potassium chloride to the water then waiting for the water to absorb as much potassium chloride as it can. If the water has absorbed all of the potassium chloride, the process is repeated. Eventually, the water becomes saturated with potassium chloride and there is additional solid potassium chloride resting on the bottom of the container. Each glass tube is filled about ¾ full with the solution. An approximately 3-in piece of clean silver wire is inserted through each rubber septum. If the wire is tarnished, it is cleaned with a Scotch-Brite pad or a fine grit sand paper. A hypodermic needle large enough for the wire to fit inside is used to insert the wire through the septum. The wire is inserted in the back of the needle. The needle with the wire in it is then poked through the septum. The wire is pushed through the needle and held as the needle is withdrawn, leaving only the wire. Approximately ⅔ of the wire is below the septum and ⅓ above. The bottom portions of the wires are then coated in silver chloride. This is done through electroplating. A conductive metal object, like a lab spatula, is placed in the same saturated potassium chloride solution and attached with a wire to the negative terminal of a 9 V battery. The portion of the silver wire that is below

the septum is placed into the potassium chloride solution and a wire connected to the positive terminal of the battery is touched to the silver wire for about 3 to 5 sec. The part of the wire in the solution appears to turn white and some bubbles form around the silver wire. The white coating is the silver chloride. The coated portion of the wire is carefully slid into the glass tube filled with potassium chloride solution and the septum is fitted snugly around the top of the glass tube. The electrode is now complete.

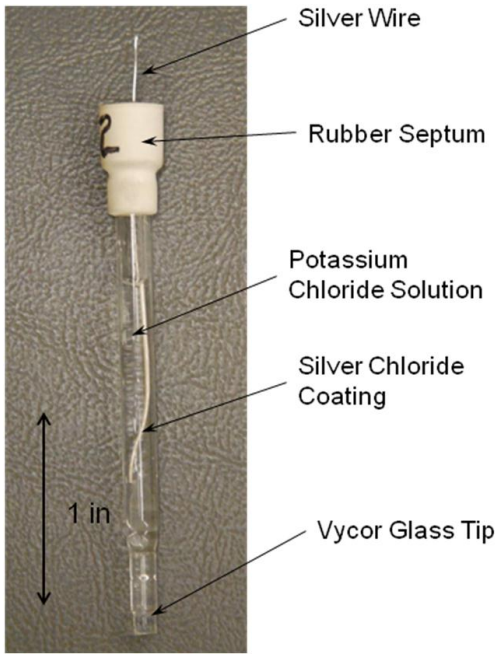

Figure 3.10: Fully assembled silver chloride electrode

3.8.1.2 Electrode Stability Assessment

Under ideal circumstances, the electrodes would have no influence on the readings being taken. In reality, the electrodes will always have some noise and some tendency to fluctuate. If the noise level is too high, the measurements will not be distinguishable from the noise.

To make sure only stable electrodes were used in the experiments, the electrodes were checked against themselves over a period of time. The electrodes were stored with their tips in a saturated potassium chloride solution in a specially made electrode holding container (Figure

3.11). Because the electrodes were in a solution that is the same as that inside the electrode and the same throughout, any potential difference measured between two electrodes was error caused by the electrodes. Theoretically they should have always shown zero potential between any given set of electrodes under these conditions. Measurements between all the electrodes were taken every other day for at least two weeks prior to running an experiment. Every possible combination was measured in order to pin point which electrodes were causing problems. Only electrodes whose readings were the most consistent and closest to zero were used in experiments.

Figure 3.11: Electrode storage and stability testing container

3.8.2 Experimental Setup

To model the detection in the field, a laboratory scale analog was constructed in a 10-in diameter by 4 in deep PVC pipe cap (Figure 3.12). The cap was inverted like a bowl, a layer of clean Ottawa sand was placed across the bottom (Figure 3.13). Then a Shelby tube was place at a desired location on top of the base layer of sand. The Shelby tube was filled with a 0.40% concentration mixture of Ottawa sand and hydrogel (Figure 3.14). The remaining volume of the container was filled with Ottawa sand to a level equal to the level of hydrogel-sand mixture in

the Shelby tube (Figure 3.15). The Shelby tube was then removed, leaving the pipe cap full of Ottawa sand with an isolated hydrogel inclusion. The entire system was saturated with distilled water using the same syringe injection technique used to saturate the triaxial samples (Figure 3.16). Once the system was saturated, the selected electrodes were inserted in the desired locations (Figure 3.17).

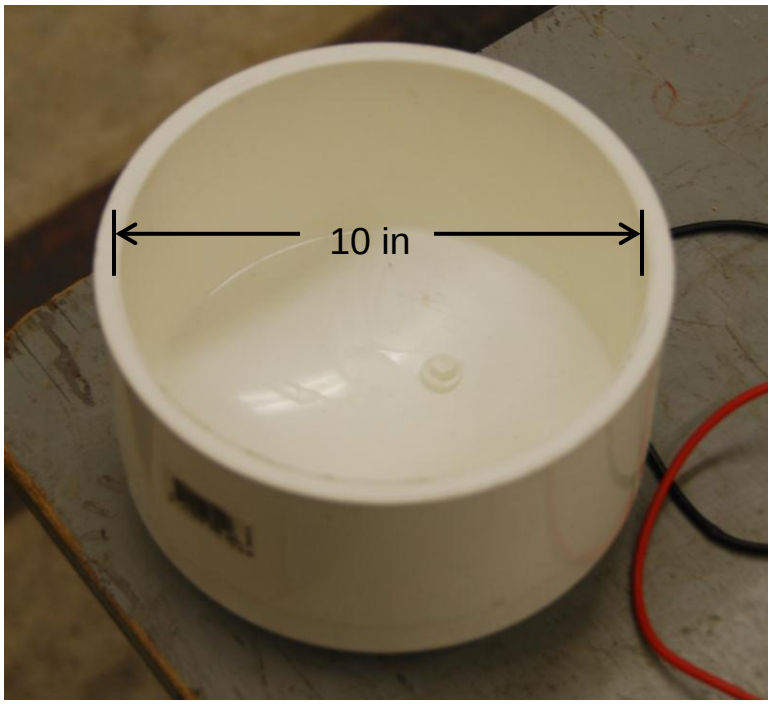

Figure 3.12: PVC pipe cap used to hold sand for self-potential experiments

Figure 3.13: Bottom layer of clean Ottawa sand

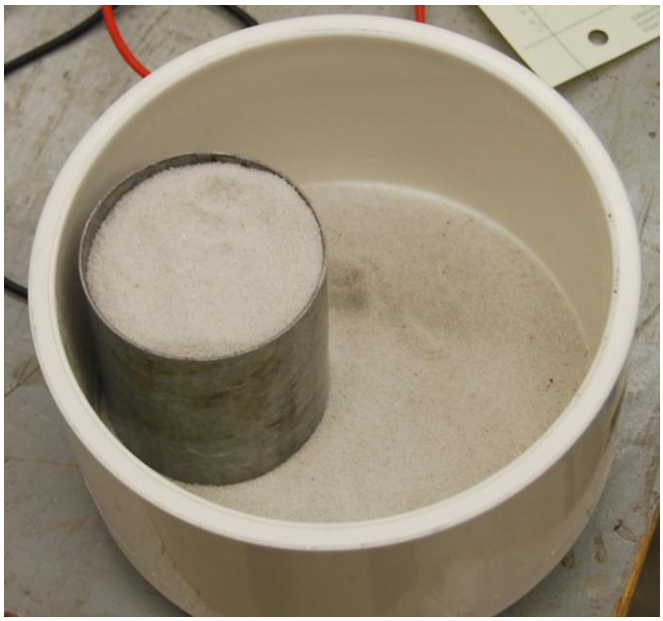

Figure 3.14: Shelby tube filled with 0.40% sand-hydrogel mixture

Figure 3.15: Clean sand backfilled around the Shelby tube just prior to Shelby tube removal

Figure 3.16: Saturated self-potential experimental setup

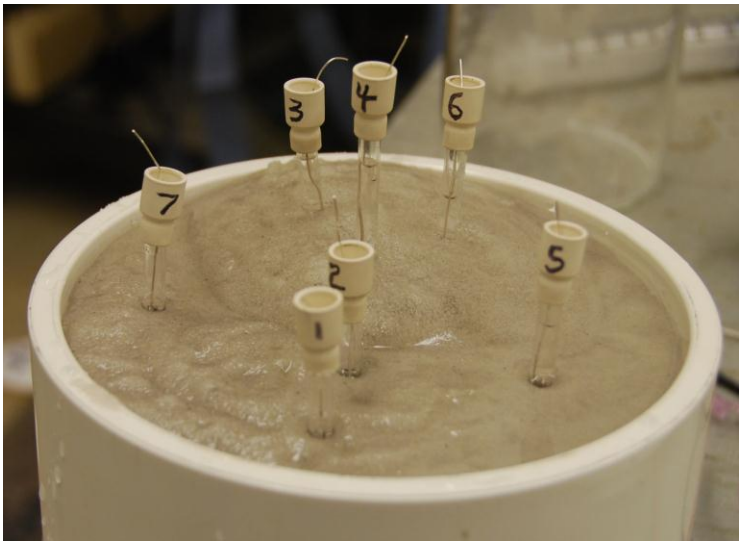

Figure 3.17: Self-potential experimental setup complete with electrodes in place

3.8.3 Data Collection

An electrical multimeter was used to measure voltage between electrodes. Theses measurements were recorded by hand. The single reference electrode method was used to map the self-potential differences. In this method, one electrode is designated the reference electrode and the potential is measured as the potential difference between the measurement electrode and the reference electrode. When a stable reference electrode is selected, this method of measurement reduces the amount of electrode bias in the measurements. The single reference method is the most straightforward method of self-potential mapping and it works well over small distances (Zhdanov 2009). For each experiment, potential readings were taken once an hour for four hours and then a final reading was taken the next day.

3.9 Capacitance Measurement Experiment

Capacitance, the ability of a material to hold an electrical charge, is a property directly related a material's ground penetrating radar (GPR) signature. Basically, materials with different levels of capacitance are easily distinguishable from each other on a GPR output. Two

experiments to measure the capacitance of different combinations of sand, air, water, and hydrogel were performed. The goal of these experiments was to evaluate whether GPR or a capacitance measuring sensor could potentially be used to detect hydrogel in the field.

3.9.1 Equipment

The sensor used during the capacitance experiments is a new type of sensor developed by Dr. Robert Dean in the Auburn University Department of Electrical and Computer Engineering. The sensor is an approximately 1-in wide by 3-in tall circuit board with two terminals at the top of the sensor. When this sensor is connected to an LCR meter, a device that measures inductance (L), capacitance (C), and resistance (R), capacitance can be measured directly. For these experiments, a Wayne Kerr model 4220 automatic LCR meter was used.

3.9.2 Experiment Setup

Since the equipment used for these experiments allowed capacitance to be directly measured, individual samples of different materials were prepared, and their capacitance was directly measured. For the first experiment, the capacitance of six different materials was measured: air, distilled water, dry Ottawa sand, distilled water saturated Ottawa sand, and distilled water saturated Ottawa sand with 0.40% hydrogel. Based on the results of the first experiment, the second experiment tested capacitance of air, distilled water, and a mixture of water and hydrogel of roughly the same ratio of hydrogel-to-water present in a 0.40% hydrogel-sand mixture. For both experiments, the materials tested were contained in clean 500 mL glass beakers, except for the air.

The experiments were run by simply inserting the sensor into the material and the reading the capacitance value from the digital readout on the LCR meter. The sensor was cleaned and

dried between measurements of different materials to prevent inaccurate readings caused by residual material on the sensor. Several readings were taken for each material.

During the first experiment, it was noticed that the sensors had a tendency to drift during measurements of the wet materials. Dr. Dean theorized that the sensor was absorbing water over time, causing the reading to change slightly. During the second experiment the sensor was "soaked" in the wet materials until the readings stabilized. This took about half an hour. Two other sensors, identical to the first, were tested in air and water to check for consistency between sensors. Also, because the first experiment showed that there was almost no difference between the capacitance of water and saturated sand but a noticeable difference between the capacitance of water and saturated sand with hydrogel, the second experiment was run on samples of air, distilled water, and distilled water with hydrogel to further isolate the variable being tested.

3.9.3 Data Collection Procedure

The capacitance readings were manually collected and recorded. For the first experiment, sets of four readings were taken within a few minutes of each other. The time between readings was not recorded. For the second experiment, only two sets of readings were taken, one initial set of readings and one final set of readings 30 min later.

3.10 Shrinkage Experiments

There is concern that once hydrogel is installed under a structure it could cause increased settlements if the water table were to drop in elevation and the swollen hydrogel particles were to shrink. To evaluate this, samples containing hydrogel were dried in an attempt to qualitatively evaluate the resulting change in volume of a small soil mass due to hydrogel drying. Two experiments were performed, one in which a sample was oven-dried and one in which samples were air-dried.

3.10.1 Equipment

The equipment used for these experiments was standard Proctor molds, a 200 °F oven without a fan, some five gallon buckets, and a camera. For both experiments samples were prepared in Proctor molds. Proctor molds were selected based on their standard size, availability in the laboratory, and ability to remove the top collar and strike the sample off. Because Proctor molds are not watertight, the samples were prepared in five gallon buckets with water fill around the Proctor mold to a level just below the top of the mold (see Figure 3.18). A digital camera was used to document the changes of the samples as they dried.

Figure 3.18: Proctor mold in five gallon bucket with water level just below the top of the Proctor mold

3.10.2 Experiment Setup

For both the oven-dried and air-dried experiments, the samples were prepared in the five gallon buckets as shown in Figure 3.18. The interior of the sample was saturated using the syringe injection method described in Section 3.4.3 for triaxial sample preparation. Samples

were left in the buckets for 24 hours to ensure they were fully saturated. During the saturation period, additional water was carefully poured on top of the sample to aid saturation. After the saturation period, the samples were removed from their buckets. The top collar was then removed, and the sample was struck even with the top of the Proctor sleeve using a metal spatula. For the oven-dried test, the sample was carefully loaded into the oven avoiding vibration. For the air-dried test, the samples were carefully place in their final positions before the collar was removed.

3.10.3 Oven Dried Experiment

Only one sample was prepared for the oven-dried experiment. The sample was prepared with 0.40% hydrogel and Ottawa sand. The sample was placed in the oven for 48 hours.

3.10.4 Air Dried Experiment

For the air-dried experiment, three Ottawa sand samples were prepared: a control sample without hydrogel, a 0.25% hydrogel and sand sample, and a 0.40% hydrogel and sand sample. The samples were left on the floor of the lab to dry for eight weeks.

3.10.5 Qualitative Observations

Because there was not an accurate way to measure the amount of volume change, the samples were simply observed at regular intervals. Taking pictures of each sample over the duration of the experiments was the qualitative method of data collection used for this experiment.

Chapter 4: Laboratory Testing Results and Discussion

4.1 Consolidated Undrained Triaxial Testing

4.1.1 Overview

Consolidated undrained (CU) triaxial tests with pore pressure measurements were performed to evaluate the effect of hydrogel on the strength and pore pressure response of Ottawa sand. Five different concentrations by mass of hydrogel were tested: 0.00%, 0.15%, 0.25%, 0.30%, and 0.40%. A minimum of four CU tests were performed on each concentration of hydrogel. Table 4.1 is a summary of the triaxial data from all of the triaxial tests performed on Ottawa sand without hydrogel presented in this paper. The missing test numbers correspond to tests that had known problems preventing those tests from providing useful information. Some test had issues but still provided some useful data. If a test is presented here and had a problem, it is noted in the *Notes* column of Table 4.1. Information on the samples with hydrogel is presented later in Table 4.4. Individual triaxial data plots not presented in this section are located in Appendix E.

Table 4.1: Basic data from triaxial tests on Ottawa sand without hydrogel

Test #	Test Date	% Hydrogel	$\gamma_{d\ intial}$ (pcf)	e_o	B	ϕ' (°)	Δu at end of test	Deformation Rate	Notes
6	4/2/2009	0.00%	97.2	0.70	0.98	33.5	-29.9	0.02 in/min	CU test, σ_3' = 2 psi, the air pressure regulator was not fully functioning, resulting in fluctuations in the data
7	4/3/2009	0.00%	99.0	0.67	0.98	32.5	-61.2	0.02 in/min	CU test, σ_3' = 2 psi, with no issues
9	4/15/2009	0.00%	97.5	0.70	0.98	31.6	-63.8	0.02 in/min	CU test, σ_3' = 2 psi, with no issues
10	4/22/2009	0.00%	99.4	0.66	0.98	30.9	-27.6	0.02 in/min	CU test, σ_3' = 2 psi, with no issues
12	5/7/2009	0.00%	93.4	0.77	0.98	30.1	-52.4	0.02 in/min	CU test, σ_3' = 2 psi, with no issues
13	5/12/2009	0.00%	97.2	0.70	0.98	32.1	-60.6	0.02 in/min	CU test, σ_3' = 2 psi, with no issues
14	5/15/2009	0.00%	98.2	0.68	0.98	32.4	-75.5	0.02 in/min	CU test, σ_3' = 2 psi, with no issues
15	5/18/2009	0.00%	99.5	0.66	0.99	33.0	-65.2	0.02 in/min	CU test, σ_3' = 2 psi, with no issues
16	5/28/2009	0.00%	95.6	0.73	0.98	33.4	-64.3	0.02 in/min	CU test, σ_3' = 2 psi, the LVDT was not working properly, sample frozen with liquid nitrogen
17	6/4/2009	0.00%	99.7	0.66	0.97	32.6	-74.6	0.02 in/min	CU test, σ_3' = 2 psi, with no issues, sample frozen with liquid nitrogen
18	6/18/2009	0.00%	102.1	0.62	0.98	33.8	-63.5	0.02 in/min	CU test, σ_3' = 2 psi, with no issues, sample frozen with liquid nitrogen
19	6/26/2009	0.00%	96.9	0.71	0.99	29.0	-31.1	0.02 in/min	CU test, σ_3' = 2 psi, with no issues, sample frozen with liquid nitrogen
20	7/7/2009	0.00%	98.3	0.68	0.97	31.1	-61.7	0.02 in/min	CU test, σ_3' = 2 psi, with no issues, sample frozen with liquid nitrogen
21	7/16/2010	0.00%	100.8	0.64	0.98	32.3	-25.0	0.02 in/min	CU test, σ_3' = 2 psi, with no issues, sample frozen with liquid nitrogen
22	7/21/2009	0.00%	99.3	0.67	0.98	30.9	-73.6	0.02 in/min	CU test, σ_3' = 2 psi, with no issues, sample frozen with liquid nitrogen
23	8/20/2009	0.00%	99.8	0.66	0.98	32.0	-73.6	0.02 in/min	CU test, σ_3' = 2 psi, with no issues, sample frozen with liquid nitrogen
28	9/30/2009	0.00%	99.6	0.66	0.98	32.2	-64.4	0.02 in/min	CU test, σ_3' = 2 psi, the LVDT was moved during the test causing a break in the data
33	11/17/2009	0.00%	95.6	0.73	0.99	31.2	-57.1	0.02 in/min	CU test, σ_3' = 2 psi, with no issues
38	1/5/2010	0.00%	96.1	0.72	0.99	31.7	-55.5	0.02 in/min	CU test, σ_3' = 2 psi, with no issues
40	1/27/2010	0.00%	91.0	0.82	1.00	32.1	-5.5	0.02 in/min	CU test, σ3' = 2 psi, with no known issues, but the does not match the other tests
41	2/1/2010	0.00%	97.5	0.70	0.98	33.2	-56.3	0.02 in/min	CU test, σ_3' = 15 psi, with no issues
42	2/3/2010	0.00%	97.3	0.70	0.98	33.3	-56.7	0.02 in/min	CU test, σ_3' = 15 psi, with no issues
43	2/4/2010	0.00%	98.0	0.69	0.98	34.3	-46.5	0.02 in/min	CU test, σ_3' = 15 psi, with no issues

4.1.2 Selection of Percent Hydrogel

Shiver (2007) concluded that increasing the concentrations of hydrogel to Ottawa sand above 0.50% did not cause additional change in the soil properties based on flexible wall permeability tests. In other words, there is a diminishing effect of hydrogel on the behavior of Ottawa sand with an upper bound of approximately 0.50%. Based on this, five concentrations of

hydrogel between 0 and 0.50% were selected for testing. These concentrations are: 0.00%, 0.15%, 0.25%, 0.30%, and 0.40%.

4.1.3 Effect of Void Ratio on Triaxial Results

Void ratio (e) is a function of its dry unit weight (γ_d) or dry density (ρ_d). Void ratio is one of the most critical properties related to the behavior of sand during shear. In general, the higher the density, or the lower the void ratio, the stronger a sample will be and vice versa. Void ratio also effects pore pressure response. Sand with a low void ratio (dense) will have a tendency to dilate during shear, generating negative pore pressures under undrained conditions. Whereas, sand with a high void ratio (loose) will tend to compress during shear, generating positive pore pressures under undrained conditions. It is important to understand how differences in void ratios between samples can impact the results of triaxial tests when assigning the effects of hydrogel to the results of triaxial tests.

4.1.3.1 Variation of Void Ratio During Sample Preparation

The triaxial samples were prepared as loose as possible to replicate the in-situ soil conditions that typify a potentially liquefiable site. The initial unit weights reported in this paper are calculated from the dimensions of the frozen samples and the dry mass of the sand recovered after the test. The void ratios were calculated based on the dry unit weights and a specific gravity of solids of 2.65 for Ottawa sand. The average unit weight of an Ottawa sand sample without hydrogel, based on the unit weights of twenty-three samples, was 97.8 lb/ft^3 with a standard deviation of 2.43 lb/ft^3. The average void ratio was 0.69 with a standard deviation of 0.043.

Samples containing hydrogel tended to be looser than samples without hydrogel. The average void ratio for eighteen samples containing various concentrations of hydrogel is 0.75

with a standard deviation of 0.027. It is thought that the hydrogel samples are consistently looser because the hydrogel swells during sample preparation, forcing the sand grains against the sides, top, and bottom of the mold. The swollen hydrogel preserves the loose structure of the sand, preventing the particles from densifying as a result of vibration during sample construction. Because the sand without hydrogel does not have the hydrogel to hold its loose structure in place, unavoidable vibrations during sample construction cause the samples to densify and have a slightly lower void ratio than the hydrogel samples.

Although the presence of hydrogel results in samples with a lower density and higher void ratio, the amount of hydrogel does not appear to have an effect on the *amount* of decreased density. Samples of all percentages of hydrogel tested had similar void ratios and densities, as shown in Table 4.2. The fact that sample density is not a function of the amount of hydrogel supports the idea that the expanding gelled pore water forces the soil particles against the sides of the mold. The hydrogel will cause the pore water to gel and expand until the soil particles become confined and can no longer move apart. Only a small amount of hydrogel is needed to cause this expansion because the voids are saturated with incompressible water. Thus any expansion caused by the hydrogel will cause the entire sample to expand because there are no empty void spaces to fill. Since the rigid mold is already full of sand, additional hydrogel cannot cause additional expansion. This results in samples of similar density and void ratio even for different percentages of hydrogel.

Table 4.2: Comparison of average density and void ratio to percent hydrogel

% Hydrogel	# of Samples	Average $\gamma_{d\ initial}$ (lb/ft^3)	Std. Dev. $\gamma_{d\ initial}$ (lb/ft^3)	Average e_o	Std. Dev. e_o
0.00	18	97.8	2.43	0.69	0.043
0.15	5	94.7	0.73	0.75	0.014
0.25	5	95.3	1.31	0.74	0.024
0.30	4	93.8	1.80	0.77	0.034
0.40	4	94.8	1.77	0.74	0.033

4.1.3.2 Effect of Void Ratio on Strength

In general, as void ratio increases, strength decreases. Because not all of the samples had the same void ratio, the effect of the void ratio on the effective angle of internal friction (ϕ') was evaluated. As described in Section 2.1.4.3, the shear strength of sand is defined by ϕ'. The larger ϕ' is, the stronger the soil. The effective friction angle of twenty-three samples without hydrogel was plotted against the initial void ratio (e_o) of those samples in Figure 4.1. Figure 4.1 demonstrates that the variability between the strengths of samples is not caused solely by differences in void ratio. The correlation coefficient (R) is only -0.25, indicating a relatively weak relationship between void ratio and ϕ' for the void ratios tested. Even if this relationship had a stronger correlation, the best fit relationship shown in Figure 4.1 only predicts a 0.4° decrease in ϕ' when comparing the predicted friction angle resulting from the average void ratio of the non-hydrogel samples ($e_{avg} = 0.69$, $\phi'_{predicted} = 32.1°$) to the predicted friction angle based on the average void ratio of the hydrogel samples ($e_{avg} = 0.75$. $\phi'_{predicted} = 31.7°$) where the average void ratios for non-hydrogel and hydrogel samples are the average of the individual initial void ratios presented in Tables 4.1 and 4.4, respectively. The fact that only a relatively small reduction in ϕ' can be expected for the larger void ratio hydrogel samples is significant because significantly larger reductions can confidently be attributed to the presence of hydrogel.

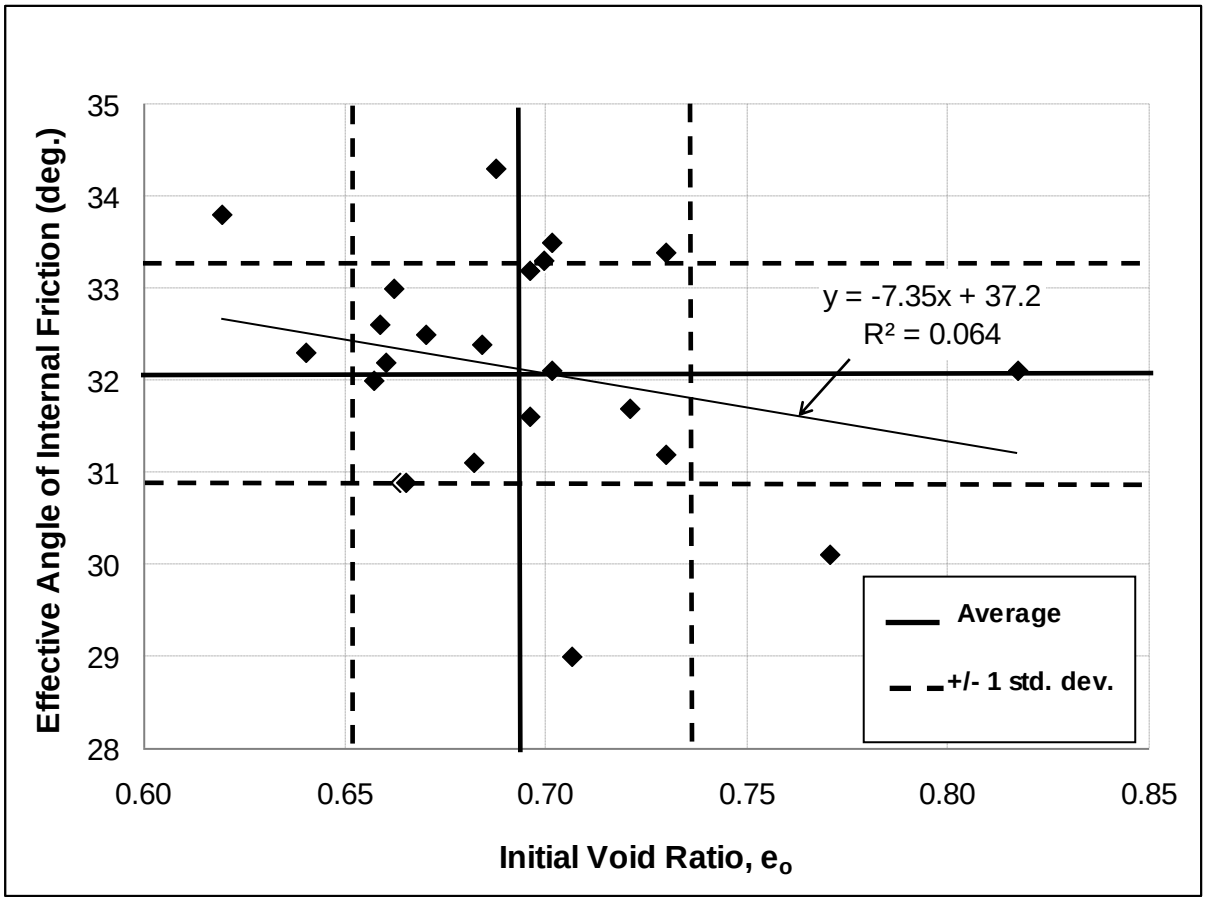

Figure 4.1: Triaxial strength results of 18 tests on clean Ottawa sand as a function of initial void ratio

4.1.3.3 Effect of Void Ratio on Pore Pressure Response

The pore pressure response of sand during a triaxial test is a function of initial void ratio and the effective confining pressure (Holtz and Kovacs 1981). When sand is sheared under drained conditions, the void spaces between the particles may increase in volume (dilate) or decrease in volume (compress). Compression occurs during shear because the particles essentially roll into the space between each other, creating a denser structure and reducing the volume of the void spaces. However, if the effective confining pressure (σ_3') is low enough, even a loose sand will dilate (Holtz and Kovacs 1981). Dilation occurs during shear because

tightly packed sand particles are forced to ride up and over each other, causing an increasing in the volume of the void spaces. In a drained triaxial test, volume changes caused by compression or dilation are measured in terms of fluctuations of the water levels in the backpressure burettes. If a triaxial test is undrained, the sample cannot change volume, but the tendencies of the sample to dilate or compress will translate into a negative or positive change in pore pressure, respectively.

For the void ratios and effective confining pressures used for this testing, the samples typically exhibited an initial positive change in pore pressure (compression tendency) until 100% of ϕ' was mobilized. After ϕ' was fully mobilized, the pore pressure decreased (dilation tendency). This behavior is demonstrated in Figure 4.2, which is the change in pore pressure recorded during a typical undrained triaxial test with σ_3' = 15 psi. The shape of the curve presented in Figure 4.2 is typical for Ottawa sand of medium density. Looser samples will generate a higher peak positive change in pore pressure, followed by a more gradual decrease in pore pressure. A denser sample would behave just the opposite, with a lower initial peak, followed by a sharper decrease in pore pressure. It is not uncommon for undrained triaxial test to generate negative pore pressures to the point of cavitation (Lambe and Whitman 1969). Cavitation occurs in a triaxial sample when the pore pressure drops below the vapor pressure of water (-14.3 psig at 72° F). In addition to the pore water vaporizing, dissolved air in the pore water will come out of solution, causing the same effect as cavitation. Evidence of cavitation was observed in many tests for this research. The result is an apparent lower limit to the decrease in pore pressure as shown in Figure 4.2.

Although it is known that pore pressure response is a function of void ratio, the differences in the pore pressure responses of the Ottawa sand tested for this research did not

always follow the expected relationship. Figure 4.3 demonstrates this point. The densest sample (e_o= 0.62) behaves as expected for a sample of this density. The loosest of the three samples (e_o= 0.77) behaves more like a loose sample than the densest of the three samples, but the e_o= 0.71 sample behaves more like a loose sample than the e_o= 0.62 sample despite the fact that it is denser.

These differences can be attributed to three sources: possible variability of the amount of expansion during freezing that ultimately results in variability of the measured sample volume, loss of sand during the sample deconstruction process needed to accurately determine the dry weight, and the variability that is inherent to testing natural materials. The effect of void ratio on the pore pressure response of Ottawa sand during shear is noticeable, but its effects are variable. It is important understand these effects and their variability when comparing the effects of hydrogel on the pore pressure response of Ottawa sand.

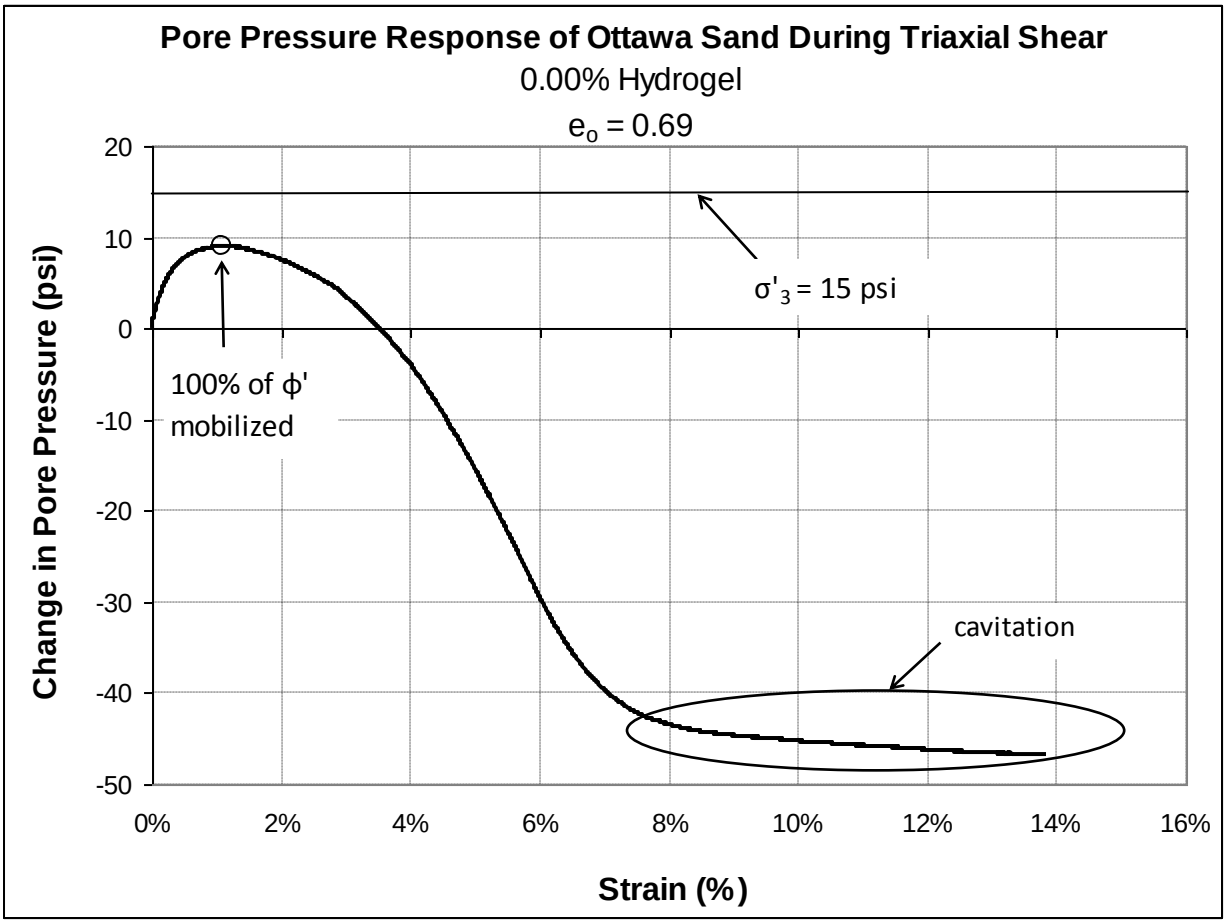

Figure 4.2: Typical pore pressure response of medium dense Ottawa sand during undrained triaxial shear

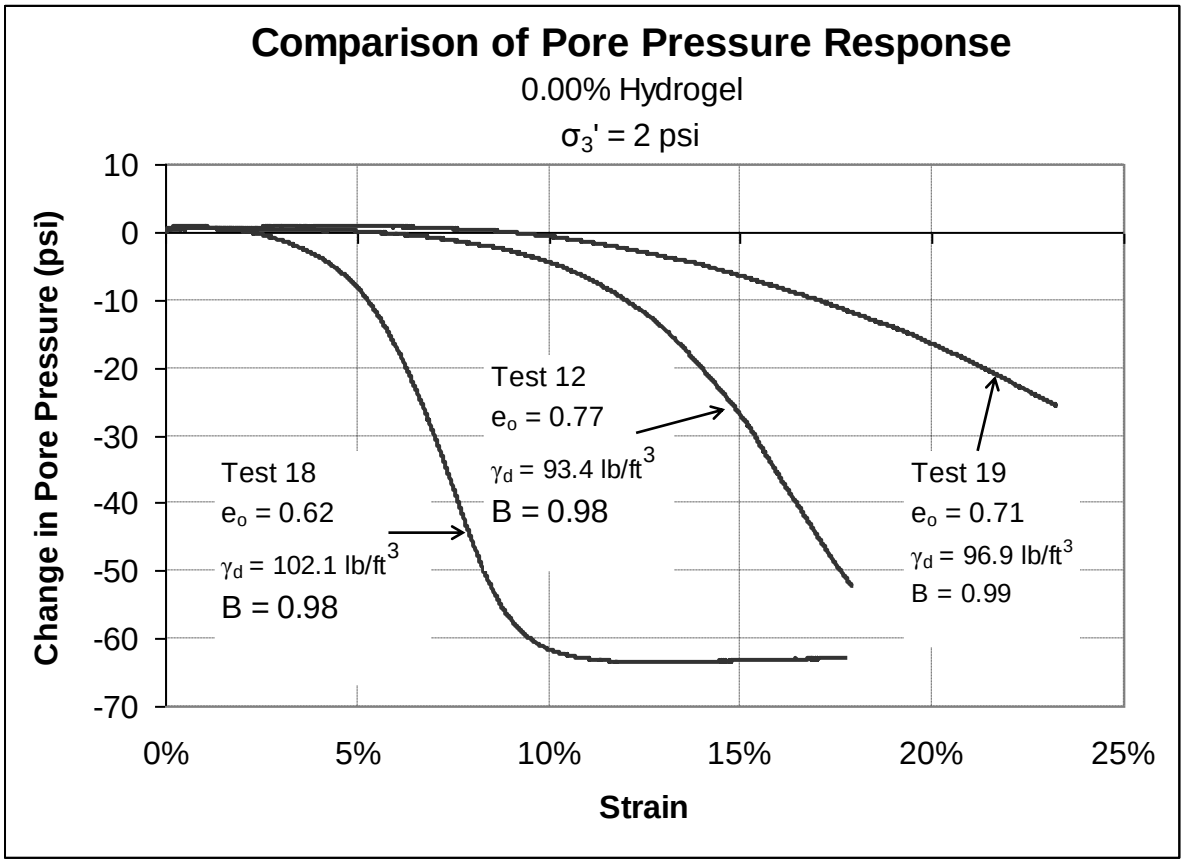

Figure 4.3: Comparison of Pore Pressure Response of the Samples with Different Initial Void Ratios

4.1.4 The Importance of Sample Saturation

Sample saturation is critical to a triaxial test. If a triaxial sample contains air in its void space, pore pressure cannot accurately be measured because some of the energy that would usually result in a change in pore pressure results in a change in density of the entrapped air. As described in Section 3.4.3, sample saturation was verified by evaluating Skempton's B coefficient (B), which is the ratio of resulting change in pore pressure to an induced change in confining pressure under undrained conditions (Equation 3.2). Although the B value is used to evaluate sample saturation, the actual degree of saturation may be higher than the B value itself (Black and Lee 1973). All CU tests for this research were run with a B value of 0.97 or higher.

4.1.5 Consolidation Pressure

Sand must be confined under some effective consolidation pressure (σ_3') to run a triaxial test. If σ_3' was equal to zero, a sample would have zero shear strength and would not be able to maintain its shape for testing. Since sand cannot hold its own shape, an unconsolidated triaxial test on a cohesionless soil is impossible. When a σ_3' is applied to a sand sample it will densify some, causing a reduction in void ratio and ultimately, a change in the pore pressure response during shear. Increasing σ_3' will also cause an increase in the deviator stress at failure, but it will not result in a different measured value of ϕ'.

In order to preserve the loosest possible structure of the samples, which replicates the field conditions most susceptible to liquefaction, it was desirable to minimize the densification due to consolidation. Initially, σ_3' = 2 psi was used for this testing. This value corresponds to soil about 5 ft below the ground surface of a fully saturated site. Since 2 psi is such a low value for σ_3', failure (100% of ϕ' mobilized) was reached at very low strain. It was difficult to discern differences in small strain pore pressure response and stress strain behavior because samples all failed at such low magnitudes of deviator stress and change in pore pressure. The transducers were also being pushed to their limit as indicated by the visible sensor noise in some of the plots, e.g., Figure 4.7. To solve this problem, σ_3' was raised to 15 psi for further testing. Raising the value of σ_3' from 2 psi to 15 psi only caused a slight increase in density. 15 psi corresponds to soil about 38 ft below the ground surface of a fully saturated site. The average additional decrease in volume due to the increase in σ_3' was only 0.26 in^3 or about 0.7% for a 2.8-in by 6-in triaxial sample, determined by monitoring the backpressure burettes as the sample was consolidated from 2 to 15 psi . This change in volume equals an approximately 0.6 lb/ft^3

increase in γ_d or a 0.1 decrease in void ratio. This small increase in density should not have resulted in a significant difference between the pore pressure responses of samples sheared with σ_3' = 2 psi and samples sheared with σ_3' = 15 psi. In general, there were no observed differences in pore response other than the increased amount of positive pore pressure generation prior to failure, which was expected.

The increase in consolidation pressure theoretically has little to no effect on the value of ϕ' obtained from a triaxial test. Effective friction angles calculated from tests with σ_3' = 15 psi yielded results on the higher end of the range as those calculated from the tests with σ_3' = 2 psi as shown in Figure 4.4. Two of the three data points are within one standard deviation. The increase in ϕ' could be caused by the increased density, or it could be the result of variability in the data. The 0.1 reduction in void ratio should not have caused such increases in ϕ' based on the relationship between friction angle and void ratio in Section 4.1.3.2.

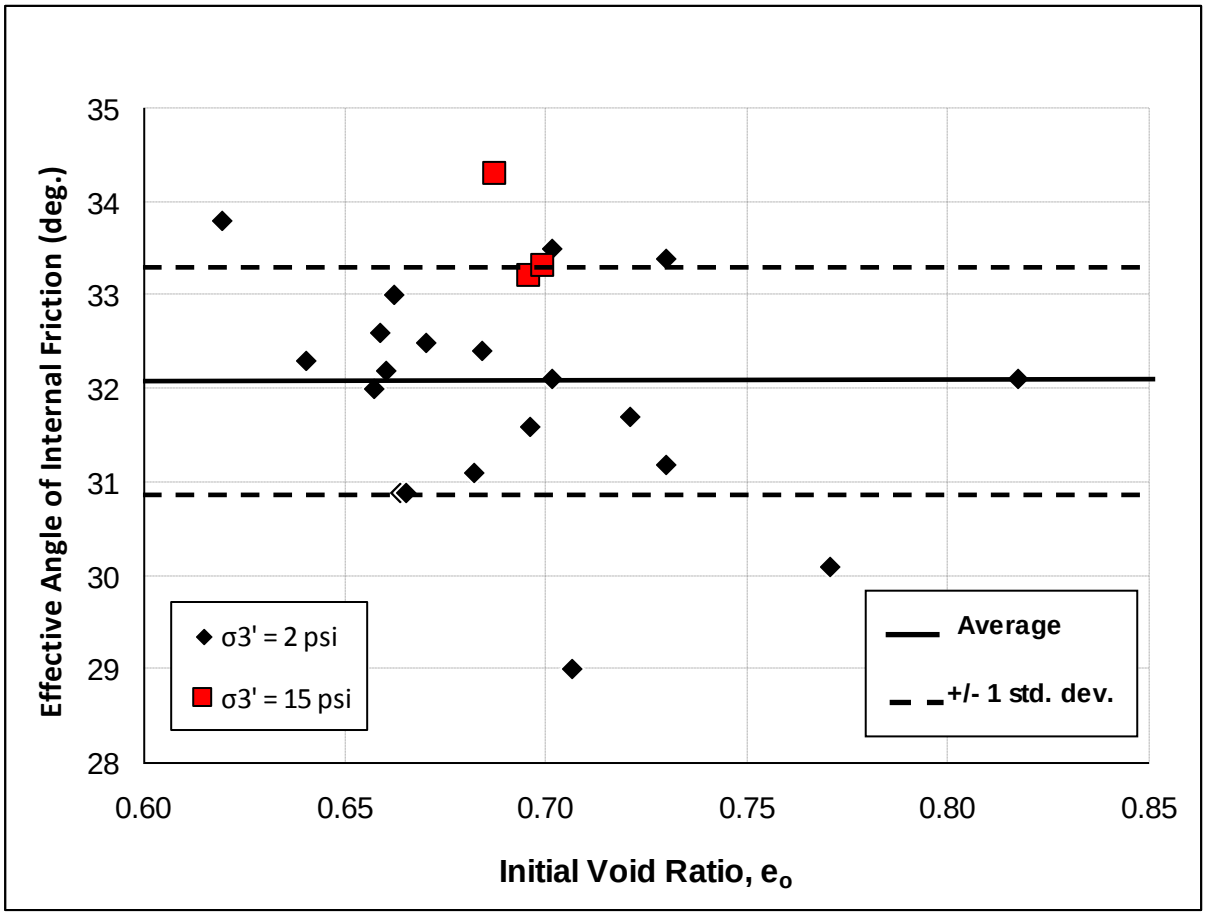

Figure 4.4: Effect of σ_3' on ϕ' of Ottawa sand withouth hydrogel

4.1.6 Effect of Freezing Method

Two different methods were used to freeze the triaxial samples. Figure 4.5 presents friction angle vs. void ratio with the freezing method denoted by different data markers. Figure 4.4 illustrates that the freezing method did not have discernable impact on ϕ'.

The liquid nitrogen-frozen samples appear to have a tendency to be less dense than the freezer-frozen samples. Actually, samples frozen with liquid nitrogen did not expand as much during freezing, and because the volume measurements were made on frozen samples, the initial void ratios of the liquid nitrogen frozen samples appear to be lower than they would be if they had expanded as much as the freezer samples. The difference in volume change is a result of the

processes discussed in Section 3.3.5. The void ratios of samples frozen both ways is actually slightly less than what is reported because of the volume change of the pore water when it melts. The void ratios are lower due to the fact that all of the samples experience some decrease in volume during thawing in the triaxial cell, but because the sample is inside the triaxial cell, volume changes due to thawing alone cannot be distinguished from volume changes due to consolidation.

It was not expected that the freezing method would have any effect on the pore pressure response. No noticeable differences between the pore pressure response of liquid nitrogen-frozen and freezer-frozen samples were observed.

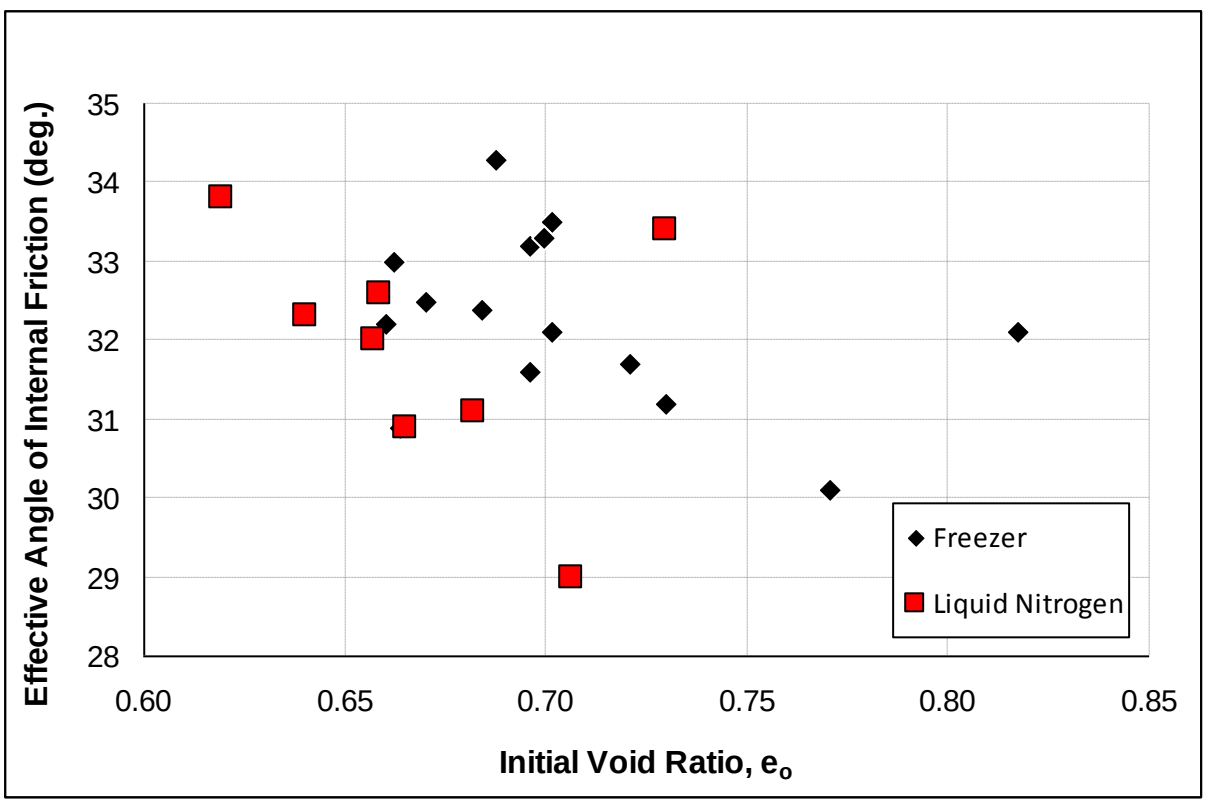

Figure 4.5: Effect of freezing method on ϕ' of Ottawa Sand without hydrogel

4.1.7 Triaxial Shear Behavior of Ottawa Sand without Hydrogel

4.1.7.1 Overview

The behavior of clean Ottawa sand during triaxial shear needed to be established to understand if any differences occurred because of the addition of hydrogel. The strength, stress strain behavior, and pore pressure response were all evaluated.

4.1.7.2 Strength

The shear strength of a sand is a function of ϕ', as described in Section 2.1.4.3. For each triaxial test, ϕ' was calculated based on the K_f line of the p'-q diagram, also known as a stress path diagram, for that test. A p'-q diagram is a representation of the stress path a sample followed during shear, where p' is the center of the effective Mohr's circle and q is the radius of the effective Mohr's circle. The K_f line defines the stress path after failure and is related to the Mohr-Coulomb failure envelope by:

$$\tan\psi' = \sin\phi' \qquad (4.1)$$

where, ψ' is the angle of the slope of the K_f line and ϕ' is the angle of the slope of the Mohr-Coulomb failure envelope as shown in Figure 4.6. The individual p'-q diagrams for each test can be found in Appendix E.

The average ϕ' for Ottawa sand without hydrogel based on twenty-three triaxial tests is 32.1°. This is close to values published by other researchers. Table 4.3 presents the values of ϕ' for Ottawa sand determined by others.

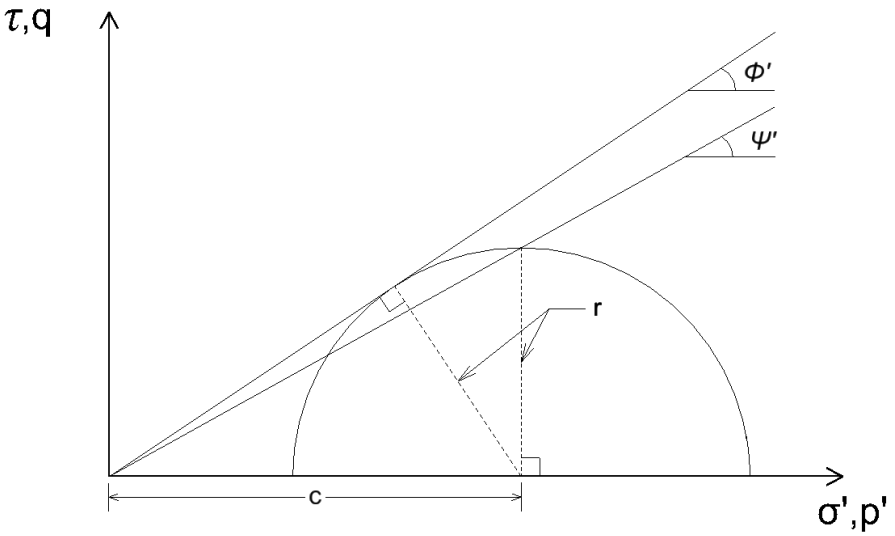

Figure 4.6: Geometric relationship between ϕ' and ψ'

Table 4.3: Comparison of published values of ϕ' for Ottawa sand

Value of ϕ'	Source
32.1°	This Paper
~30°	(Shiver 2007)
30°	(Sayles 1973)
31°	(Lee et al. 1967)
32° to 34°	(Bolton 1986)

4.1.7.3 Stress-Strain Response

4.1.7.3.1 Small Strain Response

The small strain response is the stress-strain response for strains less than about 2%. The small strain response is important because it is the zone where ϕ' is being mobilized. Since most engineered designs depend on ϕ' not being fully mobilized for stability, the small strain response can be thought of as the range of stress and strain in which engineered earth structures typically operate.

Figure 4.7 shows the small strain stress-strain response for twenty CU tests. All of the tests were run with σ_3' = 2 psi except for Tests 41, 42, and 43, which were run with σ_3' = 15 psi. The basic shape of most of the curves begins at the origin sloping steeply upward to a yield point where the curve hits a "plateau" and deforms plastically until pore pressure-induced strain hardening begins. The plastic deformation corresponded with the point where ϕ' became 100% mobilized, which typically occurred around 1% strain. The average yield stress for the 2 psi confined samples is 1.6 psi with a standard deviation of 0.65 psi, and the average yield stress for the 15 psi confined samples is 5.6 psi with a standard deviation of 0.90 psi. The yield stresses were taken as the deviator stress at 0.25% strain. 0.25% was chosen to define the deviator stress because at 0.25% most of the samples have reached their yield stress but have not begun to further increase in strength, resulting in an accurate and consistent criterion for defining yield stress.

The elastic modulus of the 2 psi confined samples was very difficult to evaluate because of the low yield stresses and is not presented in this paper. The elastic modulus of the 15 psi confined samples was estimated to be 6,500 psi based on Tests 41, 42, and 43, as shown in Figure 4.7.

Two tests, Test 7 and Test 40, do not match the general trends of the other data. Test 7 did not have a well-defined yield point and Test 40 yielded almost immediately. Test 40 did have the highest void ratio of any of the non-hydrogel samples test. This probably contributed to its low yield stress. There is no known explanation for the odd behavior of Test 7.

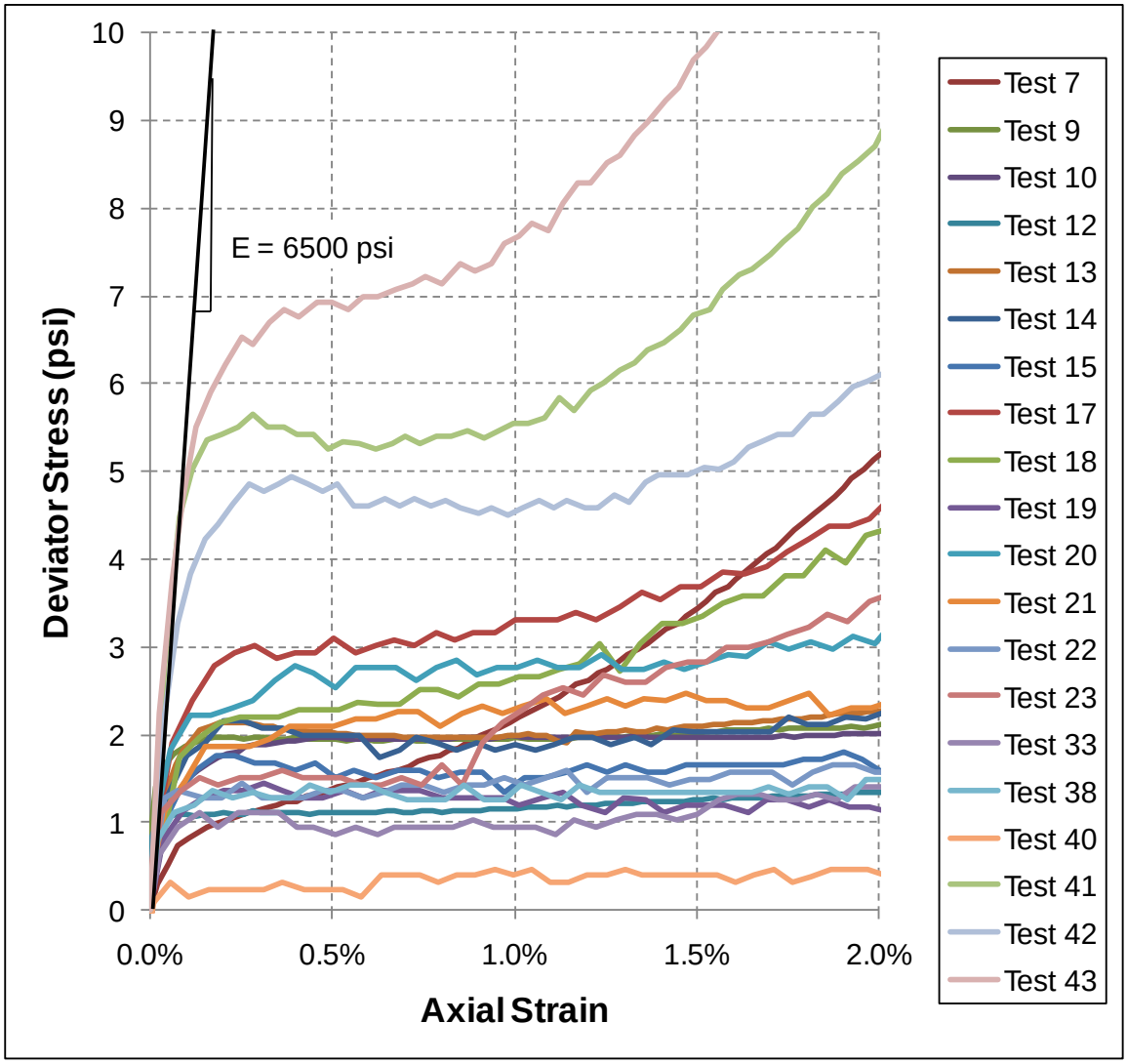

Figure 4.7: Small strain stress-strain response during undrained shear for non-hydrogel samples

4.1.7.3.2 Large Strain Response

The stress-strain response beyond the point where ϕ' is fully mobilized is purely a function of pore pressure response. Because of the effective stress equation, pore pressure has a major impact on the stress-strain behavior of soil. As noted in Section 4.1.7.4, the samples exhibited a decrease in pore pressure after yielding. The negative pore pressure causes the samples to increase in strength as strain increases. If there was no change in pore pressure after

ϕ' is mobilized, the sample would theoretically continue to yield in a perfectly plastic manner with no increase in stress. The stress peaks exhibited by some samples are a result of cavitation of the pore water. Figure 4.8 shows the large strain stress-strain response for twenty-one tests. This includes all of the tests presented in Figure 4.7 with the addition of Test 6, which was not plotted in Figure 4.7 because of issues with one of the pressure regulators that made the small strain data impossible to interpret but is not noticeable when plotted on the scale of Figure 4.8.

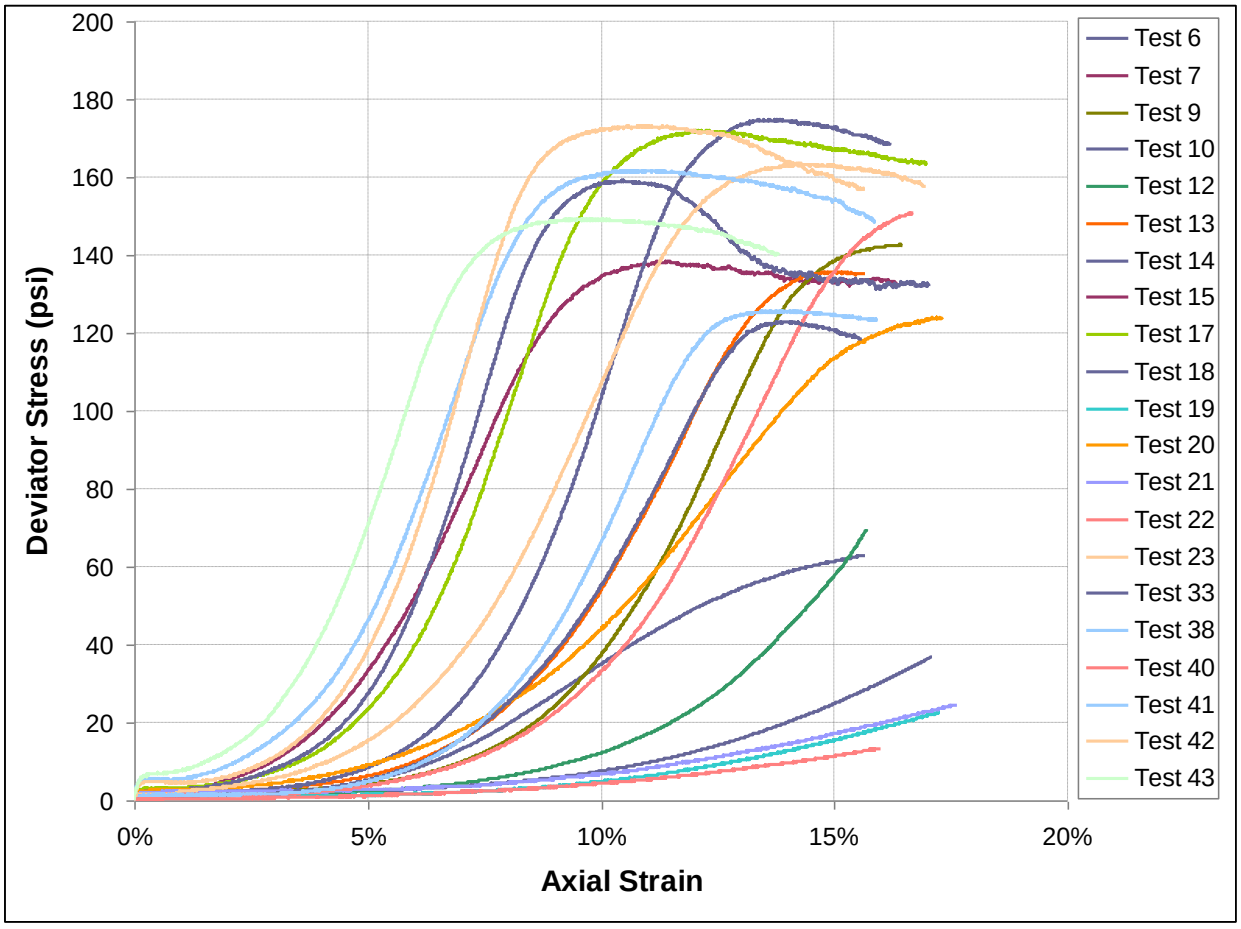

Figure 4.8: Large strain stress-strain response during undrained shear for non-hydrogel samples

4.1.7.4 Pore-Pressure Response

The pore-pressure response of samples of clean sand has many similarities to the stress-strain response. This makes sense because strength is a function of effective stress, which is in turn a function of pore pressure.

Figure 4.9 shows the pore-pressure responses of twenty triaxial tests. Results from Test 33 were not included because of an issue with the pore pressure transducer during that test. Typically samples of non-hydrogel sand exhibited a rise in pore pressure up to a magnitude close to the confining pressure. At that point, the pressure peaked or remained constant for 1 to 5% further strain, depending on the sample void ratio and the value of σ_3'. Then, as the samples were further sheared, the pore pressure decreased, resulting in the post yield strain hardening described in Section 4.1.7.3.2. Some samples reached a point where the pore pressure did not further decrease. This is thought to be the result of pore water cavitation. As noted in Section 4.1.3.3, cavitation occurs in a triaxial sample when the pore pressure drops below the vapor pressure of water (-14.3 psig at 72° F) and the water begins to boil. It is not uncommon for undrained triaxial test to generate negative pore pressures to the point of cavitation (Lambe and Whitman 1969). In addition to the pore water vaporizing, dissolved air in the pore water will come out of solution, causing the same effect as cavitation. Most of the samples show evidence of cavitation in the form of an apparent limit to pore pressure decrease. Individual pore pressure response data plots are presented in Appendix E.

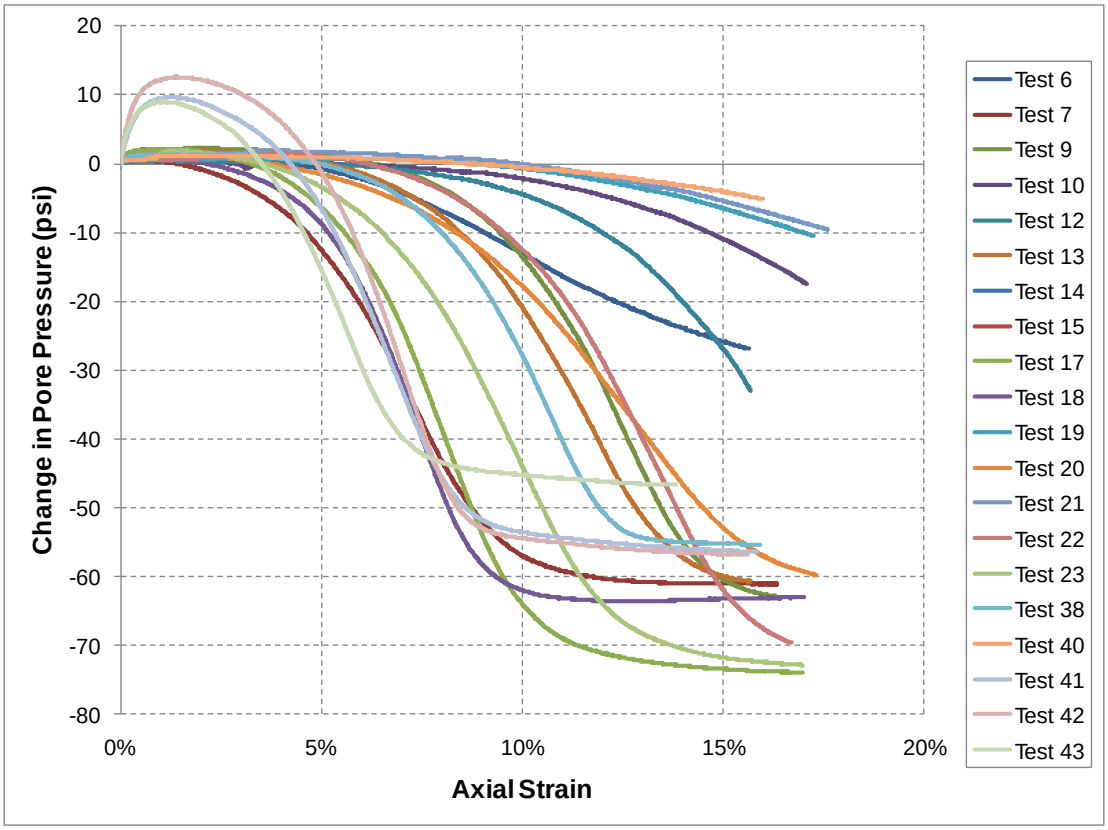

Figure 4.9: Pore-pressure response during undrained shear for non-hydrogel samples

4.1.8 Effect of Hydrogel Concentration on Triaxial Shear Behavior of Ottawa Sand

4.1.8.1 Overview

The strength, stress-strain response, and pore-pressure response of five different concentrations of hydrogel (0.00%, 0.15%, 0.25%, 0.30%, and 0.40%) were evaluated by performing CU triaxial tests. The results of these tests are compared with the results presented in Section 4.1.7 to identify consistent differences in the shear responses caused by the presence of hydrogel. Most of the tests were conducted using micro size hydrogel particles, two tests were conducted using nano size hydrogel particles. The results of the tests using different size

particles are compared and discussed. Table 4.4 is a summary of the triaxial data from all of the triaxial tests performed on Ottawa sand with hydrogel.

Table 4.4: Basic data from triaxial tests on Ottawa sand with hydrogel

Test #	Test Date	% Hydrogel	$\gamma_{d\ intial}$ (pcf)	e_o	B	ϕ' (°)	Δu at end of test	Deformation Rate	Notes
24	8/27/2009	0.40%	94.4	0.75	0.99	22.0	-1.1	0.02 in/min	CU test, σ_3' = 2 psi, with no issues
25	9/2/2009	0.40%	95.4	0.73	0.98	25.0	-2.8	0.02 in/min	CU test, σ_3' = 2 psi, with no issues
26	9/18/2009	0.25%	97.5	0.70	0.98	31.7	-17.3	0.02 in/min	CU test, σ_3' = 2 psi, with no issues
27	9/24/2009	0.25%	95.0	0.74	0.97	25.3	-8.8	0.02 in/min	CU test, σ_3' = 2 psi, with no issues
29	10/15/2009	0.15%	95.0	0.74	0.99	29.2	-22.8	0.02 in/min	CU test, σ_3' = 2 psi, with no issues
39	1/7/2010	0.15%	94.7	0.75	0.98	29.6	-5.4	0.02 in/min	CU test, σ_3' = 2 psi, with no issues
44	2/10/2010	0.25%	95.4	0.73	0.99	28.1	-15.8	0.02 in/min	CU test, σ_3' = 15 psi, with no issues
45	2/17/2010	0.15%	93.3	0.77	0.97	26.9	-11.6	0.02 in/min	CU test, σ_3' = 15 psi, with no issues
46	2/22/2010	0.30%	95.9	0.72	0.99	26.1	-2.5	0.02 in/min	CU test, σ_3' = 15 psi, with no issues
47	2/23/2010	0.40%	96.8	0.71	0.97	28.6	-22.6	0.02 in/min	CU test, σ_3' = 15 psi, with no issues
48	3/1/2010	0.15%	93.8	0.76	0.98	30.9	-60.1	0.02 in/min	CU test, σ_3' = 15 psi, with no issues
49	3/2/2010	0.15%	94.8	0.74	0.97	28.0	N/A	0.02 in/min	CD test, σ_3' = 15 psi, test was inadvertently run drained
50	3/9/2010	0.30%	93.0	0.78	0.98	27.4	-5.0	0.02 in/min	CU test, σ_3' = 15 psi, with no issues
52	3/15/2010	0.30%	93.1	0.78	0.99	26.5	-6.1	0.02 in/min	CU test, σ_3' = 15 psi, with no issues
53	3/16/2010	0.40%	92.6	0.79	0..99	27.5	-6.9	0.02 in/min	CU test, σ_3' = 15 psi, with no issues
54	3/23/2010	0.15%	96.5	0.71	0.97	28.3	-53.1	0.02 in/min	CU test, σ_3' = 15 psi, with no issues, nanoparticles
55	3/24/2010	0.25%	94.6	0.75	0.98	28.6	-12.8	0.02 in/min	CU test, σ_3' = 15 psi, with no issues
56	3/30/2010	0.30%	91.6	0.81	0.99	27.2	2.2	0.02 in/min	CU test, σ_3' = 15 psi, with no issues
57	4/20/2010	0.40%	93.5	0.77	0.99	27.0	2.2	0.02 in/min	CU test, σ3' = 15 psi, with no issues, nanoparticles

4.1.8.2 Effect of Hydrogel on Strength

Just as was done for the non-hydrogel samples, ϕ' was calculated based on the slope of the K_f line of the p'-q diagram for each test. The individual p'-q diagrams are presented in Appendix E. The calculated ϕ' angles were plotted against the amount of hydrogel as shown in Figure 4.10. Figure 4.10, the best fit linear regression, indicates that there is negative correlation between ϕ' and the amount of hydrogel. This was expected. Hydrogel has a very low

coefficient of friction and does not obey Anton's law of friction (Gong et al. 1997). Because of hydrogel's low friction, ϕ' is most likely reduced due to particle lubrication caused by the hydrogel. It was also expected that the ability of hydrogel to reduce ϕ' might have a lower limit where ϕ' is not significantly further reduced with additional amounts of hydrogel, similar to what was seen with the permeability results of Shiver (2007); however, this was not observed for the concentrations tested for this research. ϕ' for each concentration of hydrogel was also averaged and plotted against hydrogel concentration (Figure 4.11). Plotted this way, the data are still best fit by a negative correlating linear regression with a much higher R^2 value (0.974 vs. 0.626). The higher R^2 value for the averaged plot indicates that despite the scatter seen in Figure 4.10, the average trend is very well represented by a linear function.

Shiver (2007) did not observe a negative correlation between ϕ' and hydrogel concentration. His data showed that there was no discernable correlation between the concentration of hydrogel and ϕ'. It is thought that because Shiver used such a high σ_3' (45 psi) that the densification due to consolidation under the higher isotropic stress may have overridden the lubricating effects of hydrogel. Shiver also had a very small number of samples, only one test each for four concentrations of hydrogel. He could have simply had too few data points to distinguish a trend.

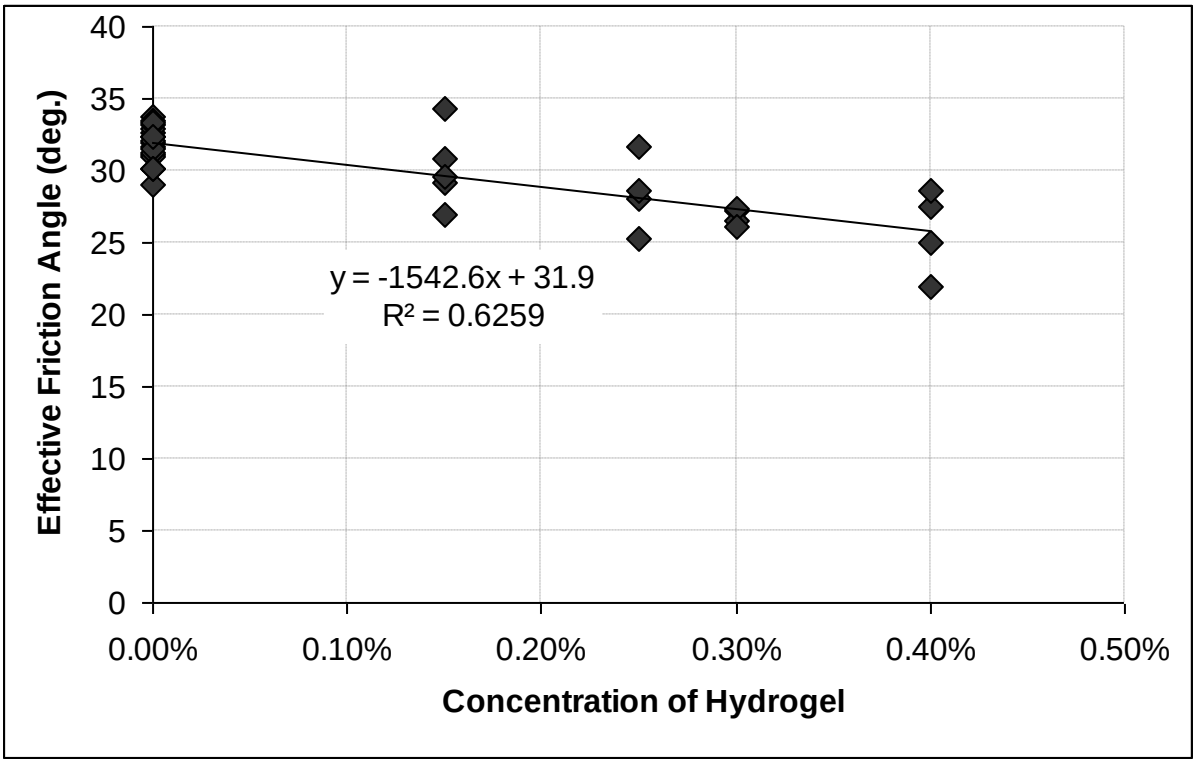

Figure 4.10: Measured friction angle for samples of different concentrations of hydrogel

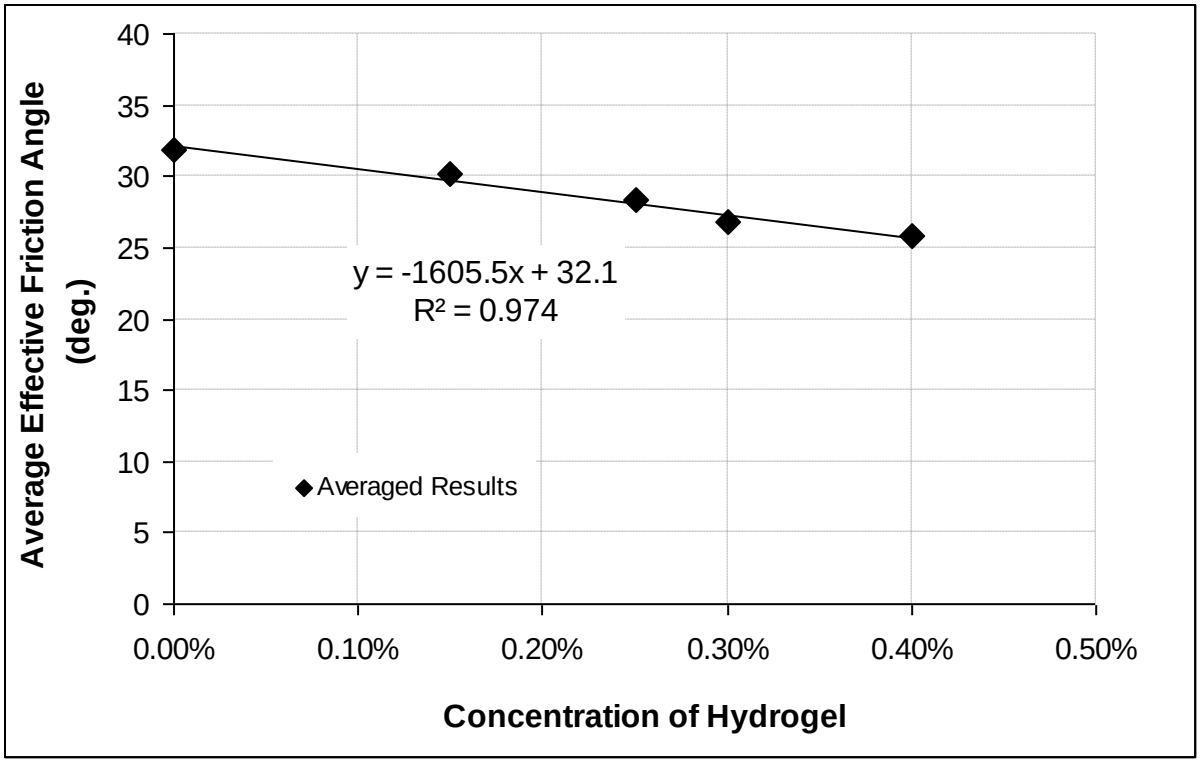

Figure 4.11: Average measured friction angle for different concentrations of hydrogel

4.1.8.3 Effect of Hydrogel on Stress-Strain Response

4.1.8.3.1 Small Strain Response

Compared to the small strain response of non-hydrogel samples presented in Section 4.1.7.3.1, samples containing hydrogel exhibited lower yield stresses and a lower modulus of elasticity. Figure 4.12 shows the small strain results of seventeen tests on different concentrations of hydrogel. The results with the lower yield stress that plot near the bottom graph were run with σ_3' = 2 psi. Additional tests were run with σ_3' = 15 psi. The average yield stress for the 2 psi confined samples is 0.9 psi with a standard deviation of 0.30 psi, and the average yield stress for the 15 psi confined samples is 3.6 psi with a standard deviation of 0.54 psi. The yield stresses were taken as the stress at 0.25% strain.

The average yield stresses for samples containing hydrogel was approximately 60% less than the average yield stresses for samples without hydrogel for both confining pressures. Figures 4.13 and 4.14 show yield stress as a function of hydrogel concentration for 2 psi and 15 psi confined samples, respectively. Both plots indicate that there is a decreasing trend between yield stress and percent hydrogel; however, the R^2 values are very low.

The elastic modulus was estimated to be 4,000 psi for samples containing hydrogel. This is 2,500 psi less than the modulus estimated for samples without hydrogel. There is no discernable relationship between modulus and concentration of hydrogel.

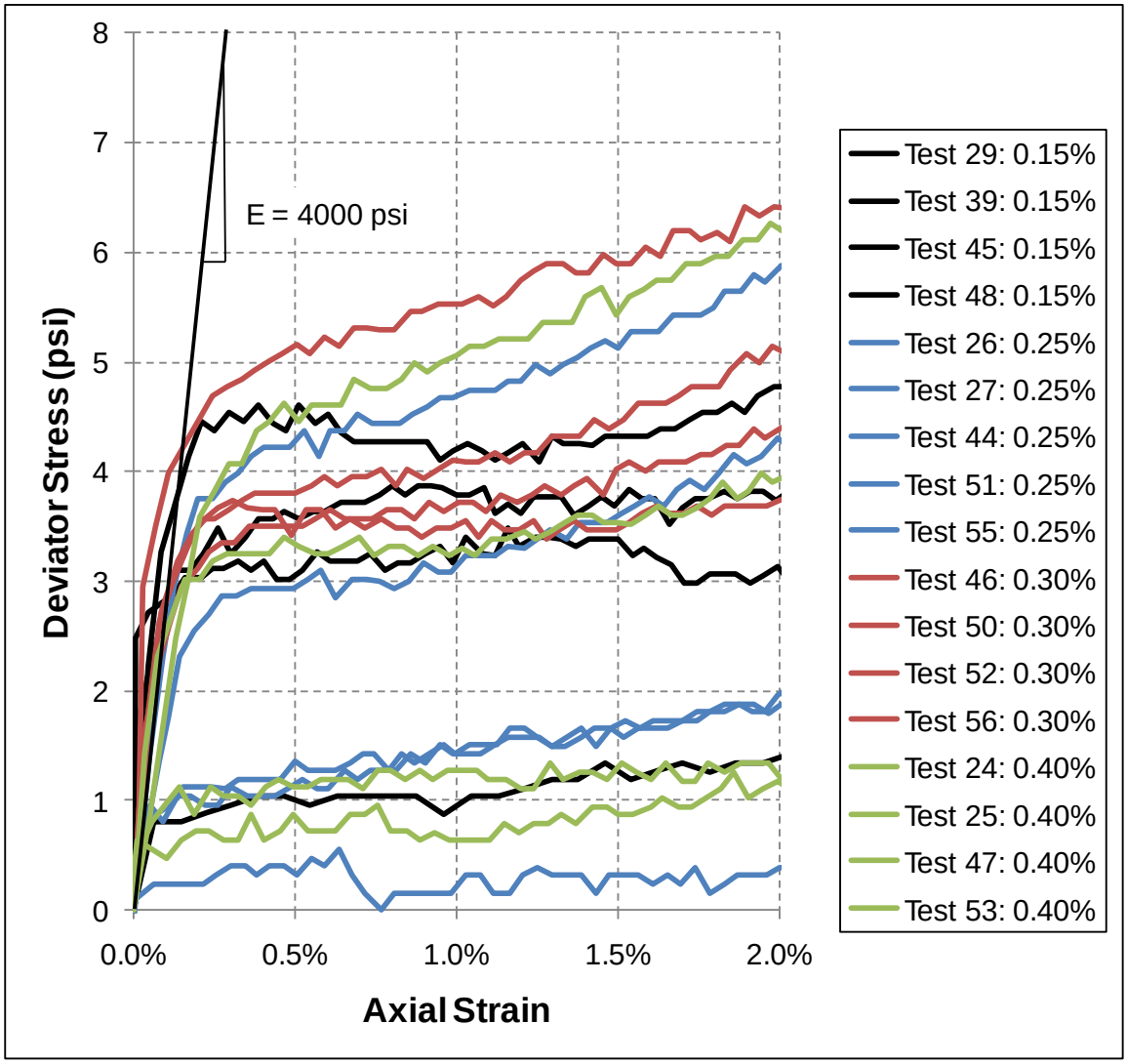

Figure 4.12: Small strain stress-strain response during undrained shear for samples containing different concentrations of hydrogel

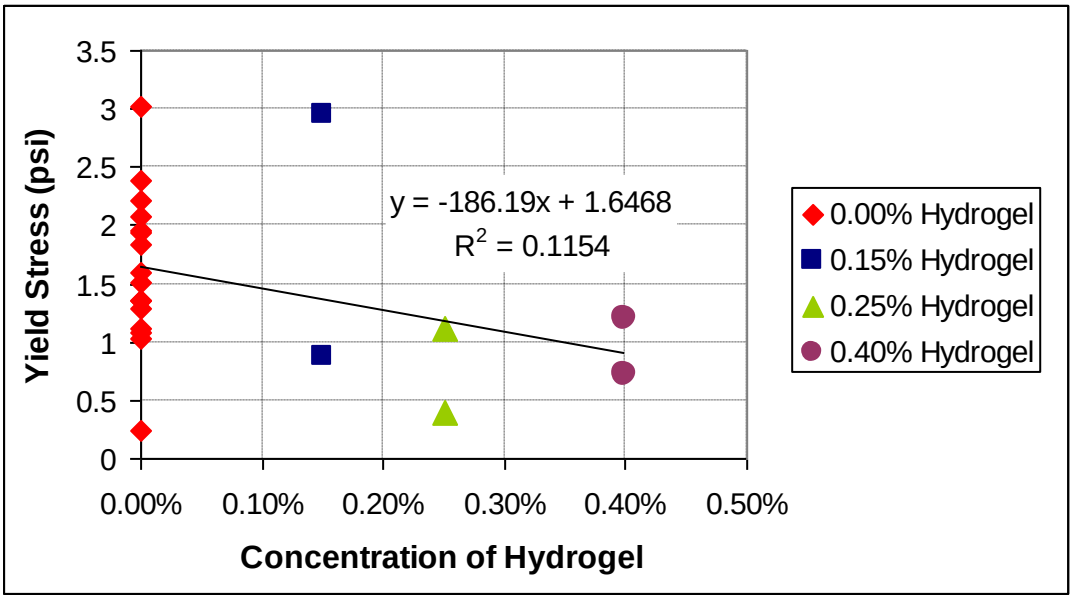

Figure 4.13: Yield Stress vs. % Hydrogel for tests run with σ_3' = 2 psi

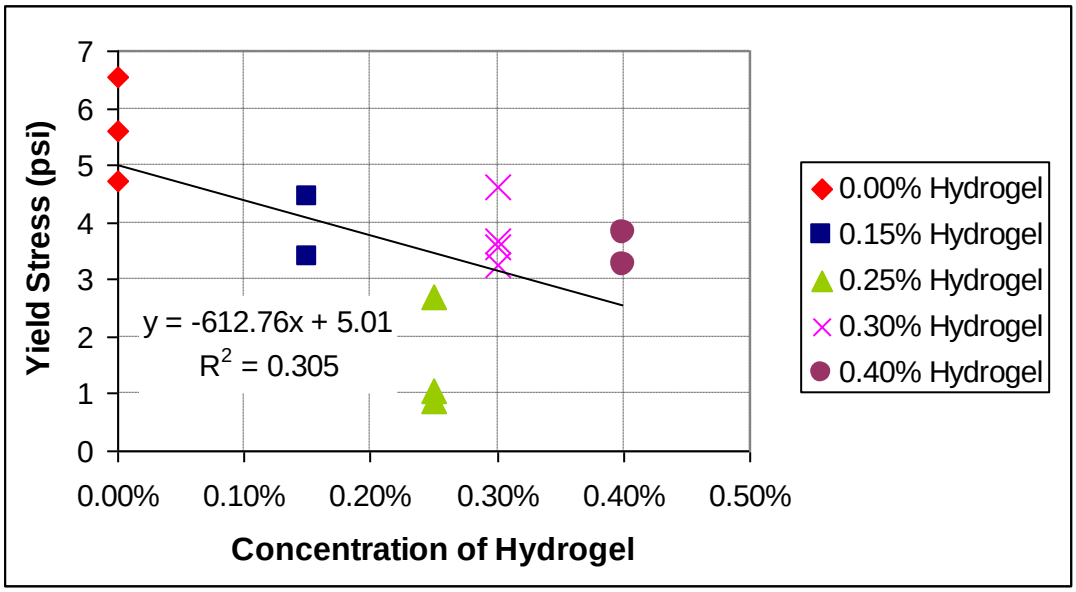

Figure 4.14: Yield Stress vs. % Hydrogel for tests run with σ_3' = 15 psi

4.1.8.3.2 Large Strain Response

As stated in Section 4.1.7.3.2, the stress-strain response beyond the point where ϕ' is fully mobilized is purely a function of pore pressure response. The large strain response for

hydrogel samples is shown in Figure 4.15. Because hydrogel reduces the samples' tendency to generate negative pore pressures at large strains, as was observed for the non-hydrogel samples, the stresses at large strain are typically lower than the large strain stresses of the non-hydrogel samples, with the exception of Test 48. Test 48, a 0.15% hydrogel sample, did not exhibit the same reduction in large strain stress as the other hydrogel samples.

It appears that only a small amount of hydrogel is required to cause a large change in pore pressure response and large strain stress-strain response. There is not a clear relationship between the amount of hydrogel and the reduction in stress. If there was a clear relationship, the different curves on the plot would be grouped with the other curves of the same color; however, this is not the case. Although the data were not perfectly sorted by concentration of hydrogel, the sample that had its strength reduced the least was a 0.15% hydrogel sample, and the sample that had its strength reduced the most was a 0.40% hydrogel sample, indicating there may be some correlation between the amount of hydrogel and the amount of stress reduction.

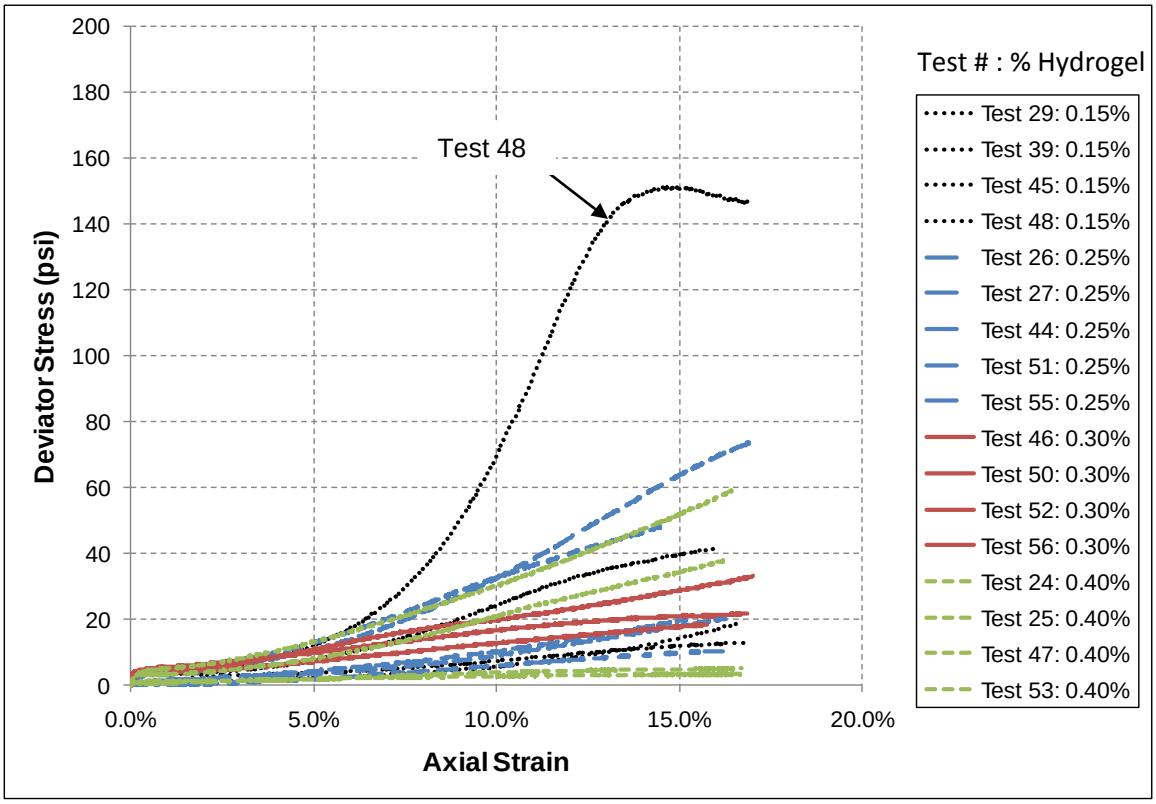

Figure 4.15: Large strain stress-strain response during undrained shear for samples containing hydrogel

4.1.8.4 Effect of Hydrogel on Pore Pressure Response

The pore pressure response of samples not containing hydrogel typically involved a rise in pore pressure to a peak corresponding to the point where ϕ' is 100% mobilized, followed by a dramatic decrease in pore pressure after the peak. For samples containing hydrogel, the small strain pore pressure response is similar. The pore pressures still rise to a peak of similar magnitude to the peaks exhibited by the non-hydrogel samples tested under the same confining pressure.

The response after the initial peak is very different for the hydrogel samples. With the exception of Test 48, all of the samples exhibited consistently smaller decreases in pore pressure than was typically observed for non-hydrogel samples. Figure 4.16 presents the pore pressure

response of tests run on samples containing hydrogel. The tests that have a lower peak increase in pore pressure were run with σ_3' = 2 psi and the ones with the higher peak increase were run with σ_3' = 15 psi.

There is not a clear indication that increased amounts hydrogel have a larger effect on pore pressure response. However, the one sample containing hydrogel that did not behave like the other hydrogel samples, Test 48, was a sample of the lowest concentration, 0.15% hydrogel. Figures 4.17 and 4.18 show the change in pore pressure at 15% strain for 2 psi and 15 psi confined tests, respectively. The data presented in these figures are for a single magnitude of strain (15%) in order to make an standardized comparison of pore pressure response with respect to the amount of hydrogel. The figures do not indicate any clear trends between % hydrogel and the amount of decrease in pore pressure. They do indicate that the presence of any concentration of hydrogel reduces the amount of pore pressure decrease compared to the pore pressure decrease of most non-hydrogel samples.

Ottawa sand with hydrogel is not soil in the traditional sense, and does not necessarily obey the laws of soil mechanics. Because of this, there is question as to whether the pore pressure response measured at the ends of the sample accurately reflects the pore pressure at the failure surface and to whether hydrogel treated Ottawa sand fully obeys the effective stress equation. Without an internal pore pressure measurement, this may remain in question to some extent. However, the results here indicate that the pore pressures are correct and that the hydrogel treated Ottawa sand does obey the effective stress equation. If a material obeys the effective stress equation and the pore pressure measurements are accurate reflections of the pore pressure at the failure surface, then the stress-strain response and the pore pressure responses should be roughly inverses of each other. That is, if the pore pressure decreases by a large

amount during a test, the stress should also increase by a corresponding large amount. If the results do not correspond, then either the pore pressure measurement is incorrect, the material does not obey the effective stress laws of effective stress or both. The stress-strain response reflected the pore pressure response for all of the tests conducted, both hydrogel treated and untreated. This indicates that, at least for the static case, the pore pressure measurements were accurate and that hydrogel treated Ottawa sand does obey the laws of effective stress.

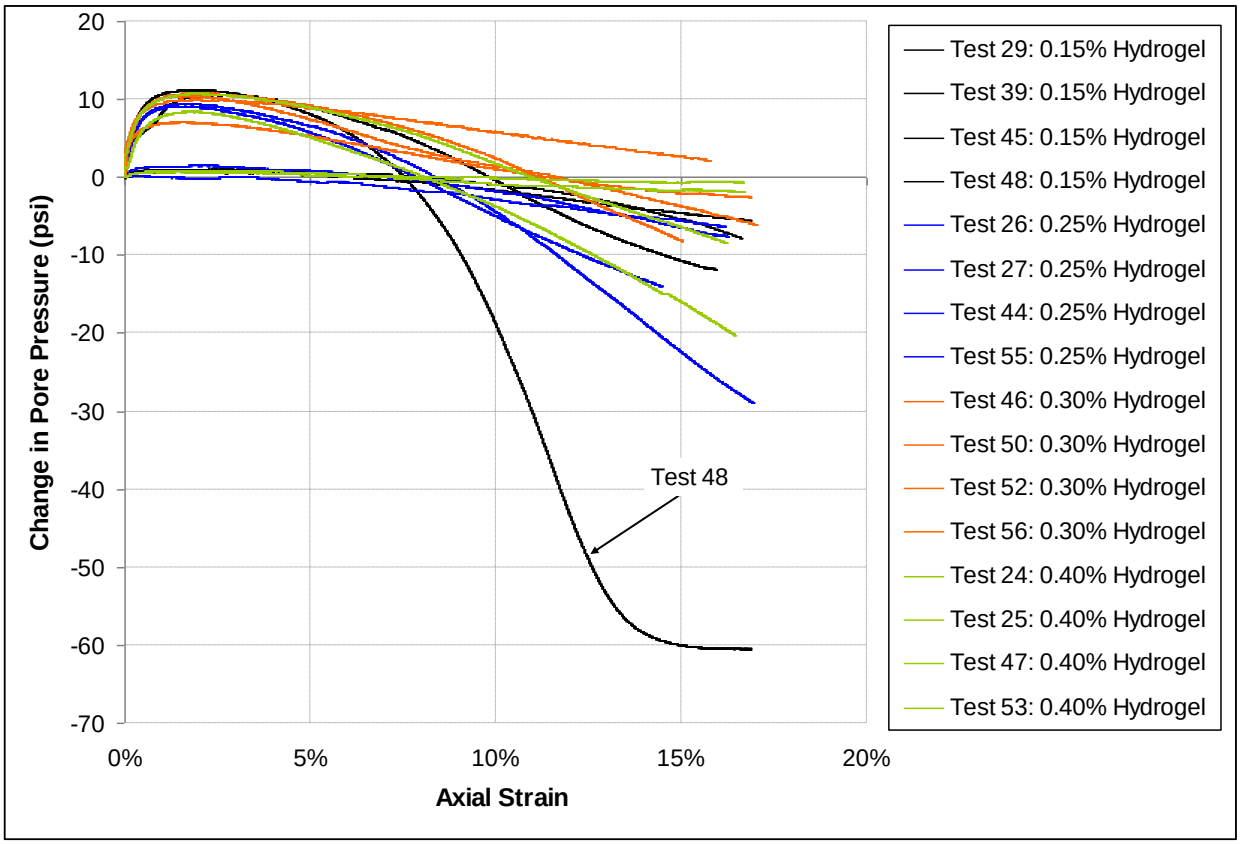

Figure 4.16: Pore pressure response during undrained shear for samples containing hydrogel

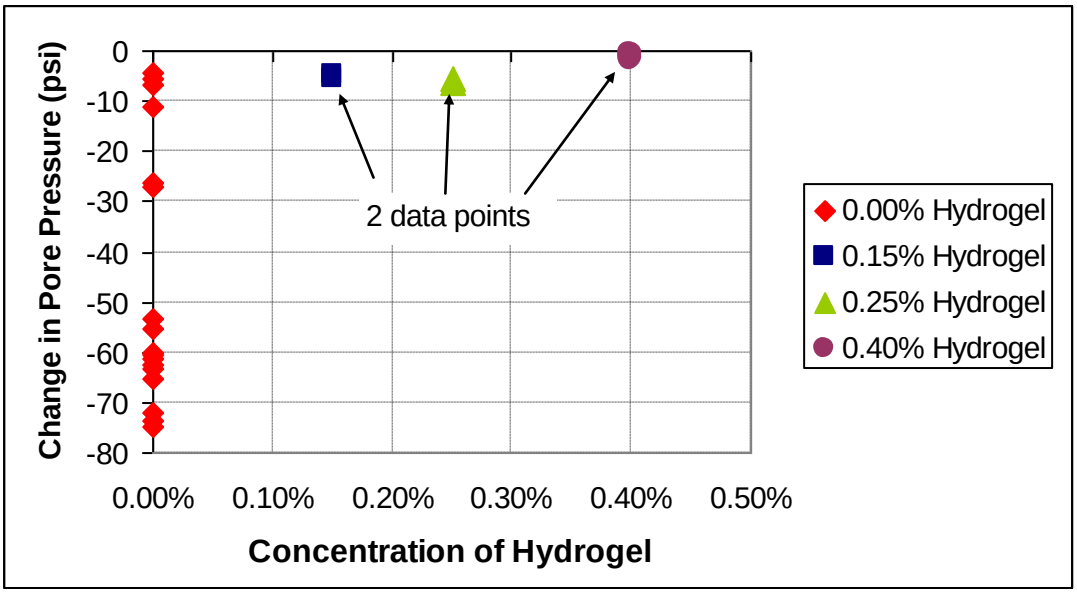

Figure 4.17: Change in Pore Pressure at 15% strain vs. % Hydrogel for 2 psi confined tests

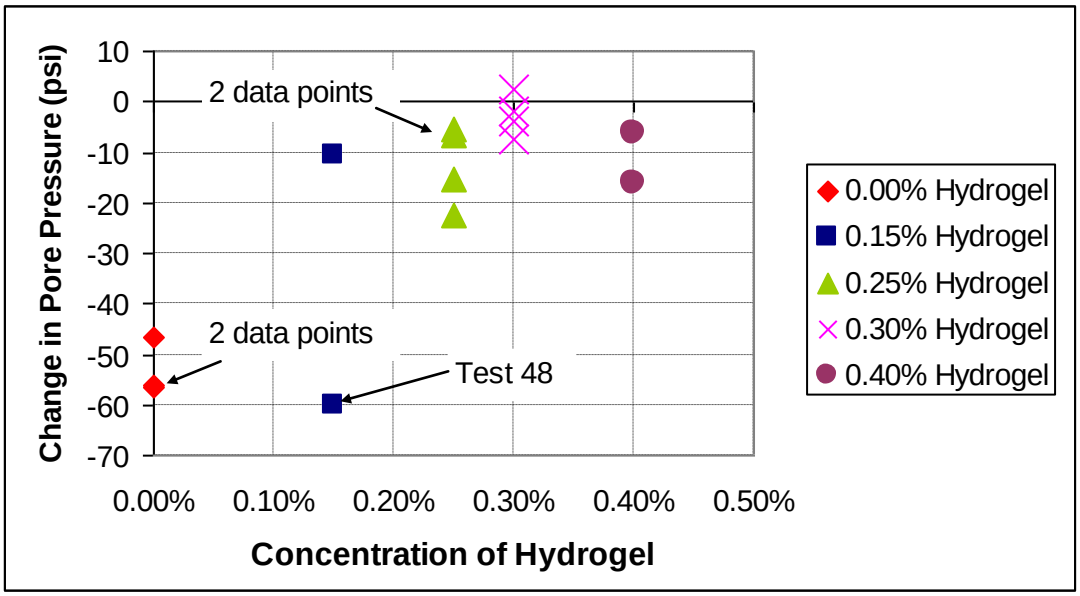

Figure 4.18: Change in Pore Pressure at 15% strain vs. % Hydrogel for 15 psi confined tests

4.1.8.5 Hydrogel Particle Size

The hydrogel particles used for most of the triaxial testing were between 1.8×10^{-3} and 3.0×10^{-3} in in diameter (micro size). Two tests were run on samples prepared with smaller

hydrogel nanoparticles, $3x10^{-6}$ to $1.4x10^{-5}$ in in diameter. The diameter of the micro size particles was known from the sieves used to sort the particles. The diameter of the nanoparticles was determined using a NICOMP 380 particle size analyzer. Samples with hydrogel concentrations of 0.15% and 0.40% were tested using the nanoparticles.

4.1.8.5.1 Effect of Hydrogel Particle Size on Friction Angle

Figure 4.19 compares the effective friction angle measured for the two tests on nanoparticle hydrogel samples to the effective friction angles measured for the samples containing micro size hydrogel. ϕ' for the nanoparticle samples was similar to ϕ' for samples with micro size particles of the same hydrogel concentration. The best fit equation (-1507.4x + 31.9) and the R^2 (0.629) value with the nanoparticle hydrogel data points are similar to that without the inclusion of the nanoparticle data points (-1542.3x + 31.9 with $R^2 = 0.626$). This indicates that nanoparticle hydrogel effect the friction angle in the same way the microparticle hydrogel does.

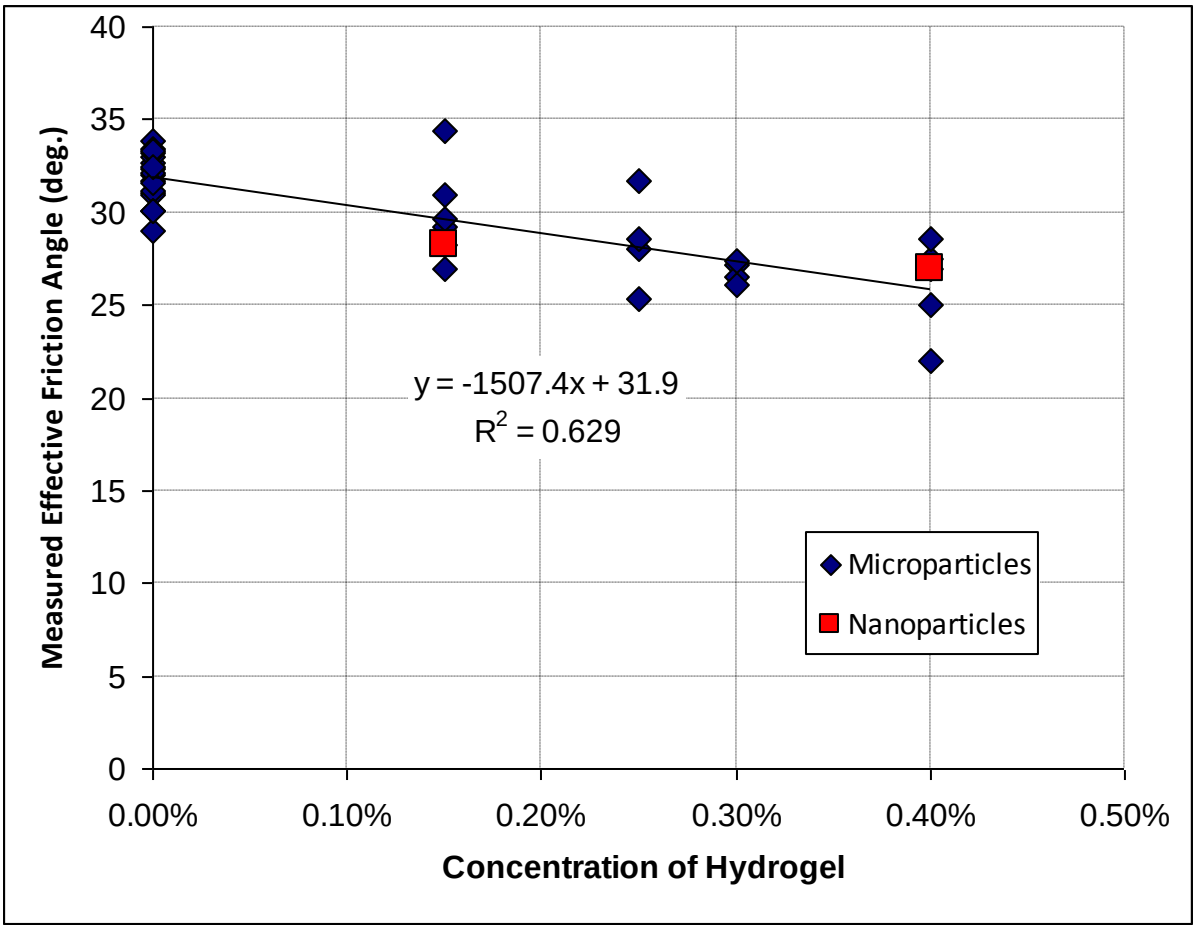

Figure 4.19: Measured effective friction angle for two samples of nanoparticle hydrogel compared to the measured effective friction angle of samples of microparticle hydrogel

4.1.8.5.2 Effect of Hydrogel Particle Size on Stress-Strain Response

Figures 4.20 and 4.21 show the small and large strain stress-strain responses for the two nanoparticle samples. The stress-strain responses of Test 41 and 52 are presented for the purpose of comparing the nanoparticle results with typical micro size hydrogel and non-hydrogel results. All of the tests presented in Figures 4.20 and 4.21 were run with σ_3'=15 psi.

For small strains, the 0.15% hydrogel nanoparticle sample behaved similarly to the microparticle hydrogel samples in terms of yield stress and elastic modulus. The 0.40% nanoparticle hydrogel sample exhibited a much higher yield stress than what is typical even for a

non-hydrogel sample and a modulus similar to that of a non-hydrogel sample. Because more tests were not performed on samples containing nanoparticle hydrogel, it is not known if the high yield stress of Test 57 is a typical or extraneous result. The facts that Test 54 matches the other data so well and that no other tests exhibited such a high yield stress seem to indicate that the results of Test 57 are not typical.

For large strains, both the 0.15% and 0.40% nanoparticle hydrogel samples exhibited stress-strain responses that fall between the typical responses of untreated hydrogel samples and samples with microparticle hydrogel.

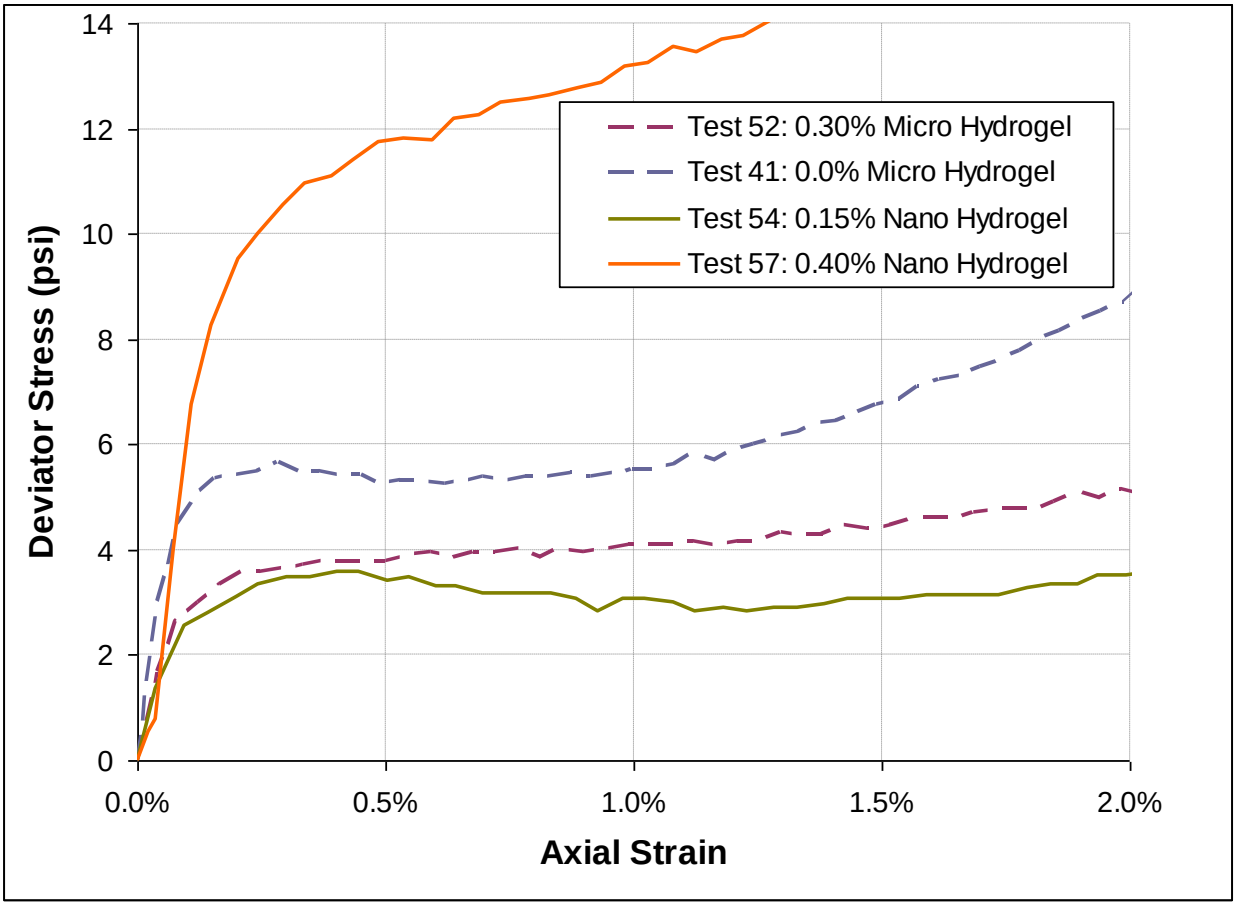

Figure 4.20: Small strain stress-strain response of nanoparticle hydrogel samples (Tests 54 and 57) compared to the response of microparticle hydrogel samples (Test 41 and 52)

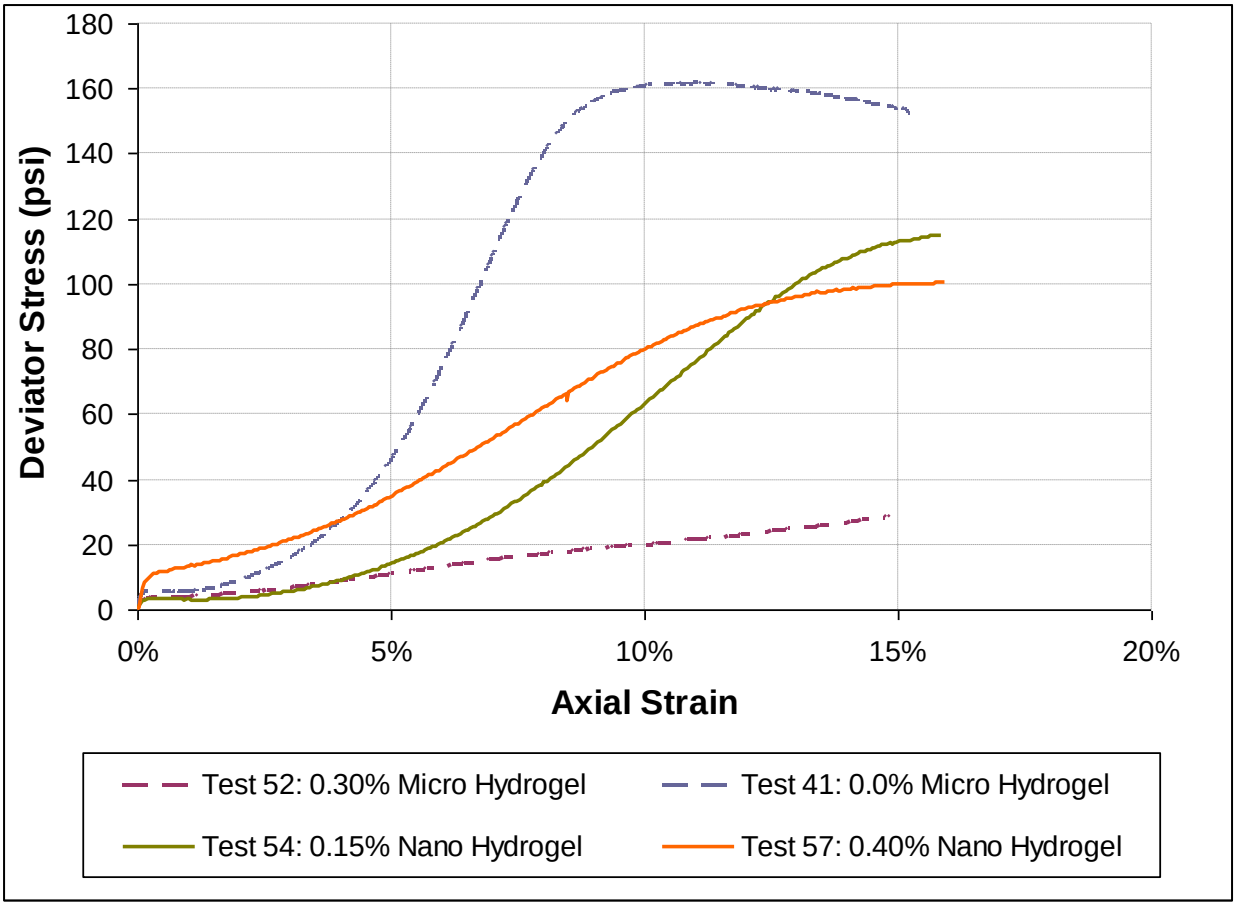

Figure 4.21: Large strain stress-strain response of nanoparticle hydrogel samples (Tests 54 and 57) compared to the response of microparticle hydrogel samples (Test 41 and 52)

4.1.8.5.3 Effect of Partice Size on Pore Pressure Response

Figure 4.22 shows the pore pressure responses of the two nanoparticle samples, Tests 54 and 57. The stress-strain responses for Test 41 and 52 (microparticle samples) are presented for the purpose of comparing the nanoparticle results with typical micro size hydrogel and non-hydrogel results. The initial increase in pore pressure is similar for all four tests except for Test 57 which was slightly lower. Test 57 also exhibited a higher yield stress, which one would expect for a smaller increase in pore pressure. After the initial peak, the samples containing nano size hydrogel exhibited a larger drop in pore pressure than was typically observed for the micro size hydrogel samples but less than what was typically observed for non-hydrogel samples.

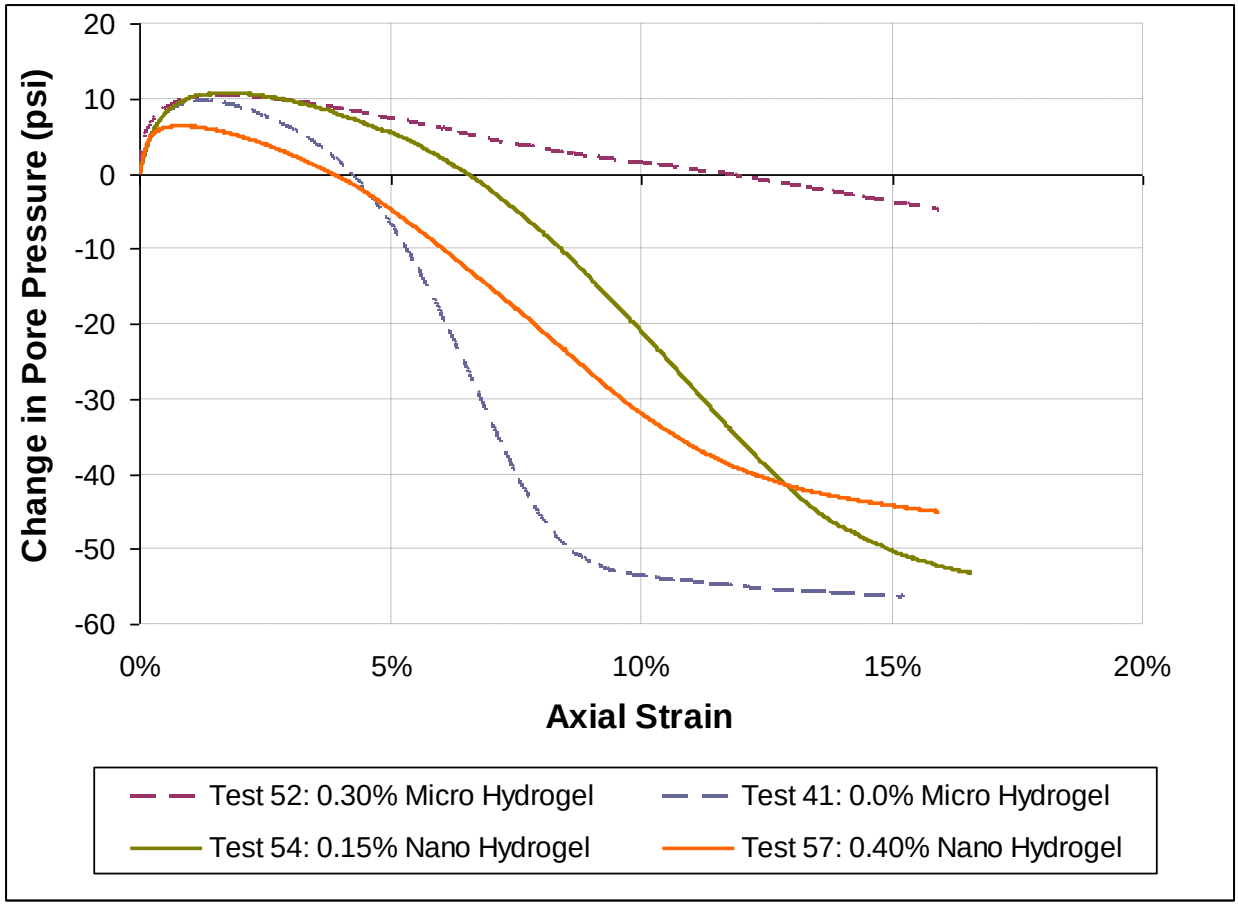

Figure 4.22: Pore pressure response of nanoparticle hydrogel samples compared to the response of microparticle hydrogel samples

4.2 Stress-controlled Cyclic Triaxial Tests

4.2.1 Overview

Stress-controlled cyclic triaxial tests were performed to evaluate the effect of hydrogel on the liquefaction susceptibility of Ottawa sand. The testing generally followed ASTM D5311 as described in Section 3.6. The tests were performed by Dr. Richard Ray at the University of South Carolina. Three sets of tests have been performed. An initial set of tests were performed in 2004 on three different concentrations of hydrogel: 0.00%, 0.16%, and 0.33%. In 2008, a second set of tests was conducted on 0.00%, 0.15%, 0.25%, 0.30%, and 0.40% samples.

However, the testing machine was not functioning properly during this set of tests, and Dr. Ray reported that the samples were not of high quality. As a result, the 2008 data are considered to be invalid. In 2010, a third set of tests was performed on the same hydrogel concentrations as the 2008 tests to replace invalid data from those tests. With the exception of one of the 0.00% hydrogel results (from 2004), all of the data presented in the body of this paper are from the 2010 testing. Additional results from the 2004 and 2008 testing are presented in Appendix F.

4.2.2 Selection of Percent Hydrogel

The percentages of hydrogel used in the 2008 and 2010 sets of tests (0.00%, 0.15%, 0.25%, 0.30%, and 0.40%) are the same as the percentages used for the static triaxial testing and consolidation testing. These concentrations were selected based on consistency in testing and the reasoning presented in Section 4.1.2. The 2004 tests were preliminary tests, using only three percentages of hydrogel: 0.00%, 0.15%, and 0.33%.

4.2.3 Factors Affecting Cyclic Triaxial Testing

4.2.3.1 Cyclic Stress Ratio (CSR)

Unlike a traditional static triaxial compression test where the deviator stress is increased until the sample fails, a deviator stress is applied in the form of a sinusoidal wave repeatedly until the sample fails. The sinusoidal wave is uniform, i.e., the maximum deviator stress is not increased to induce failure. Instead, failure (liquefaction) is induced by the repeated loading the sample. The number of cycles required to reach failure for a given cyclic deviator stress and confining stress is how failure is described. For a static triaxial compression test, the failure stress (σ'_{1f}) is a function of the effective confining stress (σ'_3). For a cyclic triaxial test, σ'_1 is varied in a controlled manner independent of σ'_3, and the number cycles to failure, N_f, is the variable. N_f is a function of both σ'_3 and σ'_1.

CSR is a way of defining the stress state of cyclically loaded soil element and is defined as:

$$\text{CSR} = \frac{\sigma_{dc}}{2\sigma_3'} \tag{4.2}$$

for a cyclic triaxial test, where σ_{dc} is the maximum cyclic deviator stress. It is important to note that CSR for a cyclic triaxial test is different than CSR measured during an earthquake or from other tests. CSR from a triaxial test cannot be directly compared to CSR as defined by equation 2.3. Ultimately, CSR is somewhat analogous to σ_3' for a static triaxial compression test. It provides a frame of reference for comparing results.

4.2.3.2 Void Ratio

Void ratio is a very important factor in cyclic triaxial testing. The densification of a loose soil structure is ultimately what leads the increased pore pressures that cause liquefaction. Thus initial void ratio has a significant impact on the results of a test. Dense samples with low void ratios are less susceptible to liquefaction, and loose samples with high void ratios are more susceptible to liquefaction. The reasoning why void ratio effects pore pressure response is the same as that for static triaxial testing presented in Section 4.1.3.3. The discussion on variation in void ratio during sample preparation presented in Section 4.1.3.1 is also valid for cyclic testing because the samples were prepared using the same methods.

4.2.3.3 Saturation

Like other geotechnical tests such as static triaxial testing, testing a sample at 100% saturation is critical for accurately understanding the pore pressure response during testing. As described in Section 3.4.3, sample saturation was verified using Skempton's B coefficient (B).

Skempton's B coefficient is the ratio of change in pore pressure to change in confining pressure under undrained conditions (Equation 3.2). Theoretically, because water is an incompressible fluid, B should equal to 1 for a fully saturated sample. In reality, the B value of a saturated sample is often close to but not equal to 1. It has been shown that the degree of saturation is often higher than the B value itself (Black and Lee 1973). All but one cyclic triaxial test for this research was performed with a B value of 0.94 or higher. One test, 0.30% A-Test 1, was performed with a B value of 0.87.

4.2.4 Test Results

4.2.4.1 Introduction

Due to the many variables involved in cyclic triaxial testing it is not easy to simplify data into one plot or table that conveys all the pertinent information in a straightforward manner. It is often desirable to compare data both against different data from an individual test and against similar data from other tests. For these reasons, some of the cyclic triaxial data will be presented multiple times in order to make visible comparisons between data plots easier for the reader.

Basic sample data is presented in Table 4.5. Some of this information is also presented on the data plots themselves. It is important to note that in many cases a single sample was tested twice, once at a low CSR and then again with a higher CSR. Tests indicated as "Test 2," with the same sample name, were run on the same samples as tests marked as "Test 1." The names of the 2010 tests follow the form: 0.XX% A – Test #, where the 0.XX% is the concentration of hydrogel by mass expressed as a percentage, A indicates which sample of that concentration (either A or B), and the test number indicates if it is the first or second test on that sample. One test on a 0.00% hydrogel sample from the 2004 testing is presented, it is

designated as 0.00% n8-04 – Test 1, which means 0.00% hydrogel sample number 8 of 2004, first test. The abbreviation Hyd. in the figures means hydrogel concentration by mass.

Table 4.5: Cyclic triaxial basic sample and test data; the % in the sample name indicates the % concentration of hydrogel by mass

Sample Name	Test	CSR	B	γ_d (pcf)	e_o
0.00% A	1 2	0.15 0.26	0.95	91.7	0.80
0.00% n8-04	1	0.19	0.97	92.4	0.79
0.15% A	1	0.23	0.95	93.5	0.77
0.15% B	1	0.14	0.95	92.5	0.79
0.25% A	1	0.27	0.94	90.7	0.82
0.25% B	1 2	0.14 0.26	0.92	91.6	0.81
0.30% A	1	0.20	0.87	93.6	0.77
0.30% B	1 2	0.10 0.16	0.94	94.4	0.75
0.40% A	1	0.22	1.00	90.2	0.83
0.40% B	1* 2	N/A 0.23	0.94	91.1	0.82

*Data for 0.40% A Test 1 was not saved prior to Test 2 and was overwritten by Test 2

4.2.4.2 Deviator Stress Behavior under Cyclic Loading

During the stress-controlled triaxial tests the isotropically consolidated sample is subjected to a cyclic axial stress or deviator stress that is applied in the form of a sinusoidal wave, in this case at 1 Hz frequency. This load wave causes a 90° change in the direction of the major principal stress occurring during the two halves of the loading cycle (ASTM 2004a). In other words, the maximum compressive force rotates from the axial direction to the radial direction through one cycle. As this loading occurs, pore pressures tend to build as the sand grains attempts to densify under undrained conditions. Once the pore pressure has reached a value close or equal to the effective confining pressure liquefaction is said to occur, and the

deviator stress wave usually degrades because the sample can no longer resist the resulting shear stress.

The samples that do not contain hydrogel behave as would be expected for a sand subjected to cyclic loading. When tested at a CSR of 0.15, Sample 0.00%A did not liquefy (Figure 4.23). It maintained a uniform sinusoidal load wave for 200 cycles. Two tests on 0.00% hydrogel samples where run at higher CSR's of 0.19 and 0.26. These samples liquefied after only 5 cycles (Figures 4.24 and 4.25), liquefaction being defined as the point at which effective stress reaches zero. This indicates that the threshold for liquefaction of plain very loose Ottawa sand during a cyclic triaxial test is somewhere between CSR = 0.15 and 0.19. At the point liquefaction occurred, the stress wave quickly diminished.

The samples containing hydrogel, on the other hand, did not exhibit the same cyclic strength as the untreated samples. Hydrogel samples liquefied (the effective stress reached zero) after less than 100 cycles in every test even with CSR lower than 0.15. The point at which liquefaction occurs can be most easily identified in the effective stress plots shown in Figures 4.52 through 4.61; however, the number of cycles to liquefaction is indicated in the captions of the stress plots (Figures 4.26 to Figure 4.35). Specifically, tests on Samples 0.15%B (Figure 4.27), 0.25%B (Figure 4.29), and 0.30% B (Figure 4.32) conducted at CSR less than 0.15 all liquefied at 52 cycles or less, indicating that hydrogel actually increases the samples' susceptibility to liquefaction, where liquefaction is being defined as the point when effective stress reaches zero. This makes sense in light of the static triaxial tests results, which indicated a reduction in shear strength with increased amounts of hydrogel.

The hydrogel samples also behave quite differently after liquefaction has occurred. With the exception of Sample 0.15%A-Test 1 (Figure 4.26), all of the samples containing hydrogel

maintain significant cyclic strength. There is a slight reduction in the maximum deviator stresses when liquefaction occurs, but this reduction is small compared to the dramatic degradation of the stress wave exhibited by the *untreated* samples (Figures 4.24 and 4.25). This behavior indicates that the hydrogel samples are maintaining shear strength even after the effective stress has reached zero. Although hydrogel does not appear to reduce liquefaction susceptibility by preventing pore pressure buildup, it does not appear to lose nearly as much strength, which is ultimately a key component of liquefaction induced failures.

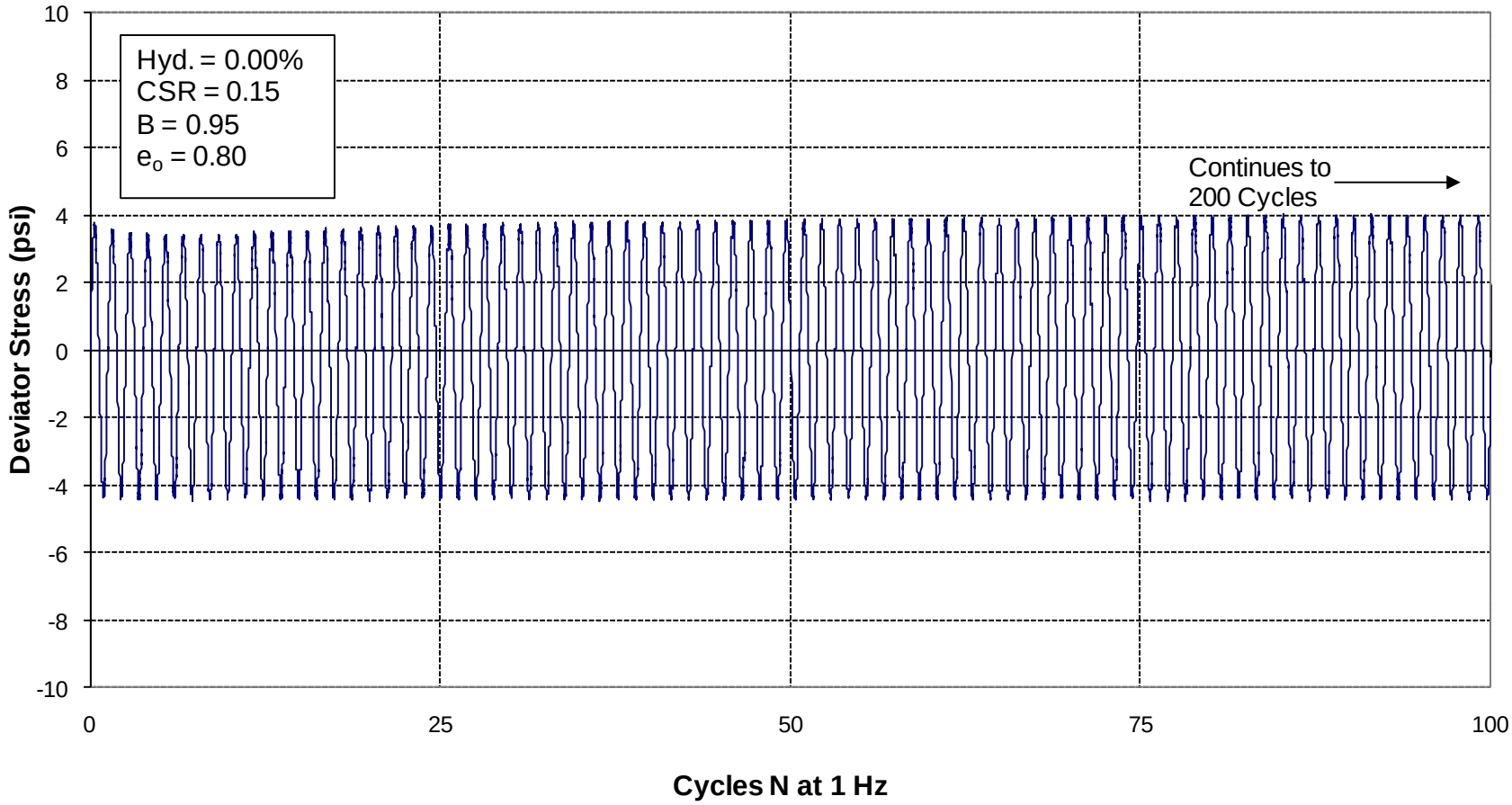

Figure 4.23: Deviator Stress vs. Cycles for Ottawa sand Sample 0.00%A-Test 1 (0.00% hydrogel); liquefaction did not occur; test was ended at 200 cycles

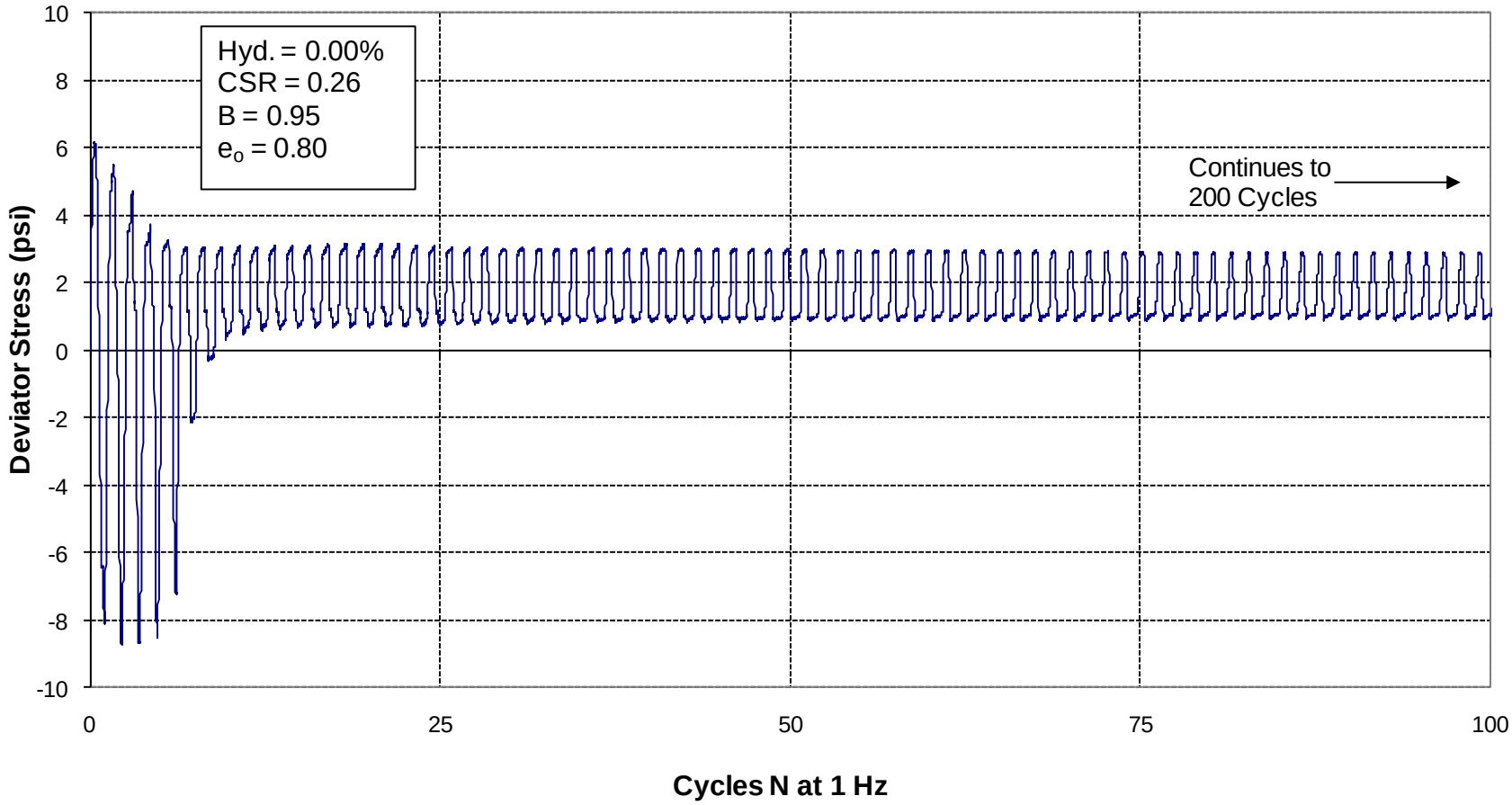

Figure 4.24: Deviator Stress vs. Cycles for Ottawa Sand Sample 0.00%A-Test 2 (0.00% hydrogel); liquefaction occurred after 5 cycles; test was ended at 200 cycles

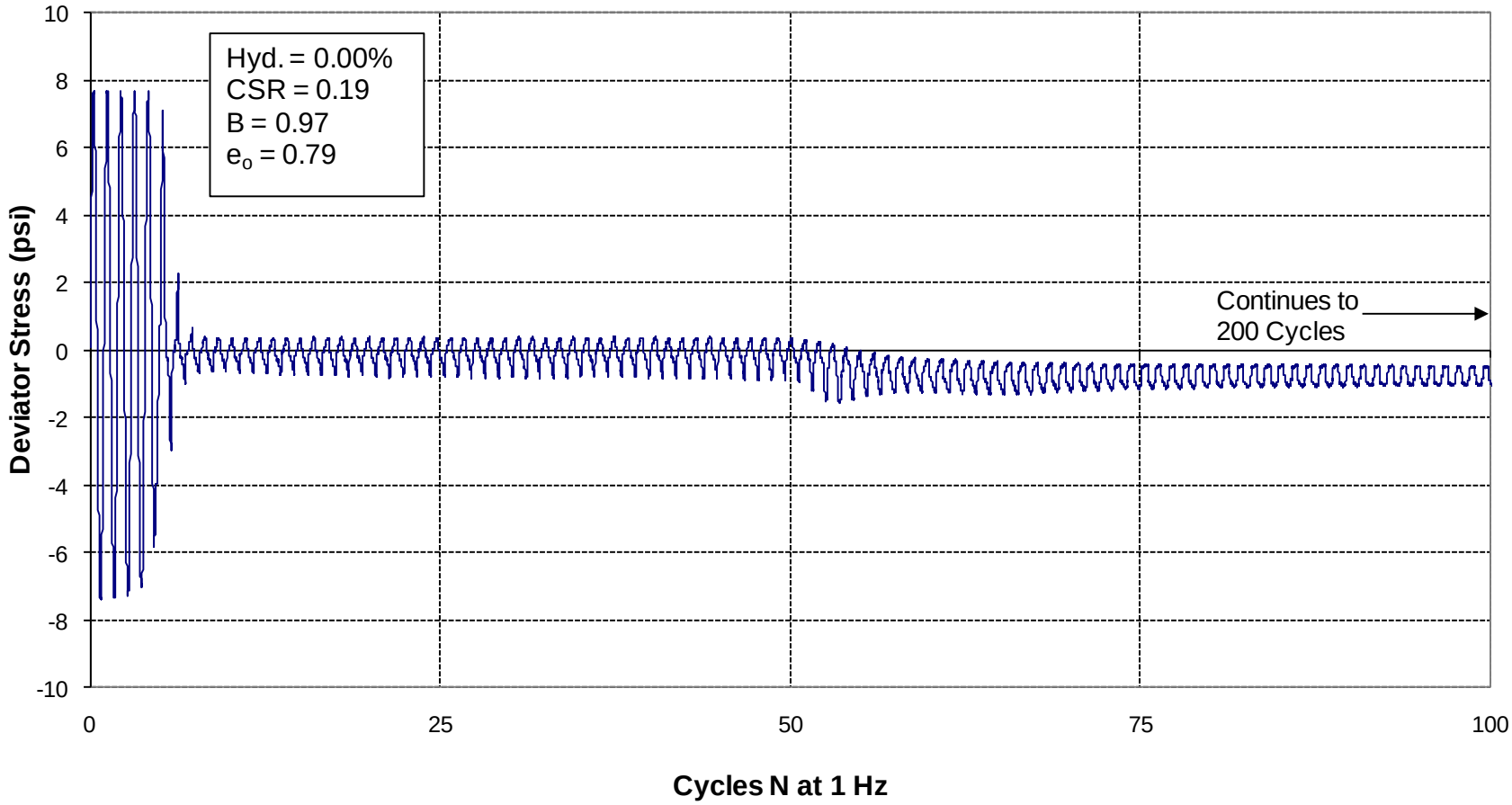

Figure 4.25: Deviator Stress vs. Cycles for Ottawa Sand Sample 0.00%n8-04-Test 1 (0.00% hydrogel); liquefaction occurred after 5 cycles; test was ended at 200 cycles

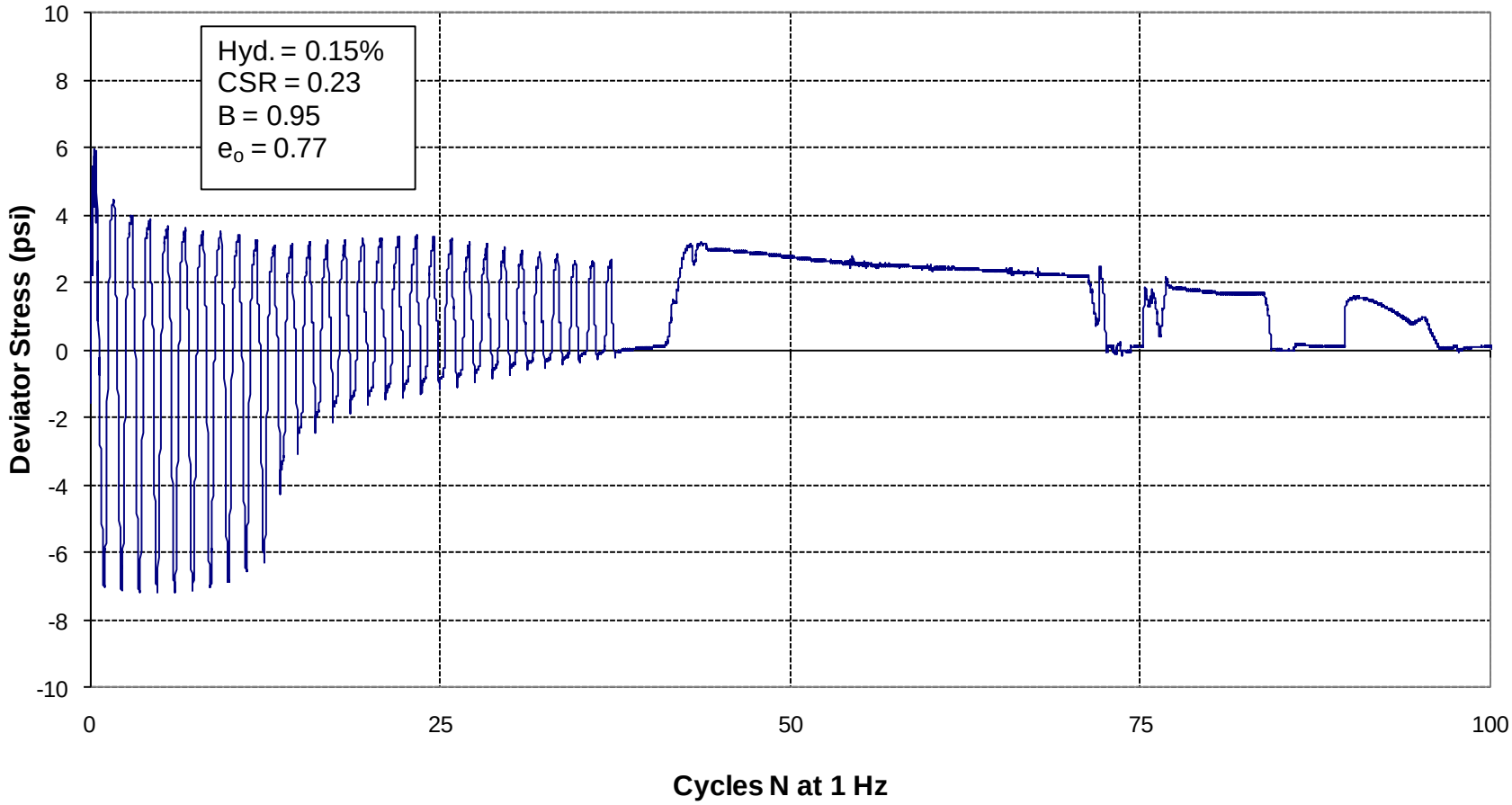

Figure 4.26: Deviator Stress vs. Cycles for hydrogel treated Ottawa sand Sample 0.15%A-Test 1 (0.15% hydrogel); liquefaction occurred after 3 cycles, significant strength was maintained through approximately 12 cycles; issues with the testing equipment occurred at 38 cycles

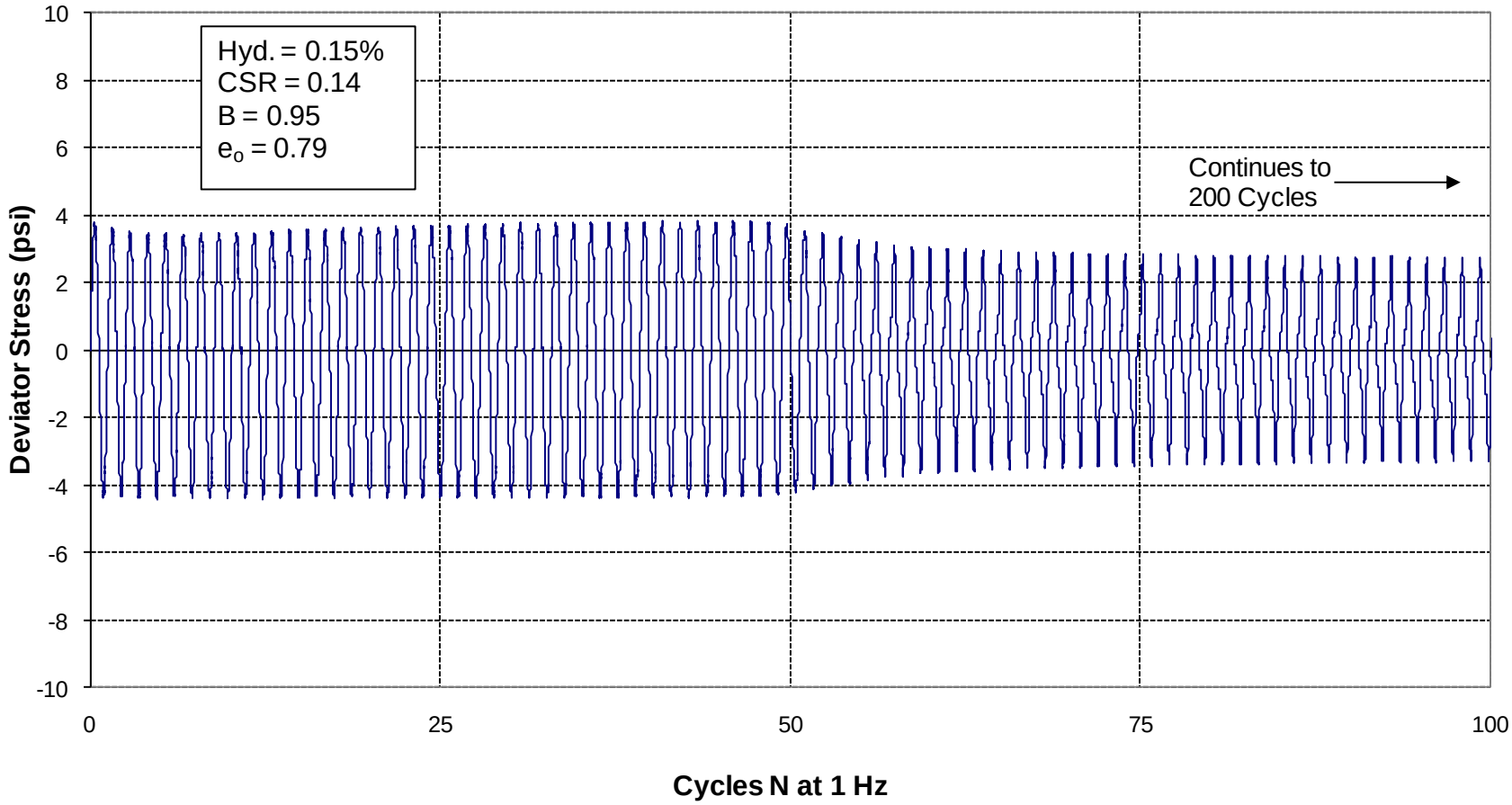

Figure 4.27: Deviator Stress vs. Cycles for hydrogel treated Ottawa sand Sample 0.15%B-Test 1 (0.15% hydrogel); liquefaction occurred after 52 cycles; significant strength was maintained until the test was ended at 200 cycles

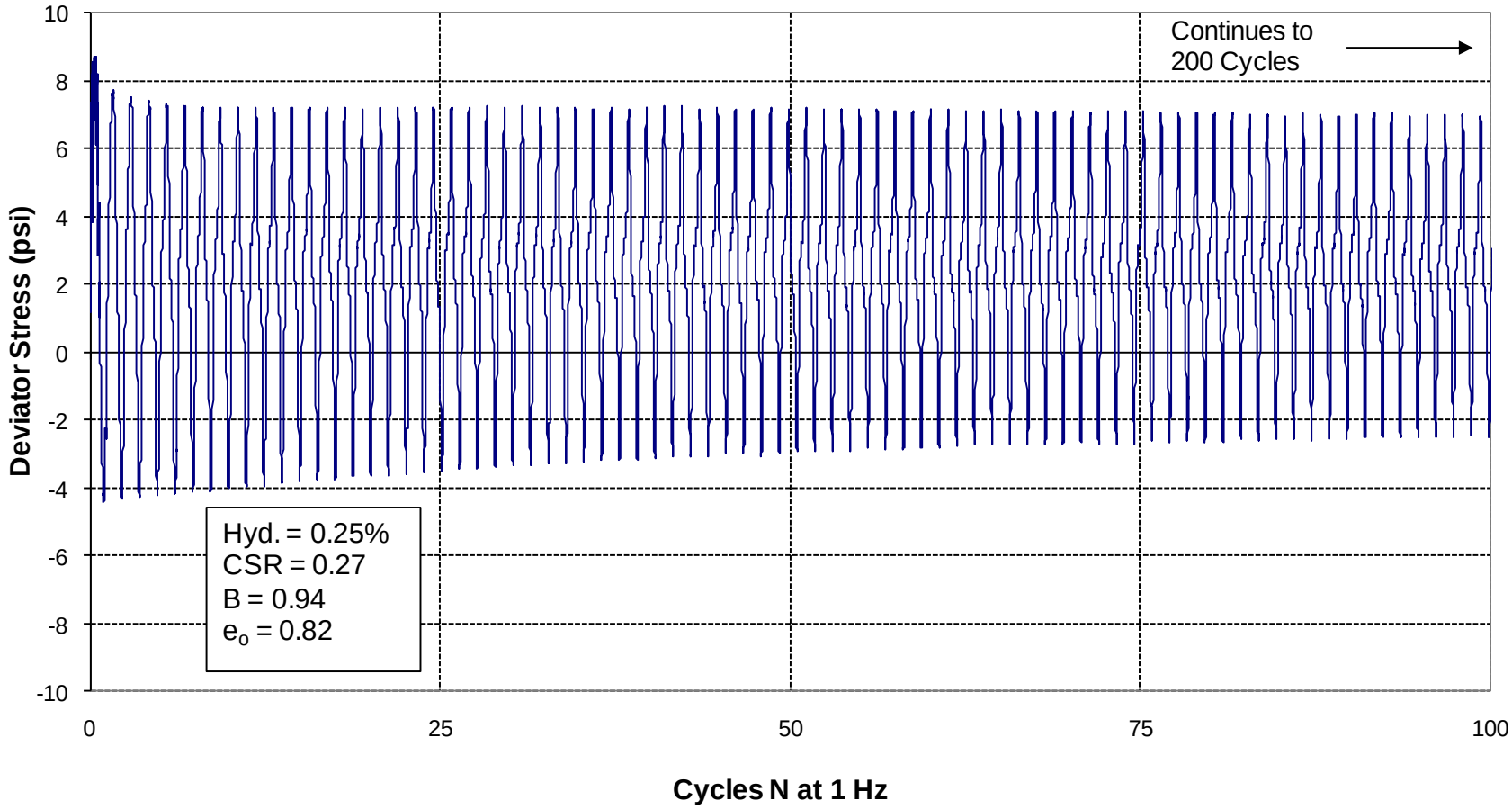

Figure 4.28: Deviator Stress vs. Cycles for hydrogel treated Ottawa sand Sample 0.25%A-Test 1 (0.25% hydrogel); liquefaction occurred after 3 cycles; significant strength was maintained until the test was ended at 200 cycles

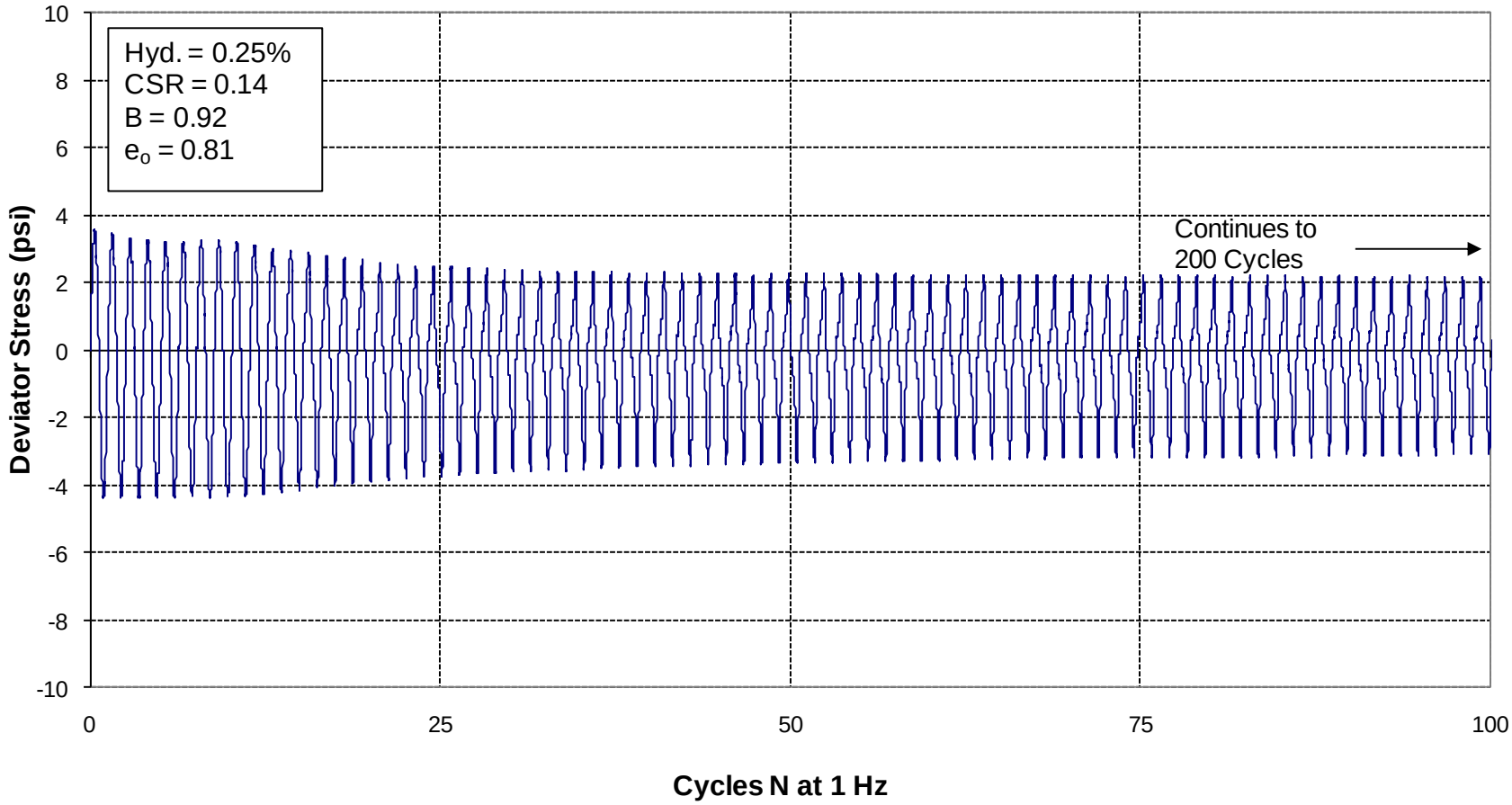

Figure 4.29: Deviator Stress vs. Cycles for hydrogel treated Ottawa sand Sample 0.25%B-Test 1 (0.25% hydrogel); liquefaction occurred after 17 cycles; significant strength was maintained until the test was ended at 200 cycles

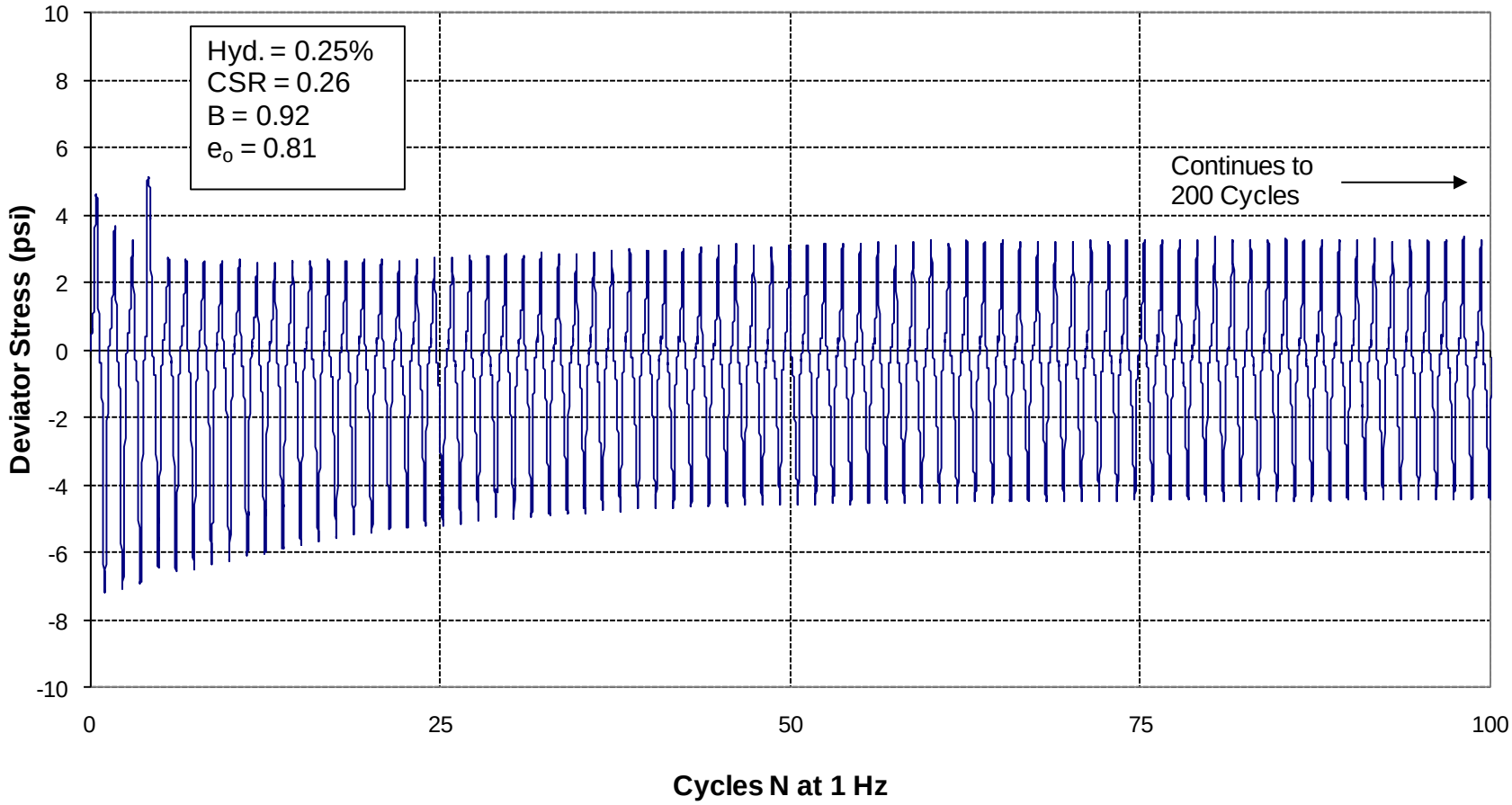

Figure 4.30: Deviator Stress vs. Cycles for hydrogel treated Ottawa sand Sample 0.25%B-Test 2 (0.25% hydrogel); liquefaction occurred immediately; significant strength was maintained until the test was ended at 200 cycles

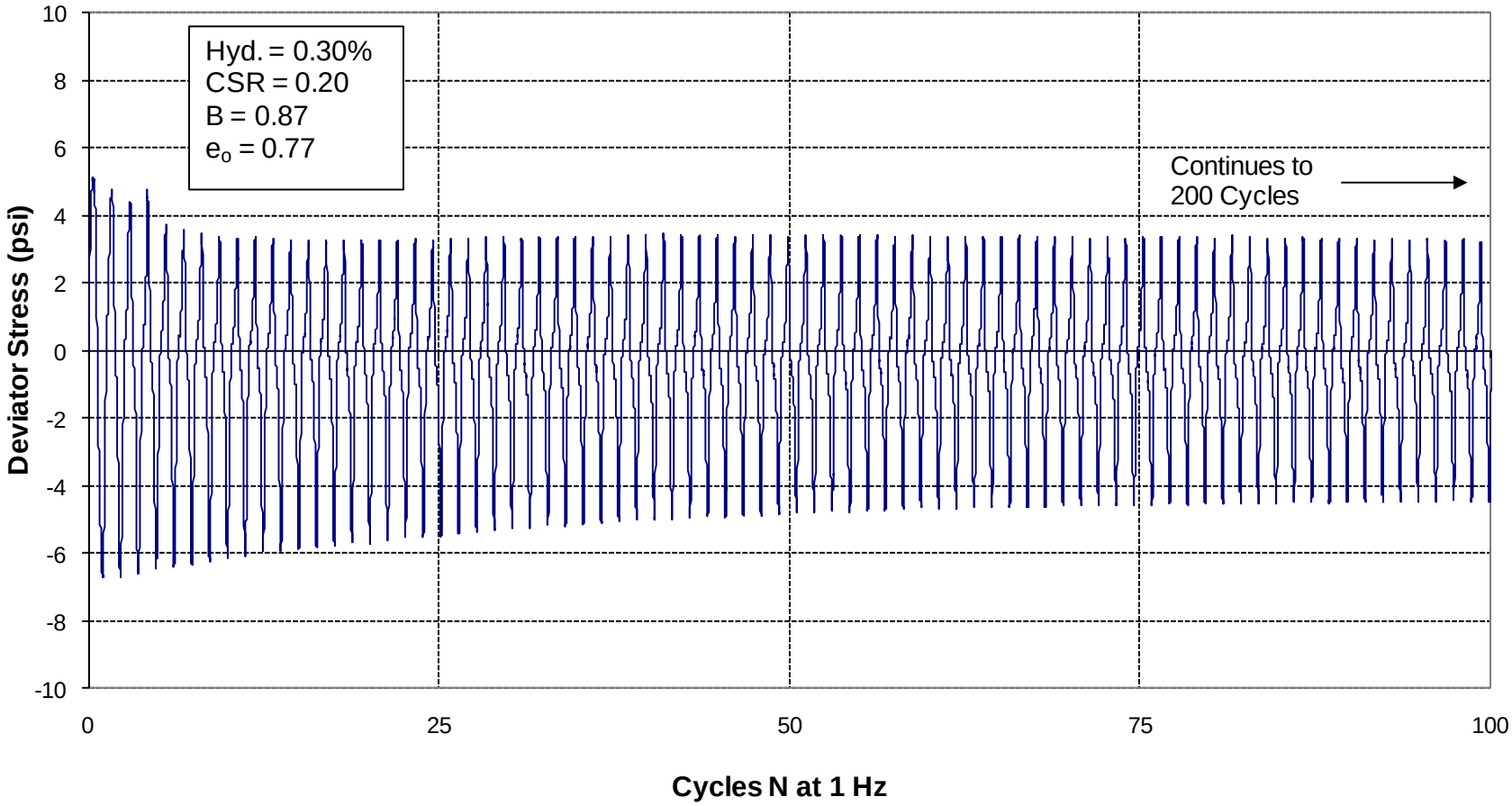

Figure 4.31: Deviator Stress vs. Cycles for hydrogel treated Ottawa sand Sample 0.30%A-Test 1 (0.30% hydrogel); liquefaction occurred after 3 cycles; significant strength was maintained until the test was ended at 200 cycles

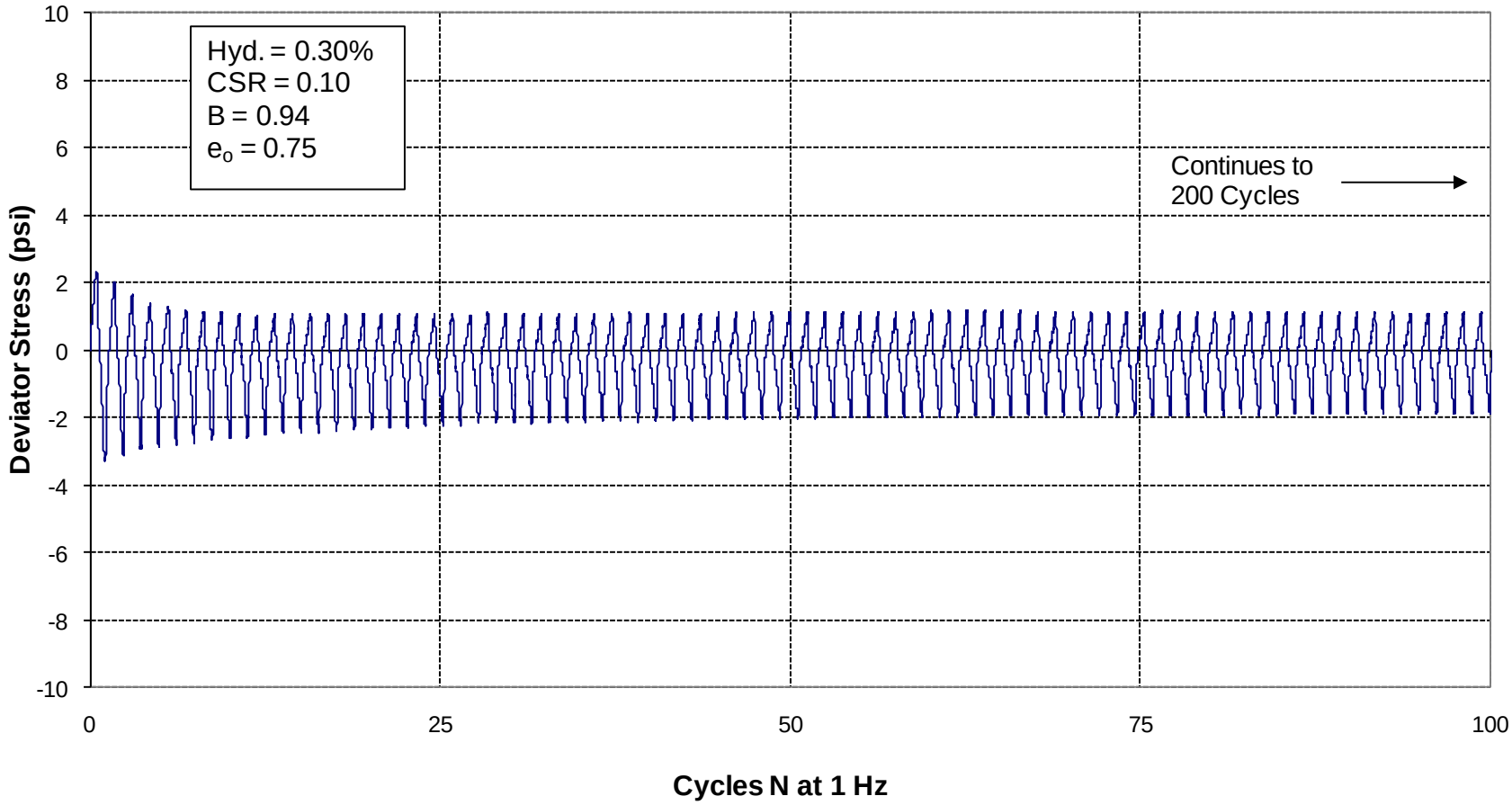

Figure 4.32: Deviator Stress vs. Cycles for hydrogel treated Ottawa sand Sample 0.30%B-Test 1 (0.30% hydrogel); liquefaction occurred after 4 cycles; significant strength was maintained until the test was ended at 200 cycles

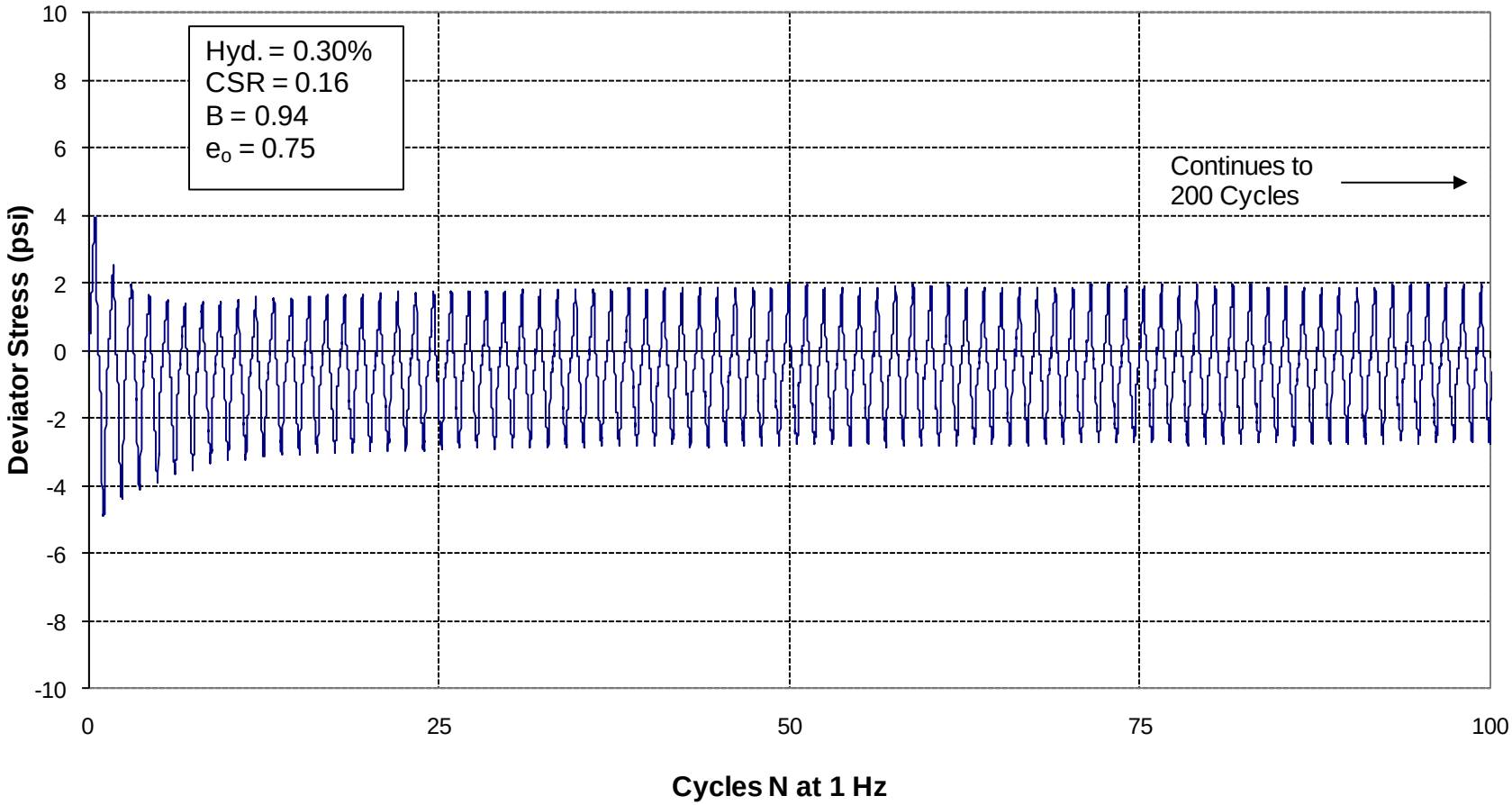

Figure 4.33: Deviator Stress vs. Cycles for hydrogel treated Ottawa sand Sample 0.30%B-Test 2 (0.30% hydrogel); liquefaction occurred immediately; significant strength was maintained until the test was ended at 200 cycles

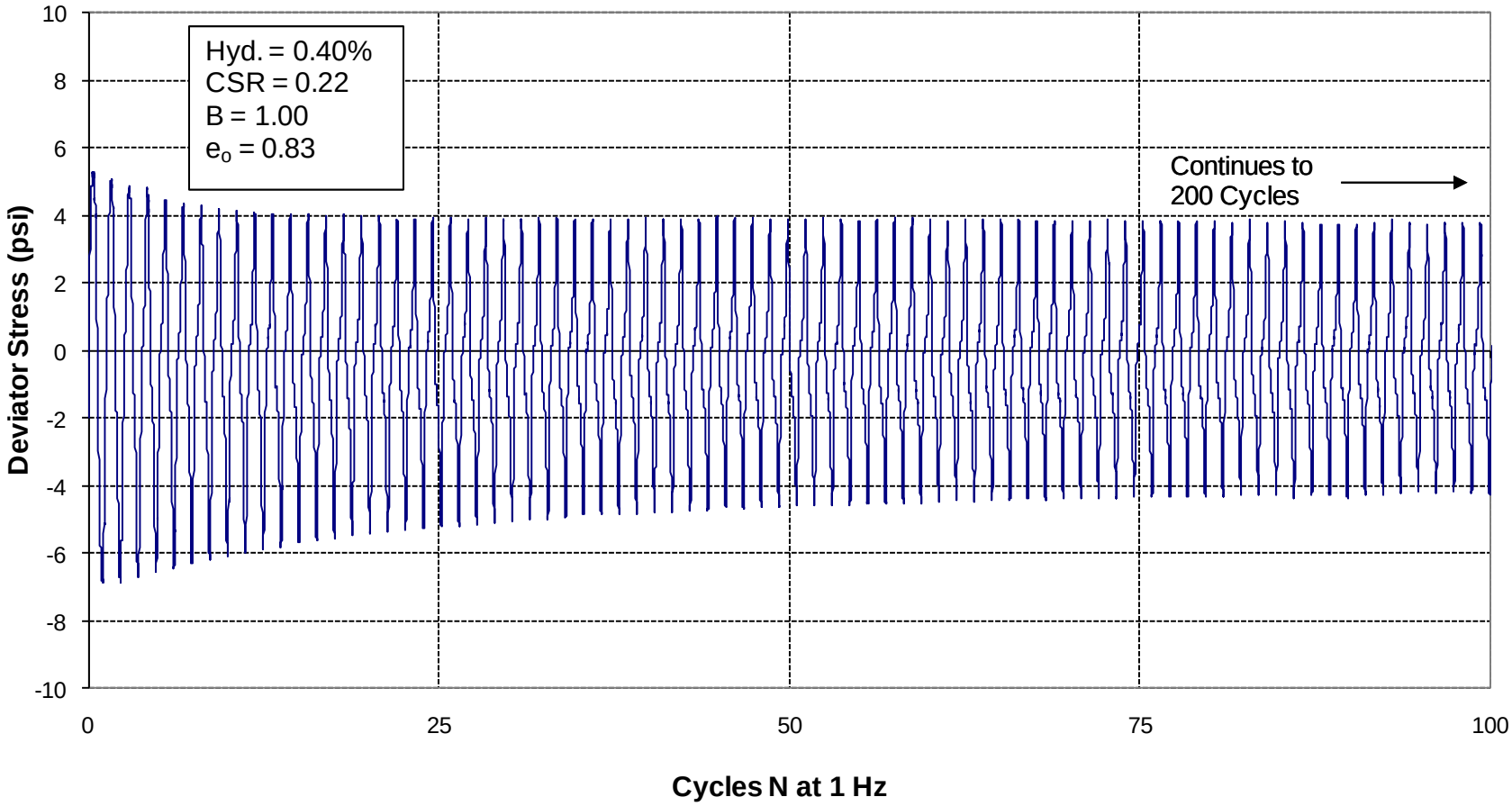

Figure 4.34: Deviator Stress vs. Cycles for hydrogel treated Ottawa sand Sample 0.40%A-Test 1 (0.40% hydrogel); liquefaction occurred after 2 cycles; significant strength was maintained until the test was ended at 200 cycles

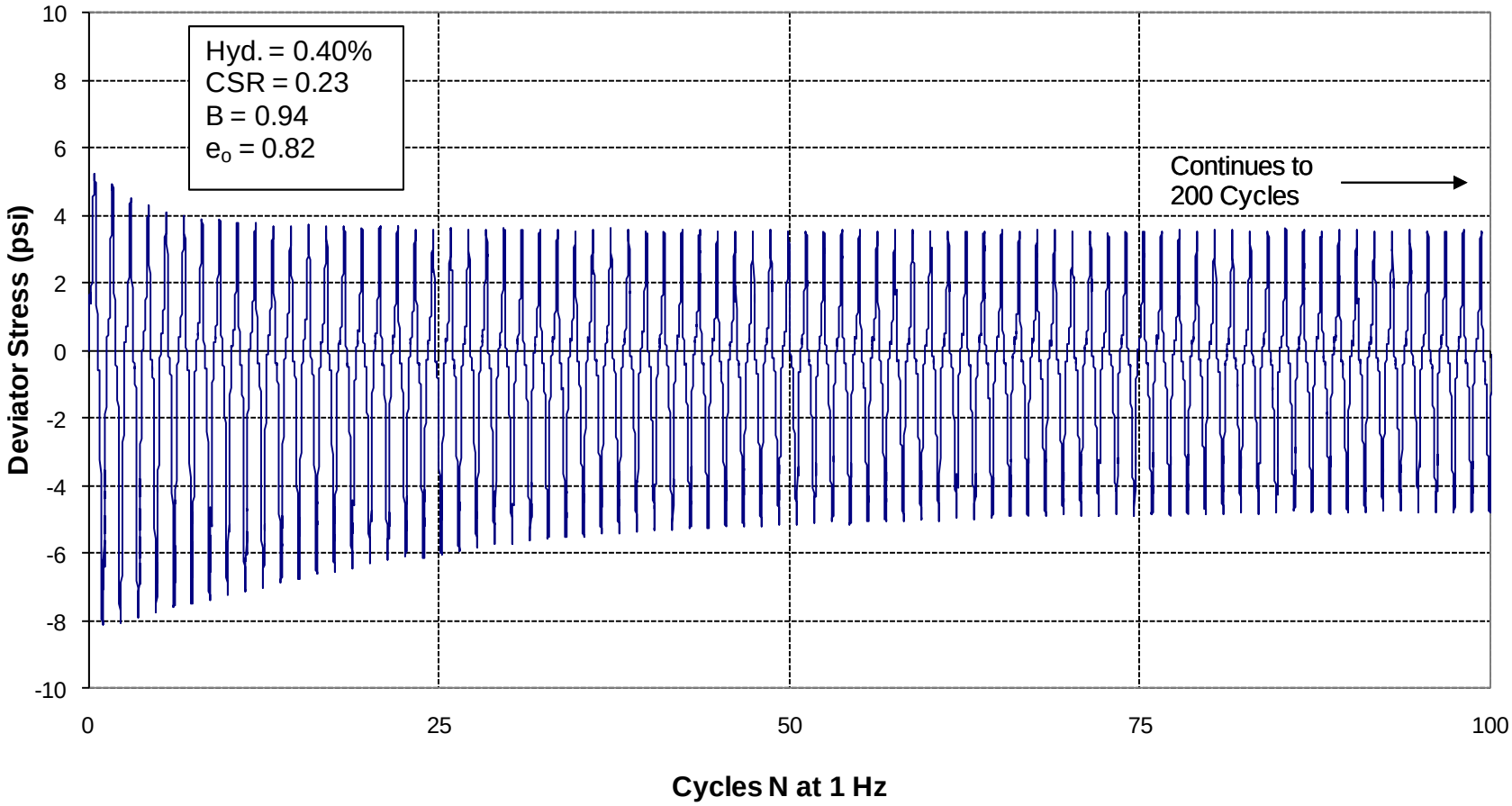

Figure 4.35: Deviator Stress vs. Cycles for hydrogel treated Ottawa sand Sample 0.40%B-Test 2 (0.40% hydrogel); liquefaction occurred immediately; significant strength was maintained until the test was ended at 200 cycles

4.2.4.3 Axial Strain Behavior due to Cyclic Loading

As the cyclic stresses are applied, corresponding strains are induced, similar to a standard triaxial compression test. Because the stresses are applied in a cyclic sinusoidal wave form, the strains also generally exhibit a similar shape. Please not that for this section, negative strains are compression and positive strains are extension.

For both treated and untreated samples, the strains remained small (< +/-1%) prior to liquefaction. This can easily be seen in Figures 4.36, 4.38, 4.40, and 4.42. After liquefaction, the non-hydrogel samples typically exhibited large strains, limiting the applied load. The strains of non-hydrogel samples lost significant strength when the effective stress reached zero (liquefaction). Because the samples lost all their strength, they compressed and did not rebound. This is why the strain versus cycles plots flat-line at approximately -10 to -15% strain in compression for the non hydrogel tests after liquefaction (Figures 4.37 and 4.38). This behavior corresponds to the stress results presented in the previous section, where we stress is reduced almost to zero. It is important to note that the samples heights are permanently reduced, as indicated by the -10 to -15% final strain.

With the exception of Sample 0.15%A (Figure 4.39), which behaved more like a non-hydrogel sample, the hydrogel samples were able to maintain a strain wave form even after the effective stress had reached zero. This indicates that the samples were able to deform elastically, allowing them to maintain more strength that the non-hydrogel samples. Figures 4.40 through 4.48 show this strain response. The hydrogel treated samples did exhibit some permanent deformation. In many of the data plots for the hydrogel treated samples (Figure 4.39 through 4.48) the waves appear to drift, usually downward (compression), no longer centering around zero strain. The amount of drift of the waves is equal to the amount of permanent strain.

Although the hydrogel treated samples do experience some permanent deformation, most of the deformation is elastic. Table 4.6 summarizes the amount of permanent strain for the tests on treated and untreated samples. With the exception of Sample 0.15%A-Test 1, all of the tests on hydrogel treated samples had significantly less permanent strain than the untreated samples that liquefied. One test on an untreated sample, Sample 0.00%A-Test 1, did not liquefy, and thus also exhibited very small permanent strain compared to the other tests on untreated samples that did liquefy.

The fact that the strains are recoverable is significant. It indicates that the treated soil would be able to deform elastically during an earthquake, dissipating energy without causing large permanent deformations, potentially reducing liquefaction induced damage. Structures founded on hydrogel treated soil would have to be strong enough to withstand the large elastic deformations during an earthquake, but they would be found on a material that will maintain strength and likely be able to support them, unlike normal liquefied sand.

Table 4.6: Summary of permanent axial strain at the end of each cyclic triaxial test the; the % in the sample name indicates the % concentration of hydrogel by mass

Sample Name	Test	CSR	Permanent Axial Strain
0.00% A	1	0.15	-0.06%
	2	0.26	-11.77%
0.00% n8-04	1	0.19	-12.05%
0.15% A	1	0.23	-12.38%
0.15% B	1	0.14	-0.04%
0.25% A	1	0.27	-1.25%
0.25% B	1	0.14	-1.91%
	2	0.26	-0.24%
0.30% A	1	0.20	-3.96%
0.30% B	1	0.10	-1.13%
	2	0.16	-1.55%
0.40% A	1	0.22	-0.09%
0.40% B	2	0.23	-0.52%

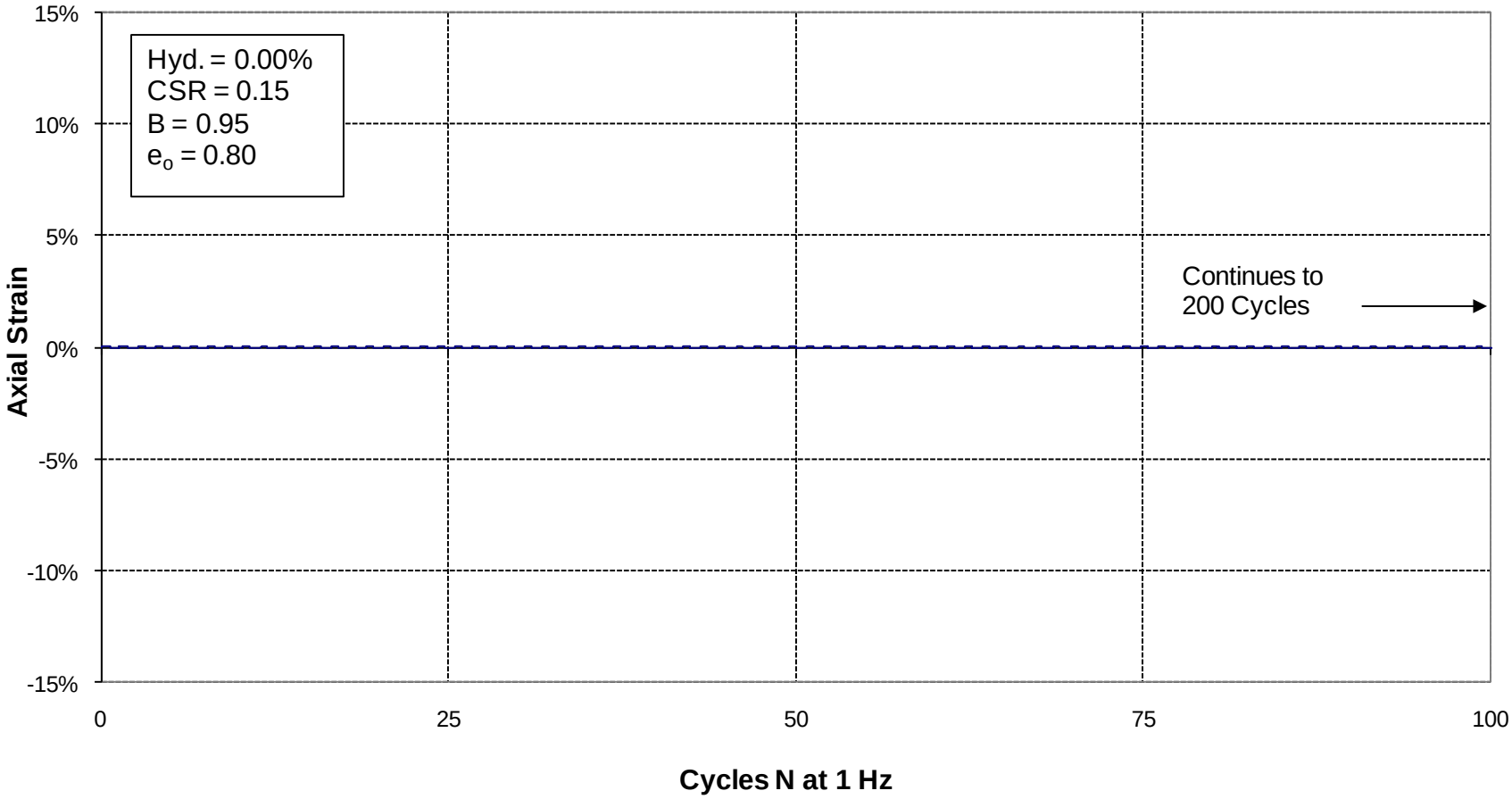

Figure 4.36: Axial Strain vs. Cycles for Ottawa sand Sample 0.00%A-Test 1 (0.00% hydrogel); liquefaction did not occur; test was ended at 200 cycles

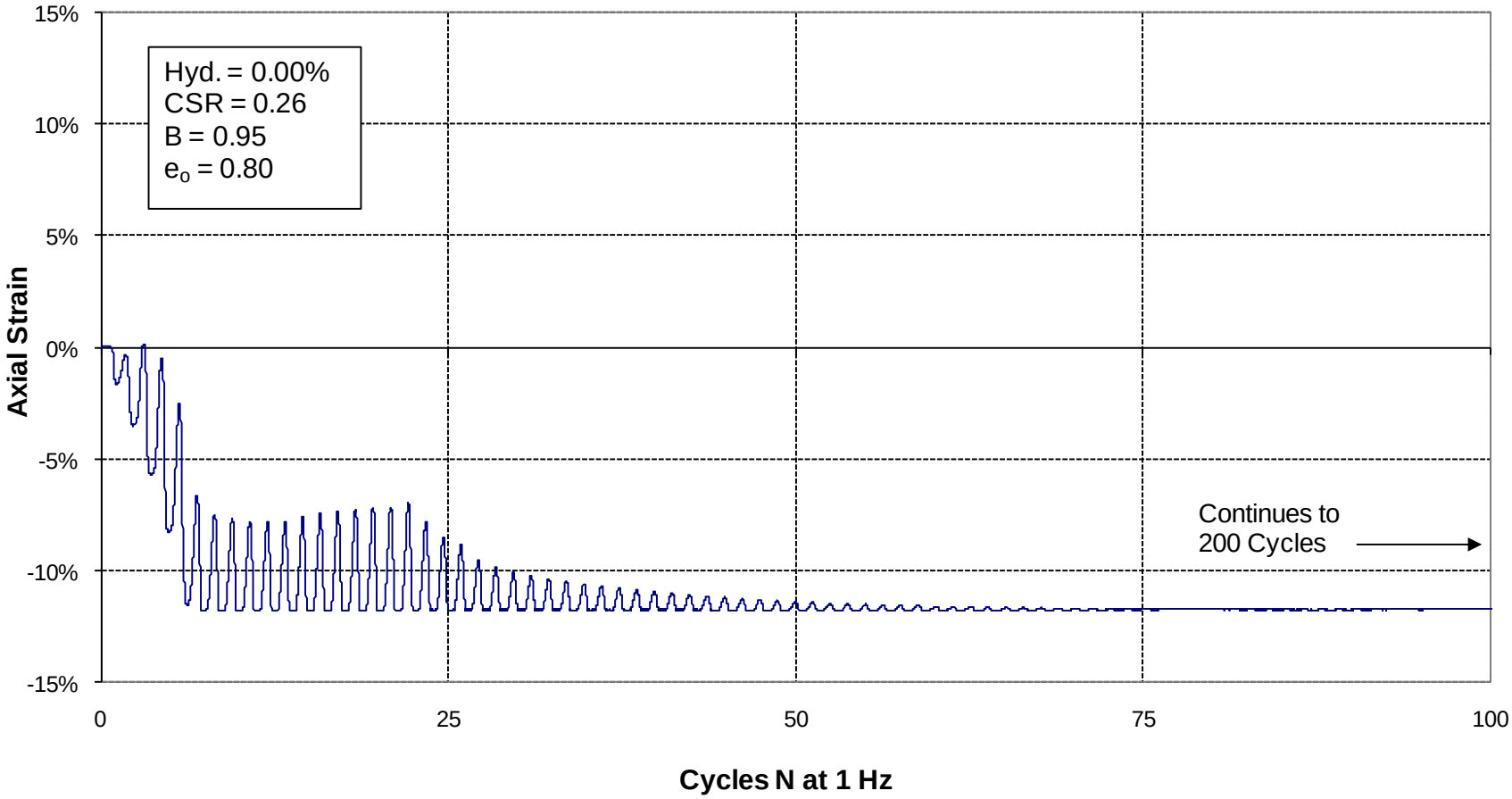

Figure 4.37: Axial Strain vs. Cycles for Ottawa sand Sample 0.00%A-Test 2 (0.00% hydrogel); liquefaction occurred after 5 cycles; test was ended at 200 cycles

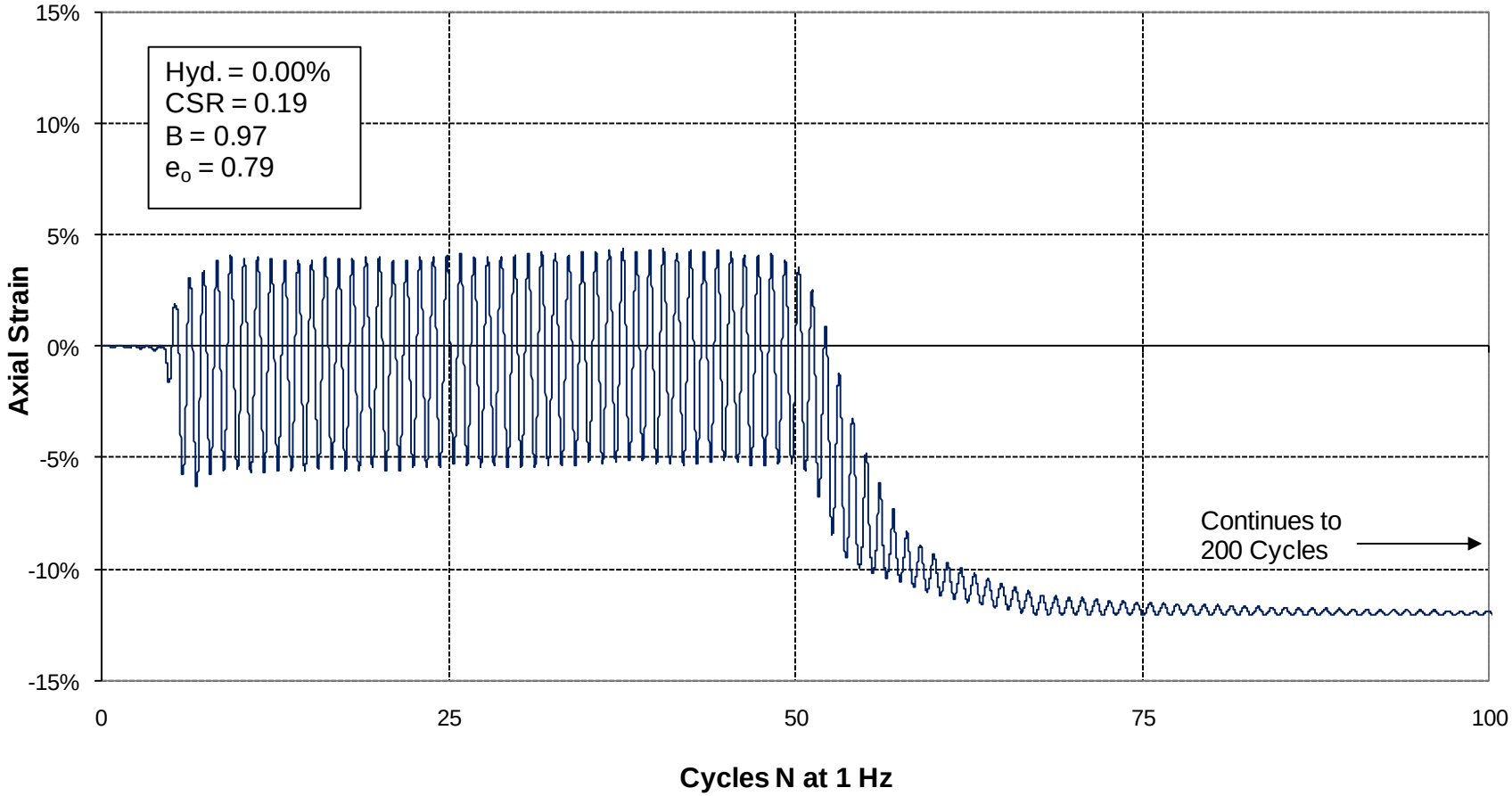

Figure 4.38: Axial Strain vs. Cycles for Ottawa sand Sample 0.00%n8-04-Test 1 (0.00% hydrogel); liquefaction occurred after 5 cycles; test was ended at 200 cycles

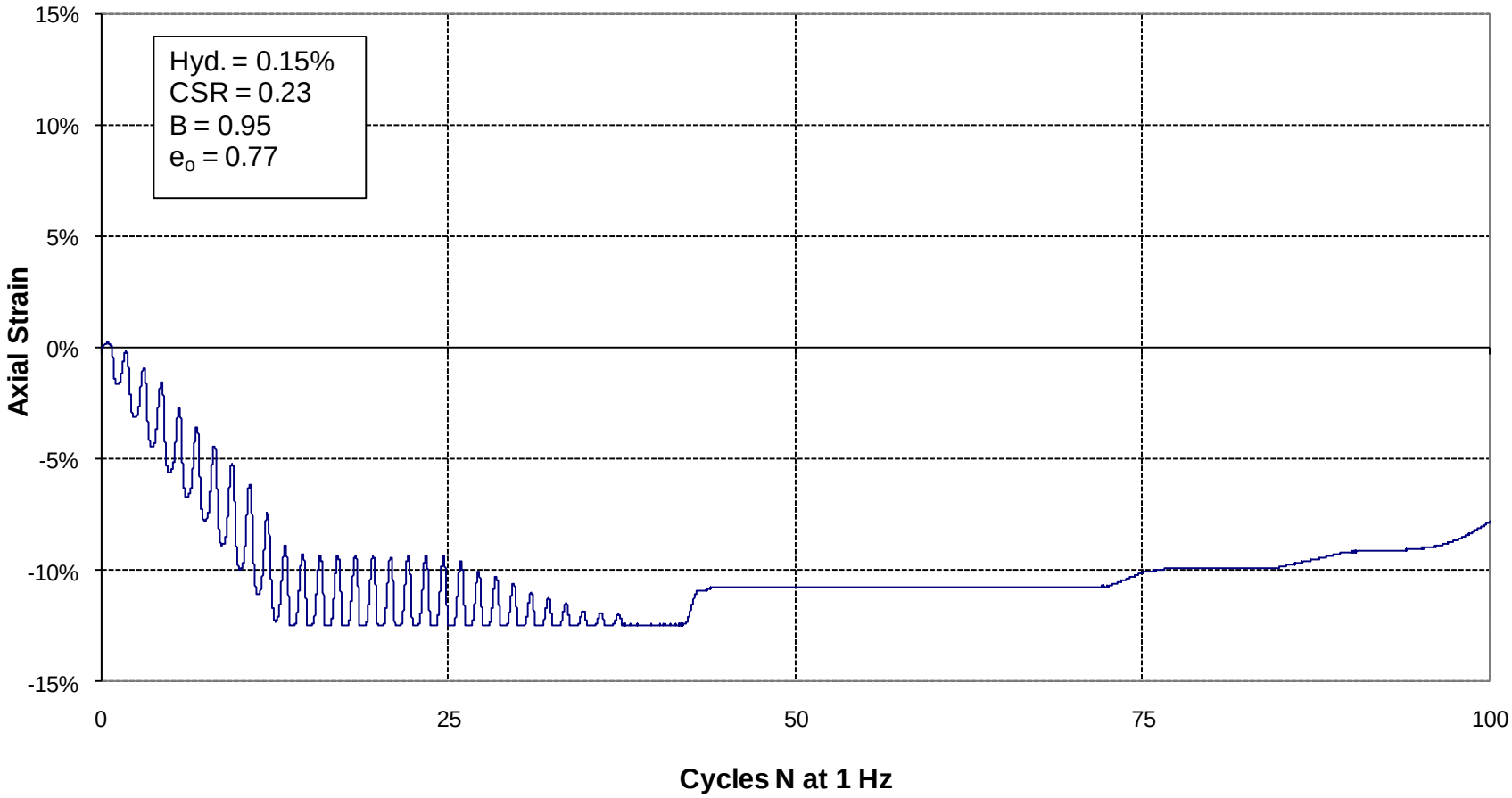

Figure 4.39: Axial Strain vs. Cycles for hydrogel treated Ottawa sand Sample 0.15%A-Test 1 (0.15% hydrogel); liquefaction occurred after 3 cycles; issues with the testing equipment occurred at 38 cycles

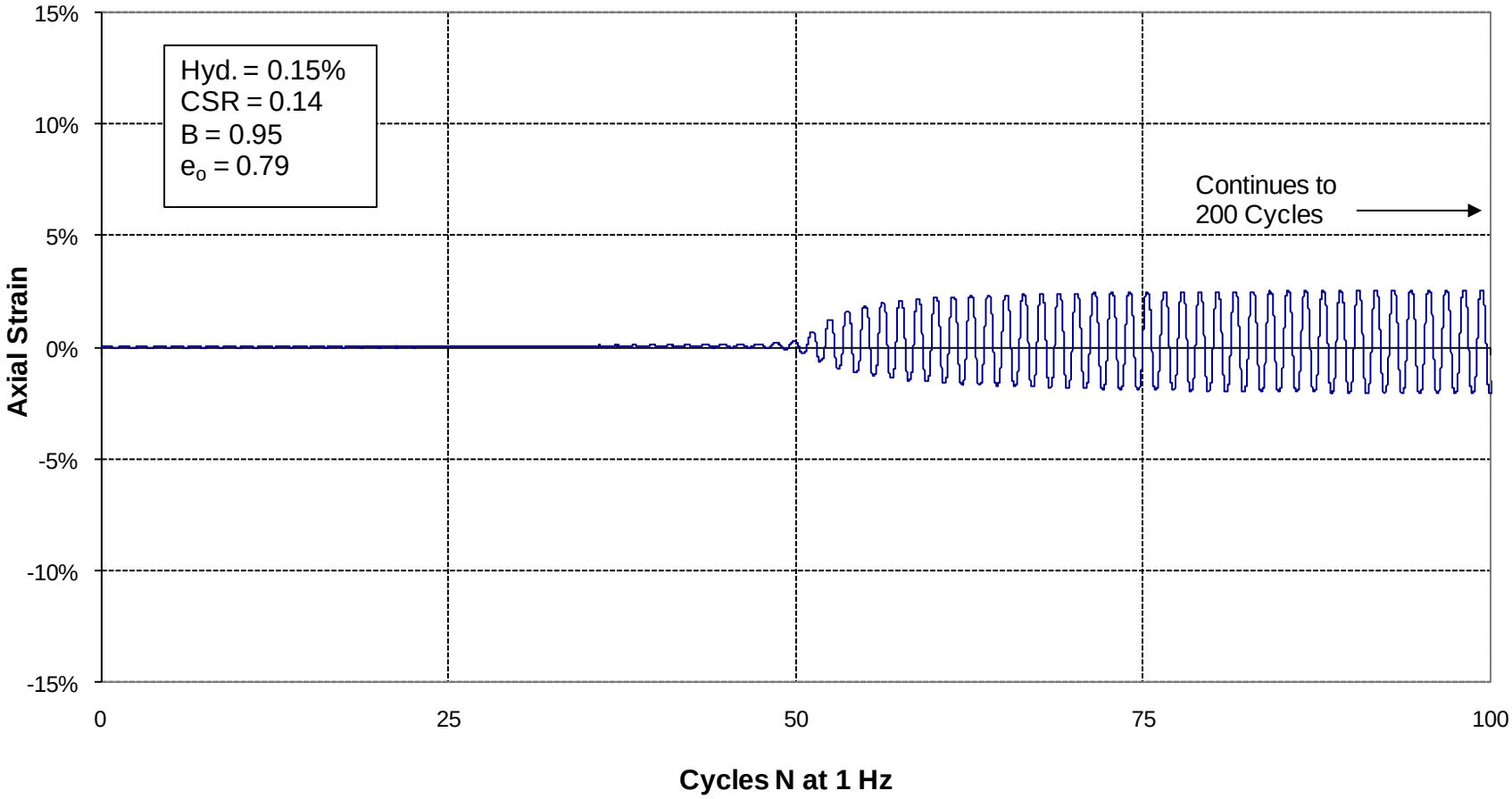

Figure 4.40: Axial Strain vs. Cycles for hydrogel treated Ottawa sand Sample 0.15%B-Test 1 (0.15% hydrogel); liquefaction occurred after 52 cycles; test was ended at 200 cycles

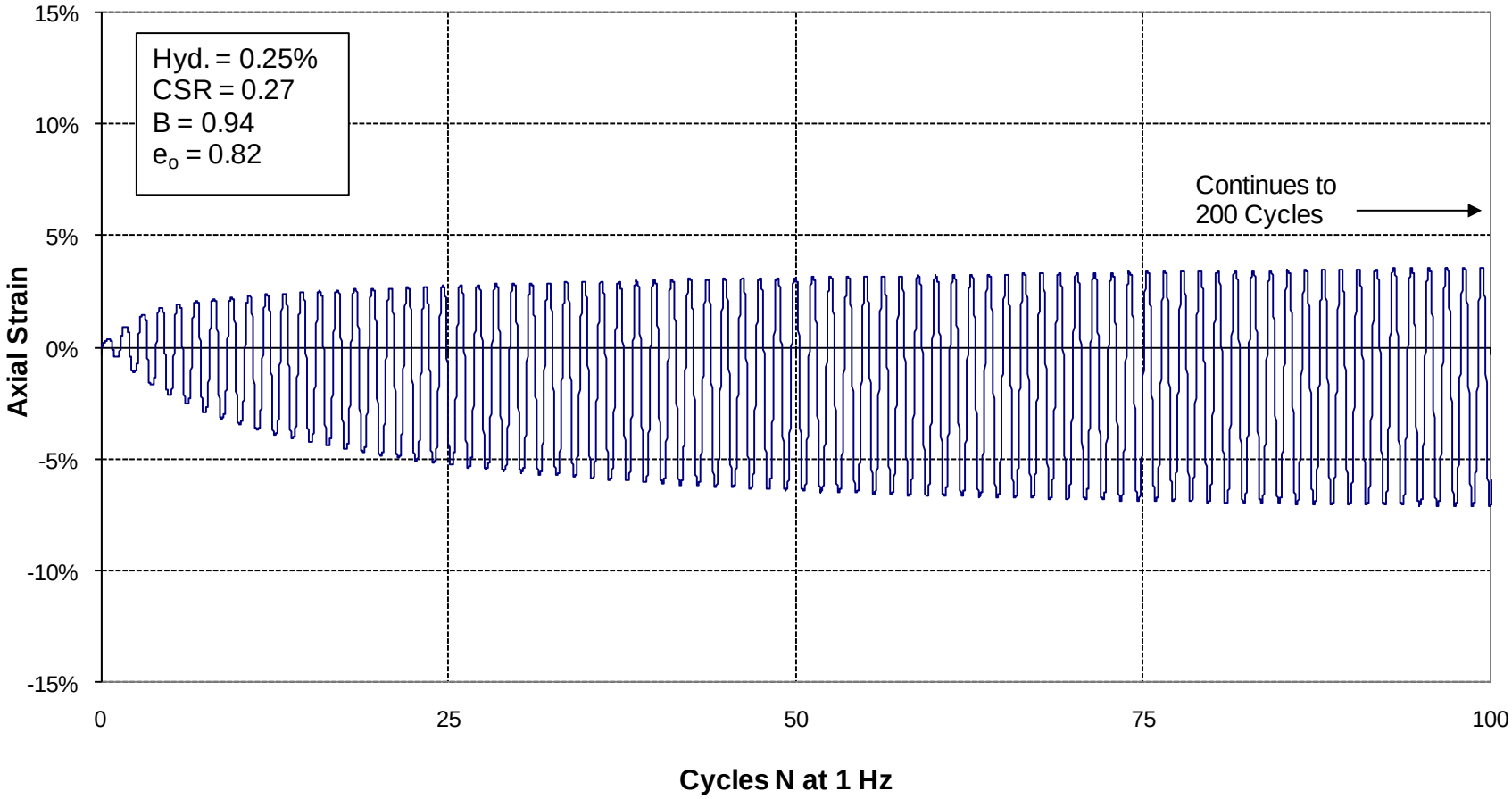

Figure 4.41: Axial Strain vs. Cycles for hydrogel treated Ottawa sand Sample 0.25%A-Test 1 (0.25% hydrogel); liquefaction occurred after 3 cycles; test was ended at 200 cycles

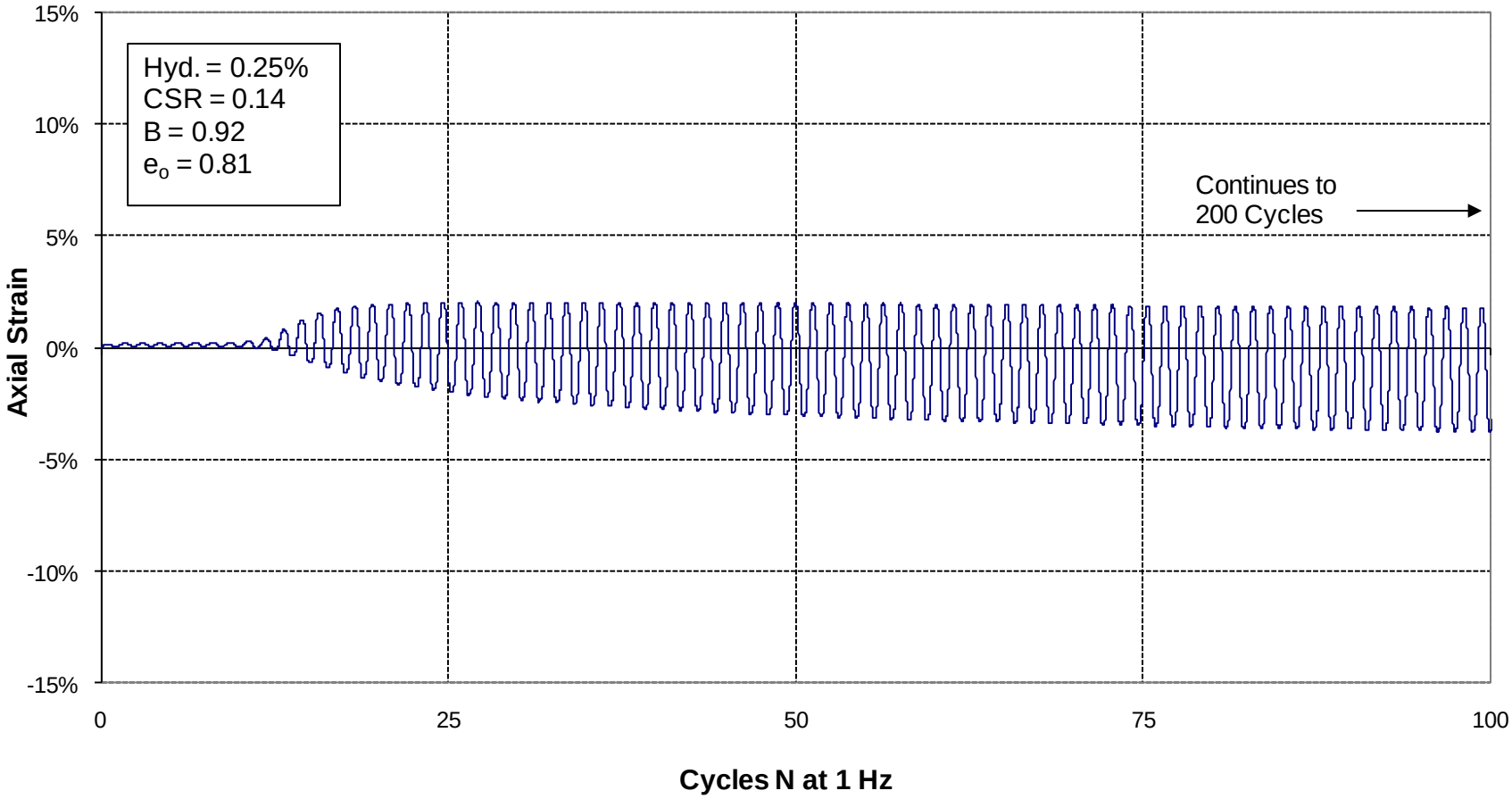

Figure 4.42: Axial Strain vs. Cycles for hydrogel treated Ottawa sand Sample 0.25%B-Test 1 (0.25% hydrogel); liquefaction occurred after 17 cycles; test was ended at 200 cycles

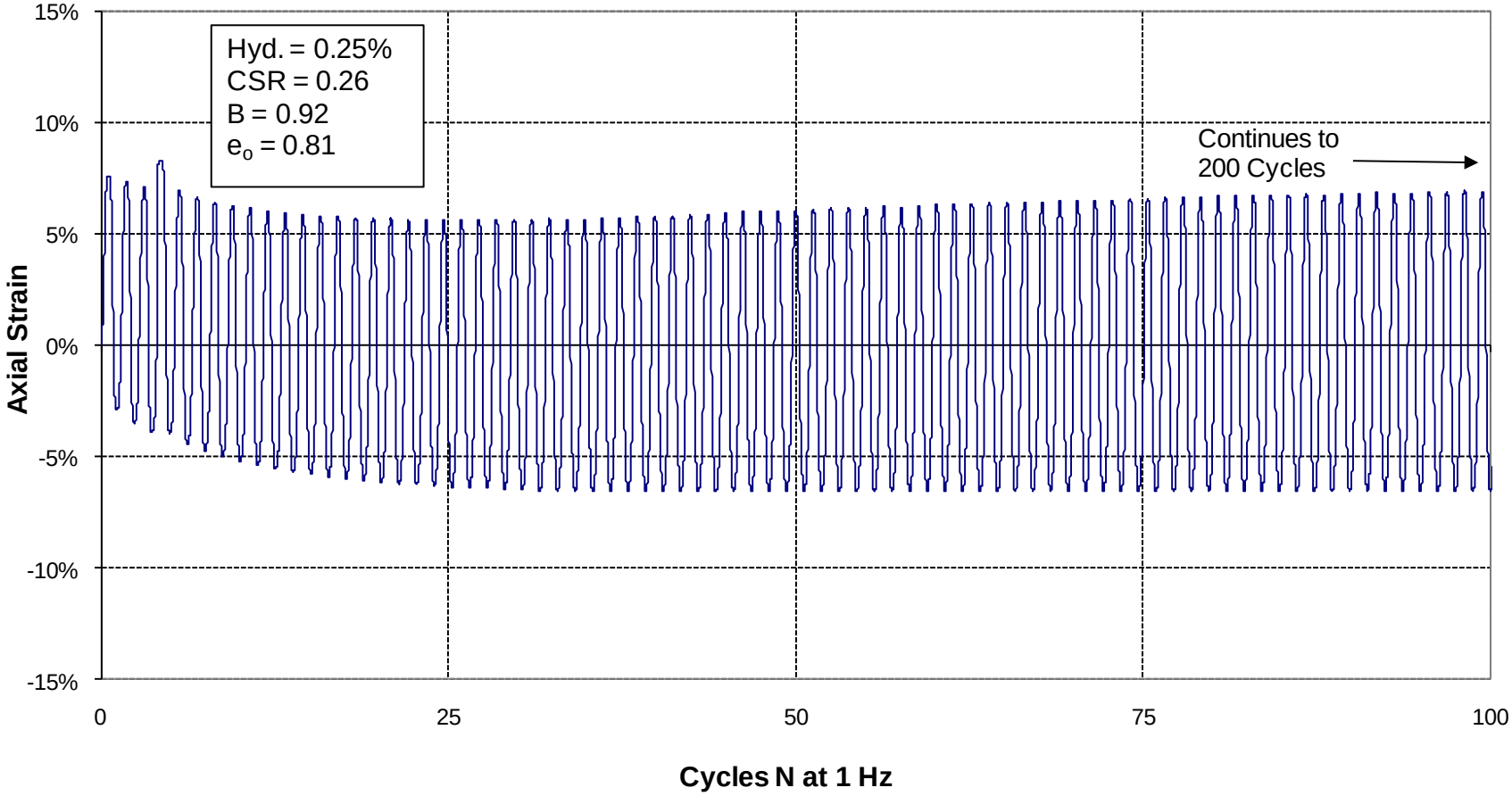

Figure 4.43: Axial Strain vs. Cycles for hydrogel treated Ottawa sand Sample 0.25%B-Test 2 (0.25% hydrogel); liquefaction occurred immediately; test was ended at 200 cycles

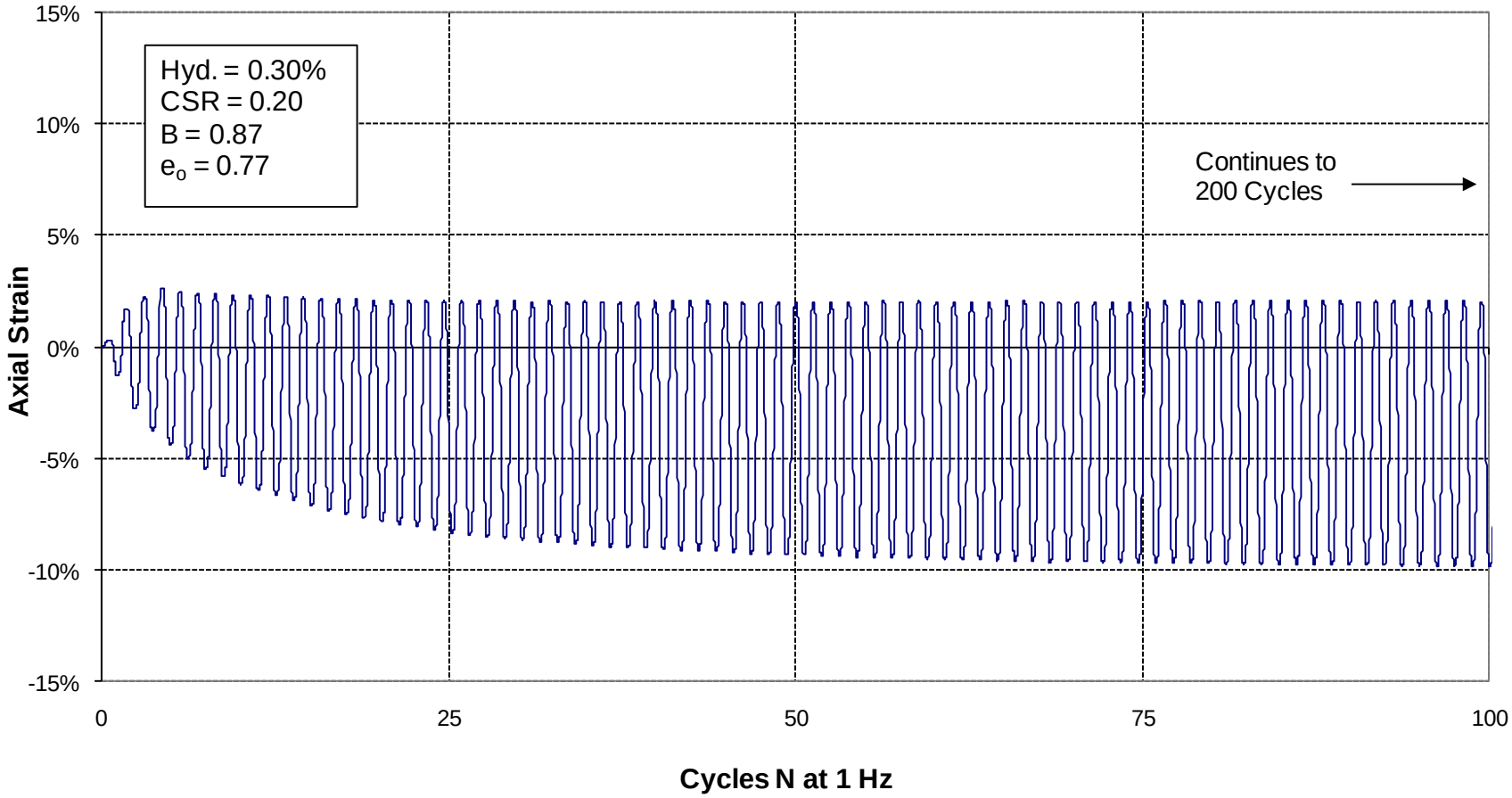

Figure 4.44: Axial Strain vs. Cycles for hydrogel treated Ottawa sand Sample 0.30%A-Test 1 (0.30% hydrogel); liquefaction occurred after 3 cycles; test was ended at 200 cycles

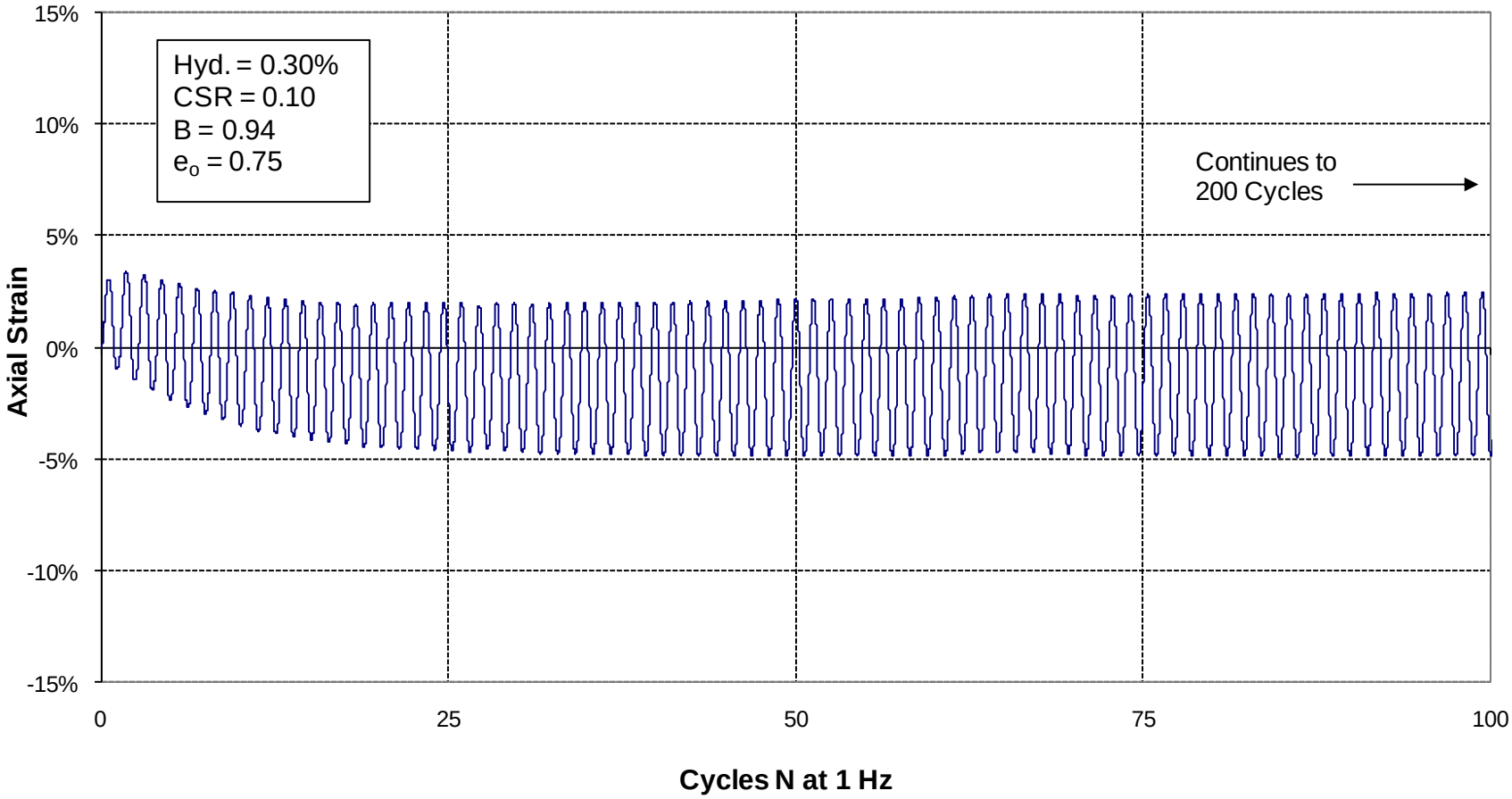

Figure 4.45: Axial Strain vs. Cycles for hydrogel treated Ottawa sand Sample 0.30%B-Test 1 (0.30% hydrogel); liquefaction occurred after 4 cycles; test was ended at 200 cycles

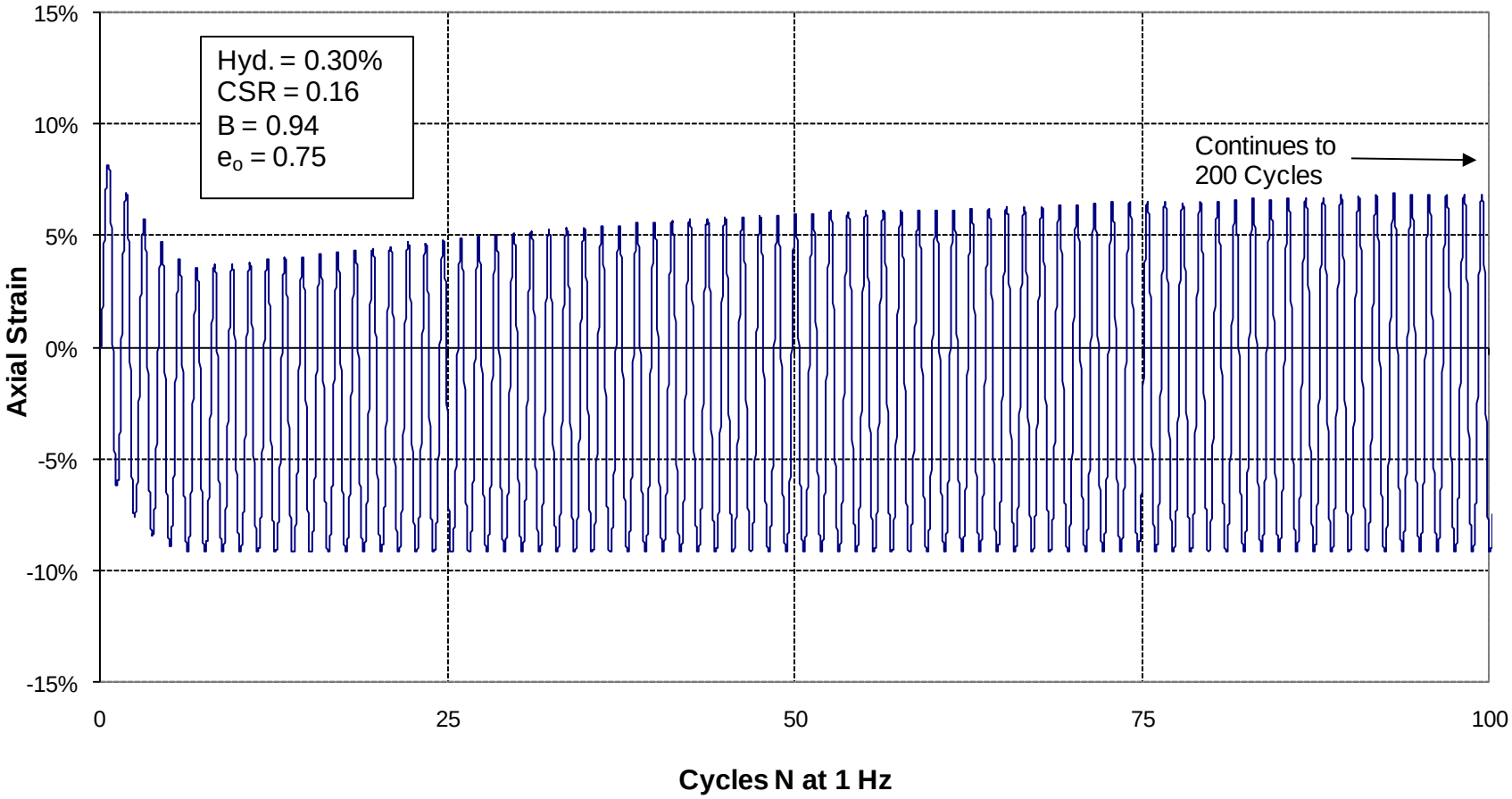

Figure 4.46: Axial Strain vs. Cycles for hydrogel treated Ottawa sand Sample 0.30%B-Test 2 (0.30% hydrogel), liquefaction occurred immediately, test was ended at 200 cycles

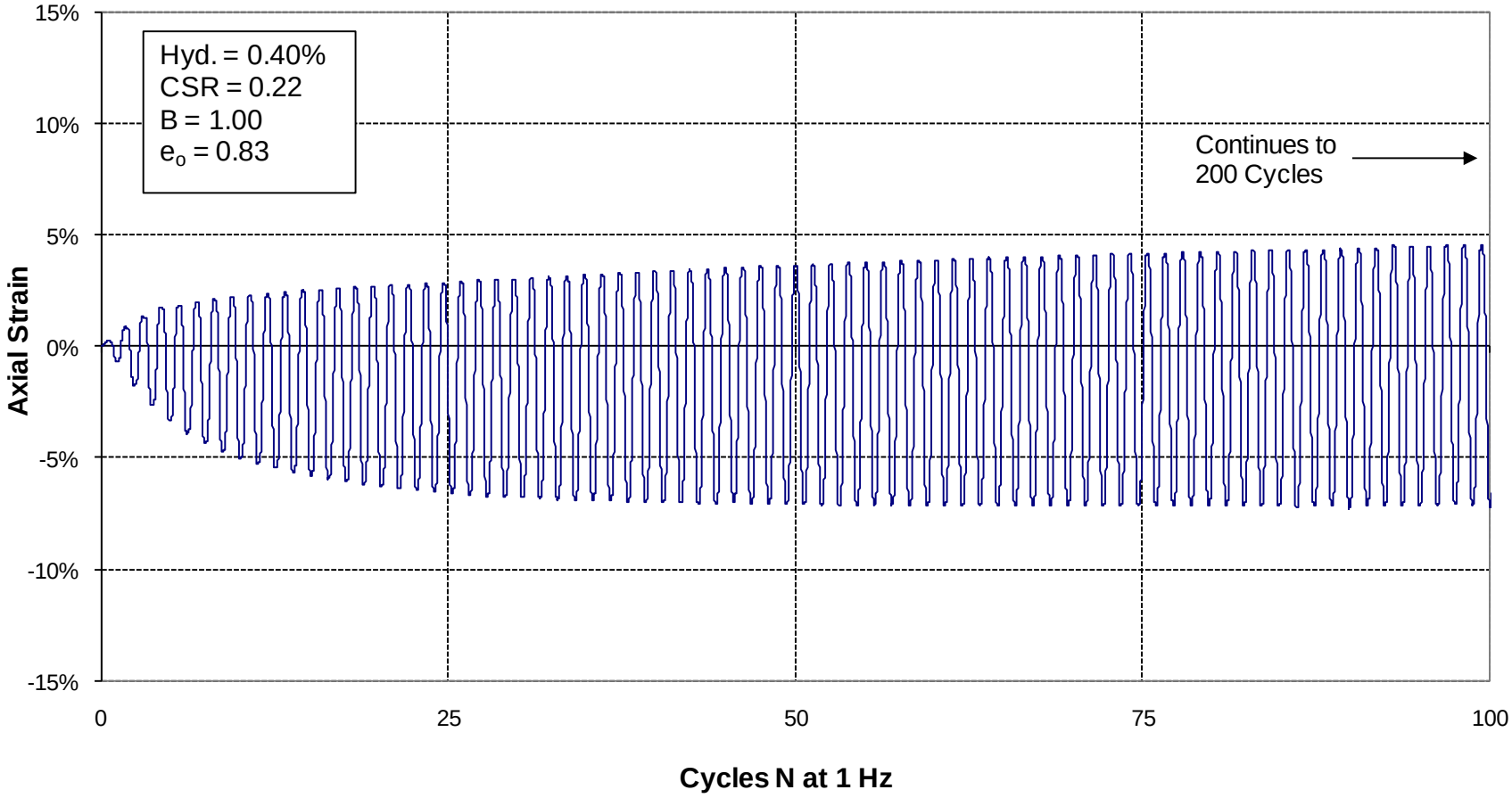

Figure 4.47: Axial Strain vs. Cycles for Sample 0.40%A-Test 1 (0.40% hydrogel); liquefaction occurred after 2 cycles; test was ended at 200 cycles

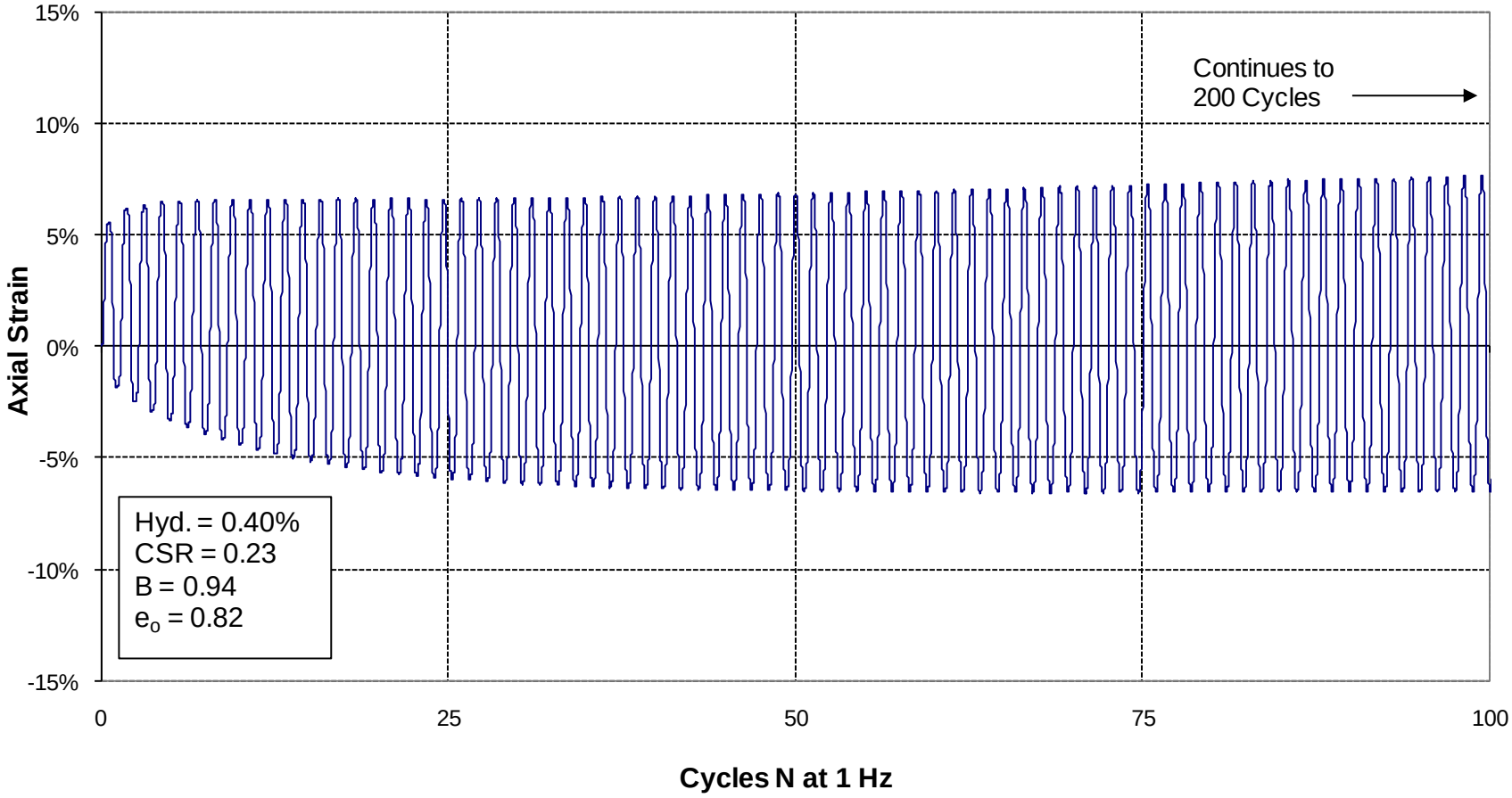

Figure 4.48: Axial Strain vs. Cycles for hydrogel treated Ottawa sand Sample 0.40%B-Test 2 (0.40% hydrogel); liquefaction occurred immediately; test was ended at 200 cycles

4.2.4.4 Effective Stress Response due to Cyclic Loading

For a triaxial test, effective stress is effective confining pressure minus pore pressure. Because effective confining pressure is held constant, effective stress is the inverse of pore pressure. Thus, plots of either effective stress vs. cycles or change in pore pressure vs. cycles show essentially the same information. Effective stress has been presented here in Figures 4.49 through 4.61.

Like strain, changes in effective stress are a result of the applied stresses. The effective stress maintains a roughly sinusoidal shape for as long as the load wave was maintained. Degradation of the load wave form is reflected in the effective stress plot as well. This is true for both hydrogel and non-hydrogel samples. The deformed shape of the effective stress wave trough of several of the samples as they approach zero is typical and an indication that liquefaction is occurring (ASTM 2004a).

The effective stress vs. cycles plots basically indicate when and how quickly the samples liquefied. Compared to the stress and strain plots, it is easiest to see when the samples liquefied in these effective stress plots. It is clear from the effective stress plots that liquefaction occurs more quickly for the hydrogel samples even of similar or lower OCR's. This can be most dramatically illustrated by comparing Figures 4.49 and 4.58.

Many of the tests, both on hydrogel and non-hydrogel samples, indicate that the effective stress reduces to a slightly negative value. This is unusual since effective stress, theoretically, cannot drop below zero. It is thought that there might be some error in the calibrating or zeroing the pressure transducers during tests. These concerns were raised to Dr. Ray who indicated that his sensors were functioning properly and correctly calibrated. Without access to the testing equipment or the raw pore pressure values, it is difficult to know why some of the effective stress

values reported were negative. The plots generally appear to a lower limit between 0 and -2 psi . This discrepancy minimal and within the range of error that could easily be associated with an average pore pressure transducer. None of the effective stresses ever reached more than 2 psi below zero.

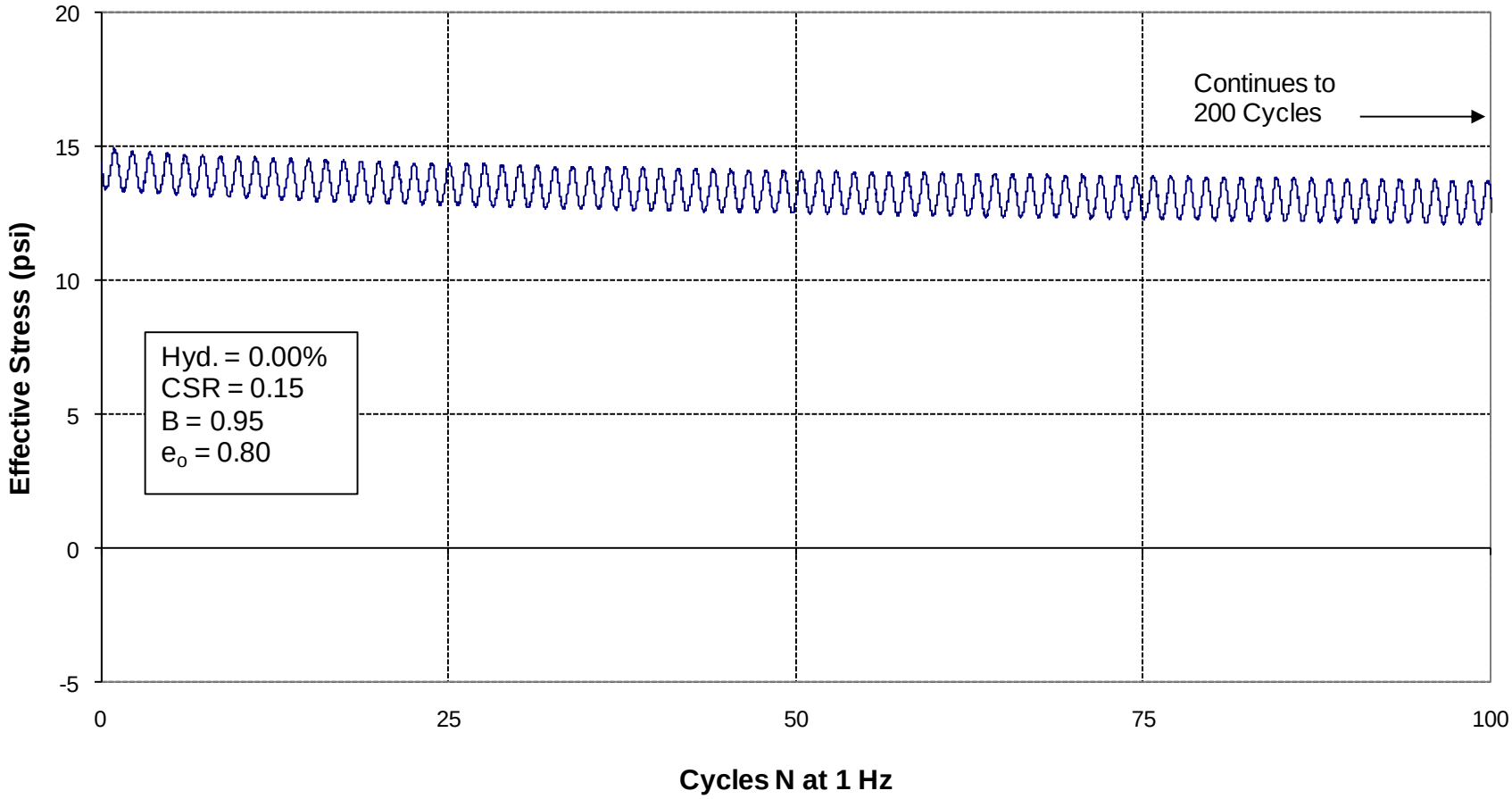

Figure 4.49: Effective Stress vs. Cycles for Ottawa sand Sample 0.00%A-Test 1 (0.00% hydrogel); liquefaction did not occur; test was ended at 200 cycles

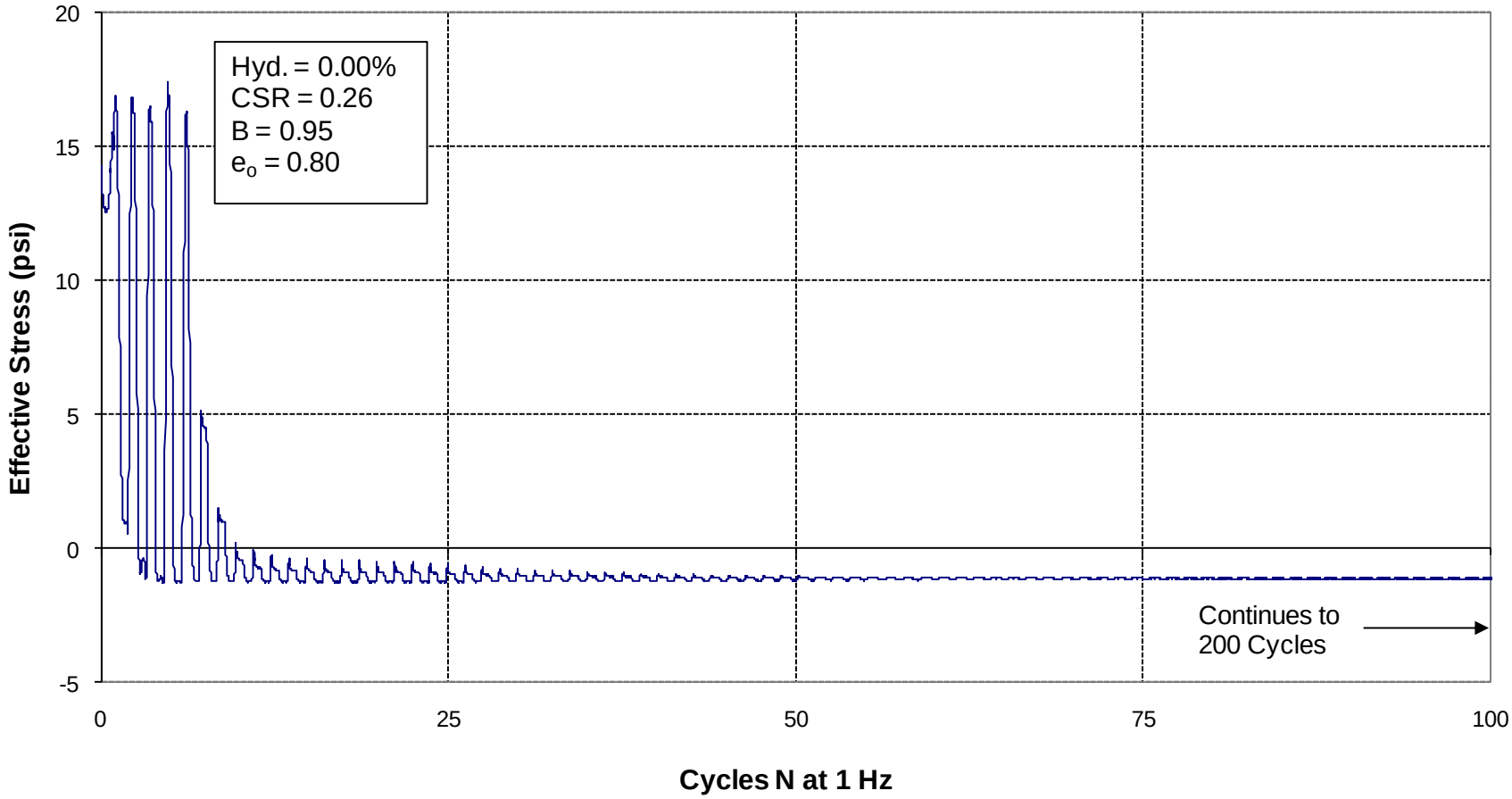

Figure 4.50: Effective Stress vs. Cycles for Ottawa sand Sample 0.00%A-Test 2 (0.00% hydrogel); liquefaction occurred after 5 cycles; test was ended at 200 cycles

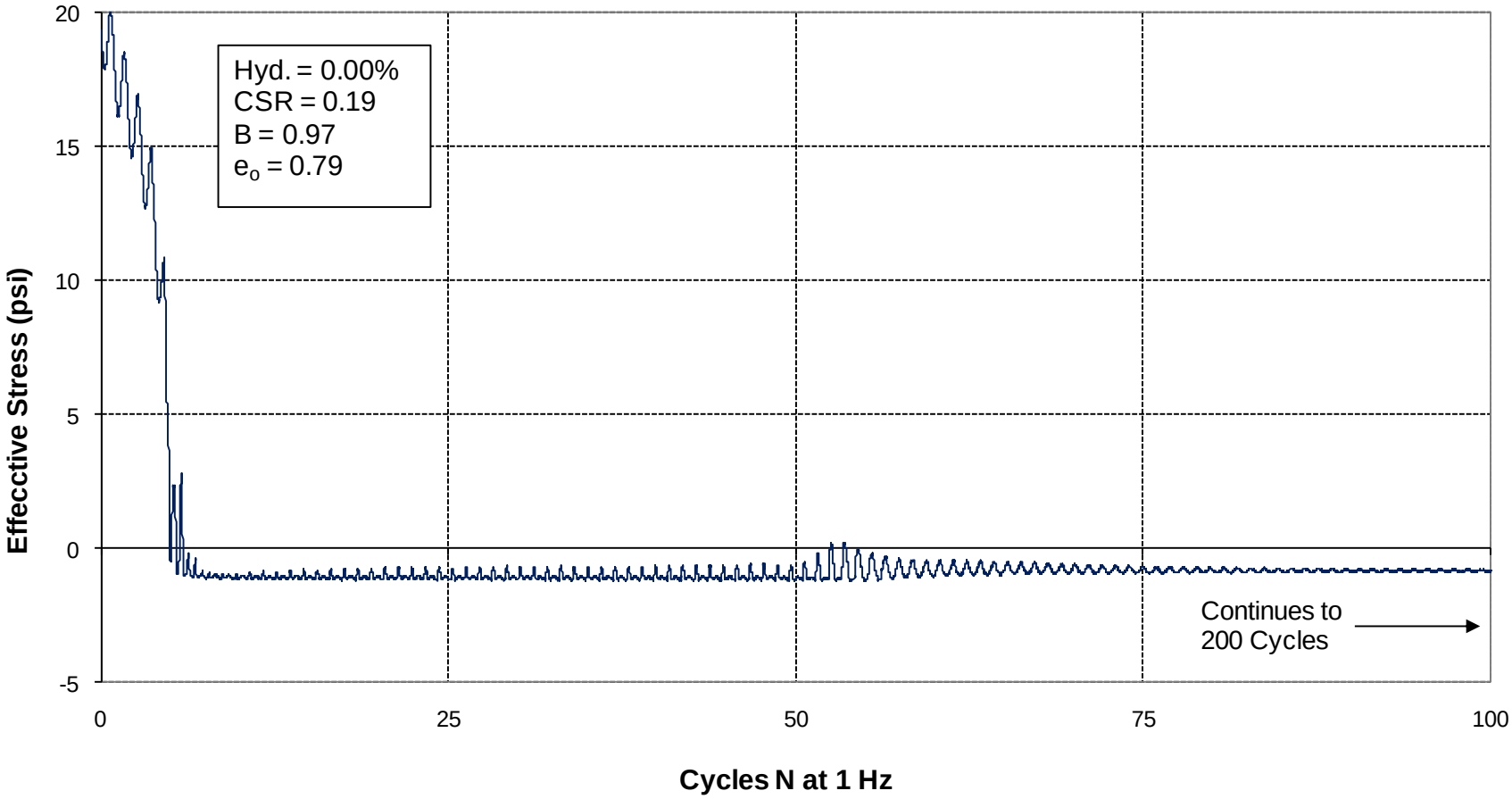

Figure 4.51: Effective Stress vs. Cycles for Ottawa sand Sample 0.00%n8-04-Test 1 (0.00% hydrogel); liquefaction occurred after 5 cycles; test was ended at 200 cycles

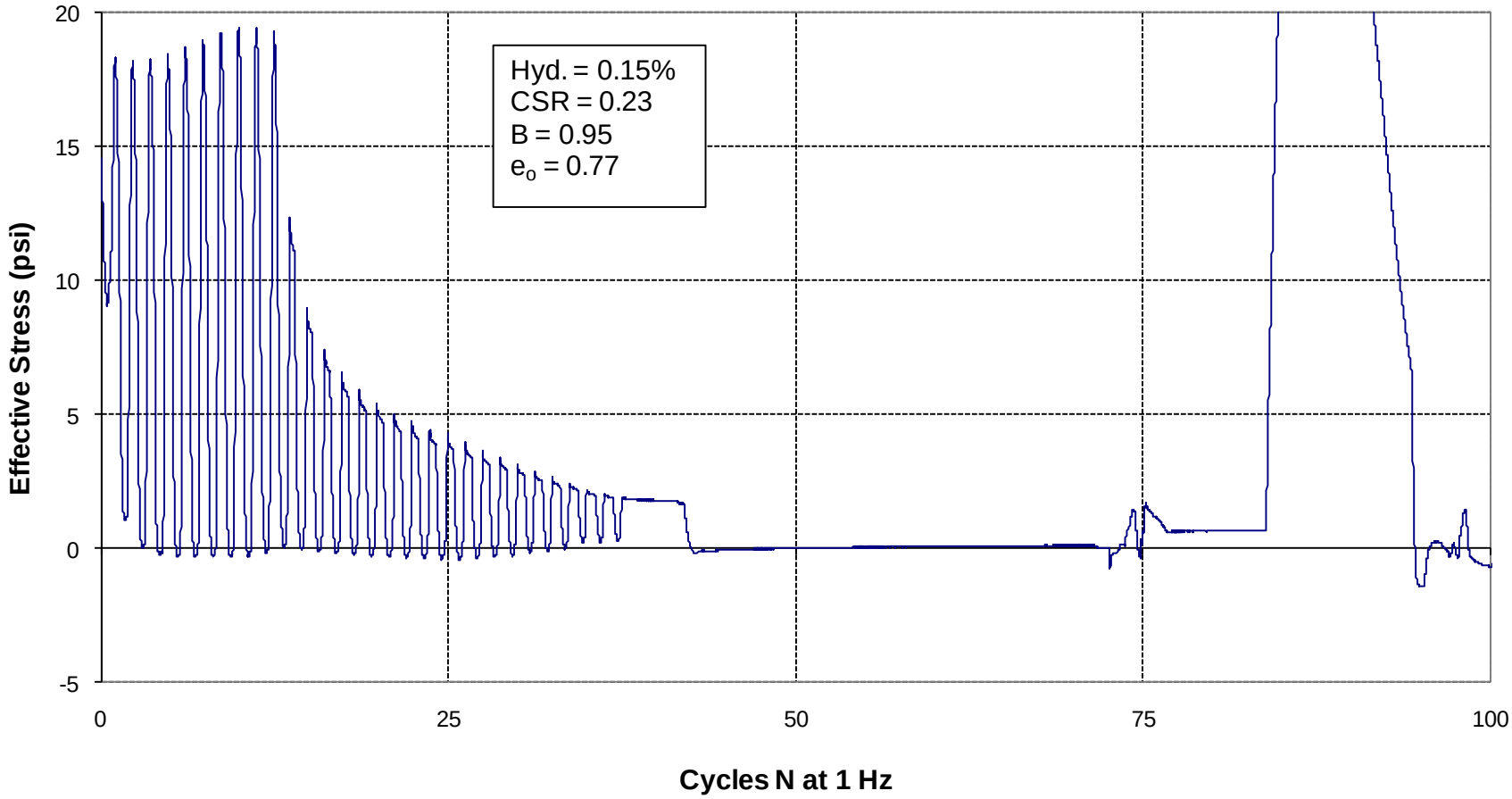

Figure 4.52: Effective Stress vs. Cycles for hydrogel treated Ottawa sand Sample 0.15%A-Test 1 (0.15% hydrogel); liquefaction occurred after 3 cycles; issues with the testing equipment occurred at 38 cycles

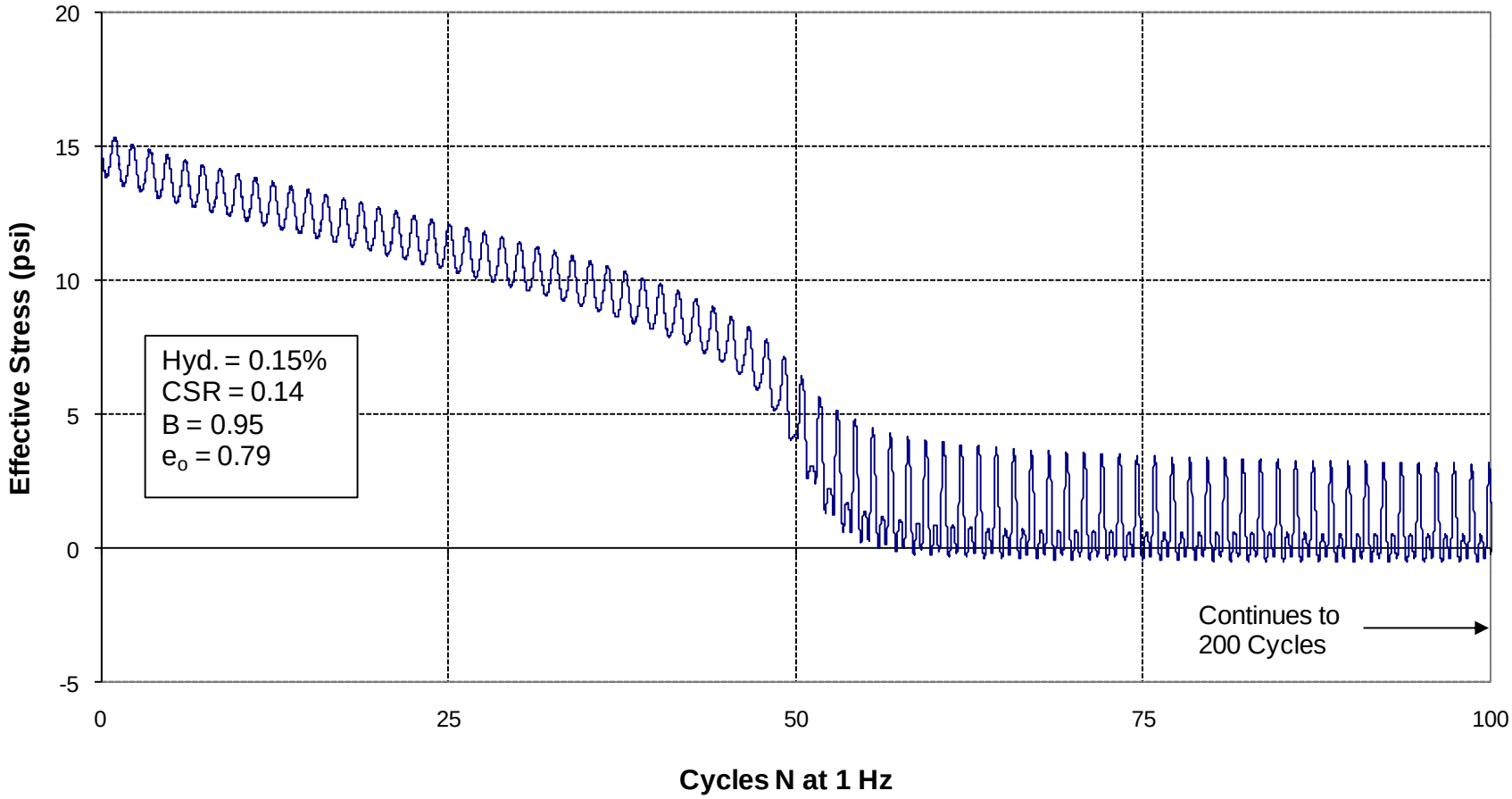

Figure 4.53: Effective Stress vs. Cycles for hydrogel treated Ottawa sand Sample 0.15%B-Test 1 (0.15% hydrogel); liquefaction occurred after 52 cycles; test was ended at 200 cycles

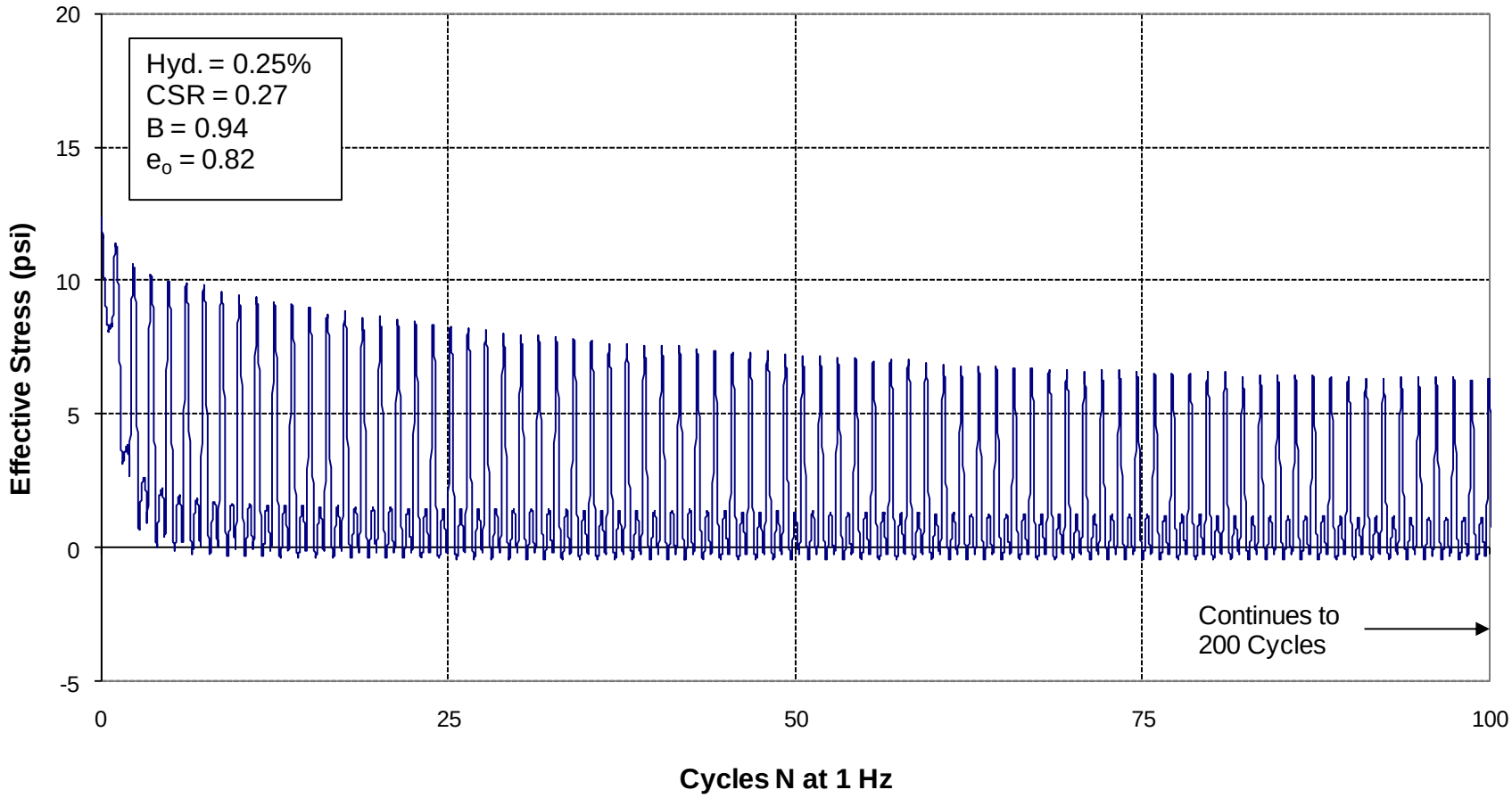

Figure 4.54: Effective Stress vs. Cycles for hydrogel treated Ottawa sand Sample 0.25%A-Test 1 (0.25% hydrogel); liquefaction occurred after 3 cycles; test was ended at 200 cycles

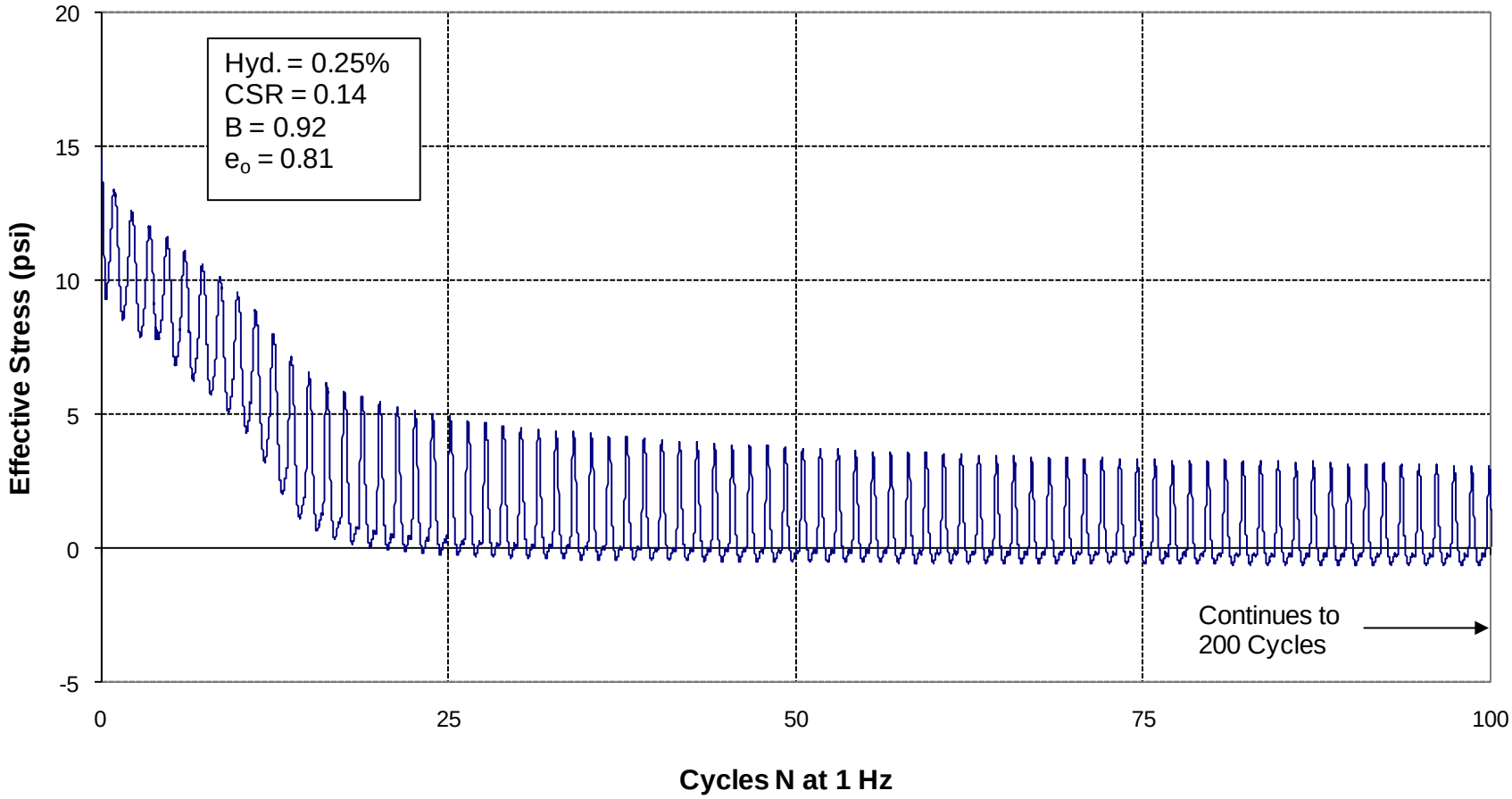

Figure 4.55: Effective Stress vs. Cycles for hydrogel treated Ottawa sand Sample 0.25%B-Test 1 (0.25% hydrogel); liquefaction occurred after 17 cycles; test was ended at 200 cycles

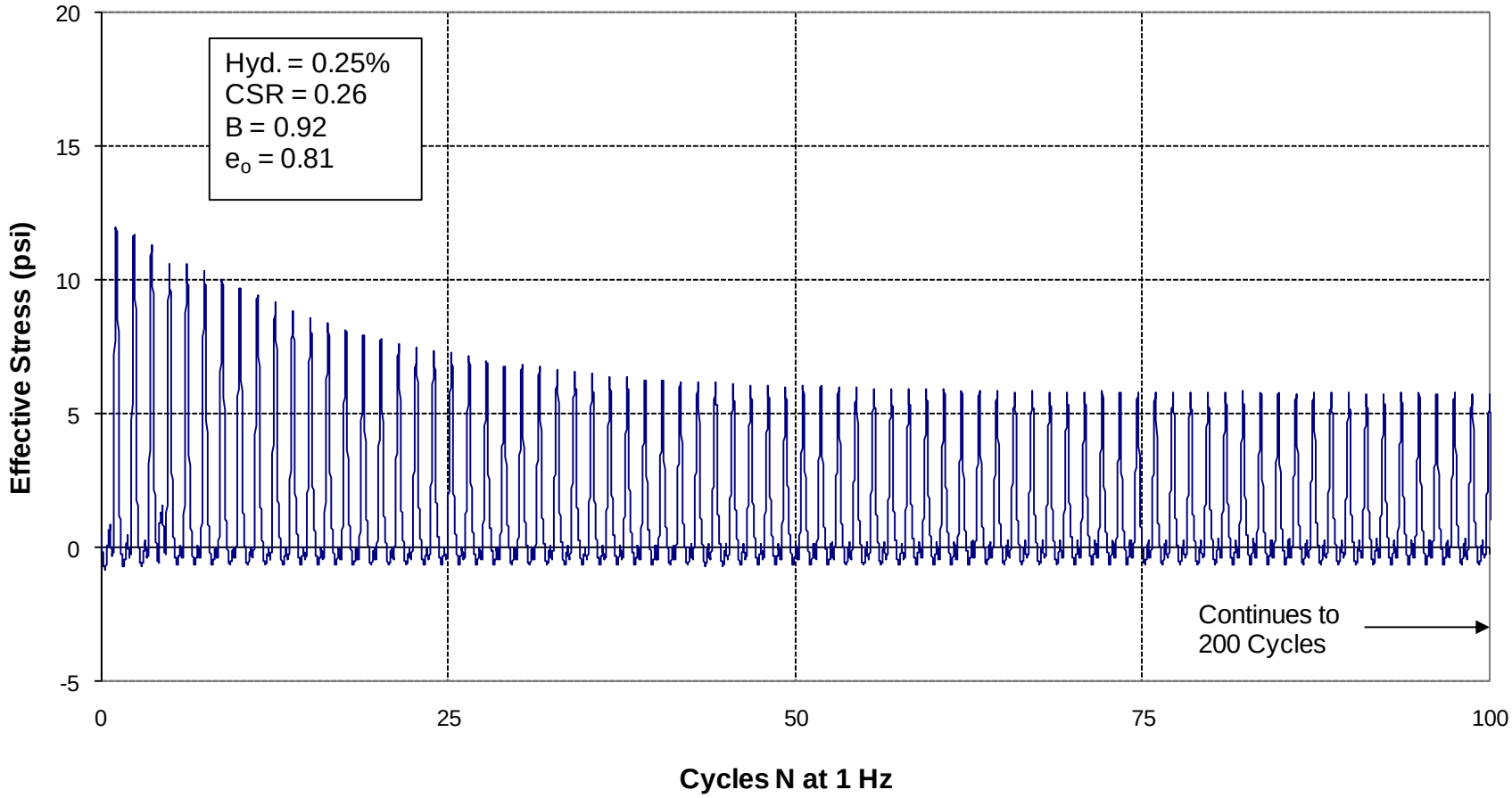

Figure 4.56: Effective Stress vs. Cycles for hydrogel treated Ottawa sand Sample 0.25%B-Test 2 (0.25% hydrogel); liquefaction occurred immediately; test was ended at 200 cycles

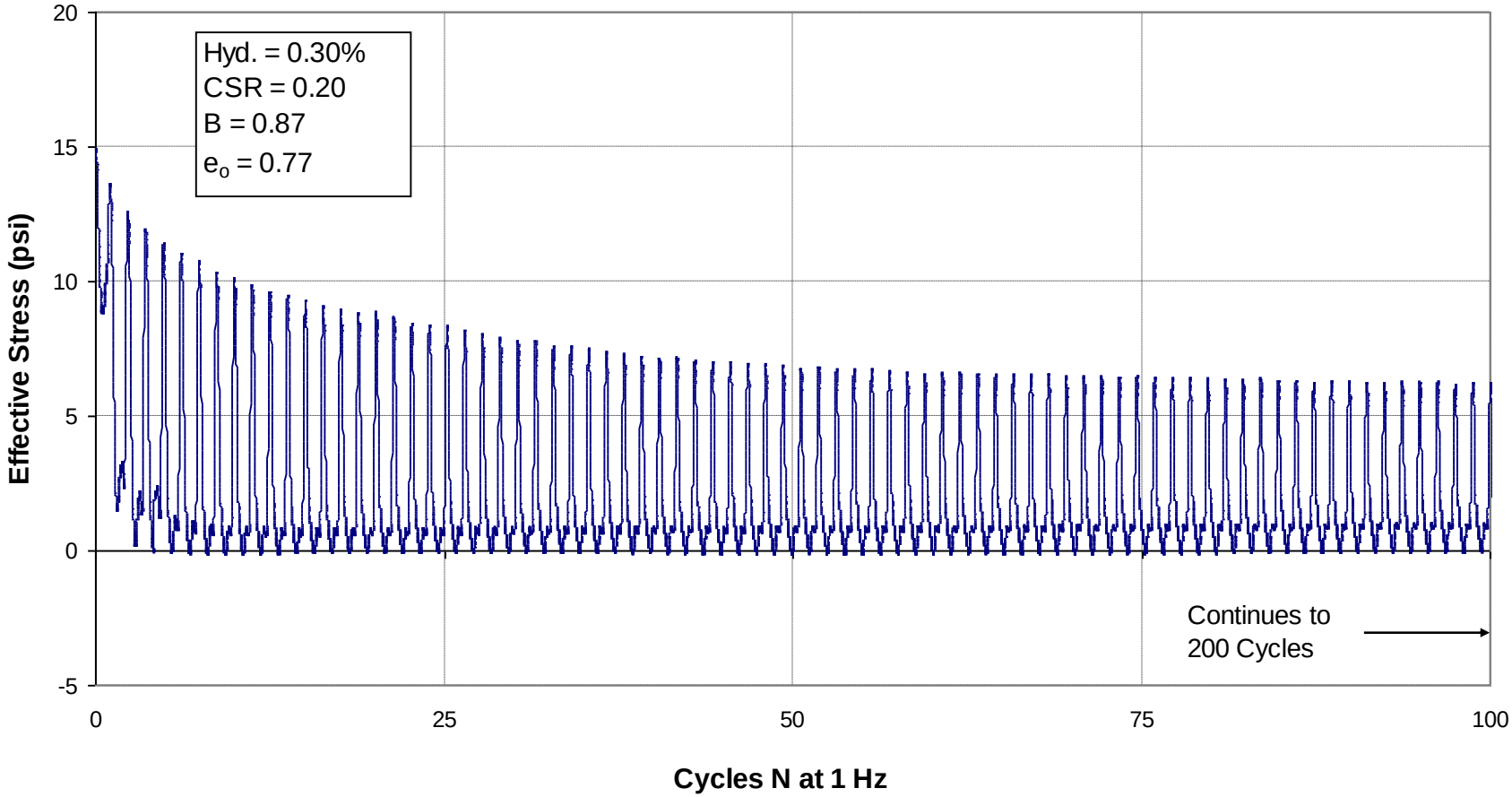

Figure 4.57: Effective Stress vs. Cycles for hydrogel treated Ottawa sand Sample 0.30%A-Test 1 (0.30% hydrogel); liquefaction occurred after 3 cycles; test was ended at 200 cycles

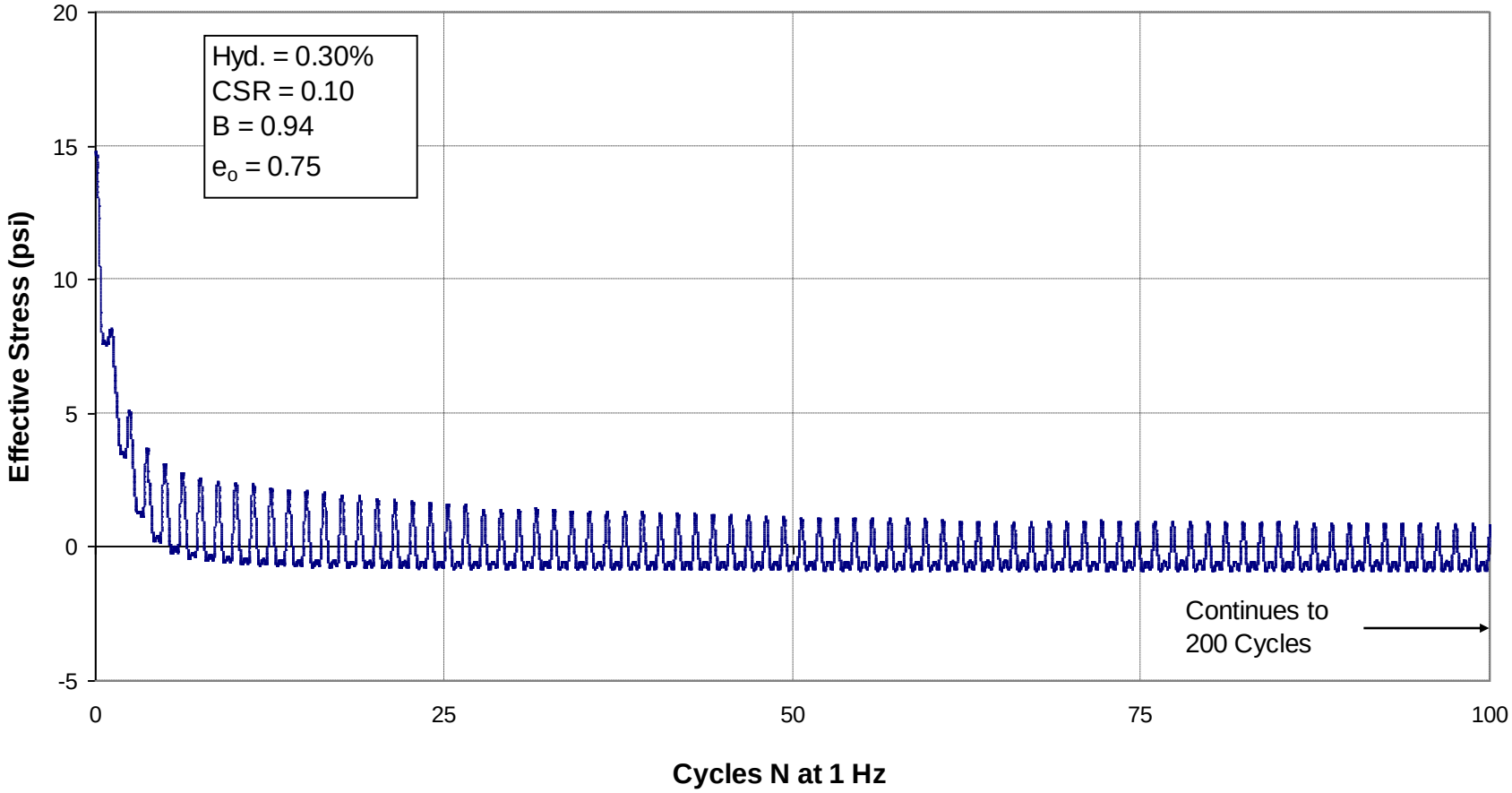

Figure 4.58: Effective Stress vs. Cycles for hydrogel treated Ottawa sand Sample 0.30%B-Test 1 (0.30% hydrogel); liquefaction occurred after 4 cycles; test was ended at 200 cycles

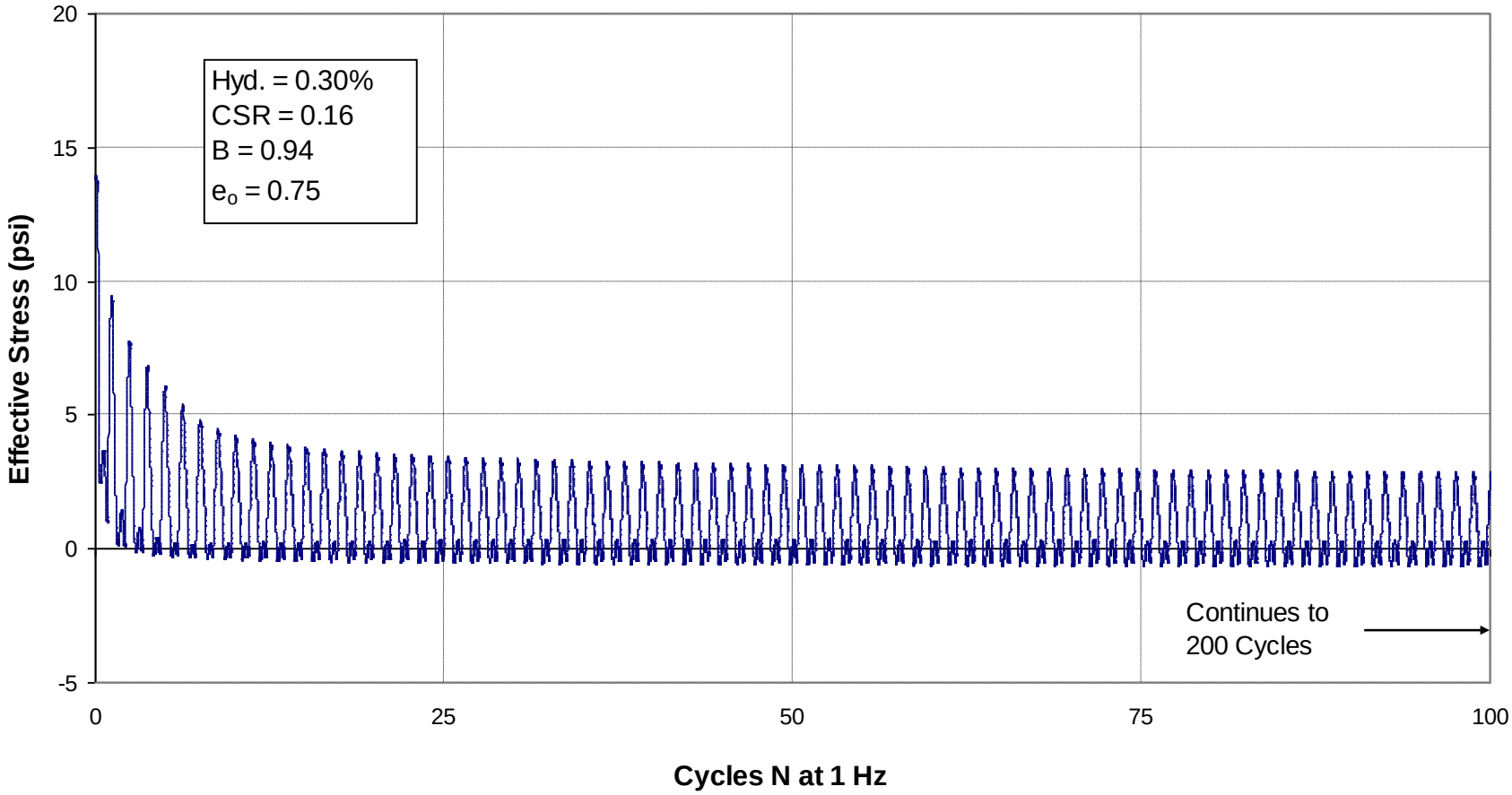

Figure 4.59: Effective Stress vs. Cycles for hydrogel treated Ottawa sand Sample 0.30%B-Test 2 (0.30% hydrogel); liquefaction occurred immediately; test was ended at 200 cycles

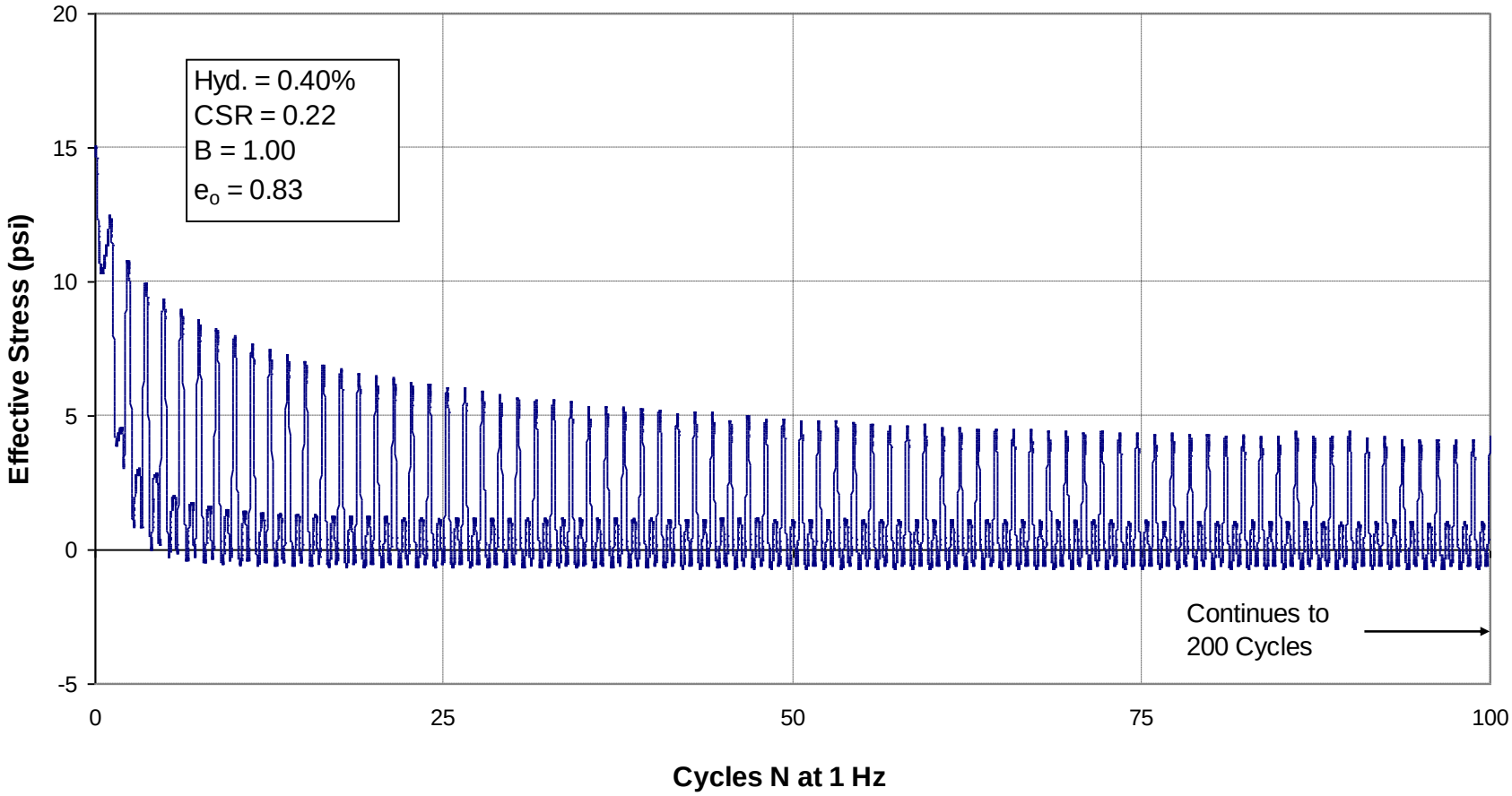

Figure 4.60: Effective Stress vs. Cycles for hydrogel treated Ottawa sand Sample 0.40%A-Test 1 (0.40% hydrogel); liquefaction occurred after 2 cycles; test was ended at 200 cycles

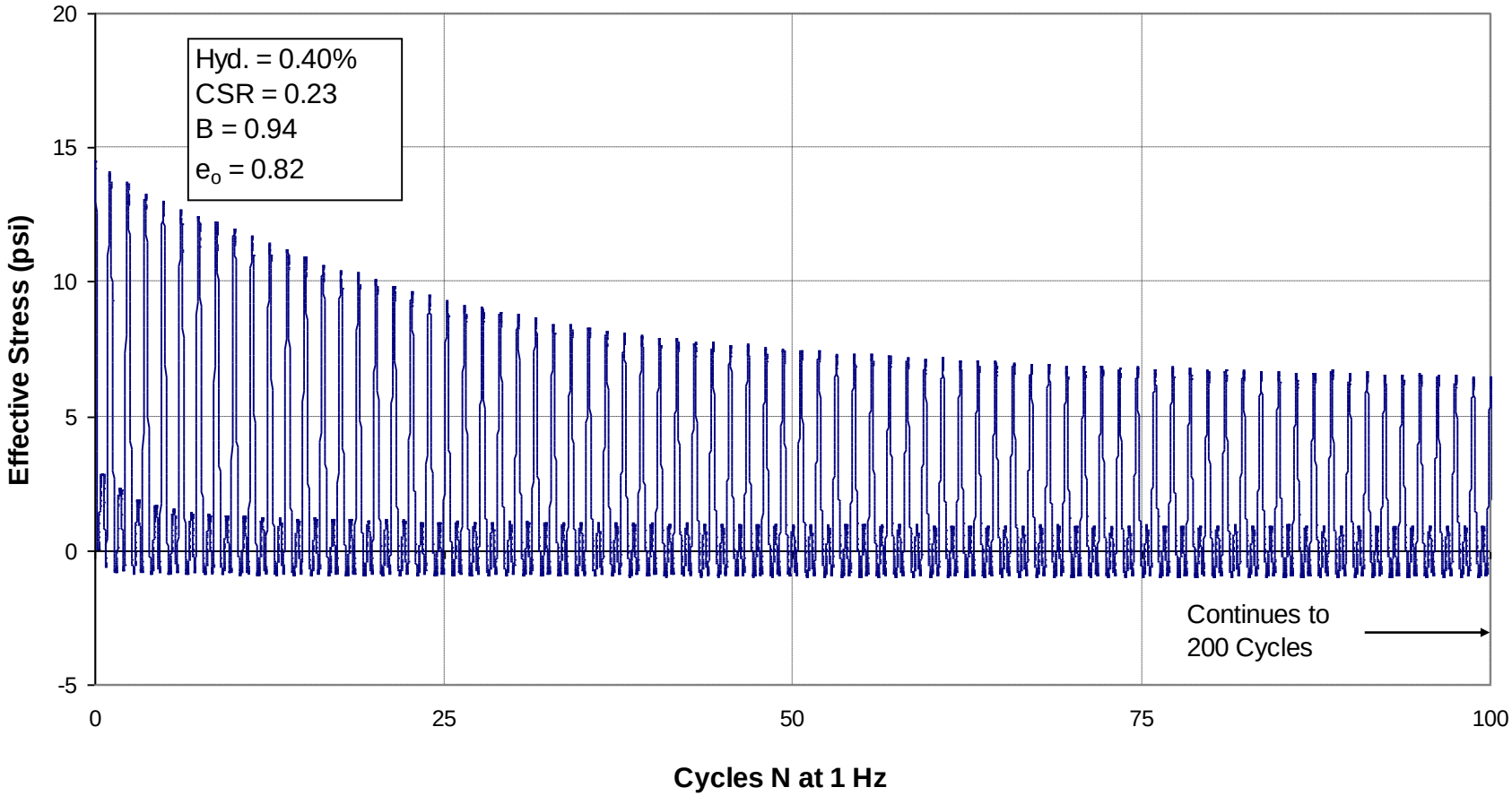

Figure 4.61: Effective Stress vs. Cycles for hydrogel treated Ottawa sand Sample 0.40%B-Test 2 (0.40% hydrogel); liquefaction occurred immediately; test was ended at 200 cycles

4.2.4.5 Combined Results

The results presented in the previous three subsections are presented again in Figures 4.62 through 4.74. In these figures, all three pieces of data (deviator stress, axial strain, and effective stress) are plotted on the same plot for each individual test. The purpose of presenting the data in this way is to make it easier to see relationships between the three types of data. More specifically, it is easier to see how stress and strain change at the point where effective stress reaches zero. Specific discussions about deviator stress, axial strain, and effective stress are presented in the previous three subsections.

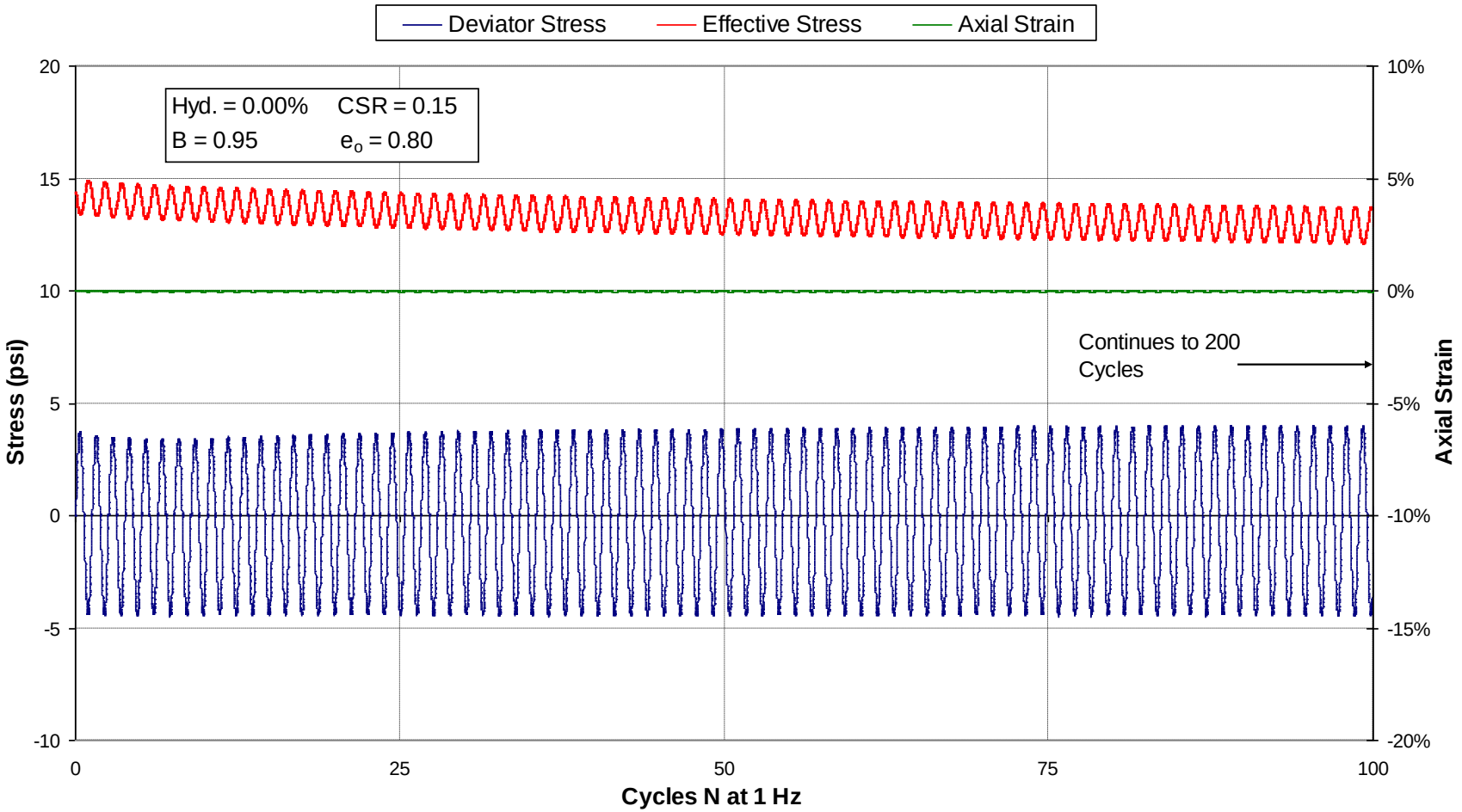

Figure 4.62: Deviator Stress, Effective Stress, and Axial Strain vs. Cycles, for Ottawa sand Sample 0.00%A-Test 1 (0.00% hydrogel); liquefaction did not occur; test was ended at 200 cycles

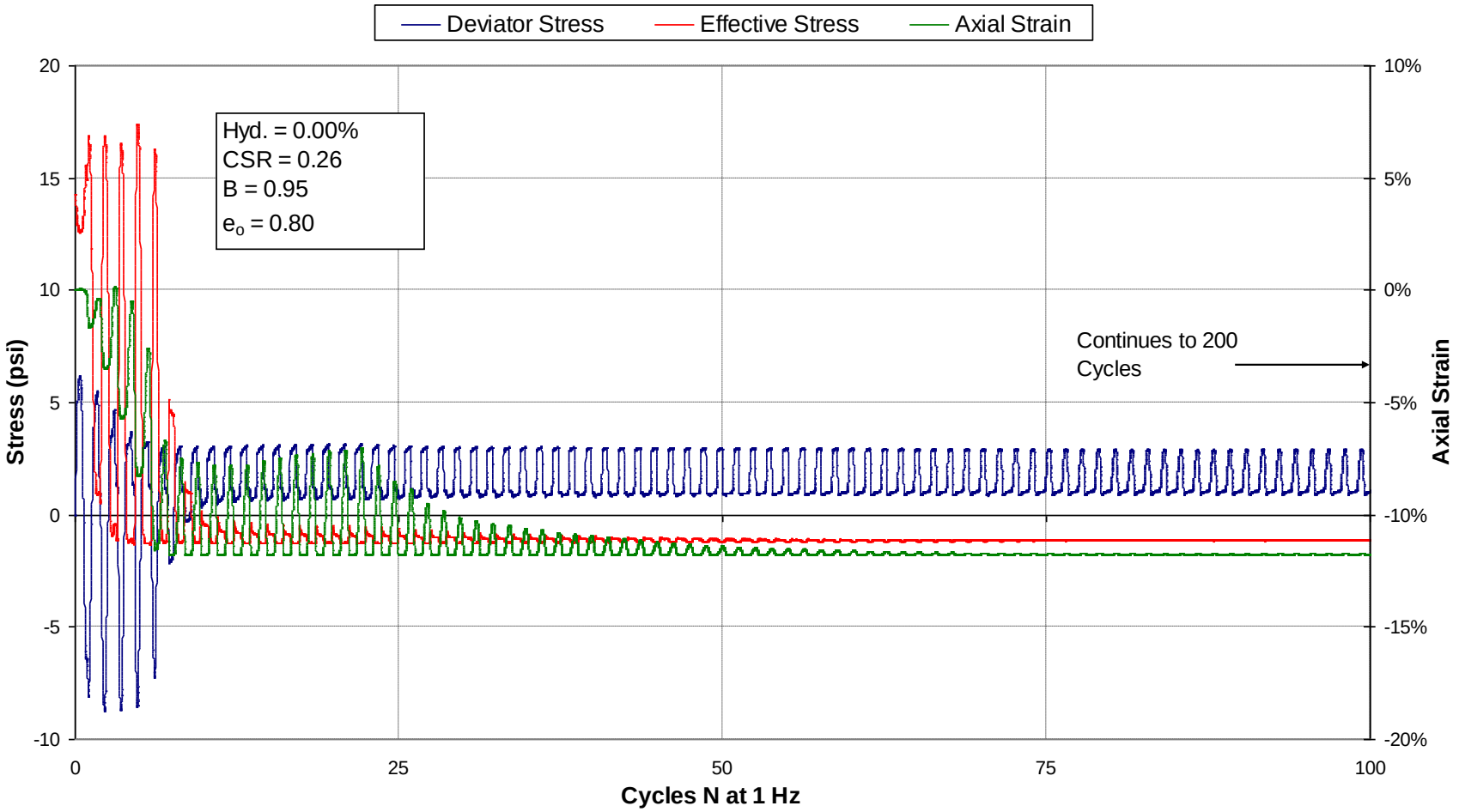

Figure 4.63: Deviator Stress, Effective Stress, and Axial Strain vs. Cycles, for Ottawa sand Sample 0.00%A-Test 2 (0.00% hydrogel); liquefaction occurred after 5 cycles; test was ended at 200 cycles

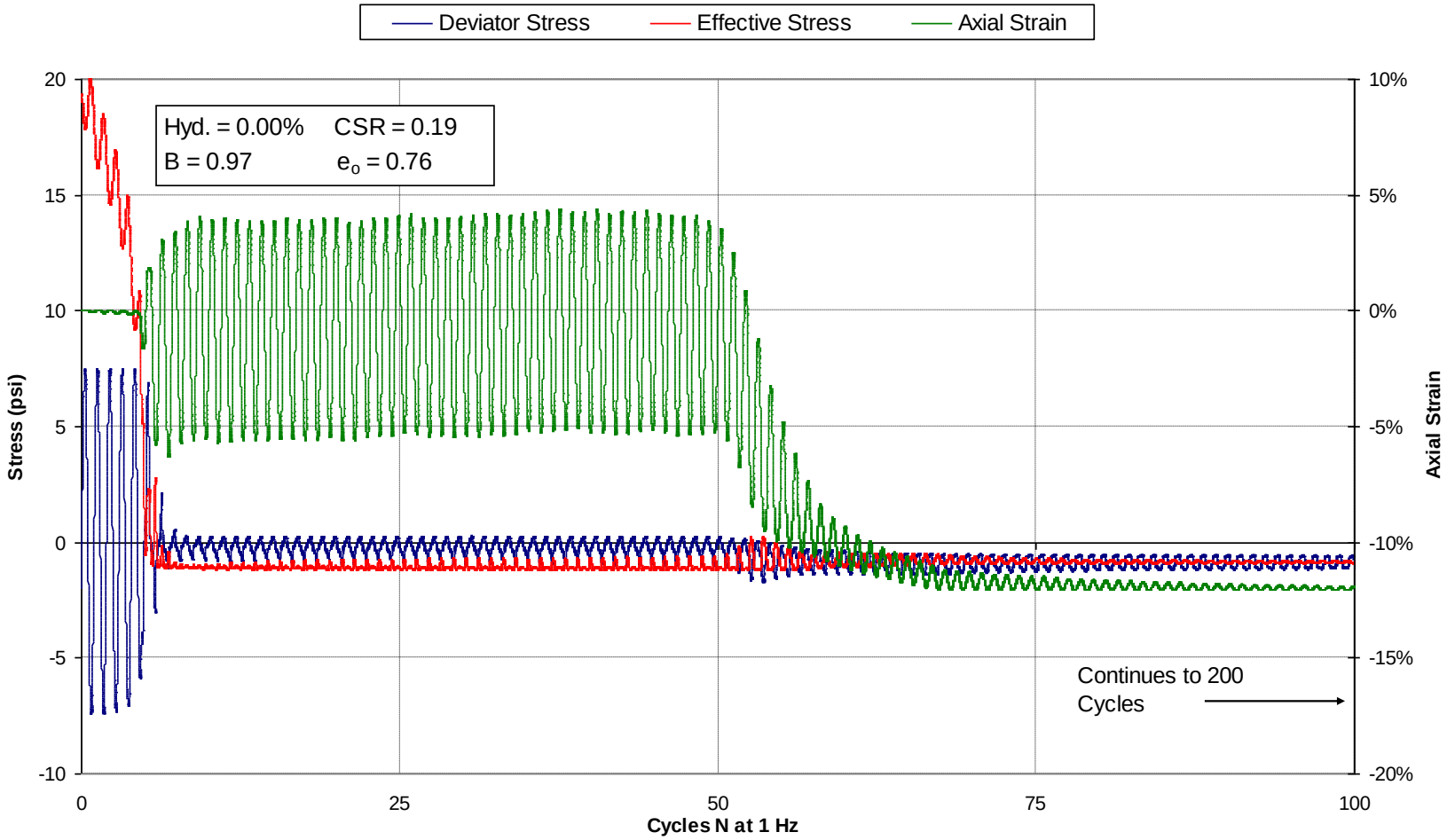

Figure 4.64: Deviator Stress, Effective Stress, and Axial Strain vs. Cycles, for Ottawa sand Sample 0.00%n8-04-Test 1 (0.00% hydrogel); liquefaction occurred after 5 cycles; test was ended at 200 cycles

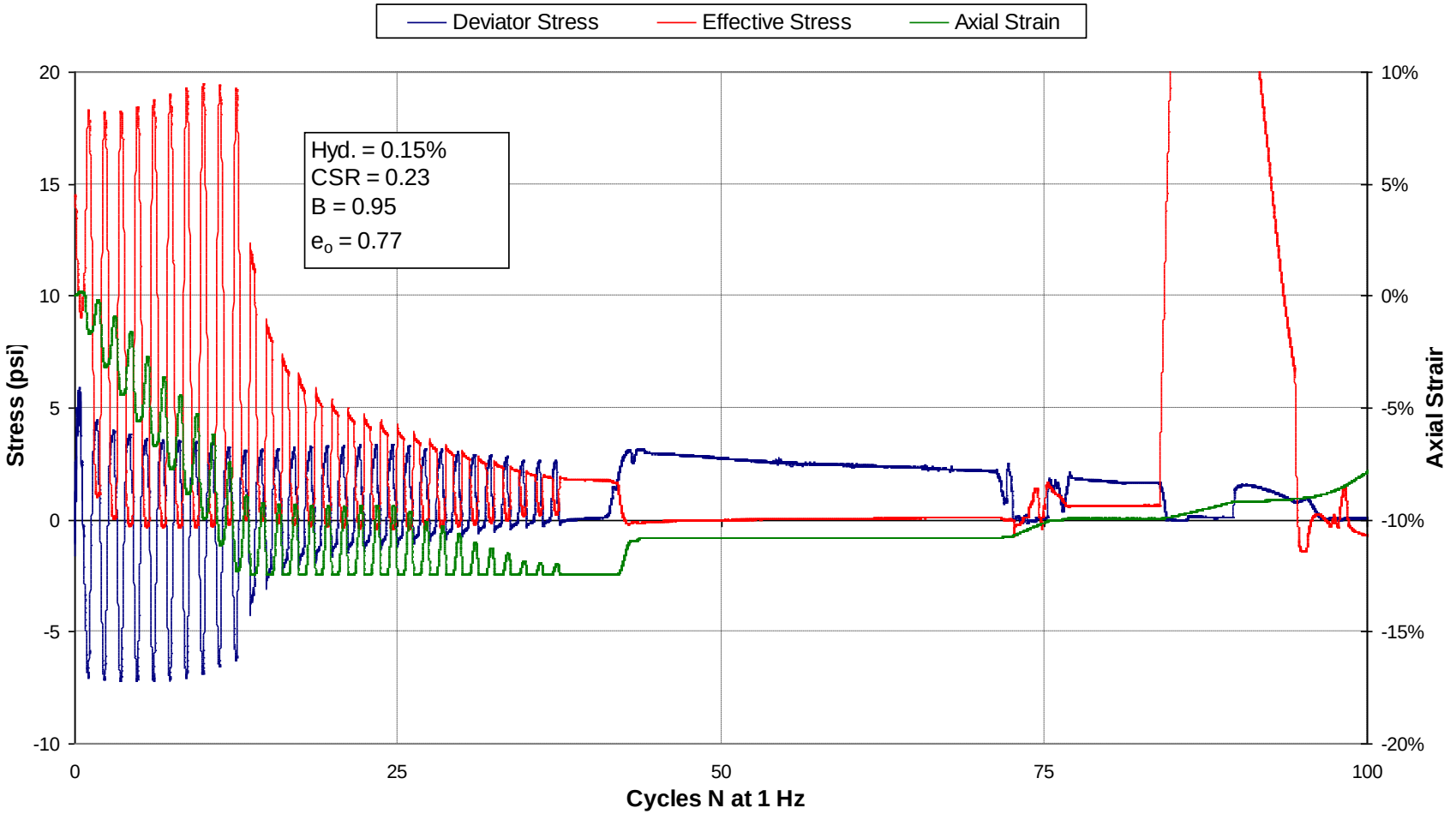

Figure 4.65: Deviator Stress, Effective Stress, and Axial Strain vs. Cycles, for hydrogel treated Ottawa sand Sample 0.15%A-Test 1 (0.15% hydrogel); liquefaction occurred after 3 cycles; issues with the testing equipment occurred at 38 cycles

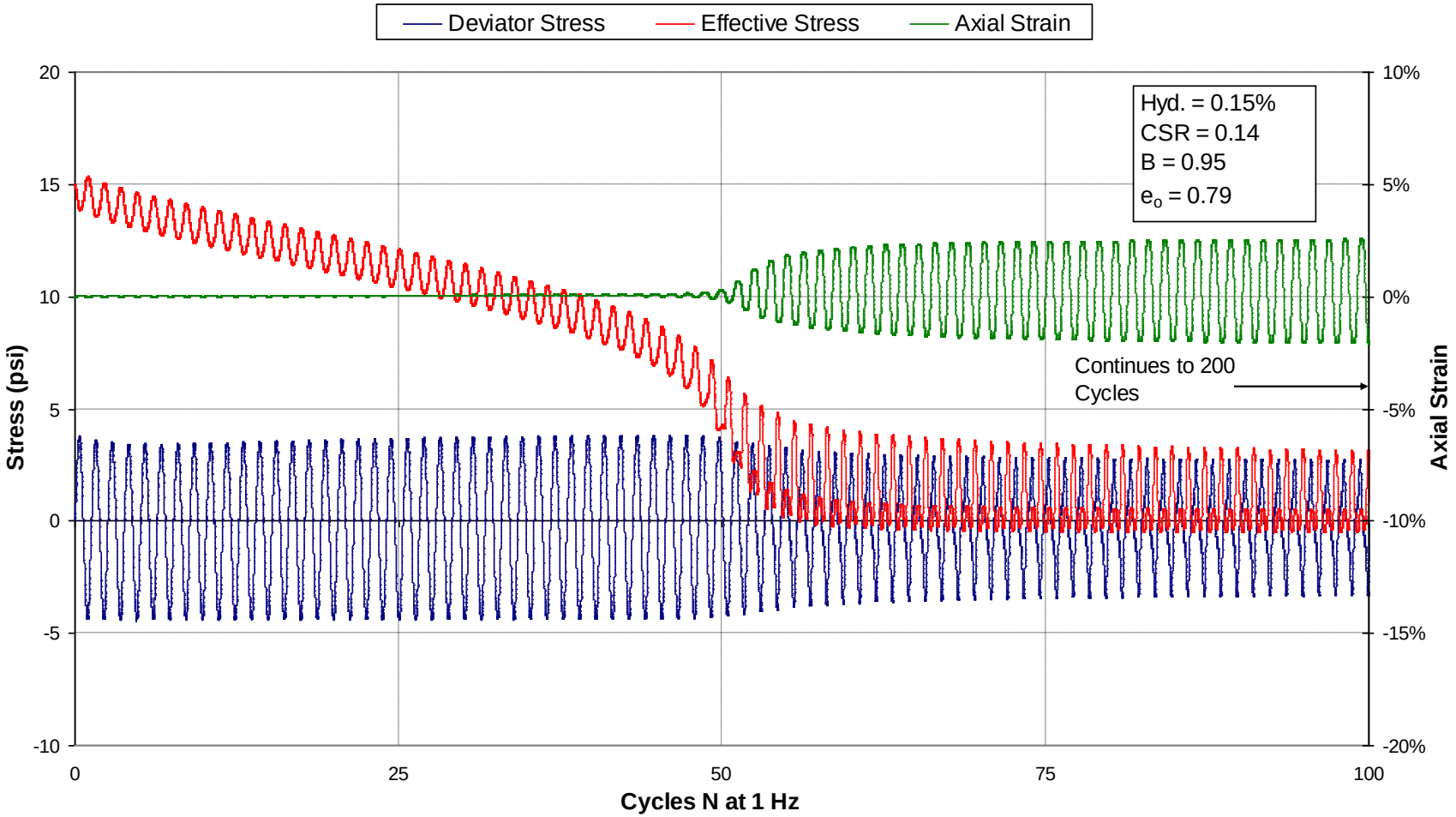

Figure 4.66: Deviator Stress, Effective Stress, and Axial Strain vs. Cycles, for hydrogel treated Ottawa sand Sample 0.15%B-Test 1 (0.15% hydrogel); liquefaction occurred after 5 cycles; test was ended at 200 cycles

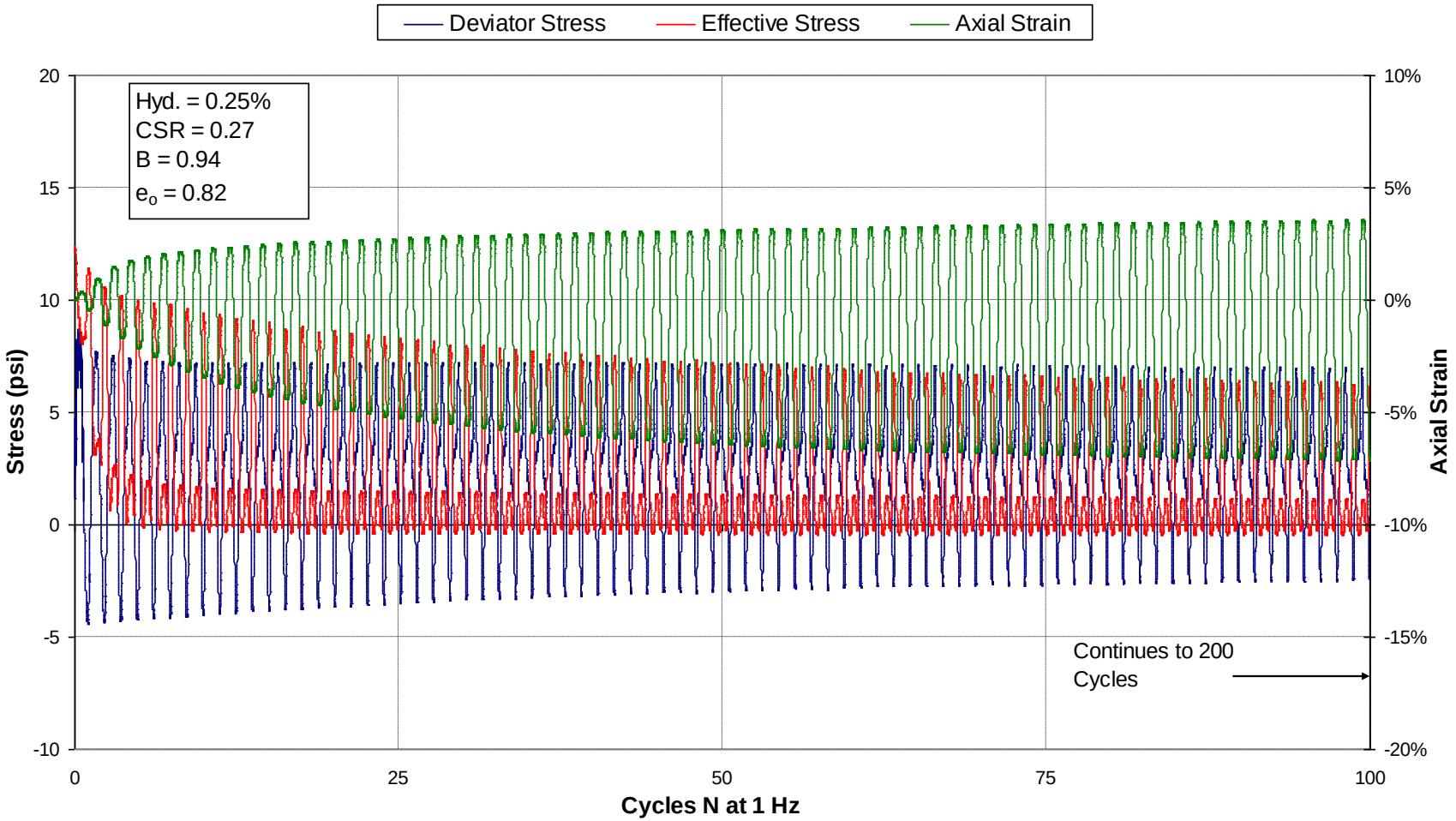

Figure 4.67: Deviator Stress, Effective Stress, and Axial Strain vs. Cycles, for hydrogel treated Ottawa sand Sample 0.25%A-Test 1 (0.25% hydrogel); liquefaction occurred after 3 cycles; test was ended at 200 cycles

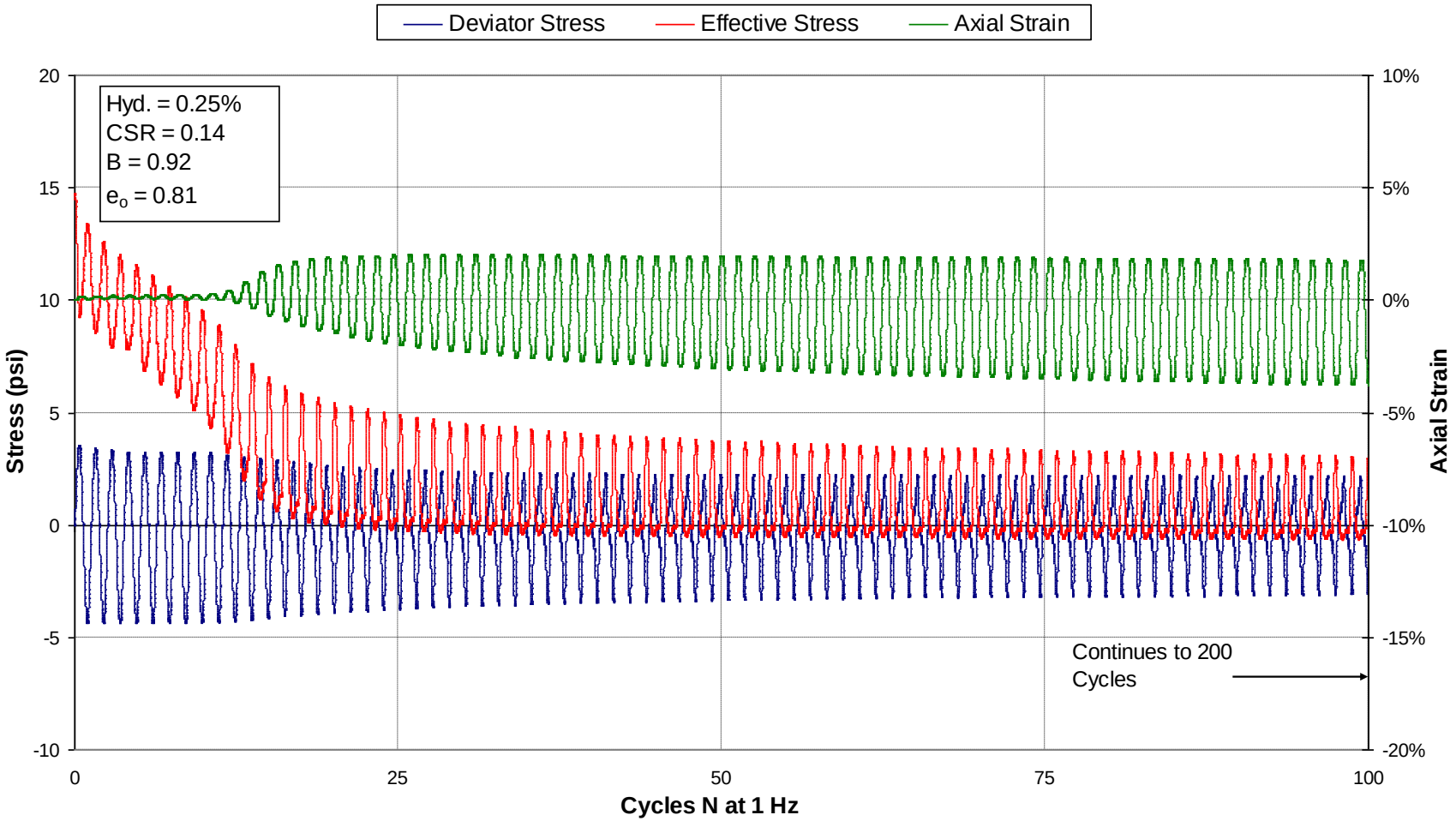

Figure 4.68: Deviator Stress, Effective Stress, and Axial Strain vs. Cycles, for hydrogel treated Ottawa sand Sample 0.25%B-Test 1 (0.25% hydrogel); liquefaction occurred after 17 cycles; test was ended at 200 cycles

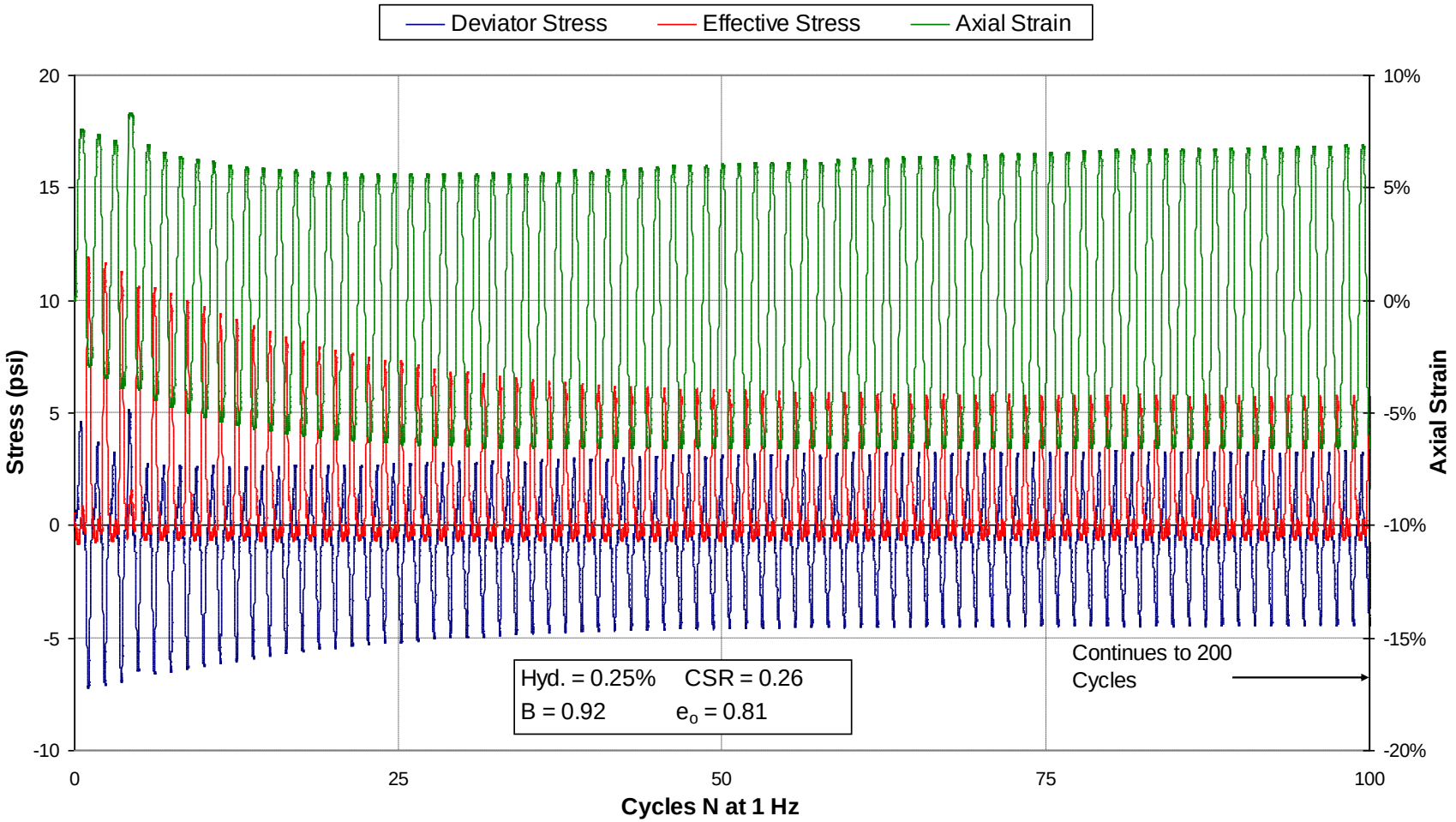

Figure 4.69: Deviator Stress, Effective Stress, and Axial Strain vs. Cycles, for hydrogel treated Ottawa sand Sample 0.25%B-Test 2 (0.25% hydrogel); liquefaction occurred immediately; test was ended at 200 cycles

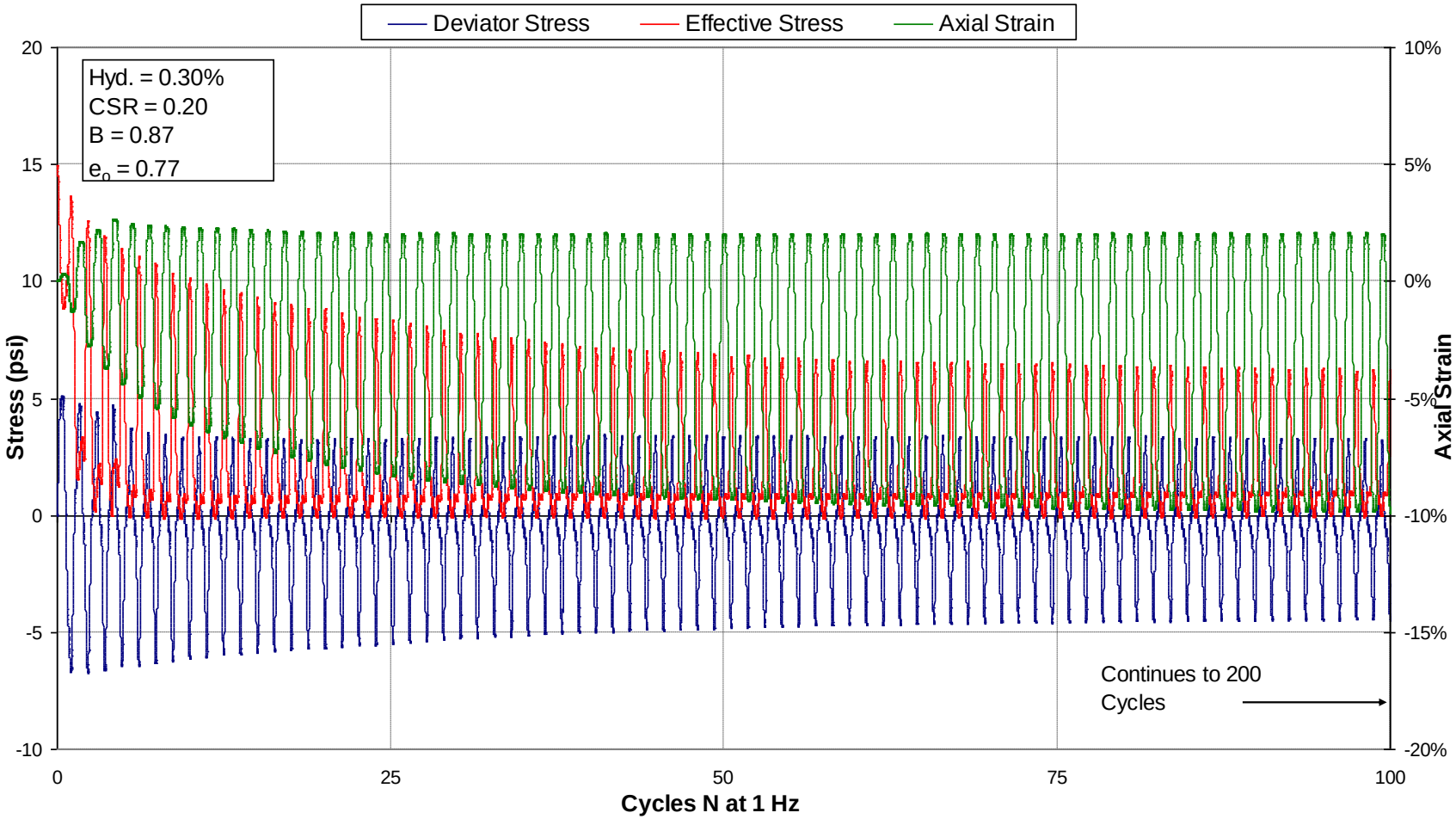

Figure 4.70: Deviator Stress, Effective Stress, and Axial Strain vs. Cycles, for hydrogel treated Ottawa sand Sample 0.30%A-Test 1 (0.30% hydrogel); liquefaction occurred after 3 cycles; test was ended at 200 cycles

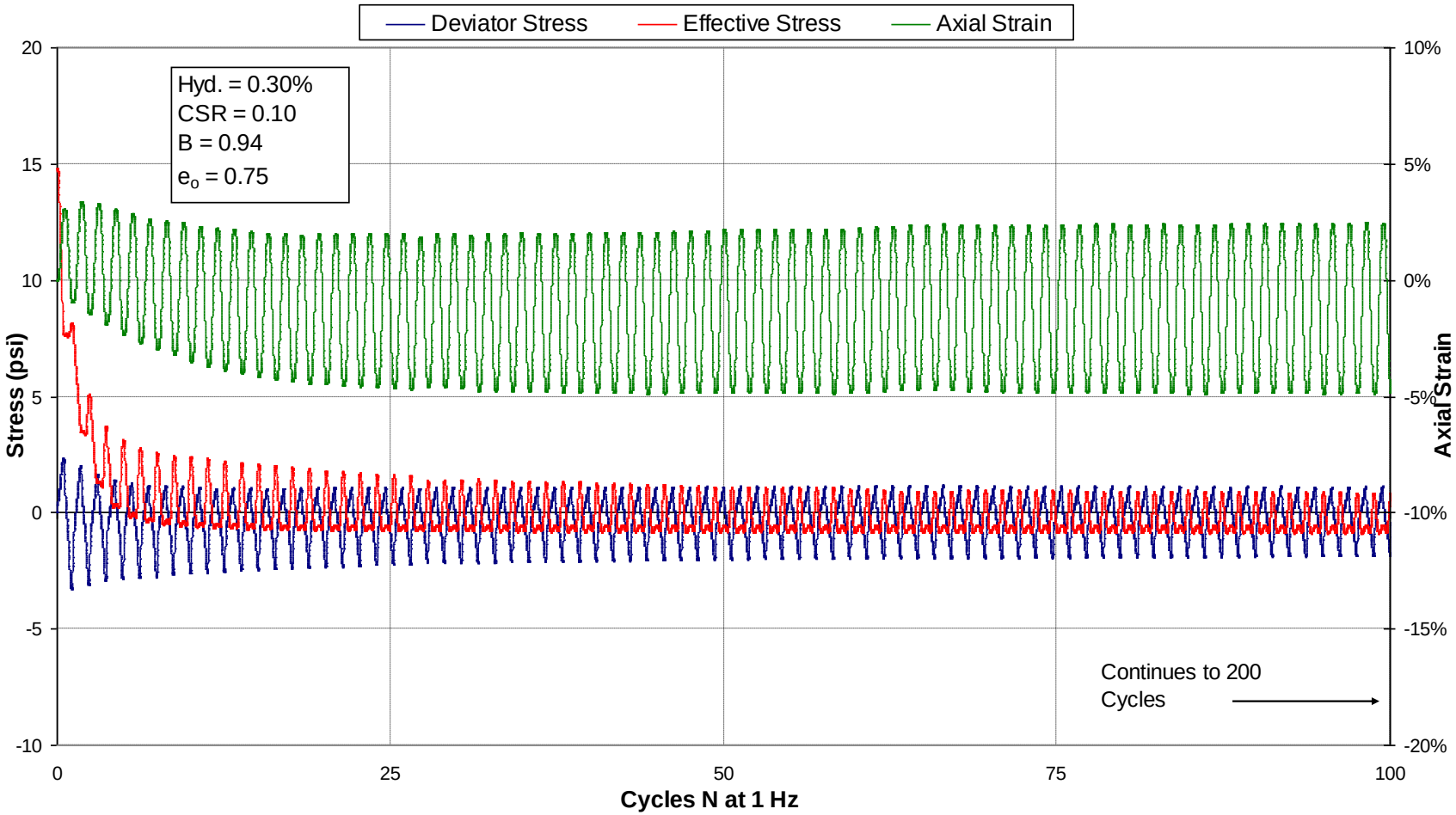

Figure 4.71: Deviator Stress, Effective Stress, and Axial Strain vs. Cycles, for hydrogel treated Ottawa sand Sample 0.30%B-Test 1 (0.30% hydrogel); liquefaction occurred after 4 cycles; test was ended at 200 cycles

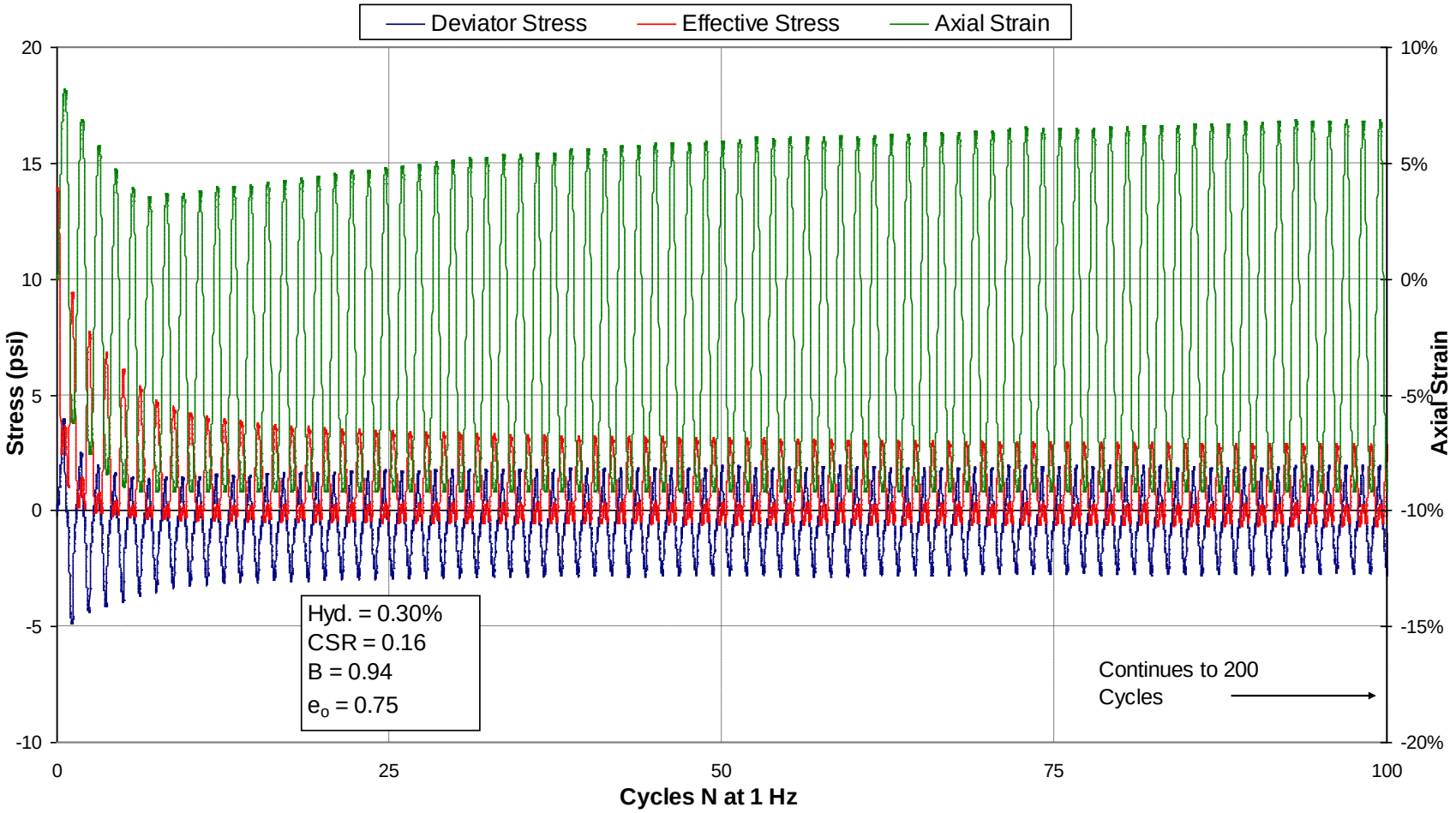

Figure 4.72: Deviator Stress, Effective Stress, and Axial Strain vs. Cycles, for hydrogel treated Ottawa sand Sample 0.30%B-Test 2 (0.30% hydrogel); liquefaction occurred immediately; test was ended at 200 cycles

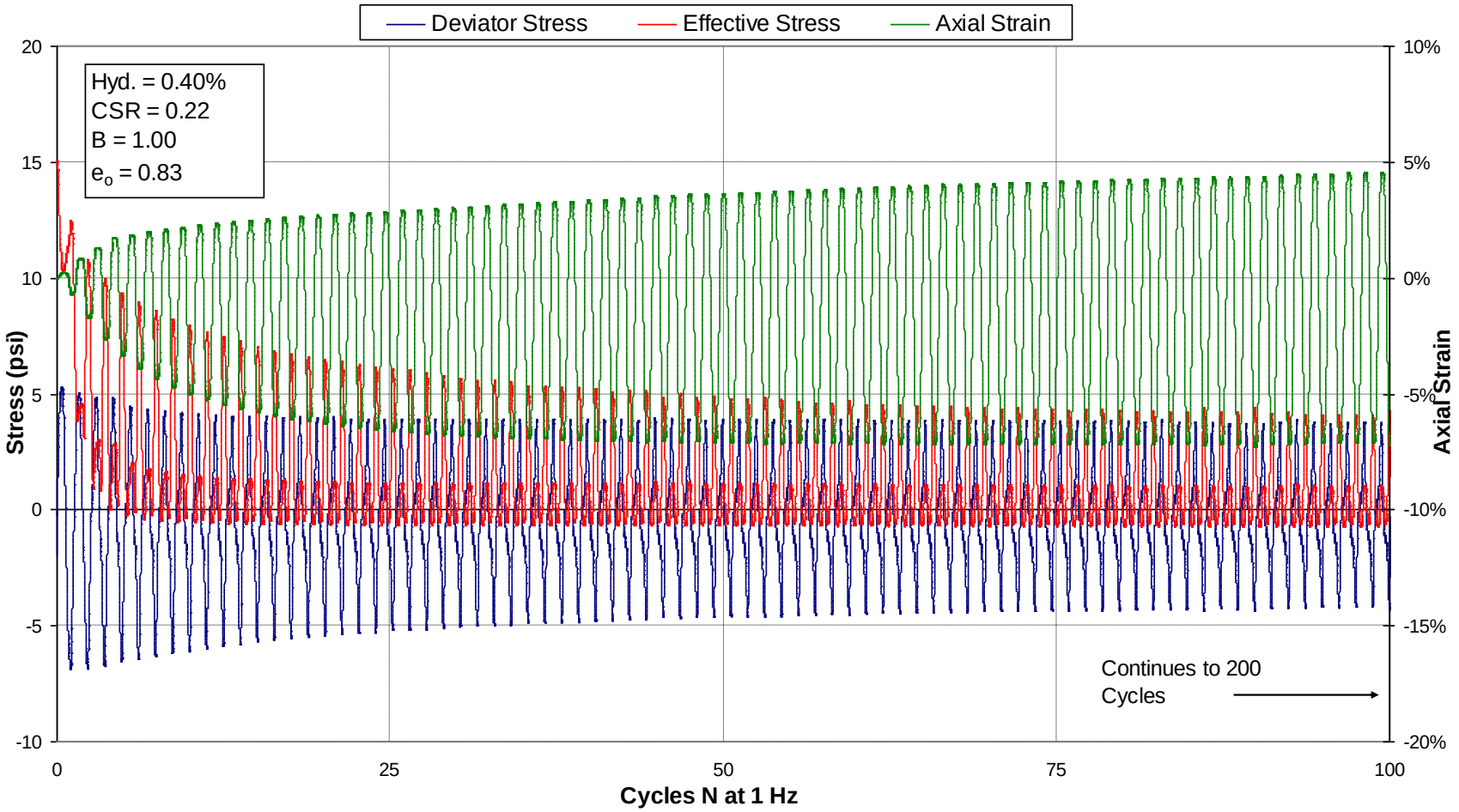

Figure 4.73: Deviator Stress, Effective Stress, and Axial Strain vs. Cycles, for hydrogel treated Ottawa sand Sample 0.40%A-Test 1 (0.40% hydrogel); liquefaction occurred after 2 cycles; test was ended at 200 cycles

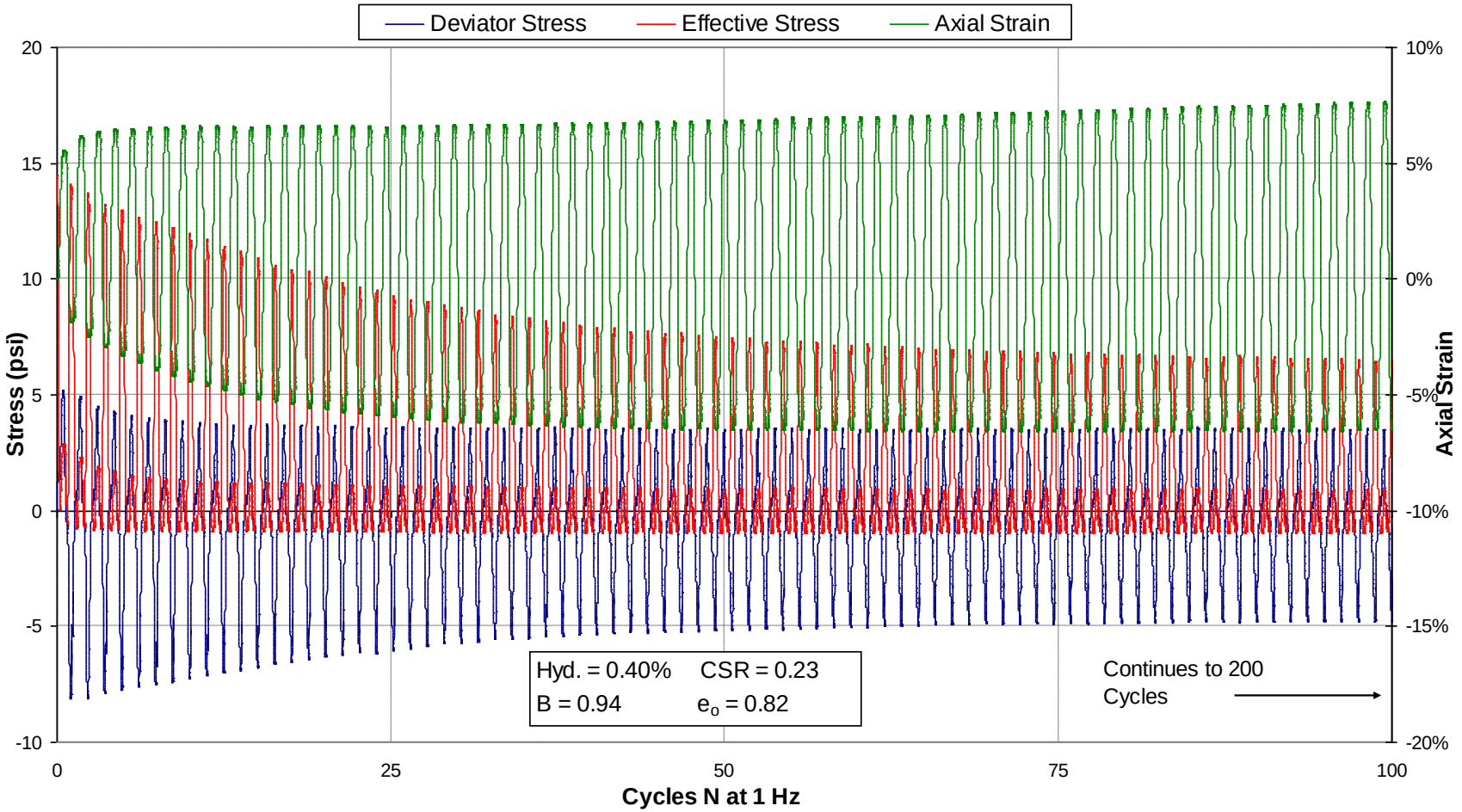

Figure 4.74: Deviator Stress, Effective Stress, and Axial Strain vs. Cycles, for hydrogel treated Ottawa sand Sample 0.40%B-Test 2 (0.40% hydrogel); liquefaction occurred after 2 cycles; test was ended at 200 cycles

4.3 One-Dimensional Consolidation Testing

4.3.1 Overview

One-dimensional consolidation testing was performed to evaluate the effect of hydrogel on the magnitude of consolidation of Ottawa sand. There is a discussion on time rate of consolidation, although quantitative calculations were not performed. The consolidation testing generally followed ASTM D2435 as described in Section 3.7. Three series of tests were performed on five different concentrations of hydrogel: 0.00%, 0.15%, 0.25%, 0.30%, and 0.40%.

4.3.2 Selection of Percent Hydrogel

The concentrations of hydrogel selected for consolidation test are the same as those selected for the CU triaxial testing. The reasoning for selecting these concentrations is discussed in Section 4.1.2. As noted in the section above, three sets of tests were run on samples of 0.00%, 0.15%, 0.25%, 0.30%, and 0.40% hydrogel.

4.3.3 Factors Affecting Consolidation Other Than Hydrogel

4.3.3.1 Stress

The consolidation of sands under low stresses is primarily a function of two things: rearrangement of the sand particles and elastic deformation of the sand particles; however, it is the rearrangement of the sand particles that causes the largest deformations. Above stresses of approximately 1000 psi (72 tsf) siliceous sands, like Ottawa sand, may begin to exhibit additional deformation due to crushing of the sand particles (Roberts 1964). For the stress range normally encountered in civil engineering problems (less than 1000 psi), the one-dimensional consolidation of sand typically plots linearly on a log σ' vs. e or ε consolidation plot, i.e. the compression index (C_c) is a constant.

Variability increased with increasing stress. That is, when comparing results of the individual tests at the same stress level, the resulting strains were not as tightly grouped at higher stresses as they were for lower stresses. This increasing variability with stress is illustrated in Figure 4.75 by comparing the results of three non-hydrogel samples. Note that for the first three stresses in Figure 4.75, the data points of all three series are closely grouped. Then, as the loadings increase, especially above 1 tsf, the data points diverge. The increase in variability could be the result of sample variability that is simply more apparent at higher stresses. It could also be the result of inconsistencies between the sand grain rearrangements that occur when sand samples are compressed. Because the void ratios of the samples were not the same, it is likely that some will compress more easily than others, possibly causing the variability. It is not likely that the variability is due to particle crushing, considering that the maximum stress applied (16 tsf) is much less than the 72 tsf stress that Roberts (1964) estimated was necessary to induce particle crushing. Increased variability with stress was also observed for samples containing hydrogel.

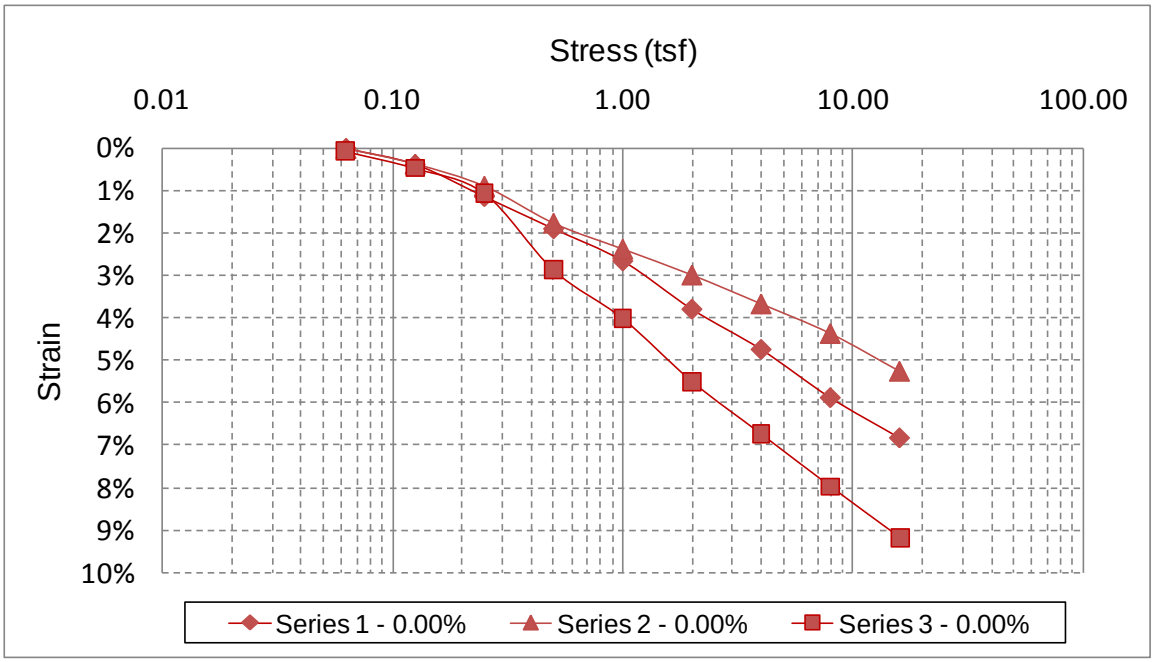

Figure 4.75: Comparison of three tests on 0.00% hydrogel samples to demonstrate the increase in variability between data points at higher stresses

4.3.3.2 Void Ratio

Because the consolidation of sand is primarily a function of particle rearrangement, the initial void ratio is a factor in determining the consolidation behavior of sands. Samples that are initially denser at the beginning of a test will not consolidate as much as samples that are looser at the beginning of a test. Note the visible difference in the slope (compression index with respect to strain, C_c') of the curves for the loose and the dense Ottawa sand in Figure 4.76.

Weight and dimensional information was not recorded for the first series of tests. This information was recorded for the second and third series of tests. The unit weights and void ratios are presented in Table 4.7. The values for unit weight and void ratio varied wildly and did not always fall within the same range of values seen for the triaxial samples. Because the consolidation samples are so small, a small error in measurement of mass or volume can result in a large inaccuracy in void ratio and unit weight. It is likely that samples that appear to have a

high void ratio (low dry unit weight) actually had a lower void ratio, but because not all of the sand was recovered after the test, the measured dry weight was lower than it should have been. This would result in a lower dry unit weight and a higher void ratio. Samples with higher than normal dry densities and lower than normal void ratios could be a result of the tester not zeroing the caliper or balance before taking measurements, causing the volume or weight measurements to be off. All of the CU triaxial sample void ratios fell within the range of 0.62 to 0.82, only one consolidation sample, Series 2 - 0.15% hydrogel, fell within this range. It does not appear that the measurements for the calculation of densities and void ratios were precise enough to draw conclusions about differences in the consolidation results with respect to density or void ratio.

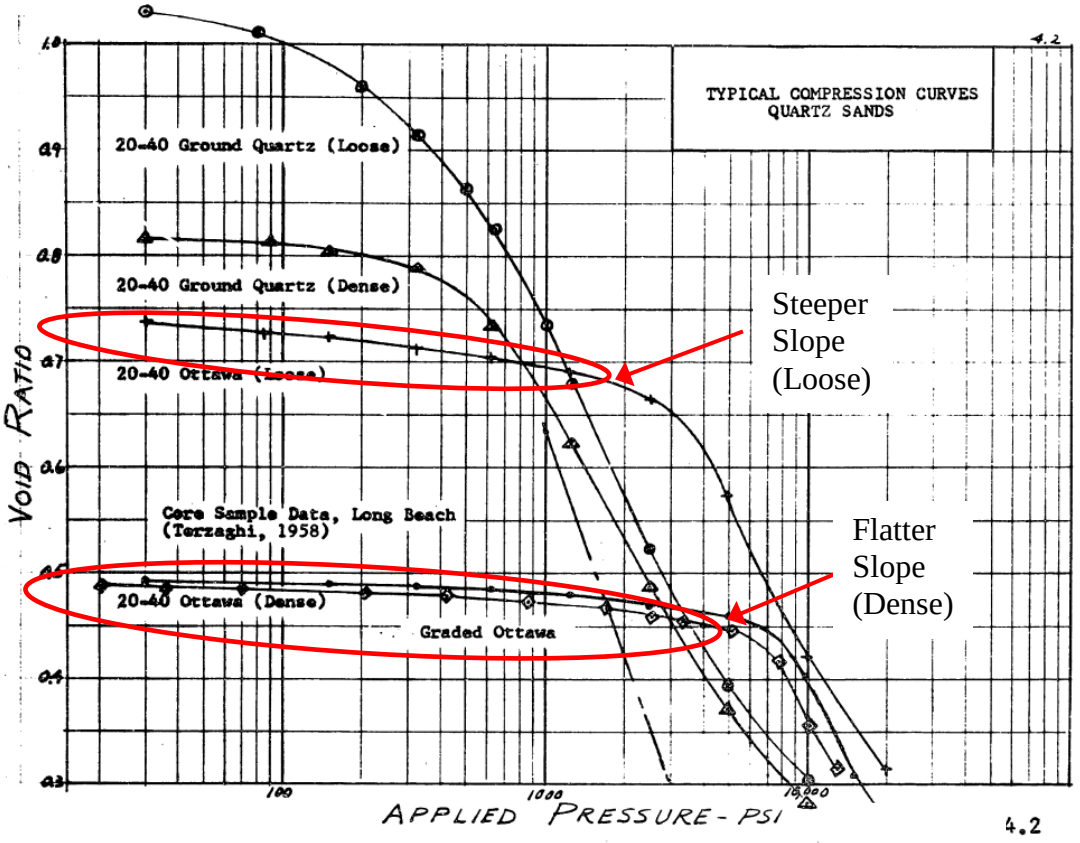

Figure 4.76: Comparison of compression curves for loose and dense Ottawa sand (Roberts 1964)

Table 4.7: Unit weights and void ratio of Series 2 and 3 samples

Series	% Hydrogel	Wet Unit Weight (lb/ft^3)	Dry Unit Weight (lb/ft^3)	Void Ratio
2	0.00%	126.8	102.6	0.61
3	0.00%	114.9	89.3	0.85
2	0.15%	118.4	95.4	0.73
3	0.15%	109.0	85.2	0.94
2	0.25%	113.9	88.8	0.86
3	0.25%	113.4	88.3	0.87
2	0.30%	132.2	109.0	0.52
3	0.30%	115.1	88.6	0.87
2	0.40%	106.8	80.4	1.06
3	0.40%	106.0	81.6	1.03
Standard Deviation:		8.37	9.02	0.171
Average:		115.7	90.9	0.83

4.3.3.3 Permeability

For fine-grained soils like clays, consolidation is a function of pore pressure dissipation which is governed by the soils permeability. With course-grained soils like sand, pore pressure dissipation is not a factor because the permeability of the material is large enough that pore pressures dissipate almost immediately. The addition of hydrogel decreases permeability (Grattoni et al. 2004; Khedr and Ahmed 1996; Shiver 2007). Because the permeability of samples containing hydrogel is much lower than that of plain sand, it was expected that hydrogel should have an effect on the consolidation of Ottawa sand. However, the reduced permeability would most affect the time rate of consolidation rather than the magnitude of consolidation, which was the focus of this research.

4.3.4 Effects of Hydrogel on Magnitude of Consolidation

Figure 4.77 presents the results of the three series of consolidation tests. Each series is denoted by different marker styles and different concentrations of hydrogel are denoted with different colors as indicated in at the bottom of the figure. The data were presented in terms of strain rather than void ratio to normalize the data so that the data would originate from roughly

the sample place on the plot. This is especially important considering the issues in calculating void ratio discussed in Section 4.3.3.2.

The 0.00% and 0.15% hydrogel samples generally exhibited similar behavior and a lower C_c' (~0.03) than most of the samples of other concentrations of hydrogel. As the concentration of hydrogel increases, C_c' typically increases; however, there is a large amount of variability in C_c' that also seems to increase with increasing amounts of hydrogel.

The results of the CU testing indicated that hydrogel lubricates the sand particles. This effect may cause the sand particles to more easily slide around each other during consolidation, resulting in larger deformations for the same pressure, and ultimately a lager C_c'. The increase in variability between C_c' may be a result of differences in hydrogel distribution throughout the sample.

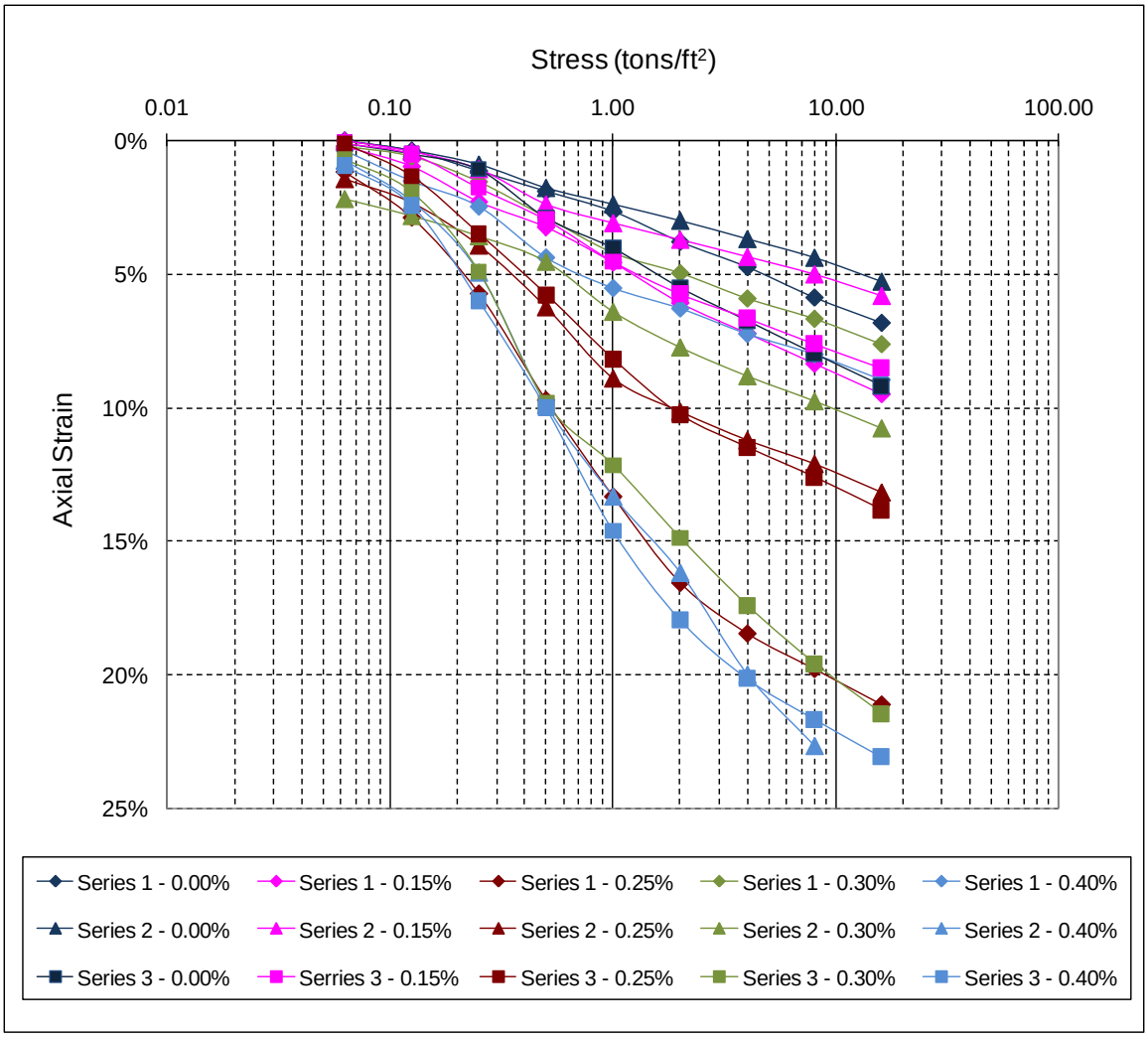

Figure 4.77: Consolidation results from three series of tests on five different concentrations of hydrogel: 0.00%, 0.15%, 0.25%, 0.30%, and 0.40%

4.3.5 Discussion of the Effects of Hydrogel on Time Rate of Consolidation

Sands consolidate quickly because of their high permeability. The time rate of consolidation of sands typically occurs so quickly that it is considered to take place instantaneously with loading. For this reason, the procedures for estimating the time rate of consolidation have been developed almost exclusively for clays.

With the addition of hydrogel, permeability of Ottawa sand is significantly reduced. Based on observations during testing, the lower permeability hydrogel-sand mixtures do

consolidate more slowly than plain Ottawa sand; however, the time required for consolidation is still much faster than that of even a high permeability clay. The triaxial samples also consolidated quickly (less than 5 min) during the consolidation phase of the setup. It is thought that consolidating or squeezing water out of the hydrogel-sand mixture (consolidation) is different than trying to flow water through it (permeability test). This concept can be illustrated with saturated household sponge. If the sponge is held against a faucet, water will not easily pass through the sponge, but if the sponge is compressed, water easily flows out. On the molecular level, the hydrogel may be acting in a similar fashion. This would explain why the permeability is very low but the rate of consolidation is not equally low. This theory may require further investigation to validate.

The reason time rate of consolidation was not quantified is two-fold. First, because the methods of estimating time rate of consolidation have been developed for clays based on the dissipation of pore pressure, their applicability to the estimation of the time rate of consolidation of sand and sand with hydrogel is not necessarily valid. Secondly, the increase in time rate of consolidation was rather small. Basically, the time required for consolidation was increased from a very small number to a slightly larger but still very small number. Despite requiring slightly more time to consolidate, it appears that sand with hydrogel could still be considered to consolidate instantaneously with loading based on the observations made during the consolidation and triaxial testing.

4.4 Electrical Self-Potential Experiments

4.4.1 Overview

One of the main concerns with using hydrogel for liquefaction prevention is the ability to know exactly where the hydrogel is in the subsurface once it has been installed. Electrical self-

potential is a geophysical subsurface investigation method based on the measurement of naturally occurring electrical currents in a soil mass. Details about the principles of electrical self-potential and equipment used are presented in Section 3.8. Three experiments were carried out to see if a mass of soil containing hydrogel within a mass of soil not containing hydrogel could be detected. A 0.40% concentration of hydrogel was used in two experiments, and a 0.25% concentration of hydrogel was used in one experiment.

4.4.2 Selection of Percent Hydrogel

Initially, 0.40% hydrogel was used in the experiments because it was the largest concentration of hydrogel being used for the triaxial and consolidation testing. Being the largest concentration meant it was the most likely to be detectable. Once it was established that 0.40% hydrogel was detectable, another experiment was run on 0.25% hydrogel to see if this lower concentration could also be detected.

4.4.3 Factors Affecting Electrical Self-Potential

In the field, naturally-occurring electrical potential stems from two sources: *dynamic* potential caused by the flow of water, other fluids, or heat and *static* potential caused by differences in the chemical composition of the subsurface. For the laboratory experiments there was no fluid flow and the temperature remained constant, eliminating dynamic potential effects. Distilled water was used to minimize the effects of any foreign molecules found in the saturating water. The PVC container that the experiment was conducted in was thoroughly washed and rinsed with distilled water to further prevent contamination. All of these efforts were aimed at isolating hydrogel as the variable.

The electrodes themselves can also introduce bias. To reduce the effects of electrode bias, several measures were taken. First, the electrodes were monitored for stability and bias as

described in Section 3.8.1.2. Second, for redundancy, multiple electrodes were used during the tests. Third, multiple measurements were taken during each experiment to track the consistency of measurements over time. These procedures allowed for selection of electrodes that have the least amount of bias and help identify any electrodes that do not match the trends of the other electrodes.

4.4.4 Experimental results and discussion

Three electrical self-potential experiments were conducted. The experiments basically consisted of a PVC container containing saturated Ottawa sand with a saturated Ottawa sand and hydrogel inclusion. Electrodes were placed in a variety of locations throughout the soil mass. Measurements were taken with respect to a preselected reference electrode. Details of the experimental setup and procedures are presented in Section 3.8.

Plan view schematics of each of the three experiments are presented in Figure 4.78. For experiments 1 and 2, a 0.40% hydrogel mixture was used in the inclusion. For experiment 3, a 0.25% hydrogel mixture was used in the inclusion. The location of the inclusion was moved between experiments to make sure the location with respect to the edges of the container was not influencing the results.

The results from these experiments are presented graphically in Figures 4.79-4.81 and numerically in Tables 4.8-4.10. In all cases, data highlighted or presented in orange indicates measurements taken between electrodes only within the hydrogel inclusion; data highlighted or presented in green indicates measurements taken between electrodes only within the clean sand; and data highlighted or presented in blue indicates measurements taken across the boundary (one electrode in the hydrogel inclusion and one in the clean sand).

When measurements are taken between electrodes located in the same media, there is much less potential difference. This can be most easily seen in Figure 4.79. Theoretically, if a material is perfectly homogenous, the potential difference would be zero between all points within that material. Although the results here were not always zero for measurements taken within a single media, they were very low, usually less than 10 mV. The reasons they are not exactly zero include the fact that sand is not perfectly homogeneous, the sand-hydrogel mixture is not perfectly homogenous, and the electrodes used are not perfectly stable or unbiased. Notable exceptions to the trend of low potential differences within a single media include measurements involving electrode 3 in Experiment 2 and electrode 5 in Experiment 3. It is likely that there was an unknown issue with electrode 3 in Experiment 2 that caused it to produce inaccurate readings. There are many possible reasons for this issue, but because the results with the other electrodes were so consistent, it is not unreasonable to discount the results of electrode 3. Electrode 5 in Experiment 3 was purposely placed on the boundary between the hydrogel inclusion and the clean sand to see how the readings would behave. Although it was considered to be outside of the inclusion, its location at the boundary probably affected the readings.

Readings taken across the boundary between the two media typically exhibited a large potential difference. The magnitude of the potential difference was not the same for all three experiments. The average potential difference across the boundary was 41.0 mV for Experiment 1, 56.5 mV for Experiment 2 (excluding results involving electrode 3), and 21.6 mV for Experiment 3 (excluding results involving electrode 5). The lower average difference observed in Experiment 3 was expected because a lower concentration of hydrogel was used for that experiment (0.25% vs. 0.40%). The difference in between Experiment 1 and 2 can be attributed to different conditions at the time of testing, such as humidity, temperature, void ratio, etc.

Ultimately, there appeared to be a measureable effect on electrical self-potential that appeared to be caused by the presence of hydrogel.

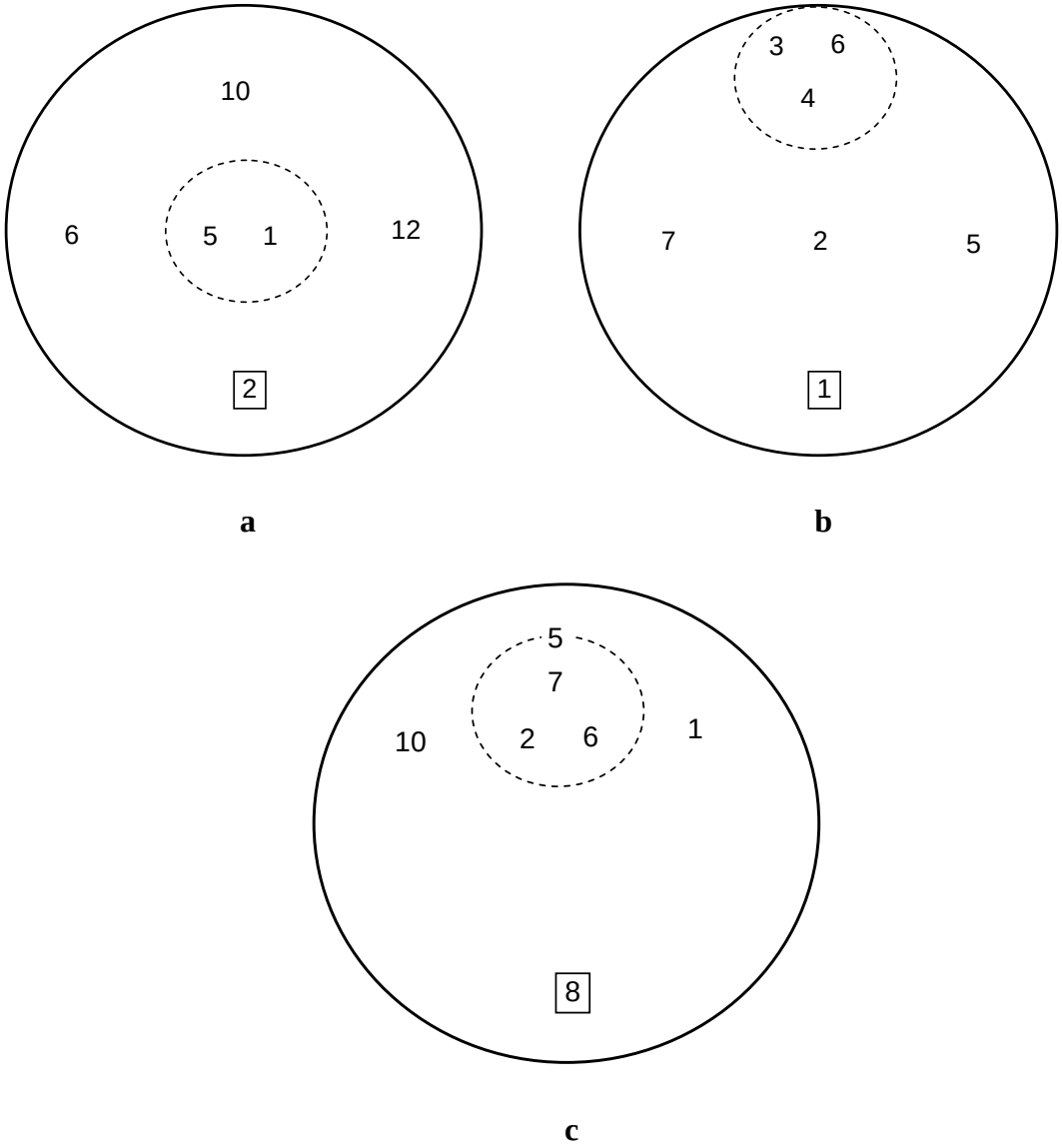

Figure 4.78: Plan view of experimental setup for Experiments 1 (a), 2 (b), and 3 (c). Note: The numbers correspond to the electrodes and their location. The boxed numbers indicate the reference electrode and the dashed circle indicates the location of the hydrogel inclusion within the sand mass. The container (large solid circle) is 10 in in diameter and the inclusion (small dashed circle) is 3 in in diameter.

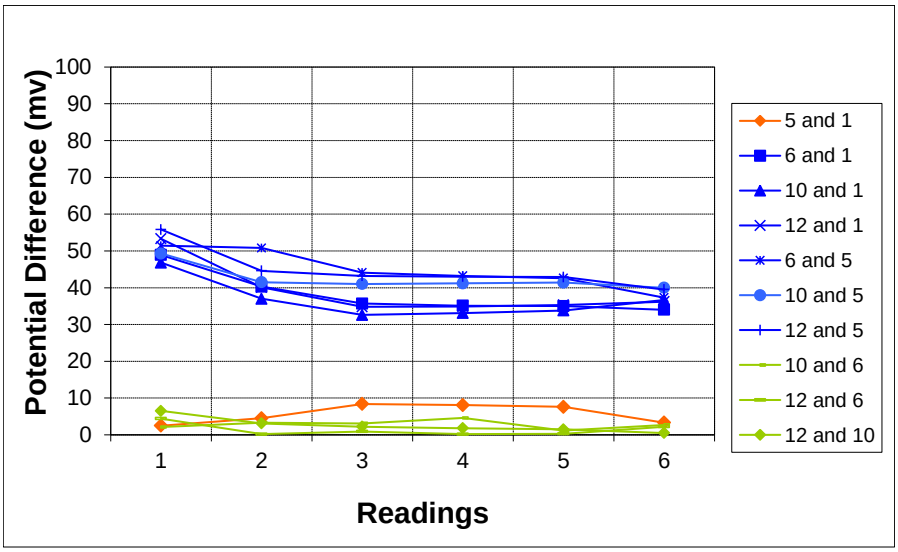

Figure 4.79: Self-potential Experiment 1 graphic presentation of results

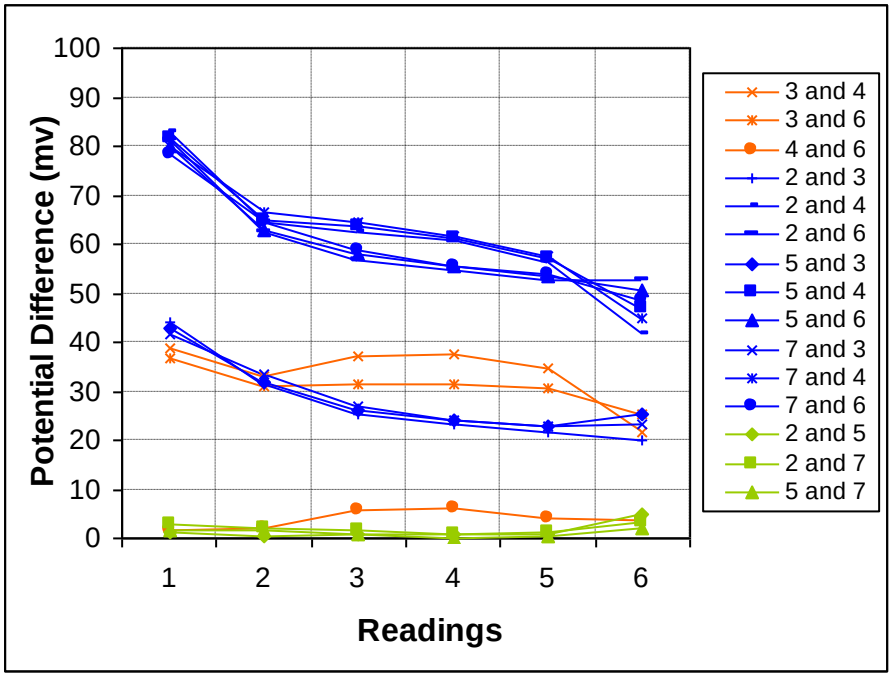

Figure 4.80: Self-potential Experiment 2 graphic presentation of results

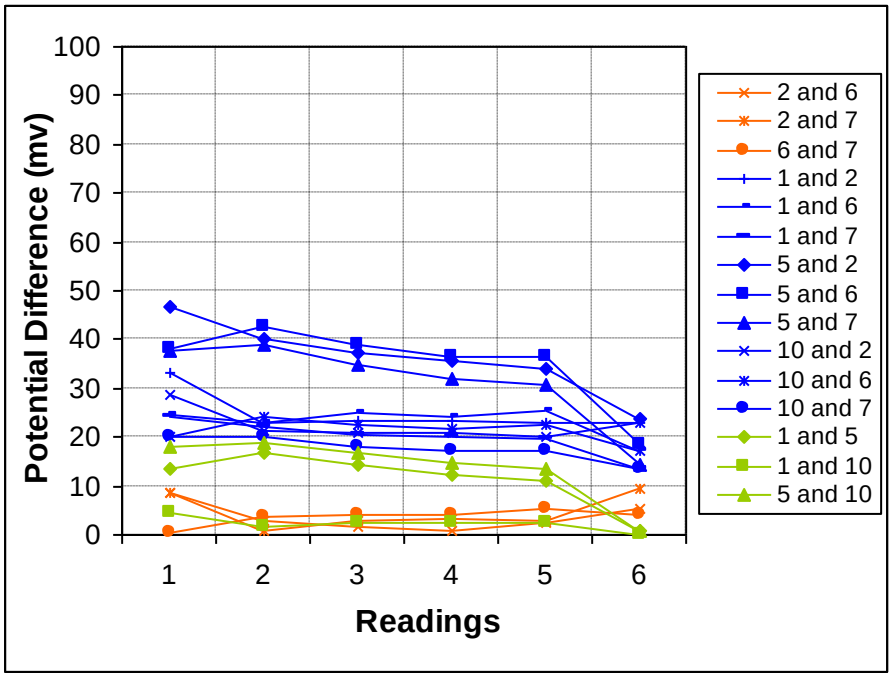

Figure 4.81: Self-potential Experiment 3 graphic presentation of results

Table 4.8: Self-potential Experiment 1 numerical results

Potential Difference (mV)	Reading 1 (0 hours)	Reading 2 (1 hours)	Reading 3 (2 hours)	Reading 4 (3 hours)	Reading 5 (4 hours)	Reading 6 (24 hours)
5 and 1	2.5	4.5	8.4	8.1	7.6	3.3
6 and 1	48.9	40.3	35.7	35.1	35.0	34.0
10 and 1	46.8	37.0	32.6	33.1	33.8	36.7
12 and 1	53.3	40.1	34.8	34.9	35.3	36.2
6 and 5	51.4	50.8	44.1	43.2	42.6	37.3
10 and 5	49.3	41.5	41.0	41.2	41.4	40.0
12 and 5	55.8	44.6	43.2	43.0	42.9	39.5
10 and 6	2.1	3.3	3.1	4.6	1.2	2.7
12 and 6	4.4	0.2	0.9	0.2	0.3	2.2
12 and 10	6.5	3.1	2.2	1.8	1.5	0.5

Table 4.9: Self-potential Experiment 2 numerical results

Potential Difference (mV)	Reading 1 (0 hours)	Reading 2 (1 hours)	Reading 3 (2 hours)	Reading 4 (3 hours)	Reading 5 (4 hours)	Reading 6 (19 hours)
3 and 4	38.6	33.0	37.3	37.5	34.6	21.6
3 and 6	36.9	31.0	31.6	31.5	30.7	25.3
4 and 6	1.7	2.0	5.7	6.0	3.9	3.7
2 and 3	44.2	31.5	25.3	23.2	21.8	20.1
2 and 4	82.8	64.5	62.6	60.7	56.4	41.7
2 and 6	81.1	62.5	56.9	54.7	52.5	52.5
5 and 3	43.0	31.9	26.3	23.9	22.7	25.3
5 and 4	81.6	64.9	63.6	61.4	57.3	46.9
5 and 6	79.9	62.9	57.9	55.4	53.4	50.6
7 and 3	41.5	33.5	27.1	24.1	23.0	23.2
7 and 4	80.1	66.5	64.4	61.6	57.6	44.8
7 and 6	78.4	64.5	58.7	55.6	53.7	48.5
2 and 5	1.2	0.4	1.0	0.7	0.9	5.0
2 and 7	2.7	2.0	1.8	0.9	1.2	3.1
5 and 7	1.5	1.6	0.8	0.2	0.3	2.1

Table 4.10: Self-potential Experiment 3 numerical results

Potential Difference (mV)	Reading 1 (0 hours)	Reading 2 (1 hours)	Reading 3 (2 hours)	Reading 4 (3 hours)	Reading 5 (4 hours)	Reading 6 (20 hours)
2 and 6	8.5	2.8	1.6	0.9	2.5	5.4
2 and 7	8.8	1.0	2.7	3.4	3.0	9.4
6 and 7	0.3	3.8	4.3	4.3	5.5	4.0
1 and 2	33.1	23.0	23.3	23.3	22.8	22.8
1 and 6	24.6	23.1	24.9	24.2	25.3	17.4
1 and 7	24.3	22.0	20.6	19.9	19.8	13.4
5 and 2	46.7	40.0	37.5	35.5	33.9	23.7
5 and 6	38.2	42.8	39.1	36.4	36.4	18.3
5 and 7	37.9	39.0	34.8	32.1	30.9	14.3
10 and 2	28.7	21.2	20.8	20.7	20.2	22.8
10 and 6	20.2	24.0	22.4	21.6	22.7	17.4
10 and 7	19.9	20.2	18.1	17.3	17.2	13.4
1 and 5	13.6	17.0	14.2	12.2	11.1	0.9
1 and 10	4.4	1.8	2.5	2.6	2.6	0.0
5 and 10	18.0	18.8	16.7	14.8	13.7	0.9

4.5 Capacitance Experiments

4.5.1 Introduction and Overview

One of the main concerns with using hydrogel for liquefaction prevention is the ability to know exactly where the hydrogel is in the subsurface once it has been installed. There are many

existing technologies that have the potential to detect hydrogel in the subsurface. One of these technologies is Ground-penetrating radar (GPR). GPR is a relatively common geophysical method that uses electromagnetic waves for subsurface investigation. The reflection of electromagnetic waves at the boundary between two materials is a function of the contrast in dielectric permittivity between the two materials (Burger et al. 2005). Dielectric permittivity is a function of a materials capacitance. Thus, the larger the difference in capacitance, the easier it is to use GPR to identifying the boundary between materials.

For this research, it is the ability to detect the boundary between saturated sand and saturated sand with hydrogel that is of interest. Two experiments were conducted (capacitance of a variety of materials was measured, 0.40% hydrogel and saturated sand, saturated sand, hydrogel and water, water, dry sand, and air). The capacitance was measured with a LCR meter and a new type of sensor developed by Dr. Robert Dean in the Auburn University Department of Electrical and Computer Engineering. Details of the experimental equipment and procedures are in Section 3.9.

4.5.2 Selection of Percent Hydrogel

All hydrogel sample used for this experiment used a hydrogel concentration of 0.40%. 0.40% hydrogel was used in the experiments because it was the largest concentration of hydrogel being studied, making it the most likely to be detectable. The capacitance of only hydrogel and water was also measured. Samples of the 0.40% hydrogel was used in the experiments because it was the largest concentration of hydrogel being used for the triaxial and consolidation testing. Being the largest concentration meant it was the most likely to be detectable. Gel and water were prepared at concentration approximately equal to a 0.40% hydrogel sand sample. The hydrogel and water were mixed at a ratio of 0.15 g of hydrogel to 1 g of water.

4.5.3 Results

Although the focus of these experiments was to determine the difference in capacitance between saturated sand and saturated sand with hydrogel, several different materials and combinations of materials were tested to see which components affected capacitance the most. In the first experiment, air, water, dry sand, saturated sand, and saturated hydrogel sand were tested. The average capacitances measured during this experiment are presented in Table 4.11. The results indicated that saturated sand and water have almost identical capacitances, and that that saturated hydrogel sand has slightly lower capacitance. It was also noticed during testing that the capacitance reading had a tendency to drift with time towards a higher capacitance for the water or saturated materials. Dr. Dean theorized that the sensor was absorbing water during testing causing the readings to drift. Based on this hypothesis, he suggested that the sensor should be allowed to sit in the materials for a period of time, so that it could become saturated and thus take a stable reading.

Based on the information, a second experiment was conducted. This experiment was performed on water and a water hydrogel mixture. The first experiment indicated that sand had almost no effect on the capacitance, so the sand was eliminated in order to further isolate hydrogel as the experimental variable. For this experiment two sensors were used. The readings from both sensors in air where compared to make sure they were providing similar measurements of capacitance. The sensor used to measure the capacitance of water indicated a capacitance of air of 393 pF, and the sensor used to measure the capacitance of water with hydrogel indicated a capacitance of air of 387 pF, a difference of only about 1.5%. The sensors were placed in their respective materials and allowed to sit until the readings stopped drifting

(about 30 minutes). The capacitances of water and water with hydrogel were measured as 1,938 pF and 1,802 pF, respectively, resulting in a contrast of 136 pF or 7.0%.

Table 4.11: Capacitance Experiment 1 results

Material	Average Capacitance (pF)
Air	386
Dry Sand	443
Water	1,719
Saturated Sand	1,727
Saturated Sand with 0.40% Hydrogel	1,640

4.5.1 Discussion

The results indicate that there is a contrast in capacitance between saturated sand and saturated sand with 0.40% hydrogel. This indicates, but does not ensure, that GPR may be a viable method of detecting of hydrogel in the field. Since there are many other variables in a field situation, it cannot be concluded that this method is viable without further research; however, its viability as a detection method is plausible.

It is also plausible that a type of sensor similar to the ones used in this experiment could be employed to measure capacitance, and thus detect hydrogel. These sensors would have some of the same limitations as GPR with the notable exception of direct measurement at a specific location within the subsurface, assuming the sensors could easily be installed at the desired locations.

For any hydrogel field detection method, the purpose is to verify the installation of the hydrogel at the desired location within the subsurface. Because the detection method can be used to do a field survey at the same location before and after the hydrogel has been installed, the method only has to be sensitive enough to show a change that can be attributed to the hydrogel.

This is important because it is much easier to identify a change caused by the hydrogel than it is to directly identify the location of the hydrogel. Since only changes within the subsurface need to be detectable, GPR or capacitance measurement may be a viable detection method despite its somewhat small capacitance contrast.

4.6 Shrinkage Experiments

4.6.1 Overview

As hydrogel absorbs water, it swells like a sponge. Conversely, when it dries, hydrogel shrinks back to its original size. Two experiments were performed to attempt to qualitatively identify the amount of shrinkage of a soil specimen containing hydrated hydrogel as a result of drying. The first experiment was conducted on a 0.40% hydrogel sample dried in an oven. The second experiment involved air drying three samples of three different concentrations of hydrogel (0.40%, 0.25%, and 0.00%).

4.6.2 Significance

In field situations, it is common for the water table to fluctuate many feet in elevation. If the addition of hydrogel to soil beneath structures causes the soil mass to shrink and swell as the water table moves up and down, significant unintended damage to an overlying structure could occur. If the presence of hydrogel prevents liquefaction during an earthquake but causes damage to that structure in this more common scenario, it is not a viable solution to the problem of liquefaction mitigation.

4.6.3 Selection of Percent Hydrogel

As with other experiments, 0.40% hydrogel was initially selected for use in these experiments because it is the largest concentration being studied, and thus, it was expected to produce the most significant results. A 0.40% hydrogel sample was used for the oven-dried

experiment. For the air-dried experiment, 0.40%, 0.25%, and 0.00% hydrogel concentrations were tested so that differences in volume change could be compared.

4.6.4 Observations and Discussion of the Oven-Dried Experiment

Before drying, the sample was prepared in a Proctor mold, with the level of the sand even with top of the Proctor mold, as described in Section 3.10. Before the sample was placed in the oven, a slightly discolored, gray spot was observed on top of the sample. It appeared that there was a significant amount of hydrated hydrogel located in this area, causing the difference in color (Figure 4.82).

After 48 hours in the 200° F oven, the discolored area had formed into a clod that had cracked and separated from the rest of the sample (Figure 4.83). It appeared that the clod had been forced upward. The level of the rest of the sand still appeared to be even with the top of the mold. The clod was carefully tilted up, revealing a several large voids (Figure 4.84). The sand, both the clod and the main sample, were cemented together with hydrogel. Cementation of the soil particles after drying was also observed when hydrogel triaxial samples were oven dried.

When these samples were prepared and saturated, there was no confining top plate like there was when the triaxial and consolidation samples were prepared. One of the functions of the top plate is to force the hydrogel evenly between the sand particles. Without the top plate is possible that a lens of swollen hydrogel caused some of the behavior observed. The voids could have been created either by hydrogel or possibly hot water vapor leaving the sample as it dried.

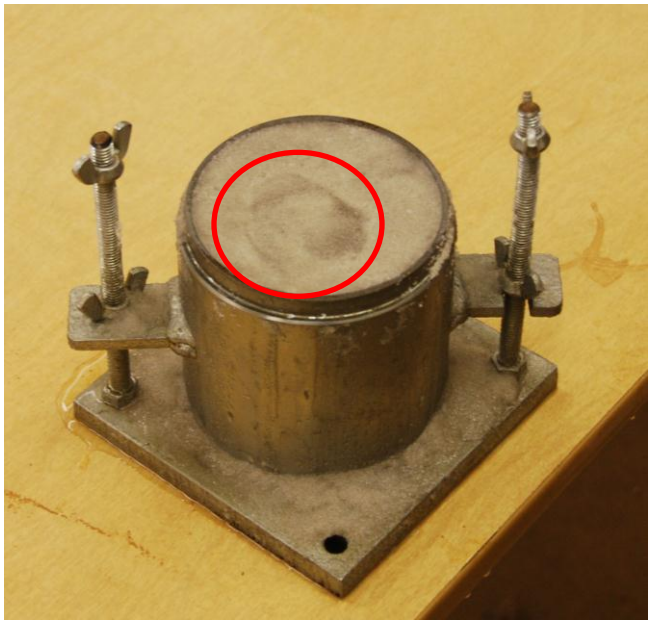

Figure 4.82: Oven-dried sample fully saturated, just before being placed in the oven (suspected hydrogel "clod" circled)

Figure 4.83: Oven-dried sample after 48 hours in the oven, the hydrogel "clod" had been forced upward during drying as shown

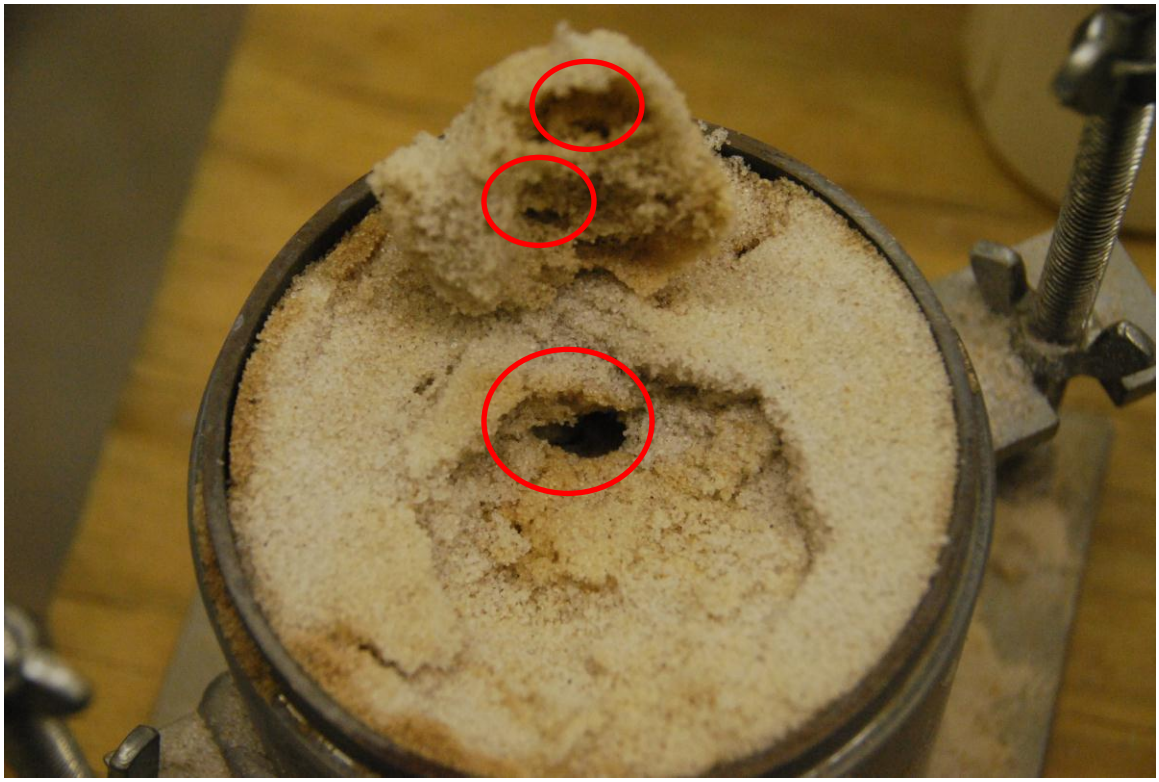

Figure 4.84: Voids (circled in red) located underneath the "clod"

4.6.5 Observations and Discussion of the Air-Dried Experiment

The oven-dried test did not provide significant insight on the issue of shrinkage as a result of dewatering. For this reason a second test was run at room temperature (~72° F) over a period of 8 weeks. Samples were prepared in the same manner as the oven dried sample was prepared in Proctor molds. For this test no discolorations or hydrogel lens could be seen on the surface of the samples at the beginning of the test. All of the samples looked like the 0.40% hydrogel sample shown in Figure 4.85 at the beginning of the test. However, after only about 12 hours of drying, cracks started to appear in on the surface of the 0.25% hydrogel sample.

After air drying for a week, the 0.25% hydrogel sample exhibited significant cracking on the surface and some vertical shrinkage on one side (Figure 4.86). The 0.40% hydrogel sample had shrunk both radially and vertically (Figure 4.87). The 0.00% hydrogel sample appeared

almost unchanged (Figure 4.88). The reddish-brown stains visible in some of the pictures are rust stains from the steel Proctor mold. After drying for almost three months, the samples exhibited little additional change from a week of drying (Figure 4.89).

After three months, hydrogel samples have a cemented crust, but feel spongy when poked with a finger. The 0.00% hydrogel sample, which exhibited almost no shrinkage throughout the experiment, was loose and dry to the touch. It had the same consistency of normal dry sand.

The 0.25% hydrogel sample behaved similarly to the oven-dried sample in that it had cracks in the surface of the sample that formed early on in the test (within one week). The irregular cracking may be a function of the sample being saturated without a top to help force the hydrogel between the sand grains, as noted in Section 4.5.4. Unlike the other samples, the 0.40% hydrogel treated sample shrank in a uniform manner without cracks. This is the behavior was expected to be observed for the hydrogel treated samples during the experiments. It is possible that the hydrogel and sand in the 0.40% hydrogel sample was better mixed than the oven dried and the 0.25% hydrogel sample.

The plain sand sample exhibited almost no shrinkage during the entire test. Unlike the thick gel in the hydrogel samples, water is not viscous enough to hold the sand particles apart. It is thought that when the plain sand sample was prepared, the sand arranged itself in a denser configuration than the hydrogel samples, which where held in a loose configuration by the gel. As the water within hydrogel evaporated, the hydrogel in the voids shrank, and the sand densified. This was not the case with the plain sand because the water was not preventing densification like the hydrogel was.

Figure 4.85: 0.40% sample at start of air-dried shrinkage test

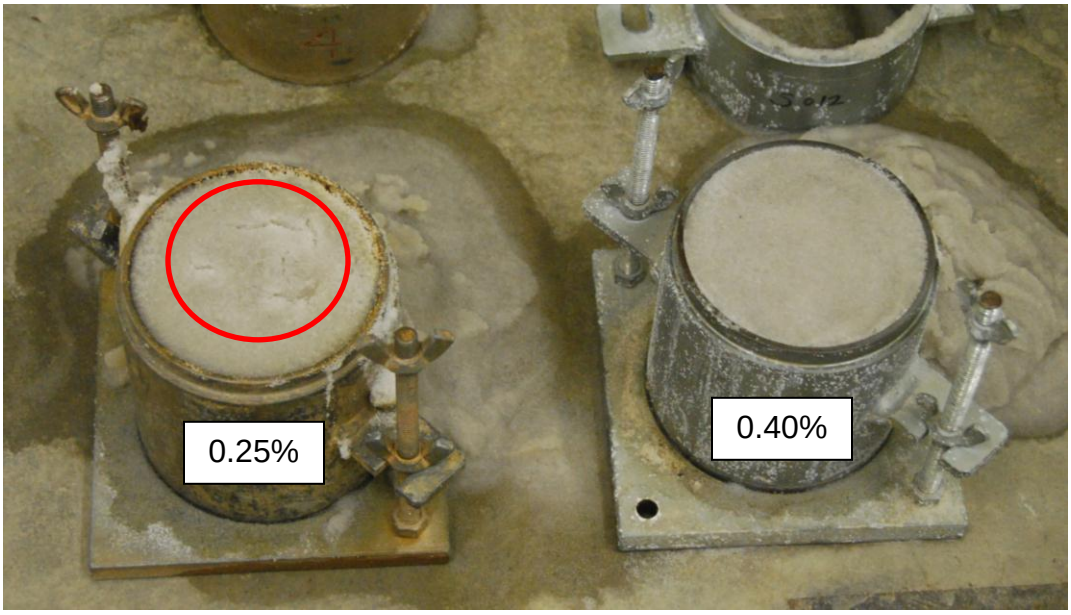

Figure 4.86: 0.25% and 0.40% hydrogel samples after 12 hours of air drying, cracks developed in the 0.25% sample (circled in red), no visible change to the 0.40% sample

Figure 4.87: 0.00% hydrogel sample after 12 hours of drying, some slight shrinkage (circled in red)

Figure 4.88: 0.25% hydrogel sample after 9 days of air drying

Figure 4.89: 0.40% hydrogel sample after 9 days of air drying

Figure 4.90: 0.00% hydrogel sample after 9 days of air drying

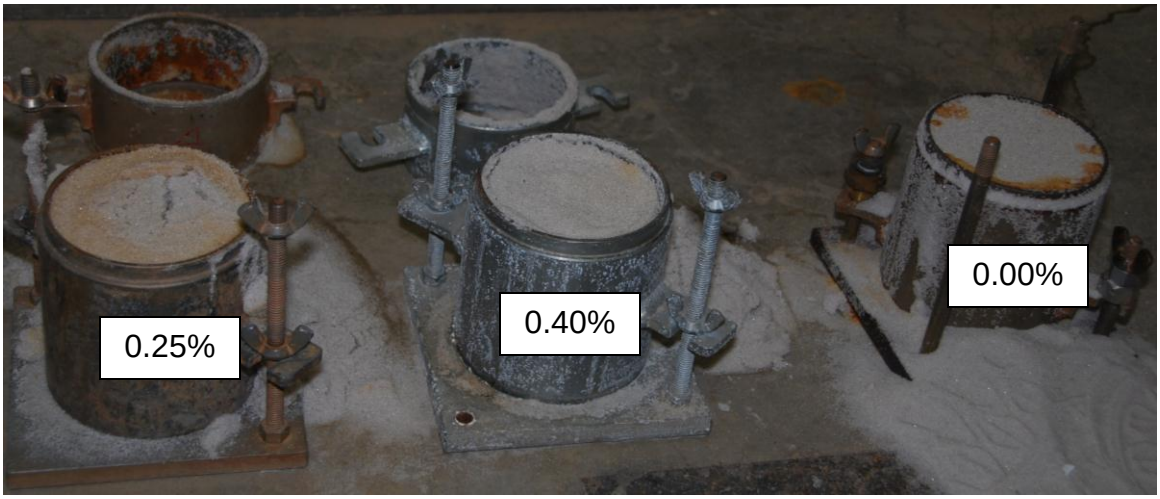

Figure 4.91: All three samples after 58 days of air drying

Chapter 5: Conclusions

5.1 Introduction

A study on the effects of polyacrylamide hydrogel on the properties of Ottawa sand was conducted. Laboratory testing included stress-controlled cyclic triaxial tests, consolidated undrained triaxial compression tests, and one-dimensional consolidation tests. Experiments evaluating the effectiveness of electrical self-potential and capacitance measurement to detect polyacrylamide hydrogel in Ottawa sand were conducted. Experiments to evaluate shrinkage of hydrogel and Ottawa sand due to dewatering were also conducted. This chapter presents conclusions based on the results of these tests and experiments. Procedures for preparing frozen soil samples in the laboratory using both a freezer and liquid nitrogen were developed. Conclusions related to methods of sample saturation and freezing are also presented.

The following conclusions are only valid for hydrogel particles between $1.8x10^{-3}$ and $3.0x10^{-3}$ in in diameter. There was not enough testing with the nanoparticle hydrogel ($3x10^{-6}$ to $1.4x10^{-5}$ in in diameter) to conclude that the smaller size does not influence hydrogel's effects on the properties of Ottawa sand. The preliminary inferences about the influence of hydrogel size on shear strength behavior are discussed in section 5.3.4. With the exception of section 5.3.4 and where referenced, the conclusion statements only pertain to the micro size hydrogel particles.

5.2 Stress Controlled Cyclic Triaxial Testing

Hydrogel does not increase the liquefaction resistance of Ottawa sand in the traditional sense. Hydrogel does not prevent the buildup of excess pore pressure during cyclic shear. The

effective stress of Ottawa sand during cyclic shear is reduced to zero as fast or faster than when hydrogel is present; however, sand treated with hydrogel maintains significant strength for many cycles after the effective stress has reached zero. Hydrogel causes the sand to maintain a higher level of shear strength that does not exist in untreated Ottawa sand at zero effective stress.

Hydrogel does not significantly increase or decrease the magnitude of the pre-liquefaction cyclic strain. Prior to liquefaction (liquefaction being defined as the point when effective stress reaches zero), both hydrogel and non-hydrogel soils exhibit strains less than 1% in either compression or extension. After liquefaction, non-hydrogel samples exhibit large (>10%), non-recoverable strains, often limited by the testing machine. Hydrogel treated samples exhibit postliquefaction strains that are smaller (typically 3%-5% depending on CSR) than untreated samples. Also, the postliquefaction strains of the hydrogel treated samples are mostly recoverable (elastic deformation), even after many cycles. Hydrogel allows Ottawa sand to deform elastically to relatively large strains (3%-5%) under conditions of zero effective stress. This is important because by deforming *elastically* treated Ottawa sand is able to dissipate energy while maintaining strength during dynamic loading, even at conditions of zero effective stress. Unlike the liquefied untreated Ottawa sand samples, the deformations of the hydrogel treated samples were small enough that they were not limited by the testing machine.

Hydrogel has little effect on the cyclic stress and strain responses of Ottawa sand before the effective stress has reached zero. Hydrogel causes pore pressure in Ottawa sand to build up more quickly than untreated samples of Ottawa sand for a given CSR under cyclic triaxial testing conditions. After zero effective stress has been reached, hydrogel prevents the total structural collapse that is typically associated with liquefied Ottawa sand under zero effective stress.

Ottawa sand with hydrogel subjected to cyclic stress retains strength; however, elastic deformations are larger than those of *non-liquefied* Ottawa sand under similar cyclic loads.

In terms of shear strength, it appears that hydrogel allows Ottawa sand to maintain shear strength at conditions of zero effective stress, implying the material exhibits cohesion, at least under the dynamic load conditions of a cyclic triaxial test. Hydrogel treated sand is not conventional soil and thus the term *cohesion* is not necessarily the most accurate way to describe its strength behavior. However, cohesion is used here to describe the strength behavior of this new material because cohesion is the most accurate conventional soil mechanics term that describes this type of strength behavior.

5.3 Consolidated Undrained Triaxial Testing

5.3.1 Shear Strength

The addition of hydrogel to Ottawa sand reduces the effective angle of internal friction. The effective friction angle of Ottawa sand as a function of concentration of hydrogel is generally described by the linear function:

$$\phi' = -1542.6x + 31.9 \qquad (5.1)$$

where ϕ' is the effective angle of internal friction expressed in degrees and x is the concentration of hydrogel by mass expressed as a decimal. The use of nanoparticle hydrogel did not appear to alter the relationship described in Equation 5.1; however, only two tests were conducted using nanoparticle hydrogel. Further testing on nanoparticle hydrogel samples is needed to validate this conclusion.

5.3.2 Stress-Strain Response

Hydrogel reduces the yield stress of Ottawa sand by approximately 60%. This was found to be true for both tests with σ_3' = 2 psi and 15 psi. Hydrogel reduces the elastic modulus of Ottawa sand by approximately 2,500 psi (27%) based on a 6,500 psi elastic modulus for plain Ottawa sand. Elastic modulus was only evaluated for tests with σ_3' = 15 psi. Specific trends relating the reduction of yield stress and elastic modulus to the concentration of hydrogel were not evident.

After yielding, stress-strain behavior is a function of pore pressure response. Hydrogel reduces the magnitude of pore pressure decrease after yielding. Thus, it also reduces the resulting strain hardening behavior proportionally.

5.3.3 Pore Pressure Response

Prior to the point where ϕ' is fully mobilized, hydrogel had no significant effect on pore pressure response. This is true for all concentrations of hydrogel tested. The maximum amount of excess pore pressure reached, which is a function of density and effective confining pressure, is roughly equal for sand with or without hydrogel of similar density tested under the same σ_3'. After the point where ϕ' is fully mobilized, the presence of hydrogel reduces the tendency of sand to dilate. Decreases in pore pressure are significantly smaller, even with only 0.15% hydrogel.

It appears that higher concentrations of hydrogel may tend to decrease the dilatant behavior of Ottawa sand. The test results were variable and did not always match this trend. Thus, a definitive conclusion can not be made based on the data presented in this paper. Discussion about the variability of the test results with regard to pore pressure response is in Section 4.1.7. These conclusions match the conclusions of Shiver (2007).

5.3.4 Hydrogel Particle Size

Most tests were conducted on $1.8x10^{-3}$ to $3.0x10^{-3}$ in (microparticles) diameter hydrogel particles. Two tests were conducted on $3x10^{-6}$ to $1.4x10^{-5}$ in (nanoparticles) diameter particles.

The shear strength of the two nanoparticle tests was not significantly different than the strengths observed for the microparticle tests. The results generally followed the relationship presented in Equation 5.1; however, more testing is needed to verify these conclusions.

The yield stress and elastic modulus exhibited by one of the nanoparticle samples was higher than all the tests using microparticles. The yield stress and the elastic modulus of the other nanoparticle sample were similar to that of the microparticle samples. With only two tests, it is not possible to draw conclusions about the effect of particle size on yield stress or elastic modulus.

Samples treated with nanoparticle hydrogel exhibited a large stress-strain response that fell between what is typical for untreated Ottawa sand and Ottawa sand treated with microparticle hydrogel. Pore pressure responses also fell between the typical responses for plain Ottawa sand and Ottawa sand with micro hydrogel. Nanoparticle hydrogel does not appear to have as large of an impact on the pore pressure response of Ottawa sand. Further research and testing is needed to validate these conclusions.

5.3.5 Sample Freezing

Freezing specimens in the laboratory is a viable method of producing loose, cohesionless soil samples that can be stored, transported, and handled. Two methods of freezing were used for this research, freezing in a freezer and freezing with liquid nitrogen. Freezing samples with liquid nitrogen offers the advantage of reduced freezing time and reduced volume change during freezing when compared to freezing specimens in a -35° F freezer and freezing with liquid

nitrogen. Specimens frozen with liquid nitrogen exhibit approximately 50% less volume increase during freezing than do freezer-frozen specimens; however, both methods result in some specimen volume increase.

Some specimens crack during freezing or mold extraction. Freezing specimens with liquid nitrogen reduces the severity of the cracking. The effects of cracks on specimen strength were not evaluated in these experiments and are still unknown.

The freezing method does not have a significant impact on the effective friction angle of Ottawa sand based on the average values of ϕ' of 32.3° and 31.9° for the freezer and liquid nitrogen methods, respectively. The freezer method produces more consistent results in terms of ϕ', as indicated by the lower standard deviation of 1.09° for the freezer-frozen specimens versus 1.53° for the liquid nitrogen frozen specimens. Both methods produce acceptable specimens that behave similarly during undrained triaxial shear testing.

5.4 Sample Saturating Using a Hypodermic Needle

Samples for this research were saturated using a new method of sample saturation—a syringe with a long hypodermic needle. The procedures are described in Section 3.3.4. This method was selected because it is faster than other methods where water must permeated through the very low permeability hydrogel treated Ottawa sand. It can also be performed outside of the triaxial cell. With some practice, several researchers were able to consistently saturate triaxial and consolidation samples using this method.

5.5 One-Dimensional Consolidation Testing

Hydrogel increases the magnitude of consolidation of Ottawa sand in a consolidometer at all stresses. The increase in magnitude of consolidation is more pronounced at higher stresses. Larger amounts of hydrogel typically cause larger increases in magnitude of consolidation.

Hydrogel increases the time required for consolidation to occur. Although the time required for hydrogel treated Ottawa sand to consolidate is larger than that of plain Ottawa sand, the amount of time required is still very short by geotechnical standards.

5.6 Electrical Self-Potential Experiments

Electrical self-potential geophysical testing was investigated as a technology that may be able to detect and verify the location of hydrogel in a field application. The ability of electrical self-potential to detect hydrogel depends on the potential difference between two materials. There is significant potential difference, approximately 40-60 mV, between 0.40% hydrogel treated Ottawa sand and plain saturated Ottawa sand. Even if the hydrogel concentration is reduced to 0.25%, an approximately 40 mV potential difference still exists. These conclusions are true for the laboratory setup described using silver chloride electrodes. Electrical self-potential shows promise of use in detecting hydrogel under field conditions.

Because of the large potential difference, other electrical based geophysical methods such as induced polarization or electric resistivity may also be viable methods of field detection.

5.7 Capacitance Measurement Experiment

Ground penetrating radar (GPR) is an established geophysical investigation technique that uses electromagnetic waves to detect differences in capacitance of materials within the subsurface. The larger the difference in capacitance between two materials, the more likely GPR will be able to detect the boundary between these materials. For this reason, capacitance of several materials was measured to evaluate the potential ability of GPR as a field investigation technique for locating subsurface hydrogel.

There is very little difference between the capacitance of water, 1,719 pF, and the capacitance of saturated Ottawa sand, 1,727 pF. There is a small difference, 87 pF (5%), in

capacitance of Ottawa sand saturated with 0.40% hydrogel and plain saturated Ottawa sand. There is a slightly larger difference between a mixture of hydrogel and water and water, 136 pF (7%). Because these contrasts exist, GPR may be a viable method for the field detection of hydrogel.

A large difference exists between the capacitance of dry and saturated materials. Water and air have a difference in capacitance of approximately 1,341 pF. The capacitance sensors used for these experiments appear to have potential applications detecting hydrogel or other materials in soil. They also have potential as a tool for measuring water content of soil.

5.8 Shrinkage Experiments

Experiments to qualitatively evaluate the amount of shrinkage of hydrogel treated Ottawa sand were conducted. Two experiments were conducted. One involved drying a hydrogel treated sample in an oven. The other involved drying two different concentration hydrogel treated samples and one untreated sample in air.

Oven-dried Ottawa sand containing hydrogel does not exhibit significant shrinkage due to the cementation effect of the dry hydrogel. Large cracks or internal voids can also form during oven drying. Air-dried Ottawa sand containing hydrogel will decrease in volume more than an equally sized sample of plain saturated sand. The volume change behavior of Ottawa sand with hydrogel due to drying appears to be inconsistent, based on preliminary tests. Issues in constructing these samples without a confining top plate make it difficult to saturate or prepare the sample at the desired void ratio. It also prevents the hydrogel from being forced evenly between the void spaces. The preparation issues, along with the fact that there is not a standard test method, make quantifying shrinkage due to drying very difficult. Initial tests indicate that shrinkage due to drying may be an issue in the field. Further experiments and testing are needed.

Chapter 6: Suggestions for Further Research

1. The ability to permeate soil with *coated* hydrogel particles is critical for the application of this technology. As soon as coated particles can been produced, experiments should be conducted to evaluate the ability to transport coated hydrogel nanoparticles through soil.

2. Experiments on the transport of other types of nanoparticles has be performed (Cheng et al. 2005; Darlington et al. 2009; Fang et al. 2009; He et al. 2009; Khodadoust et al. 2008). These studies should be used as references to develop a method of evaluating the transport of coated hydrogel particles.

3. Dyes or tracer materials should be investigated for use in locating hydrogel particles during laboratory tests and possibly field applications.

4. Methods of isolating and extracting the hydrogel from a soil sample for the purpose of evaluating the hydrogel concentration should be investigated. Easily being able to determine the amount of hydrogel present in a soil sample would be advantageous for both field and laboratory scenarios.

5. Established correlations between Atterberg limits and susceptibility to liquefaction exist. Estimates of the Atterberg limits of sand treated with hydrogel should be compared to these correlations.

6. The use of fiber optic sensors for the purpose of detecting or measuring the in situ hydrogel concentration may be possible. Fiber optic sensors should be investigated for this use.

7. There is a suspected relationship between viscosity of the pore fluid (or gel) and the soil's susceptibility to liquefaction. If a relationship between viscosity and liquefaction susceptibility is investigated, it is possible that criteria can be developed to predict how effective as certain method of pore water modification, like hydrogel treatment, may be at reducing liquefaction susceptibility.

8. Further research on the shrink and swell properties of hydrogel sand mixtures with respect to changes in water content should be evaluated.

9. Field verification of the installed hydrogel is critical to the ability to apply this technology. Potentially applicable geophysical technologies exist that were not investigated here, including seismic methods. These technologies should be evaluated for their potential to detect hydrogel.

10. In addition to the cyclic triaxial testing that has already been performed, shaking table tests should be performed to further evaluate the behavior of hydrogel treated sand under cyclic

loading. Shaking table tests should also be used to investigate structure soil interaction during dynamic loading on a larger scale.

11. Field scale experiments should be conducted using electrical self-potential and ground penetrating radar or a capacitance sensor to evaluate the viability of these methods for hydrogel detection in the field.

12. Research on the effect of hydrogel on the cohesion of Ottawa sand has not been conducted. Testing should be performed to evaluate how hydrogel affects cohesion of Ottawa sand.

13. It is theorized that the pore pressure measured at the ends of hydrogel samples may not accurately reflect the pore pressure at the center of a sample during shear. Internal evaluation of pore pressure during shear and/or cyclic shear should be evaluated.

14. Salts, such as sodium chloride, can negatively affect the ability of polyacrylamide to form a gel in the presence of water. This effect needs to be measured and analyzed to protect against degradation in saline environment.

15. Because hydrogel particles act somewhat like a sponge, confining pressure may affect the ability of hydrogel to absorb and retain water, just as a compressed sponge cannot absorb water. Shiver (2007) also suggests that confining pressure may have an effect on the ability of hydrogel to absorb water. The extent of this effect should be investigated.

16. The amount of time required for hydrogel to degrade under in-situ conditions needs to be evaluated. Important variables may include composition of the soil and/or groundwater, groundwater flow conditions, and temperature.

17. There is much debate concerning the degradation of non-toxic polyacrylamide into its monomer form, acrylamide, which is a known neurotoxin and a suspected carcinogen (2010). If polyacrylamide is deemed unsafe in the future, it would be a detrimental for this project. Environmental regulation concerning the allowed use of polyacrylamide should be monitored.

18. Other materials such as clay particles, synthetic clay particles, or other polymers may be effective at immobilizing the pore water. These materials should also be investigated for their potential to mitigate liquefaction hazards.

References

Airey, D. W., and Wood, D. M. (1987). "An evaluation of dirrect simple shear tests on clay." *Géotechnique*, 37(1), 25-35.

Andrus, R. D., and Chung, R. M. (1995). "Cost-effective ground improvement for liquefaction remediation near existing lifelines." Proceedings of the 27th Meeting of the U.S./Japan Cooperative Program in Natural Resources Panel on Wind and Seismic Effects, Tsukuma, Japan, 115-123.

Andrus, R. D., and Stokoe, K. H., II. (2000). "Liquefaction resistance of soils from shear-wave velocity." *Journal of Geotechnical and Geoenvironmental Engineering*, 126(11), 1015-1025.

ASCE. (2005). *Minimum Design Loads for Buildings and Other Structures (ASCE 7-05)*, American Society of Civil Engineers, Reston, Virginia.

Ashford, S. A., Rollins, K. M., Case Bradford, V. S., Weaver, T. J., and Baez, J. I. (2000). "Liquefaction mitigation using stone columns around deep foundations: Full-scale test results." *Transportation Research Record*(1736), 110-118.

ASTM. (2004a). "Standard Test Method for Load Controlled Cyclic Triaxial Strength of Soil." Annual Book of ASTM Standards, ASTM International, West Conshohocken, Pennsylvania.

ASTM. (2004b). "Standard Test Methods for One-Dimensional Consolidation Properties of Soils Using Incremental Loading." Annual Book of ASTM Standards, ASTM International, West Conshohocken, Pennsylvania.

ASTM. (2005). "Standard Test Method for Mechanical Cone Penetration Tests of Soil." Annual Book of ASTM Standards, ASTM International, West Conshohocken, Pennsylvania.

ASTM. (2008). "Standard Test Method for Standard Penetration Test (SPT) and Split-Barrel Sampling of Soils." Annual Book of ASTM Standards, ASTM International, West Conshohocken, Pennsylvania.

Bartlett, S. F., and Youd, T. L. (1995). "Empirical prediction of liquefaction-induced lateral spread." *Journal of Geotechnical Engineering*, 121(4), 316-329.

Bishop, A. W., and Henkel, D. J. (1962). *The Measurement of Soil Properties in the Triaxial Test*, E. Arnold, London, England.

Black, D. K., and Lee, K. L. (1973). "Saturating labroratory samples by back pressure." *Journal of the Soil Mechanics and Foundations Division*, 99(1), 75-93.

Bolton, M. D. (1986). "The strength and dilatency of sands." *Géotechnique*, 36(1), 65-78.

Boulanger, R. W., Mejia, L. H., and Idriss, I. M. (1997). "Liquefaction at Moss Landing during Loma Prieta Earthquake." *Journal of Geotechnical and Geoenvironmental Engineering*, 123(5), 453-467.

Burger, H. R., Sheehan, F. A., and Jones, C. H. (2005). *Introduction to Applied Geophysics*, W. W. Norton and Company, New York, New York.

Cheng, X., Kan, A. T., and Tomson, M. B. (2005). "Study of C60 transport in porous media and the effect of sorbed C60 on naphthalene transport." *Journal of Materials Research*, 20(12), 3244-3254.

Darlington, T. K., Neigh, A. M., Spencer, M. T., Nguyen, O. T., and Oldenburg, S. J. (2009). "Nanoparticle characteristics affecting environmental fate and transport through soil." *Environmental Toxicology and Chemistry*, 28(6), 1191-1199.

Das, B. M. (1993). *Principles of Soil Dynamics*, PWS-KENT, Boston, Massachusetts.

Debenedetti, P. G. (1996). *Metastable Liquids: Concepts and Principles*, Princeton University Press, Princeton, New Jersey.

DeJong, J. T., Fritzges, M. B., and Nusslein, K. (2006). "Microbially induced cementation to control sand response to undrained shear." *Journal of Geotechnical and Geoenvironmental Engineering*, 132(11), 1381-1392.

DeJong, J. T., Mortensen, B. M., Martinez, B. C., and Nelson, D. C. (2010). "Bio-mediated soil improvement." *Ecological Engineering*, 36(2), 197-210.

Drenevich, V. P. (1972). "Undrained cylic shear of saturated sand." *Journal of the Soil Mechanics and Foundations Division*, 98(8), 807-825.

Fang, J., Shan, X.-q., Wen, B., Lin, J.-m., and Owens, G. (2009). "Stability of titania nanoparticles in soil suspensions and transport in saturated homogeneous soil columns." *Environmental Pollution*, 157(4), 1101-1109.

Gong, J., Higa, M., Iwasaki, Y., Katsuyama, Y., and Osada, Y. (1997). "Friction of gels." *Journal of Physical Chemistry B*, 101(28), 5487-5489.

Grattoni, C. A., Luckham, P. F., Jing, X. D., Norman, L., and Zimmerman, R. W. (2004). "Polymers as relative permeability modifiers: adsorption and the dynamic formation of thick polyacrylamide layers." *Journal of Petroleum Science and Engineering*, 45(3-4), 233-245.

Greene, H. G., Gardner-Taggart, J., Ledbetter, M. T., Barminski, R., Chase, T. E., Hicks, K. R., and Baxter, C. (1991). "Offshore and onshore liquefaction at Moss Landing spit, central California--Result of the October 17,1989, Loma Prieta earthquake." *Geology*, 19(9), 945-949.

Haldavanekar, V., Bobet, A., Santagata, M., and Drnevich, V. (2004). "Soil treatment with thixotropic fluid: an autoadaptive design for liquefaction prevention." Proceedings of the 11th International Conference on Soil Dynamics & Earthquake Engineering and 3rd International Conference on Earthquake Engineering, Berkeley, California, 553-560.

Harada, N., Towhata, I., Takatsu, T., Tsunoda, S., and Sesov, V. (2000). "Development of new drain method for protection of existing pile foundations from liquefaction effects." *Soil Dynamics and Earthquake Engineering*, 26(2-4), 297-312.

Harder, L. F., Jr., and Boulanger, R. W. (1997). "Application of K_σ and K_α correction factors." Preoceedings of the NCEER Workshop on Evaluation of Liquefaction REsistance of Soils, National Center for Earthquake Engineering Research, State University of New York Buffalo, 167-190.

Hausmann, M. R. (1990). *Engineeering Principles of Ground Modification*, McGraw-Hill, New York, New York.

Hays, W., W. (1981). "Facing geologic and hydrologic hazards : earth-science considerations." Geological Survey professional paper 1240-B, G. S. U.S. Dept. of the Interior, ed., Washington, D.C.

He, F., Zhang, M., Qian, T., and Zhao, D. (2009). "Transport of carboxymethyl cellulose stabilized iron nanoparticles in porous media: Column experiments and modeling." *Journal of Colloid and Interface Science*, 334(1), 96-102.

Henn, R. W. (1996). *Practicle Guide to Grouting of Underground Strutures*, ASCE Press, New York, New York.

Holtz, R. D., and Kovacs, W. D. (1981). *An Introduction to Geotechnical Engineering*, Prentice Hall, Upper Saddle River, New Jersey.

Hynes, M. E., and Olsen, R. S. (1999). "Influence of confining stress on liquefaction resistance." Proceedings of the International Workshop on the Physics and Mechanics of Soil Liquefaction, Balkema, Rotterdam, The Netherlandds, 145-152.

ICC. (2006). *International Building Code*, International Code Council, Country Club Hills, Illinois.

Ishibashi, I., and Sherif, M. A. (1974). "Sand liquefaction in triaxial and simple shear tests." *Journal of the Geotechnical Engineering Division*, 100(8), 871-88.

Ishihara, K. (1993). "Liquefaction and flow failure during earthquakes." *Géotechnique*, 43(3), 351-415.

Ishihara, K., and Li, S. (1972). "Liquefaction of saturated sand in triaxial torsion shear test." *Soils and Foundations*, 12(2), 19-39.

Johnson, J. (2000a). "1964 Niigata earthquake, Japan." The Soil Liquefaction web site, University of Washington, Seattle, http://www.ce.washington.edu/~liquefaction/html/quakes/niigata/niigata.html (Jan 18, 2010).

Johnson, J. (2000b). "Locations." The Soil Liquefaction web site, University of Washington, Seattle, http://www.ce.washington.edu/~liquefaction/html/where/where1.html (Jan 20, 2010).

Jones, G. K. (1963). "Chemistry and flow properties of bentonite grouts in grouts." Drilling Muds in Engineering Practice, Butterworths, London, United Kingdom, 22-28.

Kayen, R. E., Mitchell, J. K., Seed, R. B., Lodge, A., Nishio, S., and Coutinho, R. (1992). "Evaluation of SPT-, CPT-, and shear wave-based methods for liquefaction potential assessment using Loma Prieta data." Proceedings of the 4th Japan-U.S. workshop on earthquake-resistant design of lifeline facilities and countermeasures for soil liquefaction, 177-204.

Khedr, S. A., and Ahmed, M. S. (1996). "Using polyacrylamide grouts for permeability control in sand." *Transportation Research Record*(1546), 131-139.

Khodadoust, A. P., Reddy, K. R., and Varadhan, S. "Transport of lactate-modified nanoscale iron particles in sand columns." New Orleans, LA, United states, 479-486.

Kramer, S. L. (1996). *Geotechnical Earthquake Engineering*, Prentice Hall, Upper Saddle River, New Jersey.

Lambe, T. W., and Whitman, R. V. (1969). *Soil Mechanics*, John Wiley and Sons, New York, New York.

Lee, K. L., Seed, H. B., and Dunlop, P. (1967). "Effect of moisture on the strength of clean sand." *Journal of Soil Mechanics and Foundation Division*, 93(6), 17-40.

Leyendecker, E. V., Hunt, R. J., Frankel, A. D., and Rukstales, K. S. (2000). "Development of Maximum Considered Earthquake Ground Motion Maps." *Earthquake Spectra*, 16(1), 21-40.

Liao, S. S., and Whitman, R. V. (1986). "Catalogue of liquefaction and non-liquefaction occurrences during earthquakes." Department of Civil Engineering, Massachusetts Institiute of Technology, Cambridge, Massachusetts.

Louie, J. N. (1996). "Earthquake Effects." The University of Nevada, Reno, http://www.seismo.unr.edu/ftp/pub/louie/class/100/effects-kobe.html (Jan 28, 2010).

Maher, M. H., and Gucunski, N. (1995). "Liquefaction, and dynamic properties of grouted sand." Soil Improvement for Earthquake Hazard Mitigation, R. D. Hryciw, ed., ASCE, New York, New York, 37-50.

Marcuson, W. F., III. (1978). "Definition of terms related to liquefaction." *Journal of Geotechnical Engineering Division*, 103(6), 565-588.

Martinez, B. C., and DeJong, J. T. "Bio-Mediated soil improvement: Load transfer mechanisms at the micro- and macro- scales." Orlando, FL, United states, 242-251.

McCarthey, D. F. (2002). *Essentials of Soil Mechanics and Foundations: Basic Geotechnics*, Prentice Hall, Upper Saddle River, New Jersey.

McCarthy, D. F. (2002). *Essentials of Soil Mechanics and Foundations: Basic Geotechnics*, Prentice Hall, Upper Saddle River, New Jersey.

McMaster, D. F., and Robinson, M. J. (1996). "Chapter 10: Chemical Grouting." Practical Guide to Grouting of Underground Strucctures, R. W. Henn, ed., ASCE Press, New York, New York.

Milsom, J. (2003). *Field Geophysics*, John Wiley and Sons, New York, New York.

Mitchell, J. K., Baxter, C. D. P., and Munson, T. C. (1995). "Performance of improved ground during earthquakes." Soil Improvement for Earthquake Hazard Mitigation, R. D. Hryciw, ed., ASCE, New York, New York, 1-36.

Mogami, T., and Kubu, K. (1953). "The behavior of soil during vibration." Proceedings, 3rd International conference on Soil Mechanics and Foundation Engineering, Zurich, 152-155.

NASA. (2010). "Road Damage Following Earthquake." NASA Images, The Internet Archive, San Francisco, California, http://libraryphoto.cr.usgs.gov/cgi-bin/search.cgi?search_mode=exact&selection=Alaska+Earthquake+1964|Alaska+Earthquake|1964 (Feb 9, 2010).

Naudet, V., Revil, A., Bottero, J. Y., and Begassat, P. (2003). "Relationship between self-potential (SP) signals and redox conditions in contaminated groundwater." *Geophysical Research Letters*, 30(21), HLS 2-1 - 2 HLS 2-4.

NRC. (1985). *Liquefaction of Soils during Earthquakes*, National Research Council, National Academy Press, Washington, D.C.

Olsen, R. S. "Cyclic liquefaction based on teh cone penetration test." *Procedings of the NCEER workshop on evaluation of liquefaction resistance of soils*, State University of New York at Buffalo, 225-276.

Page, R. A., Boore, D. M., and Yerkes, R. F. (1996). "The Los Angelos Dam Story." U.S. Geological Survey Fact Sheet-096-95, United States Geologic Survey, Washington, D.C., http://quake.usgs.gov/prepare/factsheets/LADamStory/ (Jan 25, 2010).

Park, S., Wolf, L. W., Lee, M., and Saunders, J. (2004). "Self-potential and geochemical measurements of microbially mediated bacterial sulfate reduction in saturated sediments." EOS Transactions, American Geophysical Union, abstract #B53A-0983.

Rieter, L. (1991). *Earthquake Hazard Analysis: Issues and Insights*, Columbia University Press, New York.

Roberts, J. E. (1964). "Sand Compression as a Factor in Oil Field Subsidence," Doctoral Dissertation, Massachusetts Institute of Technology, Cambridge, Massachusetts.

Robertson, P. K., Woeller, D. J., and Finn, W. D. (1992). "Seismic cone penetration test for evaluating liquefaction potential under cyclic loading." *Canadian Geotechnical Journal*, 29, 686-695.

Robertson, P. K., and Wride, C. E. (1998). "Evaluating cyclic liquefaction potential using the cone penetration test." *Canadian Geotechnicale Engineering Journal*, 27(1), 151.

Rollins, K. M., Anderson, J. K. S., McCain, A. K., and Goughnour, R. R. (2003). "Vertical composite drains for mitigating liquefaction hazard." Proceedings of the 13th International Conference on Offshore and Polar Engineering, International Society for Offshore and Polar Engineering, Honolulu, Hawaii, Paper 2003-SAK-01.

Rozycki, A., Ruiz Fonticiella, J. M., and Cuadra, A. (2006). "Detection and evaluation of horizontal fractures in earth dams using the self-potential method." *Engineering Geology*, 82(3), 145-153.

Sayles, F. C. (1973). "Triaxial and creep tests on frozen Ottawa sand." Permafrost: North American contribution [to the] Second International Conference National Academy of Sciences, Washington, D.C., 384-391.

Seed, H. B. (1968). "Landslides caused by soil liquefaction." *Journal of Soil Mechanics and Foundation Division*, 93(5), 1053-1122.

Seed, H. B. (1979). "Soil liquefaction and cyclic mobility evaluation for level ground during earthquakes." *Journal of Geotechnical Engineering Division*, 105(2), 201-255.

Seed, H. B. (1983). "Earthquake-resitant design of earth dams." Proceedings of The Symposium on Sesimic Desing of Earth Dams and Caverns, ASCE, New York, New York, 41-64.

Seed, H. B., and Booker, J. R. (1977). "Stabilization of potentially liquefiable sand deposits using gravel drains." *Journal of the Geotechnical Engineering Division*, 107(7), 757-768.

Seed, H. B., and Idriss, I. M. (1971). "Simplified procedure for evaluating soil liquefacction potential." *Journal of Geotechnical Engineering Division*, 97(9), 1249-1273.

Seed, H. B., and Idriss, I. M. (1982). "Ground motions and soil liquefaction during earthquakes." Earthquake Engineering Research Institute Monograph, Oakland, California.

Seed, H. B., and Lee, K. L. (1966). "Liquefaction of saturatedsands during cyclic loading." *Journal of Soil Mechanics and Foundation Division*, 92(6), 105-134.

Seed, H. B., Tokimatsu, K., Harder, L. F., and Chung, R. M. (1985). "The influence of SPT precedures in soil liquefaction resitance evaluations." *Journal of Geotechnical Engineering*, 111(12), 1425-1445.

Shiver, B. T. (2007). "Water stabilization using microparticles," Master's Thesis, Auburn University, Auburn, Alabama.

Stark, T. D., and Olson, S. M. (1995). "Liquefaction resistance using CPT and field case histories." *Journal of Geotechnical Engineering*, 121(12), 856-869.

Stover, C. W., and Coffman, J. L. (1993). "Seismicity of the united States, 1568-1989 (Revised)." Geological Survey professional paper 1527, G. S. U.S. Dept. of the Interior, ed., Washington, D.C.

Suzuki, Y., Tokimatsu, K., Koyamada, K., Taya, Y., and Kubota, Y. "Field correlation of soil liquefaction based on CPT data." *Proceedings of the International Symposium on Cone Penetration Testing*, 583-588.

Sykora, D. W. (1987). *Creation of a data base of seismic shear wave velocities for correlation analysis*, U.S. Army Engineering Waterways Experiment Station, Vicksburg, Mississippi.

Terzaghi, K. (1925). *Erdbaumechanik auf bodenphysikalischer grundlage*, Leipzig F. Deuticke, Vienna.

Tuttle, M., Cowie, P., Tinsley, J., Benett, M., and Berrill, J. (1990). "Liquefaction and foundation failure of Chevron oil and gasoline tanks at Moss Landing, California." *Geophys. Res. Letters*, 17(4), 56-74.

Uhlmann, D. R. (1972). "A kinetic treatment of glass formation." *Journal of Non-Crystalline Solids*, 7(4), 337-348.

USGS. (2006a). "Alaska Earthquake 1964." U.S. Geological Survey Photographic Library, United States Geologic Survey, Washington, D.C., http://libraryphoto.cr.usgs.gov/cgi-bin/search.cgi?search_mode=exact&selection=Alaska+Earthquake+1964|Alaska+Earthquake|1964 (Jan 18, 2010).

USGS. (2006b). "San Fernando Earthquake, February 1971." U.S. Geological Survey Photographic Library, United States Geologic Survey, Washington, D.C., http://libraryphoto.cr.usgs.gov/cgi-bin/search.cgi?search_mode=exact&selection=San+Fernando+Earthquake%2C+February+1971|San+Fernando|Earthquake|1971 (Jan 25, 2010).

Wang, W. (1979). "Some findings in soil liquefaction." Water Conservancy and Hydroelectric Power Scientific Research Institute, Beijing, China.

Welsh, J. P. (1991). "Chapter 8: Grouting." Underground Structures, R. S. Singha, ed., Elsevier, New York, New York.

Winterkorn, H. F., and Fang, H. Y. (1975). "Foundation Engineering Handbook." Van Nostrand Reinhold, New York, New York.

WWU. (2010). "Sand Boil produced by Liquefaction, El Centro, California." Earthquakes - General Topics, Western Washington University, Washington, D.C., http://libraryphoto.cr.usgs.gov/cgi-bin/search.cgi?search_mode=exact&selection=San+Fernando+Earthquake%2C+February+1971|San+Fernando|Earthquake|1971 (Feb 10, 2010).

Yasukawa, K., Bodvarsson, G. S., and Wilt, M. J. "Coupled self-potential and mass-heat flow code for geothermal applications." Burlingame, CA, USA, 203-207.

Youd, T. L. (1991). "Mapping of earghquake-induced liquefaction for seismic zonation." Proceedings, 4th International Conference on Seismic Zonation, Earthquake Engineering Research Institute, Sanford University, 111-147.

Youd, T. L., and Hoose, S. N. (1977). "Liquefaction susceptibility and geologic setting." Proceedings, 6th World Conference on Earthquake Engineering, New Delhi, 2189-2194.

Youd, T. L., and Idriss, I. M. (2001). "Liquefaction resistance of soils: summary report from the 1996 NCEER and 1998 NCEER/NSF workshops on evaluation of liquefaction resitance of soils." *Jouranl of the Geotechnical and Geoenvironmental Engineering*, 127(10), 297-313.

Youd, T. L., and Noble, S. K. (1997). "Magnitude scaling factors." Proceedings of the NCEER workshop on evalution of liquefaction resistance of soils, National Center for Earthquake Engineering Research, State Univiversity of New York at Buffalo, 201-215.

Youd, T. L., and Perkins, D. M. (1978). "Mapping of liquefaction induced ground failure potential." *Journal of Geotechnical Engineering Division*, 104(4), 433-446.

Zhdanov, M. S. (2009). *Geophysical Electromagnetic Theory and Methods*, Elsevier, Amsterdam, The Netherlands.

Appendix A: Testing Equipment Information

A.1 Triaxial Testing Equipment

Load Frame:

Brainard-Kilman S-600 Triaxial Load Frame; Serial Number: 1033

Brainard-Kilman E-410 Four Channel Readout; Serial Number: 1033

Test Cell:

Brainard-Kilman S-510 Triaxial Cell; Serial Number: 134

Panel Board:

Brainard-Kilman S-500 Triaxial/Permeability Panel Board; Serial Number: 1479

Brainard-Kilman E-400 Digital Readout; Serial Number: 715

Brainard-Kilman E-114 Pressure Transducer; Serial Number: 428

Range: 0 – 300 psi

Sensitivity: 0.1 psi

Excitation Voltage: 10.0 V DC at maximum 90 mA

Sensors:

Brainard-Kilman E-124 Pore Pressure Transducer; Serial Number: 332

Range: 0 – 150 psi

Sensitivity: 0.1 psi

Excitation Voltage: 10.0 V DC at maximum 90 mA

Brainard-Kilman E-214 Load Cell (0-1500lbs); Serial Number: 253

Range: 0 – 6000 lbs

Sensitivity: 1.0 lbs

Excitation Voltage: 10.0 V DC at maximum 90 mA

Boart Longyear E-312 Displacement Transducer (LVDT); Serial Number: 134

Range: 2.0 in

Sensitivity: 0.001 in

Excitation Voltage: 10.0 V DC at maximum 90 mA

Data Collection:

Optim Electronics, Megadac 5414AC; Serial Number: SO4093

Dell Inspiron 7000 laptop; Serial Number: 9103846BY15505A

Total Control Software (TCS) for Windows v 3.4.0 software; Serial Number: 500192-1-0429-0165

A.2 Consolidation Testing Equipment

Load Frame:

Soil Test C-220; Serial Number N/A

Consolidometer:

Soil Test C-251; Serial Number N/A

Sensors:

Boart Longyear E-312 Displacement Transducer (LVDT); Serial Number: 134

Range: 2.0 in

Sensitivity: 0.001 in

Excitation Voltage: 10.0 V DC at maximum 90 mA

Data Collection:

Optim Electronics, Megadac 5414AC; Serial Number: SO4093

Dell Inspiron 7000 laptop; Serial Number: 9103846BY15505A

Total Control Software (TCS) for Windows v 3.4.0 software; Serial Number: 500192-1-0429-0165

A.3 Self-Potential Testing Equipment

Multimeter:

LG Precision Co., Ltd. GoldStar DM-311; Serial Number: 311058581

A.4 Consolidation Testing Equipment

LCR Meter:

Wayne Kerr 4220

A.5 Sensor Calibrations

DURHAM GEO SLOPE INDICATOR

2175 West Park Court
Stone Mountain GA 30087
Tel: 1-800-837-0864
Technical Assistance: Ext. 2012
Fax: (770)-465-7447

Calibration Certificate

Device Calibrated:	**General Purpose Transducer**
Range:	**15.0 - 150.0 PSI**
Model No:	**E-114**
Serial No:	**428**
Readout Model No:	**E-400**
Readout Serial No:	**715**
Meter Address:	**N/A**
Equipment Condition:	**Used - Good**

Calibration Instrument:
Druck Pneumatic Calibrator 300 PSI Max
Serial No: 601315012 (.01 Resolution)
Last Calibration Date: 04-21-2008
Report #: SCC-24732

Service Used: **Precision Standards Intl.**
Equipment-Standard Used:
Limited Dead Weight Tester SN: 3627-84

Known	Before Calibration		After Calibration (Customer's Transducer)			
Applied Pressure (psi)	**Reading**	**Error**	**Reading # 1**	**Reading # 2**	**Deviation # 1**	**Deviation # 2**
0.00	**No Adjustment Necessary**		0.0	0.0	0.00	0.00
15.00			15.0	15.0	0.00	0.00
30.00			30.0	30.0	0.00	0.00
45.00			45.0	45.0	0.00	0.00
60.00			60.0	60.0	0.00	0.00
90.00			90.2	90.2	0.22	0.22
120.00			120.5	120.5	0.42	0.42
150.00			150.9	150.9	0.60	0.60
				Error:	**0.60%**	**0.60%**

Resolution: **.1 PSI**
Temperature at time of calibration ^{0}C: **23**
Excitation Voltage: **10.01 VDC**

Scale 1: **.2970** **Offset 1:** **(-) 15**
Scale 2: **.2965** **Offset 2:** **(-) 14**

*NOTE: Readouts and transducers have been calibrated at the factory and are a matched pair. In general, pressure transducers, load cells and LDT's are not interchangeable.

Calibration performed by:
Dan McMurray

Signature: _____

Associated Equipment:

Calibration Date : November 10, 2008

Calibrated @ DGSI Stone Mountain GA

Calibration Due Date : November 11, 2009

Company Name: **Auburn University**
Physical Address: **Dept. of Civil Eng.**
238 Harbert Eng. Ctr.
Auburn AL 36849-5337
Phone Number: **David Graham**
Contact: **205-427-0682**

Traceable to NIST Standards.
This calibration conforms to the latest standards set by ASTM E4.

Figure A.1: Durham Geo Calibration Certificate for Brainard-Kilman E-114 Pressure Transducer, Serial Number: 428. Page 1 of 2.

DURHAM GEO SLOPE INDICATOR

2175 West Park Court
Stone Mountain GA 30087
Tel: 1-800-837-0864
Technical Assistance: Ext. 2012
Fax: (770)-465-7447

Calibration Certificate

Model No: **E-114**
Serial No: **428**

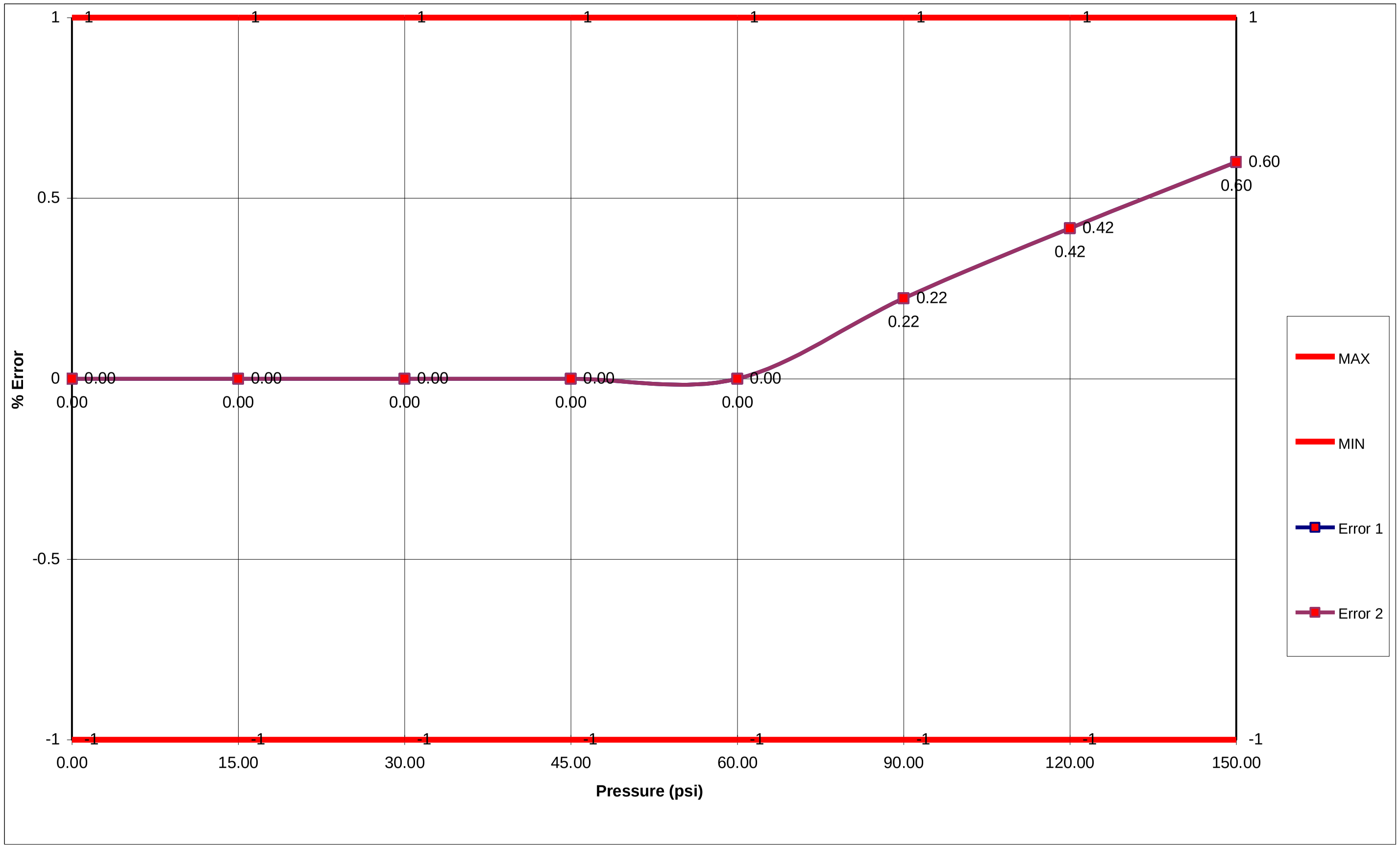

Figure A.2: Durham Geo Calibration Certificate for Brainard-Kilman E-114 Pressure Transducer, Serial Number: 428. Page 2 of 2.

DURHAM GEO SLOPE INDICATOR
2175 West Park Court
Stone Mountain GA 30087
Tel: 1-800-837-0864
Technical Assistance: Ext. 2012
Fax: (770)-465-7447

Calibration Certificate

Device Calibrated:	**Pore Pressure Transducer**
Range:	**15.0 - 150.0 PSI**
Model No:	**E-124**
Serial No:	**332**
Readout Model No:	**E-410**
Readout Serial No:	**133**
Meter Address:	**2**
Equipment Condition:	**Used - Good**

Calibration Instrument:
Druck Pneumatic Calibrator 300 PSI Max
Serial No: 601315012 (.01 Resolution)
Last Calibration Date: 04-21-2008
Report #: SCC-24732

Service Used: **Precision Standards Intl.**
Equipment-Standard Used:
Limited Dead Weight Tester SN: 3627-84

Known	Before Calibration		After Calibration (Customer's Transducer)			
Applied Pressure (psi)	**Reading**	**Error**	**Reading # 1**	**Reading # 2**	**Deviation # 1**	**Deviation # 2**
0.00	**No Prior Readings**		0.0	0.0	0.00	0.00
15.00			15.0	15.0	0.00	0.00
30.00			30.0	29.9	0.00	-0.33
45.00			44.9	45.0	-0.22	0.00
60.00			60.0	60.1	0.00	0.17
90.00			90.2	90.3	0.22	0.33
120.00			120.4	120.5	0.33	0.42
150.00			150.8	150.8	0.53	0.53
				Error:	**0.53%**	**0.53%**

Resolution: **.1 PSI**
Temperature at time of calibration ^{0}C: **23**
Excitation Voltage: **9.93 VDC**

Scale 1: **.3058**
Offset 1: **(-) 101**

*NOTE: Readouts and transducers have been calibrated at the factory and are a matched pair. In general, pressure transducers, load cells and LDT's are not interchangeable.

Calibration performed by:
Dan McMurray

Signature: _____

Associated Equipment:

Calibration Date : November 10, 2008

Initial Calibration performed @ DGSI in Stone Mtn GA

Company Name: **Auburn University**
Physical Address: **Dept. of Civil Eng.**
238 Harbert Eng. Ctr.
Auburn AL 36849-5337
Phone Number: **David Graham**
Contact: **205-427-0682**

Calibration Due Date : November 11, 2009

Traceable to NIST Standards.
This calibration conforms to the latest standards set by ASTM E4.

Figure A.3: Durham Geo Calibration Certificate for Brainard-Kilman E-124 Pore Pressure Transducer, Serial Number: 332. Page 1 of 2.

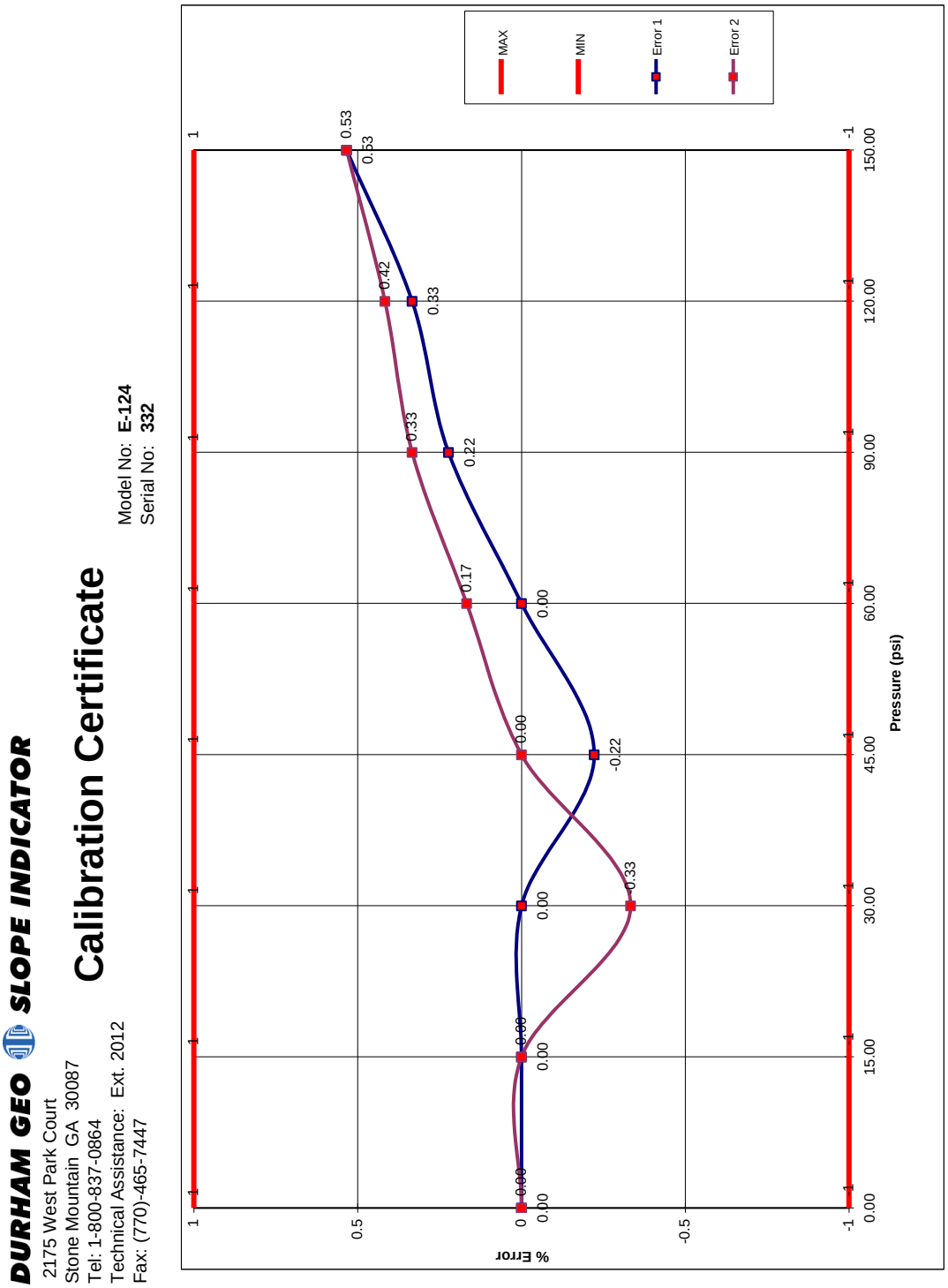

Figure A.4: Durham Geo Calibration Certificate for Brainard-Kilman E-124 Pore Pressure Transducer, Serial Number: 332. Page 2 of 2.

DURHAM GEO SLOPE INDICATOR

2175 West Park Court
Stone Mountain GA 30087
Tel: 1-800-837-0864
Technical Assistance: Ext. 2012
Fax: (770)-465-7447

Calibration Certificate

Device Calibrated:	**Pore Pressure Transducer**
Range:	**15.0 - 150.0 PSI**
Model No:	**E-124**
Serial No:	**1162**
Readout Model No:	**E-410**
Readout Serial No:	**133**
Meter Address:	**3**
Equipment Condition:	**Used - Good**

Calibration Instrument:
Druck Pneumatic Calibrator 300 PSI Max
Serial No: 601315012 (.01 Resolution)
Last Calibration Date: 04-21-2008
Report #: SCC-24732

Service Used: **Precision Standards Intl.**
Equipment-Standard Used:
Limited Dead Weight Tester SN: 3627-84

Known	Before Calibration		After Calibration (Customer's Transducer)			
Applied Pressure (psi)	Reading	Error	Reading # 1	Reading # 2	Deviation # 1	Deviation # 2
0.00	**No Prior Readings**		0.0	0.0	0.00	0.00
15.00			15.0	15.0	0.00	0.00
30.00			29.9	29.9	-0.33	-0.33
45.00			44.9	44.9	-0.22	-0.22
60.00			59.8	59.8	-0.33	-0.33
90.00			89.9	89.9	-0.11	-0.11
120.00			120.1	120.1	0.08	0.08
150.00			150.4	150.4	0.27	0.27
				Error:	**0.33%**	**0.33%**

Resolution: **.1 PSI**
Temperature at time of calibration ^{0}C: **23**
Excitation Voltage: **9.93 VDC**

Scale 2: **.1361**
Offset 2: **+ 2**

*NOTE: Readouts and transducers have been calibrated at the factory and are a matched pair. In general, pressure transducers, load cells and LDT's are not interchangeable.

Calibration performed by:
Dan McMurray

Signature: _____

Associated Equipment:

Calibration Date : November 10, 2008

Initial Calibration performed @ DGSI in Stone Mtn GA

Company Name: **Auburn University**
Physical Address: **Dept. of Civil Eng.**
238 Harbert Eng. Ctr.
Auburn AL 36849-5337
Phone Number: **David Graham**
Contact: **205-427-0682**

Calibration Due Date : November 11, 2009

Traceable to NIST Standards.
This calibration conforms to the latest standards set by ASTM E4.

Figure A.5: Durham Geo Calibration Certificate for Durham Geo Enterprises E-124 Pore Pressure Transducer, Serial Number: 1162. Page 1 of 2.

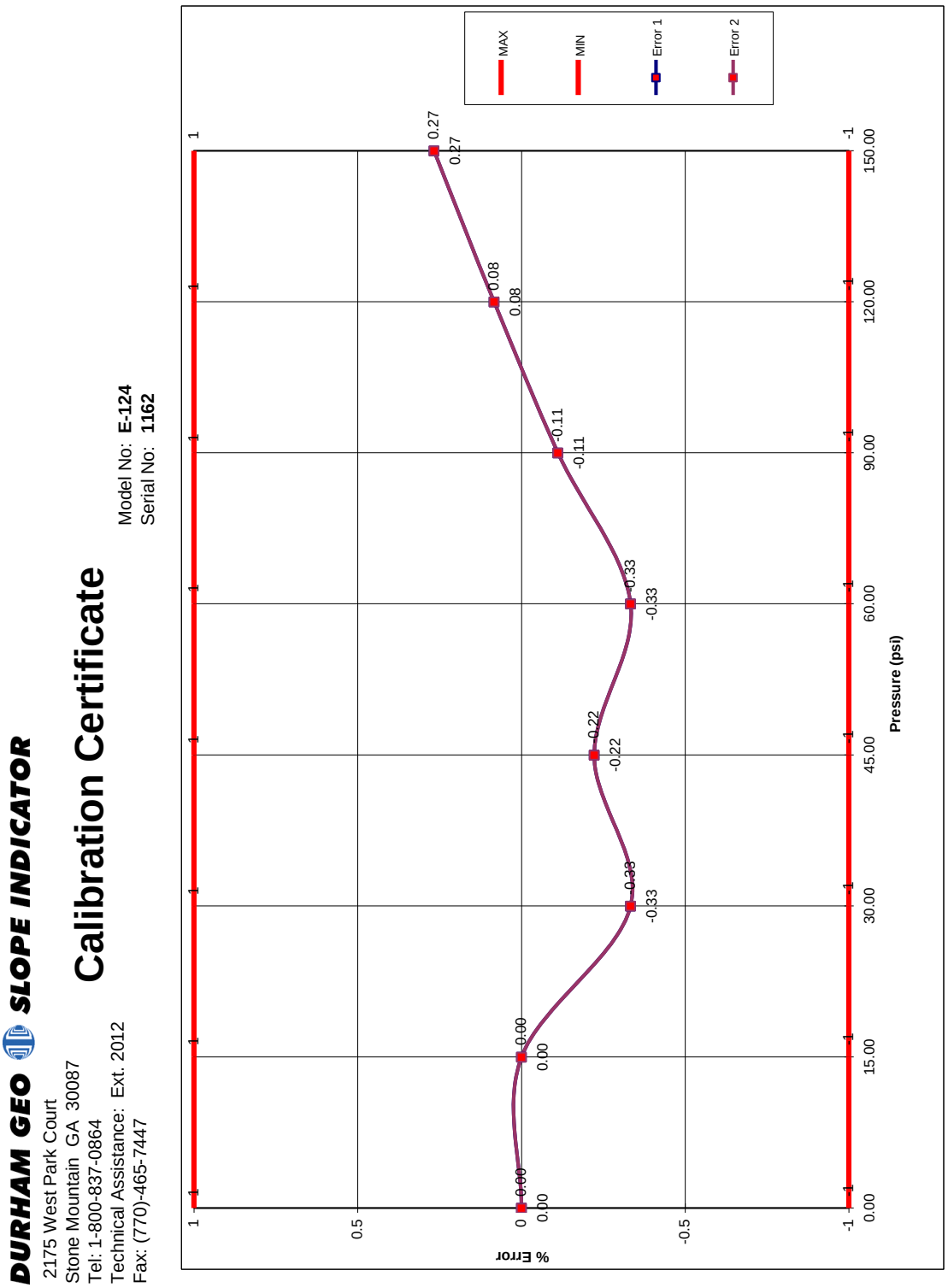

Figure A.6: Durham Geo Calibration Certificate for Durham Geo Enterprises E-124 Pore Pressure Transducer, Serial Number: 1162. Page 2 of 2.

DURHAM GEO SLOPE INDICATOR

2175 West Park Court
Stone Mountain GA 30087
Tel: 1-800-837-0864
Technical Assistance: Ext. 2012
Fax: (770)-465-7447

Calibration Certificate

Device Calibrated:	**Displacement Transducer**
Range:	**0.000 - 2.030 Inches**
Model No:	**E - 312**
Serial No:	**134**
Readout Model No:	**E-410**
Readout Serial No:	**133**
Meter Address:	**1**
Equipment Condition:	**Used - Good**

Instrument Information:
Starrett 0.0001 Div Micrometer
Serial No: **T-465**
Last Calibration Date: February 13, 2008

Service Used:
Precision Instruments Repair
Equipment-Standard Used:
Carl Ziess Calibrator #14380
Control #751 - Certificate #1228

Known	Before Calibration		After Calibration (Customer's Transducer)			
Increment (Inches)	**Reading**	**Error**	**Reading** # 1	**Reading** # 2	**Deviation** # 1	**Deviation** # 2
0.0000	**No Adjustment Necessary**		0.000	0.000	0.00	0.00
0.0500			0.050	0.050	0.00	0.00
0.2500			0.250	0.250	0.00	0.00
0.5000			0.499	0.499	-0.20	-0.20
0.7500			0.749	0.749	-0.13	-0.13
1.0000			0.999	0.998	-0.10	-0.20
1.2500			1.249	1.248	-0.08	-0.16
1.5000			1.499	1.499	-0.07	-0.07
1.7500			1.750	1.750	0.00	0.00
2.0000			2.002	2.001	0.10	0.05
2.0300			2.033	2.032	0.15	0.10
					Error:	**0.20%**	**0.20%**

Resolution: **.001 "**
Temperature at time of calibration ^{0}C: **23**
Excitation Voltage: **9.93 VDC**

Scale 0: .5604
Offset 0: + 147

*NOTE: Readouts and transducers have been calibrated at the factory and are a matched pair. In general, pressure transducers, load cells and LDT's are not interchangeable.

Calibration performed by:
Dan McMurray

Signature: _____

Associated Equipment:

Calibrated @ DGSI Stone Mountain GA

Company Name: **Auburn University**
Dept. of Civil Eng.
Physical Address: **238 Harbert Eng. Ctr.**
Auburn AL 36849-5337
Phone Number: **David Graham**
Contact: **205-427-0682**

Calibration Date : November 10, 2008
Calibration Due Date : November 10, 2009

Traceable to NIST Standards.
This calibration conforms to the latest standards set by ASTM E4.

Figure A.7: Durham Geo Calibration Certificate for Boart Longyear E-312 Displacement Transducer (LVDT); Serial Number: 134. Page 1 of 2.

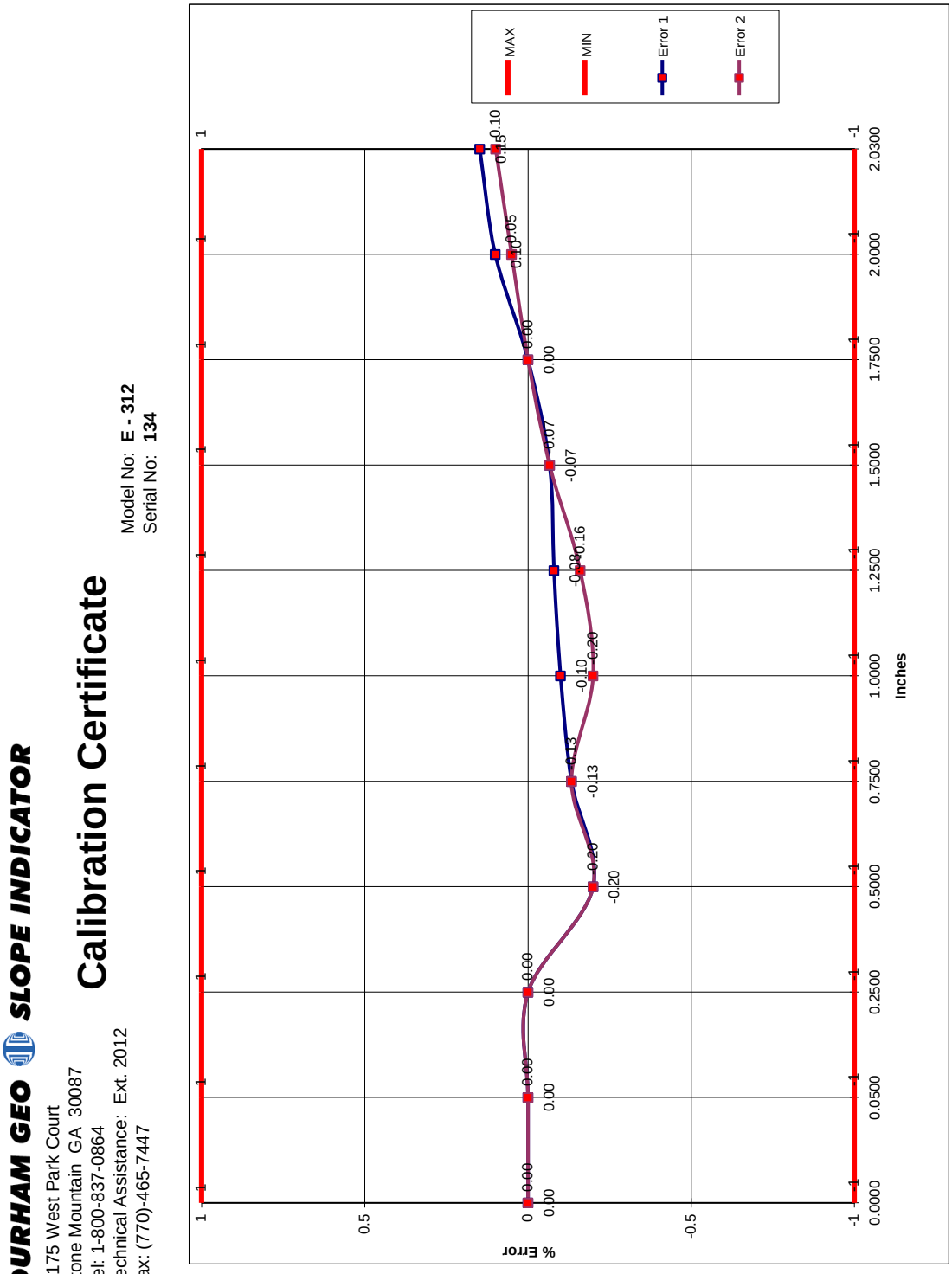

Figure A.8: Durham Geo Calibration Certificate for Boart Longyear E-312 Displacement Transducer (LVDT); Serial Number: 134. Page 2 of 2.

DURHAM GEO SLOPE INDICATOR

2175 West Park Court
Stone Mountain GA 30087
Tel: 1-800-837-0864
Technical Assistance: Ext. 2012
Fax: (770)-465-7447

Calibration Certificate

Device Calibrated:	**S - Type Load Cell**
Range:	**500 - 6,000 LBF**
Model No:	**E - 214**
Serial No:	**253**
Readout Model No:	**E-410**
Readout Serial No:	**133**
Meter Address:	**4**
Equipment Condition:	**Used - Good**

Calibration Instrument:
Interface Gold Series 10K Cylindrical Load Cell
Serial No: 141914 **(.1 LB Resolution)**
Last Calibration Date: June 3, 2008
NIST Report #: SCC-25012

Service Used:
Precision Standards International
Equipment Standard Used:
Interface Compression 25,000 lbf Cell SN:207751
NIST Report # 207751AE2008

	Customers Load Cell Readings					
Applied Load	**Before Calibration**		**After Calibration**			
Known Load (lbf)	**Reading**	**Error**	**Reading # 1**	**Reading # 2**	**Deviation # 1**	**Deviation # 2**
0.0			0	0	0.00	0.00
500.0	**New equipment, no prior readings available**		501	499	-0.20	0.20
1000.0			999	999	0.10	0.10
2000.0			1999	1999	0.05	0.05
3000.0			3000	3000	0.00	0.00
4000.0			3999	3999	0.02	0.02
5000.0			5000	5000	0.00	0.00
6000.0			6000	6000	0.00	0.00
				Error:	**0.20%**	**0.20%**

Resolution: **1 LBF**
Temperature at time of calibration ^{0}C: **23**
Excitation Voltage: **9.93 VDC**

Scale 3: **1.6713**
Offset 3: **+ 8**

*NOTE: Readouts and transducers have been calibrated at the factory and are a matched pair. In general, pressure transducers, load cells and LDT's are not interchangeable.

Calibration performed by:
Dan McMurray

Signature: _____

Associated Equipment:

Initial Calibration Performed @ Durham Geo Stone Mtn GA

Company Name: **Auburn University**
Physical Address: **Dept. of Civil Eng.**
238 Harbert Eng. Ctr.
Auburn AL 36849-5337
Phone Number: **David Graham**
Contact: **205-427-0682**

Calibration Date : November 10, 2008

Calibration Due Date : November 10, 2009

Traceable to NIST Standards.
This calibration conforms to the latest standards set by ASTM E4.

Figure A.9: Durham Geo Calibration Certificate for Brainard-Kilman E-214 Load Cell; Serial Number: 253. Page 1 of 2.

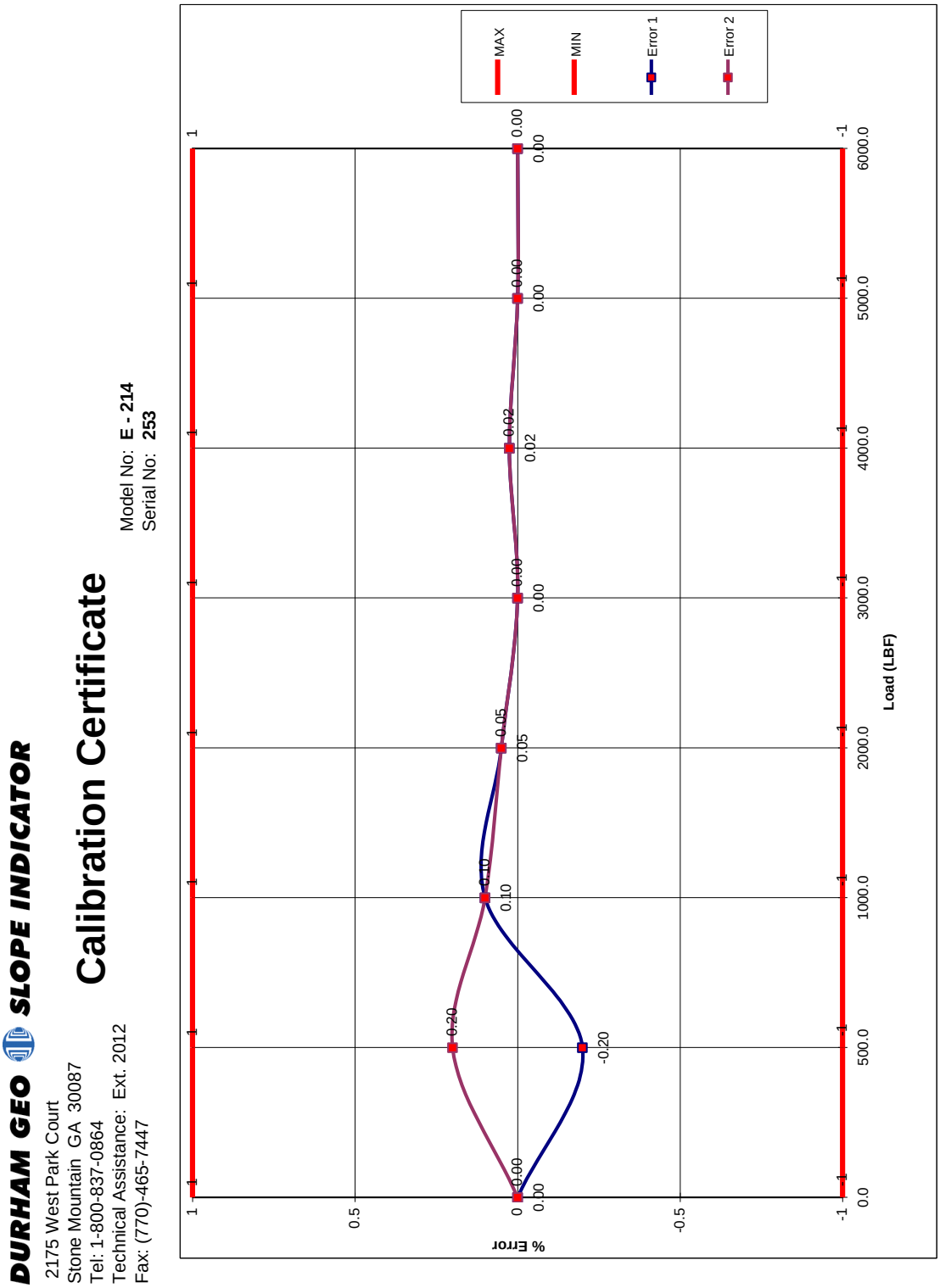

Figure A.10: Durham Geo Calibration Certificate for Brainard-Kilman E-214 Load Cell; Serial Number: 253. Page 2 of 2.

A.6 Wiring Diagram for Five Pin Connectors

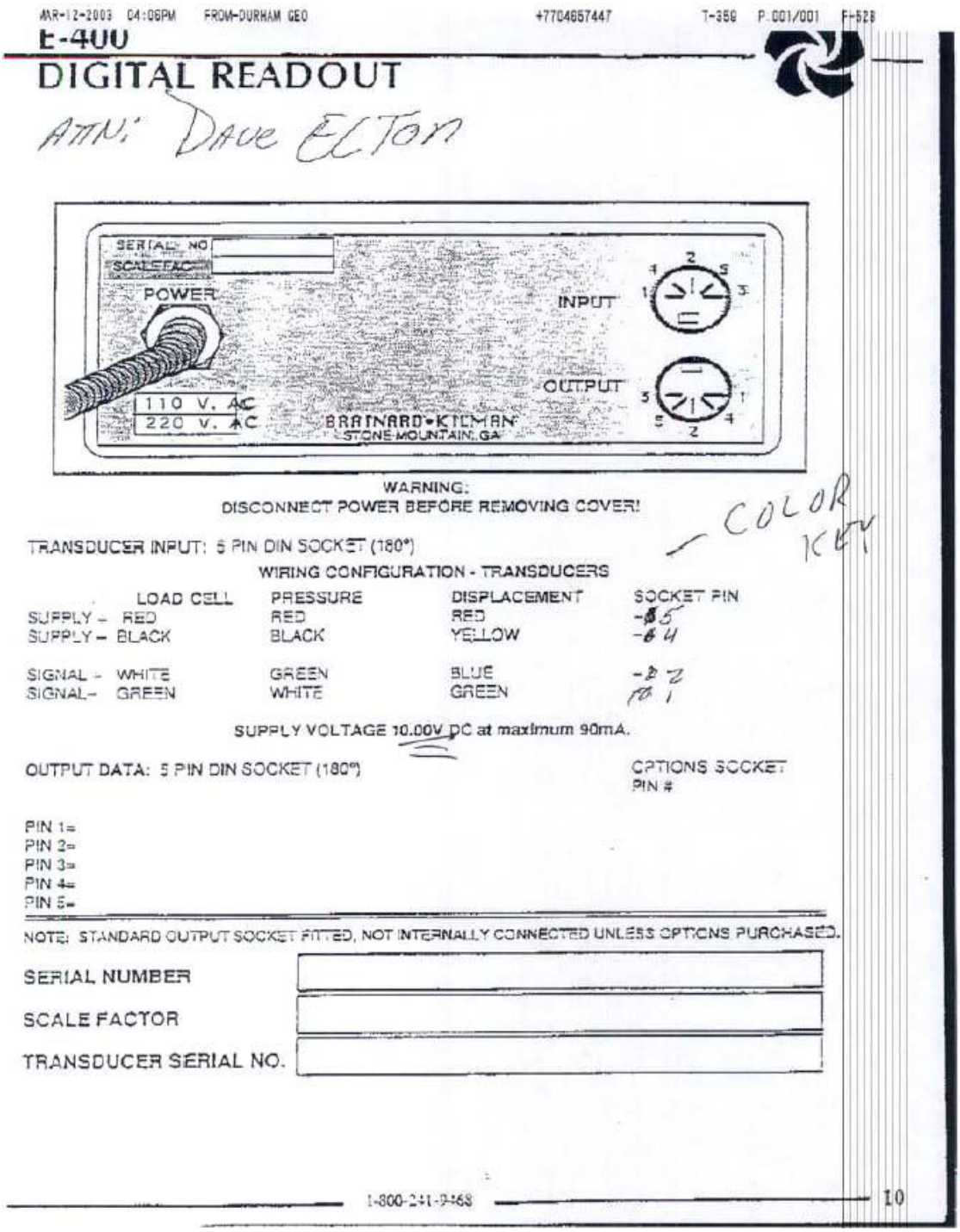

MAR-12-2003 04:08PM FROM-DURHAM GEO +7704657447 T-359 P.001/001 F-528

E-400

DIGITAL READOUT

ATTN: DAVE ELTON

SERIAL NO
SCALE FACTOR
POWER
INPUT
OUTPUT
110 V. AC
220 V. AC
BRAINARD-KILMAN
STONE MOUNTAIN, GA

WARNING:
DISCONNECT POWER BEFORE REMOVING COVER!

COLOR KEY

TRANSDUCER INPUT: 5 PIN DIN SOCKET (180°)

WIRING CONFIGURATION - TRANSDUCERS

	LOAD CELL	PRESSURE	DISPLACEMENT	SOCKET PIN
SUPPLY +	RED	RED	RED	-5
SUPPLY –	BLACK	BLACK	YELLOW	-4
SIGNAL +	WHITE	GREEN	BLUE	-2
SIGNAL–	GREEN	WHITE	GREEN	-1

SUPPLY VOLTAGE 10.00V DC at maximum 90mA.

OUTPUT DATA: 5 PIN DIN SOCKET (180°)

OPTIONS SOCKET PIN #

PIN 1=
PIN 2=
PIN 3=
PIN 4=
PIN 5=

NOTE: STANDARD OUTPUT SOCKET FITTED, NOT INTERNALLY CONNECTED UNLESS OPTIONS PURCHASED.

SERIAL NUMBER

SCALE FACTOR

TRANSDUCER SERIAL NO.

1-800-241-9468

10

Figure A.11: Wiring diagram for Durham Geo (formerly Brainard – Kilman and Boart Longyear) 5 pin socket connectors (Shiver 2007)

A.7 Durham Geo Contact Information

Durham Geo Slope Indicator (formerly Brainard-Kilman and Boart Longyear)

2175 West Park Court

Stone Mountain, GA 30087

Phone: 800-837-0864

Phone: 770-465-7557

Fax: 770-465-7447

www.durhamgeo.com

Appendix B: Step-by-Step Example of Setting Up and Using the Megadac with TCS For Windows

1. Open the data acquisition by double clicking on TCS for Windows icon

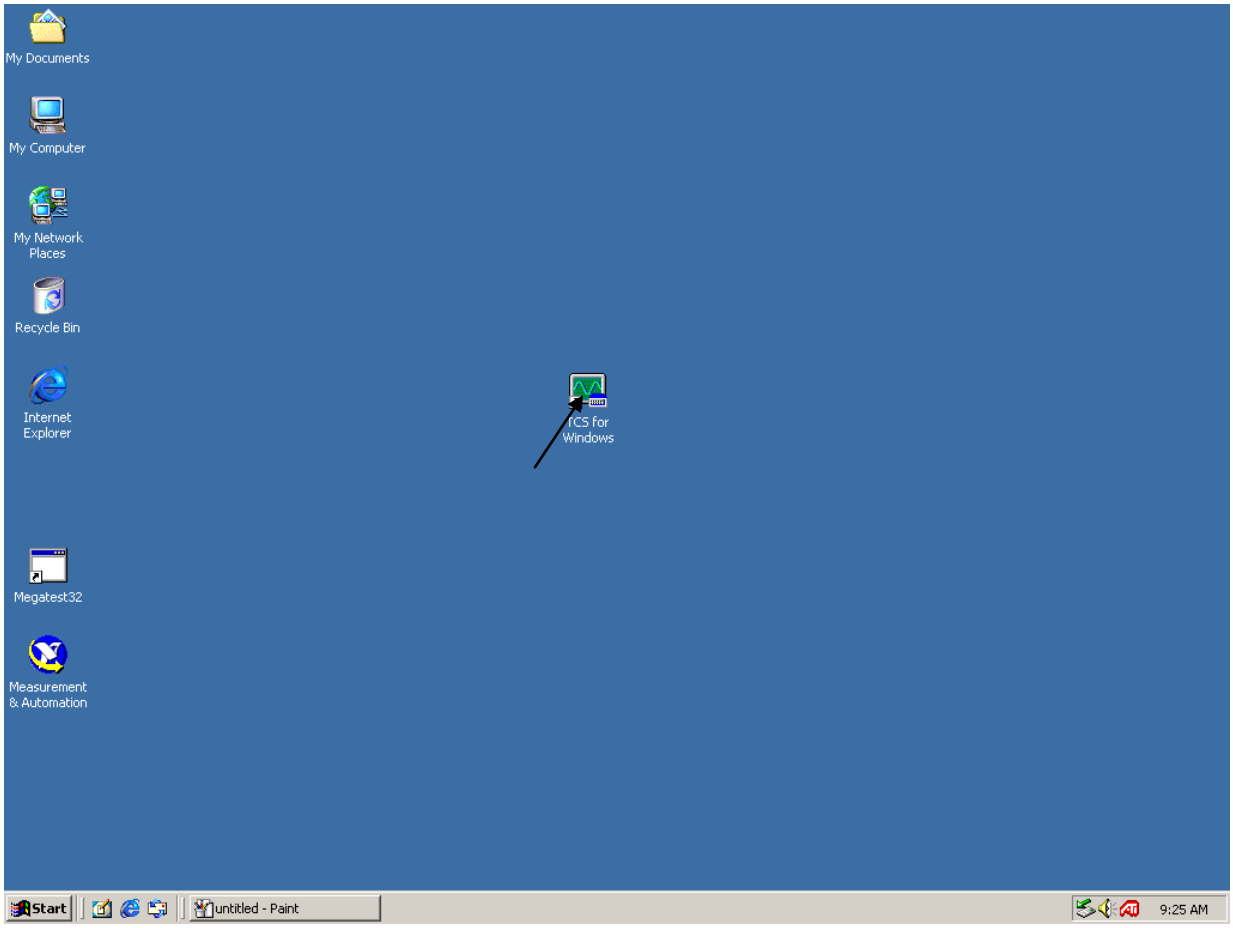

Figure B.1: Screenshot, TCS for Windows icon

2. Open or create the test you want to run by clicking file, then clicking open test if you want to open a test that is already created. Click on New Test if you are creating a new

test from scratch. We have found that once we have created a test with multiple instruments that we use over and over again; it is easier to open a test that we know is already configured properly and perform the Save Test As function and rename the test to the new test you are performing and then make the necessary changes. For your practice open Stringpot_Test.

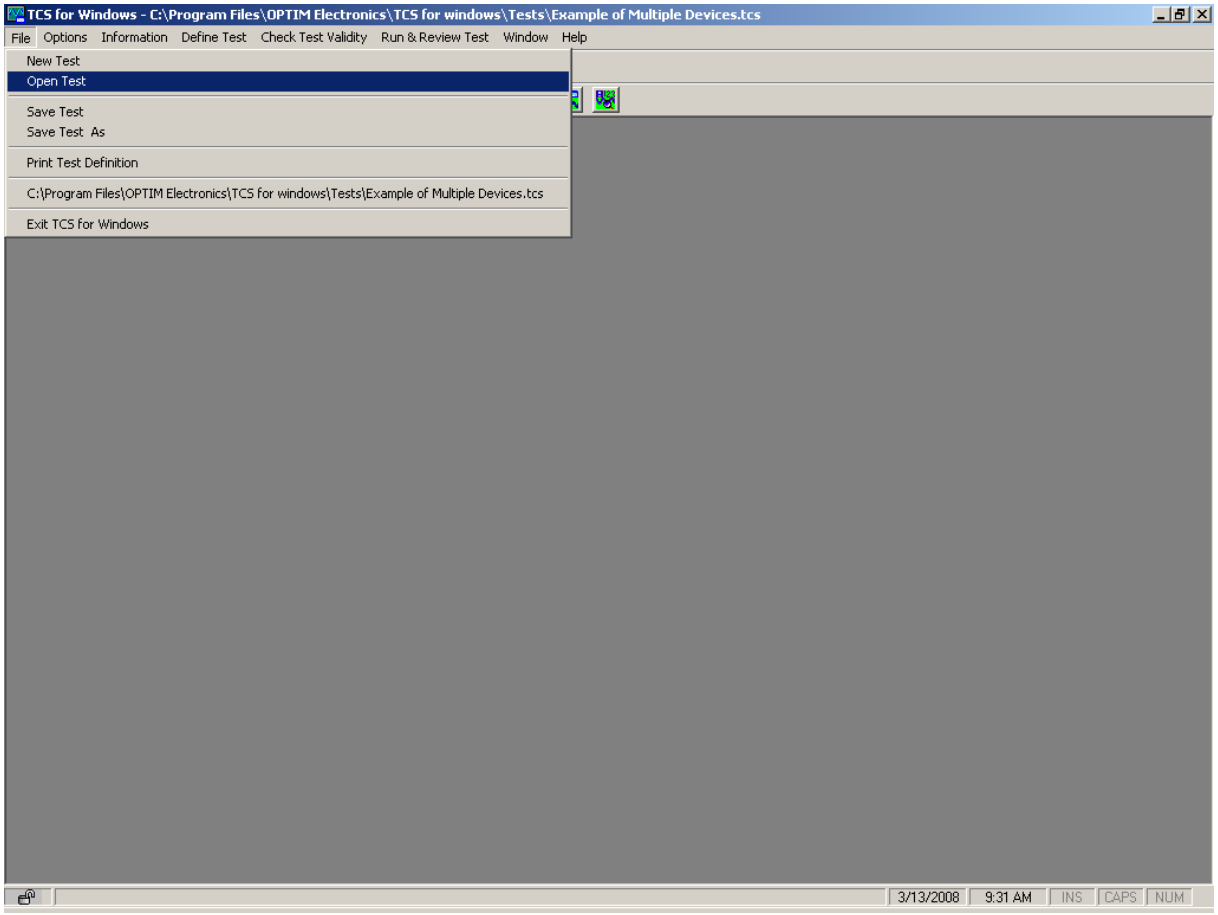

Figure B.2: Screenshot, Open Test

3. Set the Scan rate you would like by clicking on the Acquisition Recording Requirements button.

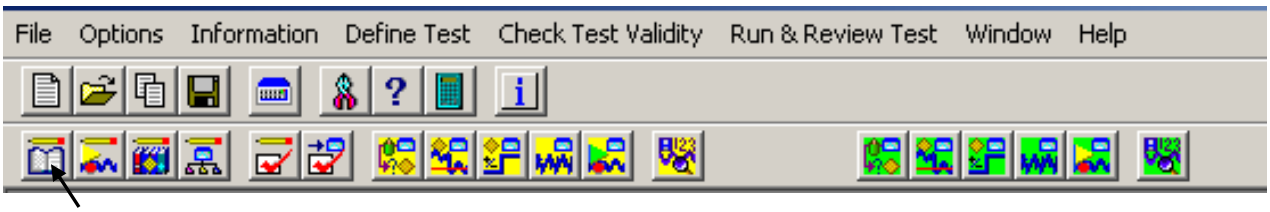

Figure B.3: Screenshot, Acquisition Recording Requirements button

4. The Scans per Second depends upon what type of testing you are doing. Here you can also set what triggers the start and stop scanning. We generally use the CPU Function Key to start and stop recording which means that we have to manually hit the record button on the computer. Here is also where you can put in any Pretrigger and Posttrigger time. We generally set the Record Location to MEGADAC RAM, the Archive Method to When Recorded and the Archive Location to Host Computer. When done close the Acquisition Recording Requirements Screen. It is important to note that you do not need to hit the save button after each change is made. TCS for Windows automatically stores your changes until you try to close the program, then a prompt will come up asking if you would like to save the changes made to the program. Even though this prompt comes up, I make it a practice that after I make a change on a page I hit the save button. I encourage you that while you are practicing and learning the system that you don't save any changes to our program. If you would like to make changes, perform the save as function and then rename the file. That way when we talk on the phone we can be looking at the same program on my computer and your computer.

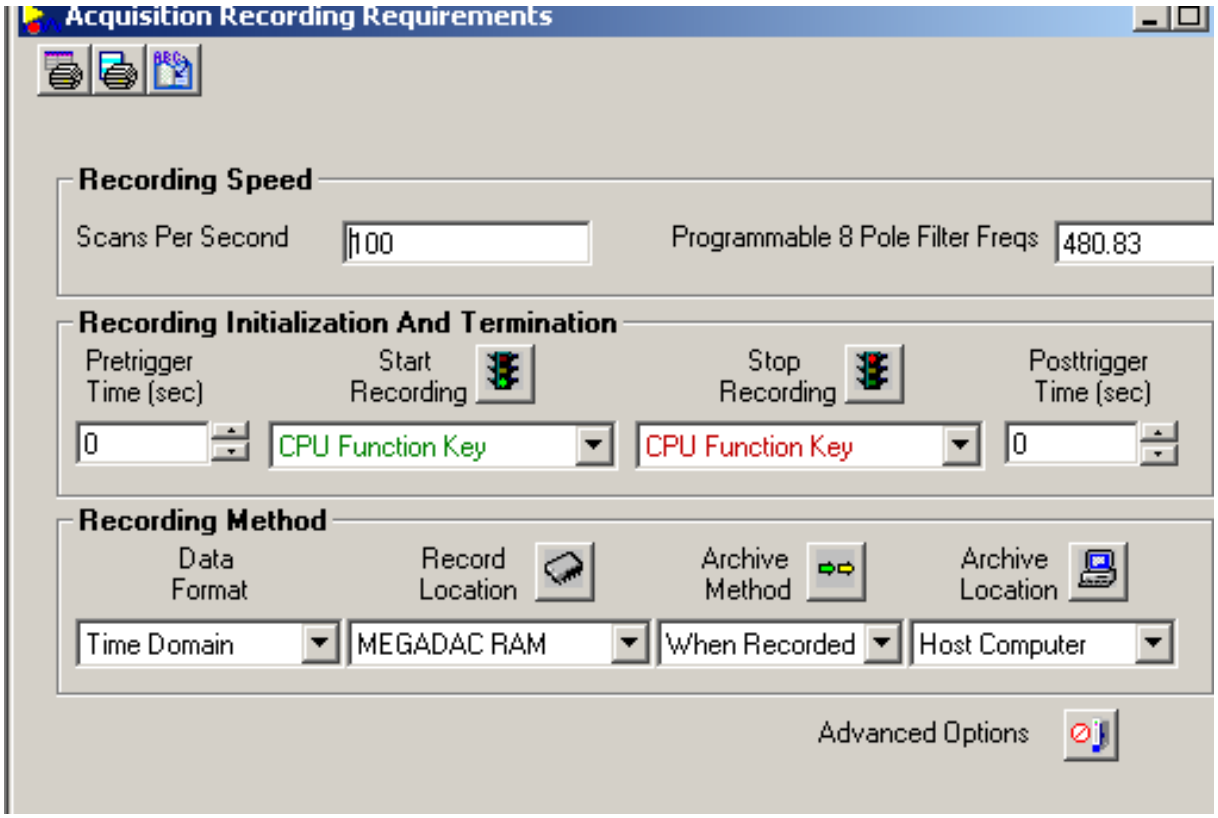

Figure B.4: Screenshot, Acquisition Recording Requirements window

5. Click on the Sensor Library Definitions button to set up the Test Sensors.

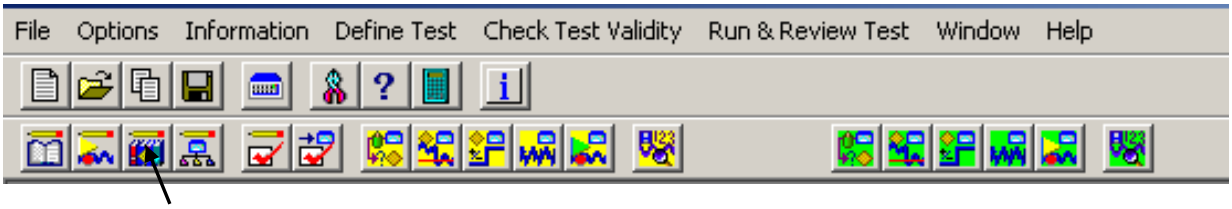

Figure B.5: Screenshot, Library Definitions button

6. This is where you configure what sensors you are going to use on you test. On the right side is the Global Sensor Library. This is where you should store all of the sensors that you have or will use. I suggest that once you have all of your sensors configured right and working, that you make a file called master or backup that you save, which will not be used or changed. This way if a change is accidentally made to the global sensor

library, then you can go back and copy the master to get back to the original working file. On the left side is where you copy the sensors from the global sensor library to the Test's Sensors side. The test sensors side generally has just the sensors that you plan on using in the test. If you have sensors on the test sensor side that is not being used on the test it doesn't affect anything. The way to copy a sensor from Global Sensor Library to the Test's Sensor is to simply drag the sensor you would like from the Global Sensor Library over into the Test's Sensor's, Sensor Library file and then click copy.

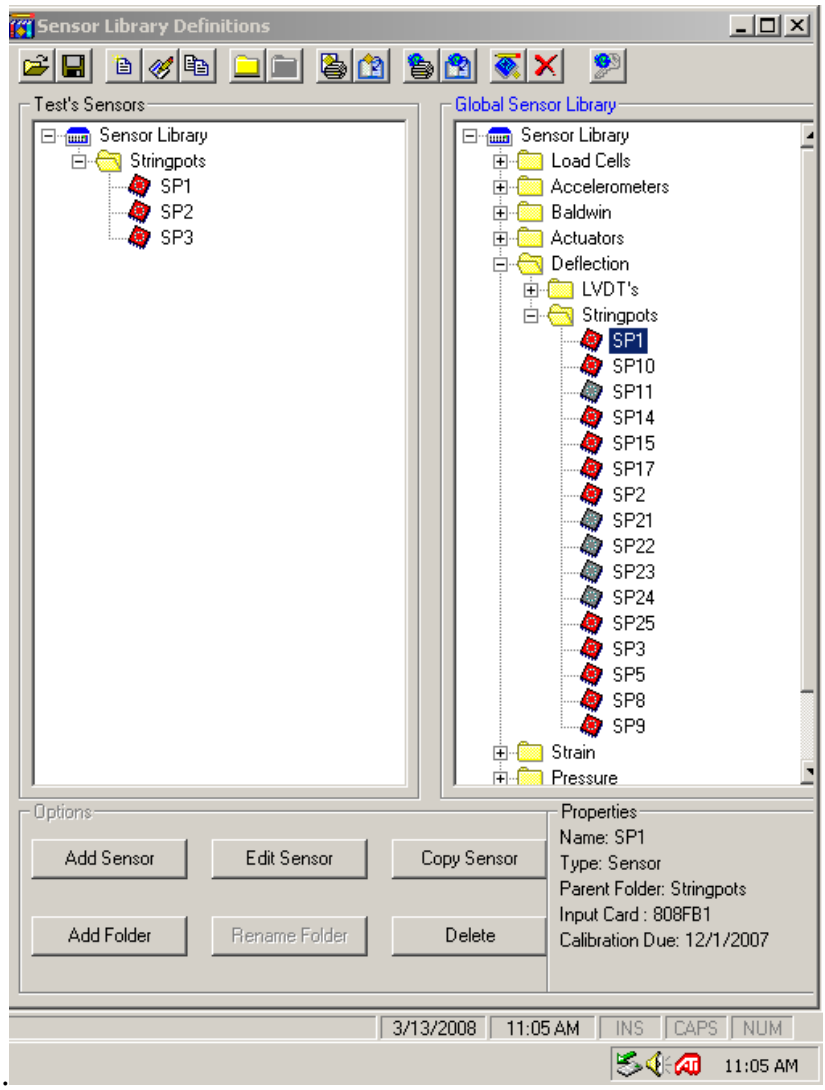

Figure B.6: Screenshot, Sensor Library Definitions window

7. Each sensor must be configured and its calibration entered so that the Megadac can convert the DC voltage into the proper value and units. When you copy the Sensor over to the Test's Sensor, all of the configurations and calibrations go with it. It is good practice to double check the Sensors configuration and calibration on the Test's Sensor side to make sure everything is configured right. This is done by double clicking the sensor (i.e. SP1). The Sensor Definition page comes up and here you identify what sensor you are using by naming it, giving it a number if desired. You can add any comments about the sensor. It is important that you select the correct Input Module. In this case the Input Module selected is 808FB1. This page is also where you select the Excitation Source, whether the Megadac is providing the excitation or some external source. On this page you also select the Excitation Type and the Excitation Value. The excitation value is very critical. If you put 5 V as your Excitation Value and the 808FB1 Module's jumper is set up for 10 V, the test will run and you will not know that there is a problem until you start to evaluate your data and the values are nowhere where you expected them to be. So a very critical step in ensuring that your test is set up properly is to 1-know the excitation value of the sensor that you are using, 2-make sure that you put the Excitation Value to match that sensor and 3-Ensure that the jumper on the 808FB1 Module is set to mach the Excitation Value.

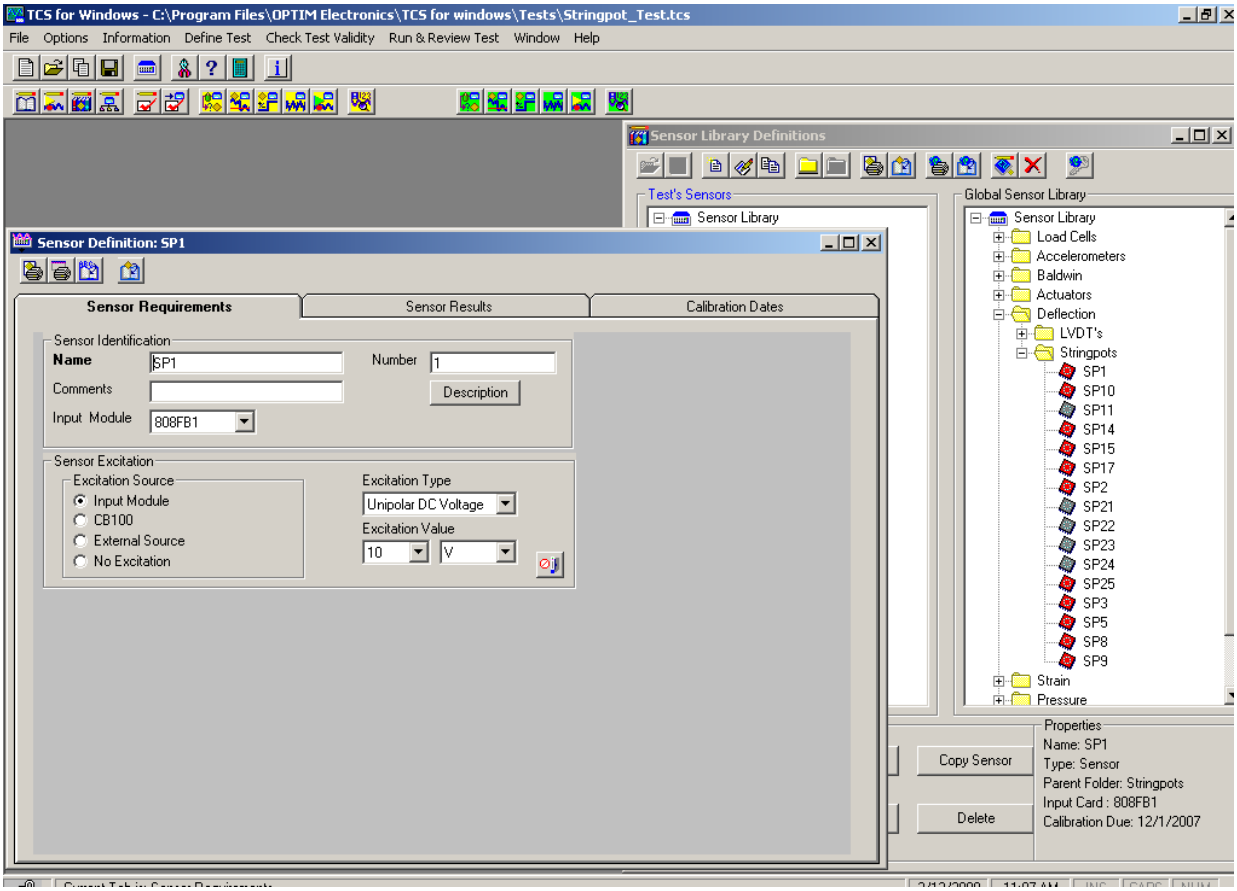

Figure B.7: Screenshot, Sensor Definition window, Sensor Requirements tab

8. The next step to set up the Sensors configuration is to enter its units and calibration. This is done by clicking the Sensor Results Tab on the Sensor Definition Page that was already brought up from the last step. Here you set up the Curve Model, the Engineering Units, the curve type and the sensors calibration. There are also other functions on this page that allow you to create your own calibration for a sensor, but we will not present this information at this time, but we can explain it to you easier over the phone. Most instruments when you buy them have a calibration sheet with them. We generally just insert the factories calibrations into the right side where it has Sensor Value (mV) and Engineering Units. For our example we are looking at SP1 and our calibration sheet says that the Pos. Sensor is 49.93 mV/V/in, which translates into 499.3 mV per inch. Once

you have entered your sensors calibration you can view the curve by clicking on the view curve button at the bottom.

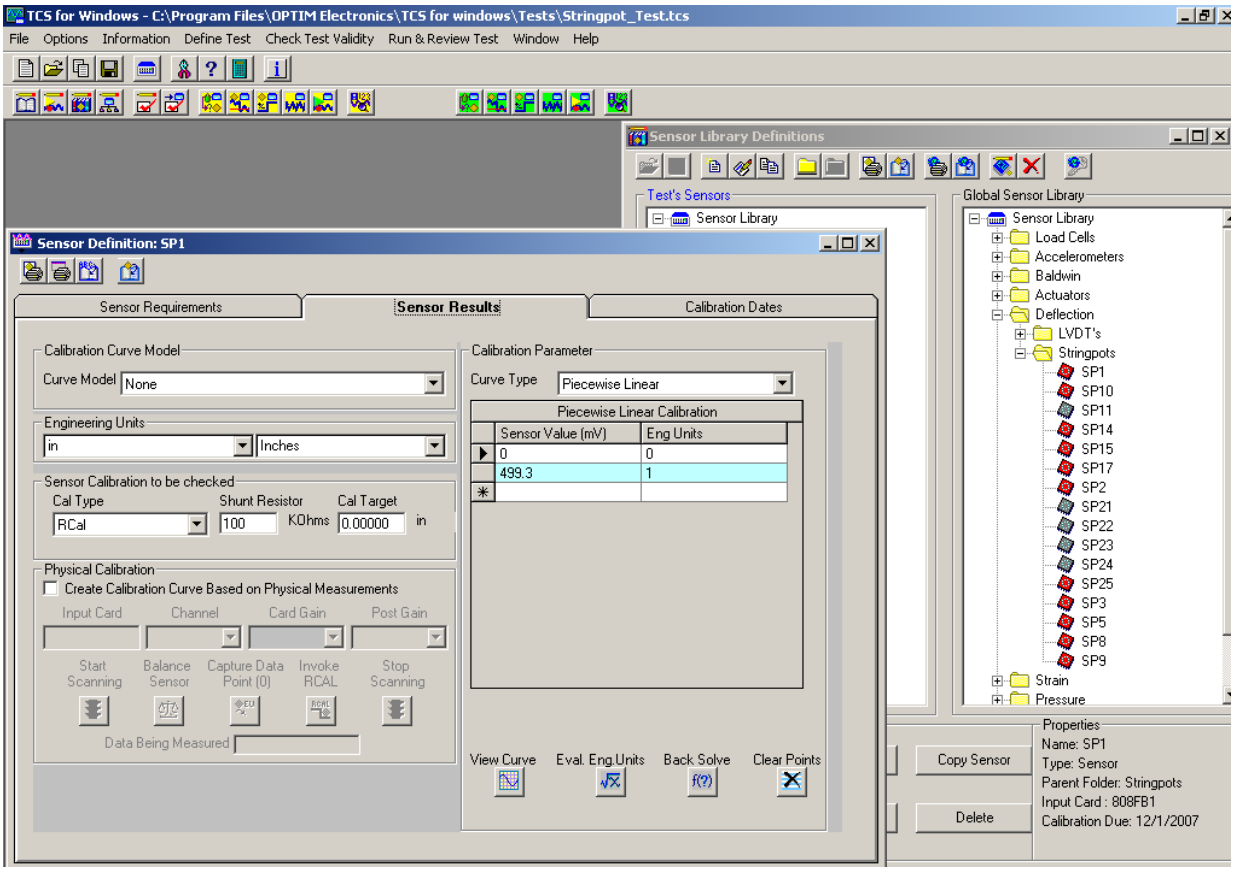

Figure B.8: Screenshot, Sensor Definition window, Sensor Results tab

9. Click on Tag and Channel Definitions button.

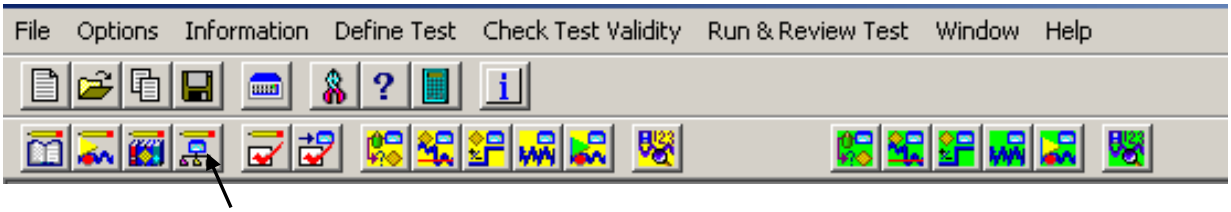

Figure B.9: Screenshot, Tag and Channel Definitions button

10. This is where you insert into the program the sensors that you plan to use on the test. When creating a new test, this screen will come up with no information in the spaces.

There are 6 fields that we generally fill in on a new sensor. 1: Name the sensor. 2: Assign the channel the sensor will be hooked up to. 3: Make sure the card gain is set appropriately (1 or 100). 4: Assign the appropriate P-Gain. 5: Pick the appropriate sensor from the pull down list as you hover over the sensor field on the right side of the screen. When you pick this sensor it automatically fills in the input card configured for that sensor and its calibrations. 6: Select whether or not you want to zero or balance your sensor (I.E. strain gauges). It is important that after setting up a sensor that you look at the Max Full and Min Full and see if your sensor's range fits within this range. Also pay attention to the resolution to make sure that is what you are expecting.

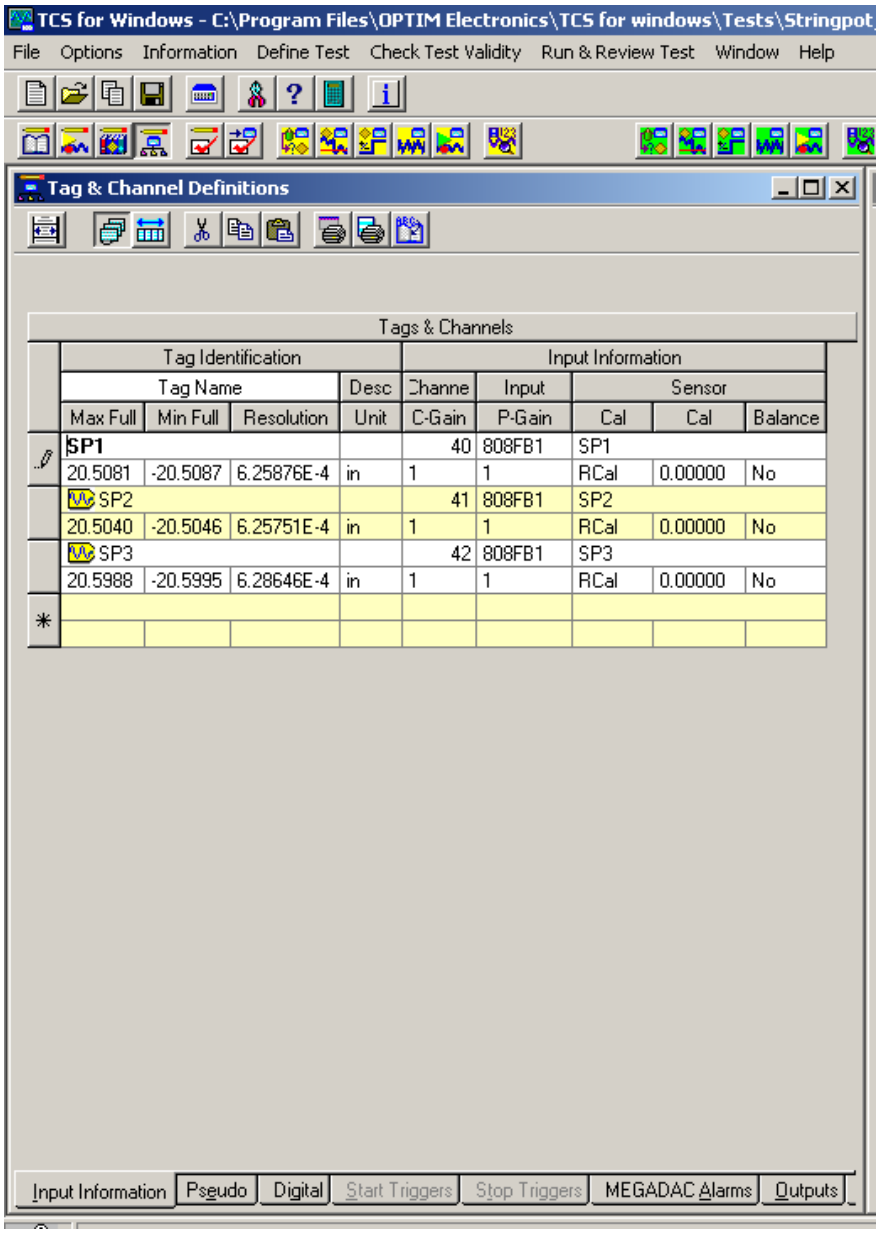

Figure B.10: Screenshot, Tag and Channel Definitions window

11. Now that you have configured your tags and channels the next step is to hook up your sensor or sensors to the channels you have configured them to. For your first time I would suggest that you find a sensor that has to be excited by 10VDC and gives out a 0-10VDC output. If you do not have one that fits this description an easy way to test your setup is to just use a variable DC power supply making sure to not exceed 10 VDC. The

STB AD808FB1 board has eight channels as numbered on the drawing below. The terminals V and R are the excitation voltage that comes from the megadac. It will either be 5 or 10VDC depending on how you have the jumper set on the 808FB1 card in the megadac frame (how the jumpers work can be discussed over the phone. The V is the Positive, and the R is the Negative. The + and – terminals between the V and R are for the output of your sensor (0-10VDS). If you are setting it up with a Variable DC Power supply just to test if you are seeing a signal, hook up the + from the power supply to the + on the board and the – of the power supply to the – on the board. Ensure that before hooking the power supply up that it is set at less than 10VDC. Once you have hooked up your sensor or variable power supply, you are ready to run a sample test to see if you are getting data.

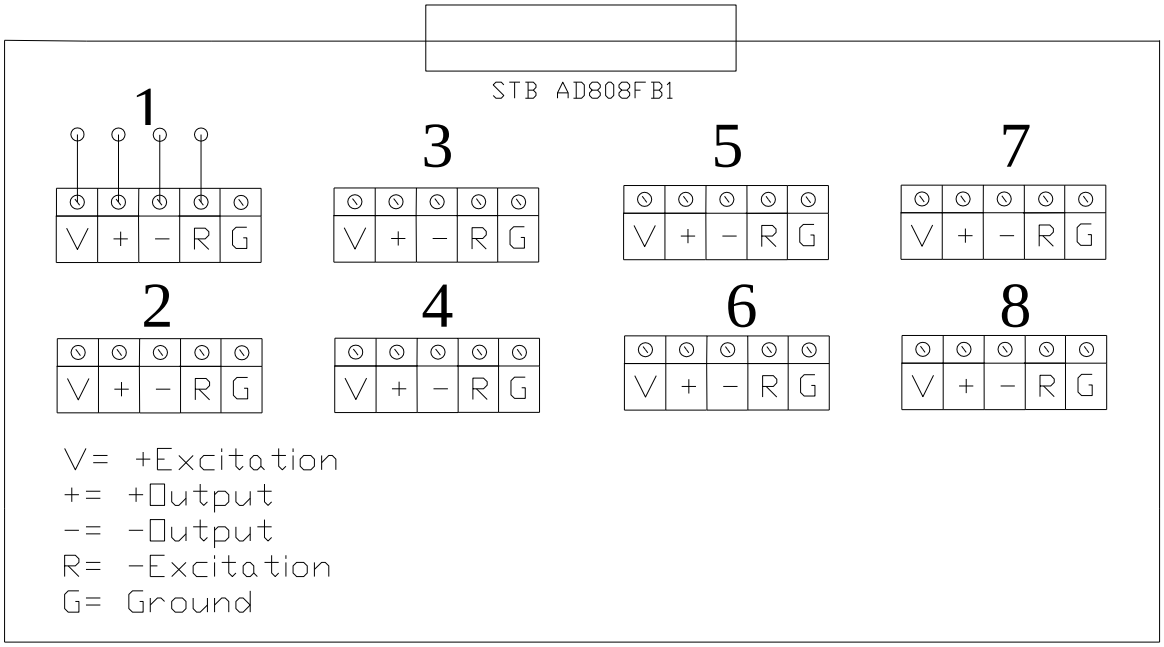

Figure B.11: STB AD808FB1 board schematic diagram

12. It is also important to see that the Megadac channels are set up with the right input card (i.e. 808FB1) and card gain. To do this:

    1: Click on Megadac information button.

    2: Click on Get Configuration button

    3: Click on Map Input Channels. Double Check that you have the right cards configured and the proper card gains. If it is not configured right make the necessary changes and then click the save map to megadac button. Also save this to a file by clicking save map to file on PC.

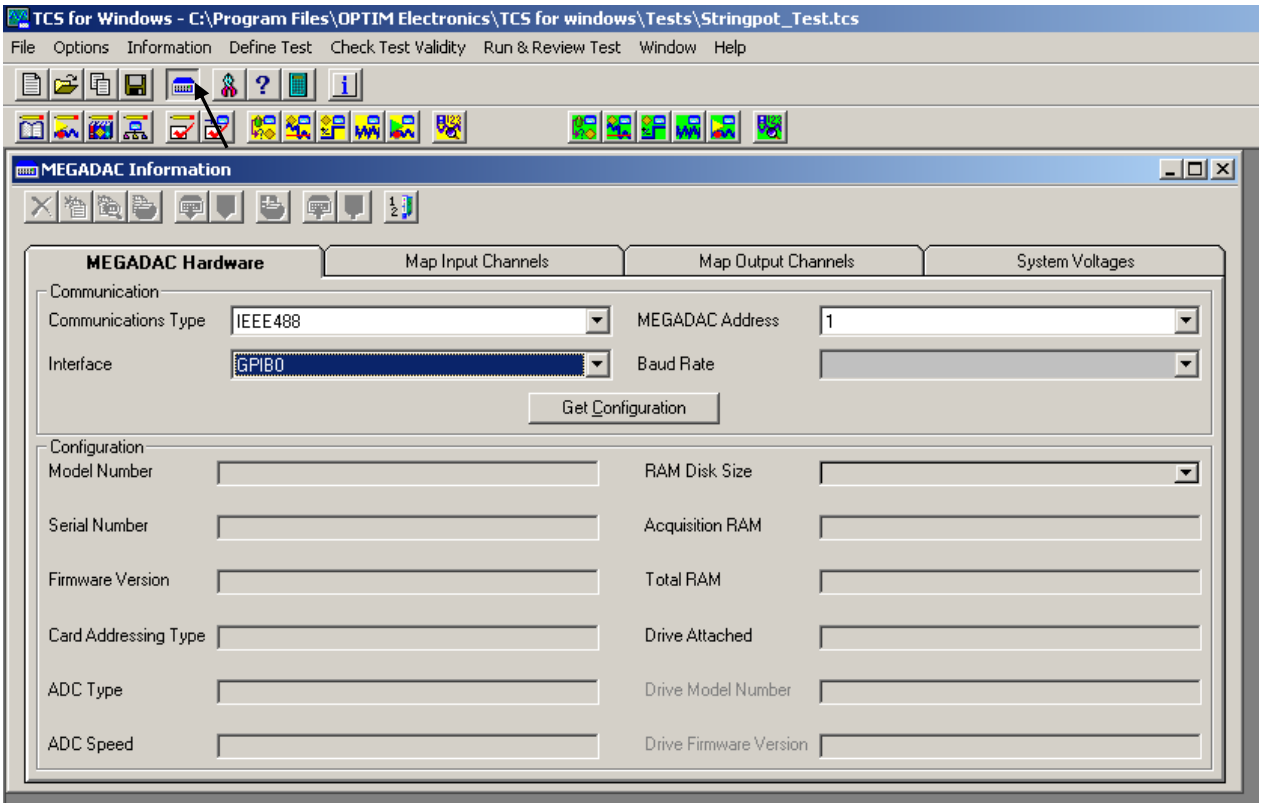

Figure B.12: Screenshot, Megadac button and Megadac Information window

13. Once you are to this step you are ready to use the sample run mode of the program, and see if you are reading the sensor or sensors that you have hooked up. Click on Sample Run.

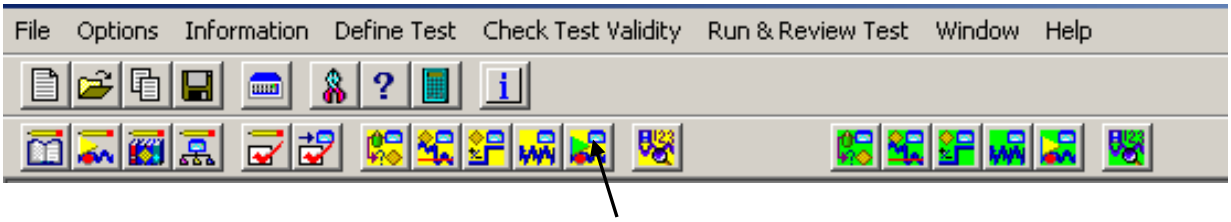

Figure B.13: Screenshot, Sample Run button

14. Once you are ready to read your sensor, ensure that the megadac is turned on and the communication cable is hooked up. Click the Scan button. After a few seconds, if everything is configured and hooked up right, data will come up in the data Units column. If you would like to view the data on a plot, click on the 7th button from the right of the Sample Run Screen and plots will come up. I will not go into detail right now on how the plots work and the different capabilities, but I will let you know that you can do multiple things with plots. The one part that is a general practice of ours is to click on the plot screen on the button that has the red circle shaped figure. This will allow the plots to automatically adjust its scale so that you can see the smaller movements on the plot. Also on this screen if you had configured a sensor to be zeroed or balanced, then you could click the Bal button and it would zero your sensor. If you want to record data in this Sample Run mode you click the Rec button while it is already scanning. Once you are done recording click the Rec button again to stop recording data. It is important to know that if you use the sample run mode you can download the test that you have just run and put it into a program such as excel, but it does not archive it anywhere. So the second time you run a test in Sample Run mode and record, the last test will be overwritten. So our general practice is to only use sample run while setting up our tests to ensure that all of the sensors are working properly and taking data.

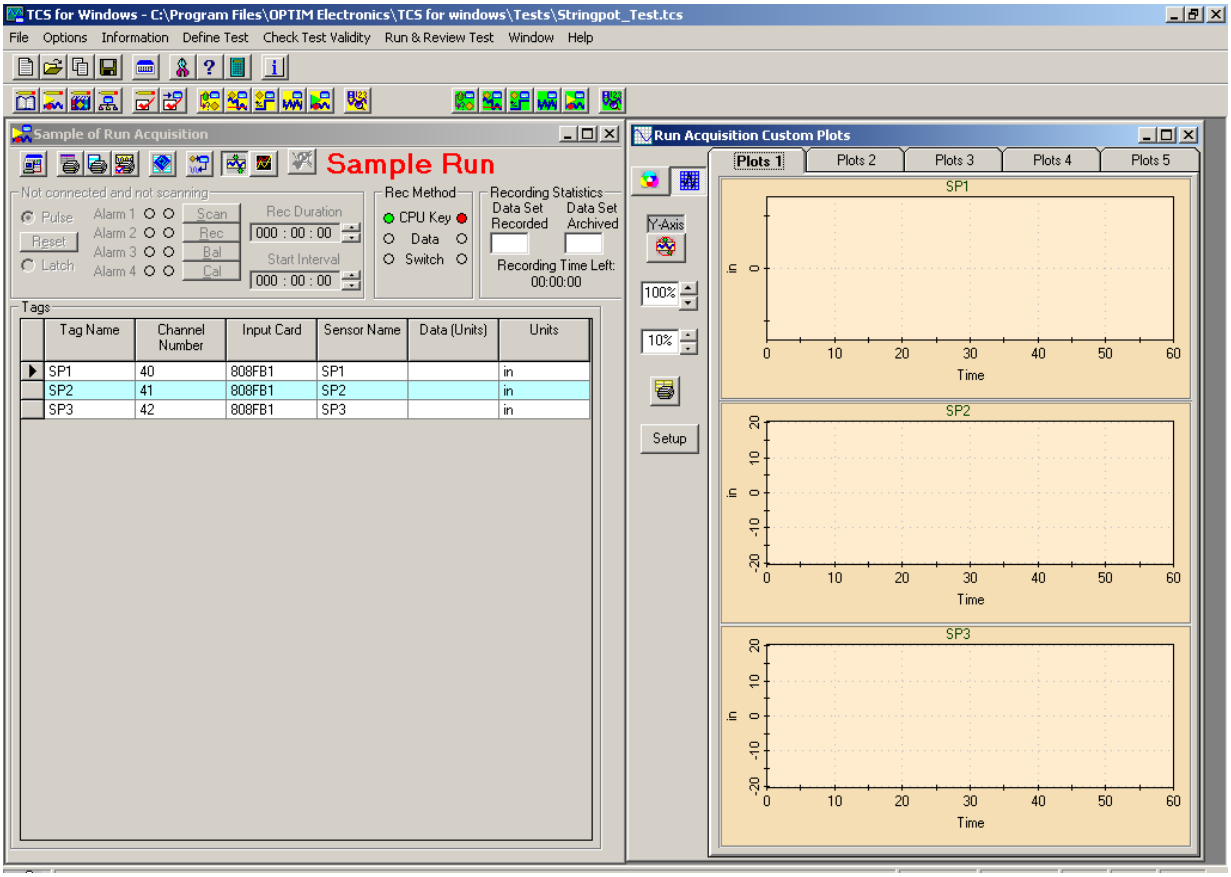

Figure B.14: Screenshot, Sample of Run Acquisition window

15. Once we are sure that it is working properly then we run our test in the Live Run mode. Click the Run Acquisition Button (Live Run).

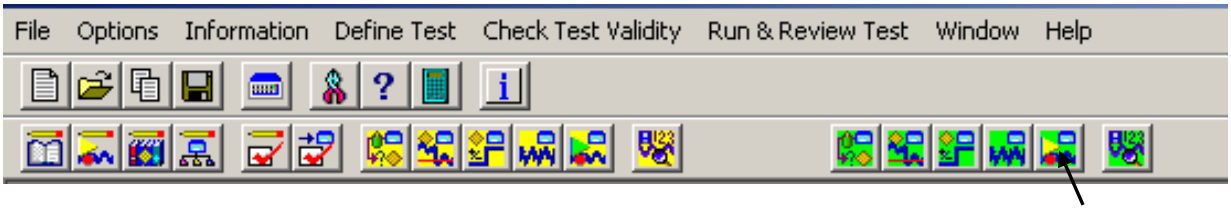

Figure B.15: Screenshot, Run Acquisition button

16. On this screen the same steps apply as the sample run mode, except that in the live run mode once you hit the Scan button a prompt will come up asking if you want to run in Live run mode because the critical fields will be locked. This means that once you say yes, you cannot change any of the configurations of the test. You can always perform the

save as function and rename the test if you need to make adjustments to the configuration of the test. The other difference in the Live Run Mode is that each time you record a new test it archives it and does not overwrite the last test run. This is where it is critical that you write down which test number relates to which sample you are testing. As you get familiar with this page while running tests, watch the two boxes Data Set Recorded and Data Set Archived. While recording the first test, the number 1 will come up in the Data Set Recording box. Once you stop the recording you will see the number 1 in the Data Set Archived box. This can sometime be confusing for example if you are running your 2nd test in the live run mode, as you are recording you will see the number 1 in the Data Set recorded box and while still recording you will see the #1 in the Data Set Archived box. Not until you stop recording will you see the #2 come up in the Data Set Archived box. In other words every time while recording whether it be the 1st or 5th test, the #1 will show up in the Data Set Recording Box: but once you stop the recording the test # that you are recording will show up in the Data Set Archived box.

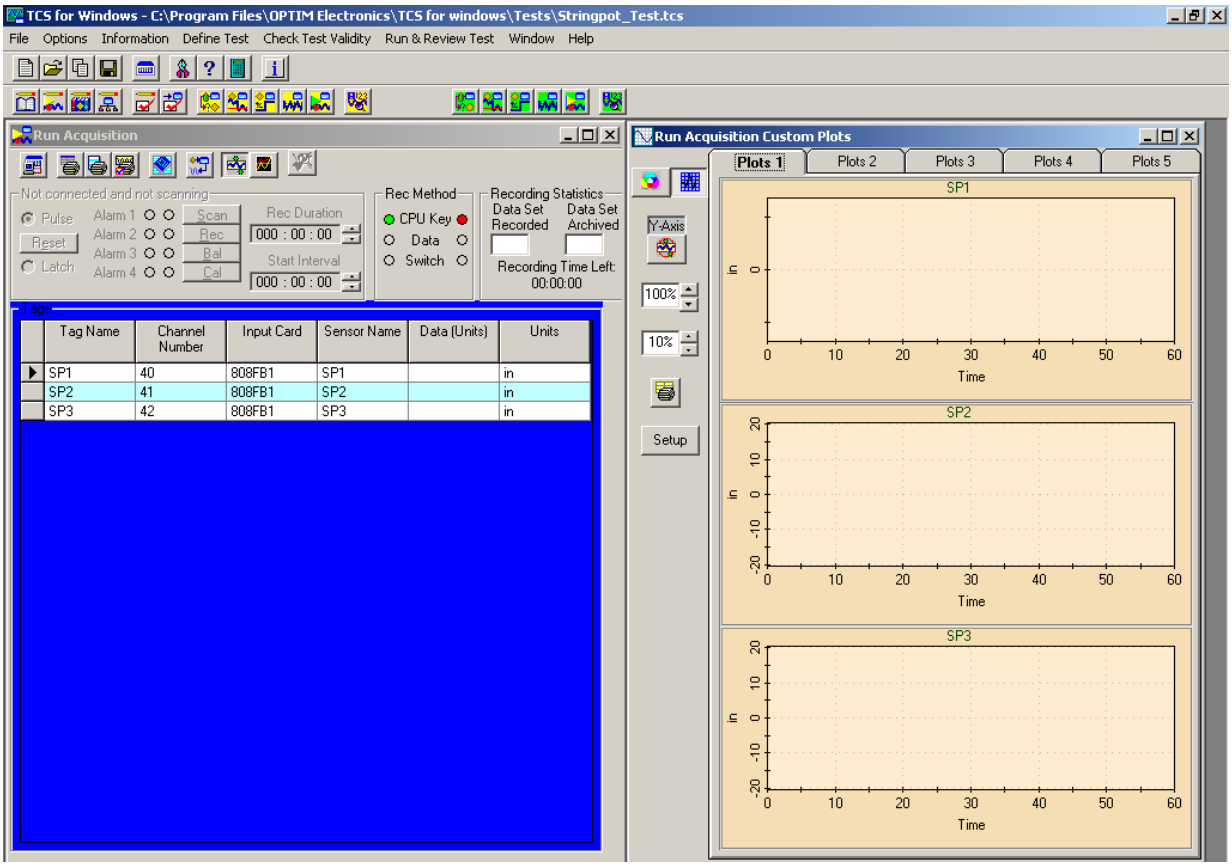

Figure B.16: Screenshot, Run Acquisition window

17. Click on the Process Recorded Data-Live Run button.

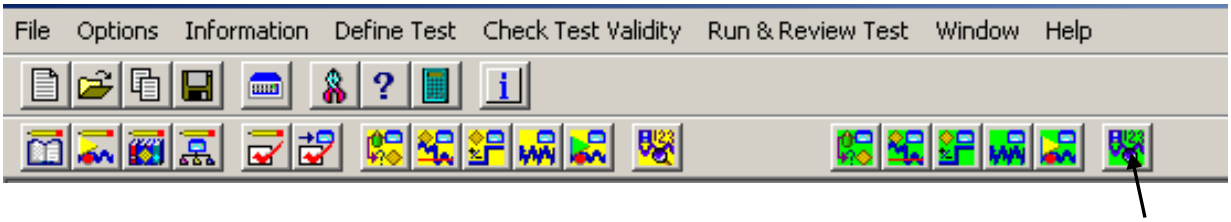

Figure B.17: Screenshot, Process Recorded Data button

18. This is where you download the data that is on the megadac to your laptop. The functions of the Process Recorded Data in Sample Run and Live Run are the same except that Live run has archiving capabilities. When the screen comes up the Tab Data Set Selection will be brought up. Here you can either review the data or export the data to

your computer. I will not go into detail about reviewing data right now but we can discuss it over the phone. To export data there are 9 steps.

1: Uncheck the Review checkmark.

2: Click or check the Export Entire Data Sets Box.

3: On this example screen that is shown below, it does not show any Data Sets at the bottom because I had not performed any tests. If you had performed a test and recorded it then it would show up down on the bottom. Many times we run 10 to 15 tests which show up in numerical order from greatest to least, which means the last test recorded shows up at the top. This is where it is critical that you beforehand you had hand written what sample correlated with what test number. Before moving on to the next step make sure that the test # that you want to export is highlighted. This is done by clicking on the box to the left of the test number.

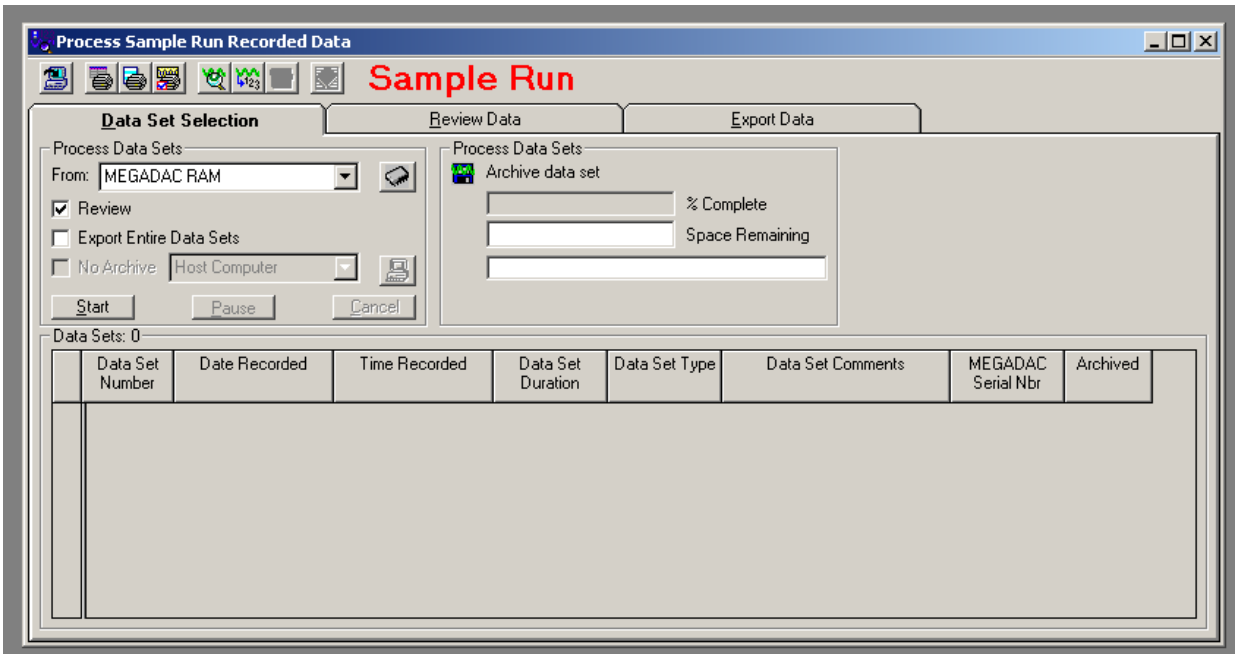

Figure B.18: Screenshot, Process Sample Run Recorded Data window, Data Set Selection tab

4: Click on the Export Data Tab

5: Make sure that the Export Format is compatible with the program that you plan on using for viewing the data (i.e. excel). Since we use excel, we select ASCII Fixed Width.

6: Select the Export Path where you would like the data to be exported to on your computer (i.e. desktop or C drive).

7: Name the Test in the Export File name field. Make this identifiable to the test you are exporting.

8: Make sure that all of the data points that you want exported have their boxes checked.

9: Click the Start button and then a screen will come up saying how much time is left until it is finished exporting.

Repeat these 9 steps for each Data Set you want to export.

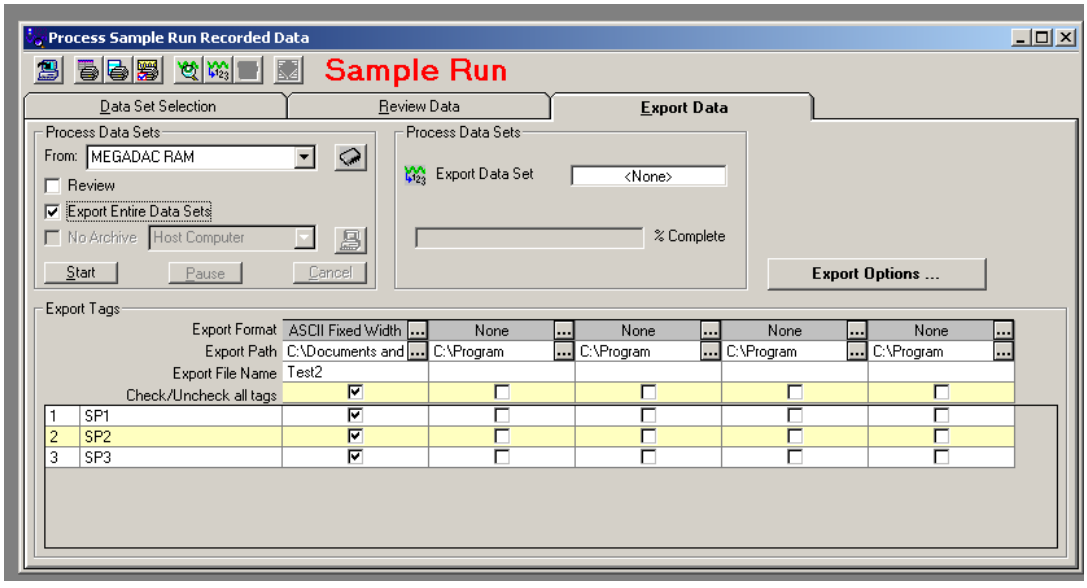

Figure B.19: Screenshot, Process Sample Run Recorded Data window, Export Data tab

19. Once you have exported all of the Data Sets that you need, you can now use a program such as excel to view and analyze the data. The steps that I take to open a test in excel is

1: Open excel

2: Click File/Open

3: Find to the place that you had the megadac export your test to (i.e. desktop or C drive).

4: The file will not show up on the screen because the test is an .ASC file. In the Files of Type field click the pull down arrow and select all files. This will bring up all of the tests that you just exported.

5: Select the test you want to open in excel and click open.

20. When excel tries to open the file: 1: Select Delimited

2: Space

3: Next

4 Finish

21. When the file come up there are a few minor things to make note of.

1: If you named a sensor using spaces it will take up multiple columns and will confuse you of what data goes to what sensor.

2: At about the 21st row you will have a row that says Good and Bal alternatively. This indicates that there were no major errors for each sensor. If they all say Good and Bal then we usually ignore it or delete that row.

3: The values come into excel in scientific form so you need to format it so that it is in numeric form with the amount of digits after the decimal point.

4: Once you have spaced everything and formatted it the way you want to save it.

1: Click File/Save As

2: Select the file location where you would like to save it.

3: Name the file without quotation marks and without the .ASC

4: Click the pull down arrow on the save as type and select Microsoft Excel Workbook (*.xls)

5: Click Save

Appendix C: Detailed Consolidated Undrained Triaxial Procedures

Procedures after (Shiver 2007)

C.1 Preparing the Sand / Hydrogel Mixture

1. Place 300 grams of Ottawa sand into four 1000 mL beakers.
2. Calculate the desired amount of hydrogel per beaker: [(% hydrogel / 100) x (1200 g of sand)] / 4.

Note: 1500 grams of sand is enough to over-fill a 6" long, 2.8" diameter mold.

3. Place the proper amount of hydrogel into each beaker.
4. Tilt the beaker approximately 45° and rotate until you can no longer see hydrogel powder.
5. Combine the contents of the four beakers into one beaker and rotate (as in step 4) 3-4 times.

Note: It is important to not over-mix the samples, or segregation will occur. Rotate only until hydrogel powder is no longer visible.

C.2 Preparing the Mold

1. Coat the inside of the mold with Molykote® 33 Light low temperature grease, wipe off excess with a paper towel.
2. Cut a latex membrane (either used sample membranes or latex gloves) roughly twice the size of the mold opening.

3. Lay the latex over the mold opening and secure with a rubber band or an O-ring (Figure C.1) (it is important that this seal is tight, so the rubber band may have to be double looped).

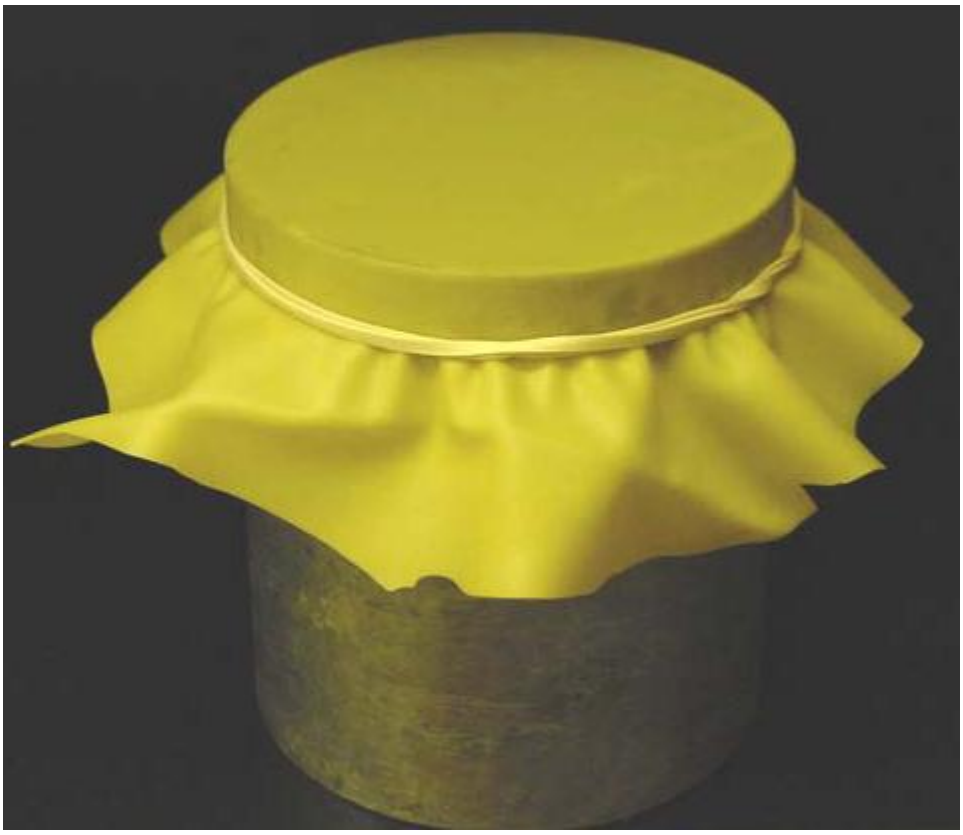

Figure C.1: Latex membrane secured over the mold with rubber bands during mold preparation. Notice there are no wrinkles under the rubber band (Shiver 2007)

4. Stretch the latex by pulling down on the sides until there are no wrinkles under or above the rubber band.
5. Flip the mold over so that the latex now serves as the bottom of the mold.
6. Place the mold in the confining frame and place the top plate on top.
7. Adjust horizontal bar so that the thumb-screw will secure the top plate when tightened.
8. Swing the bar out and remove the top plate to allow soil placement.
9. Place the mold in the freezer or the liquid nitrogen freezing vessel.

10. Fill the mold following the procedures of C.3
11. After striking off the mold, place top plate on top being very careful not to cause vibration.
12. Swing the bar over and tighten screw, again being careful not to cause vibration.
13. Allow the sample to freeze at -35° for at least three hours or freeze with liquid nitrogen following the procedures of C.6.

C.3 Adding Sand/Hydrogel Mixture to the Mold

1. Place mold in freezer.
2. Place the sand/hydrogel mixture into the funnel/tube device by placing the sand in the funnel and pinching the tube approximately 6" from the free end so that the mixture will not flow out.
3. Place the tube in the mold no more than ¼" from the bottom, and let the mixture flow out by releasing grip on the tube.
4. Maintain the ¼" spacing while evenly distributing the mixture into the sample.
5. Fill until the mold is slightly over full.
6. Strike off the top of the mold with a straight edge (a piece of cardboard with a straight edge works well for this) being careful to not cause vibration.

C.4 Wetting the Sample

1. Fill syringe with deaired water.

Note: Deaired water is water with the dissolved air removed from it either by boiling or vacuum. This project used the Nold Deaerator whose operation is described in "The Nold Deaerator owner's manual."

2. Attach needle and inject water into the sample at various locations through the holes in the top plate.

Note: Water should be injected no faster than 1 mL per 5 seconds and at least five injection points evenly distributed around the sample.

3. While injecting water, slowly raise the needle from bottom to top.
4. When water is observed coming out of all the holes on the top plate the specimen should be saturated. Confirm this by injecting water into various locations and depths to see if water comes out of all top cap holes at all locations of injection.

Note: The needle may become clogged from time to time. Clear the clog by taking the needle out of the sample and off the syringe. Then use a solid needle that fits inside the needle to push out the clog.

C.5 Extracting the Sample

1. Remove sample from freezer (be sure to use insulating gloves as frostbite of the skin is possible).
2. Use a wrench to loosen the screw.
3. Strike the top plate with the wrench to remove it from the mold.
4. Due to water expansion during freezing, the top of the sample may need to be squared off. This is done with a steel rasp. It is important that the top be as square as possible so that the load put upon it during testing is perpendicular.
5. Remove latex membrane and rubber band.
6. Place sample in Shelby tube extractor flush with the butt plate.
7. Turn the Shelby tube extractor on, the lever now allows for movement of the piston forward and backward.

8. Be sure the piston is lined up with mold by moving the piston very close to the sample. If the sample is not properly in line with the piston, the sample may break or the mold can be deformed.
9. Apply pressure to the sample – a loud pop may be heard when the sample breaks free from the mold, but this is normal.
10. As the sample is extracted support it with your free, gloved hand.
11. Once the sample is removed, isolate from air by wrapping it completely in plastic wrap (or foil), secure wrap with rubber bands, and place back into freezer until testing.

Note: If a sample is left in the freezer for a long period of time without being wrapped, sublimation will occur, leaving the sample unsaturated.

C.6 Freezing with Liquid Nitrogen

1. Construct the sample in the cylindrical polystyrene freezing vessel following the procedures above.
2. Obtain approximately 3 L of liquid nitrogen in an appropriate vessel.

Note: Please know and follow the appropriate safety precautions when using liquid nitrogen. There is danger of frost burns and asphyxiation.

3. Carefully pour the liquid nitrogen into the annular space around the mold at the rate no faster than 1 L per minute. Leave about ¼" above the top of the liquid nitrogen to allow excess water to "bleed" out. As always, avoid vibration.
4. Continue to add liquid nitrogen as necessary to keep the level in the freezing vessel near the top of the mold.
5. After 10 minutes from the initial addition of liquid nitrogen, carefully move the entire freezing vessel into a -35° F freezer.

6. After an hour, the sample can be extracted.

C.7 Equipment Overview

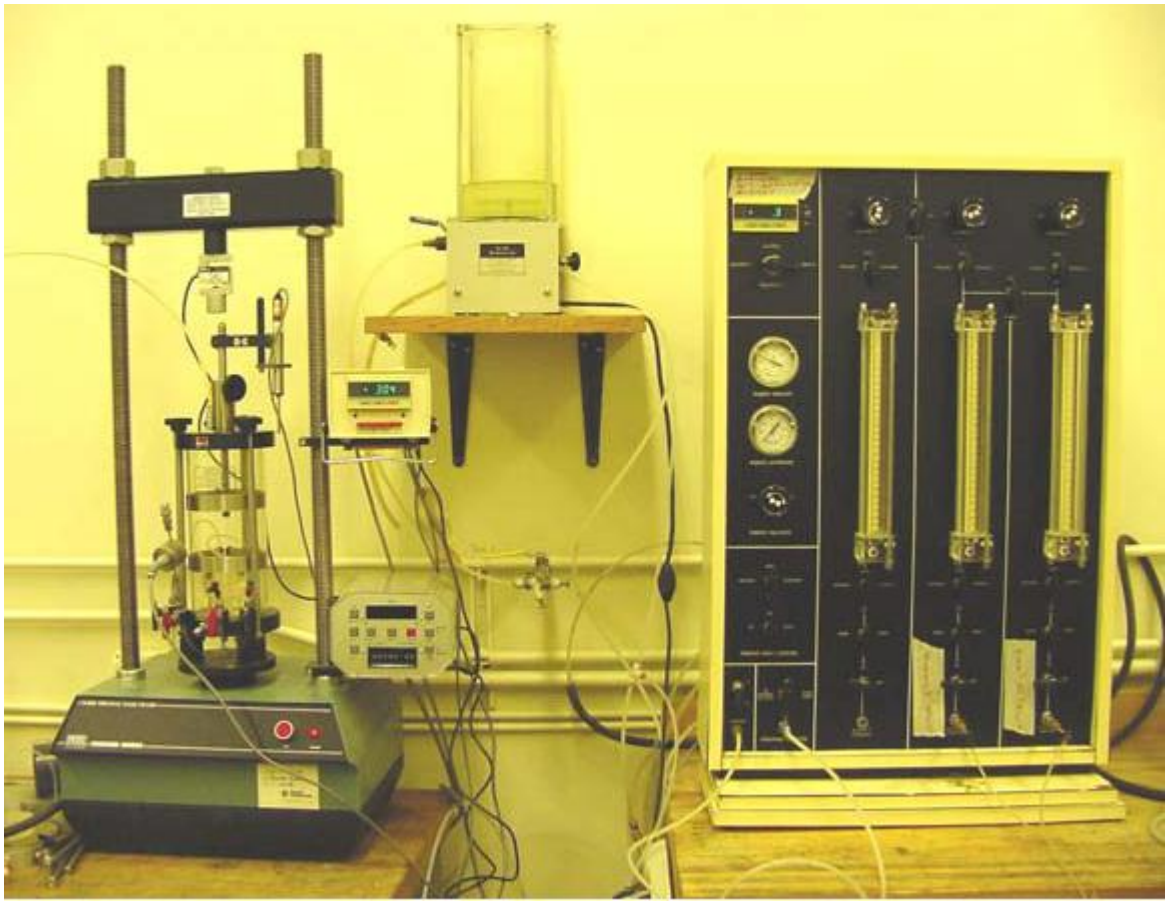

Figure C.2: (left to right): The Triaxial Test Cell and Load Frame, the Nold Deaerator, and the Panel Board that controls both the Triaxial Test Cell and the Nold Deaerator (Shiver 2007).

C.7.1 Triaxial Testing Accessories

Accessories for triaxial testing including membranes and o-rings were obtained from:

Durham Geo

2175 West Park Court

Stone Mountain, Georgia 30087

(800) 837- 0864

Membranes are thin rubber tubes that fit around the sample and seal it from chamber conditions; therefore, it must not have any holes. A new membrane was used for every test. O-rings seal the ends of the membrane tube and connect it to the caps in the triaxial cell. O-rings were re-used for tests.

C.7.2 The Panel Board

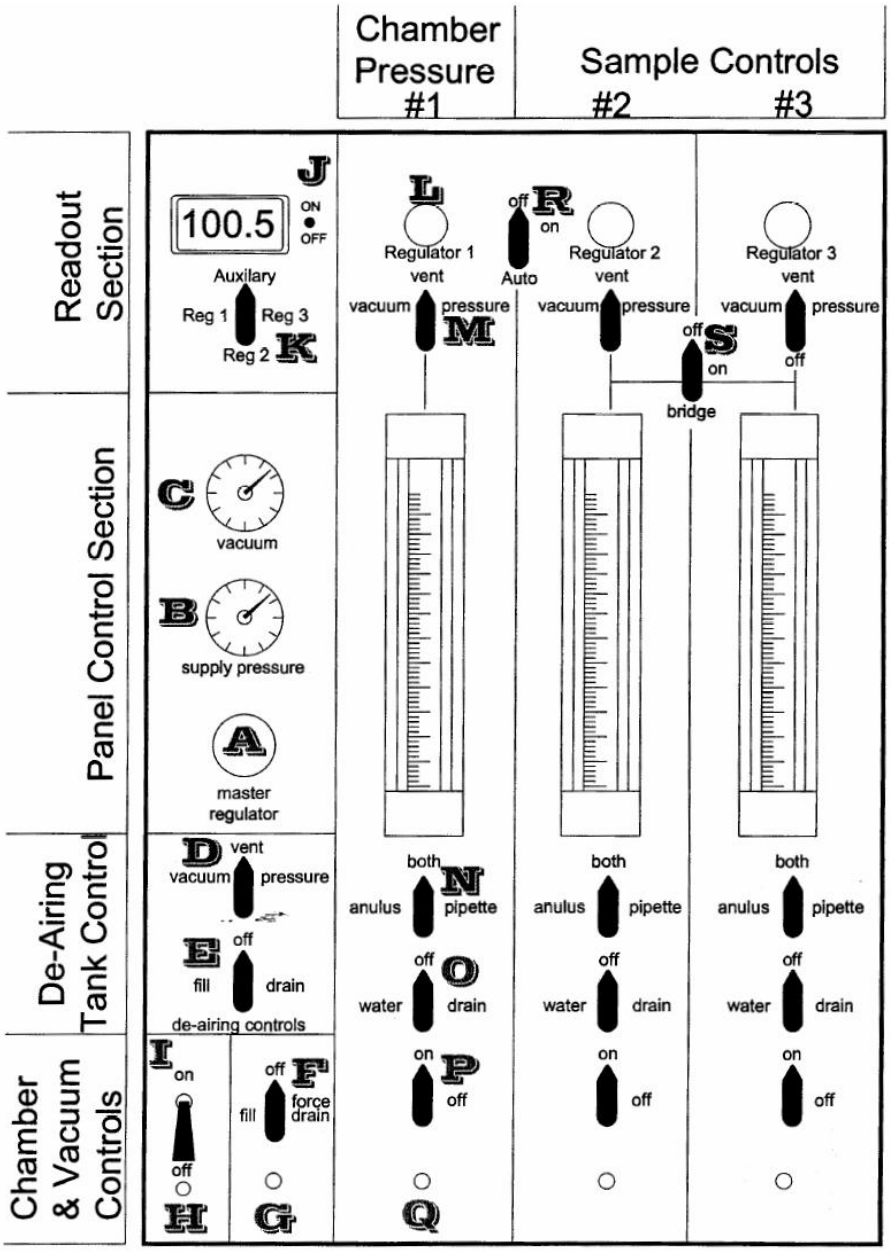

Figure C.3: Schematic of the panel board with annotations of controls. The long tubes are referred to as reservoirs (Shiver 2007).

C.7.2.1 Organization of the Panel Board

The panel board is organized into three separate channels that occupy the right ¾ of the board.

The channels are completely separate from each other, and the controls for each are separated

visually by a long, vertical white line. The channels are numbered 1, 2, and 3 from left to right. Referring to the diagram (fig. 2.10) with the symbols given here in parentheses, each channel has its own pressure regulator (L), pressure/vent selector (M), annulus and pipette, annulus/pipette selector (N), water/drain selector (O), channel on/off valve (P), and quick connect fitting (Q). Channel 1 is used to control the chamber of the test cell that the specimen sits in and supplies chamber pressure. Channel 2 is used to control the influent water from the bottom and supplies back pressure. Channel 3 is used to control the effluent water, which exits from the top of the specimen and also supplies back pressure. The part that each channel controls depends on where the tubes leaving the channels (from Q) are attached on the test cell. It is important to make sure the proper channels on the panel board are connected to the proper ports on the test cell.

C.7.2.2 Panel Board Controls and Their Functions

Master Regulator (A): The master regulator is connected to the house pressure supply and controls the maximum amount of pressure that is available to any channel. For example, if the master regulator reads 90 psi, the maximum amount of pressure you can apply to channel 1 is 90 psi. As with all of the regulators, turning it clockwise increases pressure, turning it counterclockwise decreases pressure.

Supply Pressure Gage (B): The supply pressure gage simply displays the maximum available pressure as regulated by the master regulator.

Digital Pressure Gage On/Off Switch (J): Turns the digital pressure gage readout on and off. Leave it on.

Digital Pressure Gage Channel Selector (K): The digital pressure gage channel selector allows you to choose which regulator pressure to view. For example, when switched to regulator 3, the pressure that the channel 3 L valve is set to will be displayed. To view pressures that regulators on the Auxiliary Panel are set to, switch to "Auxiliary", and then flip the switch above the desired channel regulator to "on".

Pressure/Vent/Vacuum Selector (M): The pressure/vent selector lets you choose between applying the pressure (to the annulus/pipette) that the channel pressure regulator (L valve) is set to, or venting the channel annulus/pipette to atmospheric pressure. The vacuum was not needed during testing.

Annulus/Pipette Selector (N): The annulus/pipette selector lets you choose between letting water flow into or out of the just the annulus (the larger cylinder that contains the pipette), just the pipette (the small cylinder with mL increments labeled on it), or both at the same time.
Note: The term "reservoir" will be used to refer to both annulus/pipette for a channel (fig 2.10) (e.g. reservoir 1, 2, or 3). If just the annulus or pipette is used, then "annulus" or "pipette" will be referred to for a channel (e.g. pipette 1 or annulus 3).

Water/Drain Selector (O): The water/drain selector lets you choose between adding or draining water from the annulus/pipette. "Water" connects the deaired water tank to the annulus/pipette. "Drain" lets water out of the annulus/pipette.

Channel On/Off Valve (P): The channel on/off valve serves as the barrier between the panel board and the tube (connected to the Panel Board at Q) leading to the test cell. When the valve is on, the conditions applied to the channel are connected to the tube leading to the test cell.

Quick Connect Port (Q): The quick connect port connects a particular panel board channel to a test cell port.

Autoload ®: The autoload feature allows the use of one regulator (L2) to control the pressure regulation for both channels 1 and 2, by only adjusting the pressure regulator on channel 2 (L2). When the valve is turned on, any adjustment to the channel 2 pressure regulator (L2) will cause a simultaneous, proportional change to the applied pressure in channel 1. For example, if you have the Autoload on and you increase the pressure regulation in channel 2 by 5 psi (by turning L2), you have also increased the pressure regulation pressure in channel 1 by 5 psi. In a sense, L2 becomes L1 and L2 when the autoload is on. This feature insures that the pressure in channel 1 always remains above the pressure in channel 2.

Bridge (S): The bridge function is similar to the autoload. When the bridge is turned on (and M3 is turned to "off"), L2 and M2 become the controls for channel 3 as well as channel 2, making the pressure conditions in channel 2 and 3 identical. For example, when channel 2 is vented, channel 3 is also vented – when channel 2 is at 50 psi, channel 3 is also at 50 psi.

C.7.3 The Triaxial Test Cell

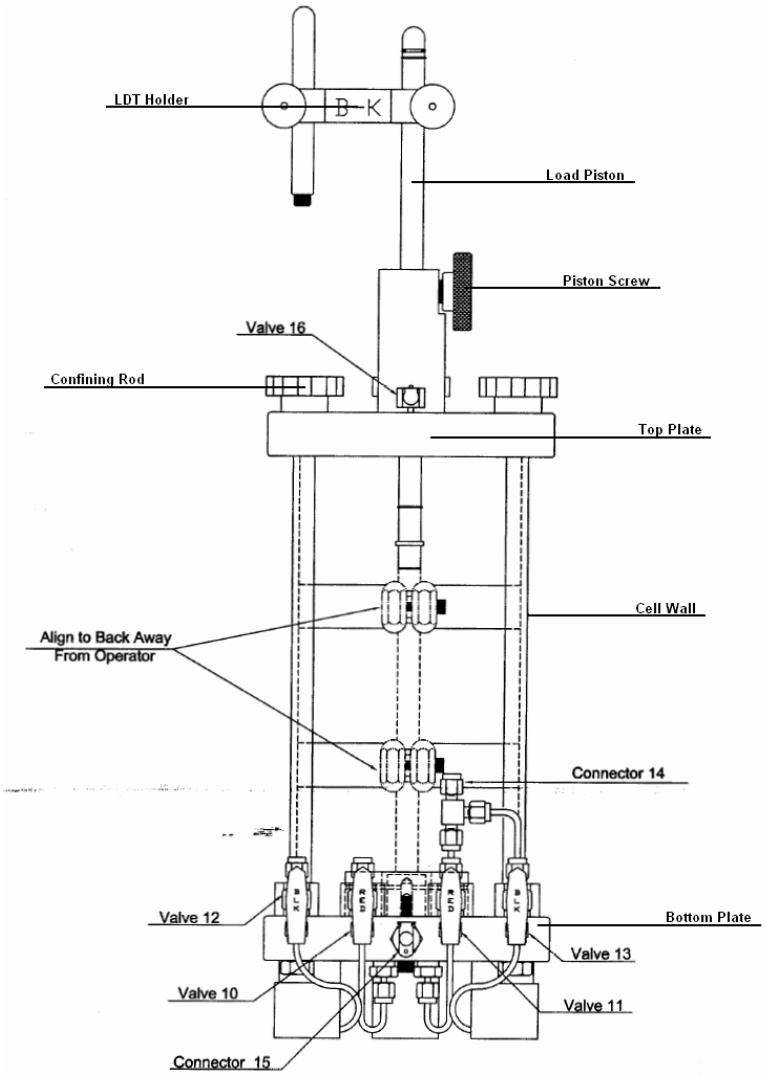

Figure C.4: Schematic of the triaxial test cell with labels of parts and controls (Shiver 2007)

C.7.3.1 Triaxial Test Cell Controls and Their Functions

LVDT Holder: Holds the displacement transducer (LVDT) that measures vertical displacement during testing.

Load Piston: Transfers load to the sample during testing.

Piston Screw: Can be screwed or unscrewed to either inhibit or allow travel of the piston.

Top Plate: Holds the piston and creates the top of the test cell.

Cell Wall: Plexiglass tube that surrounds the sample.

Bottom Plate: Holds the bottom cap and creates the bottom of the test cell.

Connector 14: Connects the pore pressure transducer to the test cell.

Connector 15: Chamber connection. A tube connects between this connection and Q1 on the panel board. Allows for chamber pressure control.

Valve 10: Red valve that connects Q2 on the panel board to the bottom of the sample.

Valve 11: Red valve that connects the bottom of the sample to the pore pressure transducer.

Valve 12: Black valve that connects Q3 on the panel board to the top of the sample.

Valve 13: Black valve that connects the top of the sample to the pore pressure transducer.

Valve 16: Vent for the cell. An open tube is attached to it.

Confining Rod (3): Tighten to hold the test cell together while it is under pressure.

C.8 Consolidated Undrained Triaxial Setup and Post Test Procedure

C.8.1 Preparing the Frozen Sample for the Triaxial Cell

1. Remove the specimen from freezer and unwrap.
2. Weigh the sample and record as “sample wet”.
3. Measure the height and diameter of the sample with calipers (measure the height and diameter each at five different locations on the sample; these values will then be used to calculate an average height and an average diameter for the sample). Record these values as “height” and “diameter”.
4. Attach the latex membrane to the membrane stretcher and apply a vacuum with the house vacuum so that the membrane is pulled flush to stretcher.
5. Place the sample inside the membrane stretcher.
6. Turn the vacuum off and remove the membrane from the stretcher; now the membrane should be wrapped snuggly around the sample.

Note: The membrane will extend beyond the sample ends on the top and bottom. This excess length will be used to attach the membrane to the top and bottom caps of the triaxial cell.

7. Fold the excess length back onto the sample so that the membrane does not extend past the ends.
8. The sample is now ready to be placed in the triaxial cell (the sample can be placed back in the freezer until the lines of the cell are flushed).

C.8.2 Flushing the Triaxial Lines with Deaired Water

1. Be sure there is a full tank of deaired water in the Nold Deaerator. It is recommended that a fresh tank be made before each test and that the tank is filled and deaired while the sample is thawing.
2. Be sure valve D is turned to vent.
3. Refer to figures C.3 and C.4.
4. Connect the pore pressure transducer to the triaxial cell using “connector 14”. This will occupy two of the four valves on the triaxial cell, one from the top cap and one from the bottom cap (Figure C.5), and the average pore pressure from the two will be output (it is recommended the transducer be placed on the opposite side of the cell from the panel board).

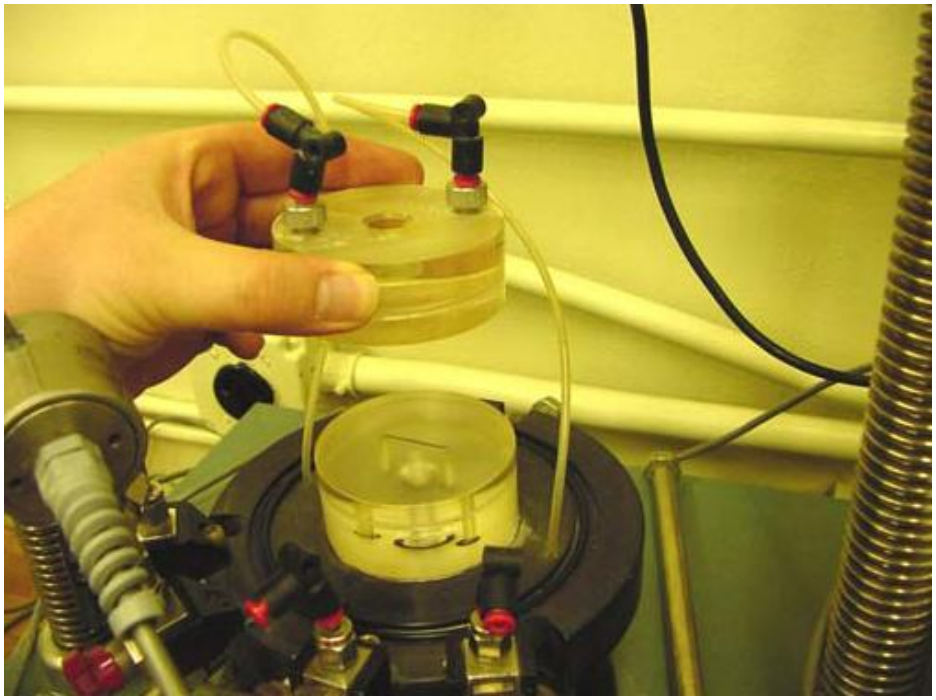

Figure C.5: Top and bottom caps on triaxial cell. Arrow points to the trench between holes on the bottom cap (Shiver 2007)

5. Turn M1, M2, and M3 to “vent” and turn P1, P2, and P3 to “off” on the panel board.
6. Fill panel board reservoirs by turning N1, N2, and N3 to “both” and then O1, O2, and O3 to “water”. When the reservoirs fill, turn O1, O2, and O3 to “off”.

Note: Be careful not to overfill the reservoirs, as this can damage the regulators.

7. Connect tubes from panel board to triaxial cell. G to connector 15, Q2 to valve 10, and Q3 to valve 12.
8. Close valves 10, 11, 12, and 13.
9. Turn Q2 and Q3 to “on”.
10. Remove the deairing valve on the pore pressure transducer and open valves 10 and 11.

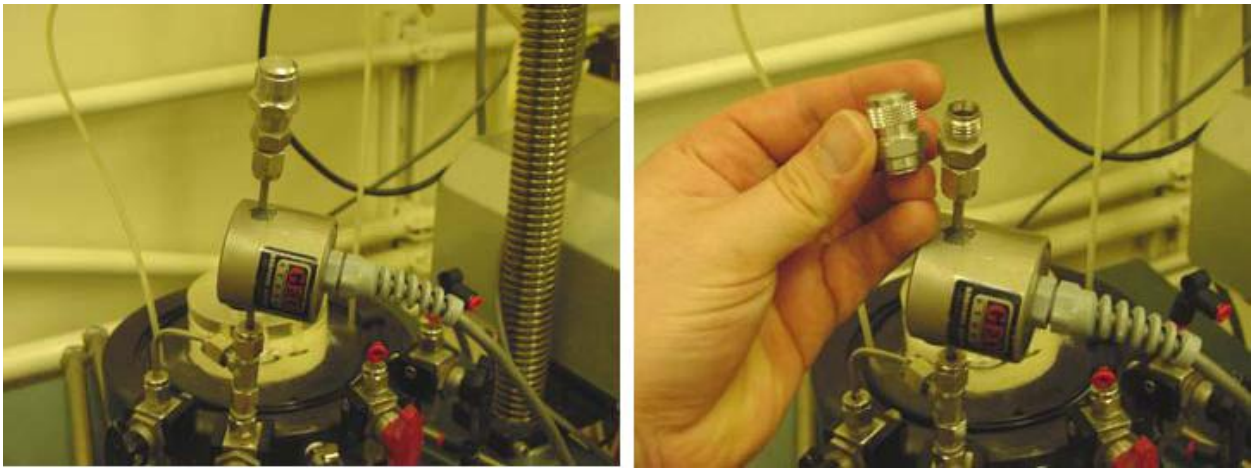

Figure C.6: Deairing valve on pore pressure transducer (Shiver 2007)

11. Water will now flow out of one hole of the bottom cap
12. When no air can be seen coming out of this hole, use a small piece of membrane and cover both holes on the bottom cap and apply pressure with a finger – this will force water through the trench (fig. 2.10) between the holes and out through the pore pressure transducer
13. Once no air is seen exiting the pore pressure transducer, close valves 10 and
14. Use a female-female connector to splice the tubes that lead to the top cap.

15. Open valves 12 and 13; water will now flow through the tube.
15. When no air is seen in the tubes or exiting the pore pressure transducer, close valves 12 and 13.
16. Replace deairing valve on the pore pressure transducer.
17. The lines are now flushed.

C.8.3 Placing the Sample in the Triaxial Cell and Cell Assembly

1. Clean the grooves and o-rings in the top and bottom plates of sand and debris (if it is not clean, a leak will develop when the cell is pressurized).
2. Remove sample from freezer (if needed).
3. Place deaired porous stone on top of the bottom cap.

Note: Porous stones are deaired by placing them into a desiccator filled half way with deaired water. The desiccator is then placed under a vacuum of at least 20 in Hg. The stones are submerged in the deaired water and will be deaired after approximately 20 minutes under the vacuum.

4. Open valve 10 and press down on the stone. Water should seep out of the top of the stone. When it does close the valve to ensure stone saturation.
5. Dip a piece of filter paper in deaired water to saturate it.
6. Slowly lay the piece of filter paper over the stone starting at one edge and moving to the opposite in a “rocking chair” type motion (Figure C.7). Laying the filter paper down all at once will trap air underneath it. Push trapped air bubbles out with fingers.
7. Place the bottom end of the specimen over the filter paper and porous stone. The bottom of the sample is used because it will be smooth and perpendicular.
8. Pull the excess membrane down over the bottom cap.

9. Slide an o-ring down over the sample and into the groove in the bottom cap. Be sure there are no wrinkles underneath the o-ring and that it is secure in the cap groove.

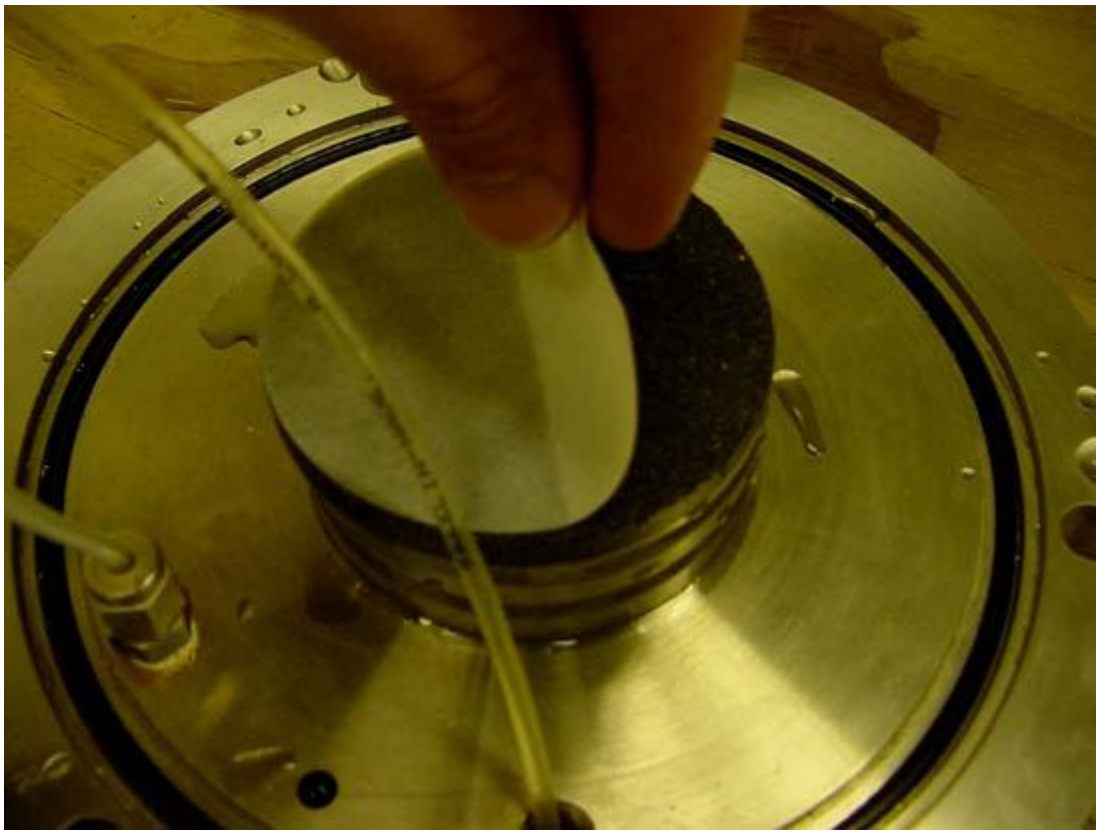

Figure C.7: Placing the filter paper on the porous stone in "rocking chair" motion (Shiver 2007)

10. Using a syringe (without the needle), from the hypodermic needle used before, squirt deaired water on top of the specimen (only enough to wet the top). This will allow for the filter paper to go on without producing trapped air bubbles.
11. Dip a piece of filter paper in deaired water to saturate it.
12. Slowly lay the piece of filter paper over the top of the sample starting at one edge and moving to the opposite in a "rocking chair" motion (Figure C.7). Laying the filter paper down all at once will trap air underneath it.

13. Place a deaired porous stone on top of the filter paper, and squirt more water on top of the stone.
14. Place the top cap on top of the porous stone.
15. Pull excess membrane up over the top cap.
16. Place an o-ring in the groove of the top cap making sure there are no wrinkles underneath the o-ring and that it is secure in the groove
17. Pull the top cap tubes out of female-female connector and connect them to the top cap.
18. Flush the trench between the top cap holes by removing the deairing valve on the pore pressure transducer and opening valves 12 and 13. This will allow water to flow from the top reservoir through the trench and out the pore pressure transducer.
19. When no air is exiting the pore pressure transducer, close the valves and replace the deairing cap on the pore pressure transducer.
20. Place the plexiglass cell wall over the sample and into the groove surrounding the sample on the base plate (be sure the o-ring is in the groove).
21. Loosen the piston screw on the top plate (i.e. the piston moves freely) if needed.
22. Place the bottom end of the piston in the cutout on the top cap making sure it is all the way in.
23. Slide the top plate down the piston on top of the cell wall in the corresponding grooves (be sure the o-ring is in the groove).
24. When the top cap is in place, tighten the piston screw (i.e. the piston does not move freely).
25. Attach the three steel confining rods in the grooves around the cell and tighten by hand until they cannot be tightened anymore.

26. Place the LVDT in its support attached to the piston. The LVDT will rest on top of the top plate. Displace the LVDT as little as possible, so the full travel of the LDT can be used.
27. Lower load cell on to the top of the piston using the bolts that control the height of the horizontal bar to which the load cell is attached to.
28. When the load cell is just touching the piston (i.e. one or two pounds is read on the load cell readout) tighten the bolts so that the horizontal bar cannot move.
29. Vent the cell by connecting an open tube to valve 16.
30. Turn F to "fill", and the cell should begin filling with water.
31. When the cell is filled, turn F to "off", and remove the vent tube.
32. Be sure all reservoirs are filled. If filling is required turn the corresponding N valve to "both" and O valve to fill.
33. Disconnect the tube from G.
34. Connect this tube to Q1.
35. Be sure valves 10 and 12 are closed.
36. Turn K to "regulator 2".
37. Turn L2 counter-clockwise until the digital readout reads zero (the digital readout may need to be cleared).
38. Turn K to "regulator 1".
39. Turn L1 clockwise until pressure reads a pressure equal to the desired effective confining stress (σ_3') for the test
40. Turn "autoload" switch to "on".

Note: "autoload" operation is explained in Brainard-Kilman (Durham-Geo)

S-500 Triaxial/Permeability Panel Board owner's manual.

41. If the pressure reading changes, make adjustments using L1

42. Turn K to "regulator 2". It should still be reading zero.

43. Turn L2 clockwise until pressure reads 40 psi.

44. Turn K to "regulator 2". It should be reading 40 psi + σ_3'. If it does not, make adjustments by turning L1.

45. Make sure both channels are reading the desired pressures.

46. Turn M1 and M2 to "pressure".

47. Turn P1 and P3 to "on".

48. Open valves 12 and 10.

49. The sample is now under pressure – let the sample thaw for at least three hours.

50. Triaxial setup is now complete (Figure C.8).

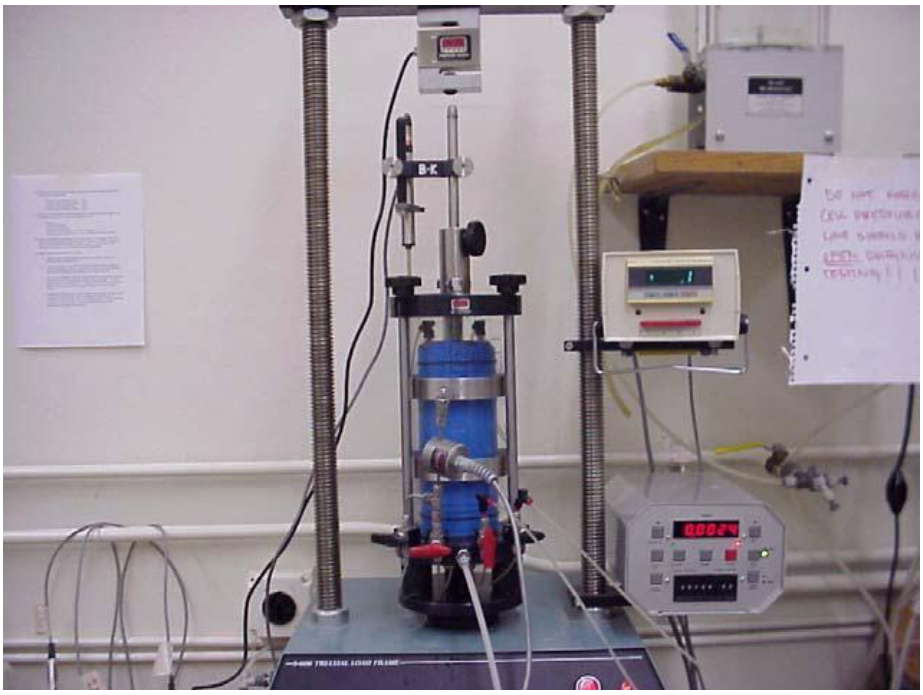

Figure C.8: Assembled triaxial test cell with sample (Shiver 2007)

C.8.4 Post Test Procedure

1. Fill a squirt bottle with tap water.
2. Obtain a pan for use in oven drying, the bigger the better, as long as it will fit in the oven.
3. Weigh the pan, and record as “pan weight”.
4. Turn P1, P2 and P3 to “off”.
5. Turn M1, M2, and M3 to “vent”. A hissing sound should be heard as the pressure is released.
6. Drain reservoir 3.
7. Turn P3 to “on”.
8. Open valve 12.
9. Water from inside the sample will flow into reservoir 3 as pressure is released.
10. Disconnect the tube running between Q1 and connector 15.
11. Connect one end of this tube to G and the other to valve 16.
12. Connect a drain tube to connector 15. The drain tube is any long tube with one end open and the other end with a male quick connect fitting. Place the open end in the drainage bucket to the right and below the triaxial load frame before connecting the other end to connector 15.
13. Water from the cell should now be flowing into the drainage bucket.
14. Turn F to “force drain”. This will pressurize the cell and force water out the drain tube. Hold on to the drain tube as it may be forced out of the bucket and squirt water.
15. When the cell is empty, turn F to “off”, and remove tube from valve 16.
16. Tighten the Piston Screw.
17. Raise the horizontal bar that the load cell is on approximately 6” above the load piston.

18. Loosen and remove the Confining Rods.
19. Remove the top plate; set it aside. The piston will still be in the top cap and may need to be maneuvered to get it out.
20. Remove tubes from valves 10 and 12 and connector 15.
21. Remove pore pressure transducer from connector 14 and set aside.
22. Remove the base plate (with the sample and cell wall still resting on it), and set it on the table next to the load frame.
23. Remove cell wall; set it aside. The sample should still be standing on its own.
24. Remove the tubes going to the top cap.

Note: From this point on do not lose any sand from the sample. All sand should go into the pan.

25. Remove the top o-ring and top cap. Rinse the bottom of the top cap off with the squirt bottle into the pan and set aside.
26. With fingers, get the porous stone and filter paper from the top of the sample. Rinse them off into the pan; set aside.
27. Slowly turn the base plate on its side so that the sample is now laying flat in the pan.
28. Slowly remove the base plate and bottom cap from the sample. Rinse them into the pan; set aside.
29. Rinse and remove o-ring from the pan.
30. Remove and rinse porous stone and filter paper from the bottom cap into the pan; set aside.
31. Very carefully squeeze the sample sand out of the membrane into the pan.
32. Rinse the membrane into the pan; discard.

33. Rinse hands into the pan.
34. Place the pan into a 200° F oven for at least 24 hours.
35. Once the sample is dry, weight the pan and sample together and record as "pan + sample".
36. Subtract "pan weight" from "pan + sample" and record as "sample dry"
37. Calculate the unit weight of the sample by dividing "sample dry" by the volume of the sample using the average height and diameter of the sample.
38. Testing for sample is complete.

Appendix D: Detailed Consolidation Sample Construction and Setup Procedure

Basic procedures originally developed by Mikkel Watts

D.1 Preparing the Sand / Hydrogel Mixture

1. Place 300 grams of Ottawa sand into one 1000 mL beaker.

Note: 300 grams of sand is enough to over-fill the brass consolidation ring used as the mold.

2. Calculate the desired amount of hydrogel per beaker: (% hydrogel / 100) x (300 g of sand).
3. Place the hydrogel into the beaker.
4. Tilt the beaker approximately 45° and rotate until you can no longer see hydrogel powder (about five rotations).
5. Combine the contents of the four beakers into one beaker and rotate (as in step 4) 3-4 times.

Note: It is important to not over-mix the samples, or segregation will occur. Rotate only until hydrogel powder is no longer visible.

D.2 Preparing the Brass Ring Mold

1. Grasp the brass ring in one hand and open a latex glove with your free hand as shown in Figure D.1.

2. Wrap the base of the brass ring with one layer of the glove. There will be extra glove on the side of the brass ring.
3. Tighten around the sides of the glove until the base of the brass ring is relatively smooth, as shown in Figure D.2.
4. Leave a little give in the glove for the porous stone that will be inserted between the glove and the brass ring.
5. Insert a porous stone into the bottom of the ring; be sure not to rip the glove when sliding the stone into the ring under the glove.
6. Prepare the confining frame.

Figure D.1: Glove and brass ring

Figure D.2: Glove on the brass ring

D.3 Preparing the Confining Frame

1. Place the prepared ring mold in the confining frame on a square piece of foam.

Note: The purpose of the foam is to keep the rubber glove from being in direct contact with the metal plate and breaking.

2. Place the top plate on top.
3. Adjust horizontal bar so that the thumb-screw will secure the top plate when tightened.
4. Swing the bar out and remove the top plate to allow soil placement (Figure D.3).
5. Place the mold in a -35° F freezer.

Figure D.3: Brass ring mold in confining frame, ready for the sand/hydrogel mixture to be added

D.4 Preparing the Confining Frame

1. Pour the sand / hydrogel mixture, prepared earlier, through a funnel and into the brass ring.
2. Keep the end of the funnel a quarter of an inch above the sand level in the mold while pouring.
3. Move around the brass ring while pouring, keeping the top level of the sand relatively flat (Figure 5).
4. Stop pouring the sand mixture into the mold when the mold starts to overflow.
5. Use a straight edge to strike the top of the mold flush.
6. Saturate the sample according to the procedures of D.5.
7. Carefully place the top plate on the brass ring.
8. Be sure to line the holes, on the top plate, up with the opening on the brass ring.

9. Tighten the thumbscrew, again being careful not to cause vibration.
10. Allow the sample to freeze at -35° for at least three hours.

Figure D.4: Placing the sand in the mold using a funnel

D.5 Saturating the Sample

1. Fill a syringe with 60 mL of tap water.
2. Inject the syringe through a hole in the top plate to the base of the mold while slightly pressing on the syringe's plunger.

Note: If pressure is not applied while the syringe is being injected, sand will clog the needle.

3. With the syringe fully inserted to the base of the mold, begin to withdrawal the syringe while injecting water no faster than 1 mL per second.

Note: If the syringe is withdrawn to fast the sample will have dry spot when finished. If the rate of injection is to fast the sample will have water voids from sand displacement.

4. Repeat steps 2 and 3 at 6 or more locations across the sample.
5. When water is observed coming out of all the holes on the top plate the sample should be saturated.

Note: The needle may become clogged from time to time. Clear the clog by taking the needle out of the sample and off the syringe. Then use a solid needle that fits inside the needle to push out the clog.

D.6 Extracting the Sample

1. Take the mold system out of the freezer and allow it to thaw slightly at room temperature for 5-7 minutes.
2. Remove the swing arm from the top of the mold.
3. Lift the sample off of the bottom plate.
4. With a hammer or wrench, gently tap on the top plate to remove it.
5. With the top plate removed, the sample is ready for a warm water bath to loosen the sample from the brass mold.
6. The water bath will make it possible to extract the sample without breaking it.
7. Place warm water half an inch high in a pan and add the mold to the pan of water glove side down, as shown in Figure D.5.
8. Make sure that the water does not rise above the brass ring and make contact with the frozen sample.

Figure D.5: Sample and mold in warm water bath

Note: The water should not be able to reach the frozen sample from below because the rubber glove creates a seal between the water and the sample.

9. Let the brass ring and frozen sample system sit in the water bath for roughly 3 minutes.

Note: The edge of the frozen sample will began to look glossy when the sample is ready to be extruded.

10. When the sample looks ready to be extracted remove it from the water bath and apply pressure to the stone by hand until the sample begins to slide out.
11. Eject the sample onto a piece of aluminum foil or plastic wrap (Figure D.6).
12. Quickly and carefully move the sample to a -35° F freezer to refreeze the edges.
13. Allow the sample to refreeze in the deep freezer for 10 minutes.

Figure D.6: Extracted sample

14. Once the sample is removed, isolate it from air by wrapping it completely in plastic wrap (or foil), secure wrap with rubber bands, and place back into freezer until testing.

D.7 Consolidation Test Setup

1. Place a porous wet stone into the base of the brass mold.
2. Cut a piece of filter paper to the diameter of the porous stone.
3. Wet the filter paper and place it on the top of the porous stone.
4. Place the brass ring over the brass base mold.
5. Place the frozen sample in the brass ring.

Note: The sample will probably not fit into the ring at first. Allow the sample to rest over the opening for 1 minute. Try rotating the sample clockwise until it begins to slide in the ring. Don't force the sample into the ring. If the sample does not slide in tightly allow it to thaw another minute and try twisting it into place again. Repeat this process until the sample finally fits into place.

6. Place the entire brass base, brass ring, and sample system (consolidometer) onto the consolidation frame.

7. Place the top part of the consolidometer over the consolidometer base, and secure it with the six machine screws.
8. Place a saturated piece of filter paper onto the sample in the brass ring.
9. Place a porous stone on top of the filter paper and sample in the consolidometer.
10. Install the piston, held in place using four small springs.
11. Adjusting the counterweight so that the loading arm is balanced and not putting any load on the sample.
12. Adjust the loading arm to be level using the spirit level on arm
13. Attach the displacement transducer (LVDT) to the top of the consolidometer using the cross bar and vertical threaded rods.
14. Allow the sample to thaw in the consolidation machine for at least 3 hours before running a testing.

Figure D.7 shows an example of a properly constructed consolidometer in the consolidation frame for reference.

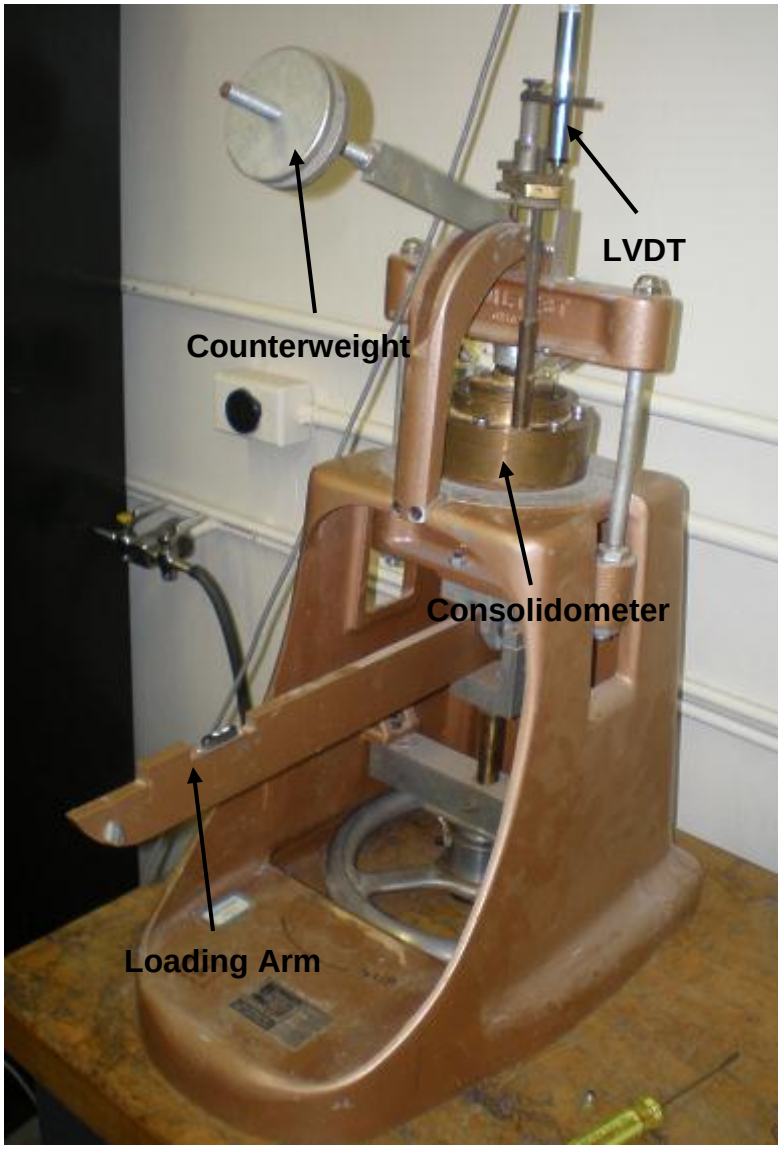

Figure D.7: Assembled consolidometer in the consolidation frame with parts labeled

Appendix E: Individual Triaxial Data Plots

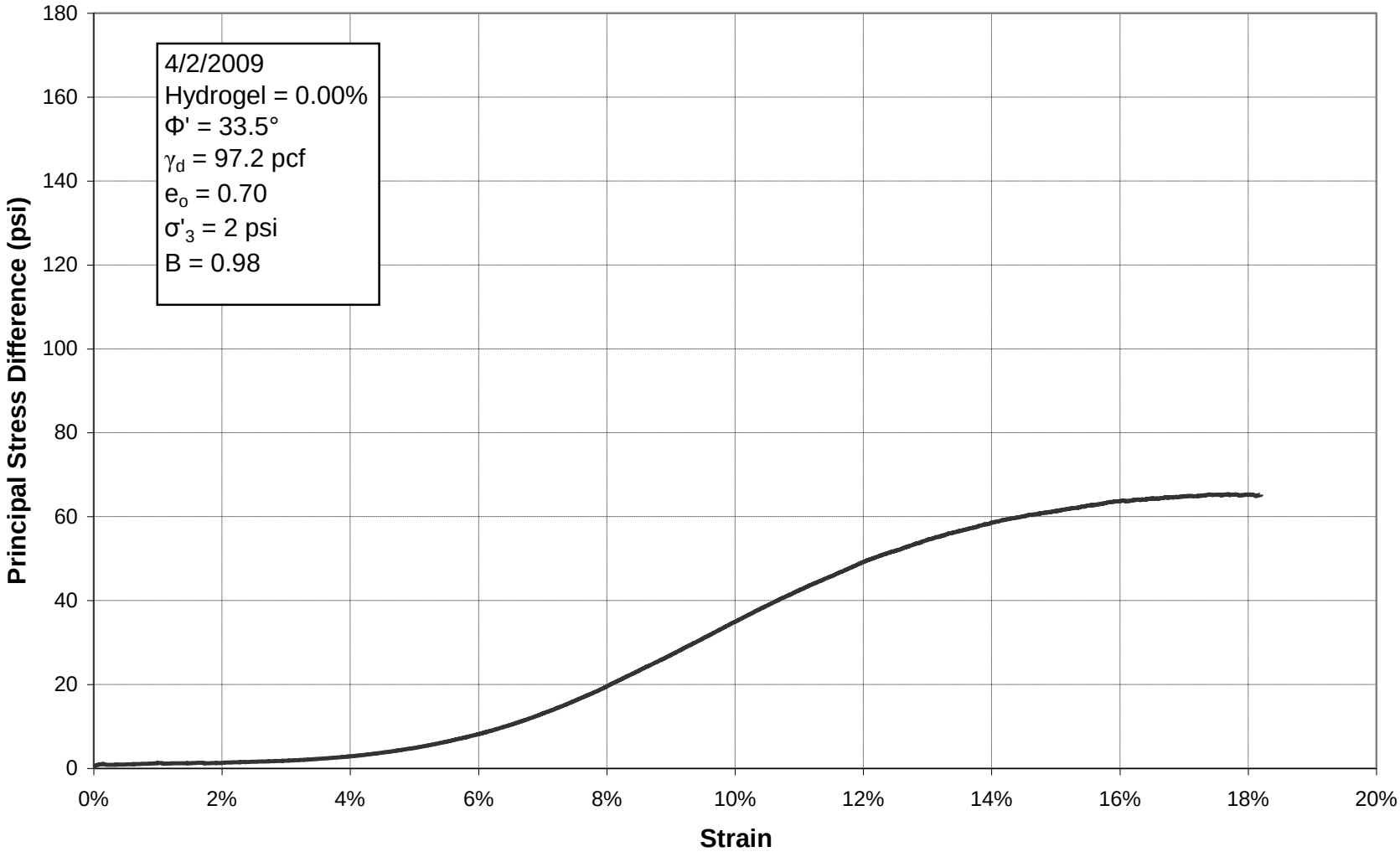

Figure E.1: Principal Stress Difference vs. Strain for Triaxial Test 6, 0.00% Hydrogel

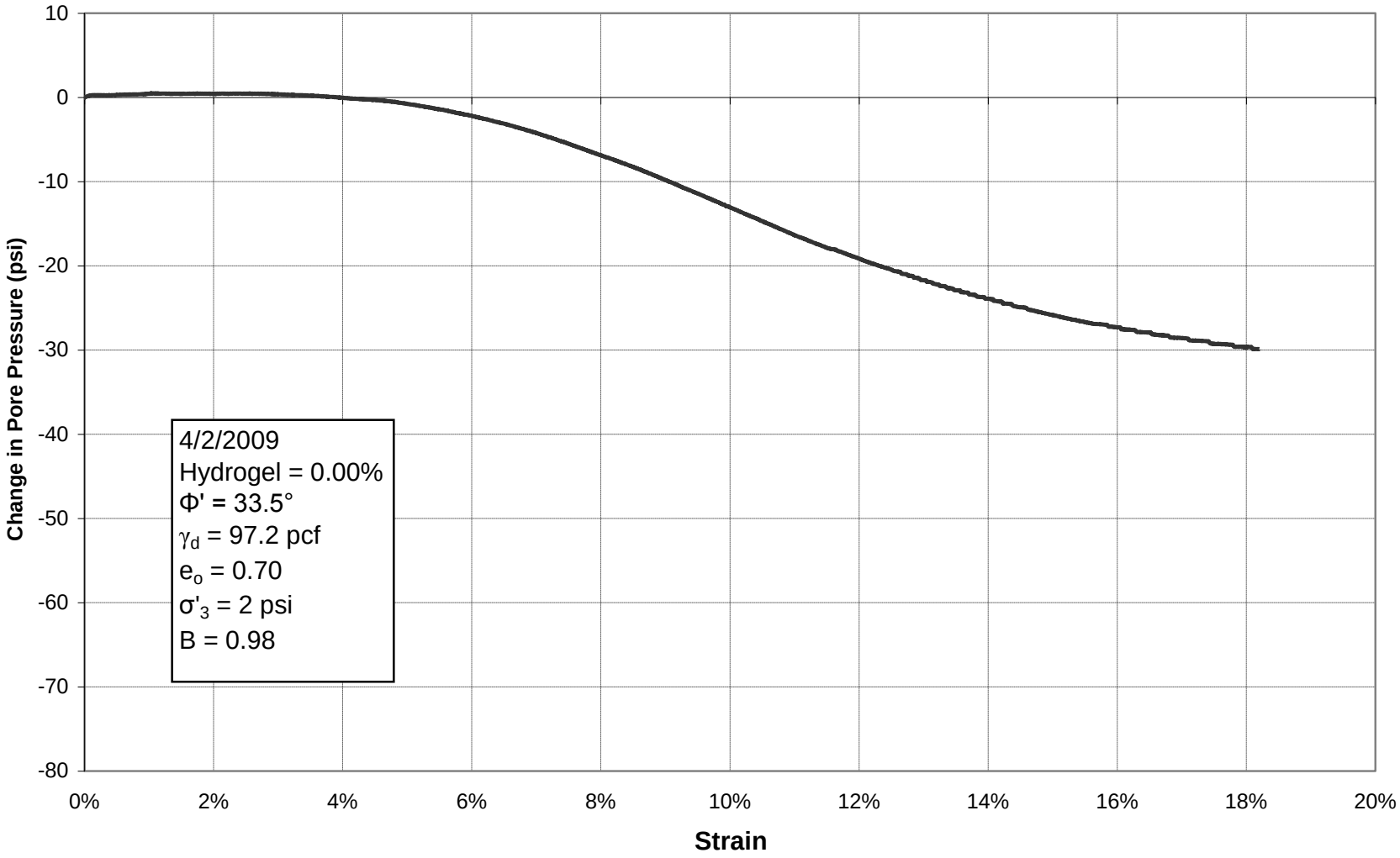

Figure E.2: Change in Pore Pressure vs. Strain for Triaxial Test 6, 0.00% Hydrogel

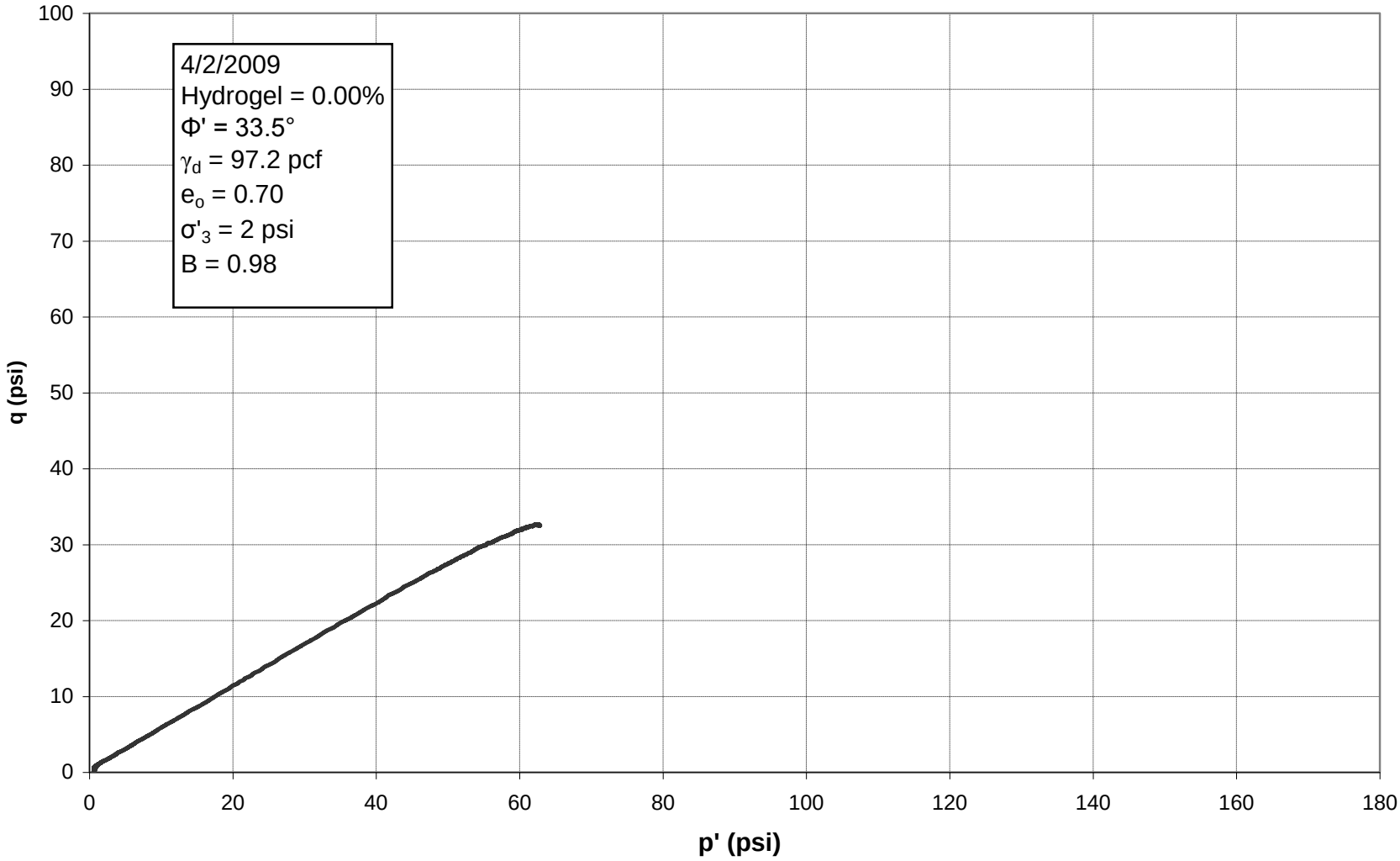

Figure E.3: p'-q Diagram for Triaxial Test 6, 0.00% Hydrogel

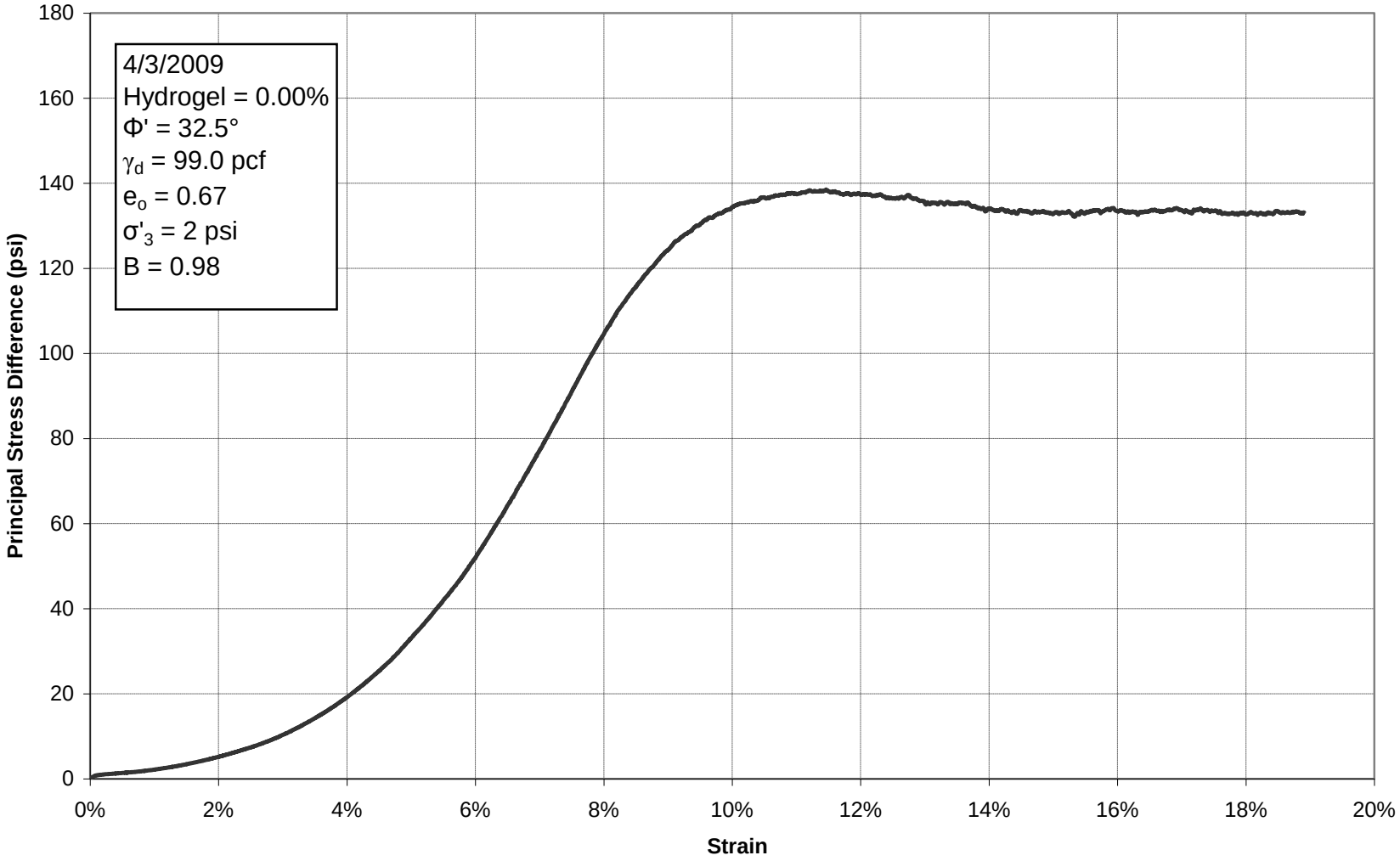

E.4: Principal Stress Difference vs. Strain for Triaxial Test 7, 0.00% Hydrogel

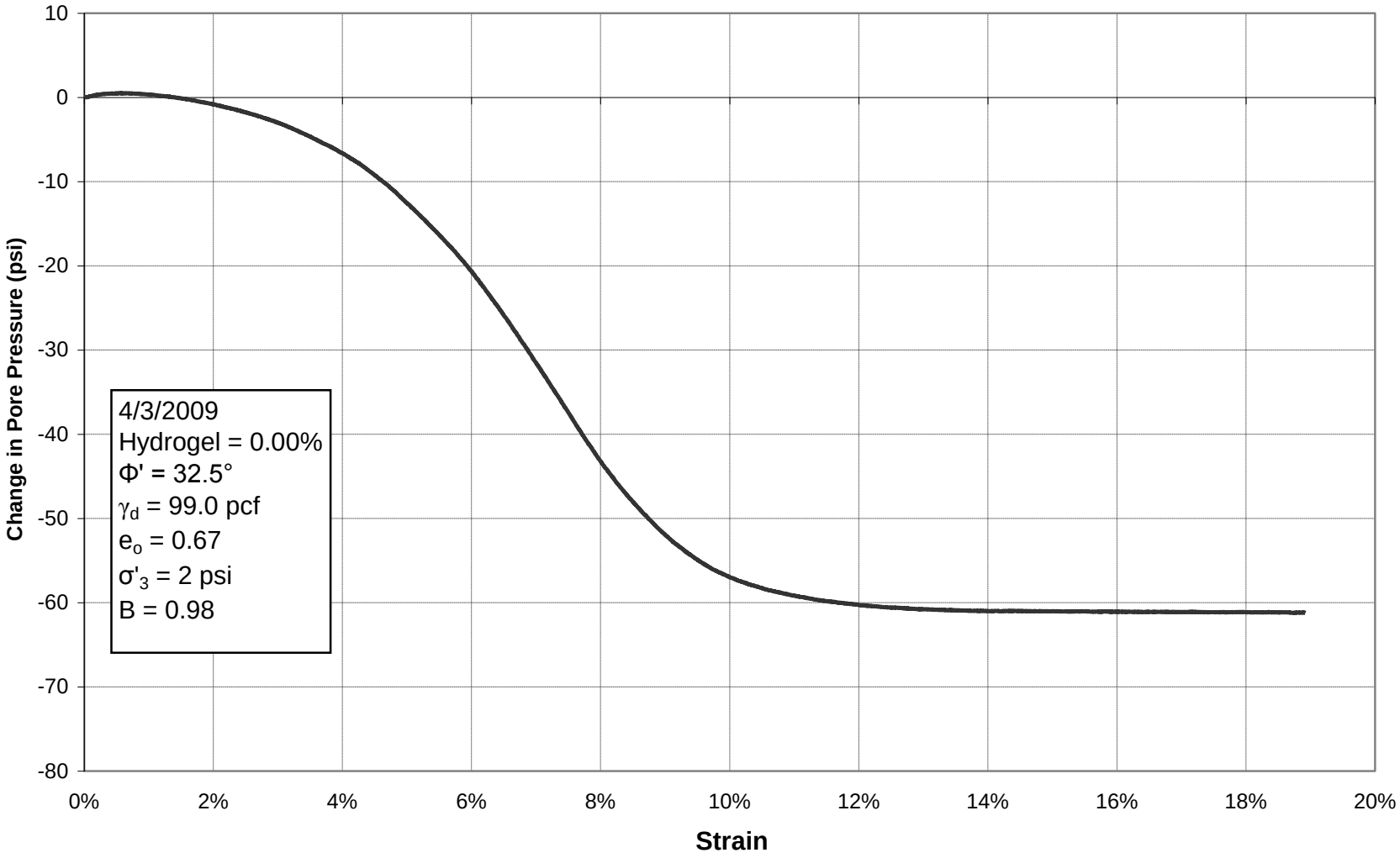

Figure E.4: Change in Pore Pressure vs. Strain for Triaxial Test 7, 0.00% Hydrogel

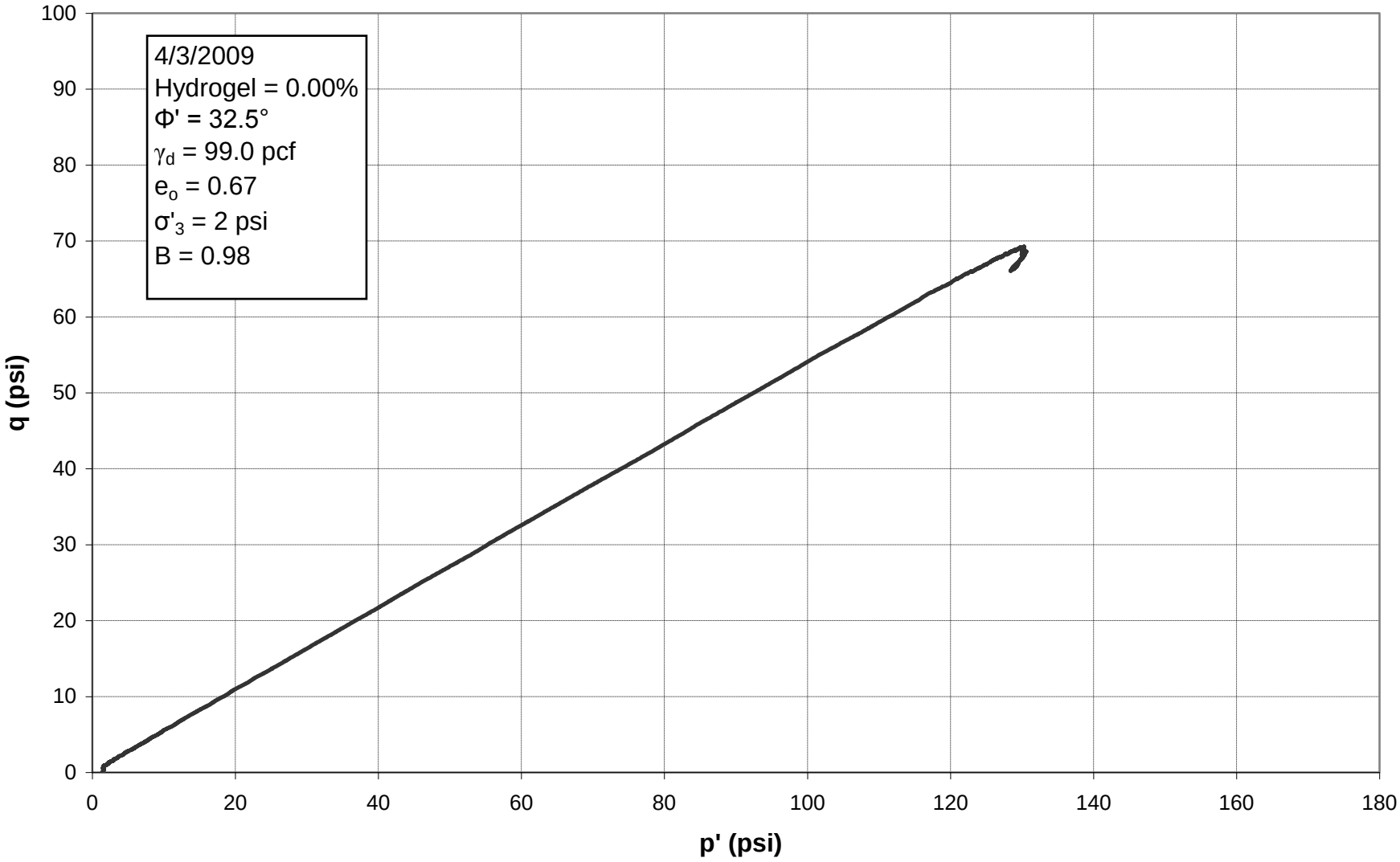

Figure E.5: p'-q Diagram for Triaxial Test 7, 0.00% Hydrogel

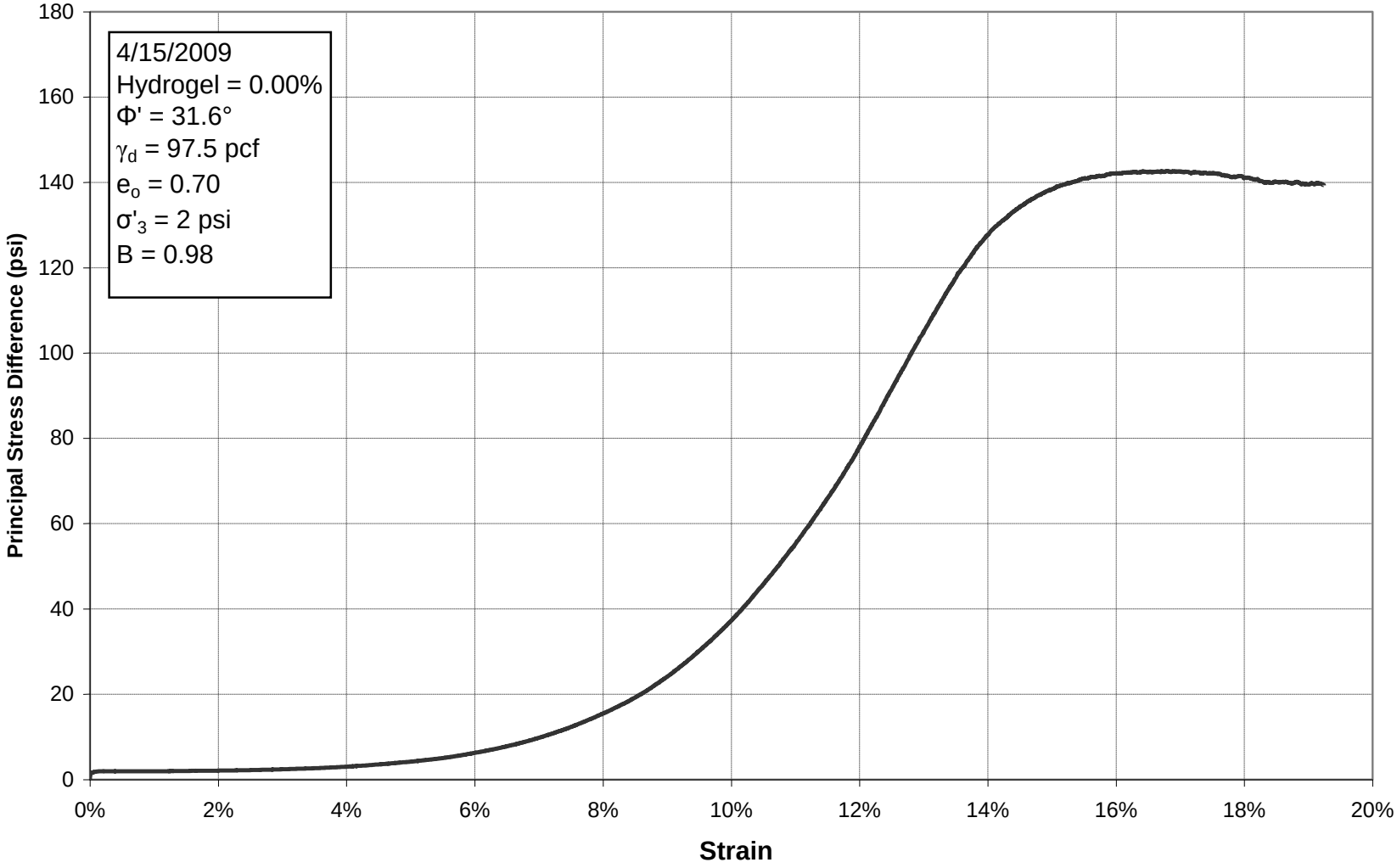

Figure E.6: Principal Stress Difference vs. Strain for Triaxial Test 9, 0.00% Hydrogel

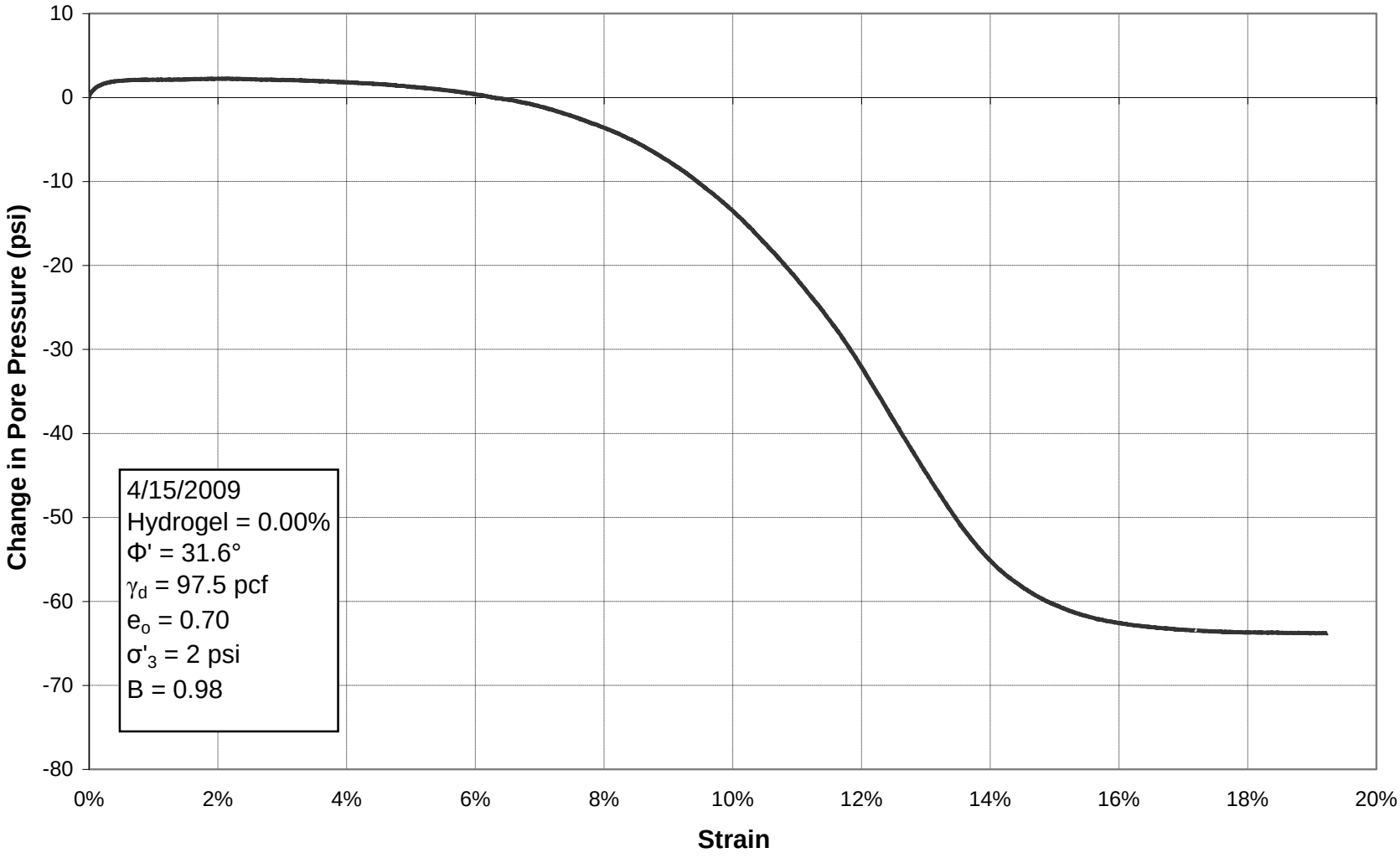

Figure E.7: Change in Pore Pressure vs. Strain for Triaxial Test 9, 0.00% Hydrogel

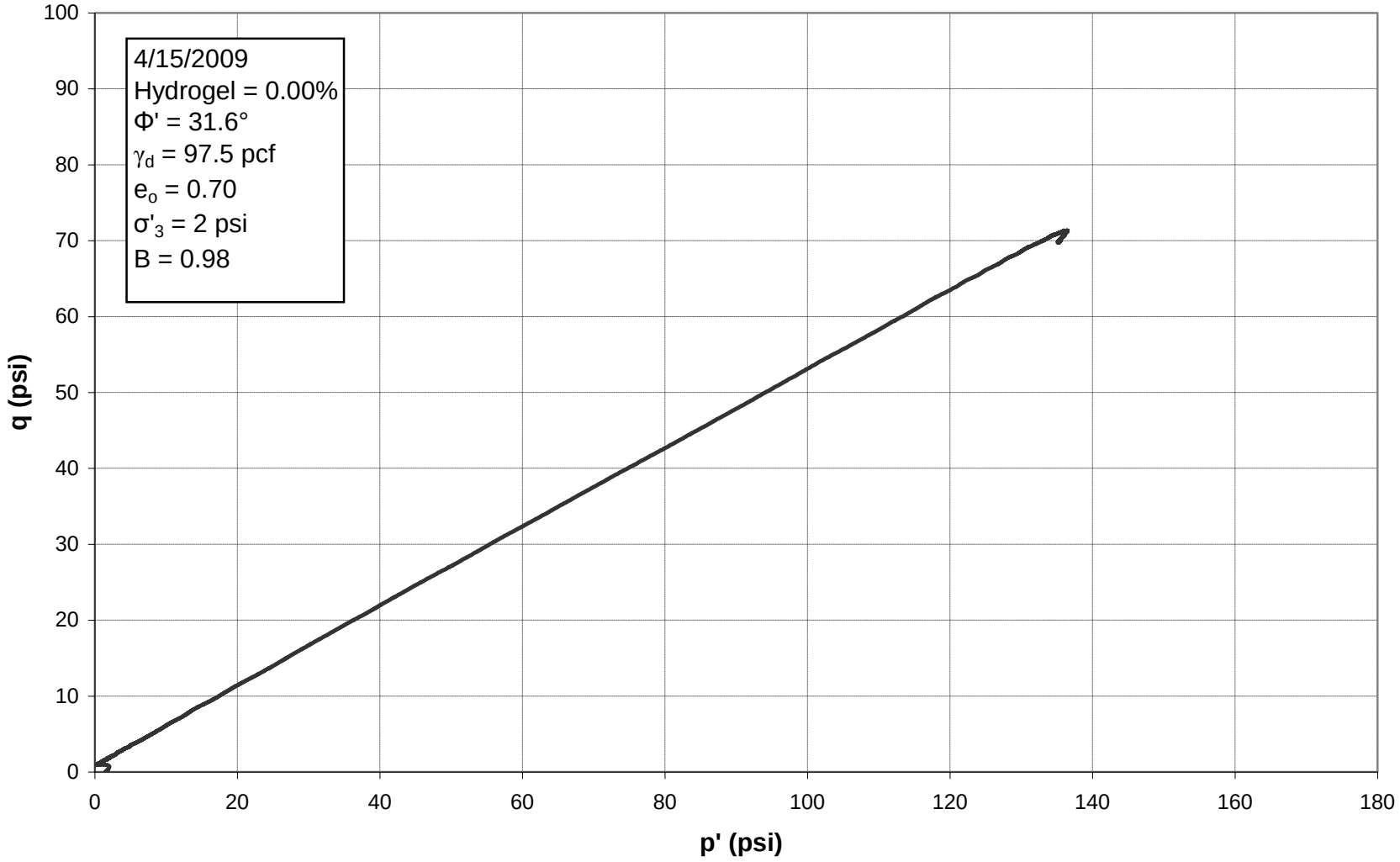

Figure E.8: p'-q Diagram for Triaxial Test 9, 0.00% Hydrogel

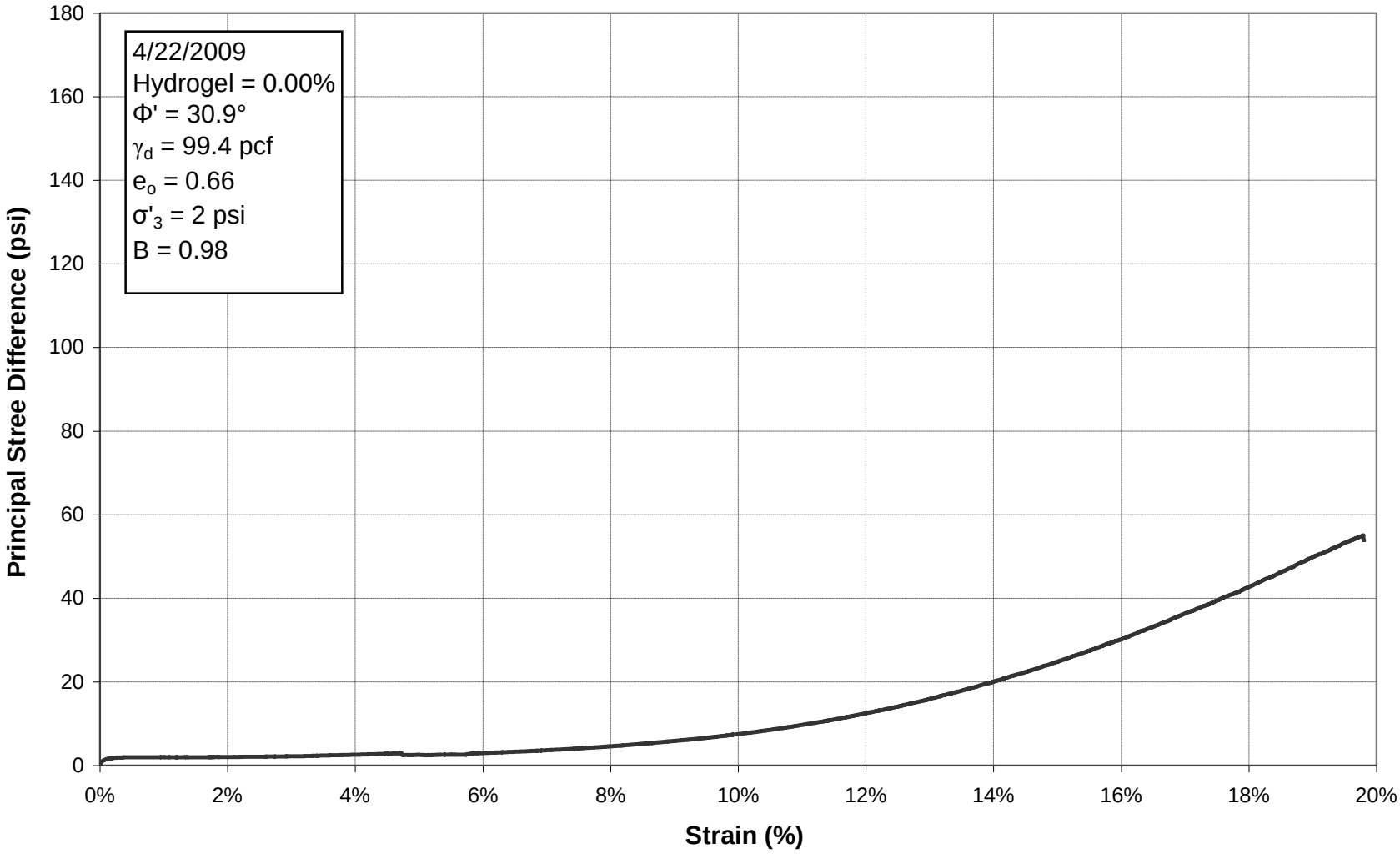

Figure E.9: Principal Stress Difference vs. Strain for Triaxial Test 10, 0.00% Hydrogel

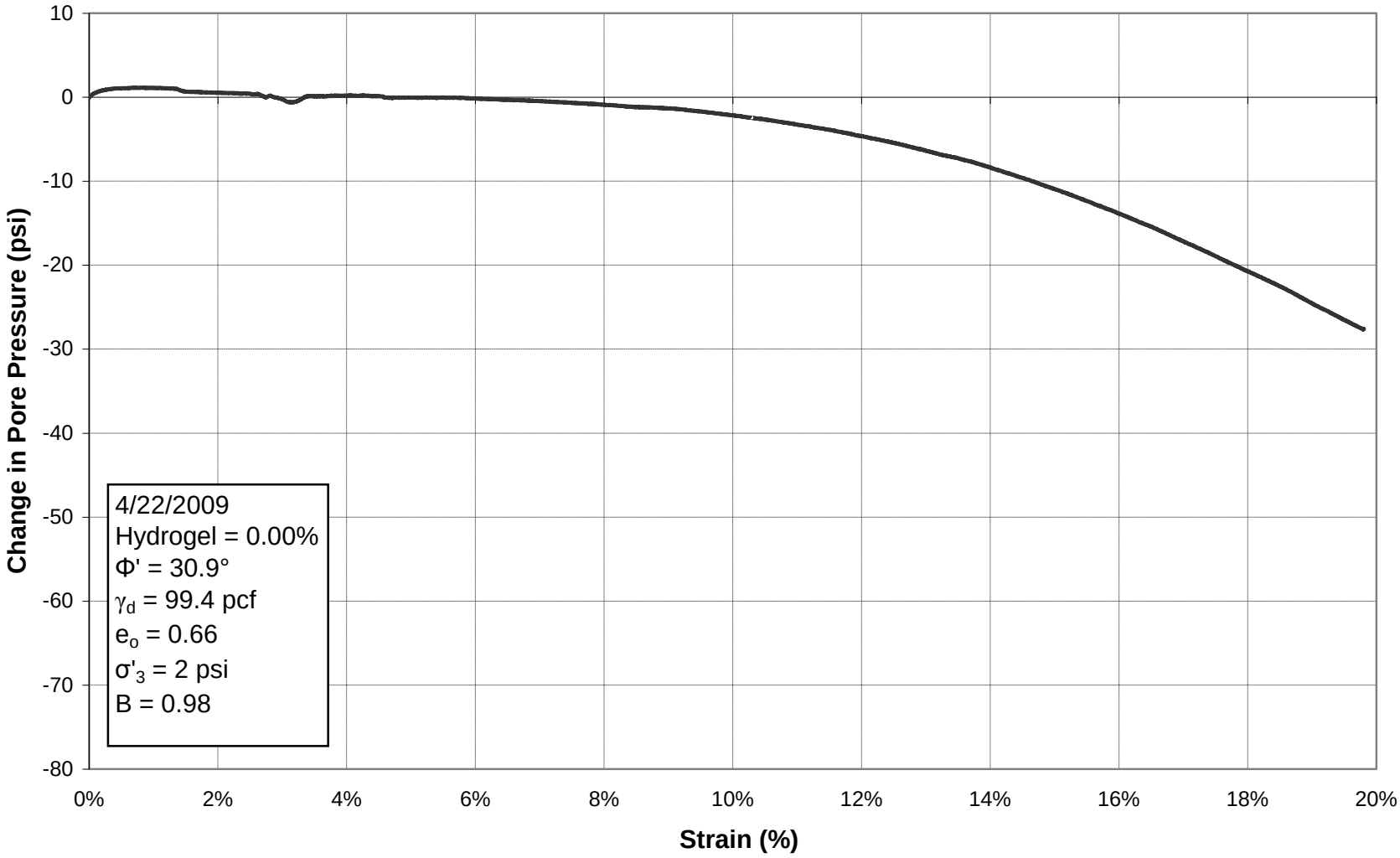

Figure E.10: Change in Pore Pressure vs. Strain for Triaxial Test 10, 0.00% Hydrogel

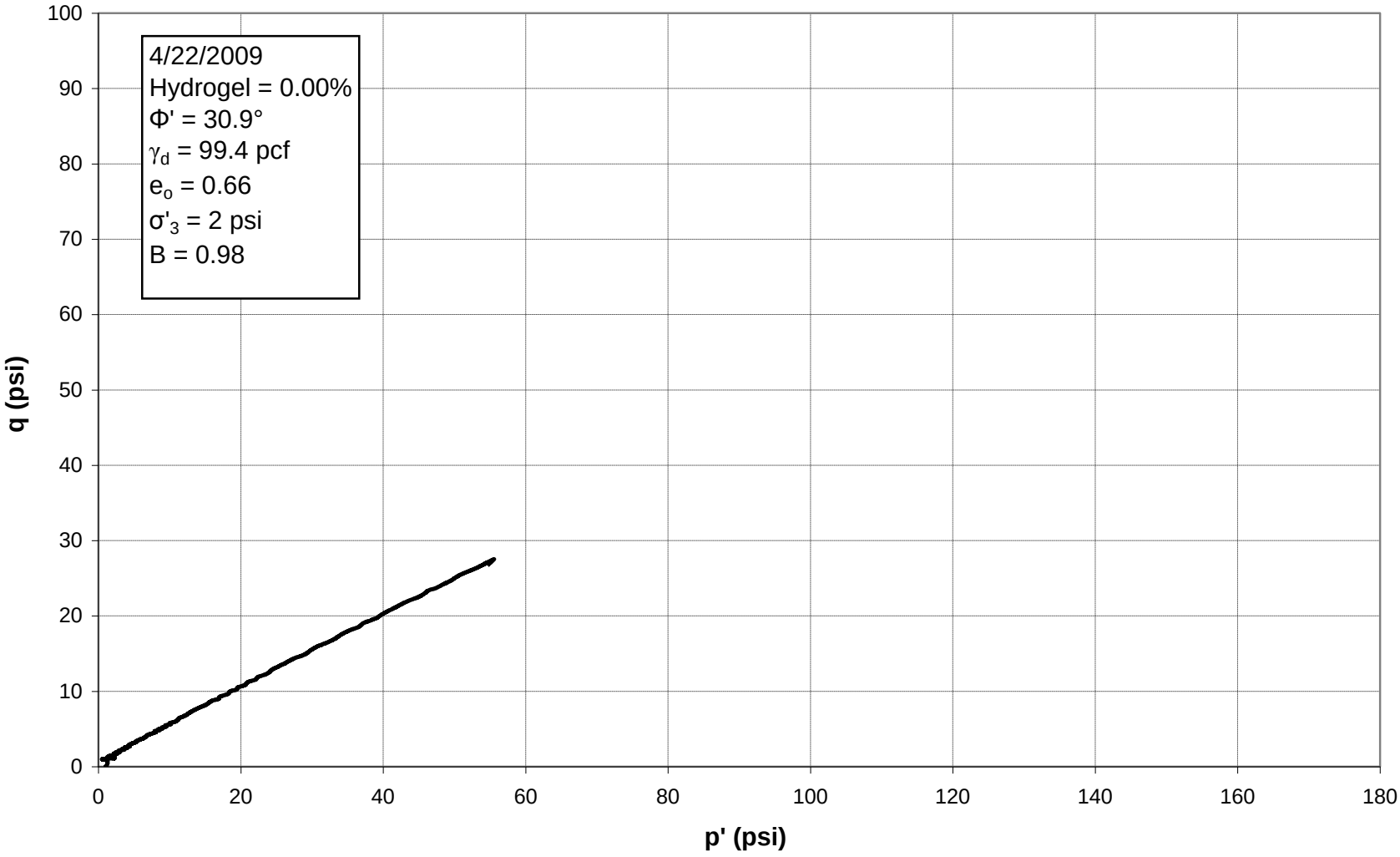

Figure E.11: p'-q Diagram for Triaxial Test 10, 0.00% Hydrogel

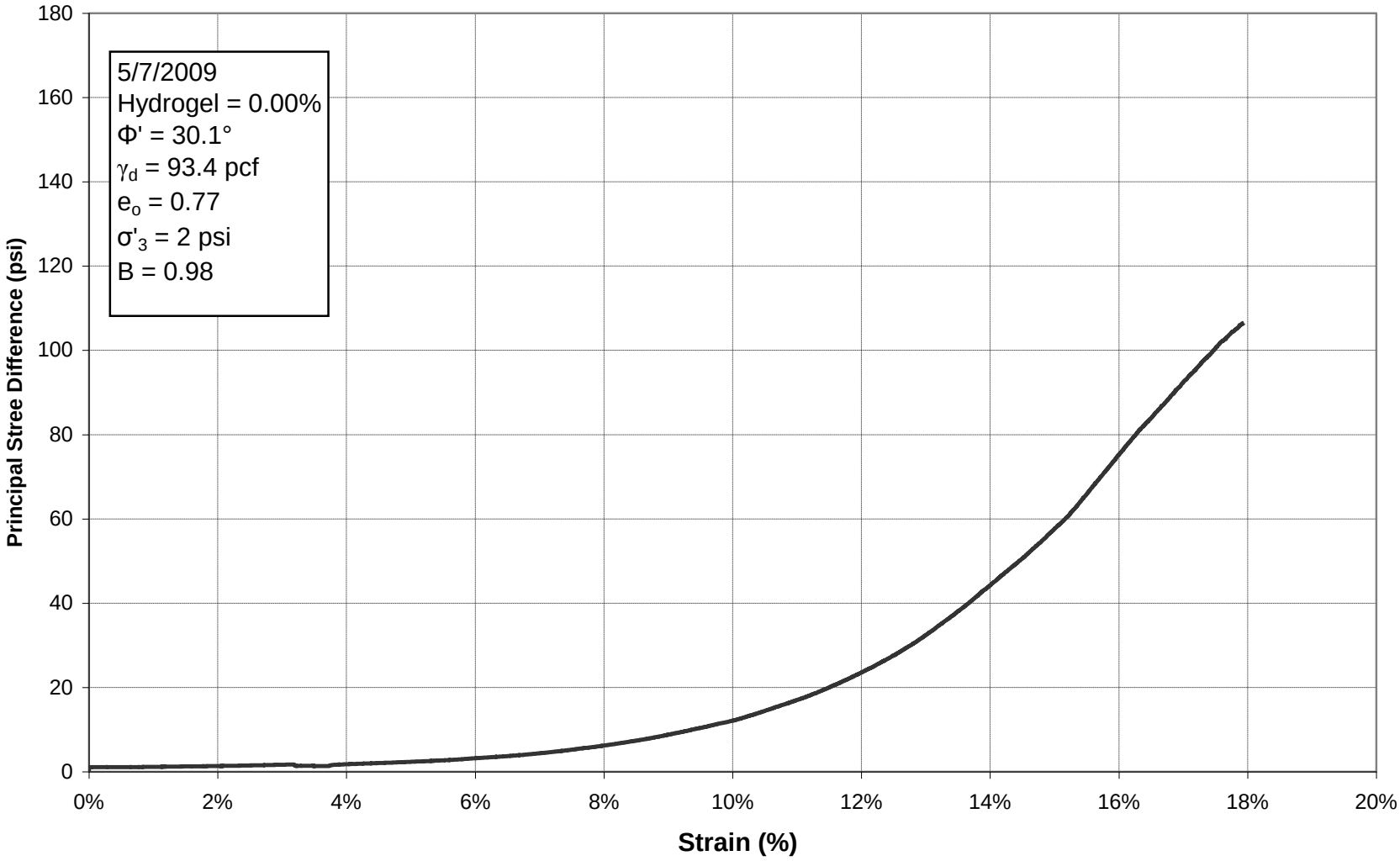

Figure E.12: Principal Stress Difference vs. Strain for Triaxial Test 12, 0.00% Hydrogel

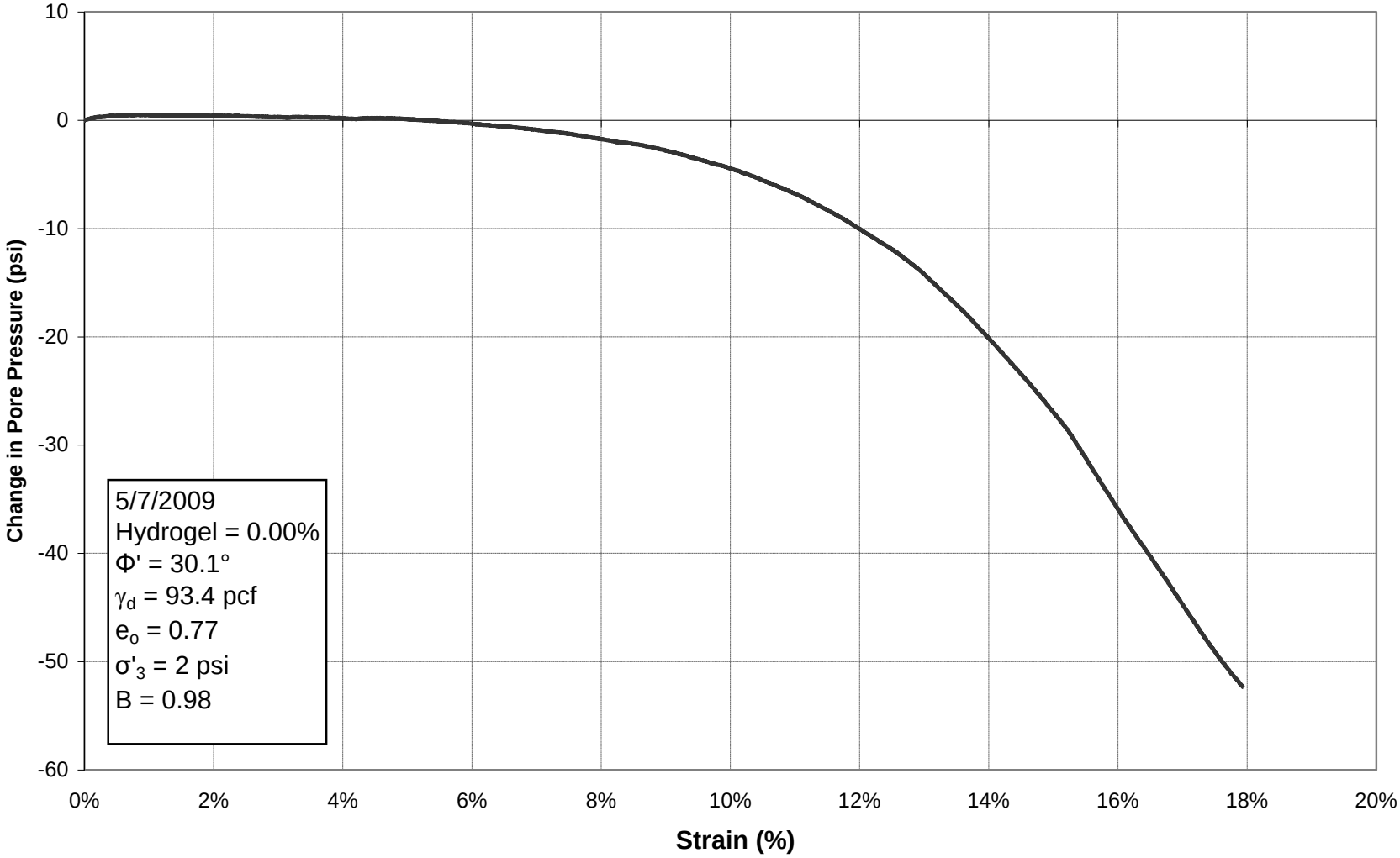

Figure E.13: Change in Pore Pressure vs. Strain for Triaxial Test 12, 0.00% Hydrogel

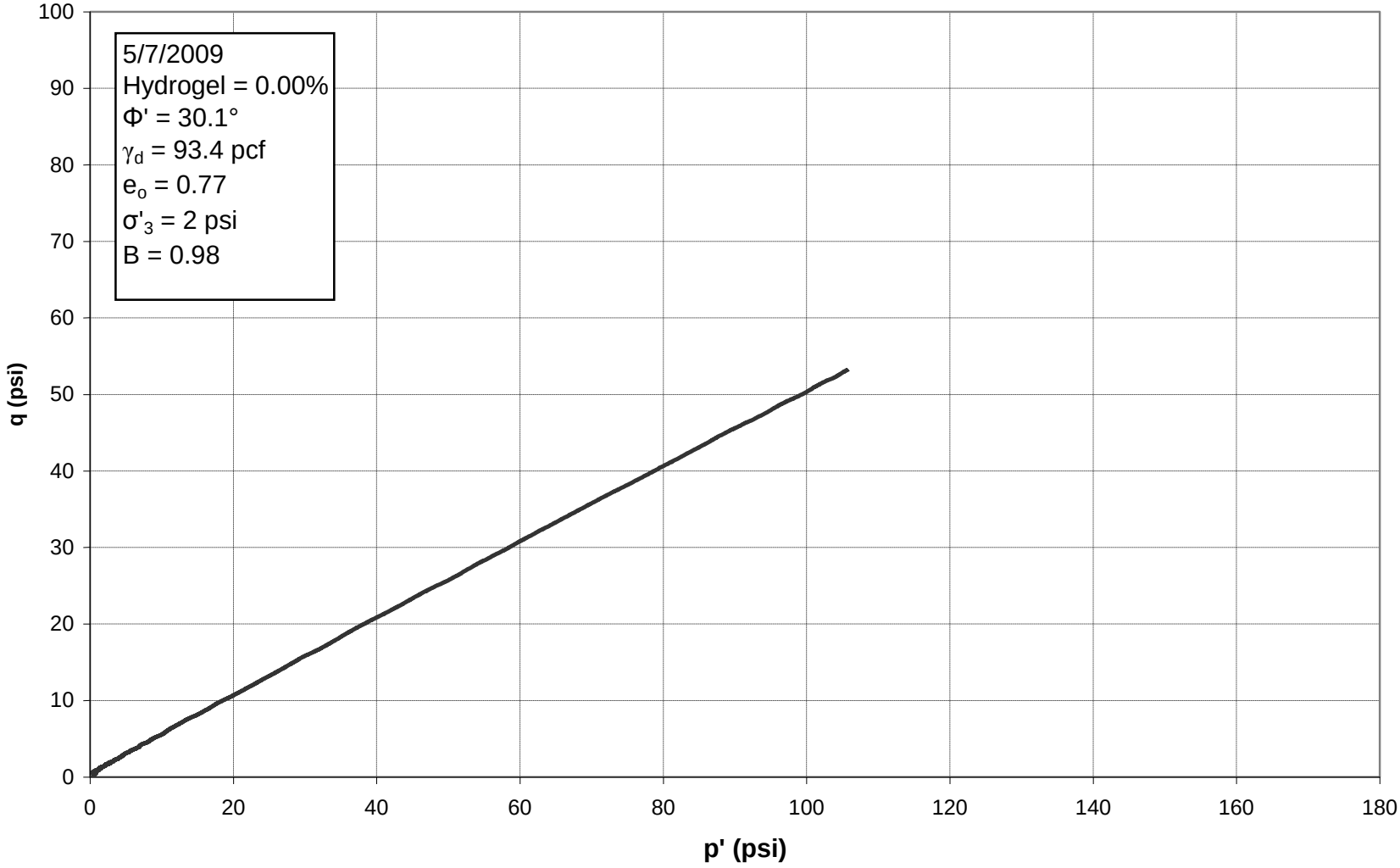

Figure E.14: p'-q Diagram for Triaxial Test 12, 0.00% Hydrogel

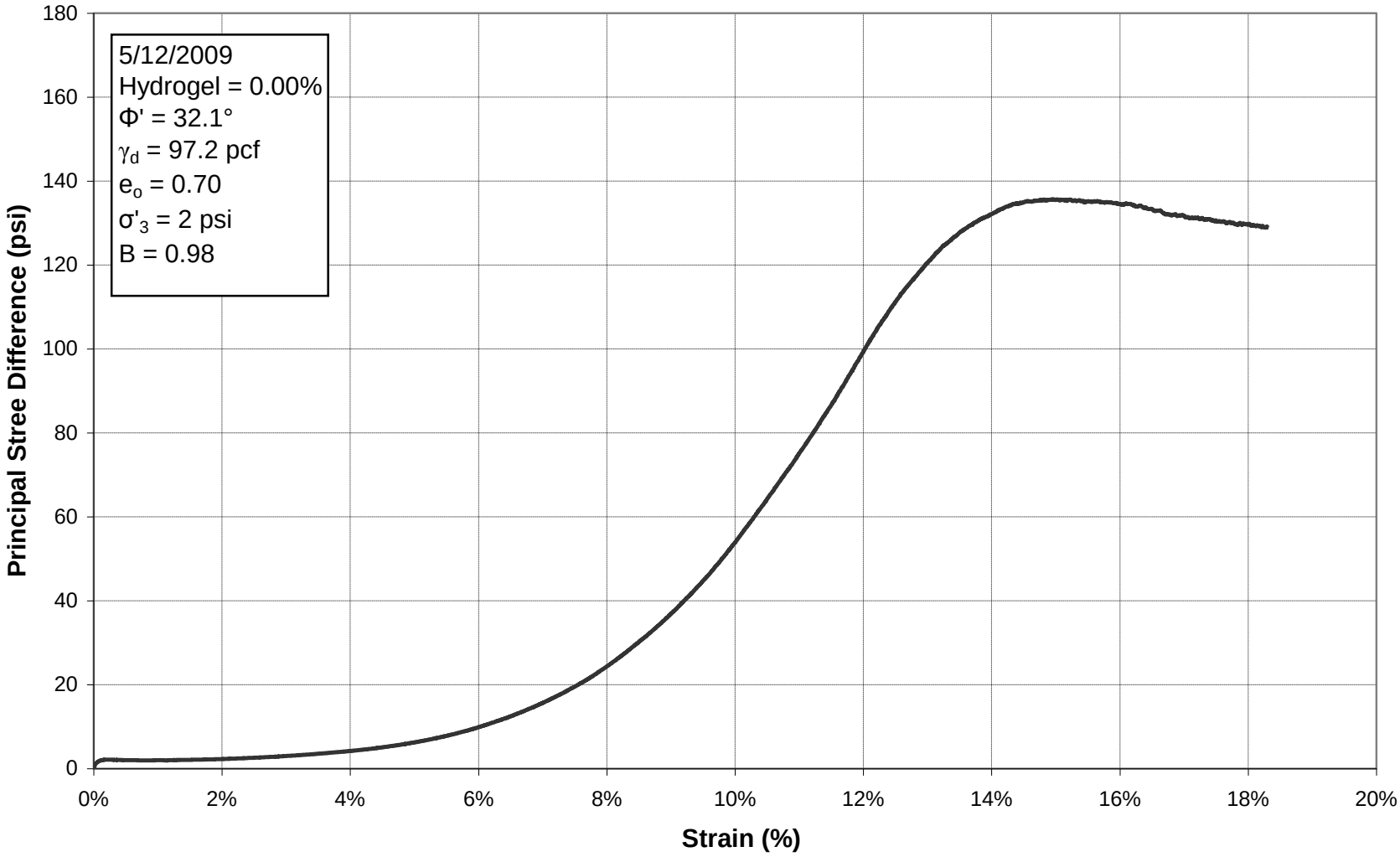

Figure E.15: Principal Stress Difference vs. Strain for Triaxial Test 13, 0.00% Hydrogel

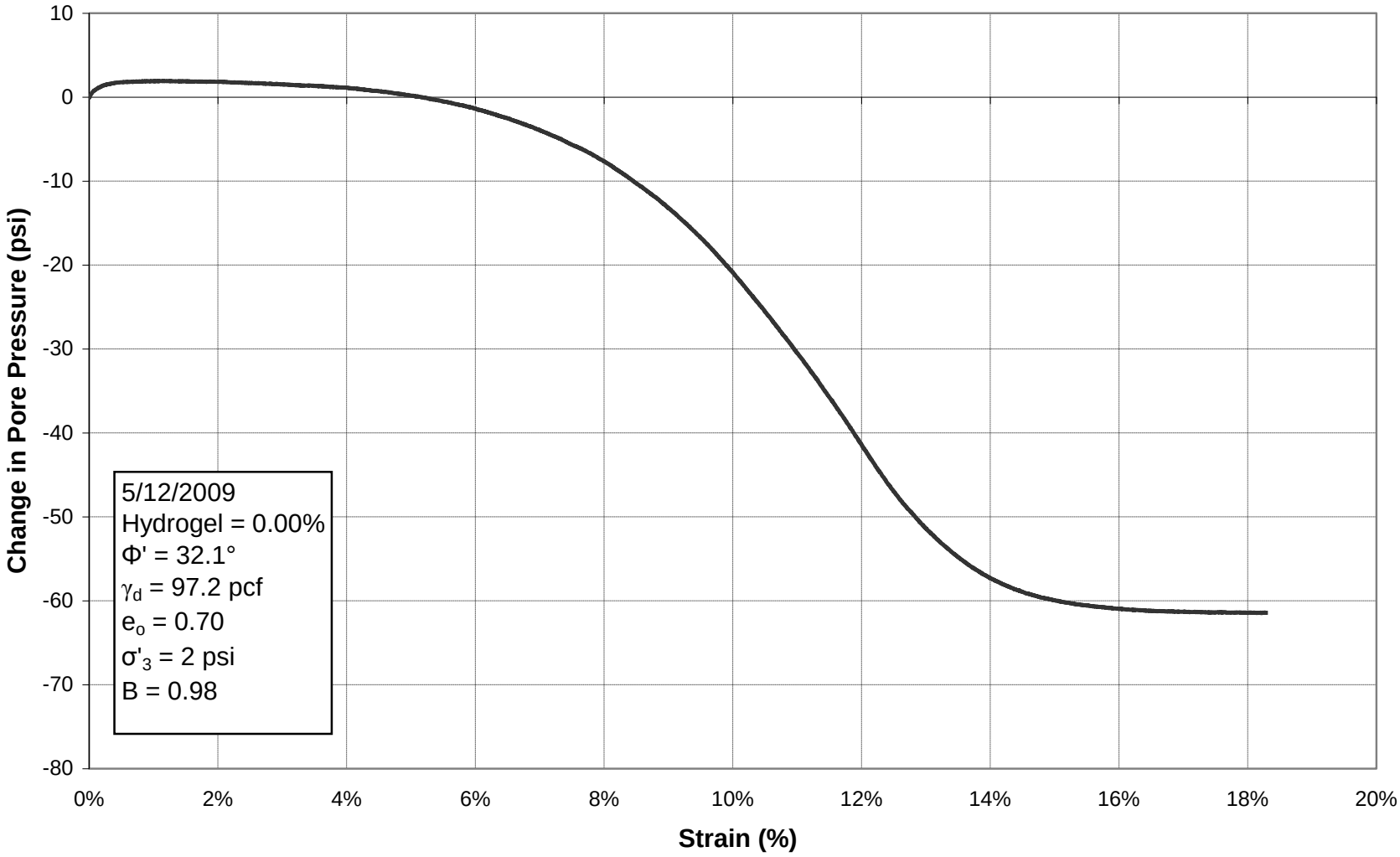

Figure E.16: Change in Pore Pressure vs. Strain for Triaxial Test 13, 0.00% Hydrogel

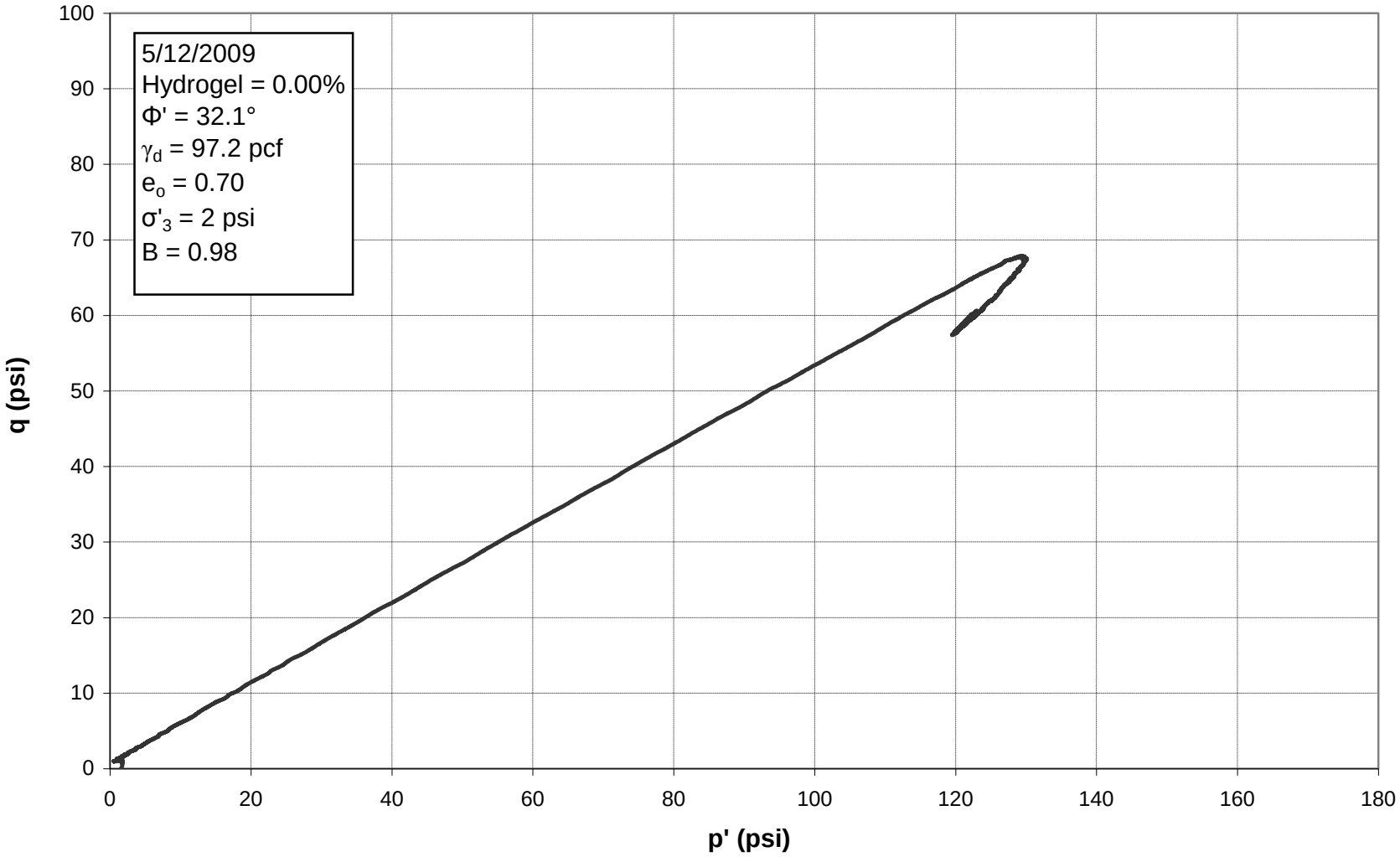

Figure E.17: p'-q Diagram for Triaxial Test 13, 0.00% Hydrogel

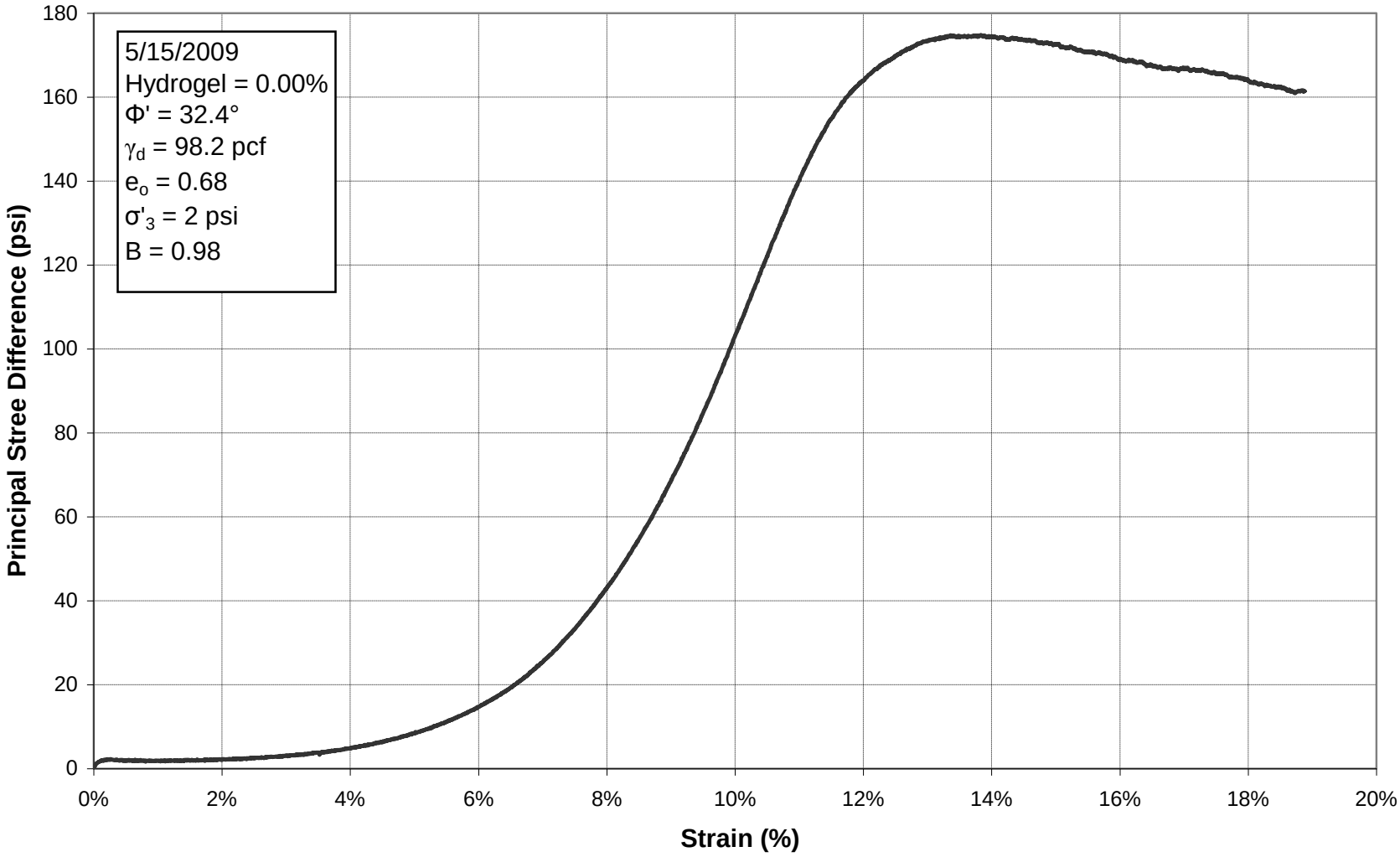

Figure E.18: Principal Stress Difference vs. Strain for Triaxial Test 14, 0.00% Hydrogel

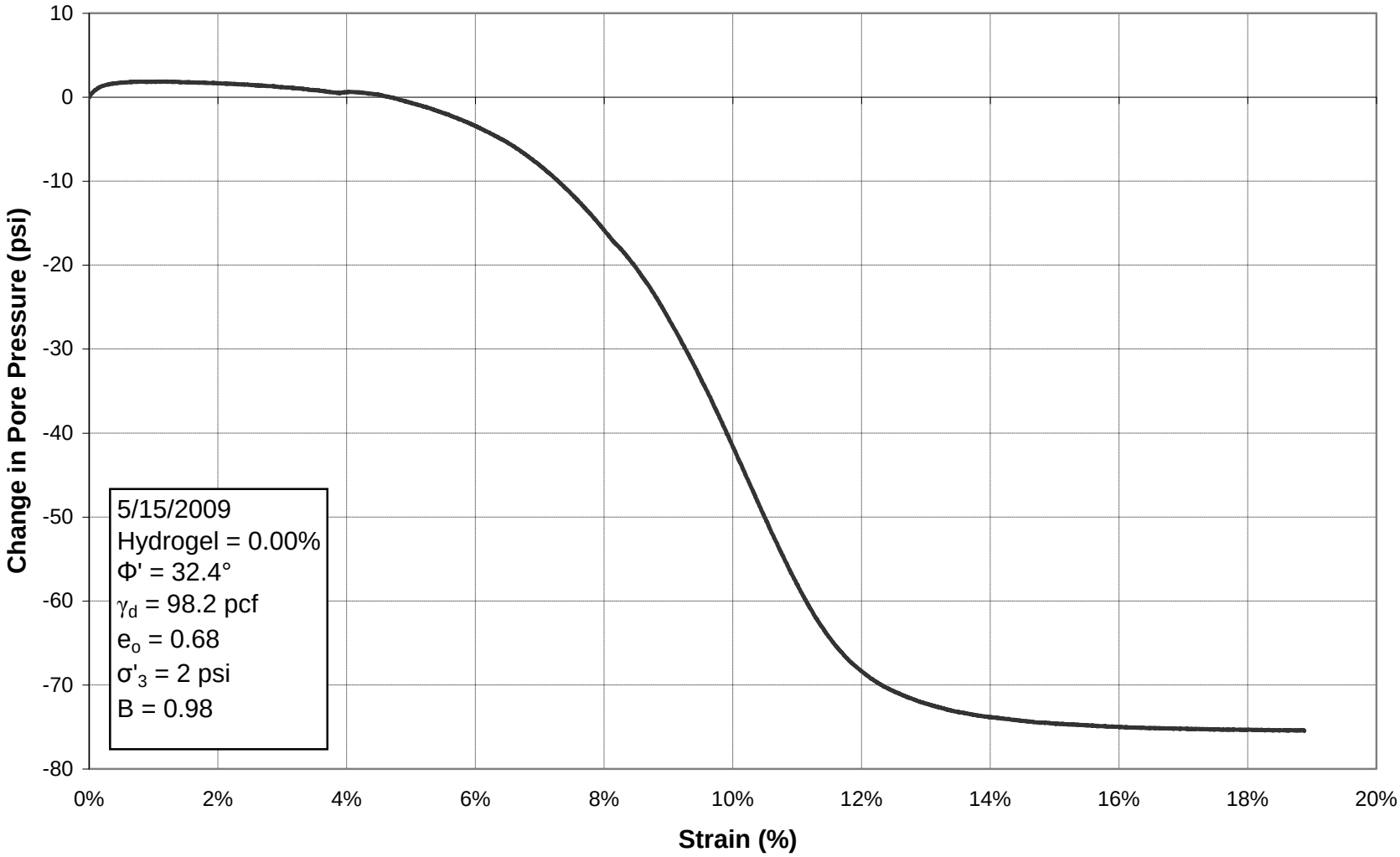

Figure E.19: Change in Pore Pressure vs. Strain for Triaxial Test 14, 0.00% Hydrogel

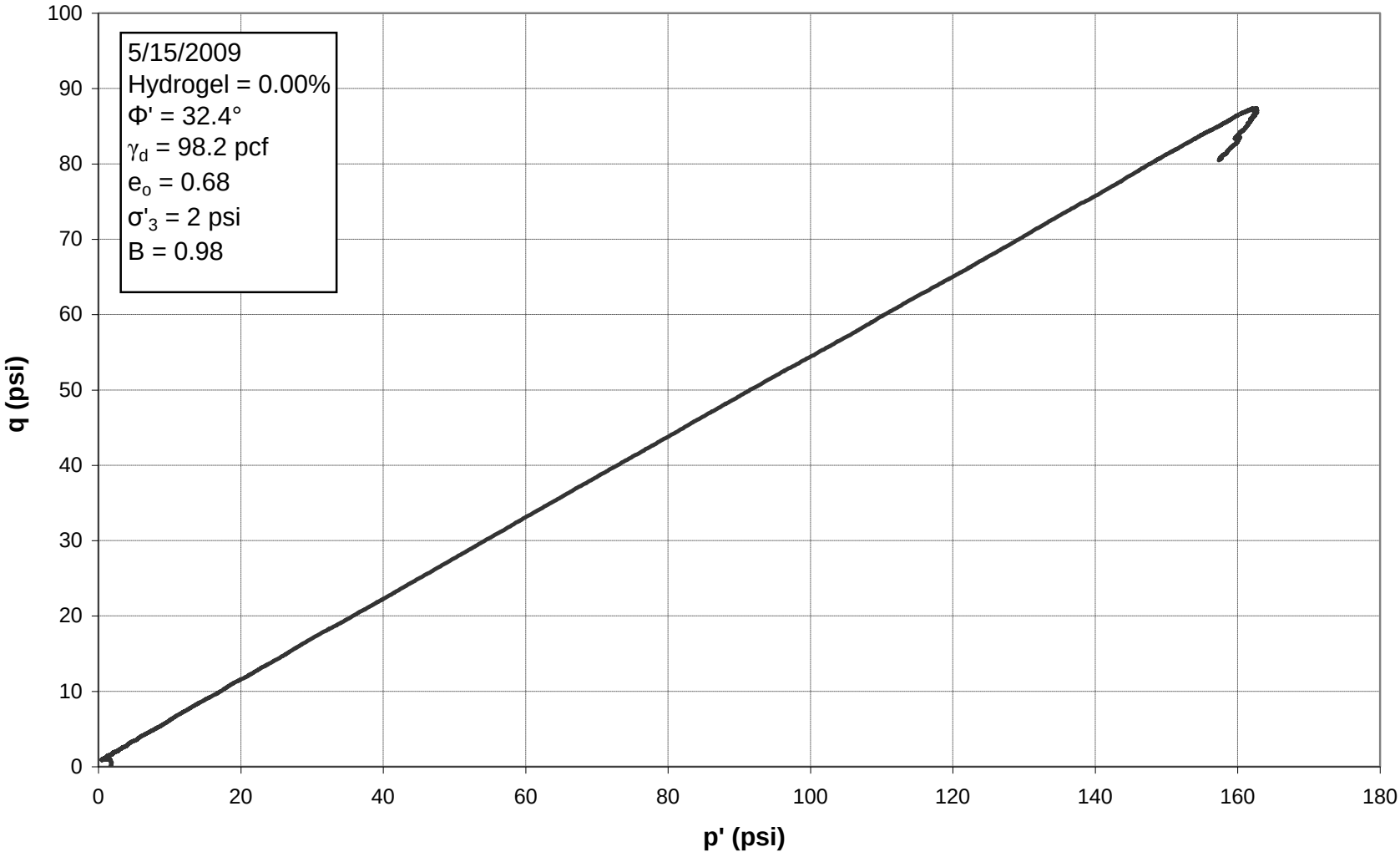

Figure E.20: p'-q Diagram for Triaxial Test 14, 0.00% Hydrogel

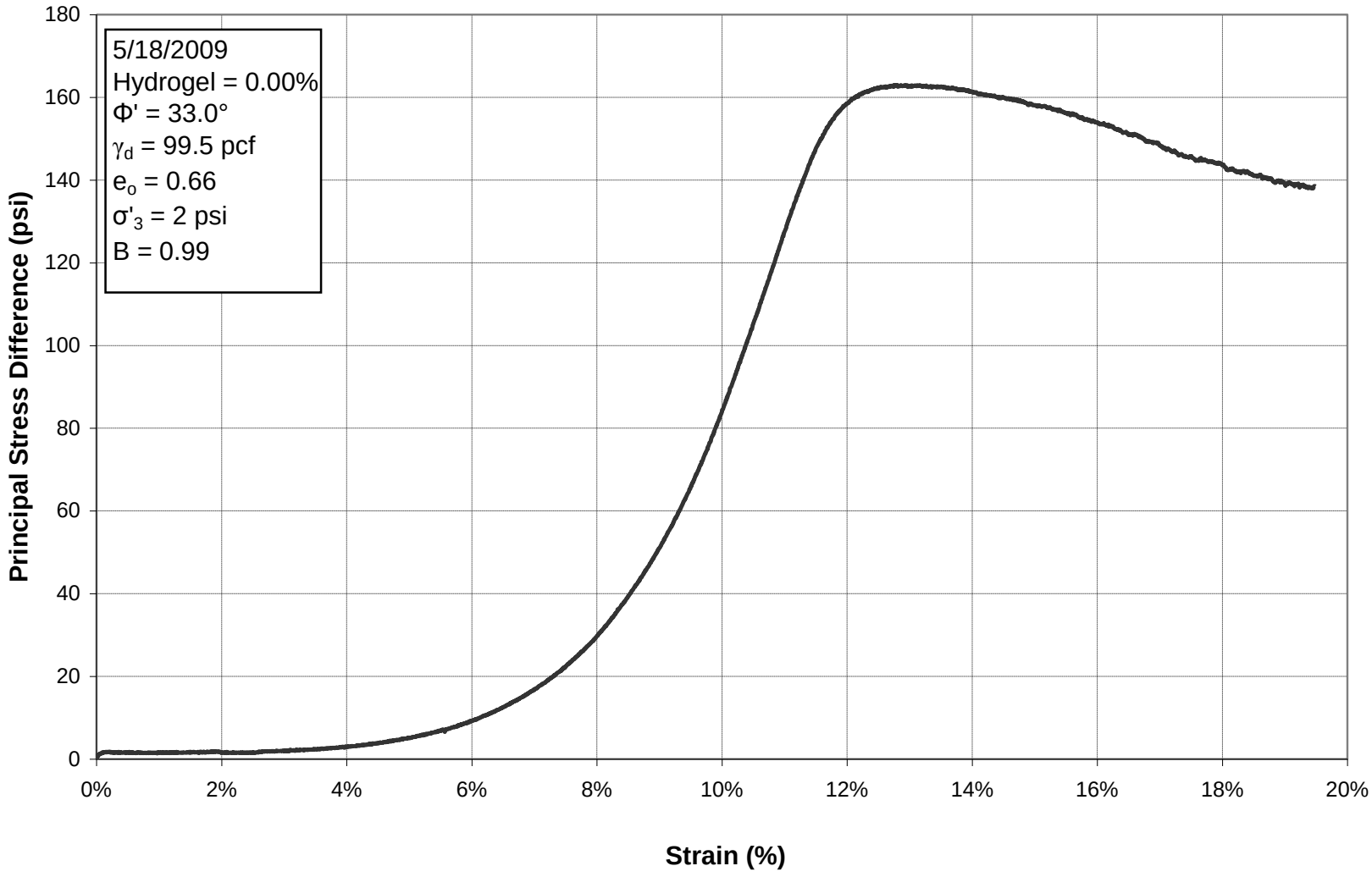

Figure E.21: Principal Stress Difference vs. Strain for Triaxial Test 15, 0.00% Hydrogel

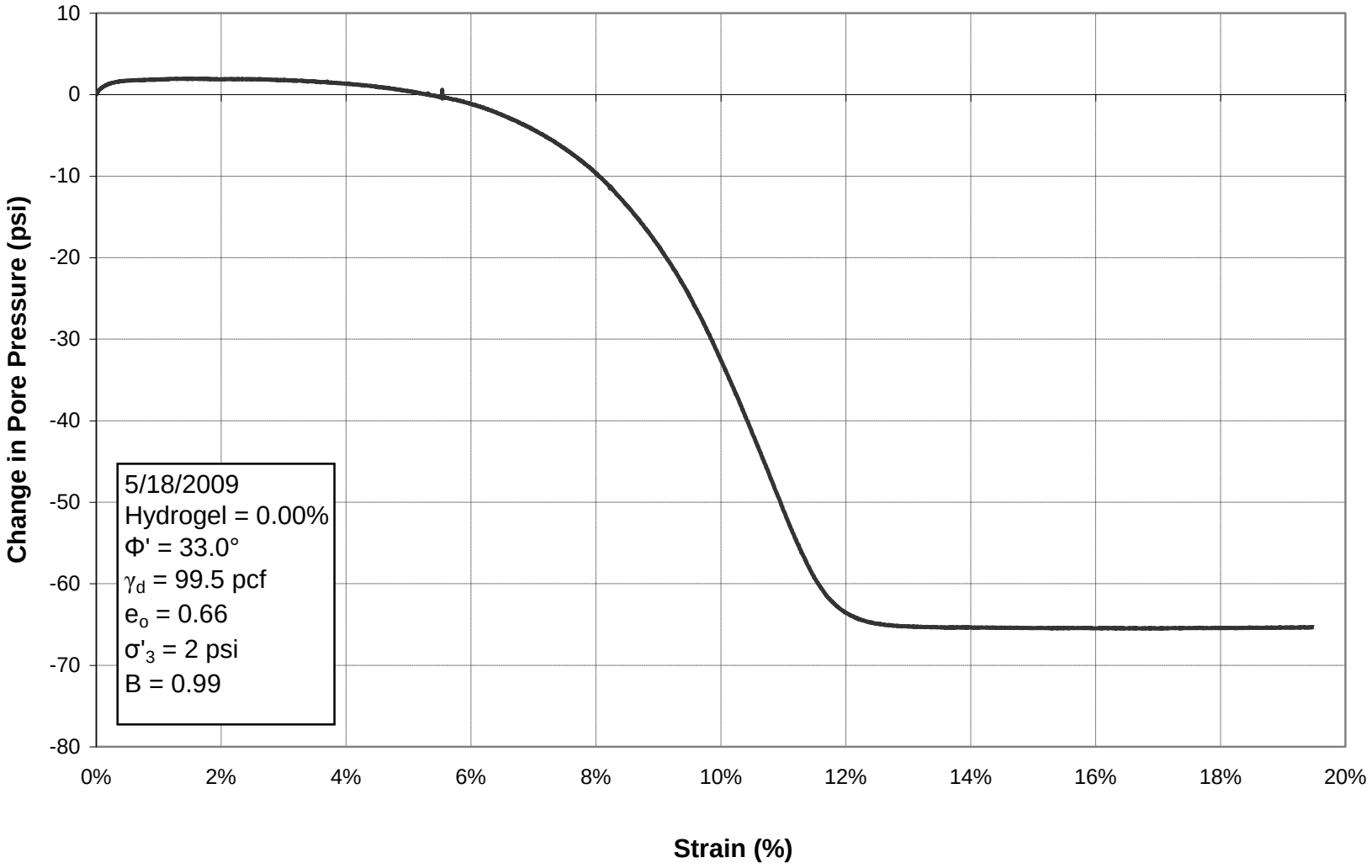

Figure E.22: Change in Pore Pressure vs. Strain for Triaxial Test 15, 0.00% Hydrogel

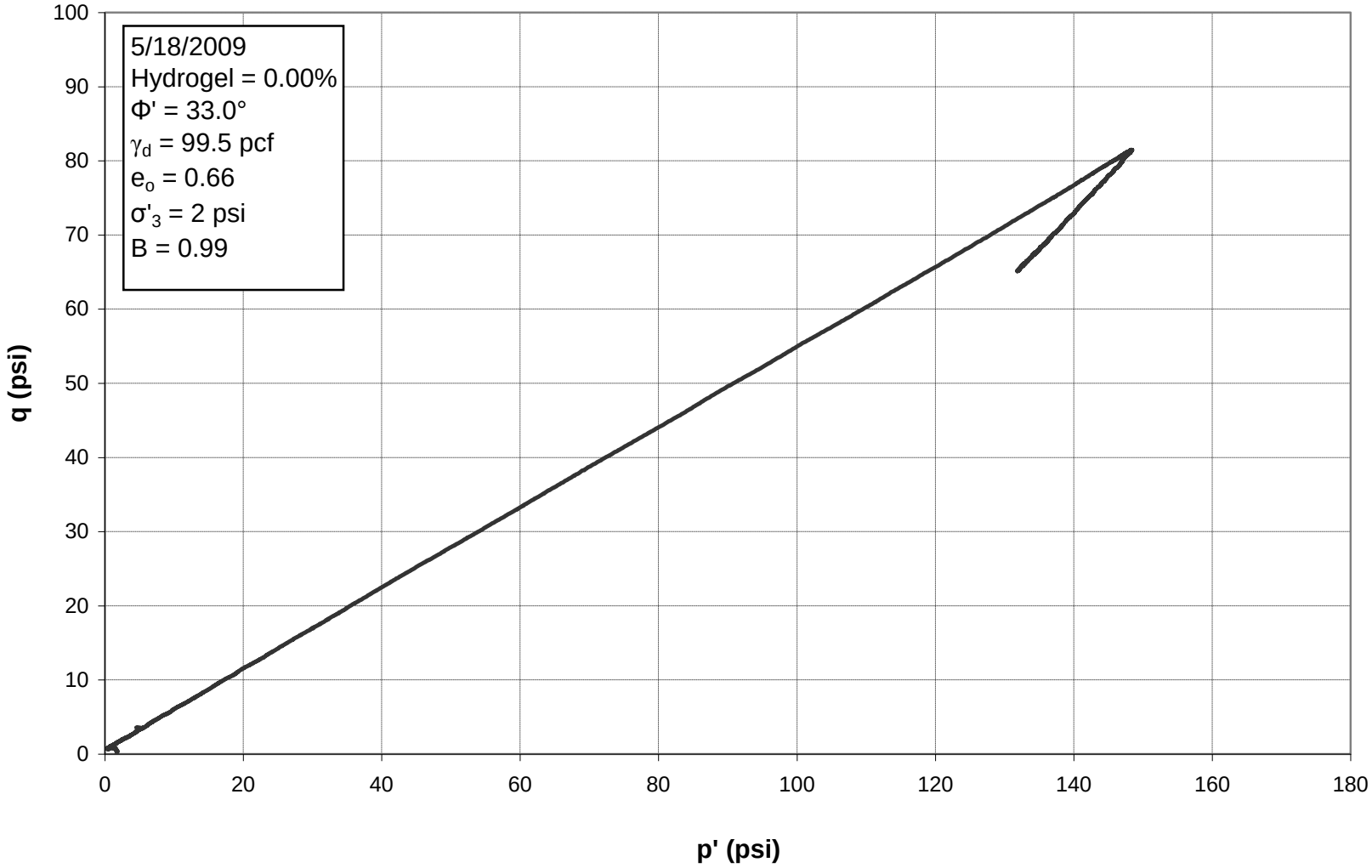

Figure E.23: p'-q Diagram for Triaxial Test 15, 0.00% Hydrogel

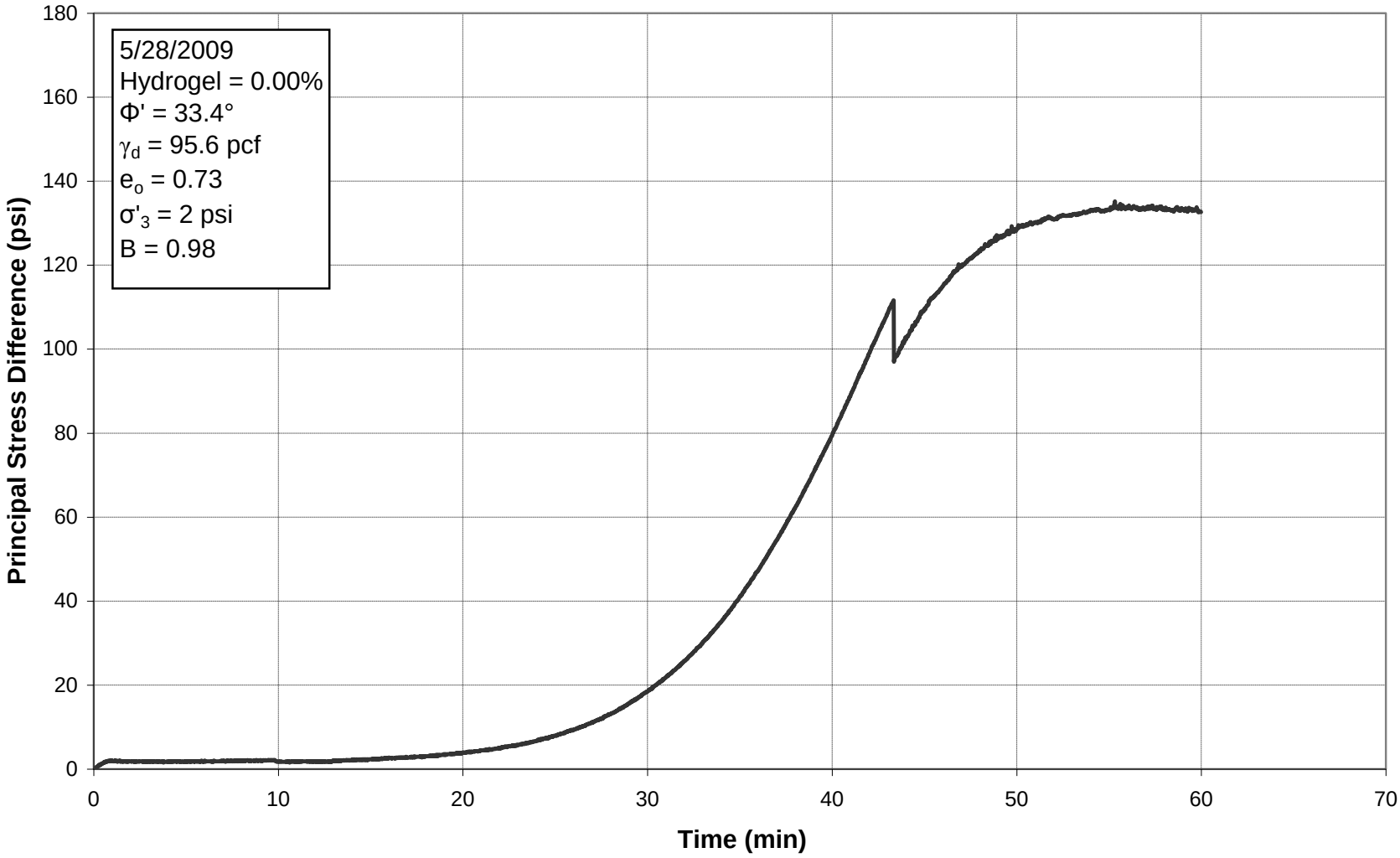

Figure E.24: Principal Stress Difference vs. Time for Triaxial Test 16, 0.00% Hydrogel (there was an issue with the LVDT during this test, as a result time has been substituted for strain in this plot)

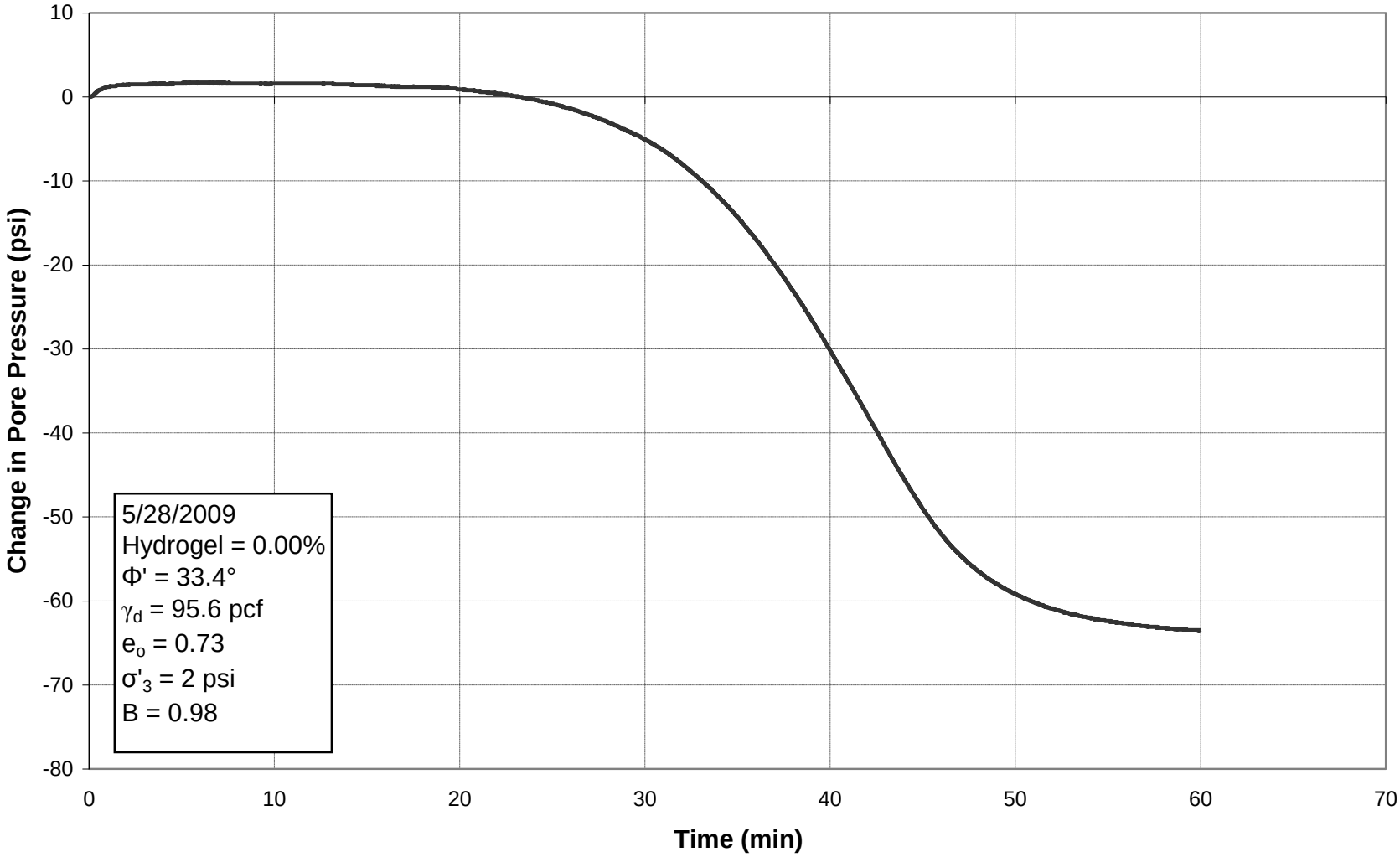

Figure E.25: Change in Pore Pressure vs. Time for Triaxial Test 16, 0.00% Hydrogel (there was an issue with the LVDT during this test, as a result time has been substituted for strain in this plot)

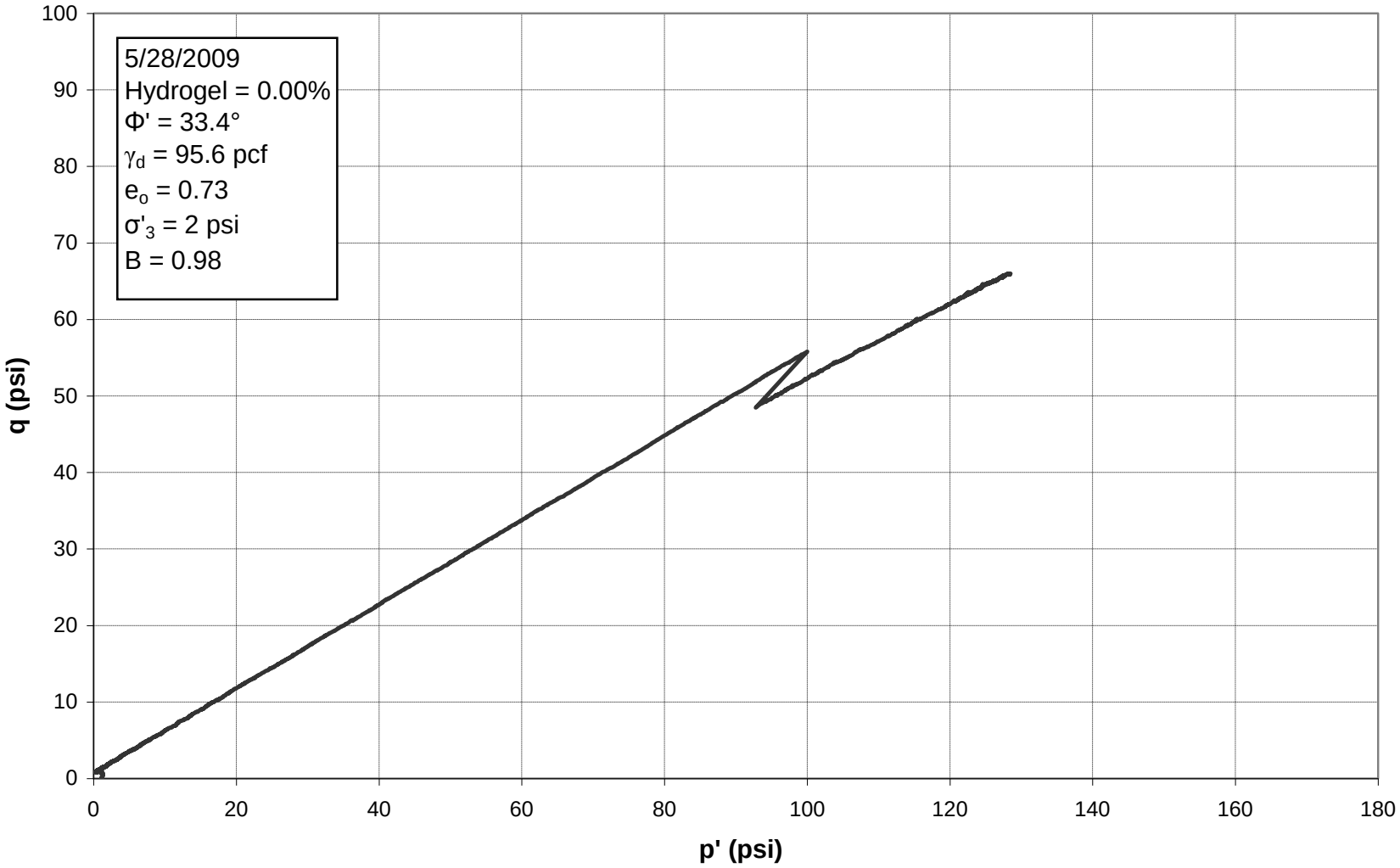

Figure E.26: p'-q Diagram for Triaxial Test 16, 0.00% Hydrogel

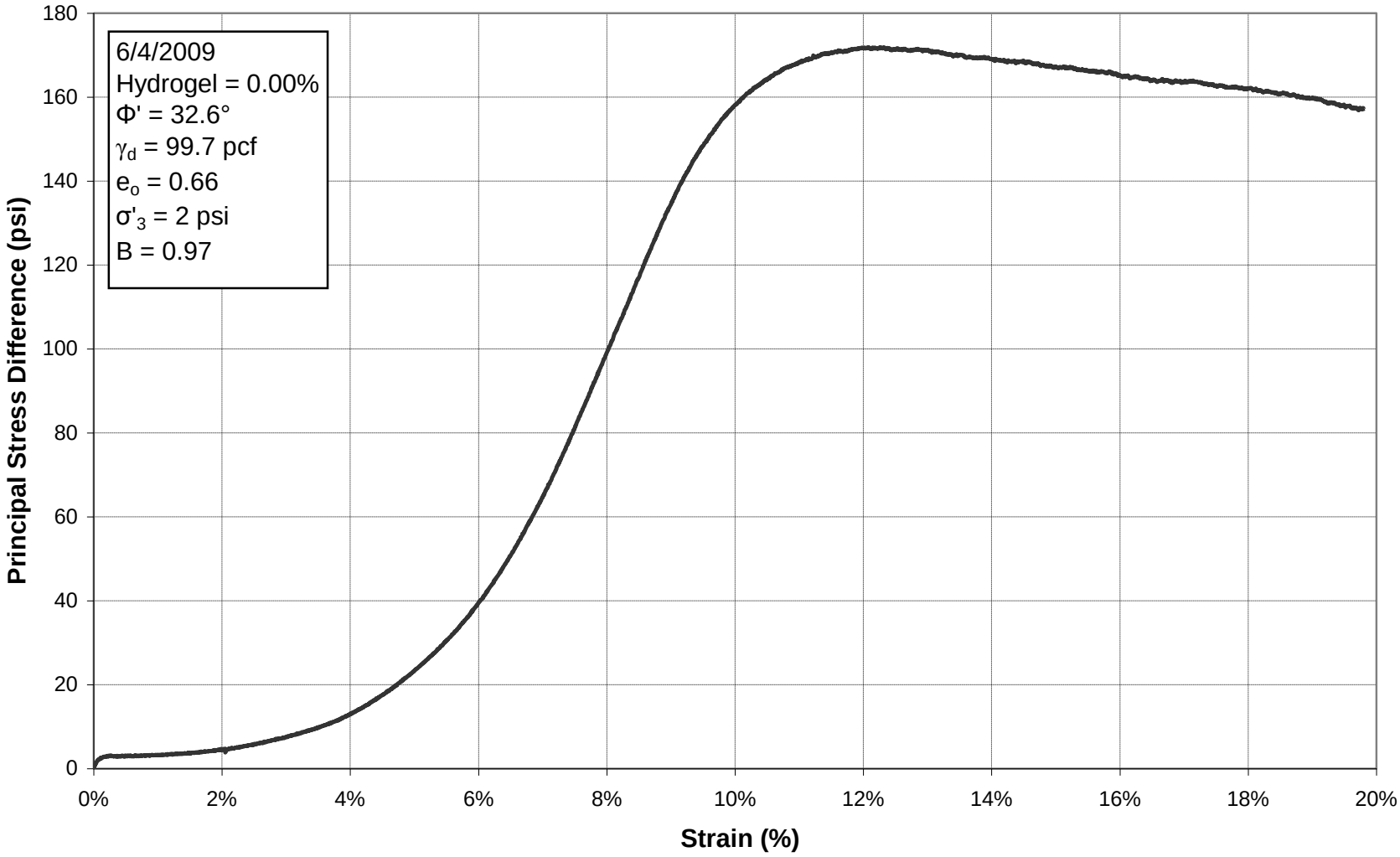

Figure E.27: Principal Stress Difference vs. Strain for Triaxial Test 17, 0.00% Hydrogel

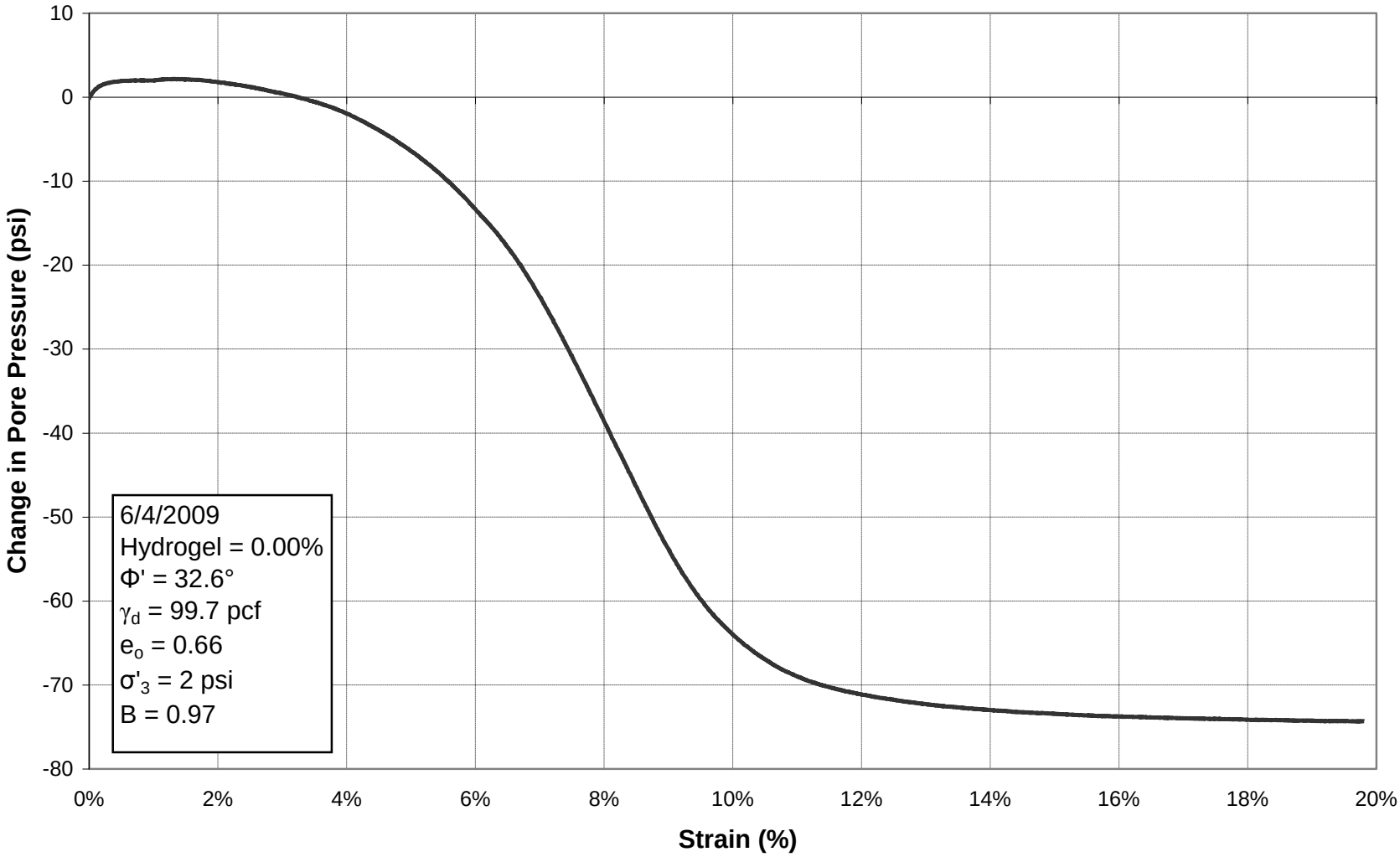

Figure E.28: Change in Pore Pressure vs. Strain for Triaxial Test 17, 0.00% Hydrogel

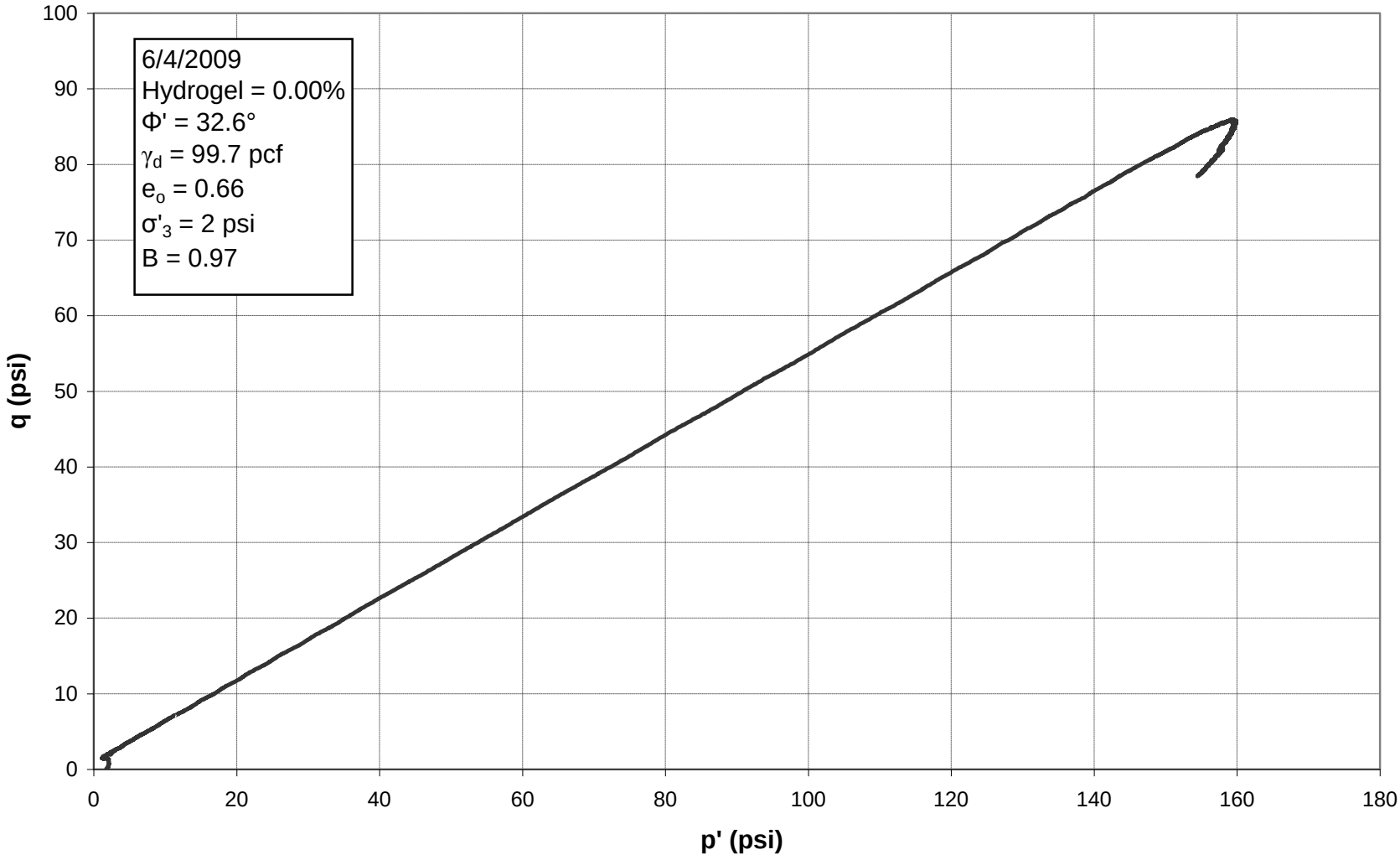

Figure E.29: p'-q Diagram for Triaxial Test 17, 0.00% Hydrogel

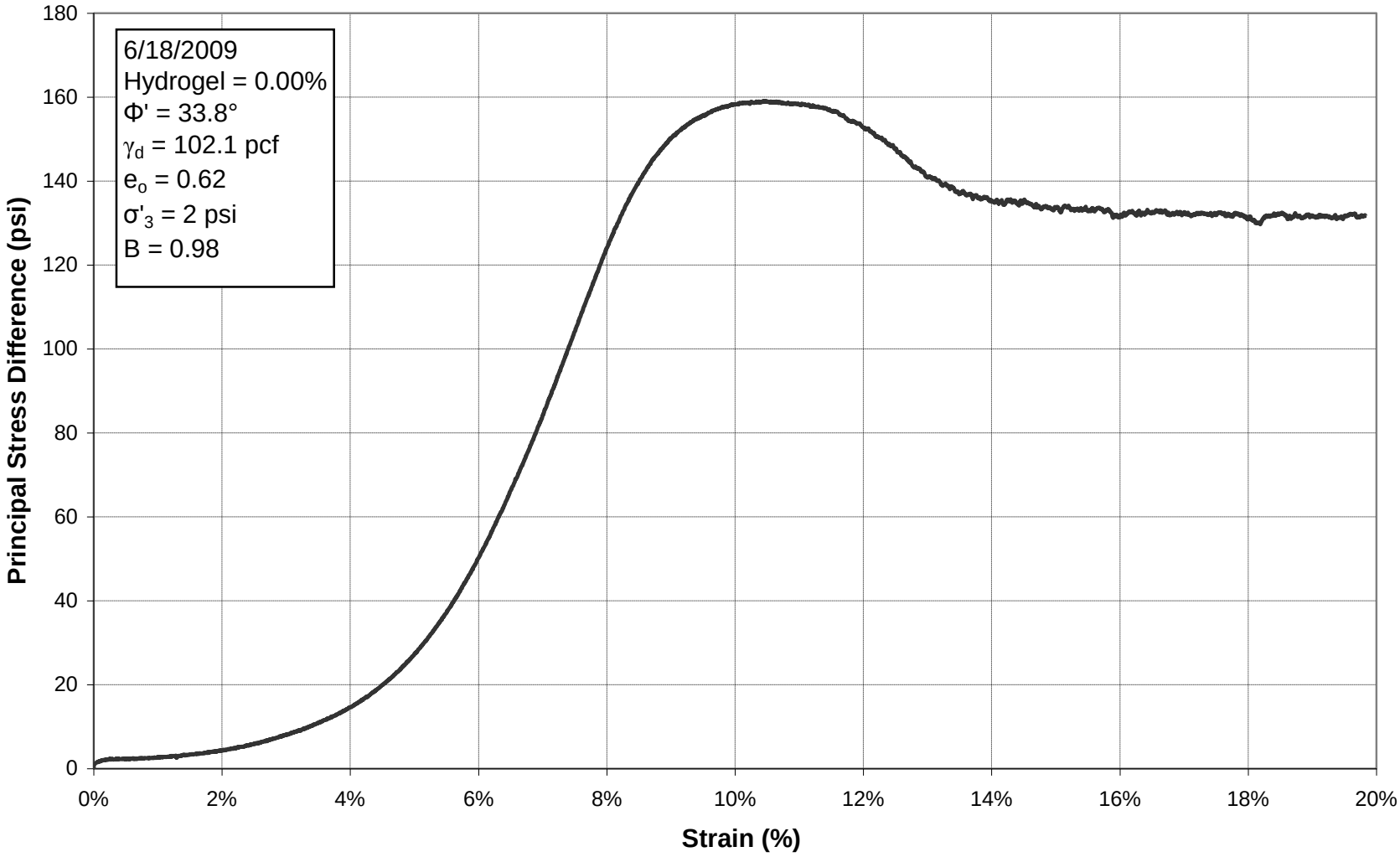

Figure E.30: Principal Stress Difference vs. Strain for Triaxial Test 18, 0.00% Hydrogel

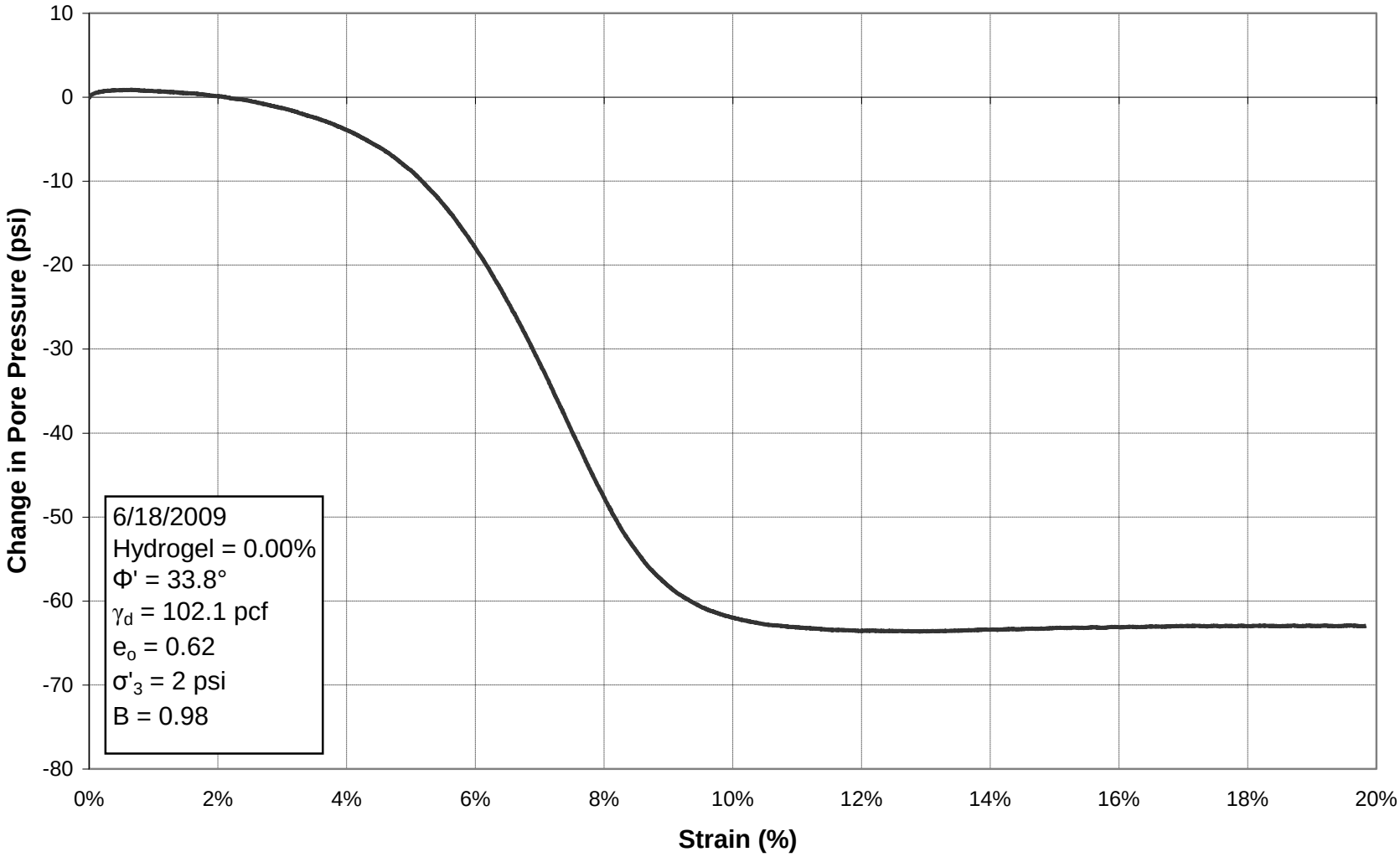

Figure E.31: Change in Pore Pressure vs. Strain for Triaxial Test 18, 0.00% Hydrogel

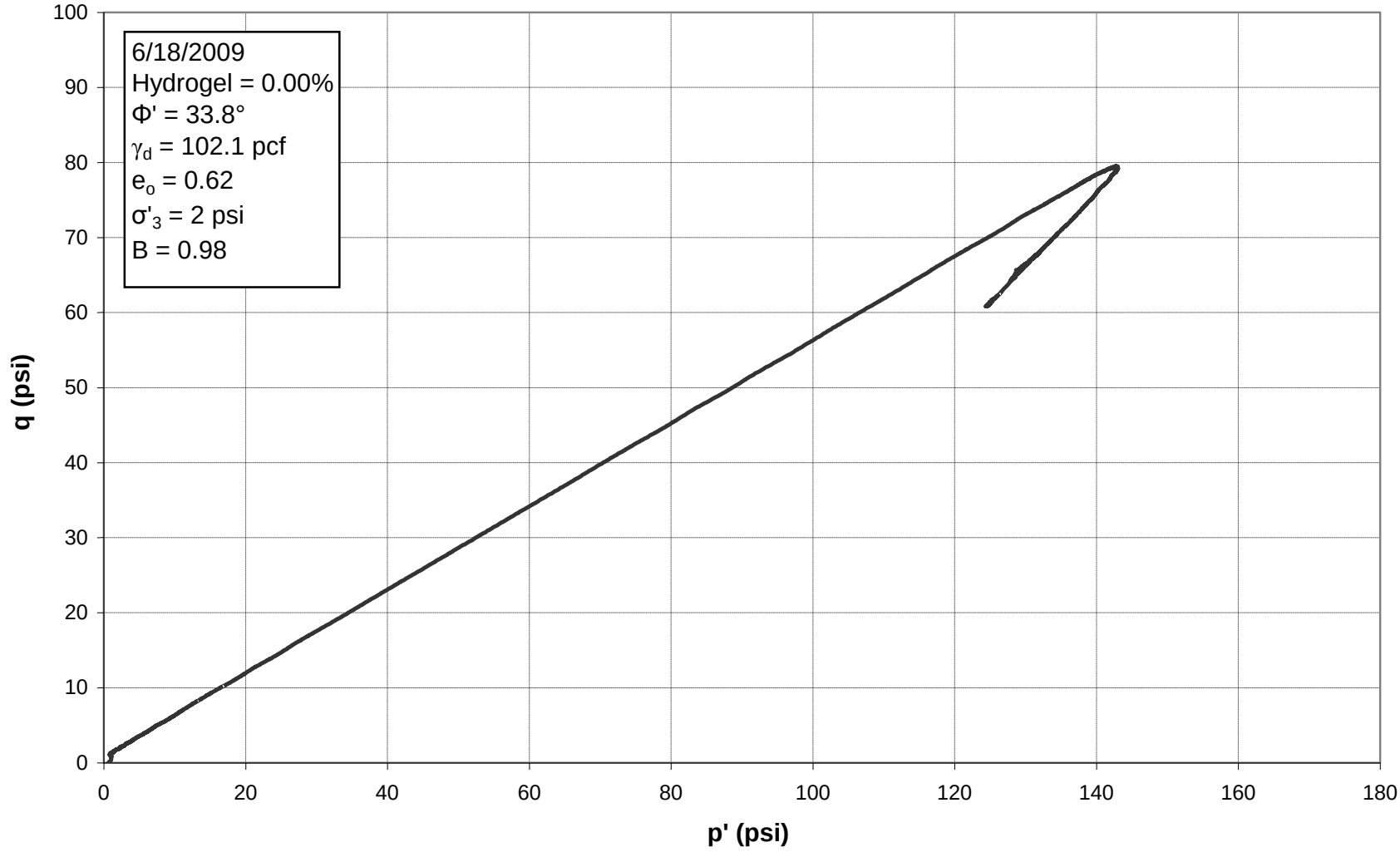

Figure E.32: p'-q Diagram for Triaxial Test 18, 0.00% Hydrogel

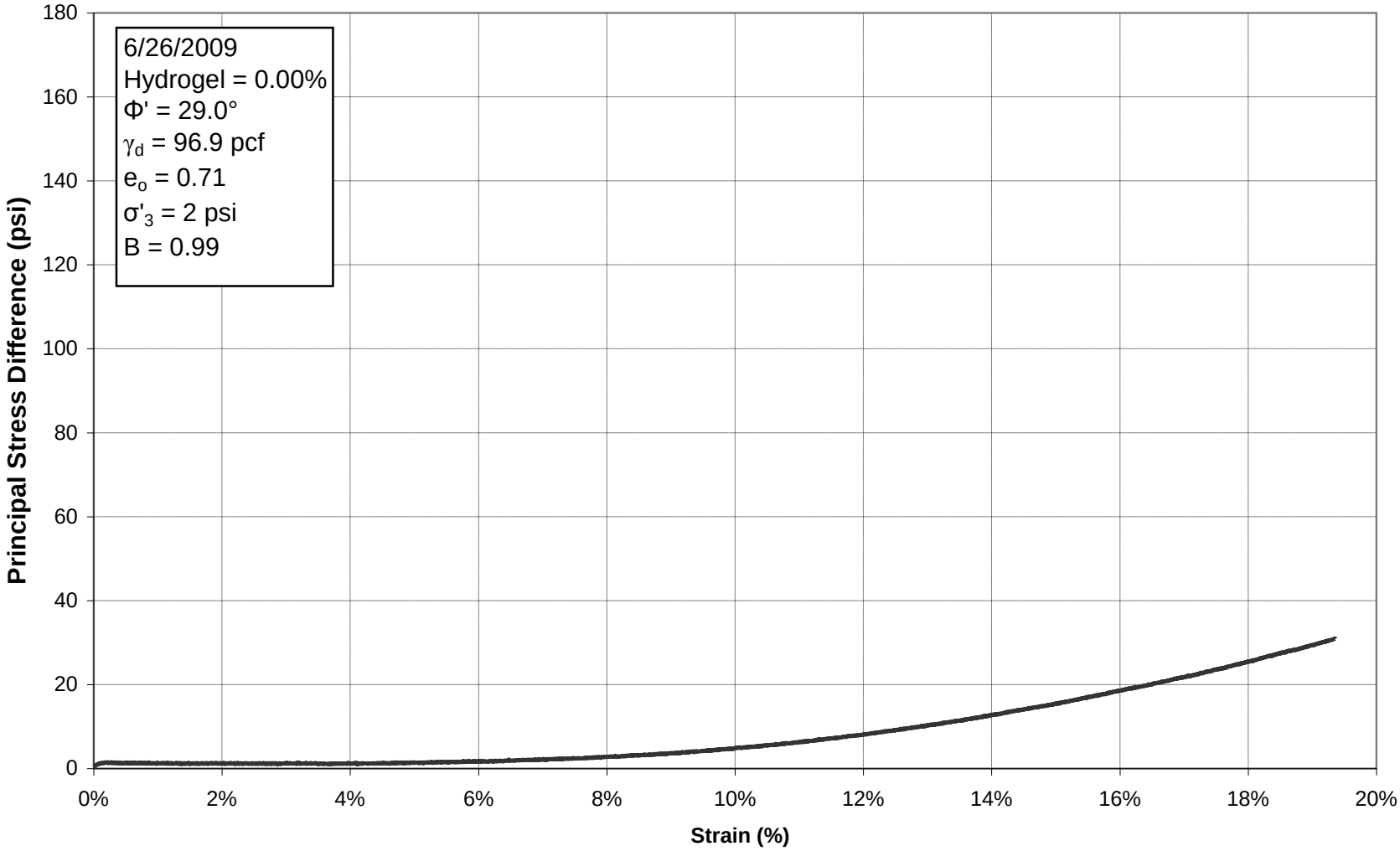

Figure E.33: Principal Stress Difference vs. Strain for Triaxial Test 19, 0.00% Hydrogel

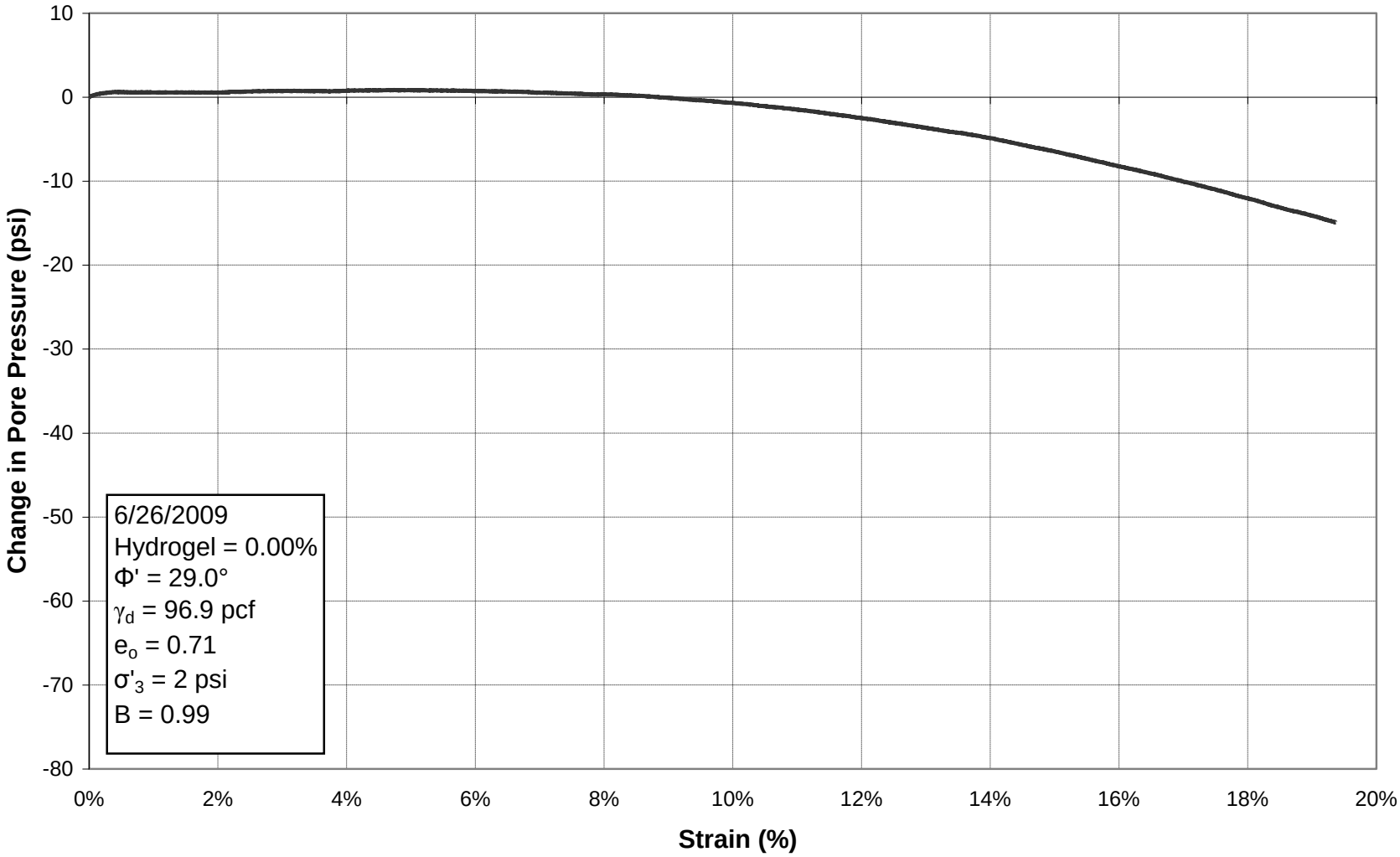

Figure E.34: Change in Pore Pressure vs. Strain for Triaxial Test 19, 0.00% Hydrogel

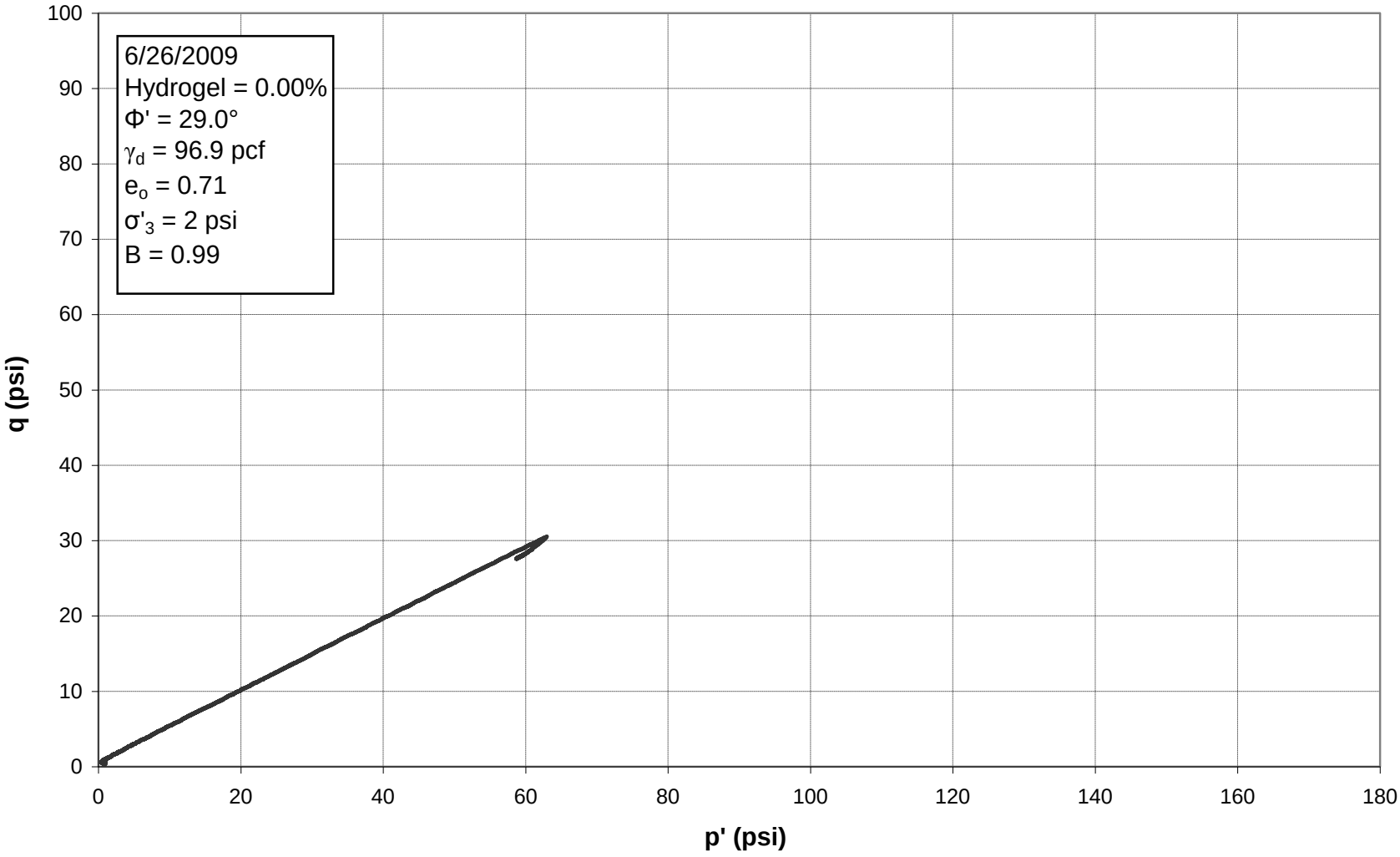

Figure E.35: p'-q Diagram for Triaxial Test 19, 0.00% Hydrogel

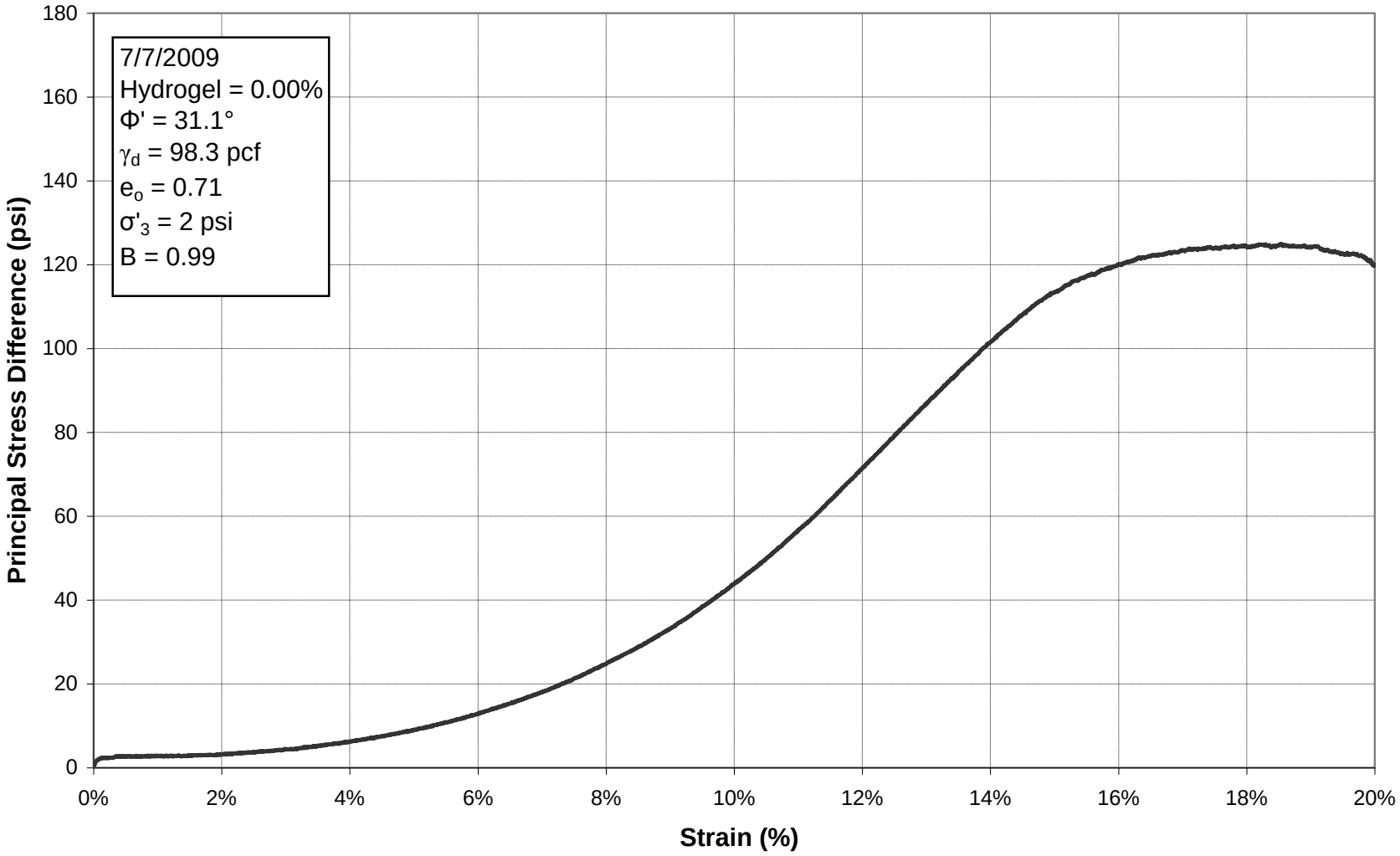

Figure E.36: Principal Stress Difference vs. Strain for Triaxial Test 20, 0.00% Hydrogel

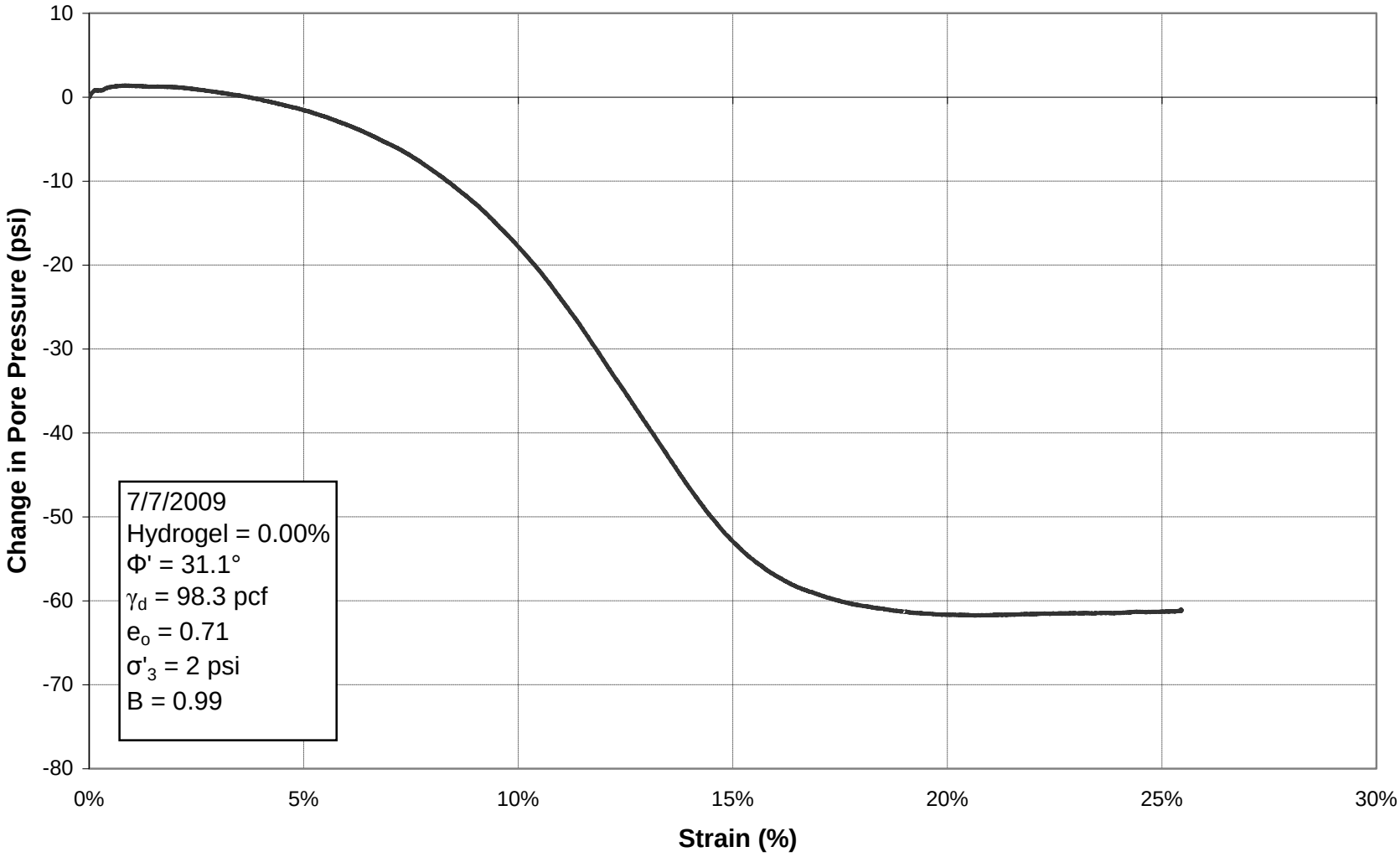

Figure E.37: Change in Pore Pressure vs. Strain for Triaxial Test 20, 0.00% Hydrogel

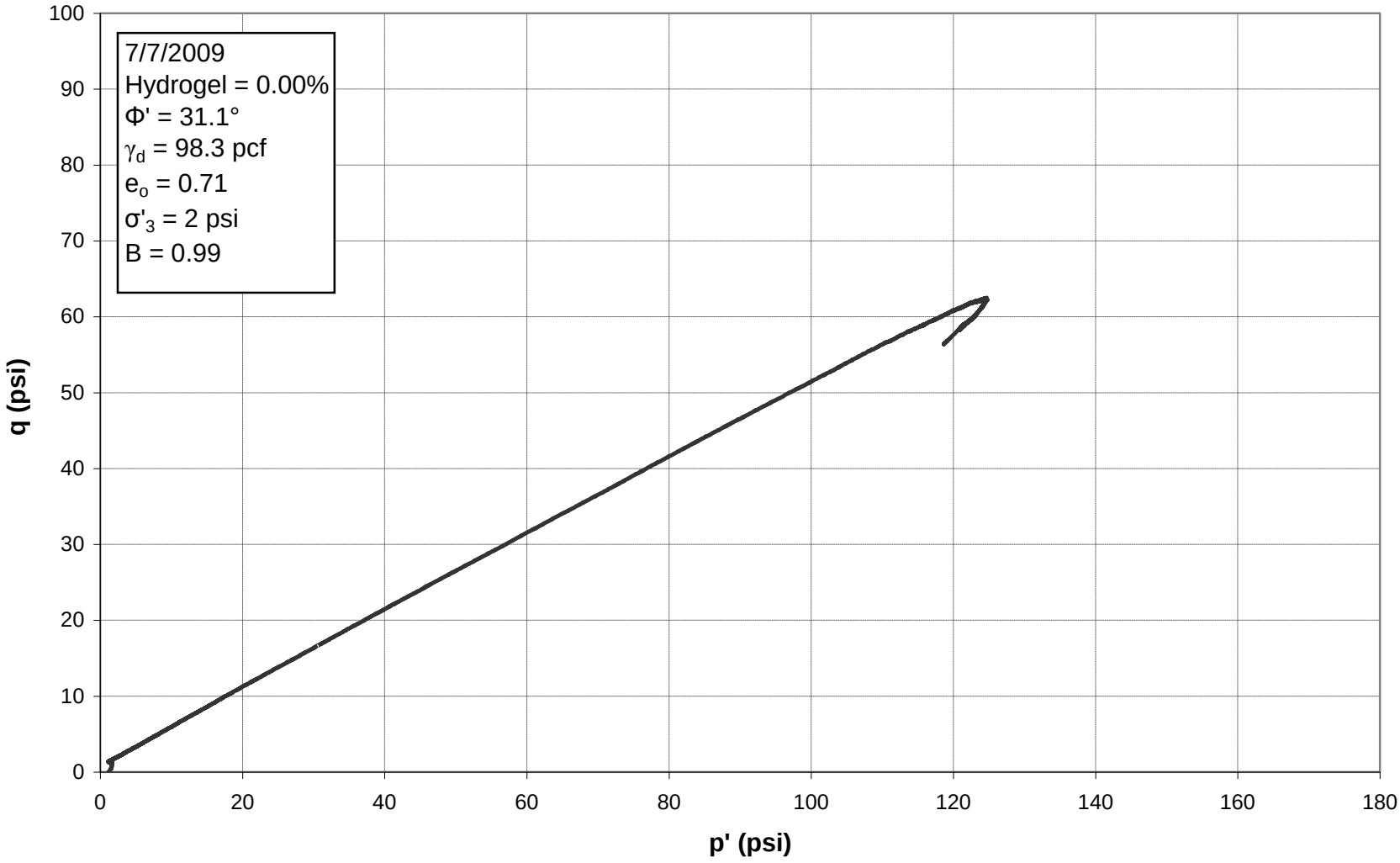

Figure E.38: p'-q Diagram for Triaxial Test 20, 0.00% Hydrogel

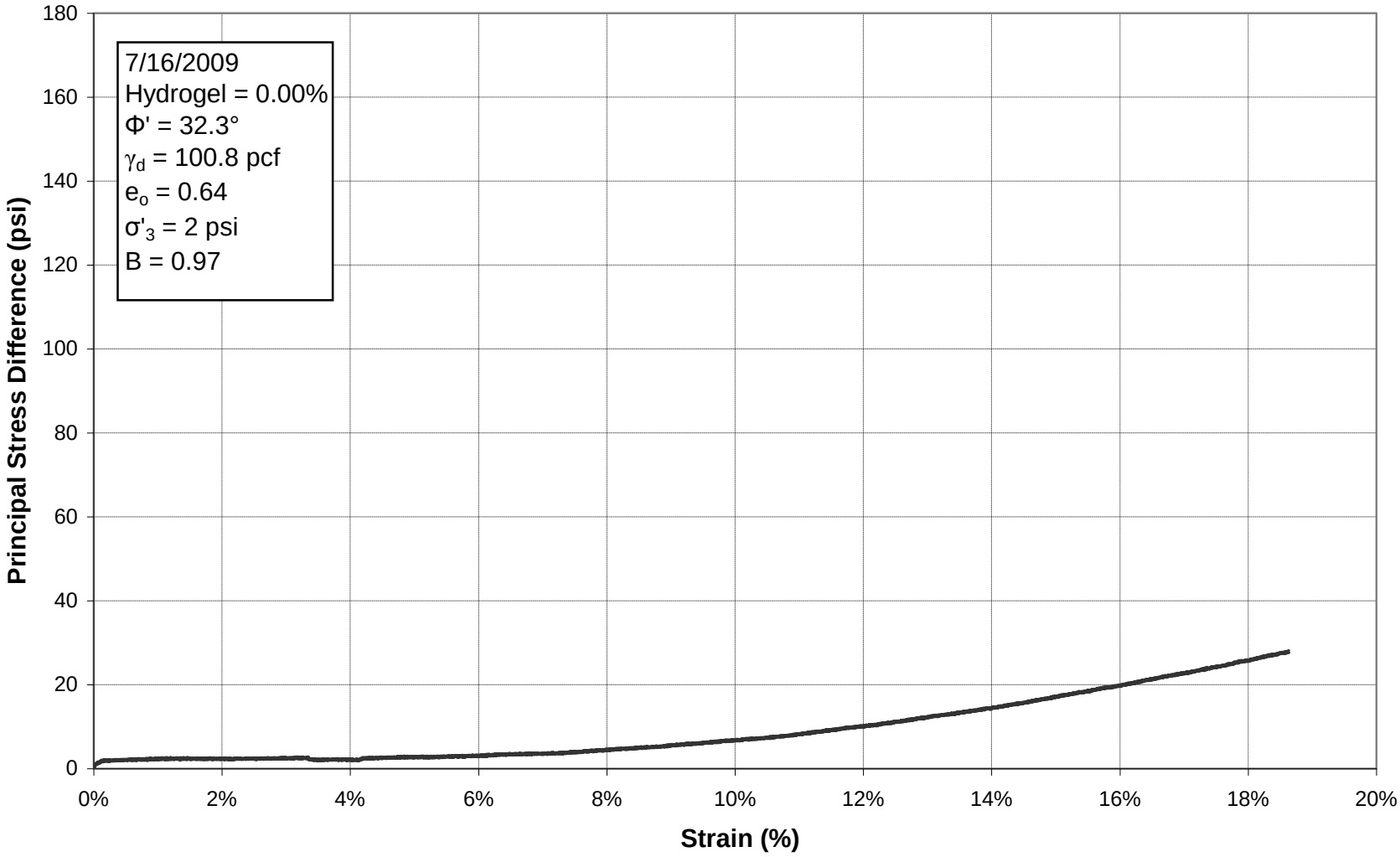

Figure E.39: Principal Stress Difference vs. Strain for Triaxial Test 21, 0.00% Hydrogel

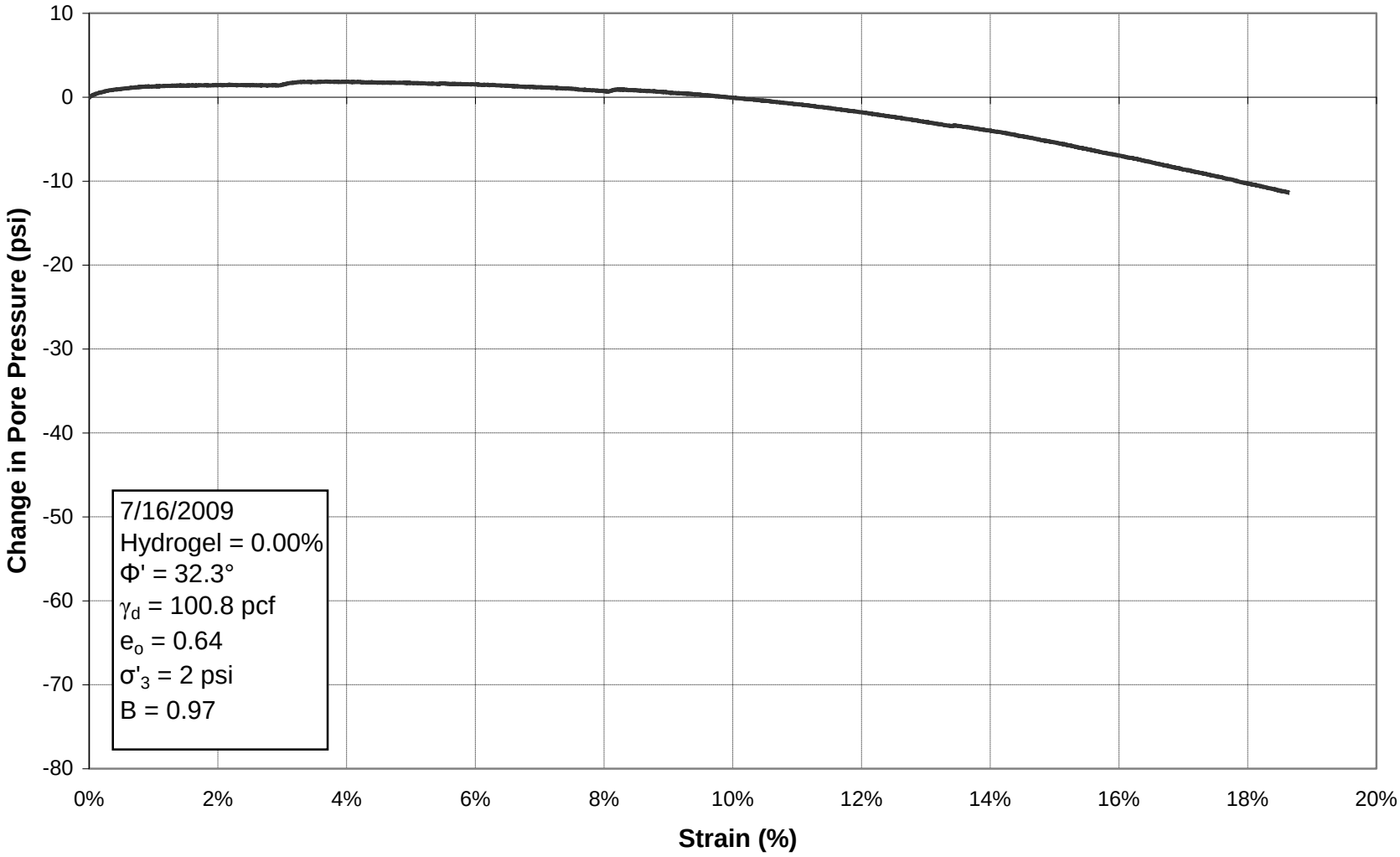

Figure E.40: Change in Pore Pressure vs. Strain for Triaxial Test 21, 0.00% Hydrogel

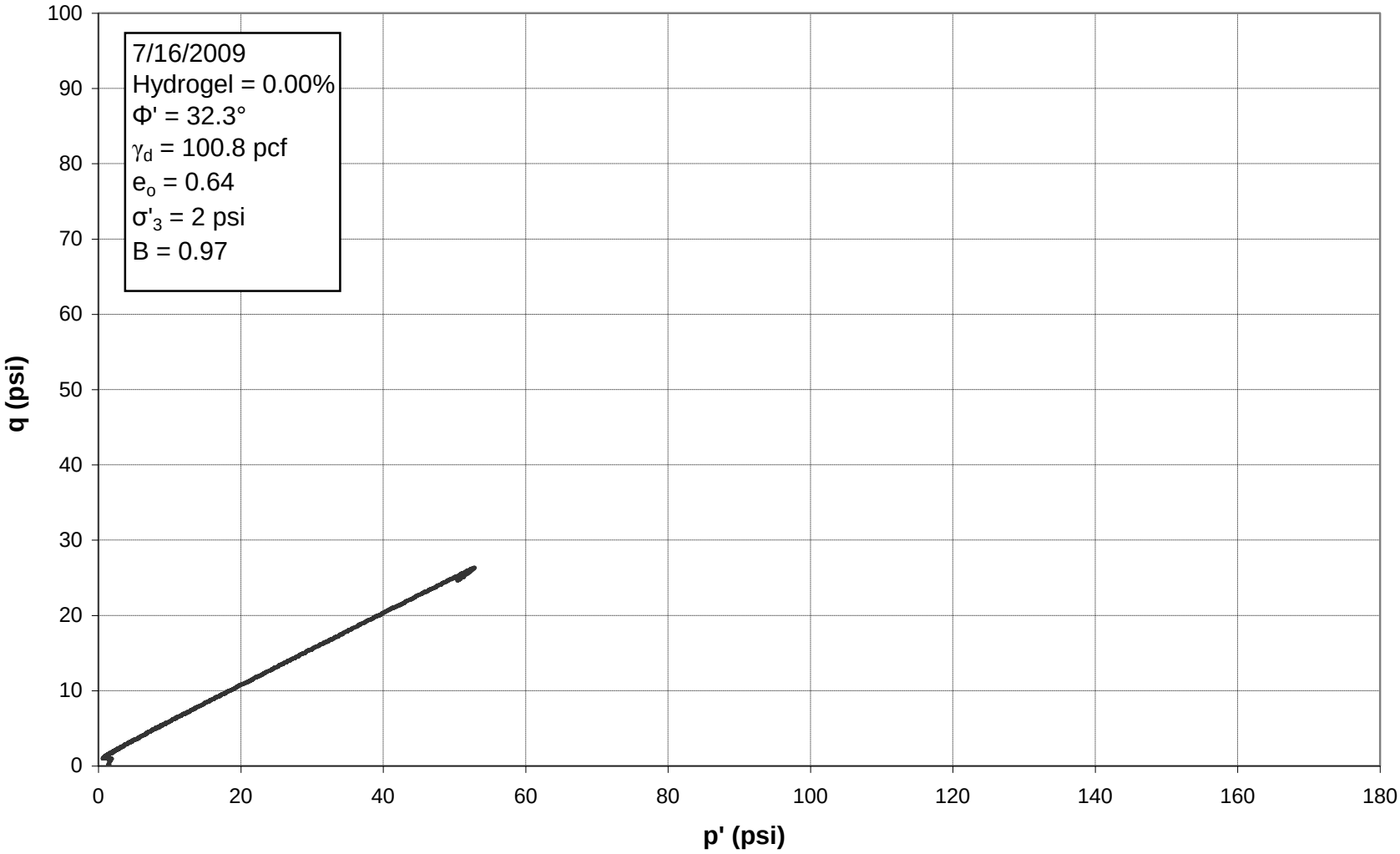

Figure E.41: p'-q Diagram for Triaxial Test 21, 0.00% Hydrogel

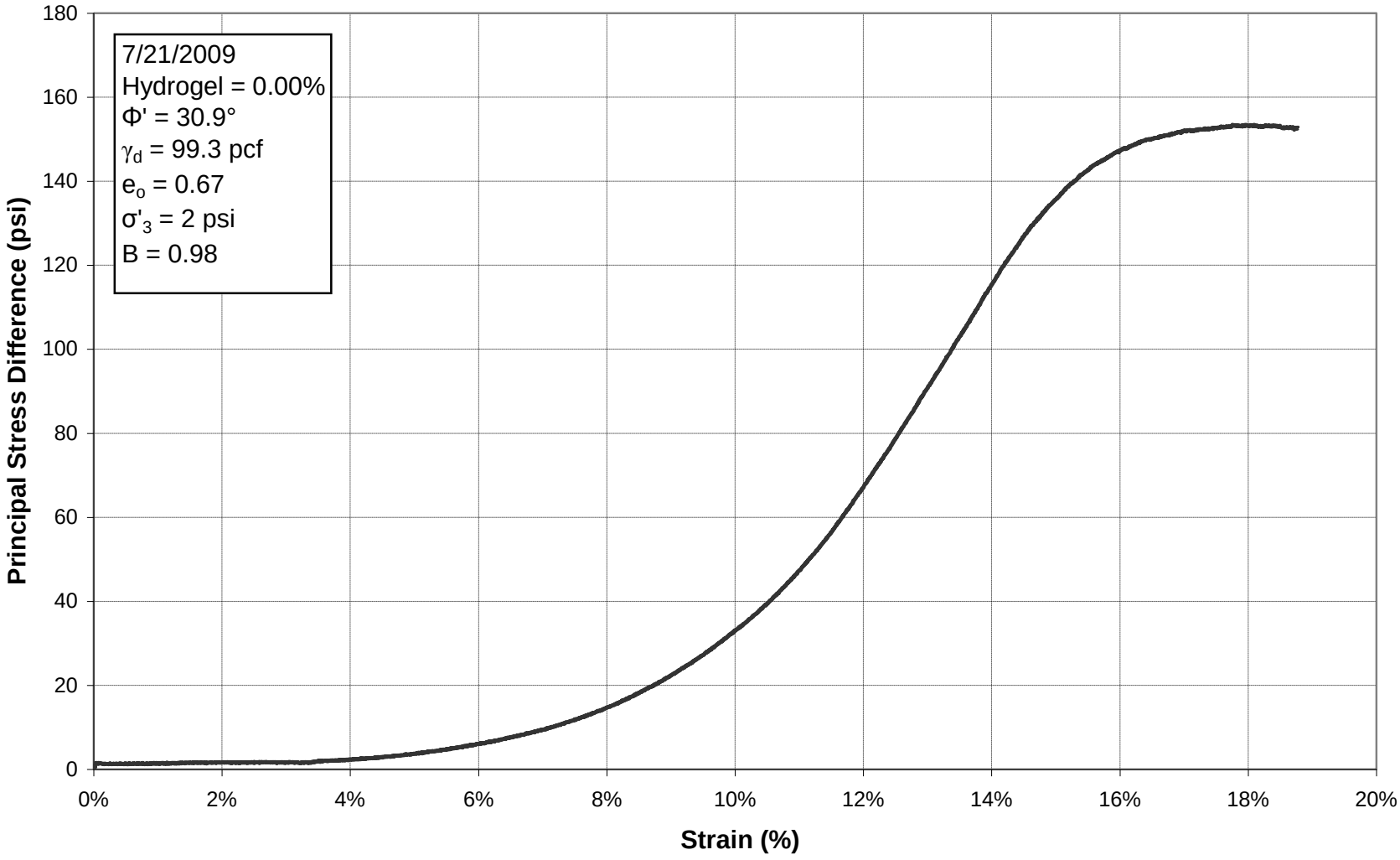

Figure E.42: Principal Stress Difference vs. Strain for Triaxial Test 22, 0.00% Hydrogel

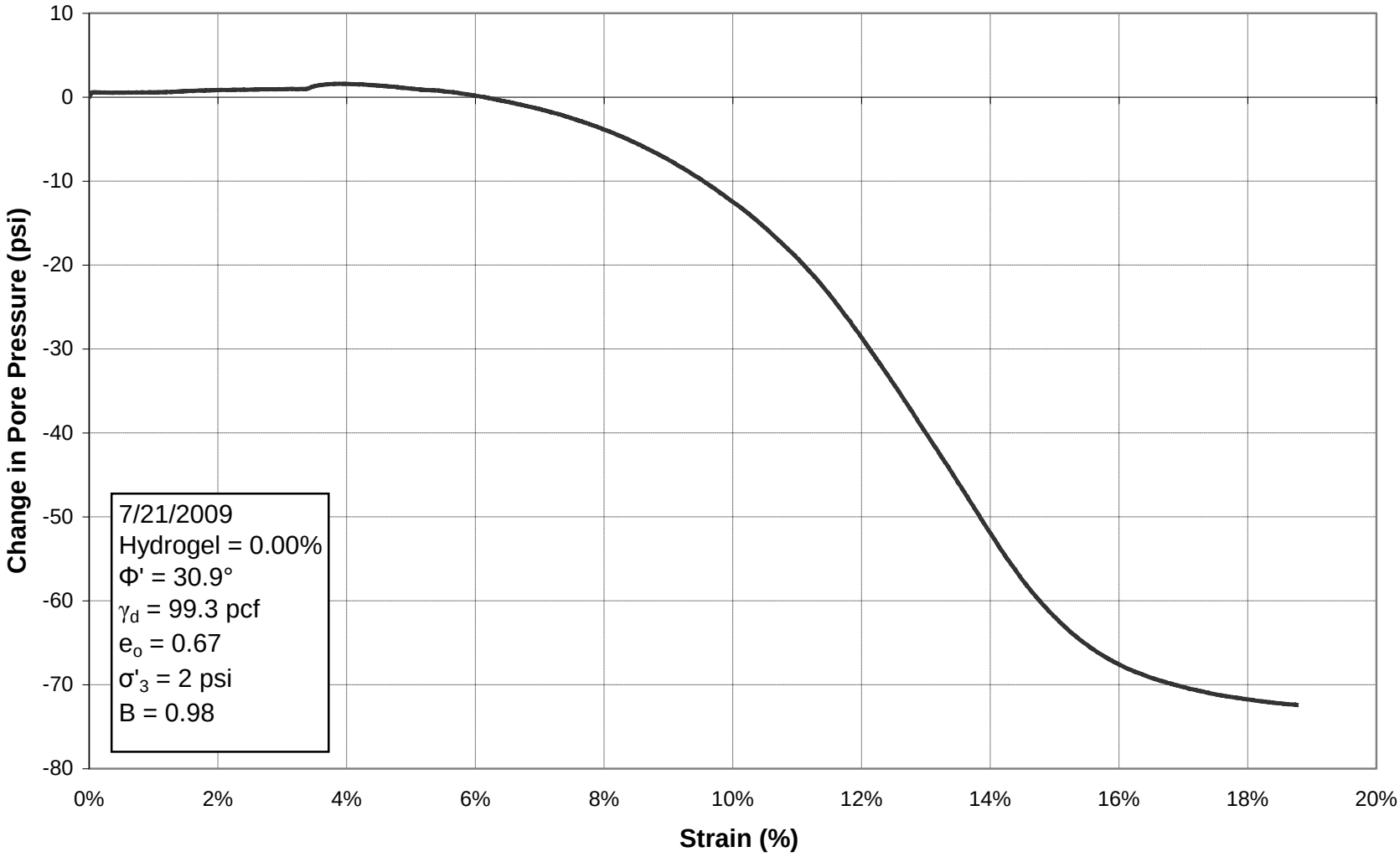

Figure E.43: Change in Pore Pressure vs. Strain for Triaxial Test 22, 0.00% Hydrogel

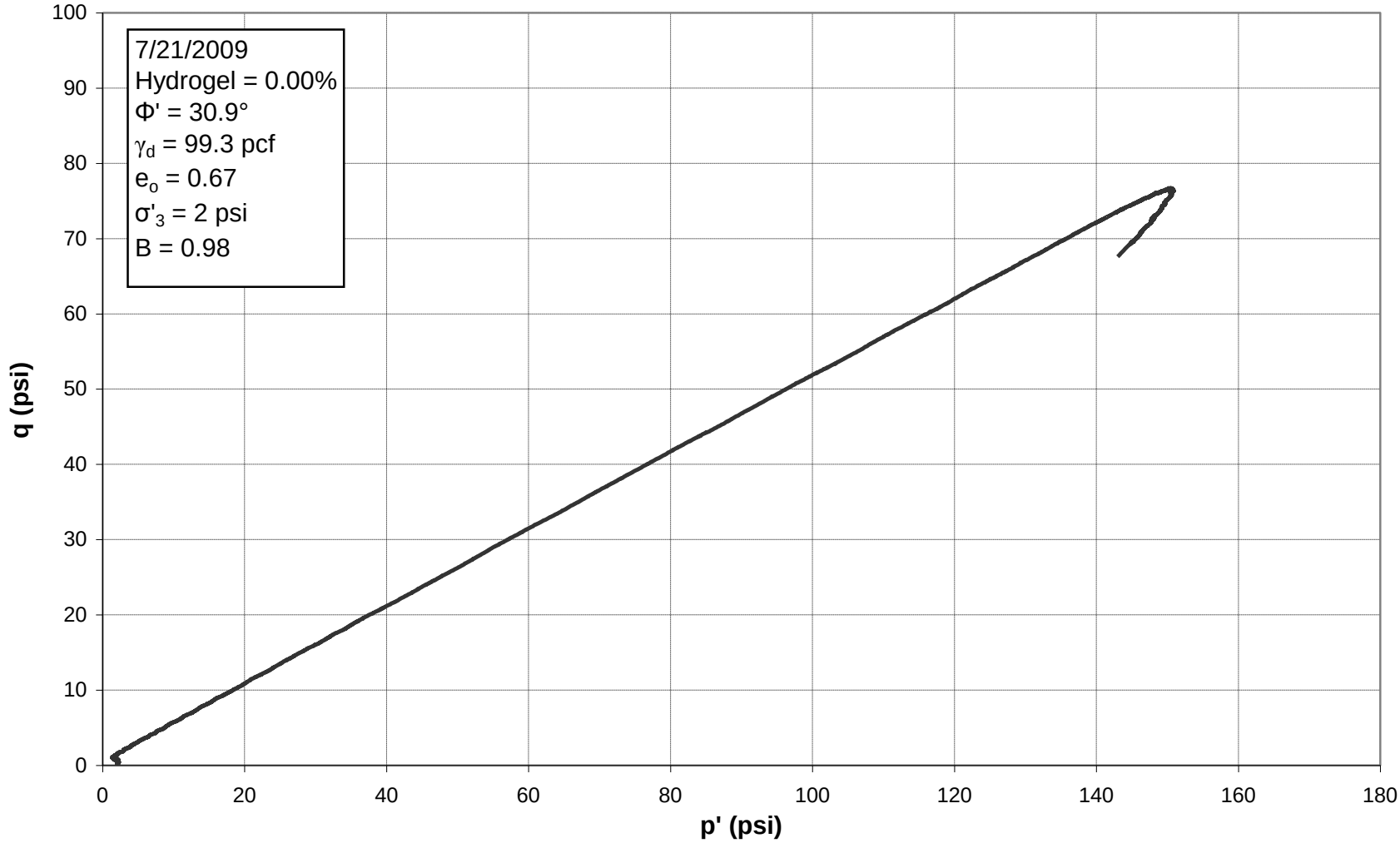

Figure E.44: p'-q Diagram for Triaxial Test 22, 0.00% Hydrogel

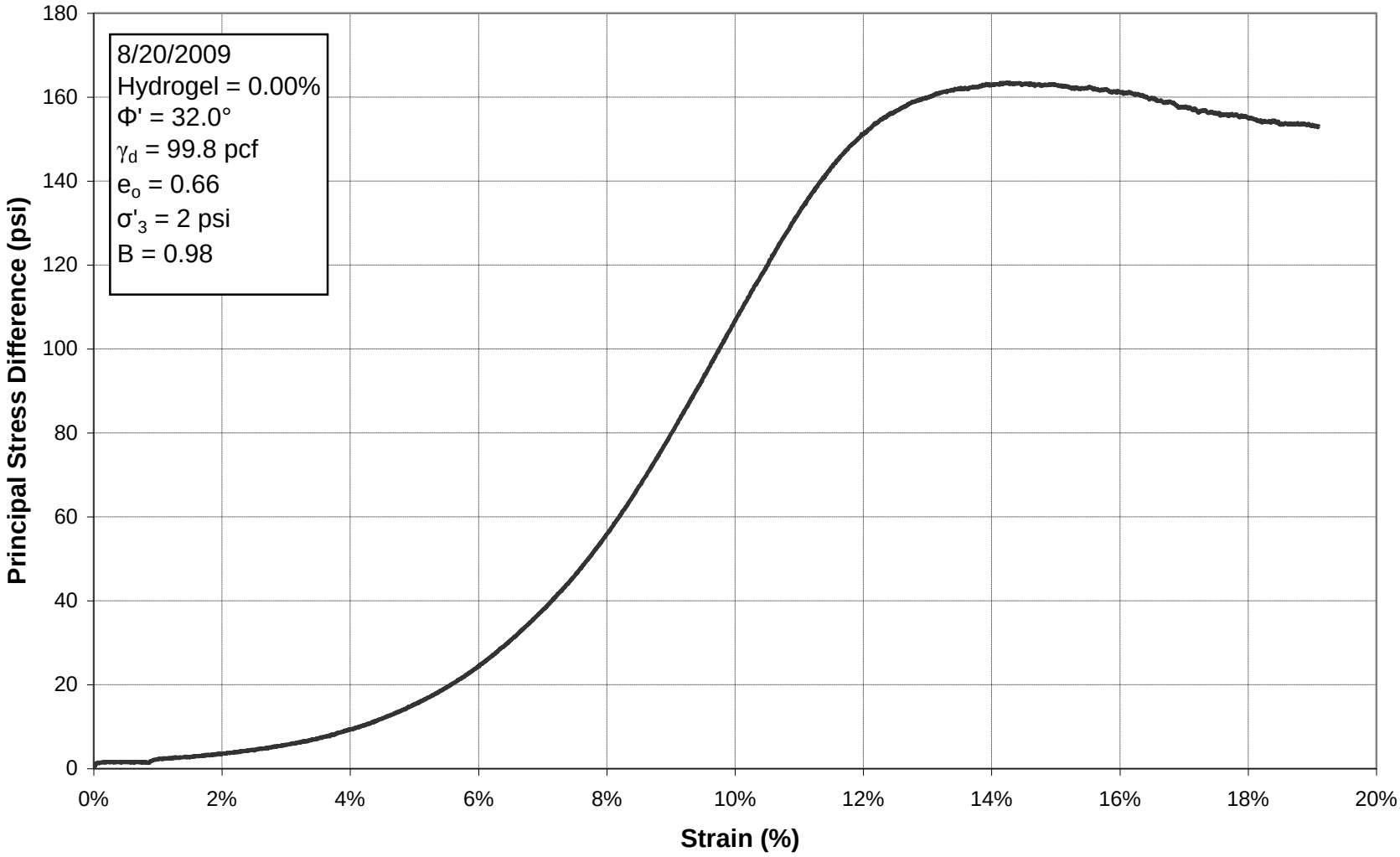

Figure E.45: Principal Stress Difference vs. Strain for Triaxial Test 23, 0.00% Hydrogel

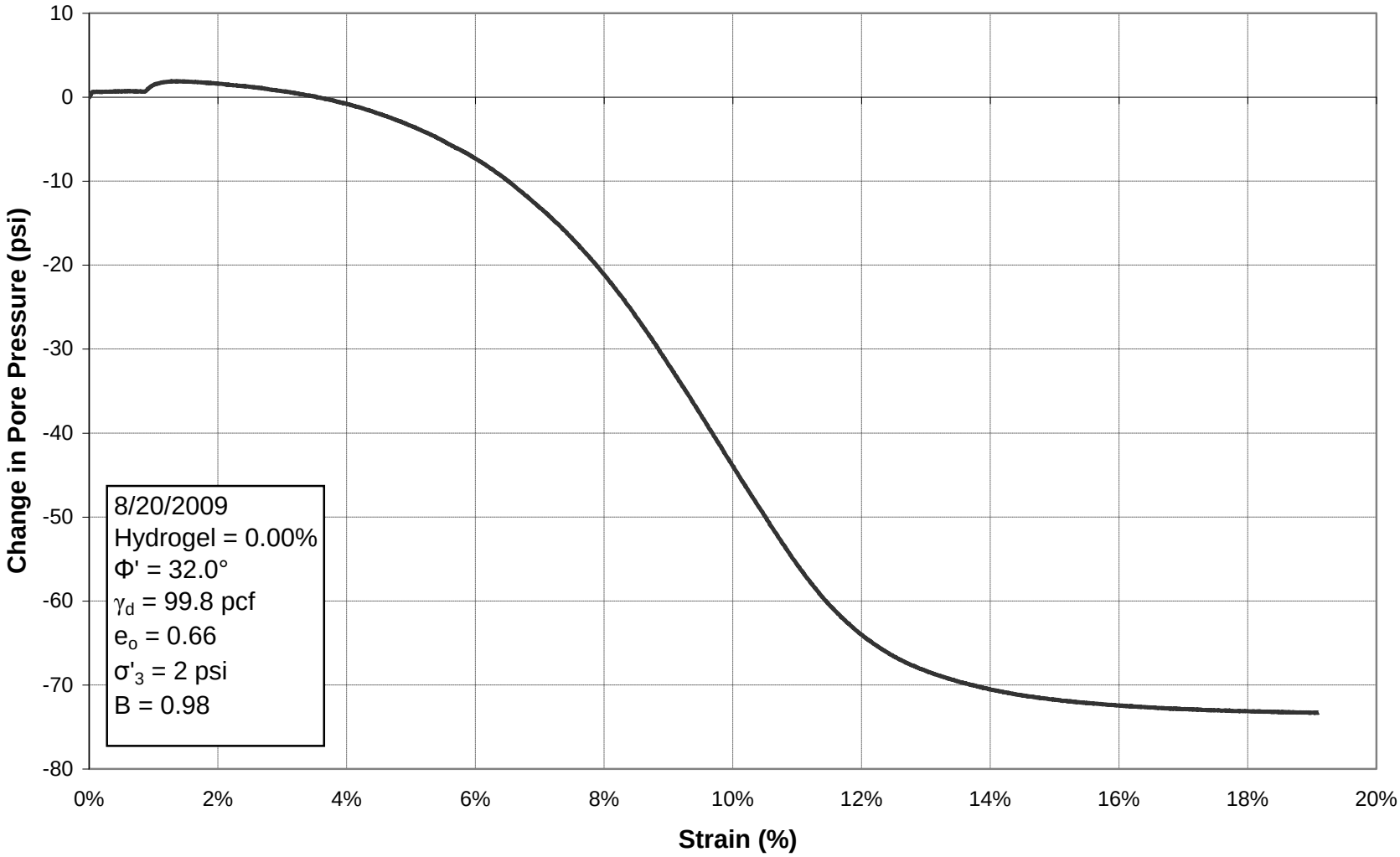

Figure E.46: Change in Pore Pressure vs. Strain for Triaxial Test 23, 0.00% Hydrogel

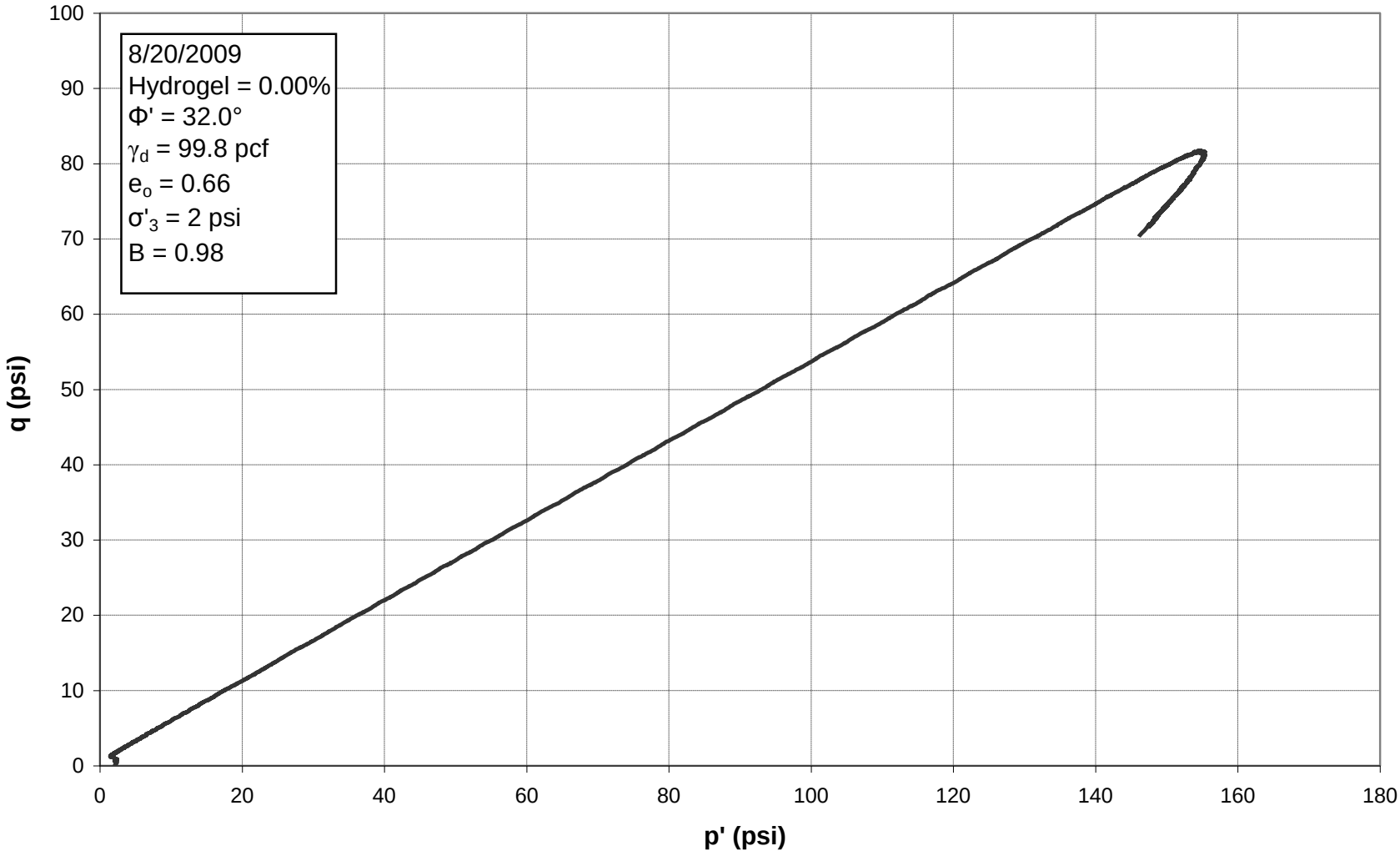

Figure E.47: p'-q Diagram for Triaxial Test 23, 0.00% Hydrogel

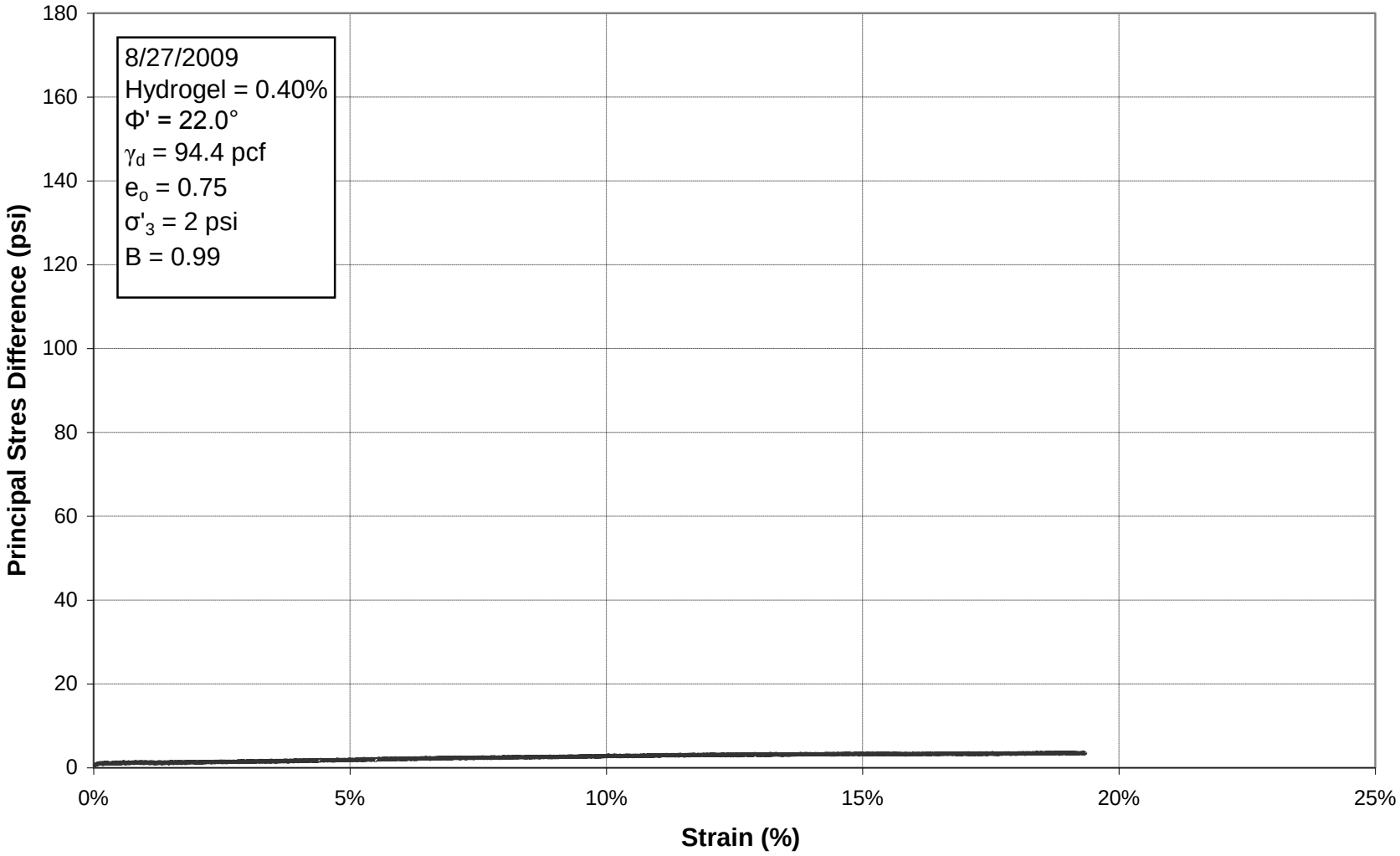

Figure E.48: Principal Stress Difference vs. Strain for Triaxial Test 24, 0.40% Hydrogel

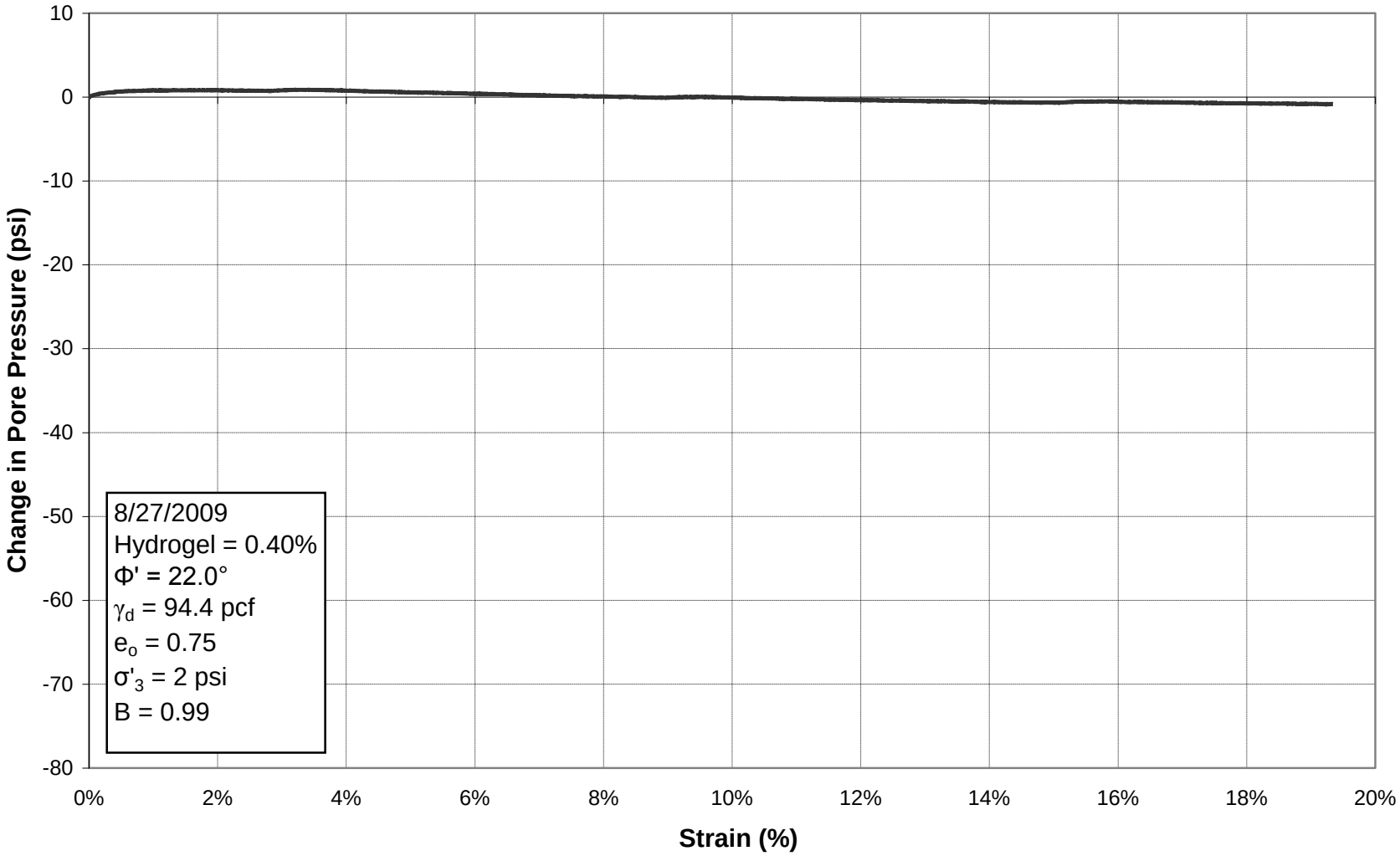

Figure E.49: Change in Pore Pressure vs. Strain for Triaxial Test 24, 0.40% Hydrogel

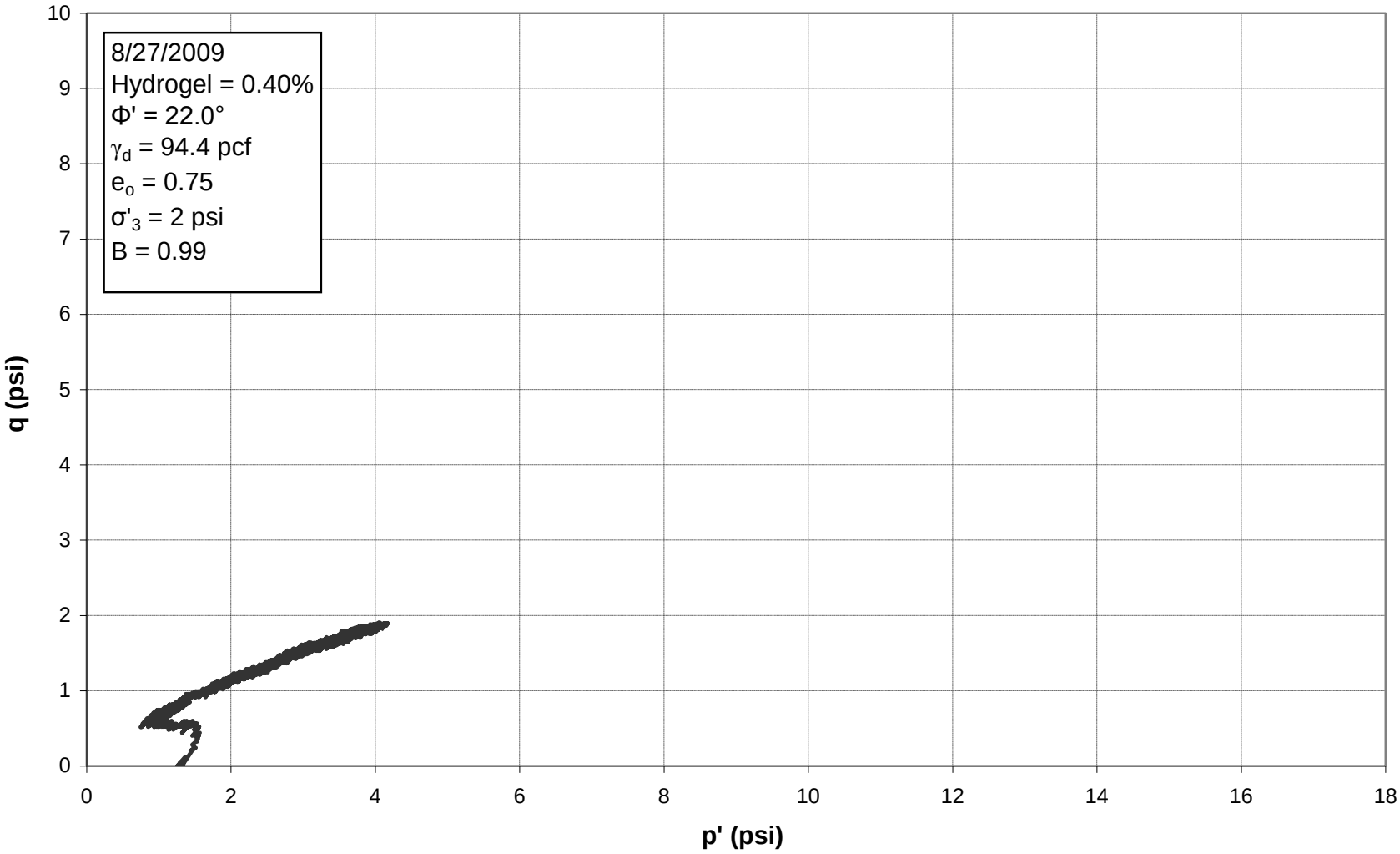

Figure E.50: p'-q Diagram for Triaxial Test 24, 0.40% Hydrogel (the axes have been scaled down by a factor of ten compared to the other p'-q diagrams to better show the data)

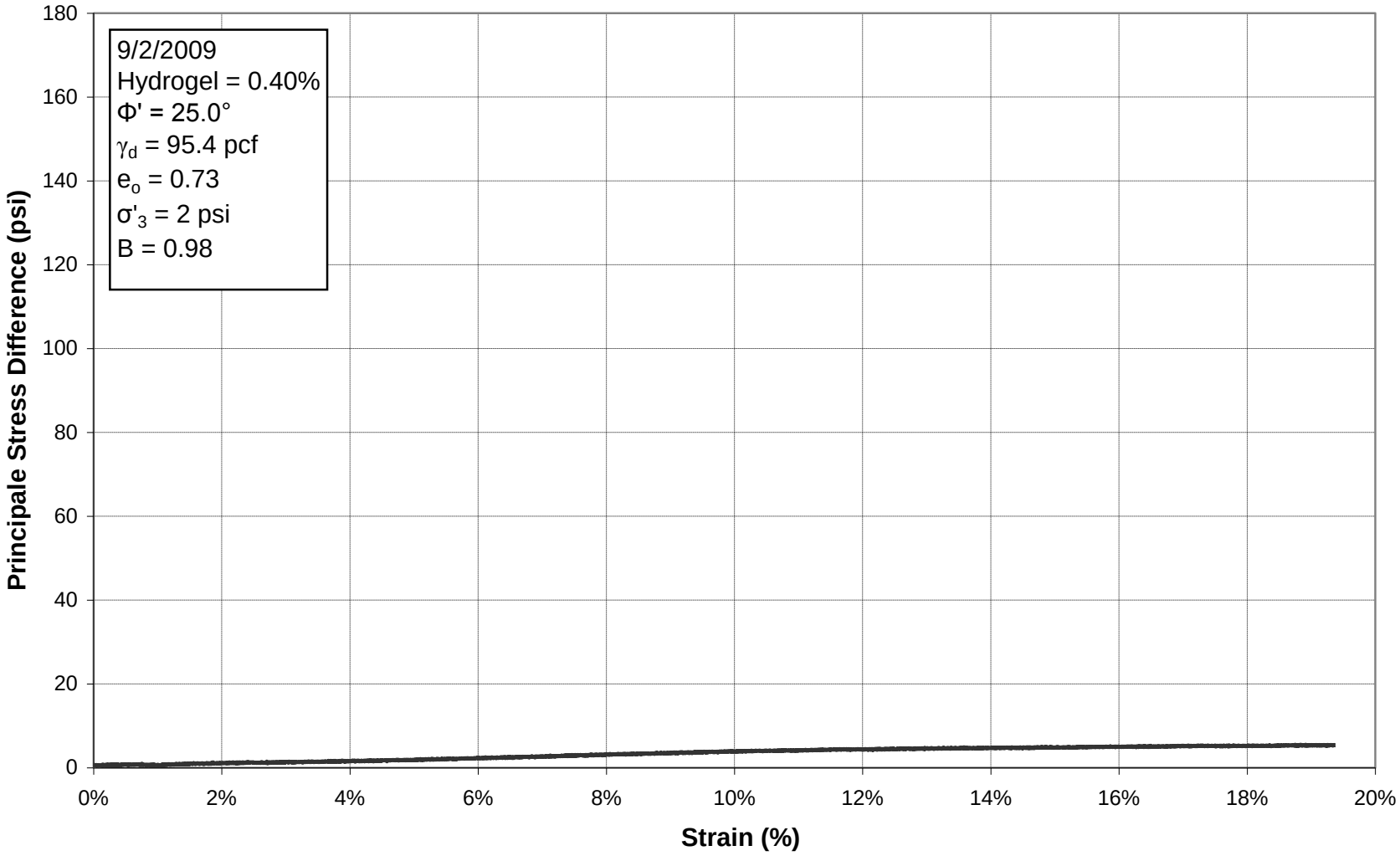

Figure E.51: Principal Stress Difference vs. Strain for Triaxial Test 25, 0.40% Hydrogel

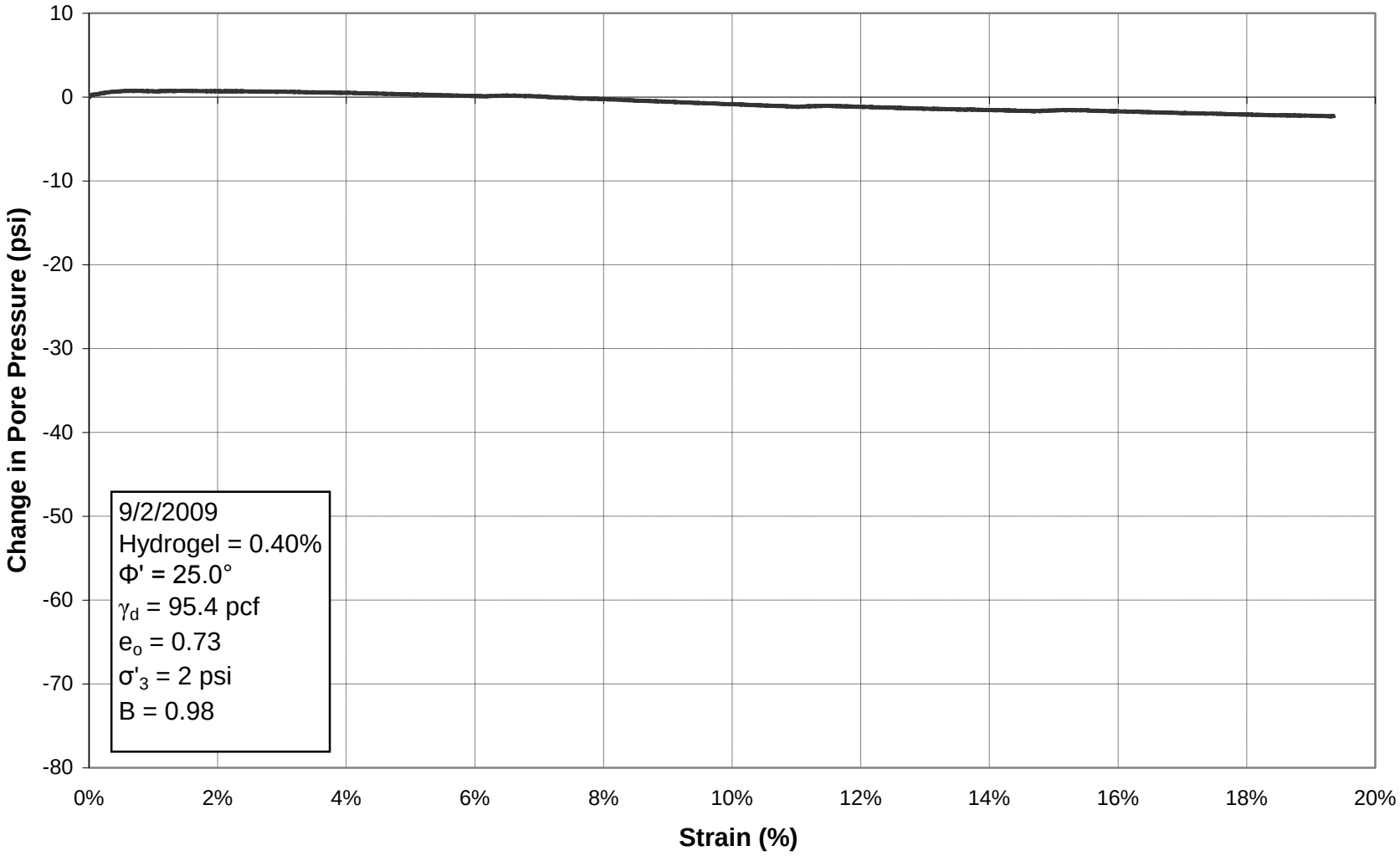

Figure E.52: Change in Pore Pressure vs. Strain for Triaxial Test 25, 0.40% Hydrogel

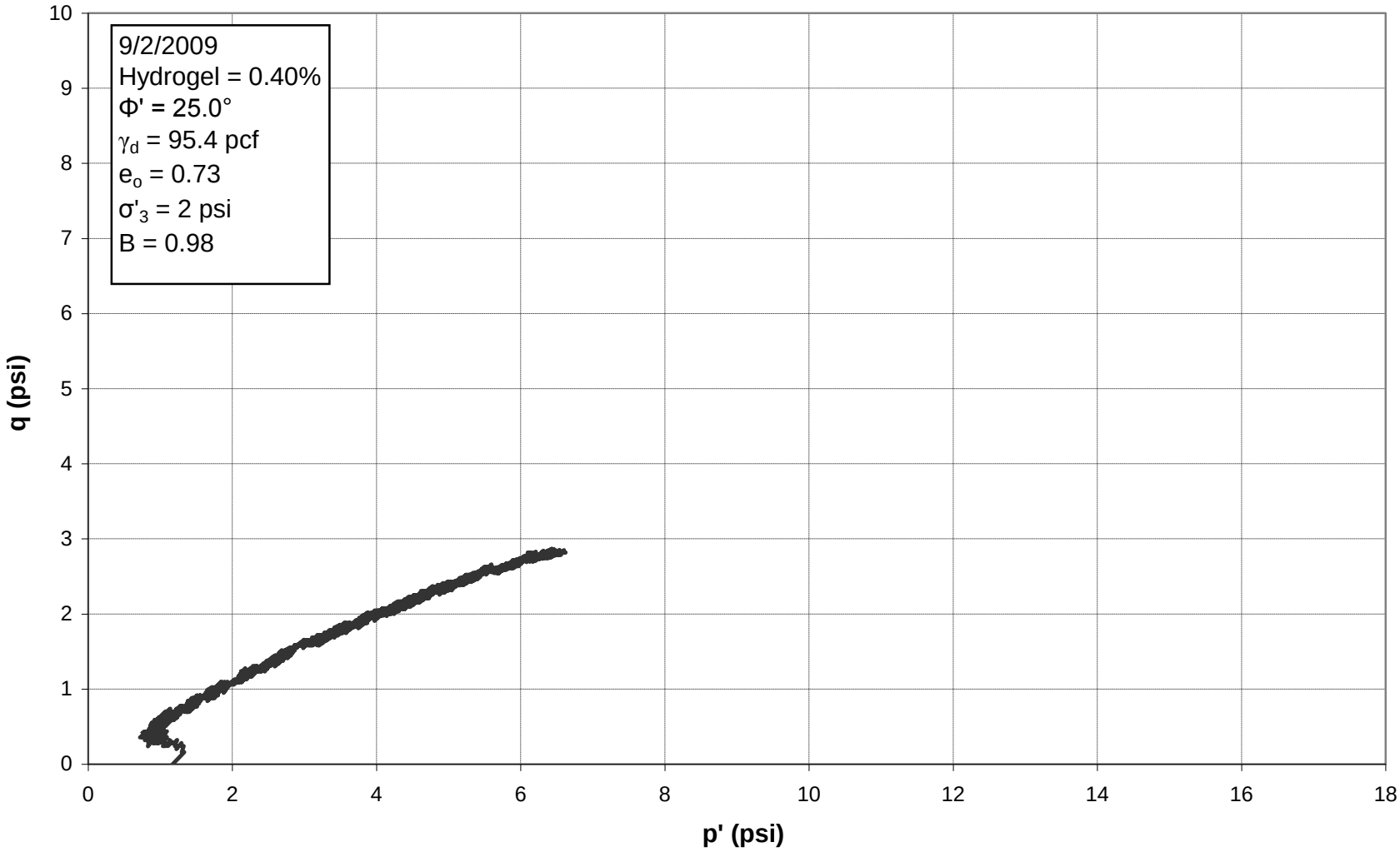

Figure E.53: p'-q Diagram for Triaxial Test 25, 0.40% Hydrogel (the axes have been scaled down by a factor of ten compared to the other p'-q diagrams to better show the data)

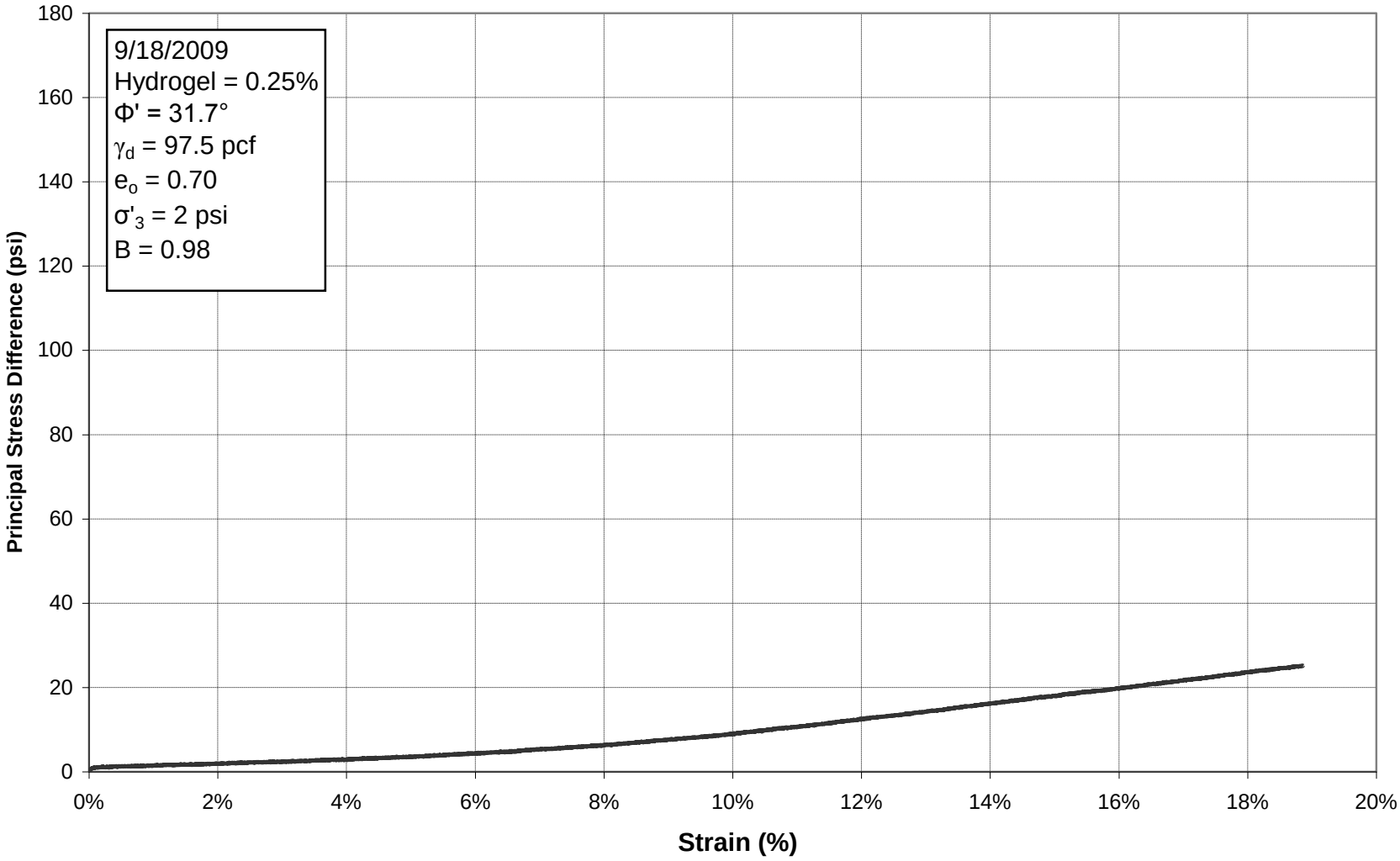

Figure E.54: Principal Stress Difference vs. Strain for Triaxial Test 26, 0.25% Hydrogel

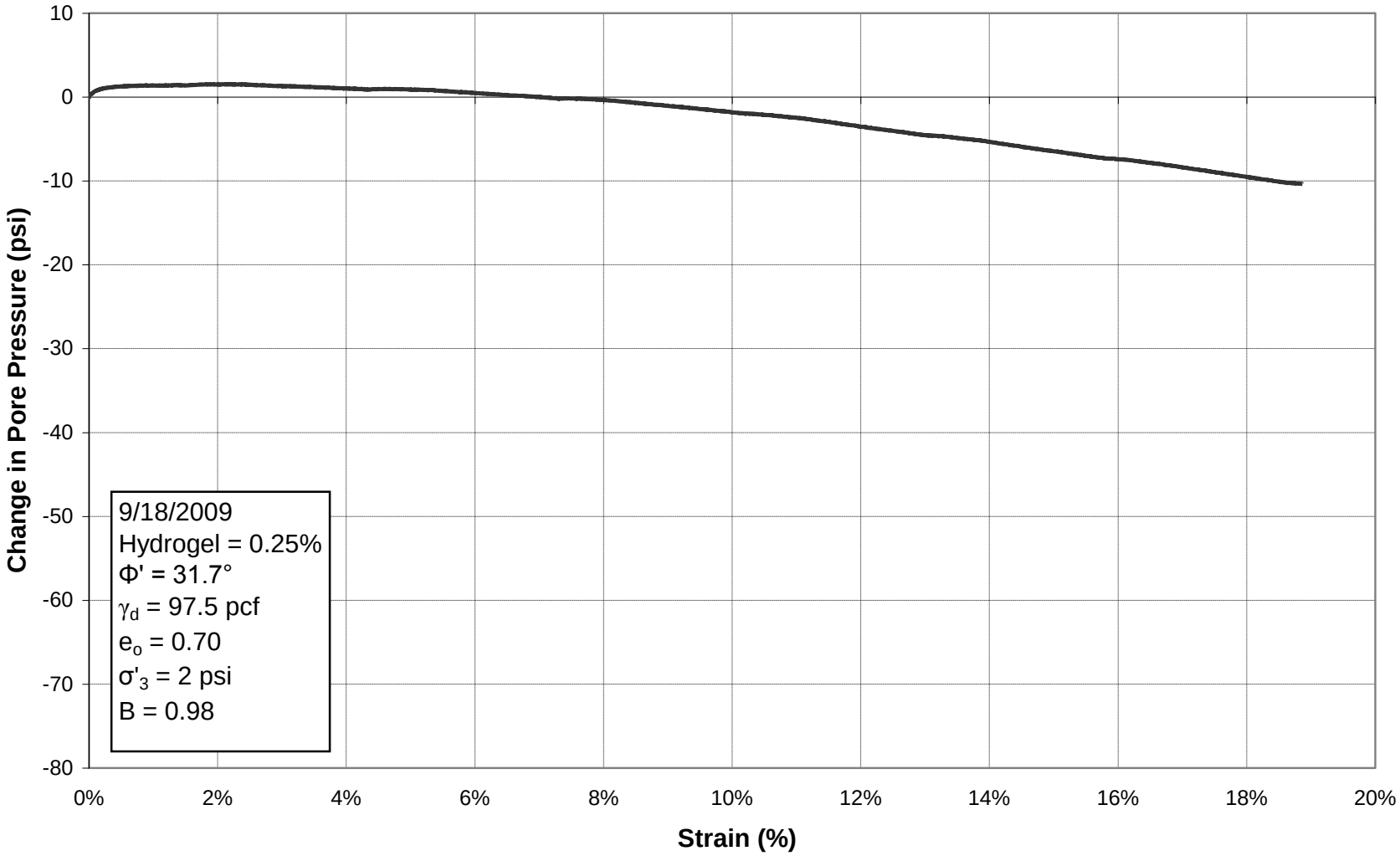

Figure E.55: Change in Pore Pressure vs. Strain for Triaxial Test 26, 0.25% Hydrogel

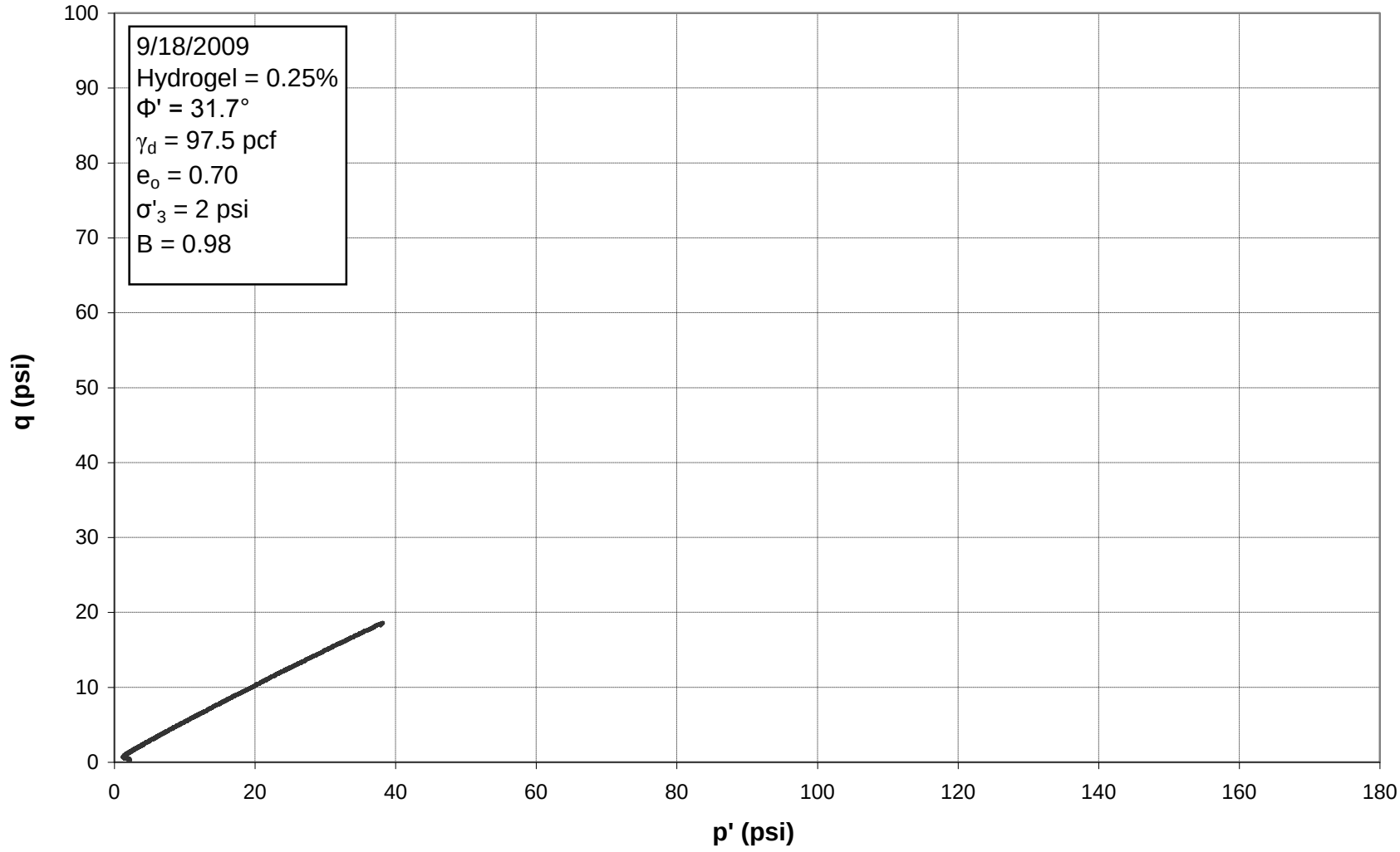

Figure E.56: p'-q Diagram for Triaxial Test 26, 0.25% Hydrogel

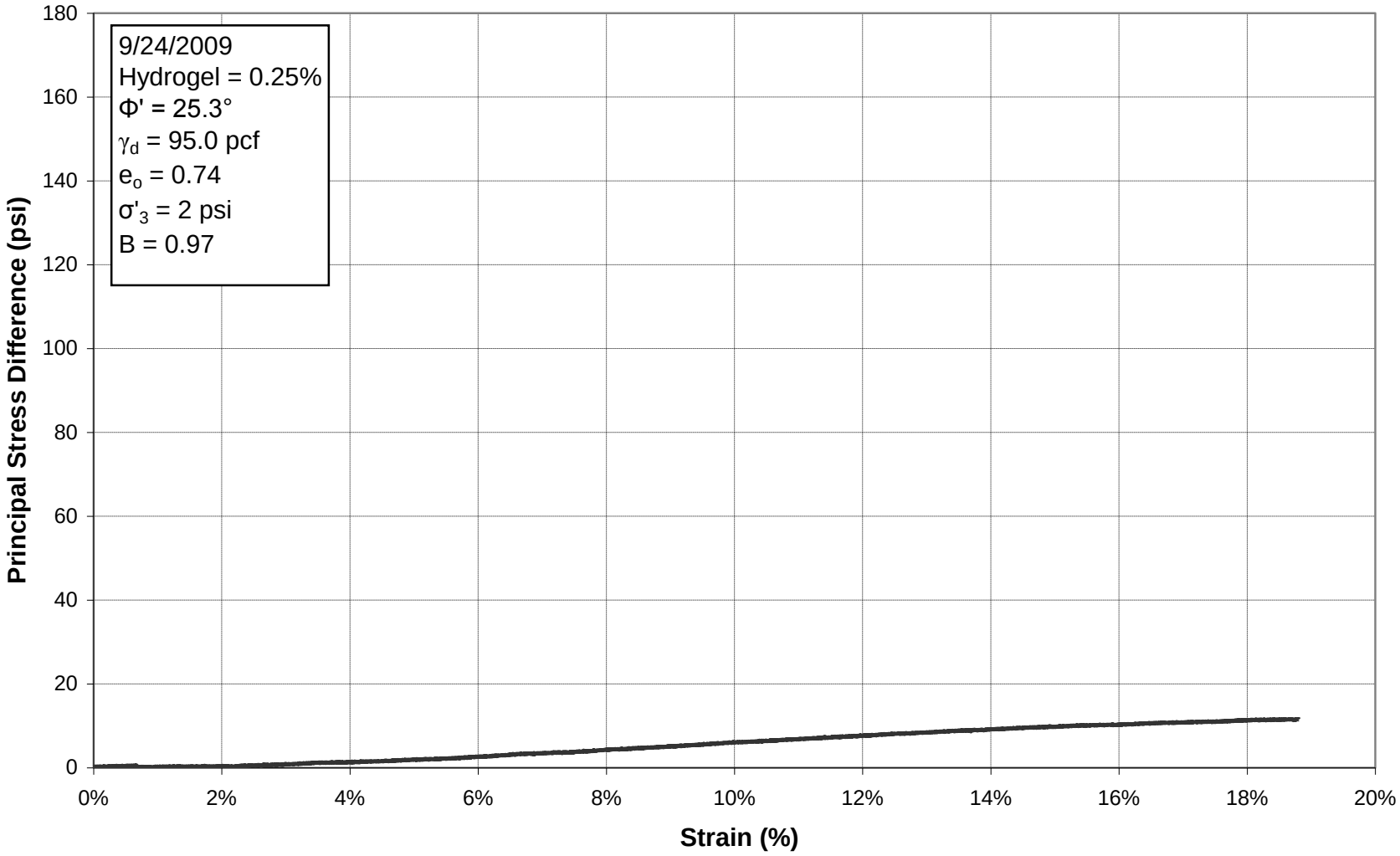

Figure E.57: Principal Stress Difference vs. Strain for Triaxial Test 27, 0.25% Hydrogel

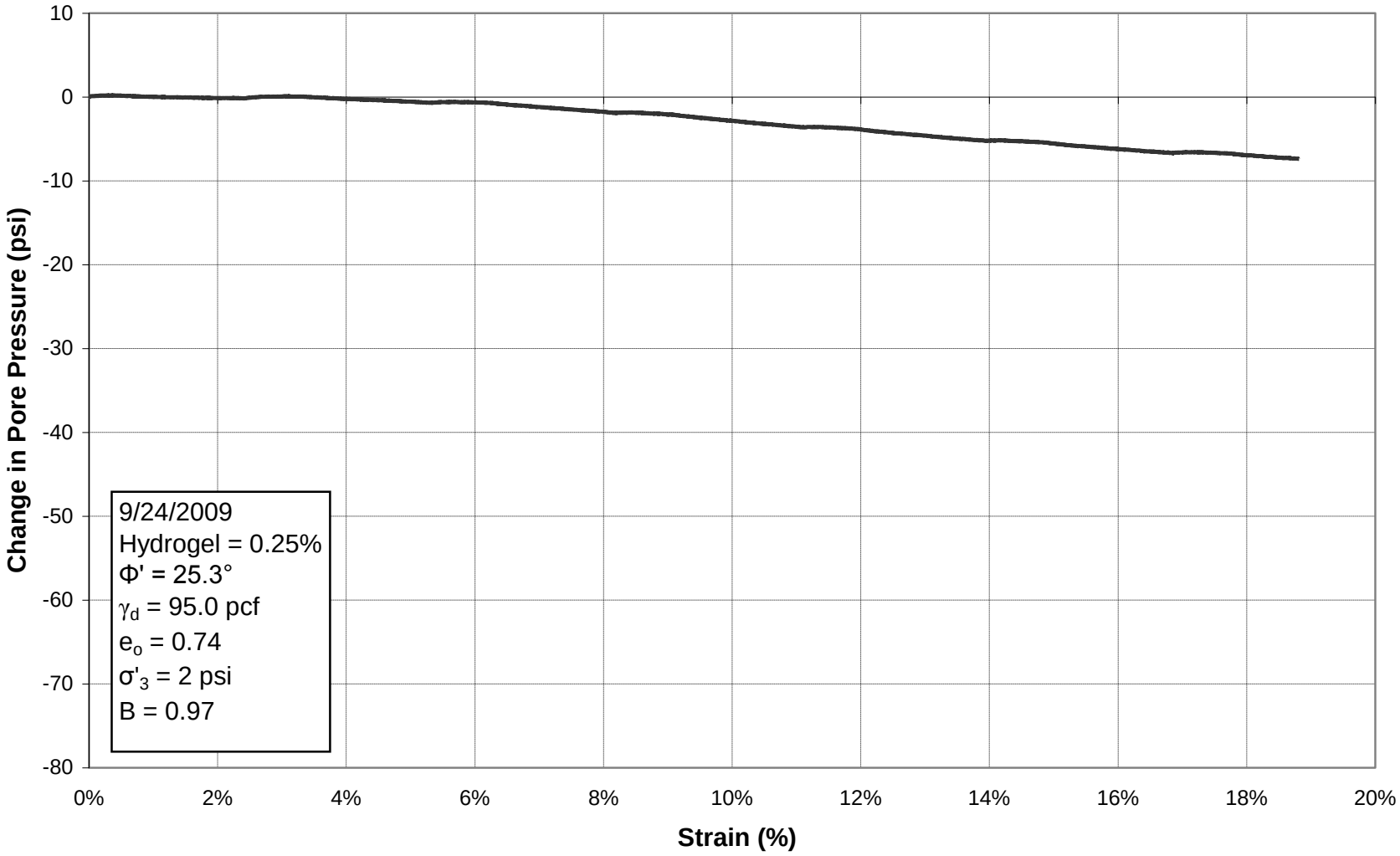

Figure E.58: Change in Pore Pressure vs. Strain for Triaxial Test 27, 0.25% Hydrogel

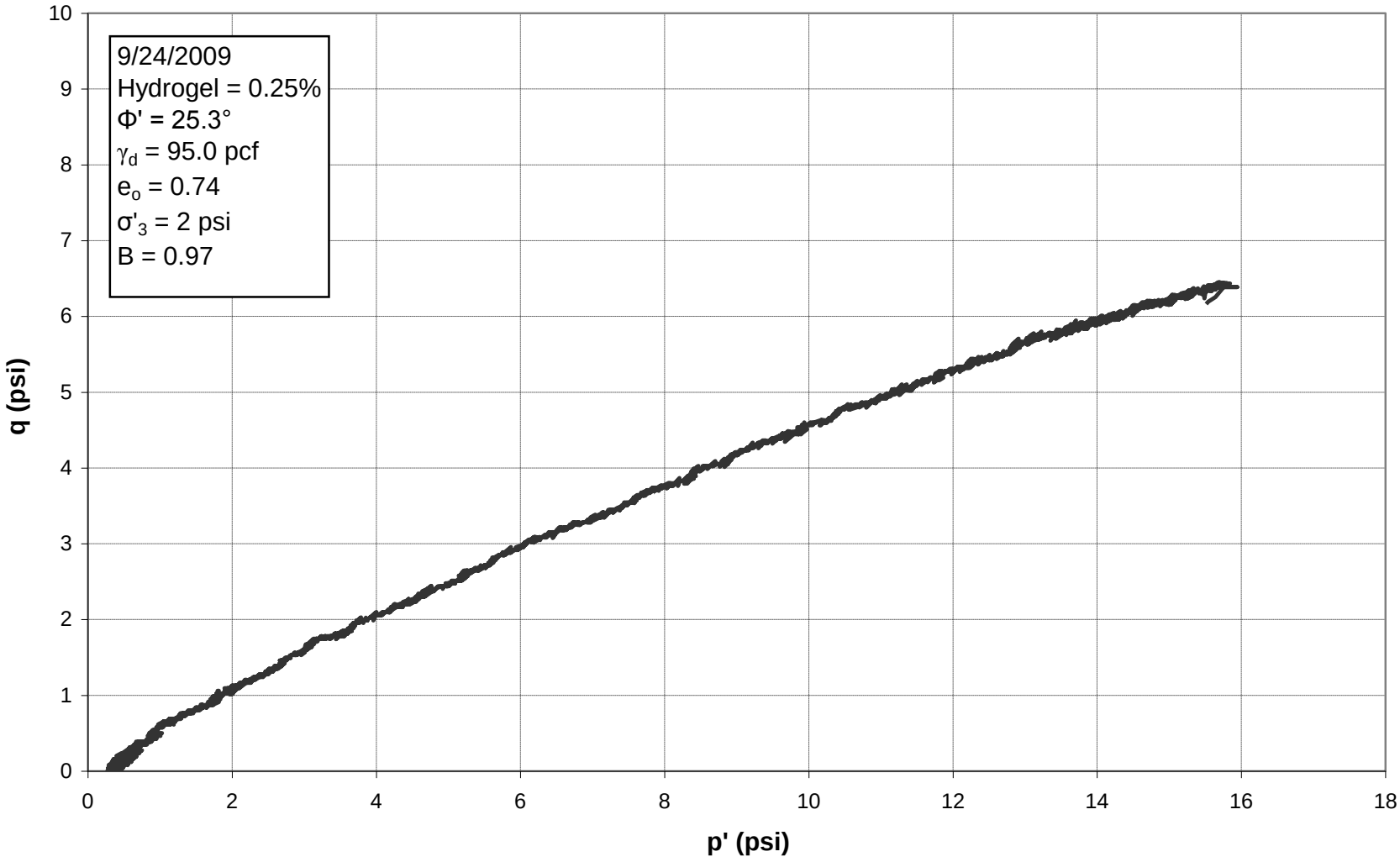

Figure E.59: p'-q Diagram for Triaxial Test 27, 0.25% Hydrogel (the axes have been scaled down by a factor of ten compared to the other p'-q diagrams to better show the data)

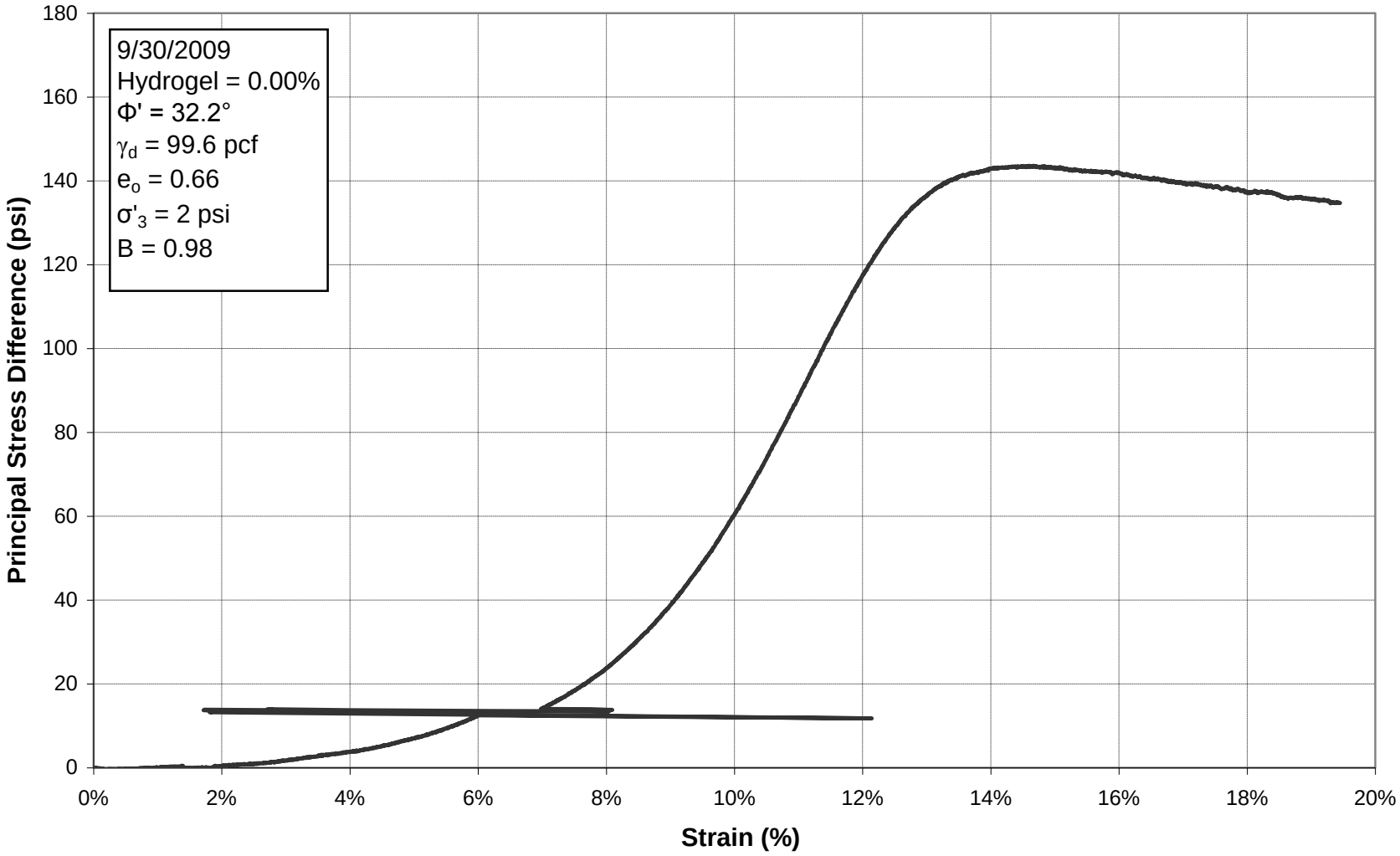

Figure E.60: Principal Stress Difference vs. Strain for Triaxial Test 28, 0.00% Hydrogel (The spike in the data is a result of the LVDT being adjusted during the test)

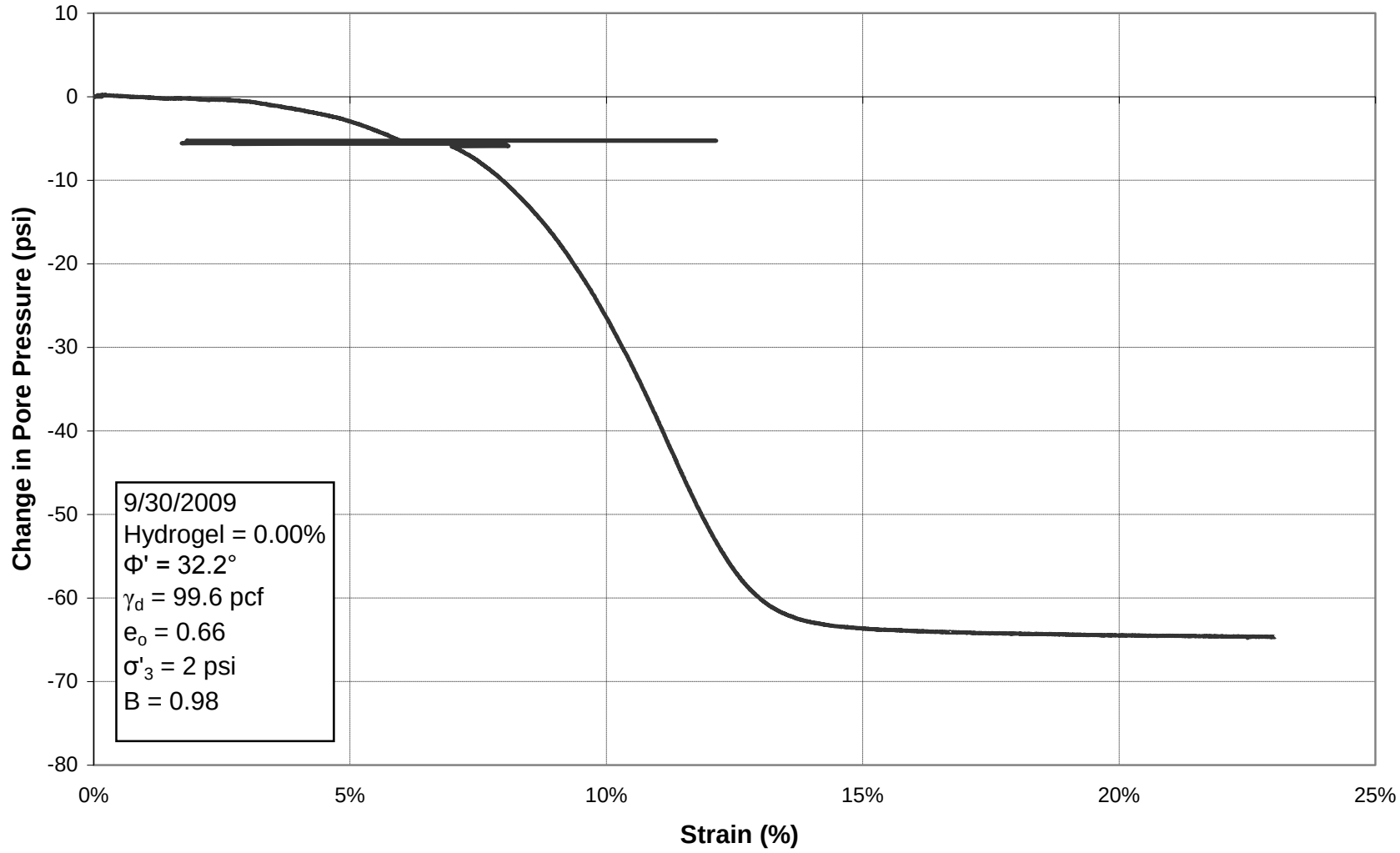

Figure E.61: Change in Pore Pressure vs. Strain for Triaxial Test 28, 0.00% Hydrogel (The spike in the data is a result of the LVDT being adjusted during the test)

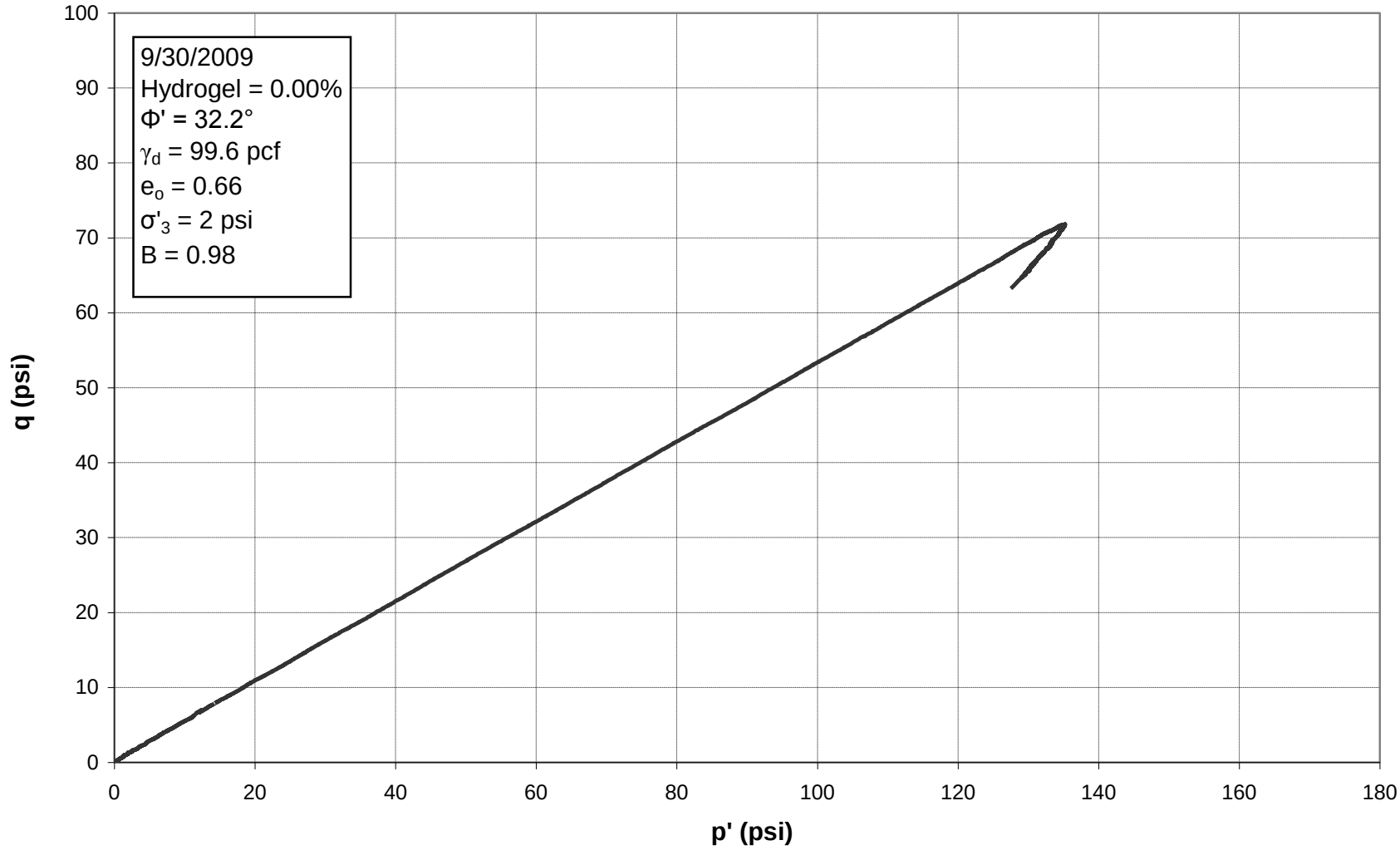

Figure E.62: p'-q Diagram for Triaxial Test 28, 0.00% Hydrogel

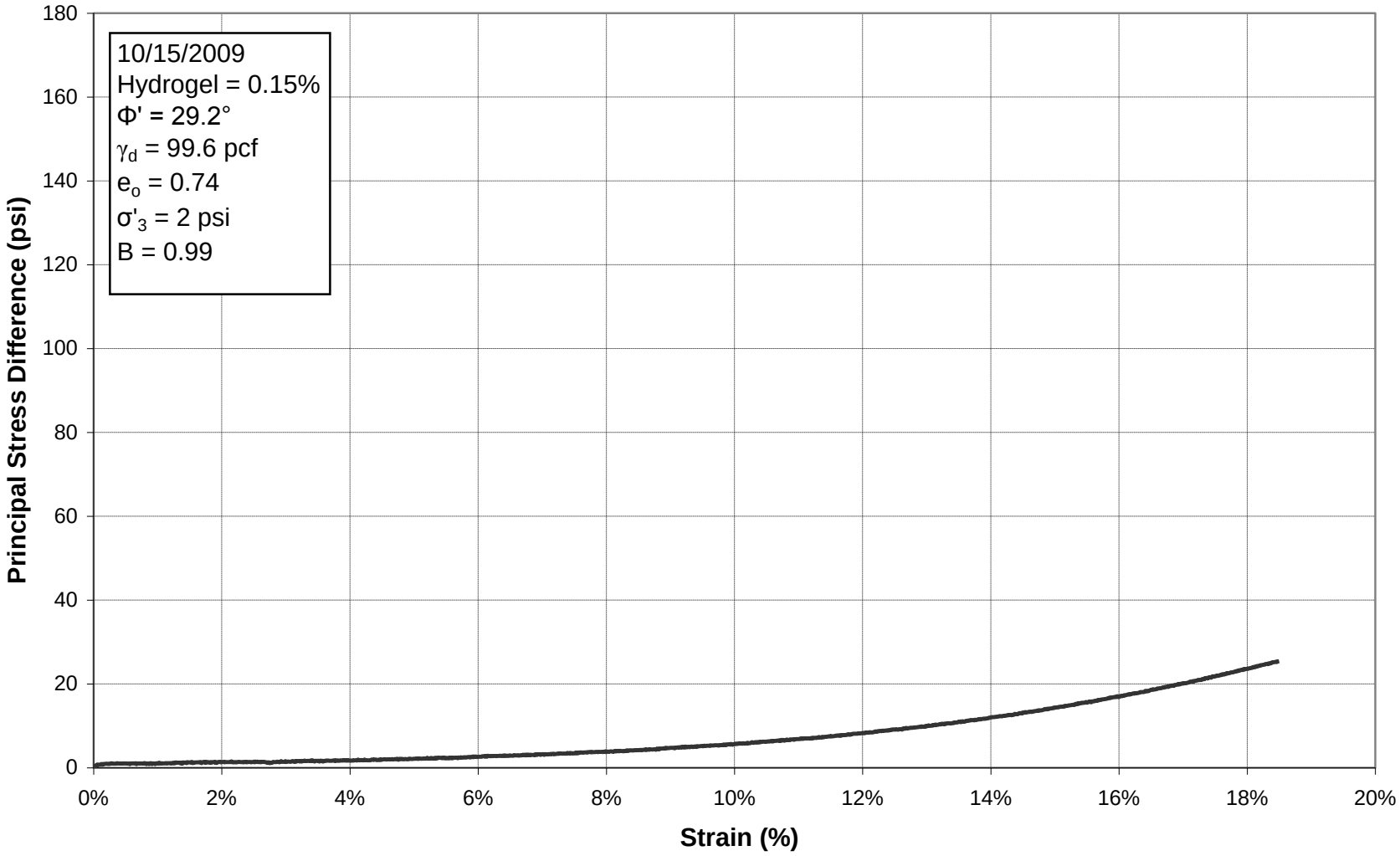

Figure E.63: Principal Stress Difference vs. Strain for Triaxial Test 29, 0.15% Hydrogel

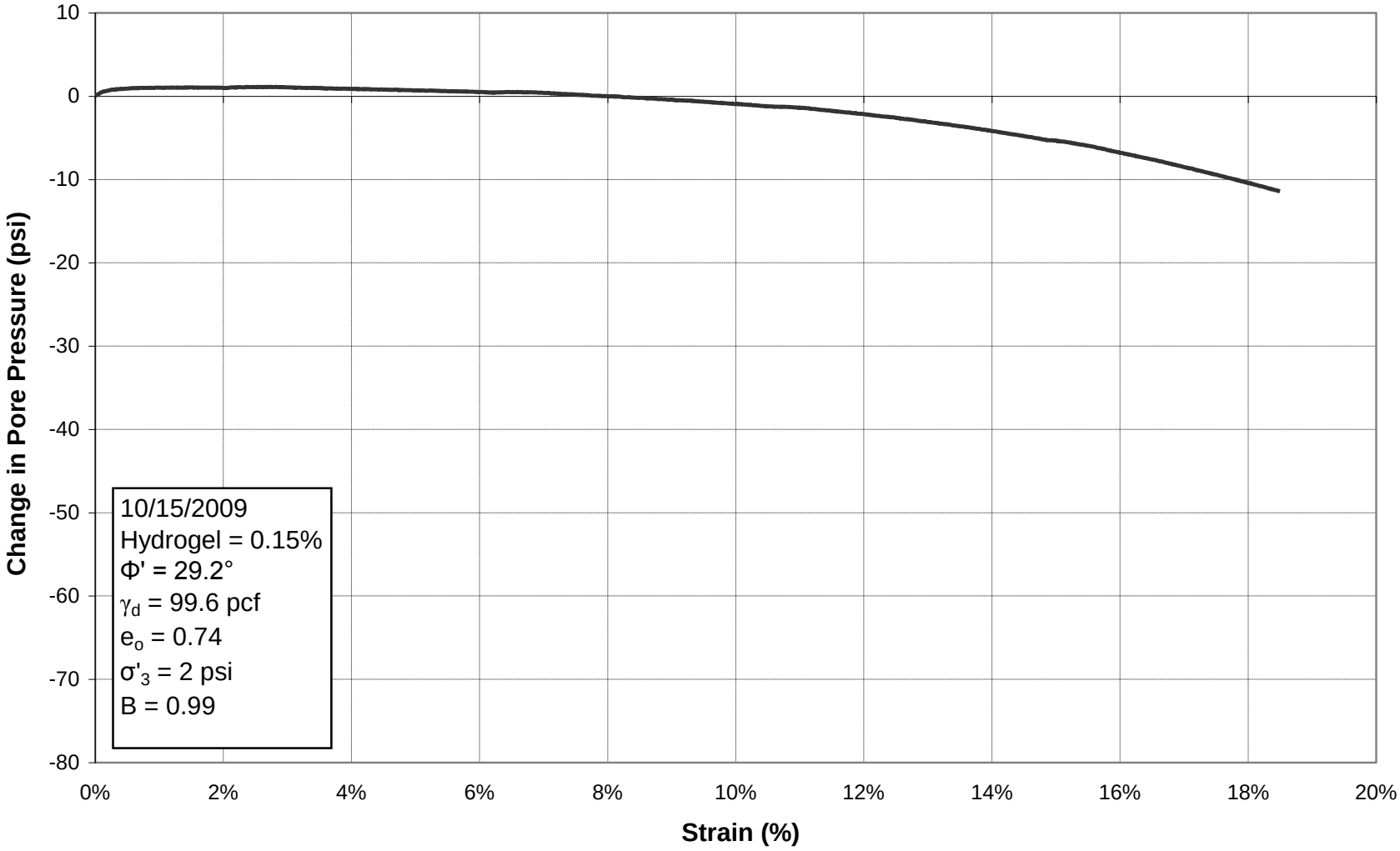

Figure E.64: Change in Pore Pressure vs. Strain for Triaxial Test 29, 0.15% Hydrogel

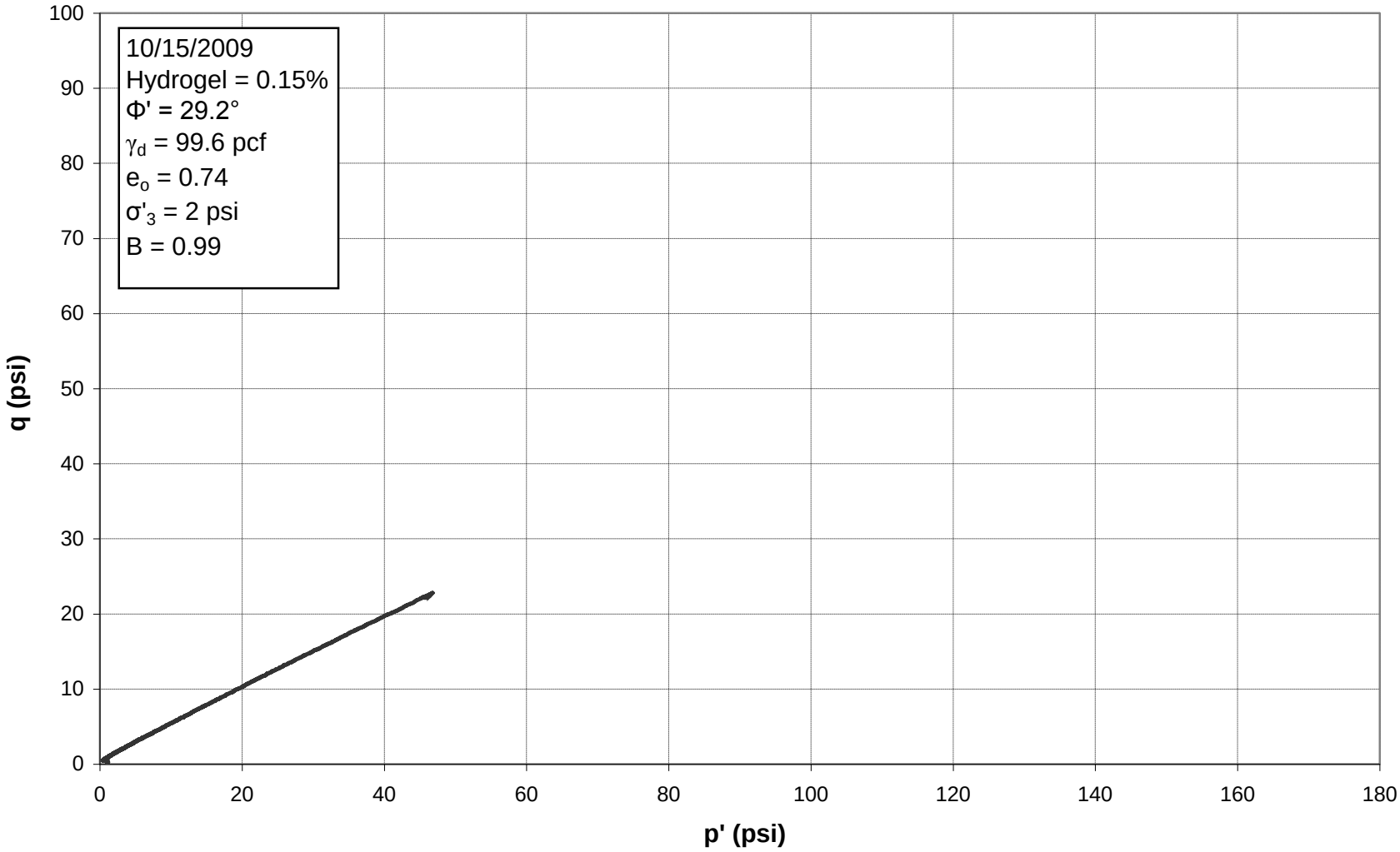

Figure E.65: p'-q Diagram for Triaxial Test 29, 0.15% Hydrogel

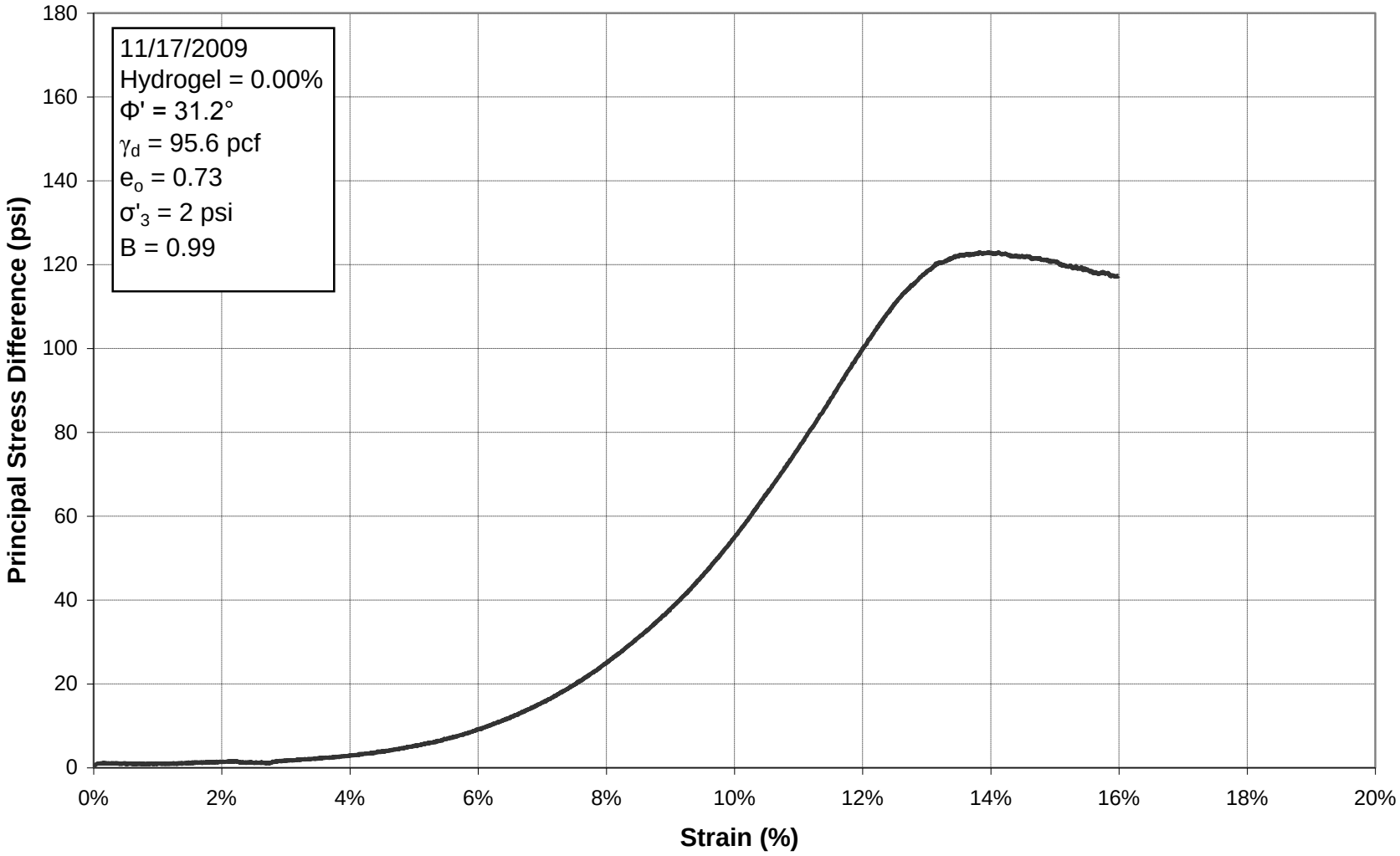

Figure E.66: Principal Stress Difference vs. Strain for Triaxial Test 33, 0.00% Hydrogel

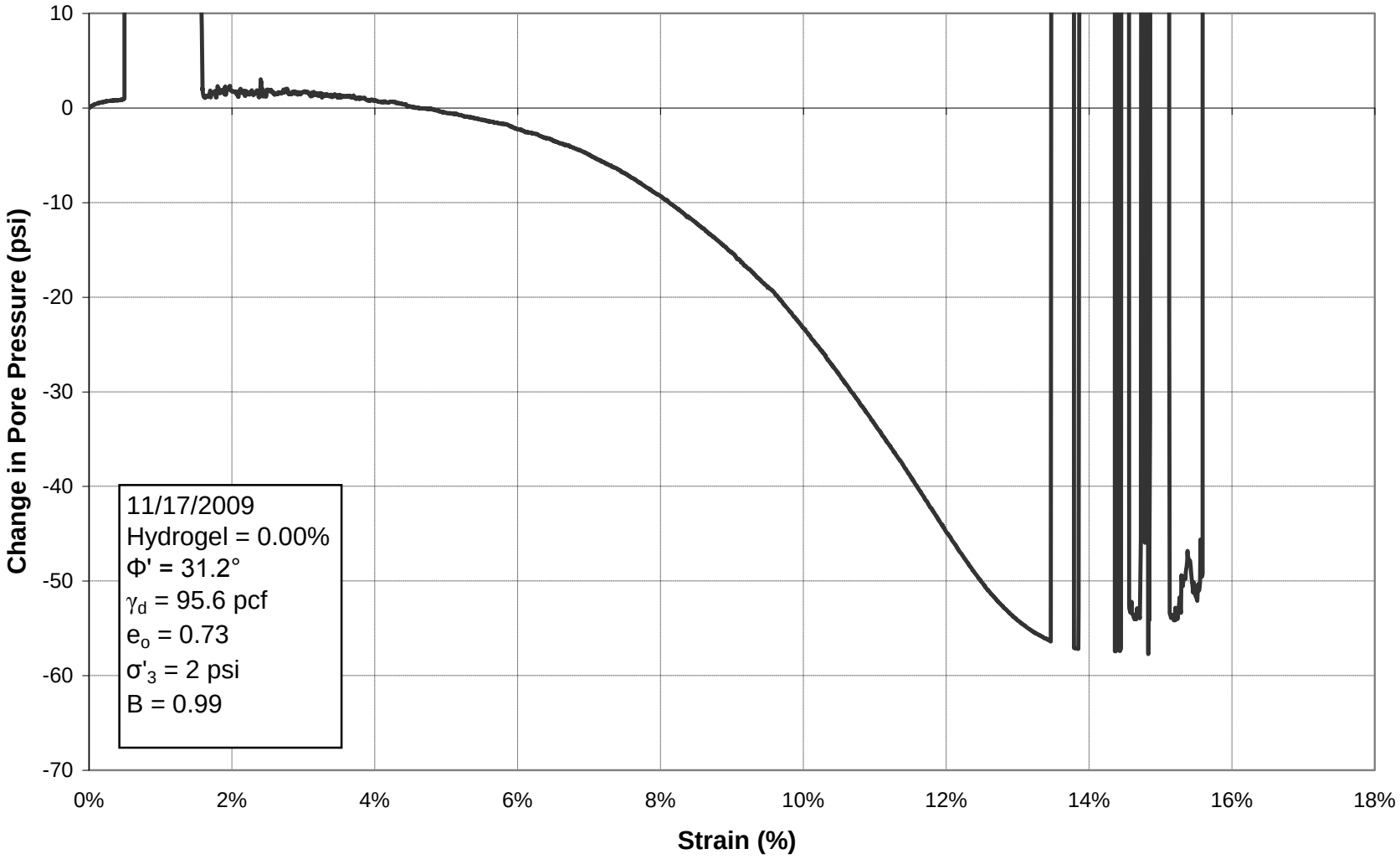

Figure E.67: Change in Pore Pressure vs. Strain for Triaxial Test 33, 0.00% Hydrogel (the spikes in the data are a result of a short in the pore pressure transducer wiring)

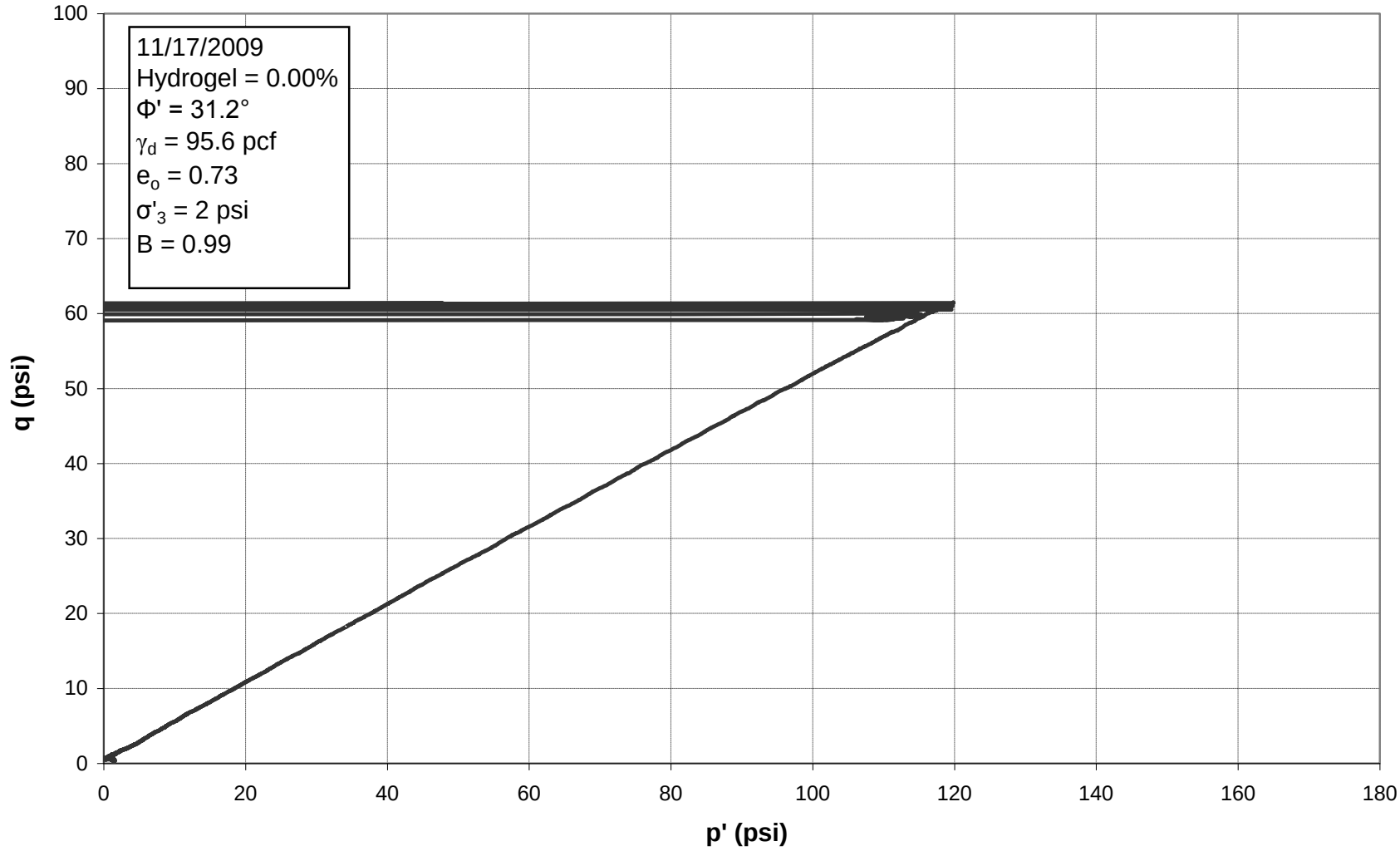

Figure E.68: p'-q Diagram for Triaxial Test 33, 0.00% Hydrogel (the spikes in the data are a result of a short in the pore pressure transducer wiring)

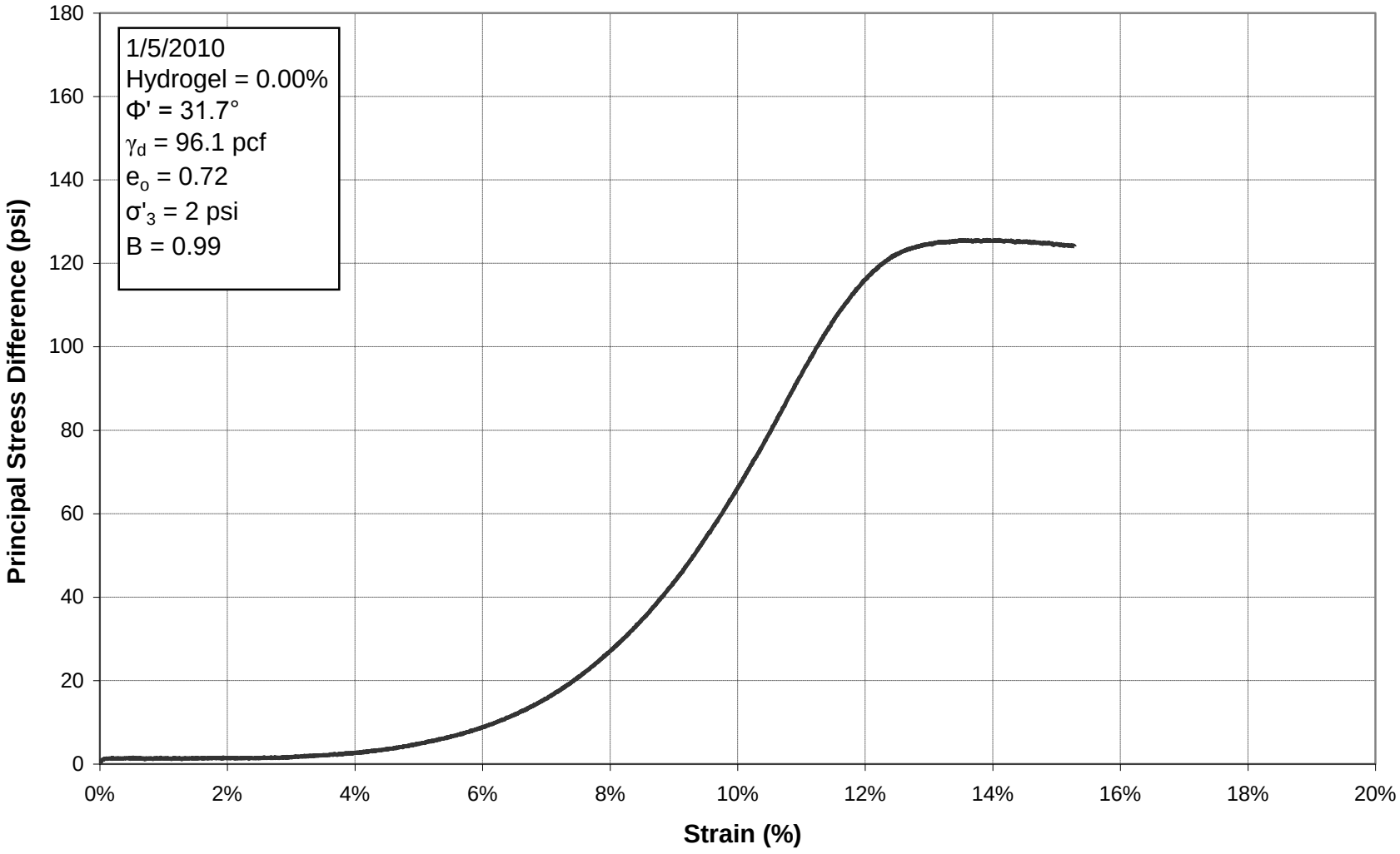

Figure E.69: Principal Stress Difference vs. Strain for Triaxial Test 38, 0.00% Hydrogel

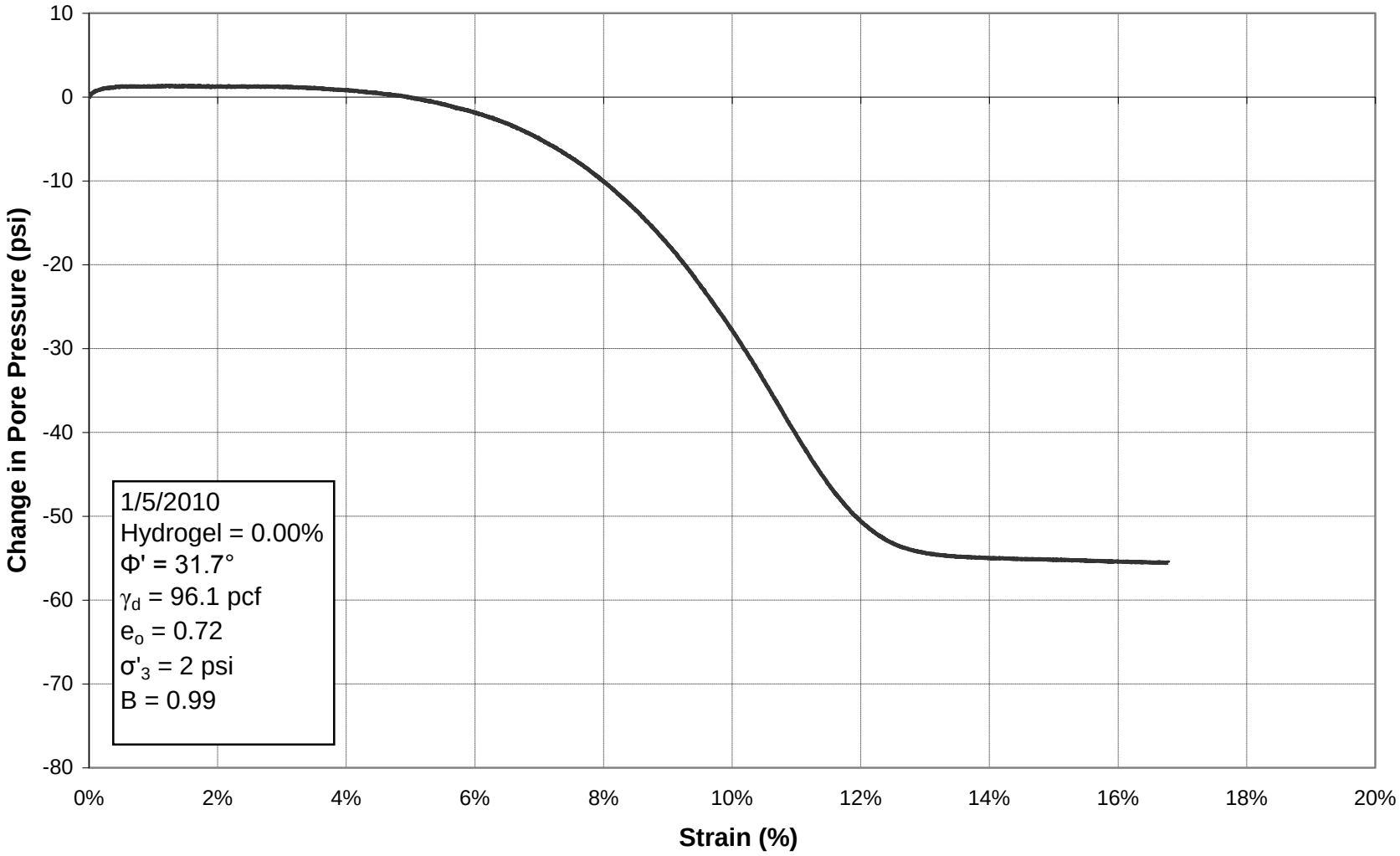

Figure E.70: Change in Pore Pressure vs. Strain for Triaxial Test 38, 0.00% Hydrogel

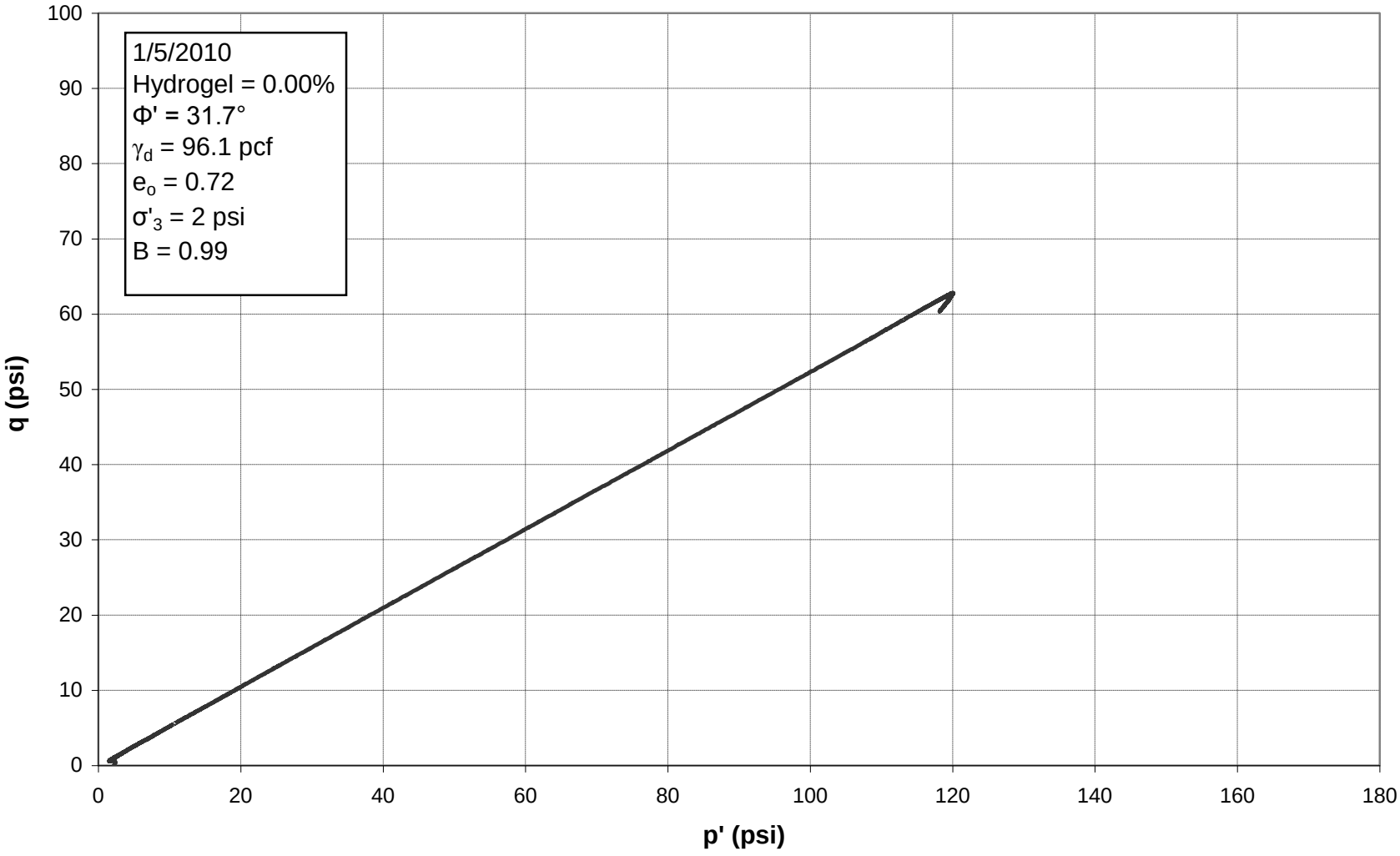

Figure E.71: p'-q Diagram for Triaxial Test 38, 0.00% Hydrogel

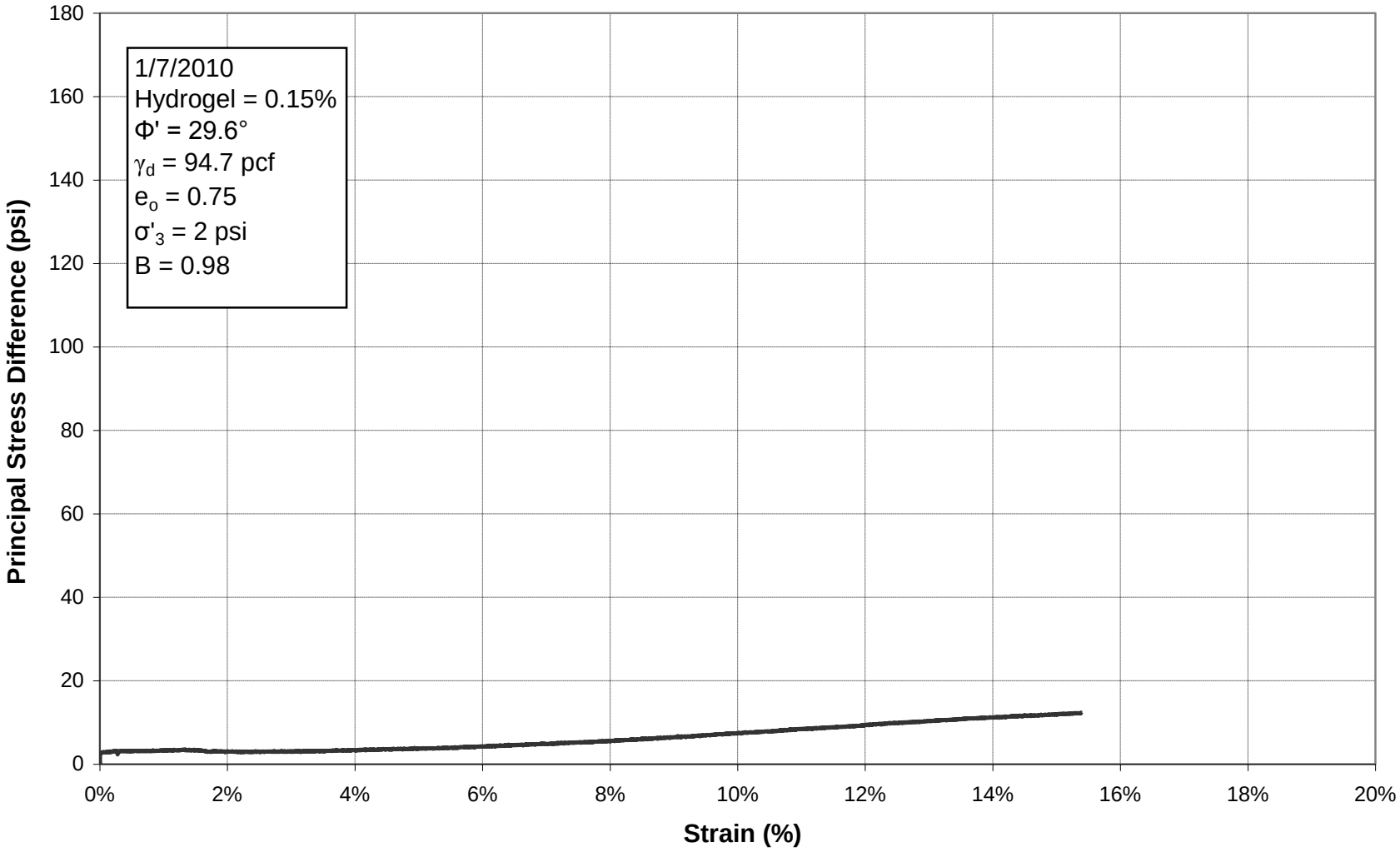

Figure E.72: Principal Stress Difference vs. Strain for Triaxial Test 39, 0.15% Hydrogel

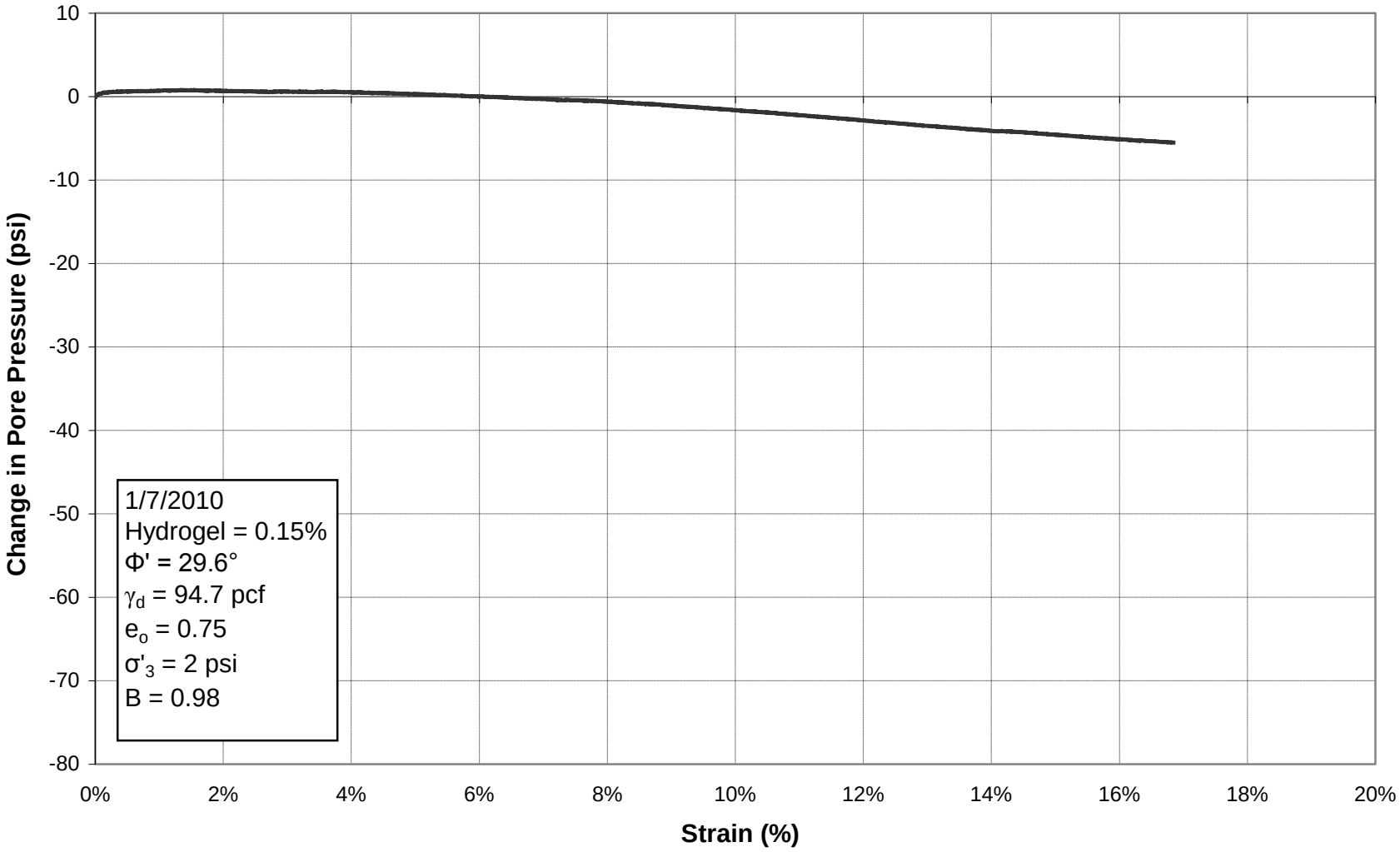

Figure E.73: Change in Pore Pressure vs. Strain for Triaxial Test 39, 0.15% Hydrogel

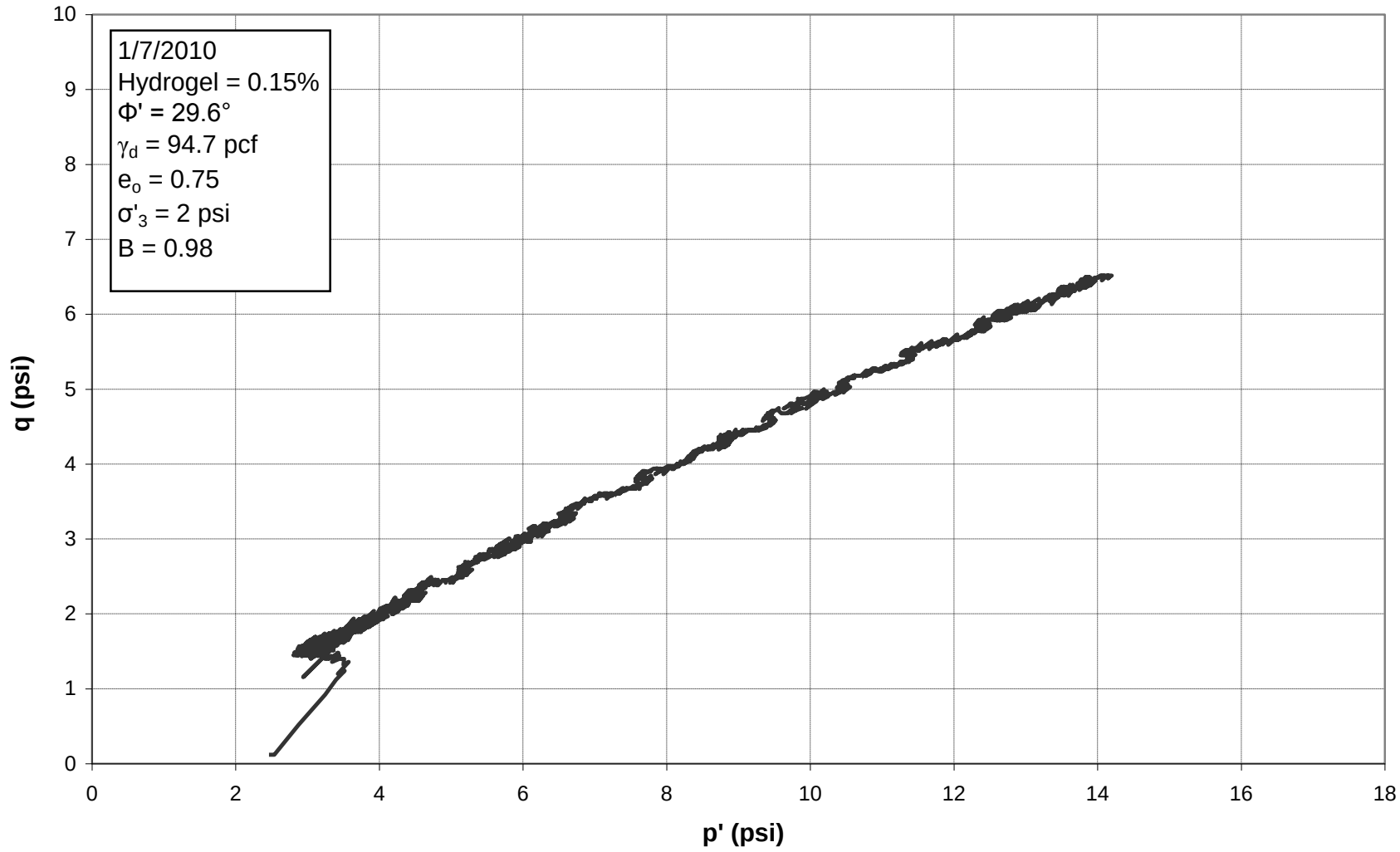

Figure E.74: p'-q Diagram for Triaxial Test 39, 0.15% Hydrogel (the axes have been scaled down by a factor of ten compared to the other p'-q diagrams to better show the data)

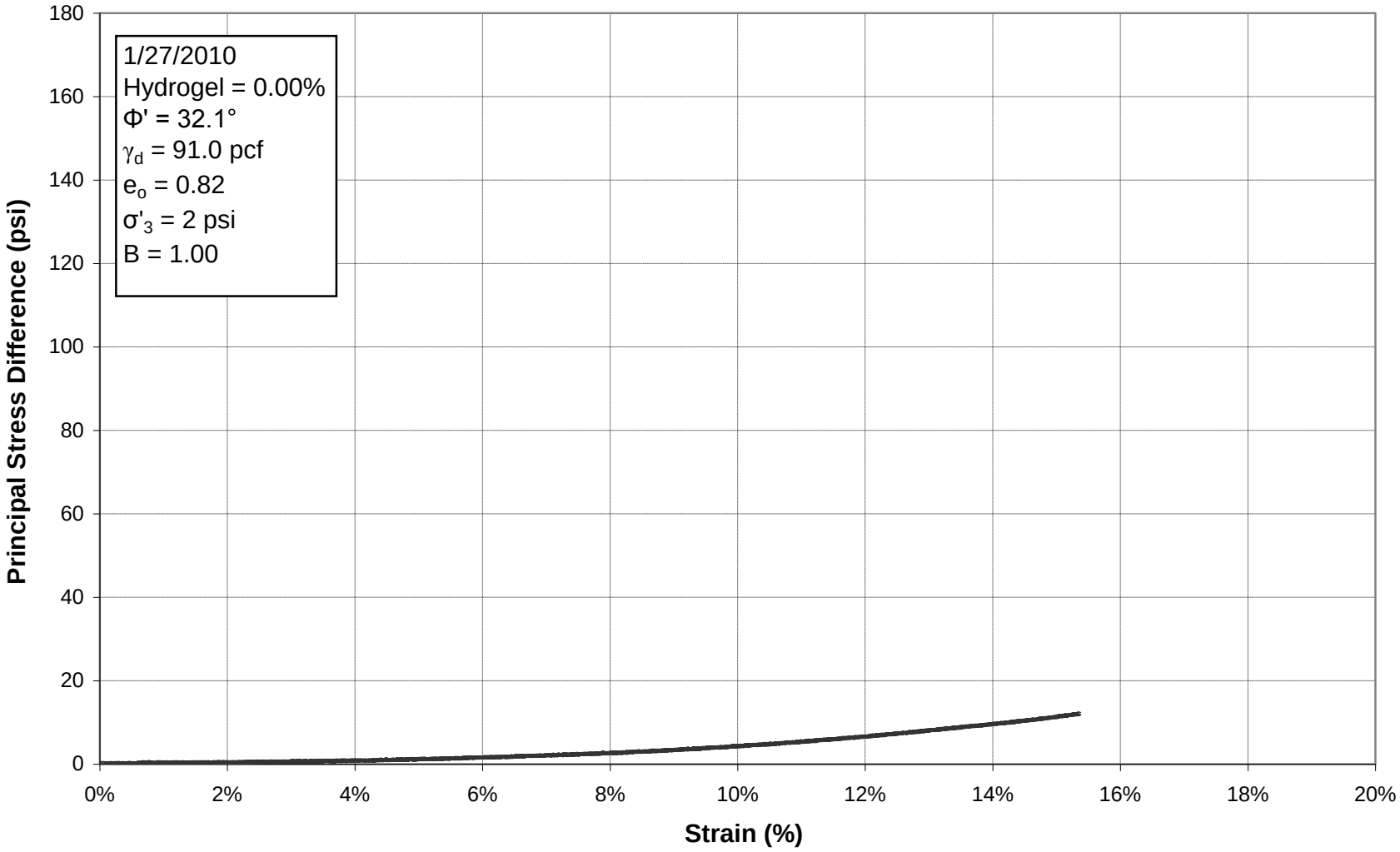

Figure E.75: Principal Stress Difference vs. Strain for Triaxial Test 40, 0.00% Hydrogel

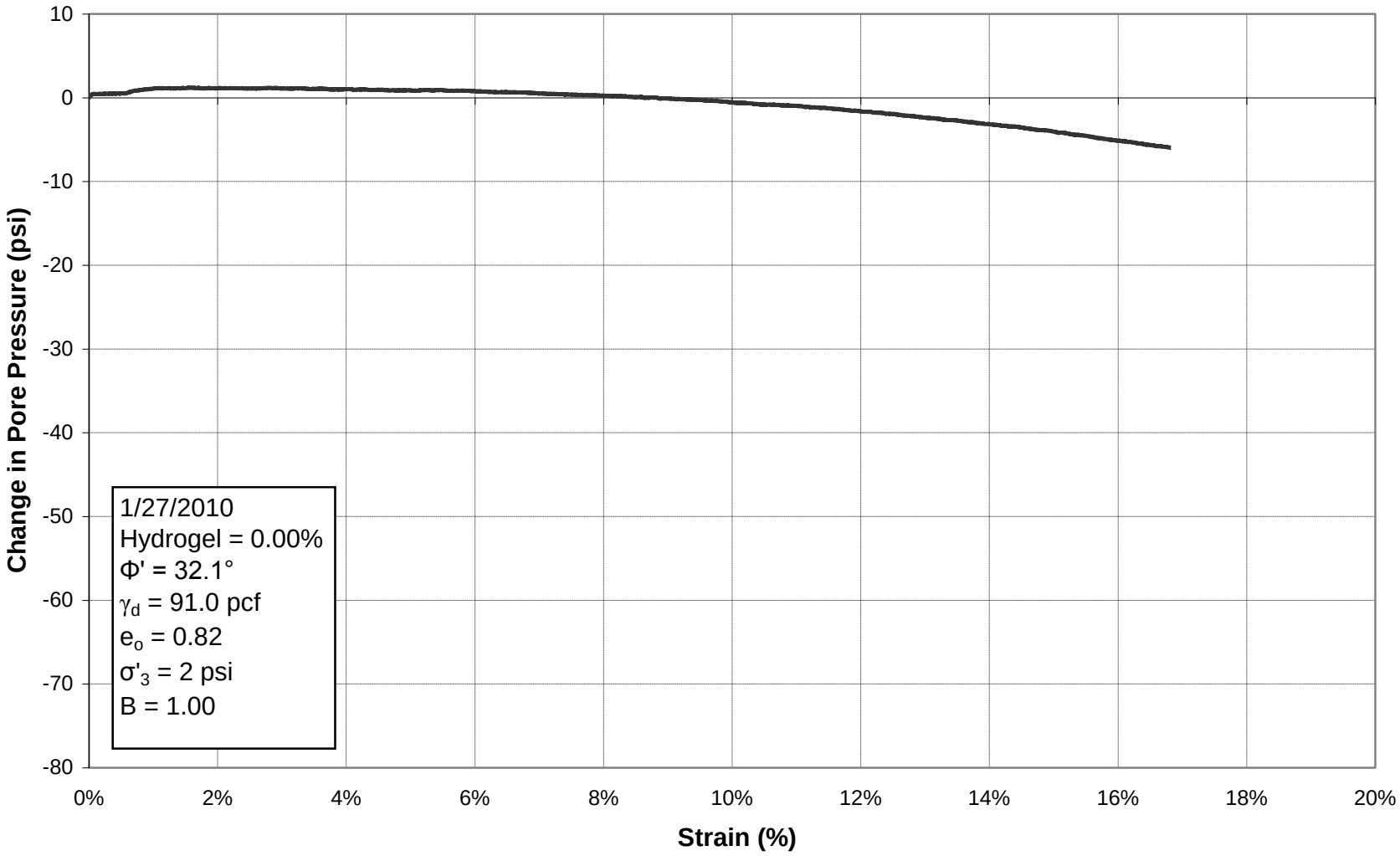

Figure E.76: Change in Pore Pressure vs. Strain for Triaxial Test 40, 0.00% Hydrogel

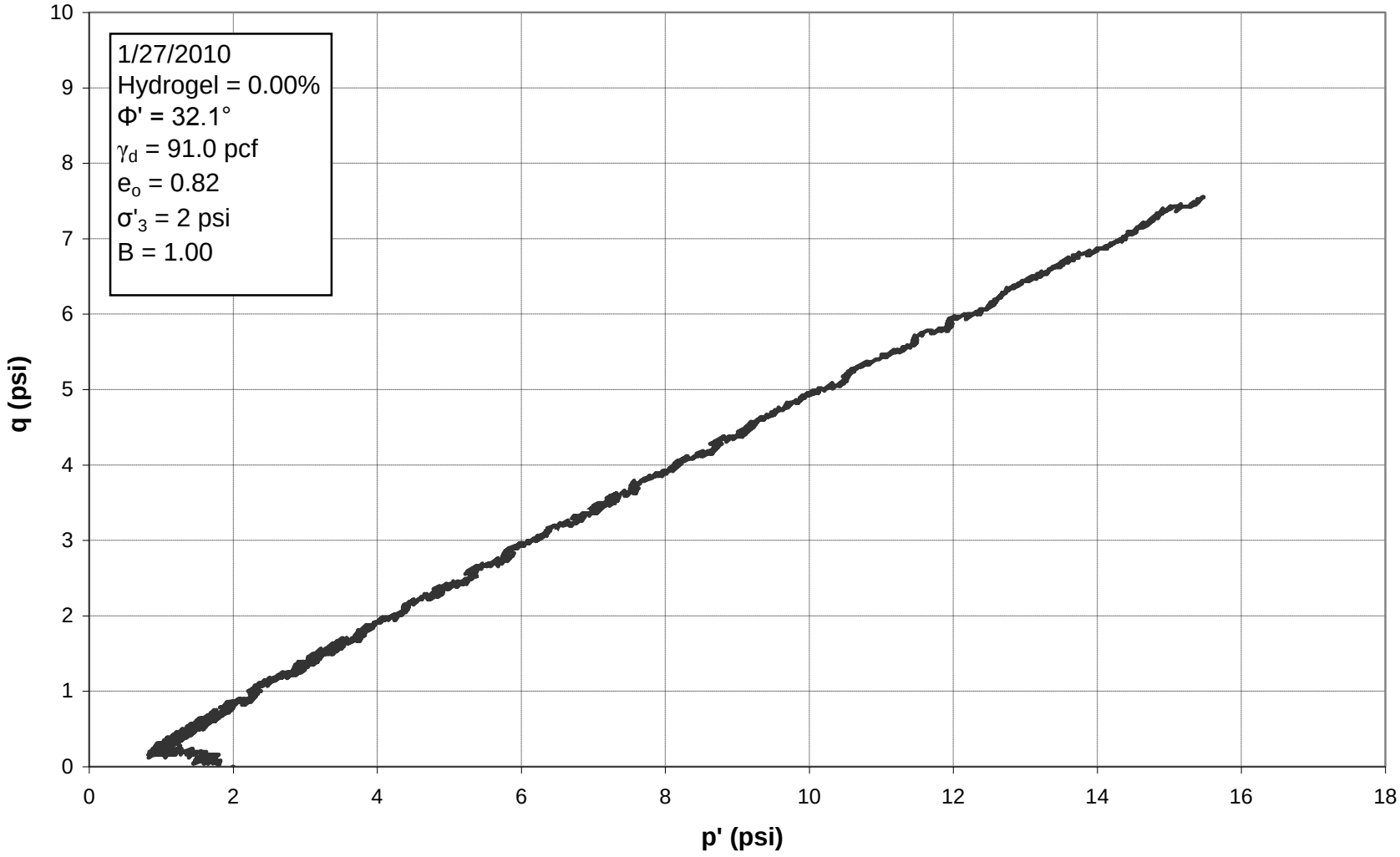

Figure E.77: p'-q Diagram for Triaxial Test 40, 0.00% Hydrogel (the axes have been scaled down by a factor of ten compared to the other p'-q diagrams to better show the data)

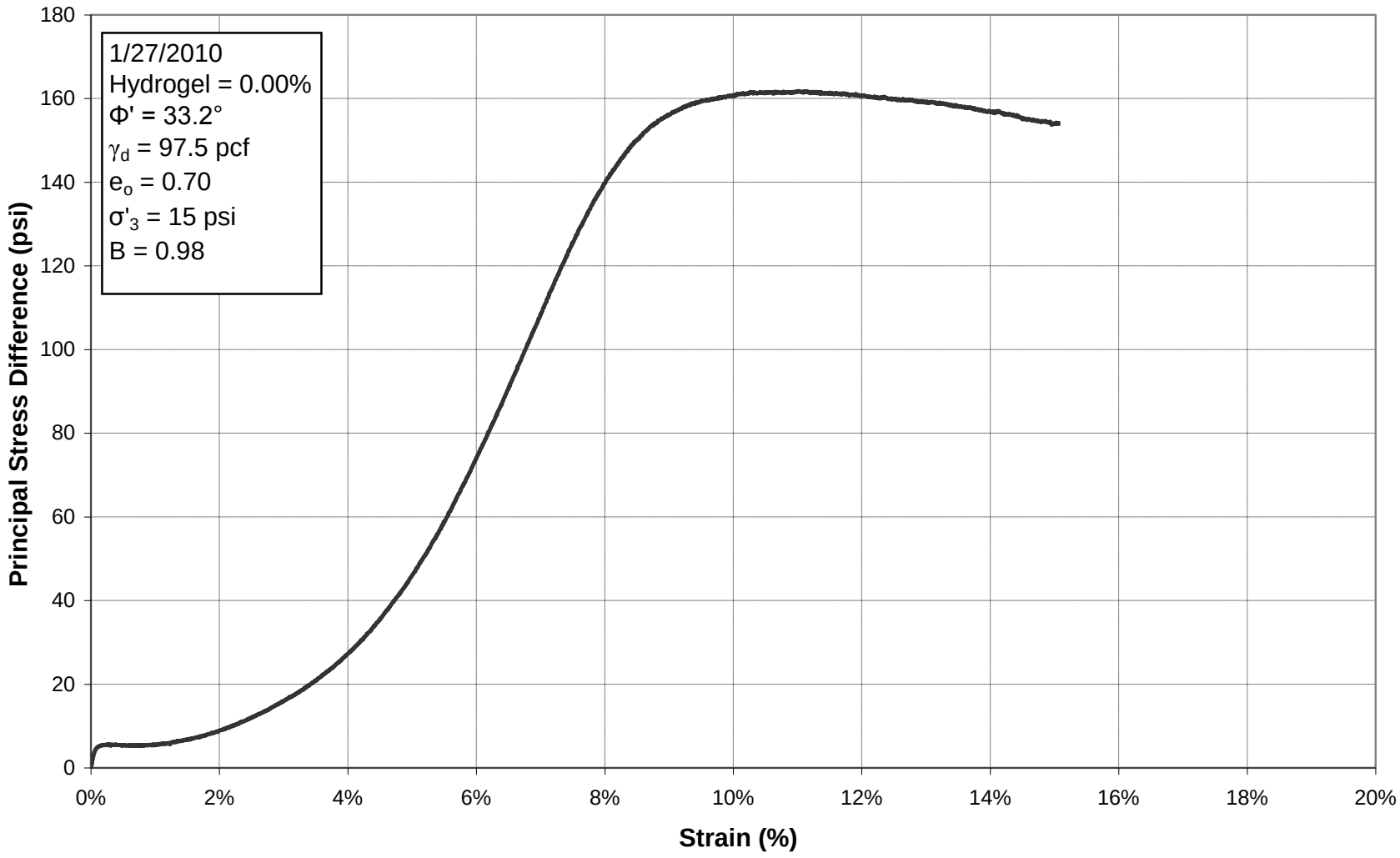

Figure E.78: Principal Stress Difference vs. Strain for Triaxial Test 41, 0.00% Hydrogel

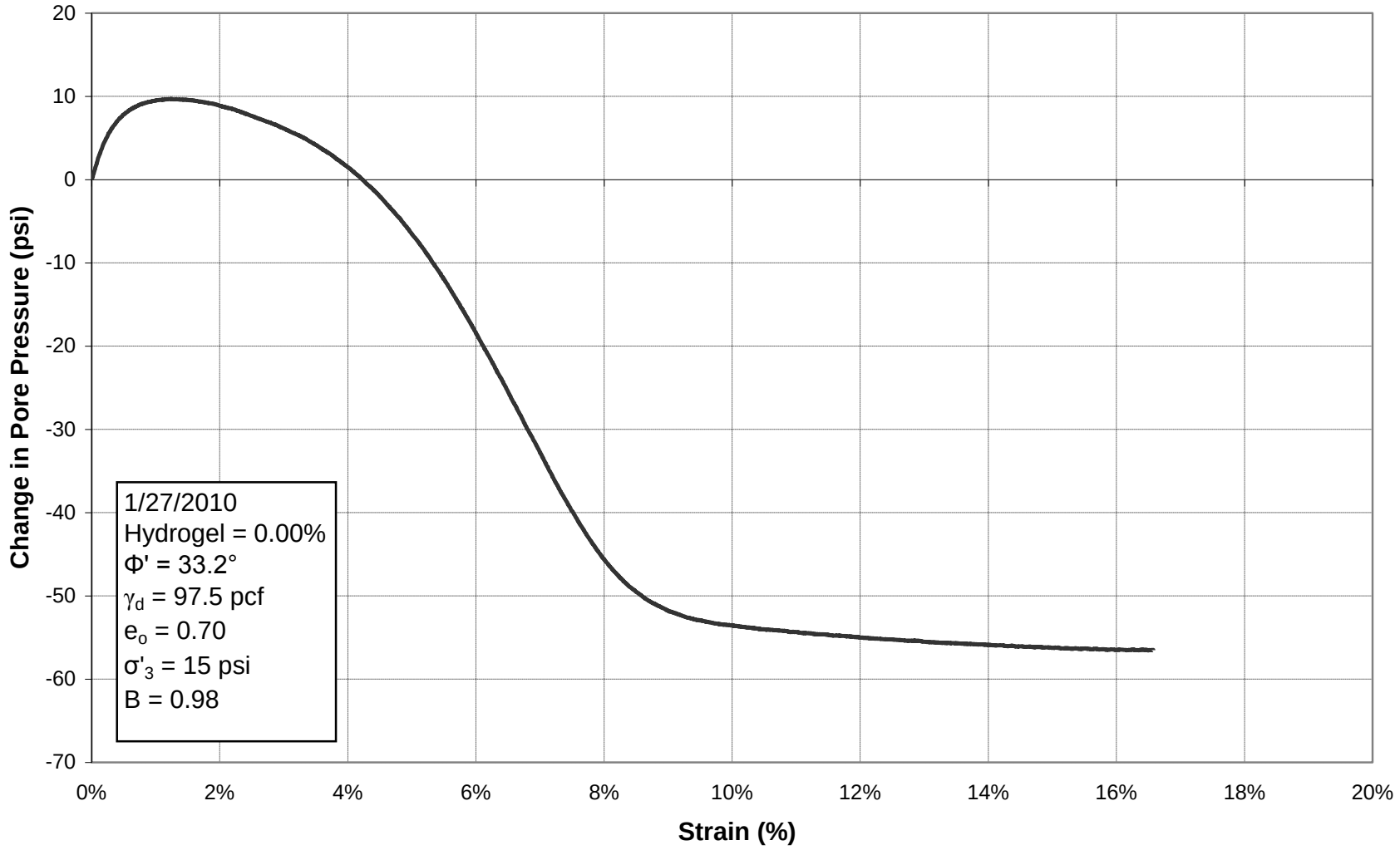

Figure E.79: Change in Pore Pressure vs. Strain for Triaxial Test 41, 0.00% Hydrogel

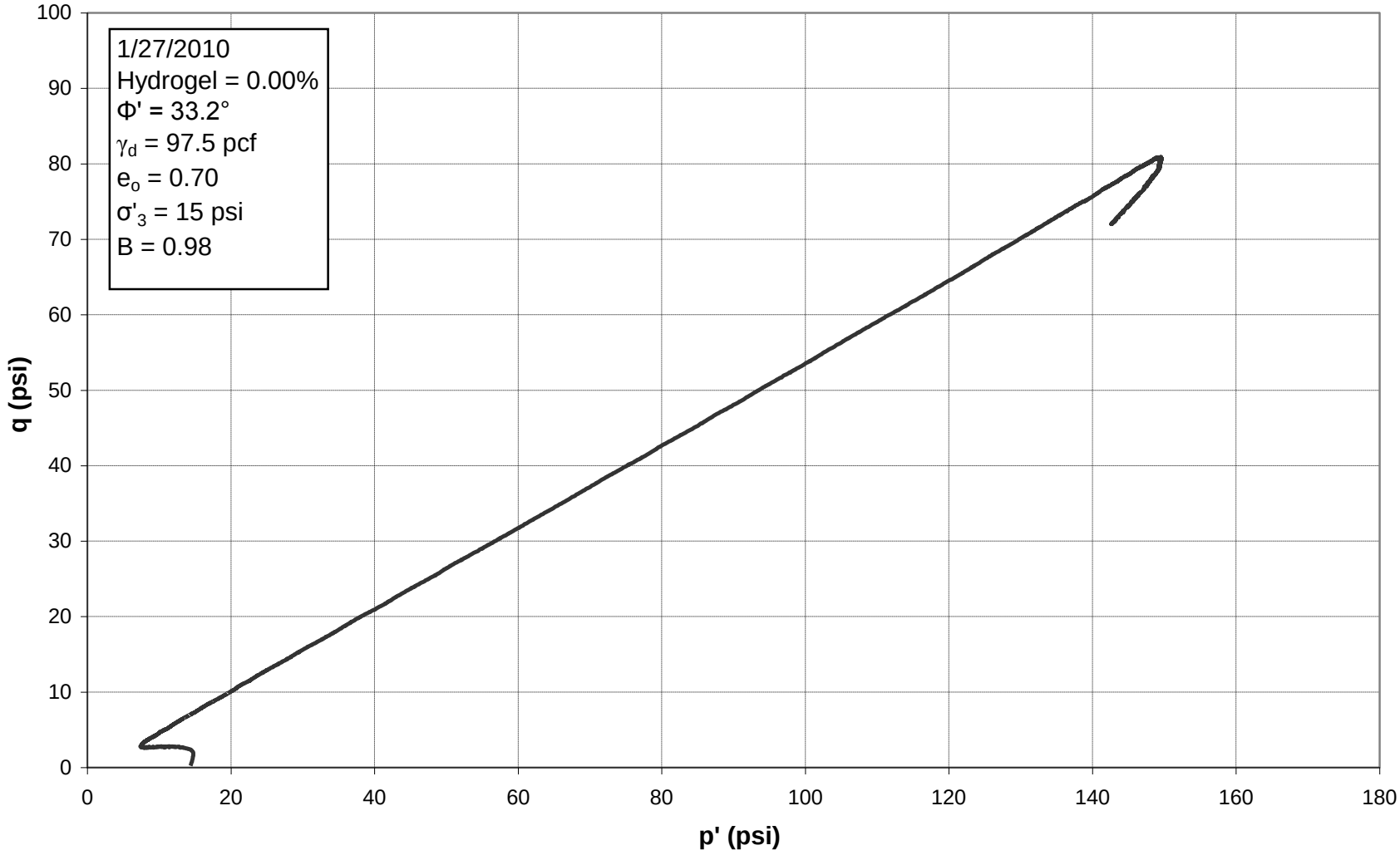

Figure E.80: p'-q Diagram for Triaxial Test 41, 0.00% Hydrogel

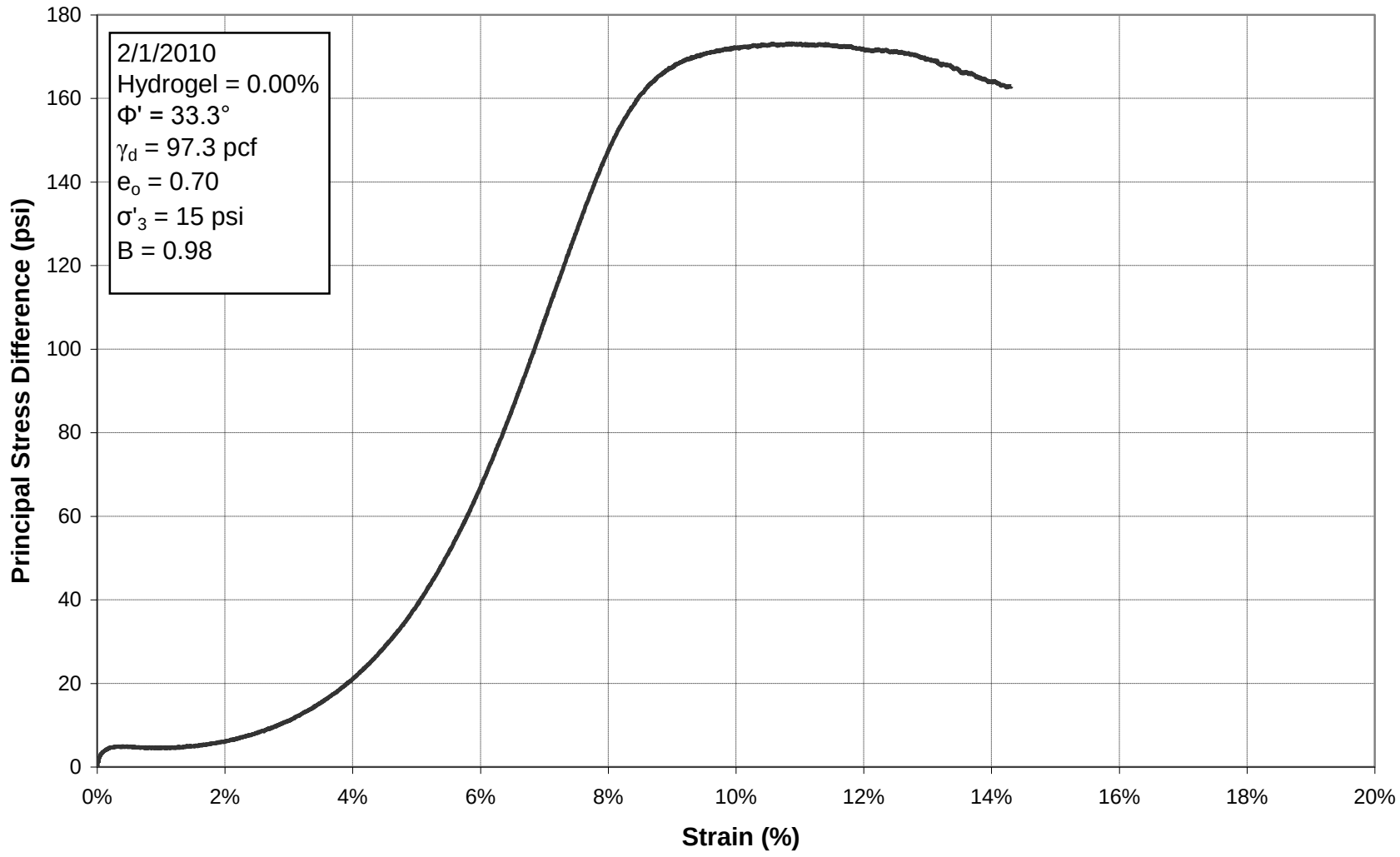

Figure E.81: Principal Stress Difference vs. Strain for Triaxial Test 42, 0.00% Hydrogel

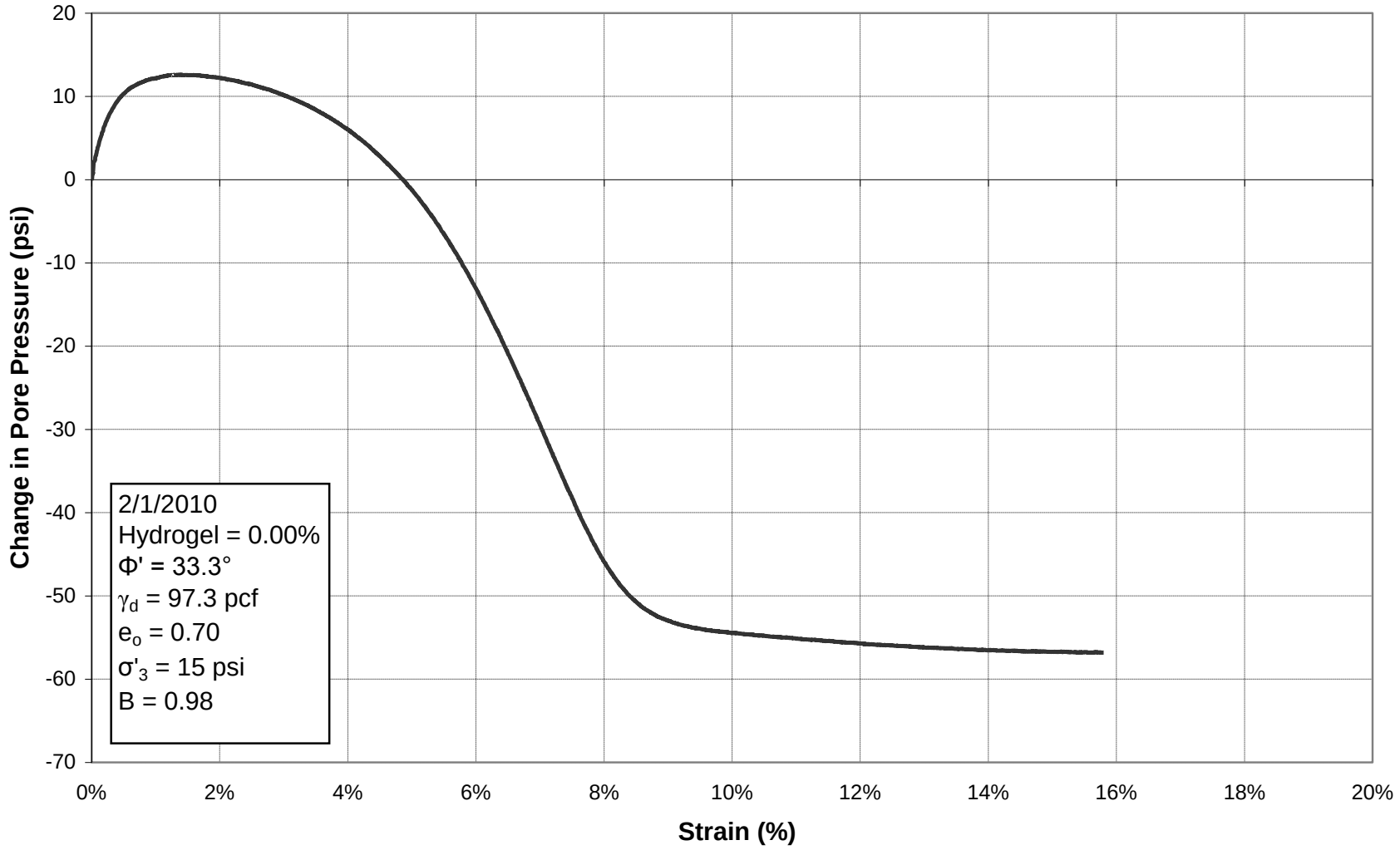

Figure E.82: Change in Pore Pressure vs. Strain for Triaxial Test 42, 0.00% Hydrogel

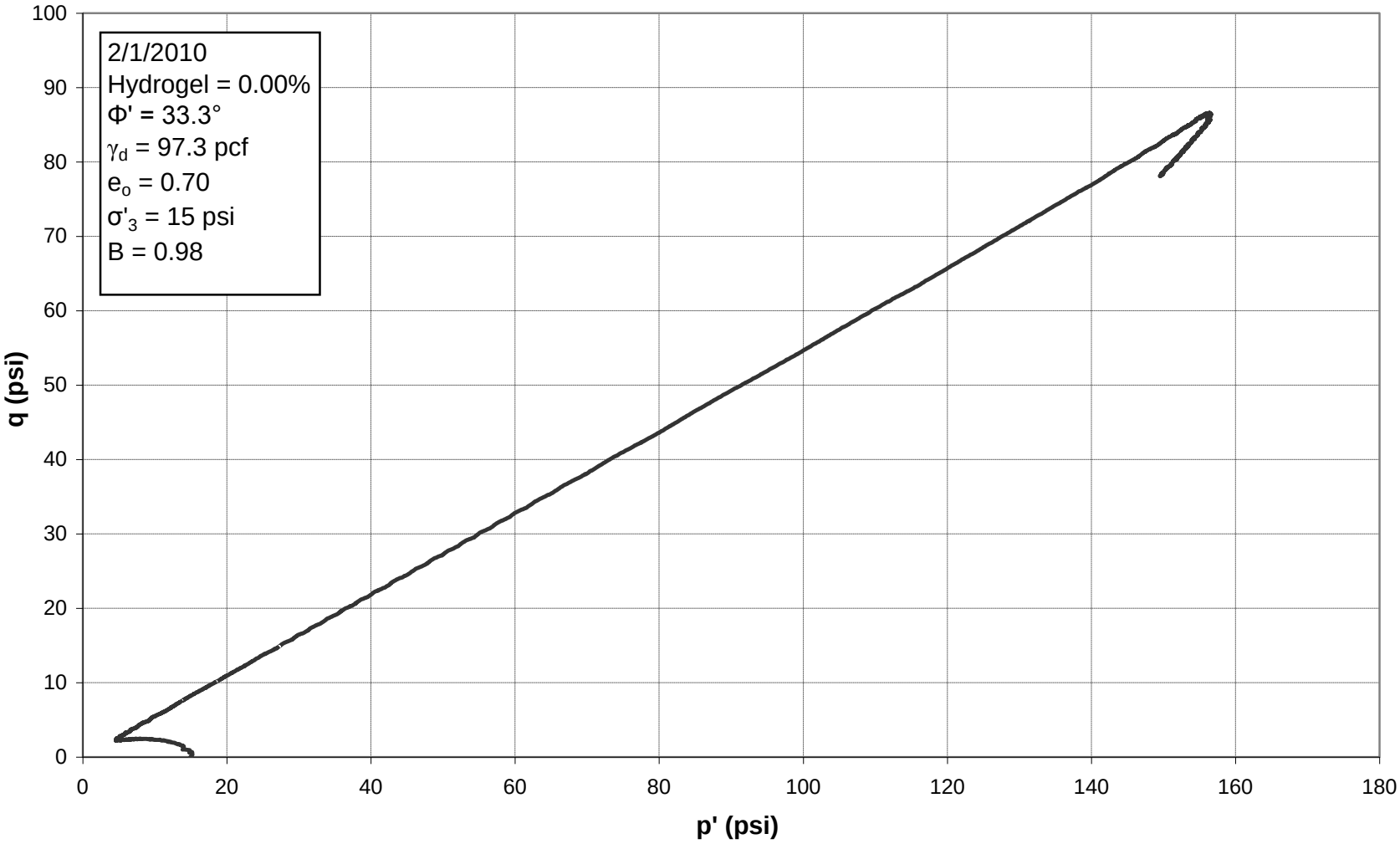

Figure E.83: p'-q Diagram for Triaxial Test 42, 0.00% Hydrogel

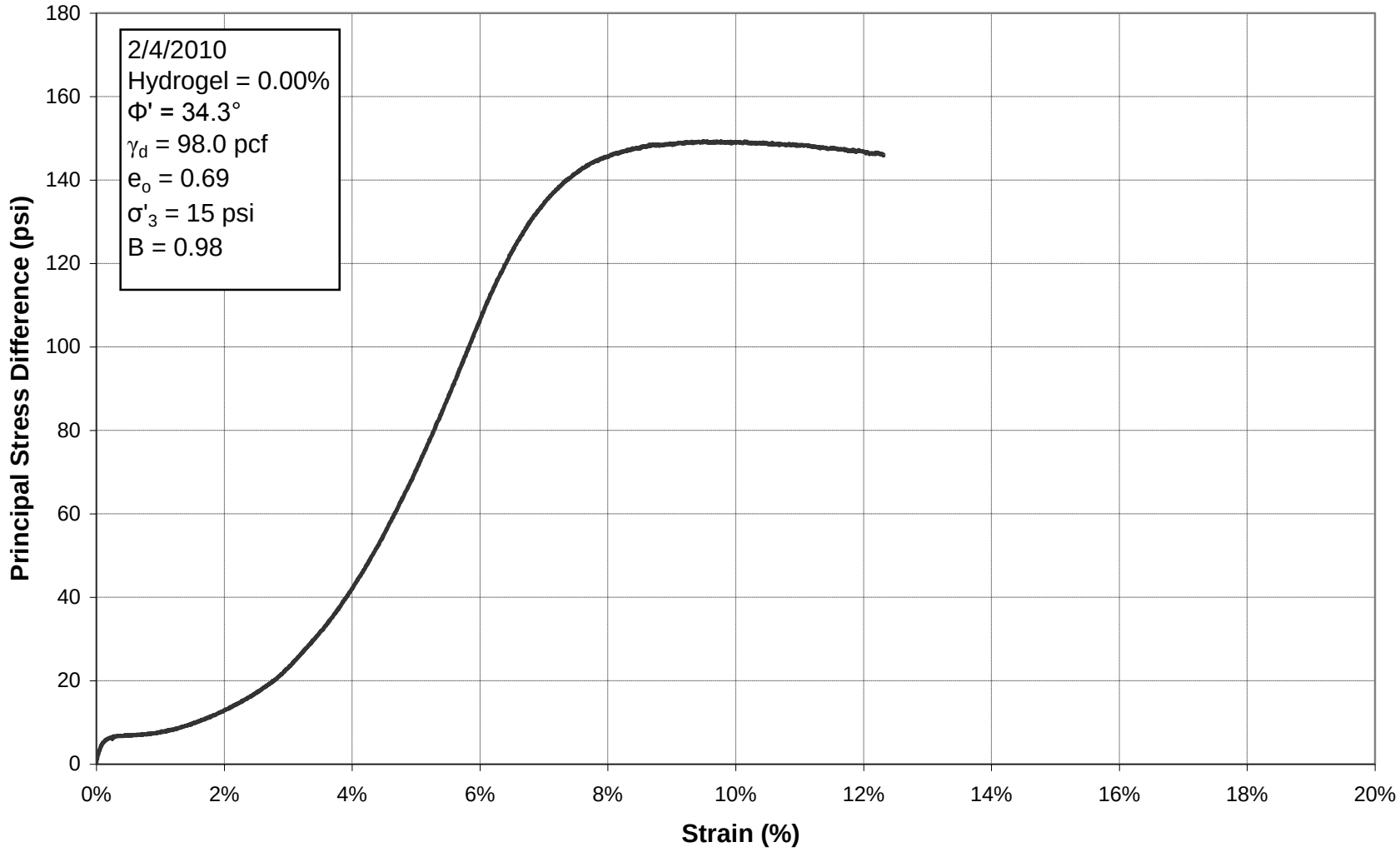

Figure E.84: Principal Stress Difference vs. Strain for Triaxial Test 43, 0.00% Hydrogel

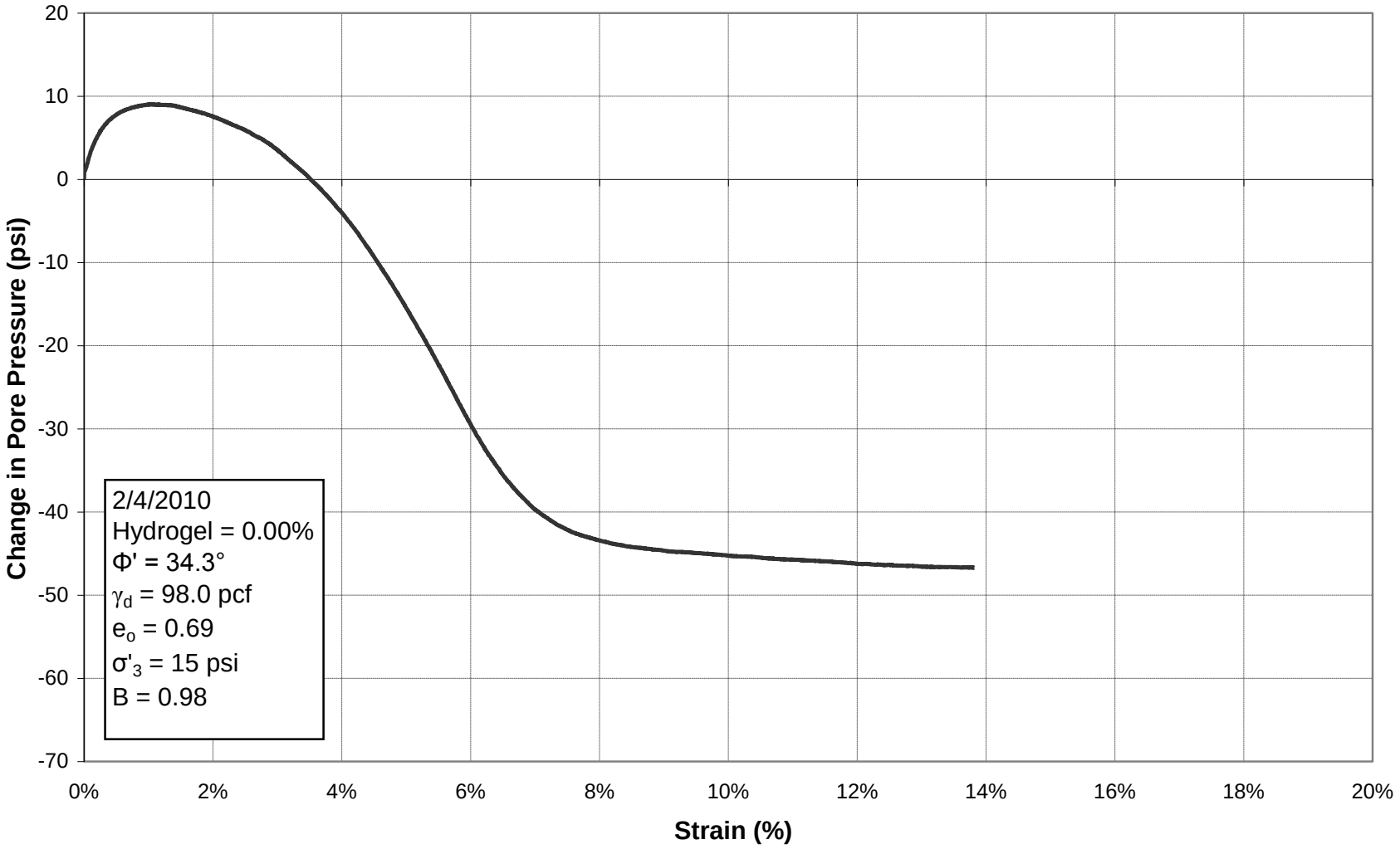

Figure E.85: Change in Pore Pressure vs. Strain for Triaxial Test 43, 0.00% Hydrogel

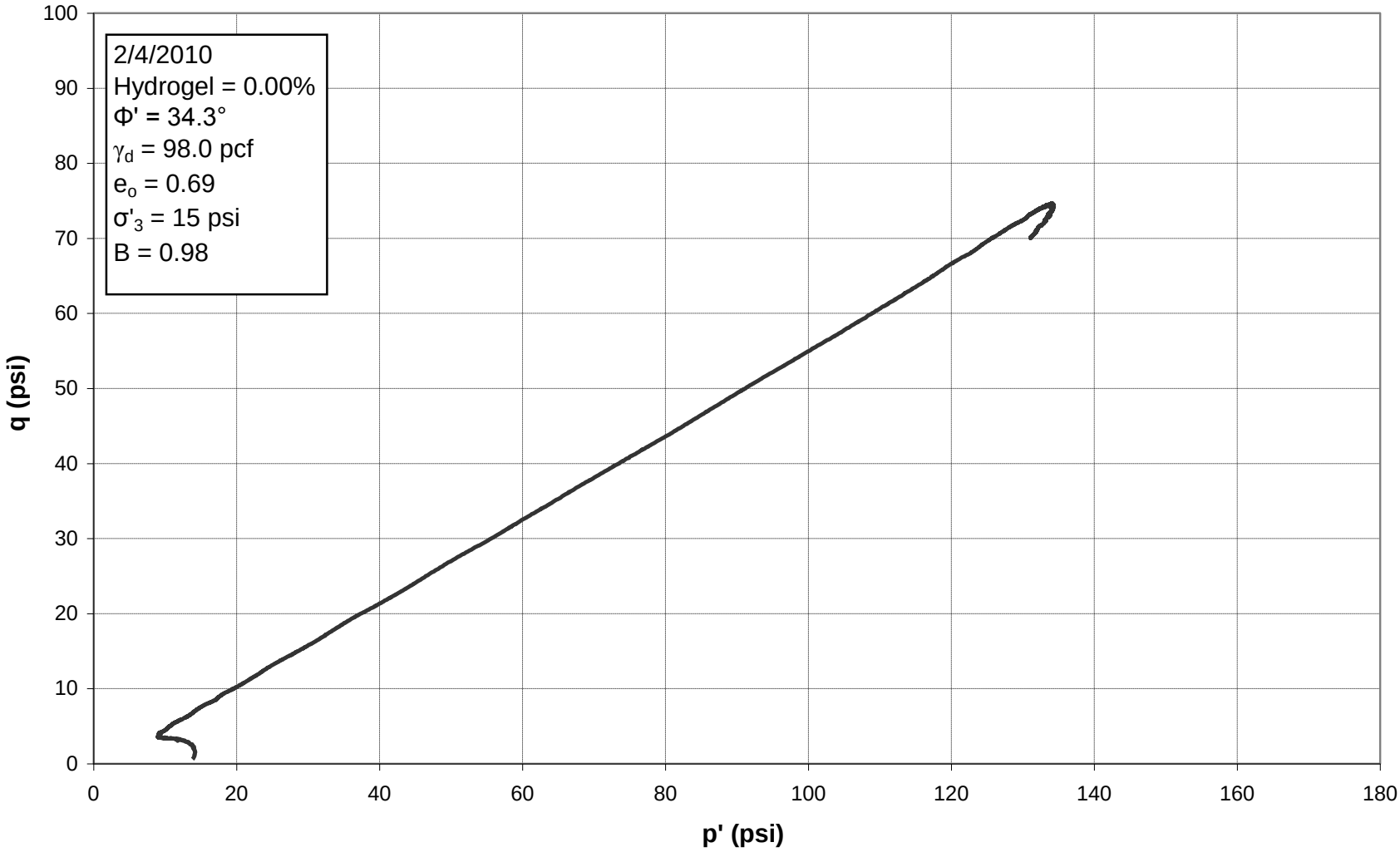

Figure E.86: p'-q Diagram for Triaxial Test 43, 0.00% Hydrogel

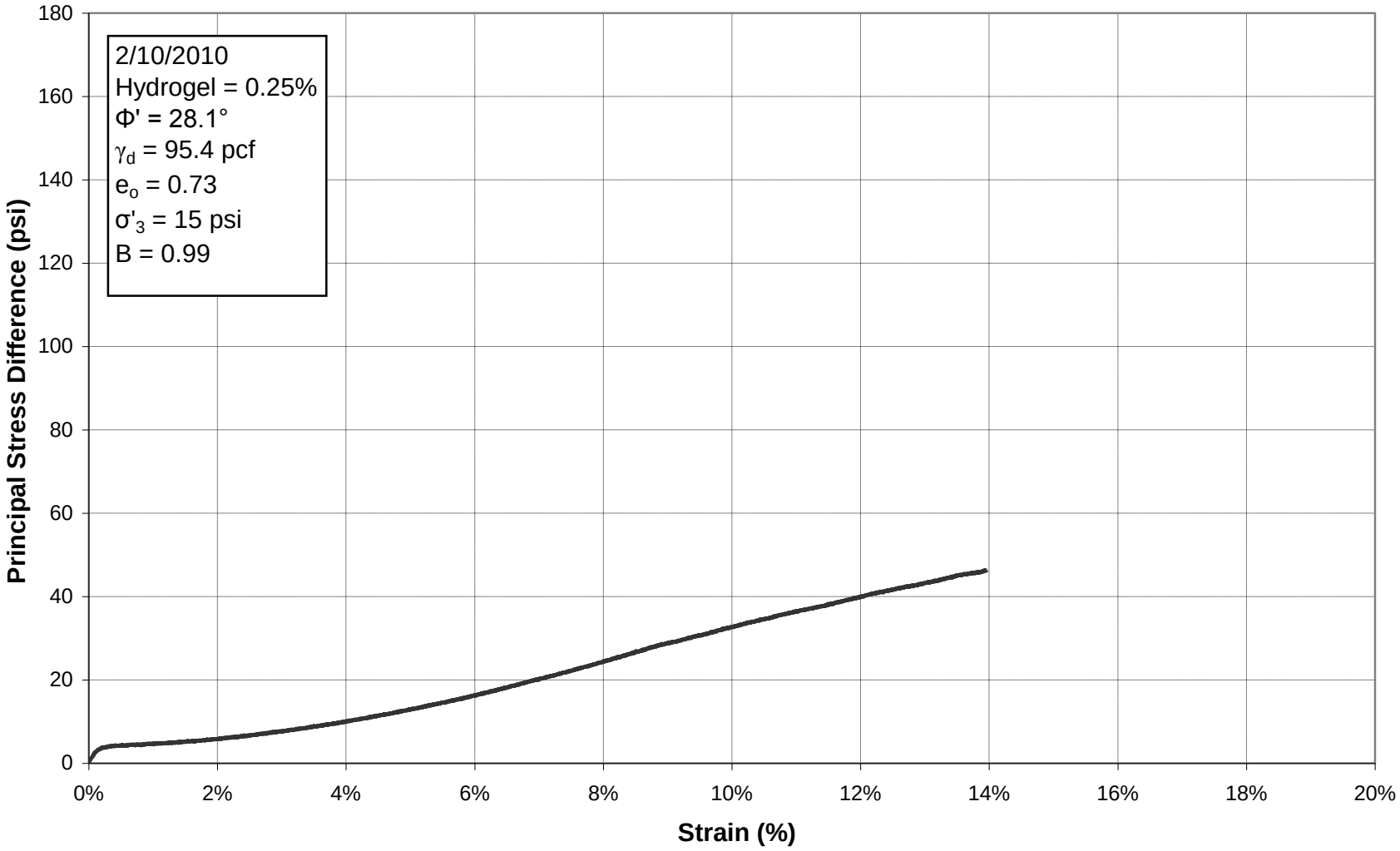

Figure E.87: Principal Stress Difference vs. Strain for Triaxial Test 44, 0.25% Hydrogel

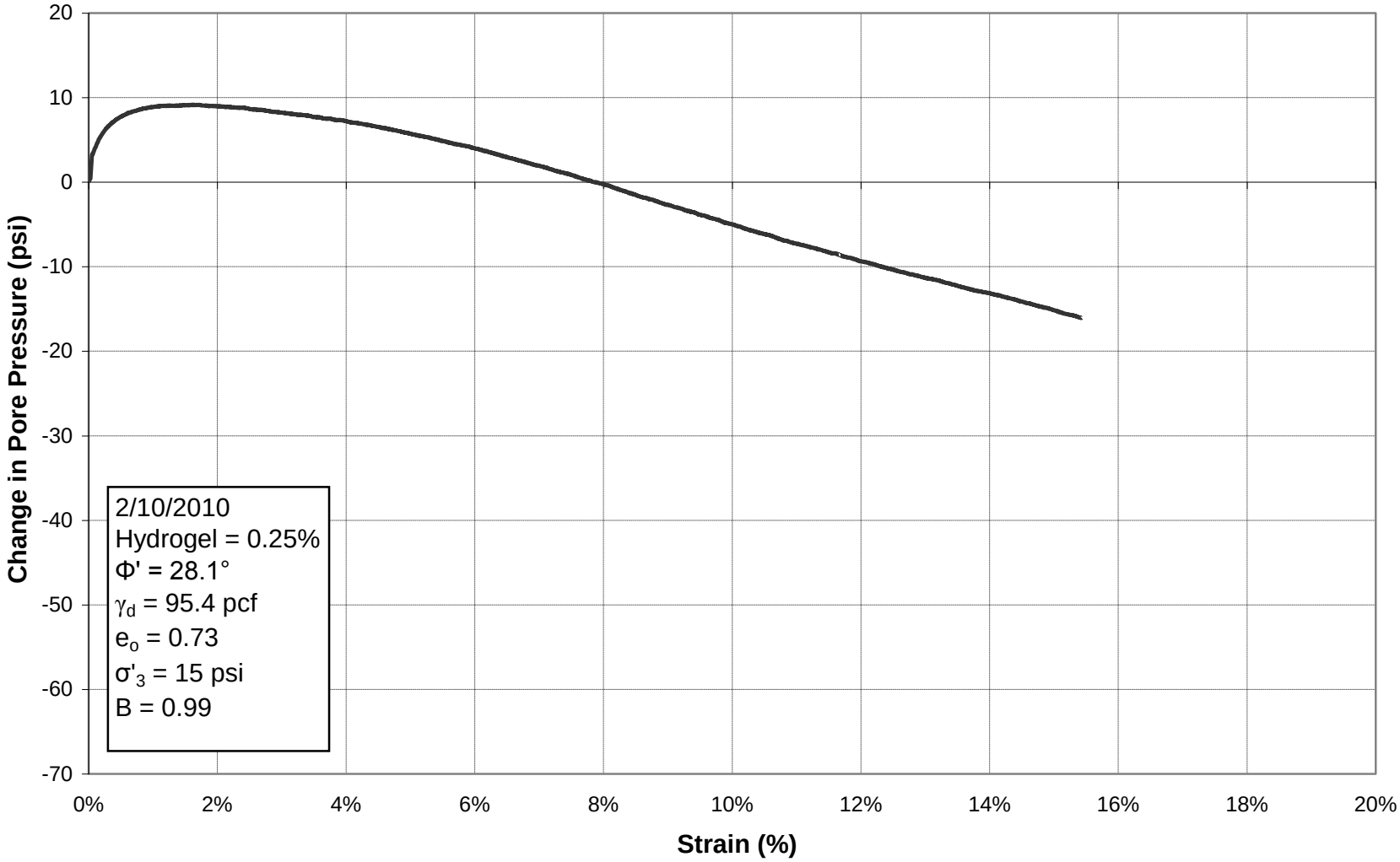

Figure E.88: Change in Pore Pressure vs. Strain for Triaxial Test 44, 0.25% Hydrogel

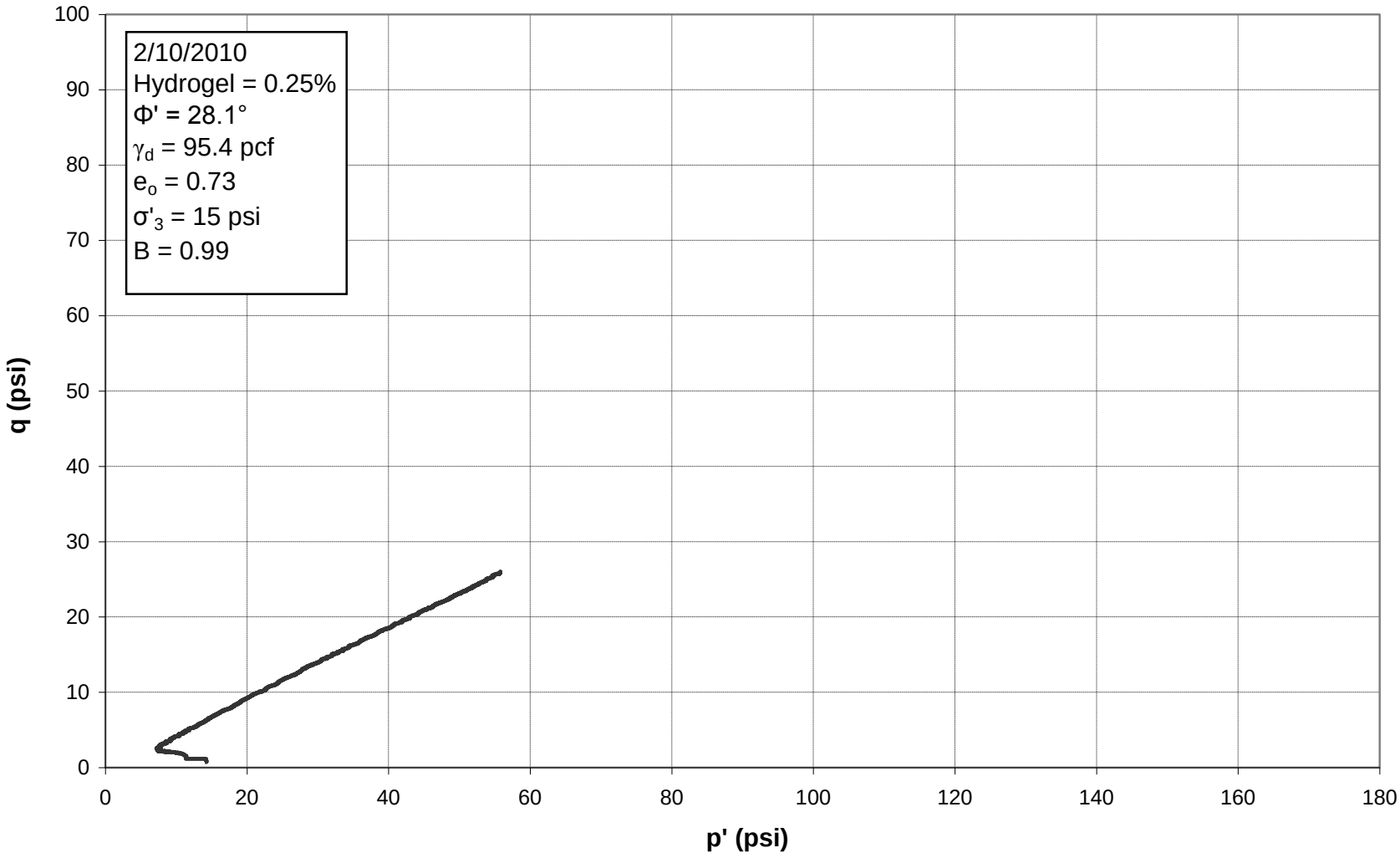

Figure E.89: p'-q Diagram for Triaxial Test 44, 0.25% Hydrogel

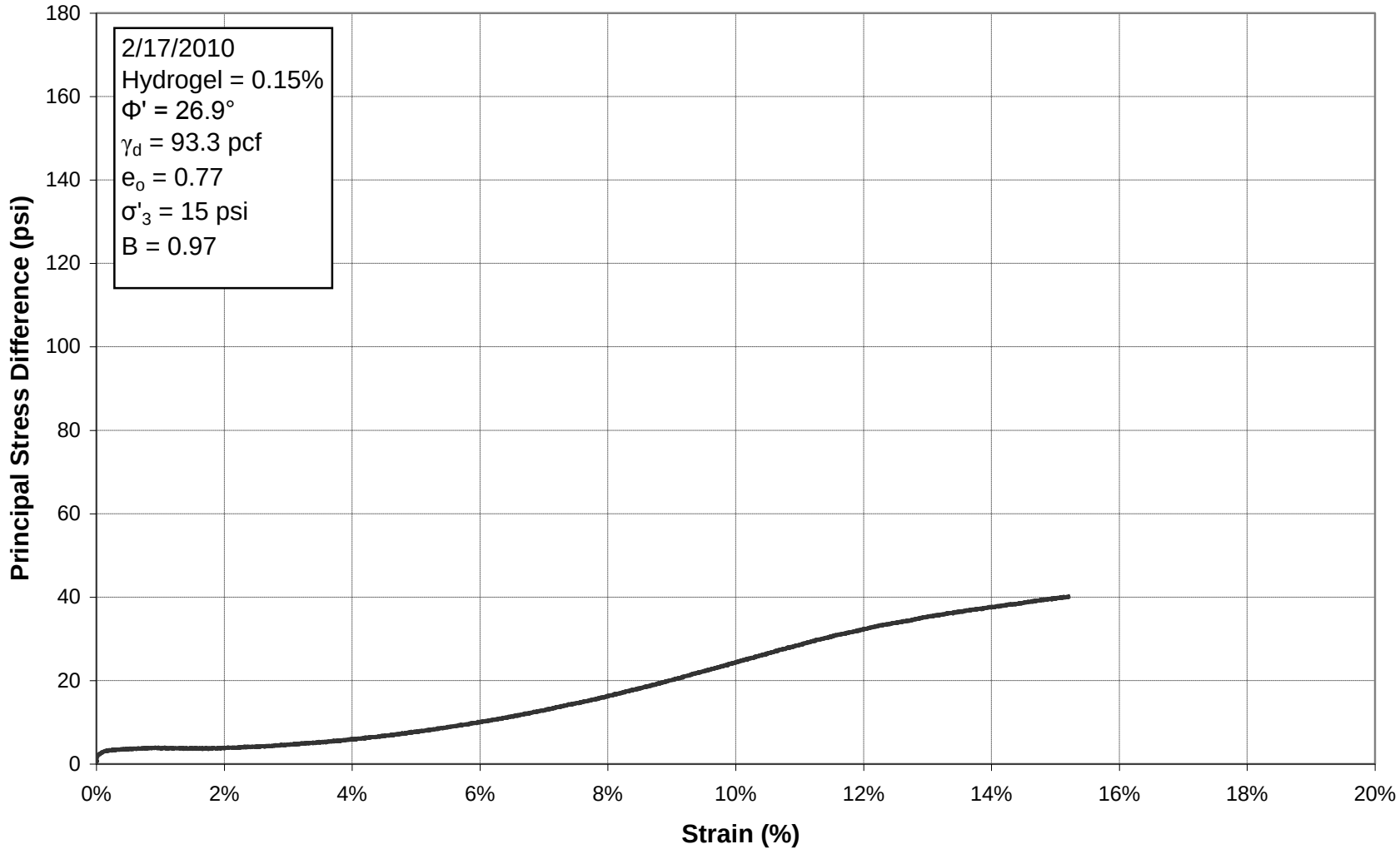

Figure E.90: Principal Stress Difference vs. Strain for Triaxial Test 45, 0.15% Hydrogel

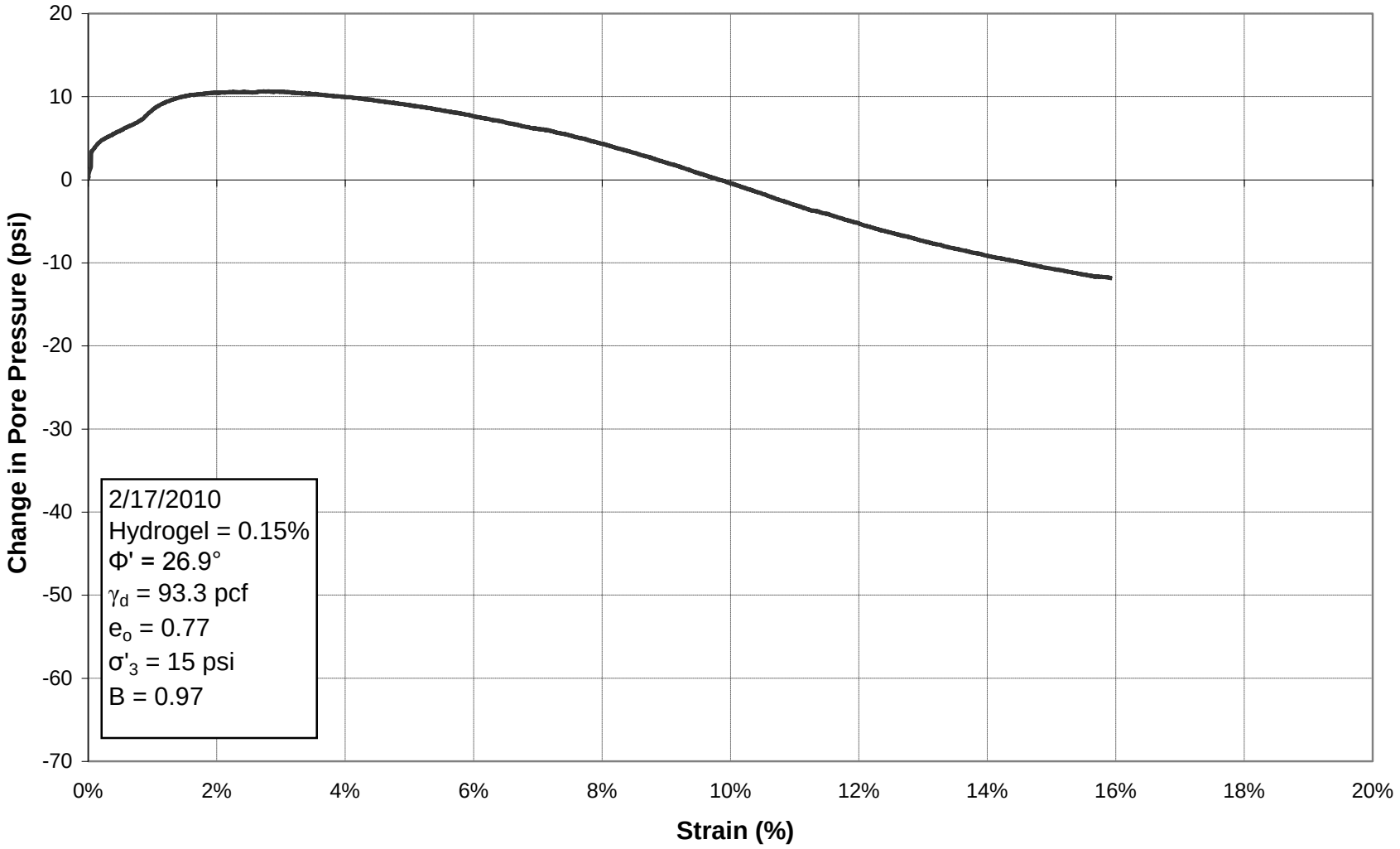

Figure E.91: Change in Pore Pressure vs. Strain for Triaxial Test 45, 0.15% Hydrogel

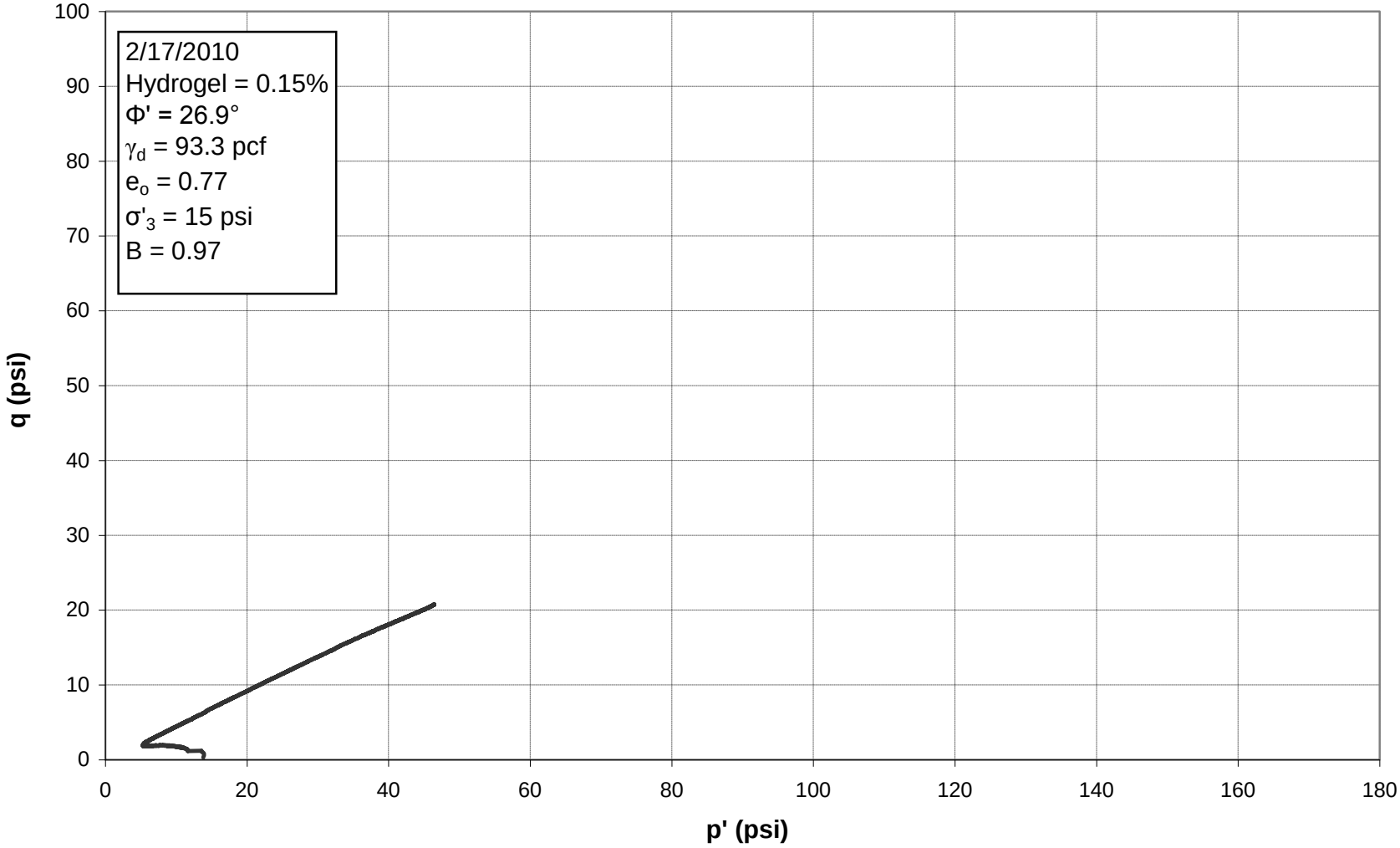

Figure E.92: p'-q Diagram for Triaxial Test 45, 0.15% Hydrogel

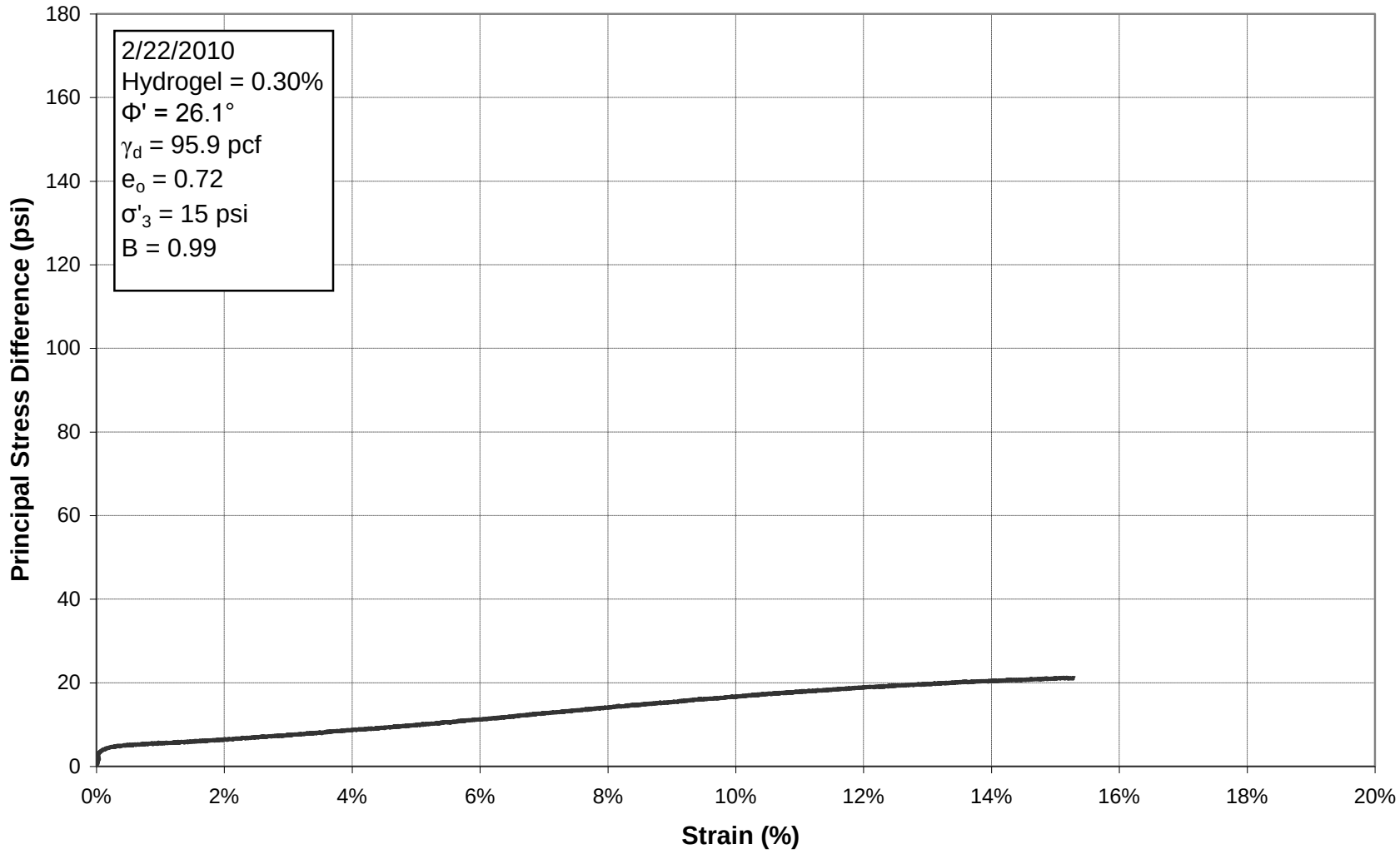

Figure E.93: Principal Stress Difference vs. Strain for Triaxial Test 46, 0.30% Hydrogel

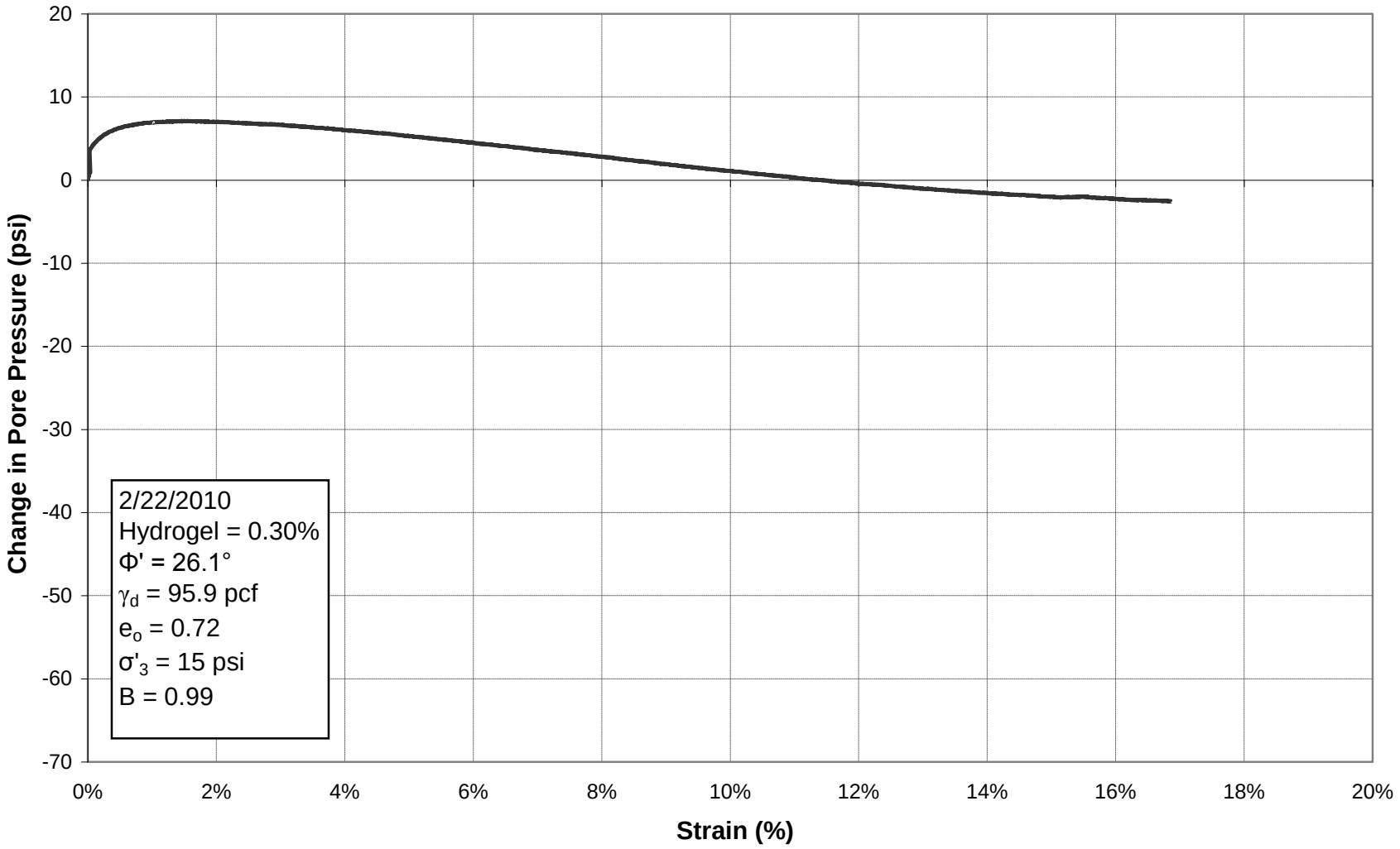

Figure E.94: Change in Pore Pressure vs. Strain for Triaxial Test 46, 0.30% Hydrogel

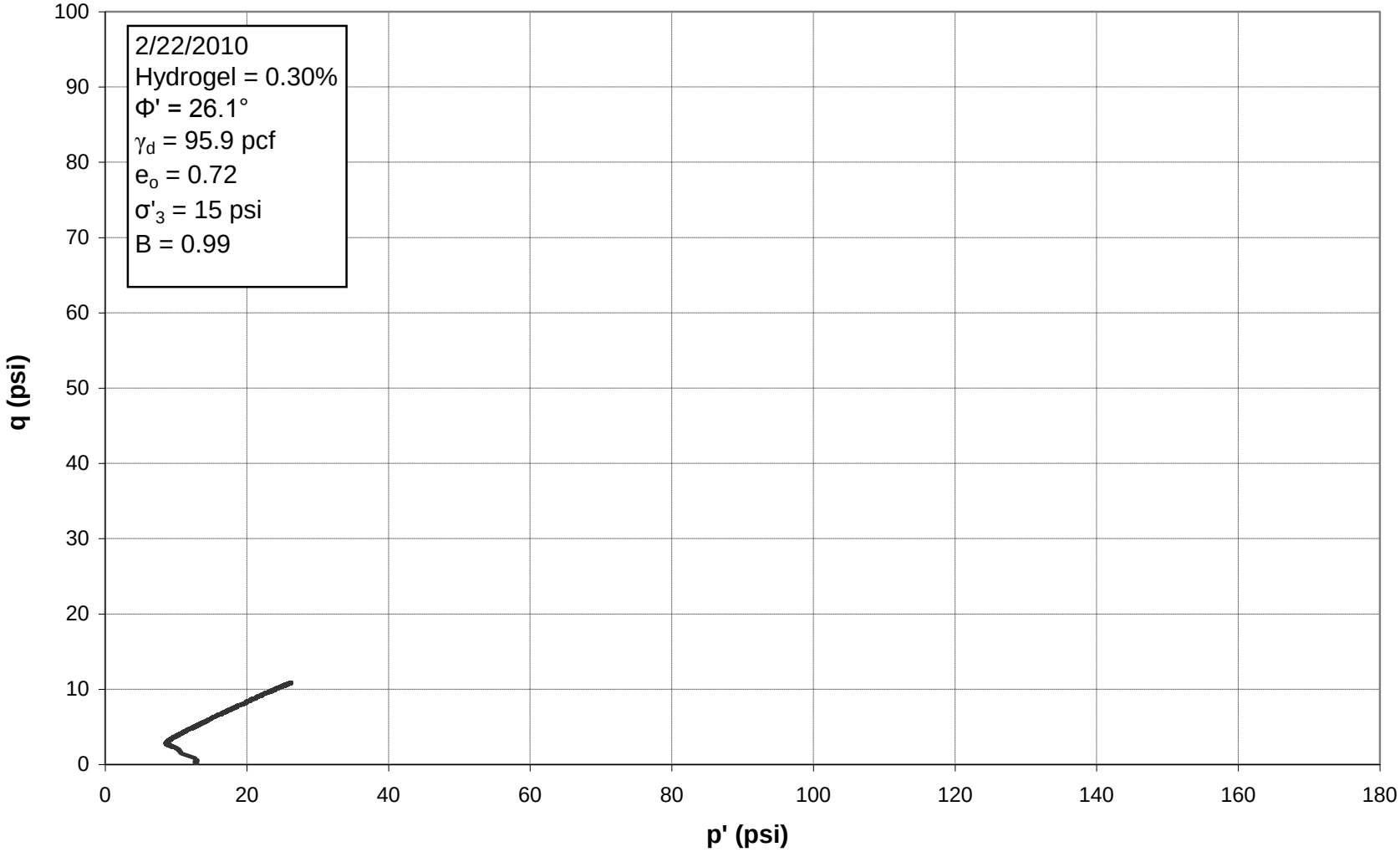

Figure E.95: p'-q Diagram for Triaxial Test 46, 0.30% Hydrogel

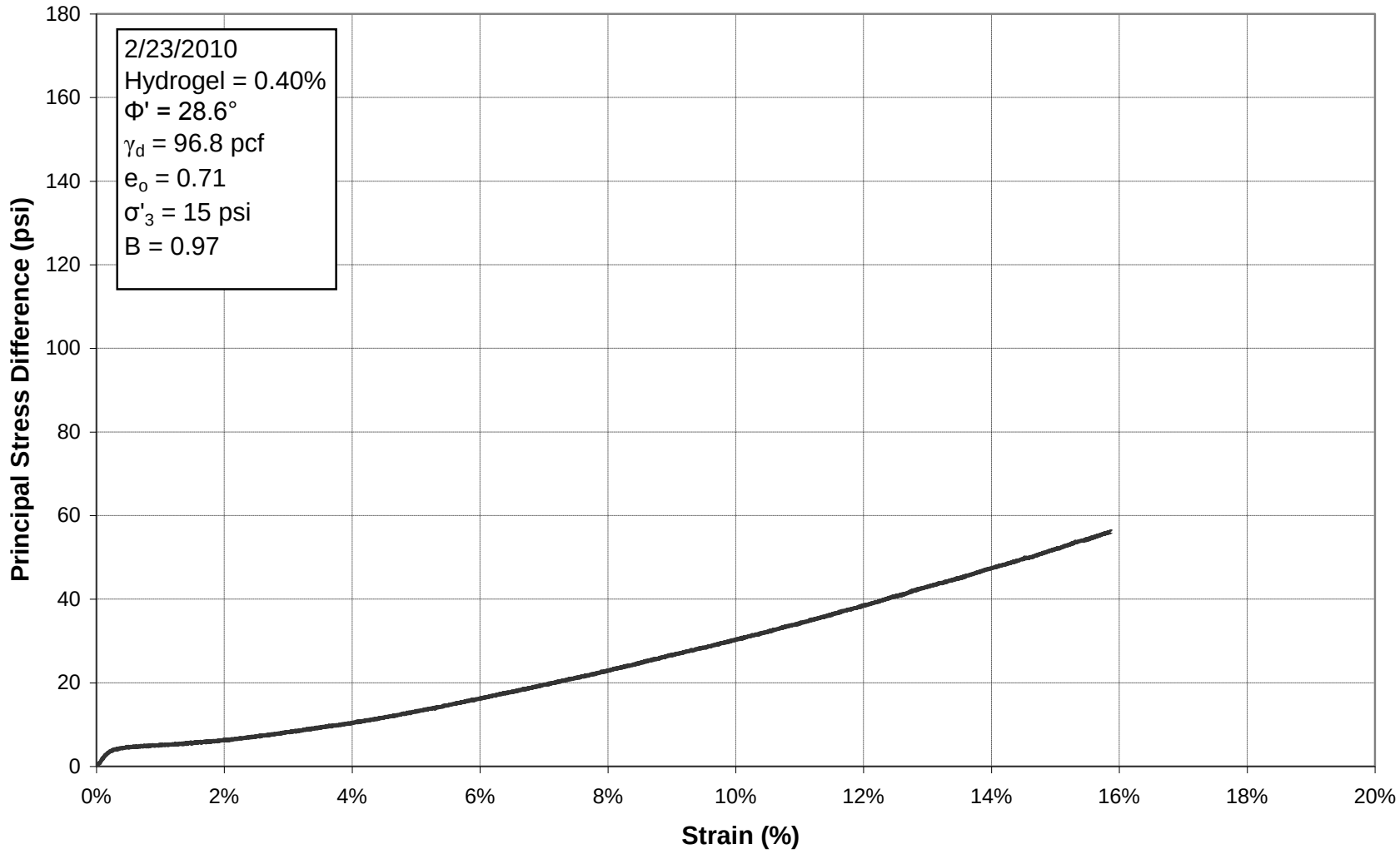

Figure E.96: Principal Stress Difference vs. Strain for Triaxial Test 47, 0.40% Hydrogel

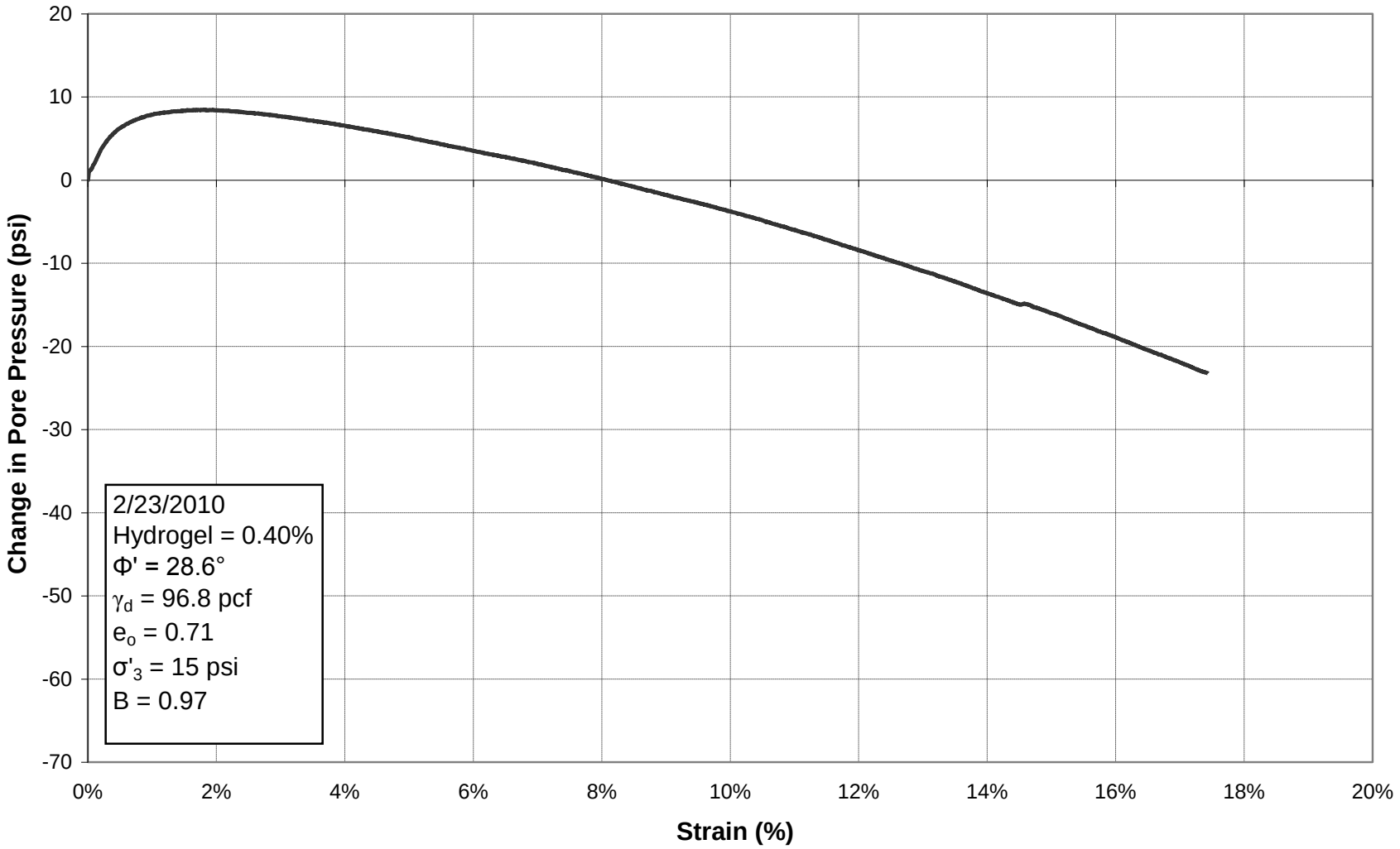

Figure E.97: Change in Pore Pressure vs. Strain for Triaxial Test 47, 0.40% Hydrogel

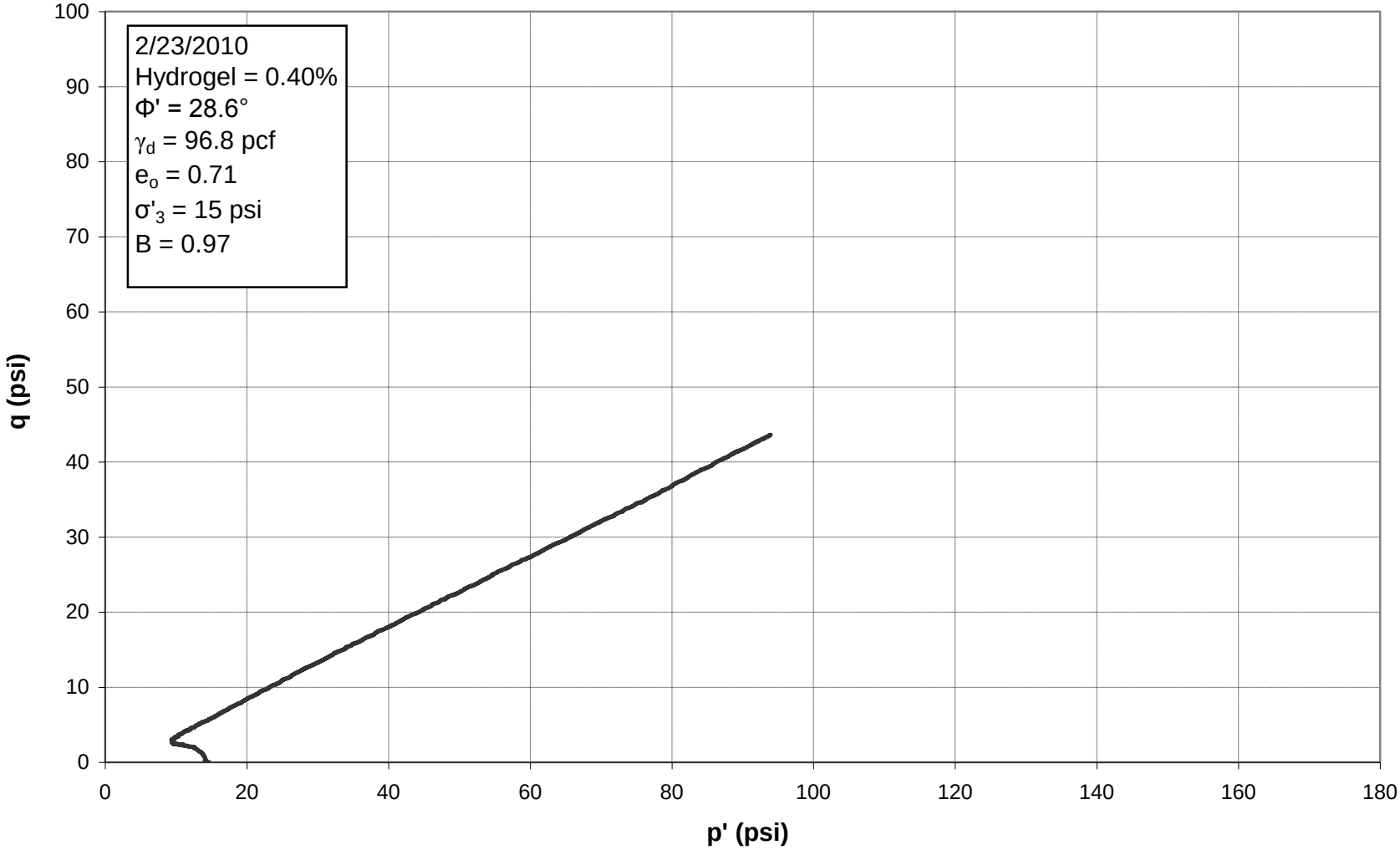

Figure E.98: p'-q Diagram for Triaxial Test 47, 0.40% Hydrogel

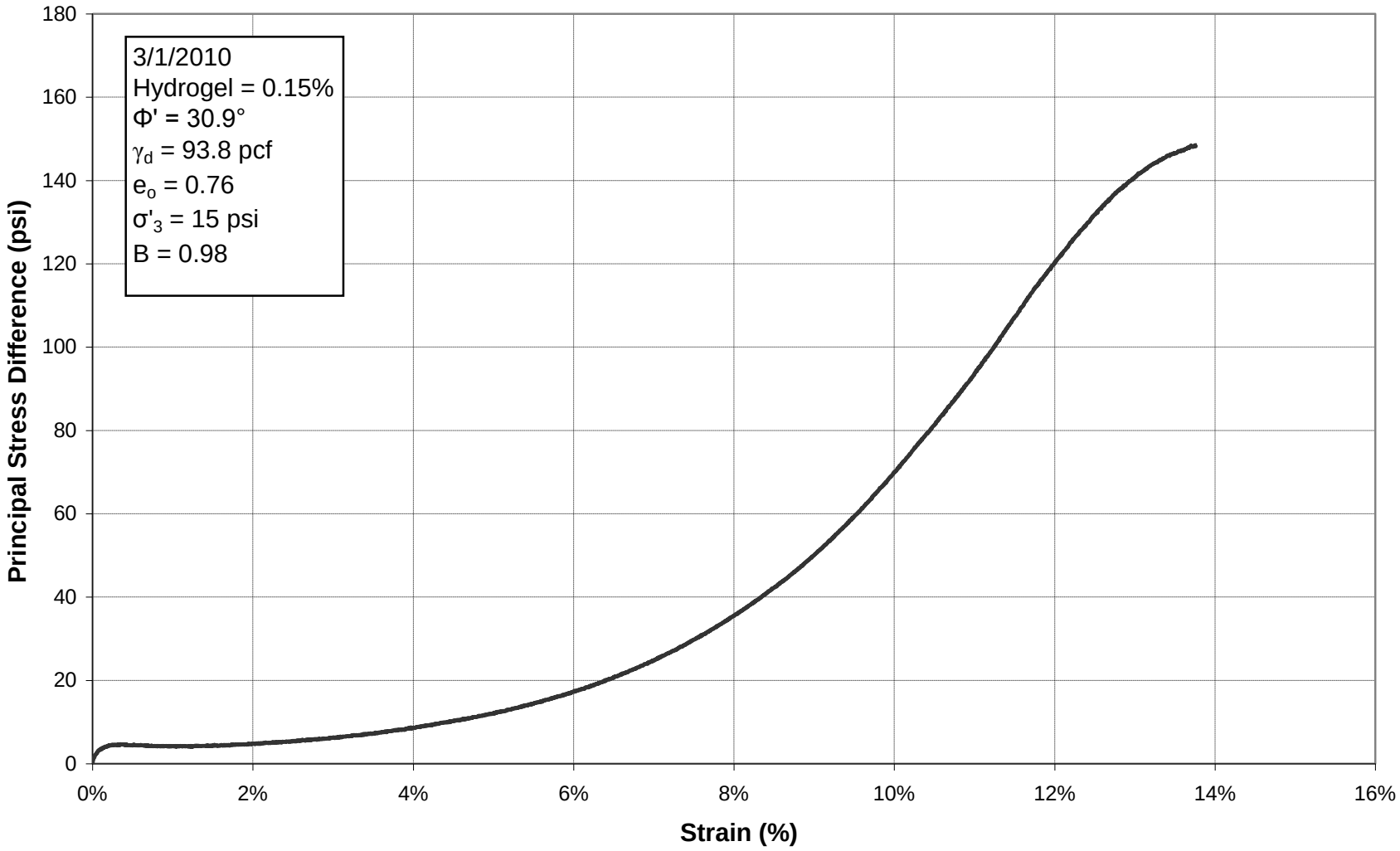

Figure E.99: Principal Stress Difference vs. Strain for Triaxial Test 48, 0.15% Hydrogel

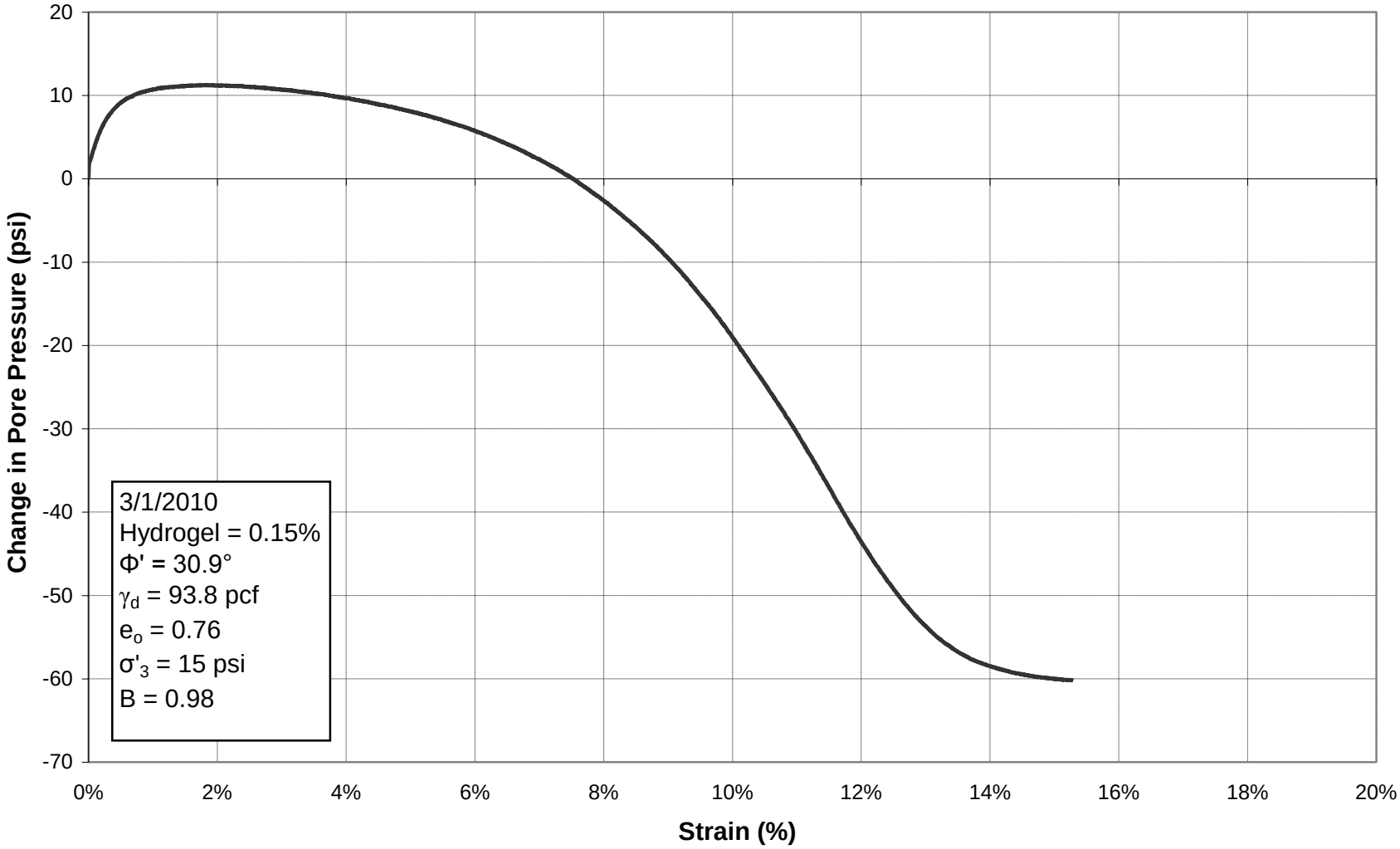

Figure E.100: Change in Pore Pressure vs. Strain for Triaxial Test 48, 0.15% Hydrogel

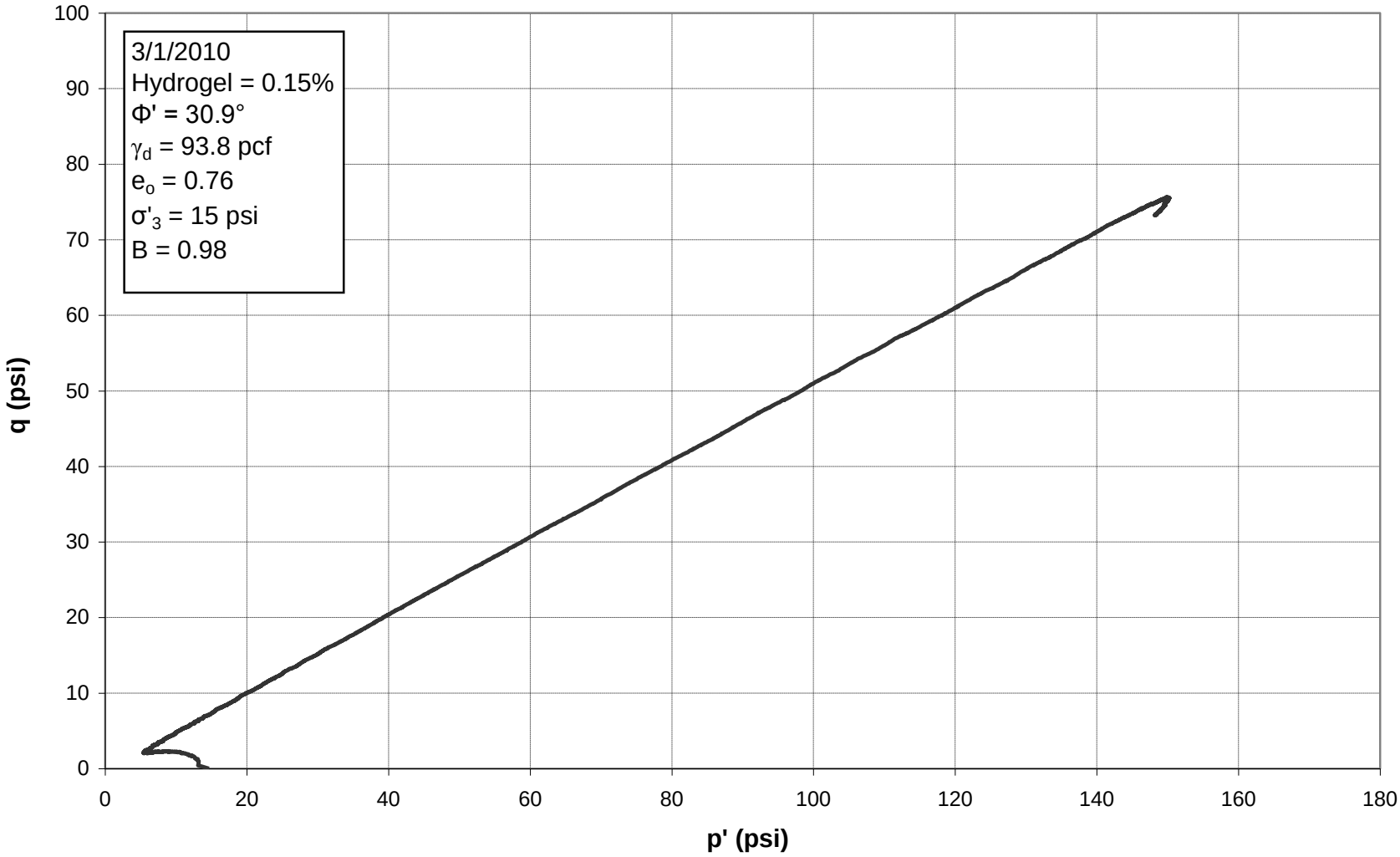

Figure E.101: p'-q Diagram for Triaxial Test 48, 0.15% Hydrogel

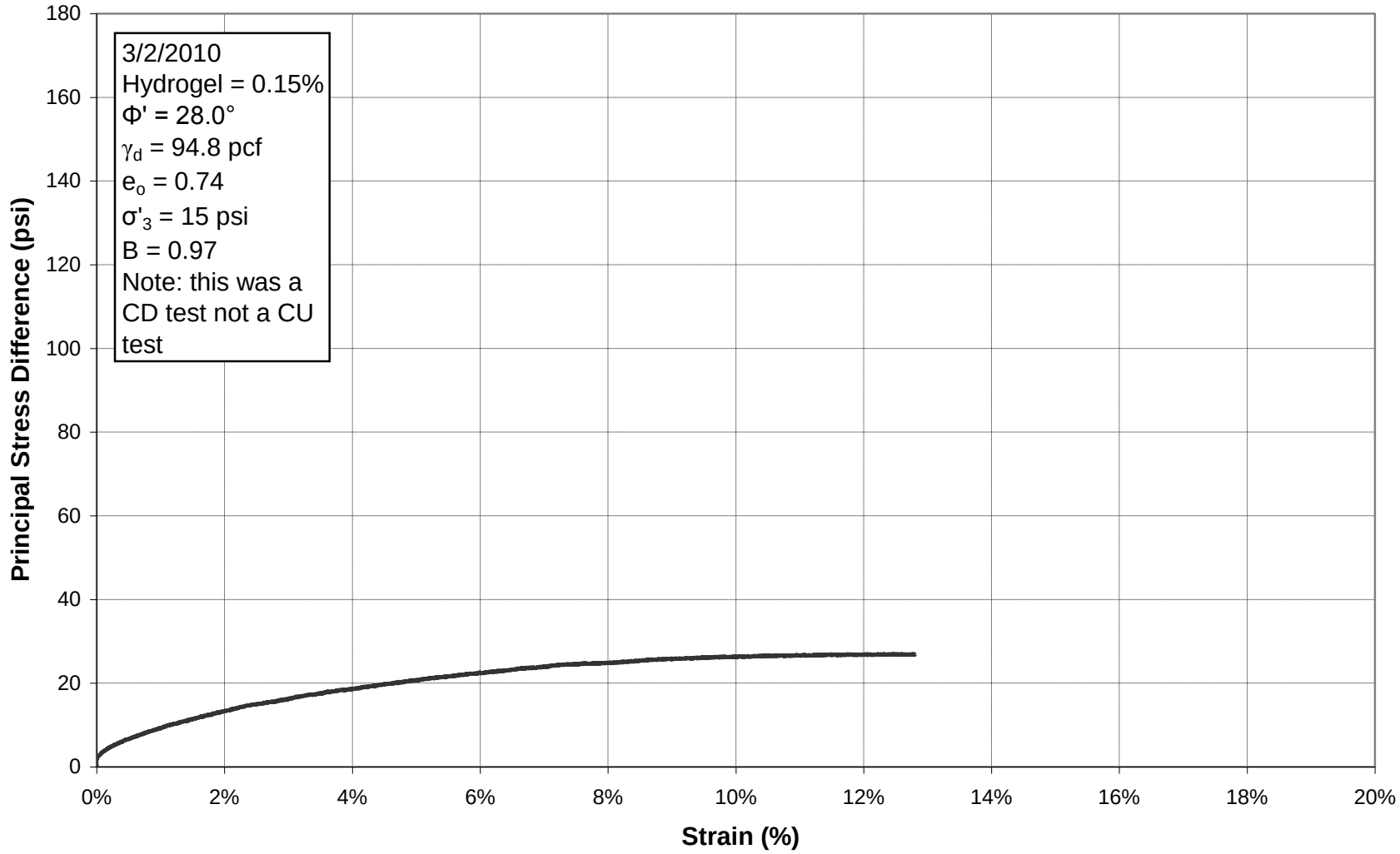

Figure E.102: Principal Stress Difference vs. Strain for Triaxial Test 49, 0.15% Hydrogel (this test was inadvertently run as a drained test)

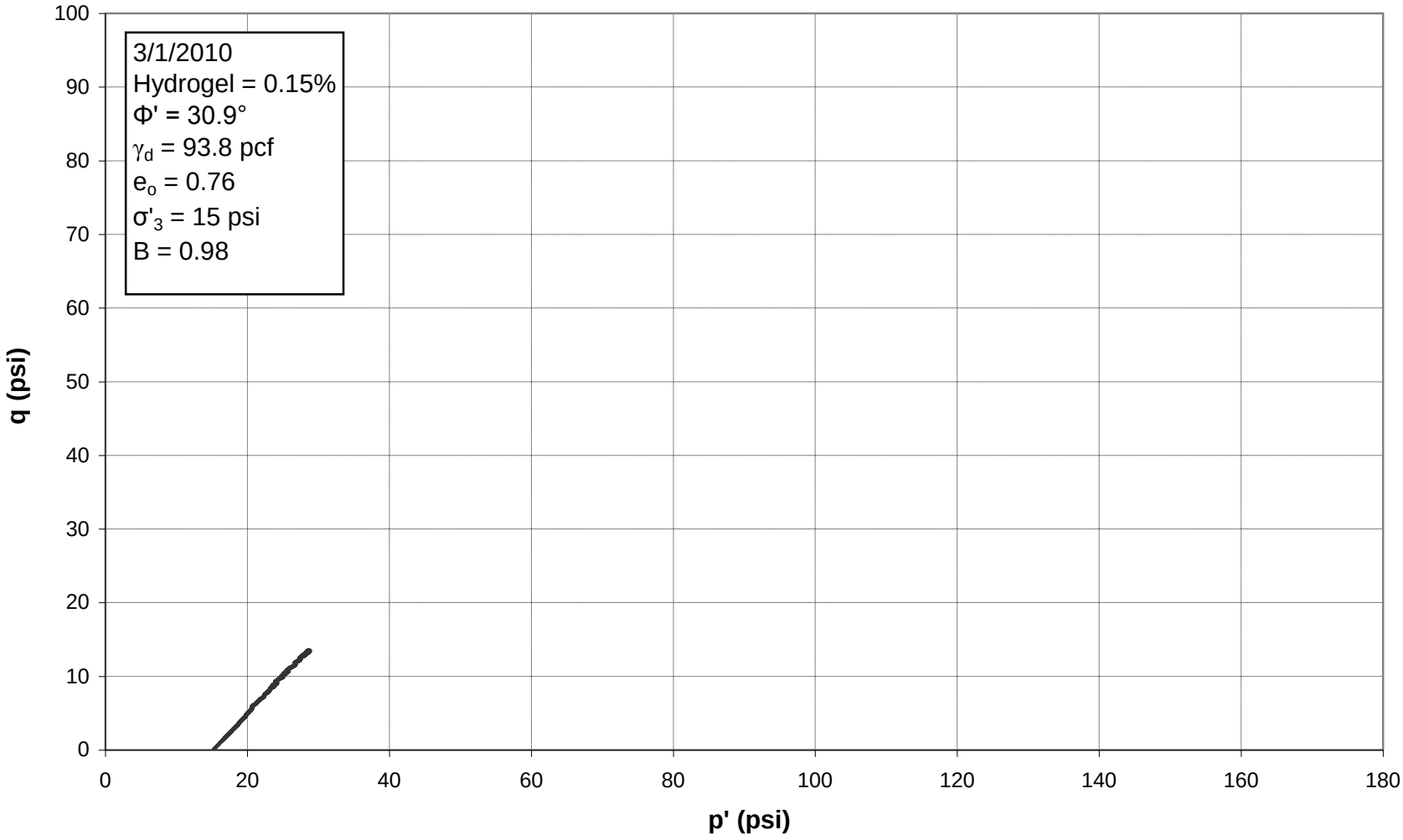

Figure E.103: p'-q Diagram for Triaxial Test 49, 0.15% Hydrogel (this test was inadvertently run as a drained test)

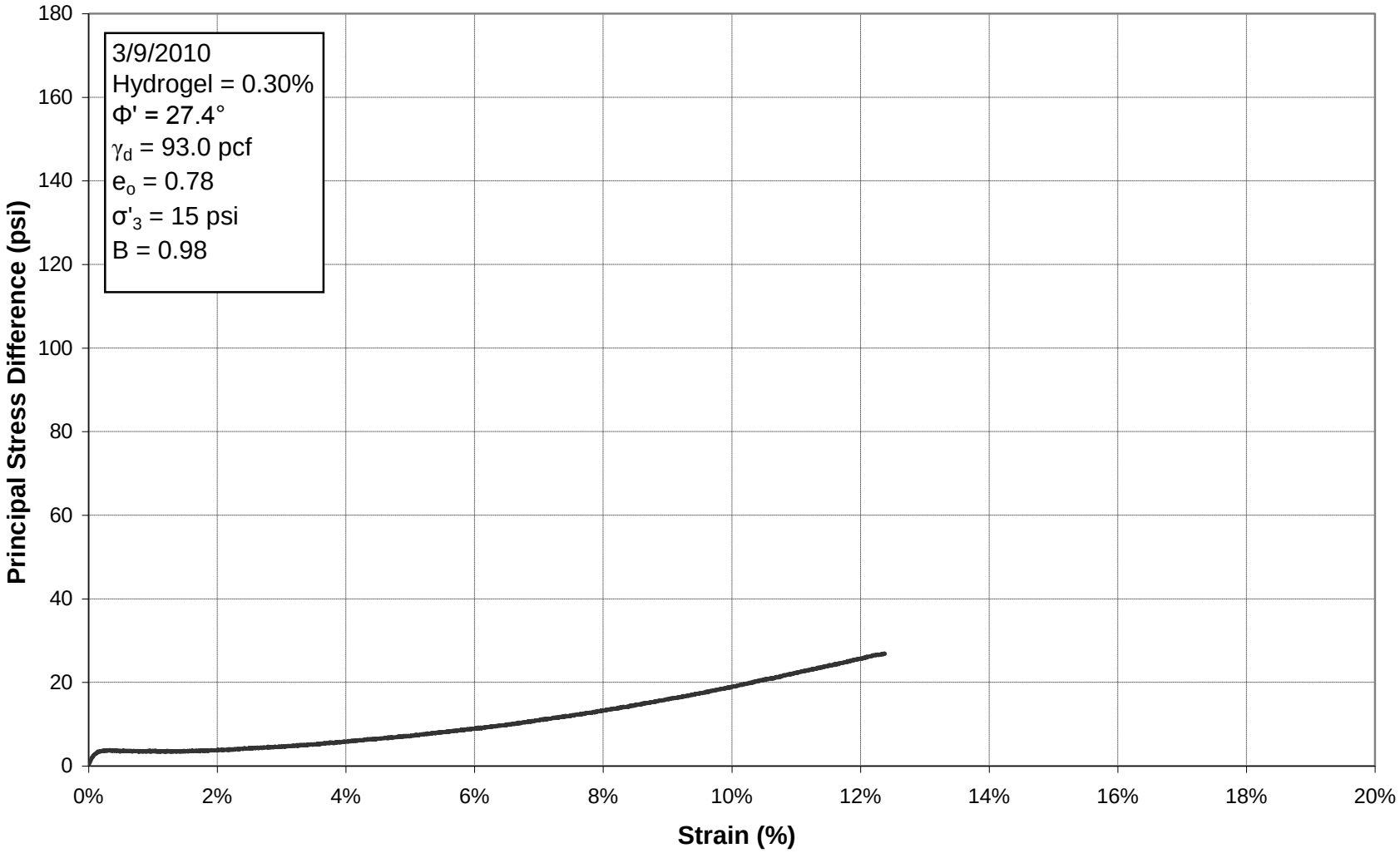

Figure E.104: Principal Stress Difference vs. Strain for Triaxial Test 50, 0.30% Hydrogel

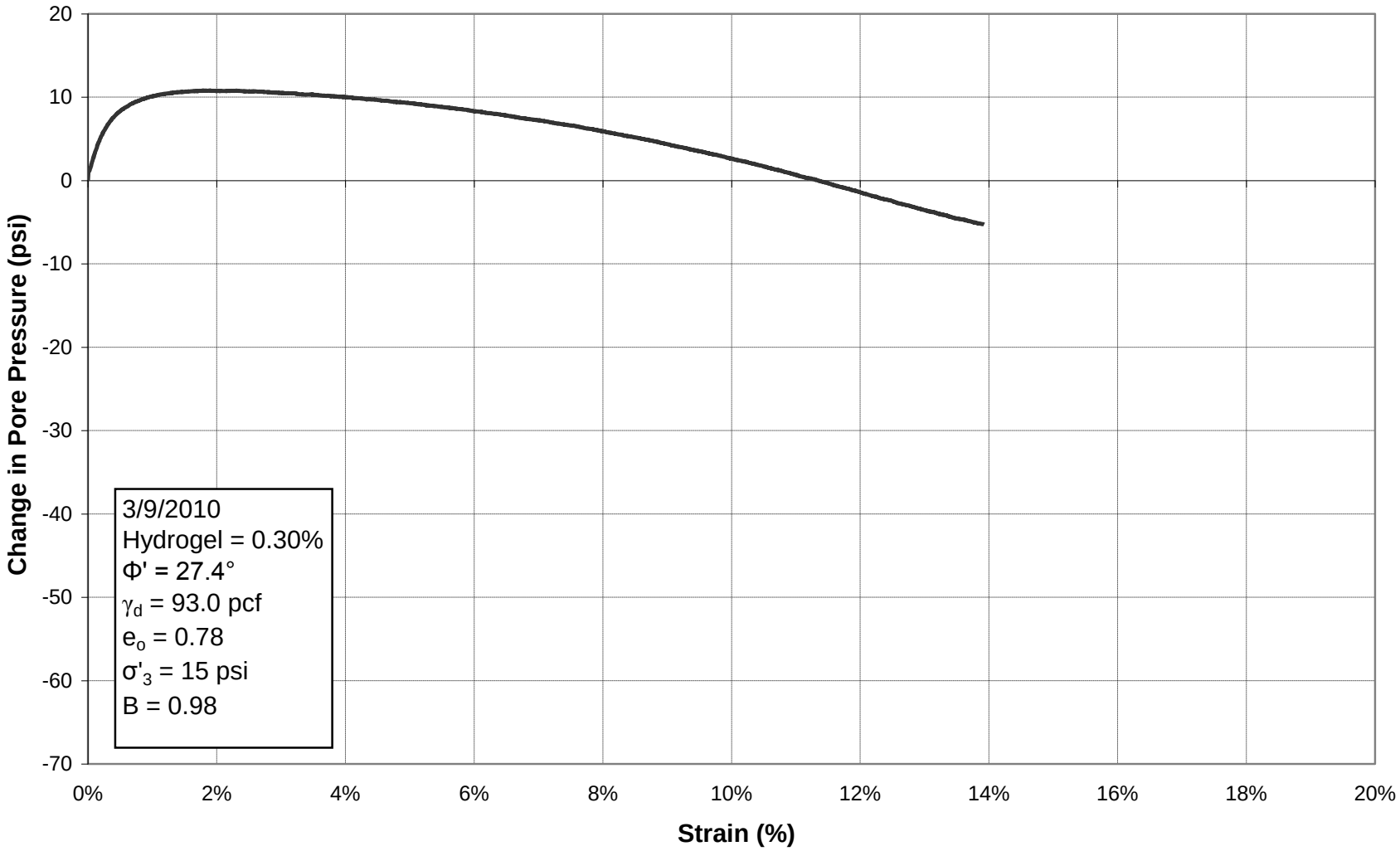

Figure E.105: Change in Pore Pressure vs. Strain for Triaxial Test 50, 0.30% Hydrogel

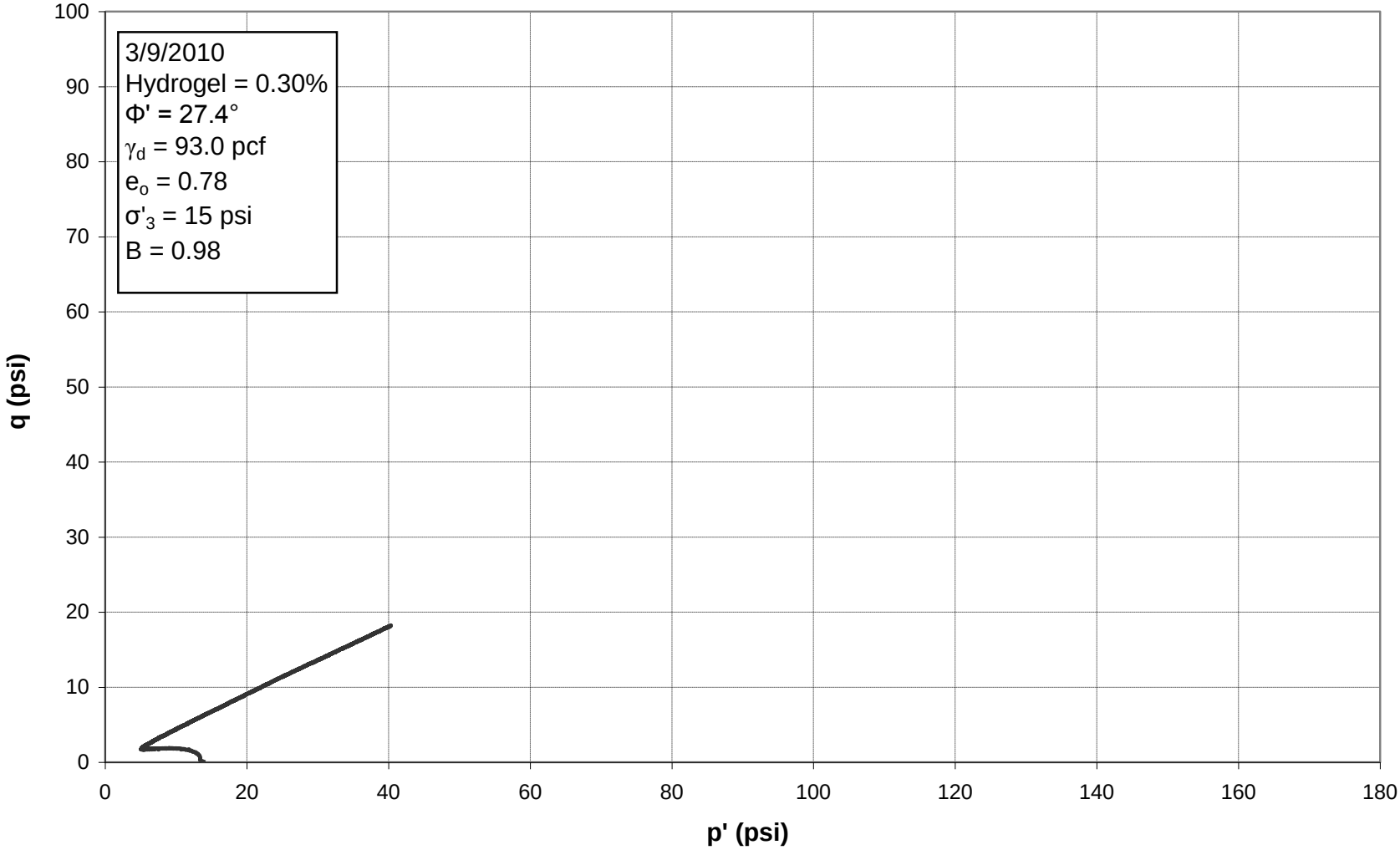

Figure E.106: p'-q Diagram for Triaxial Test 50, 0.30% Hydrogel

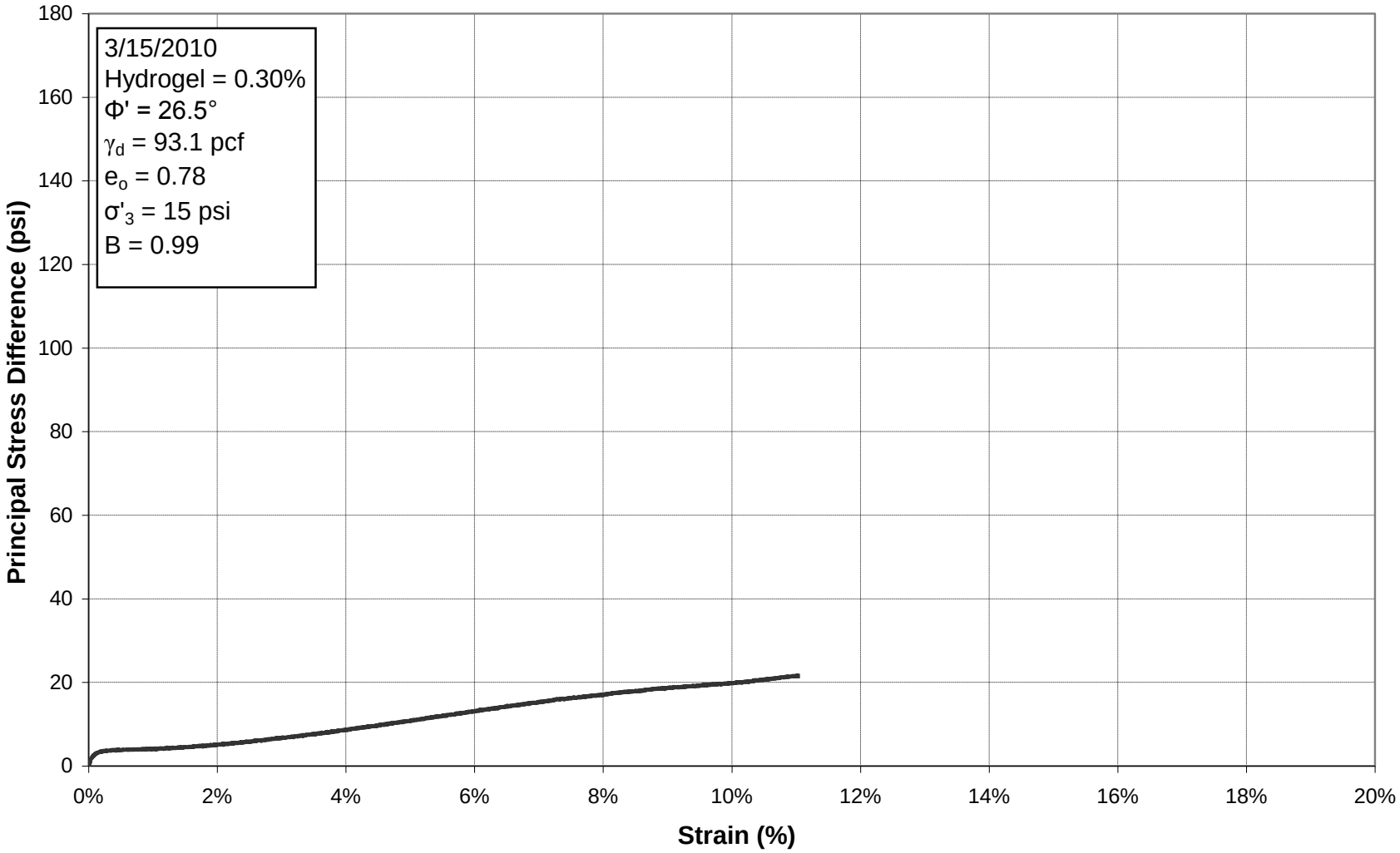

Figure E.107: Principal Stress Difference vs. Strain for Triaxial Test 52, 0.30% Hydrogel

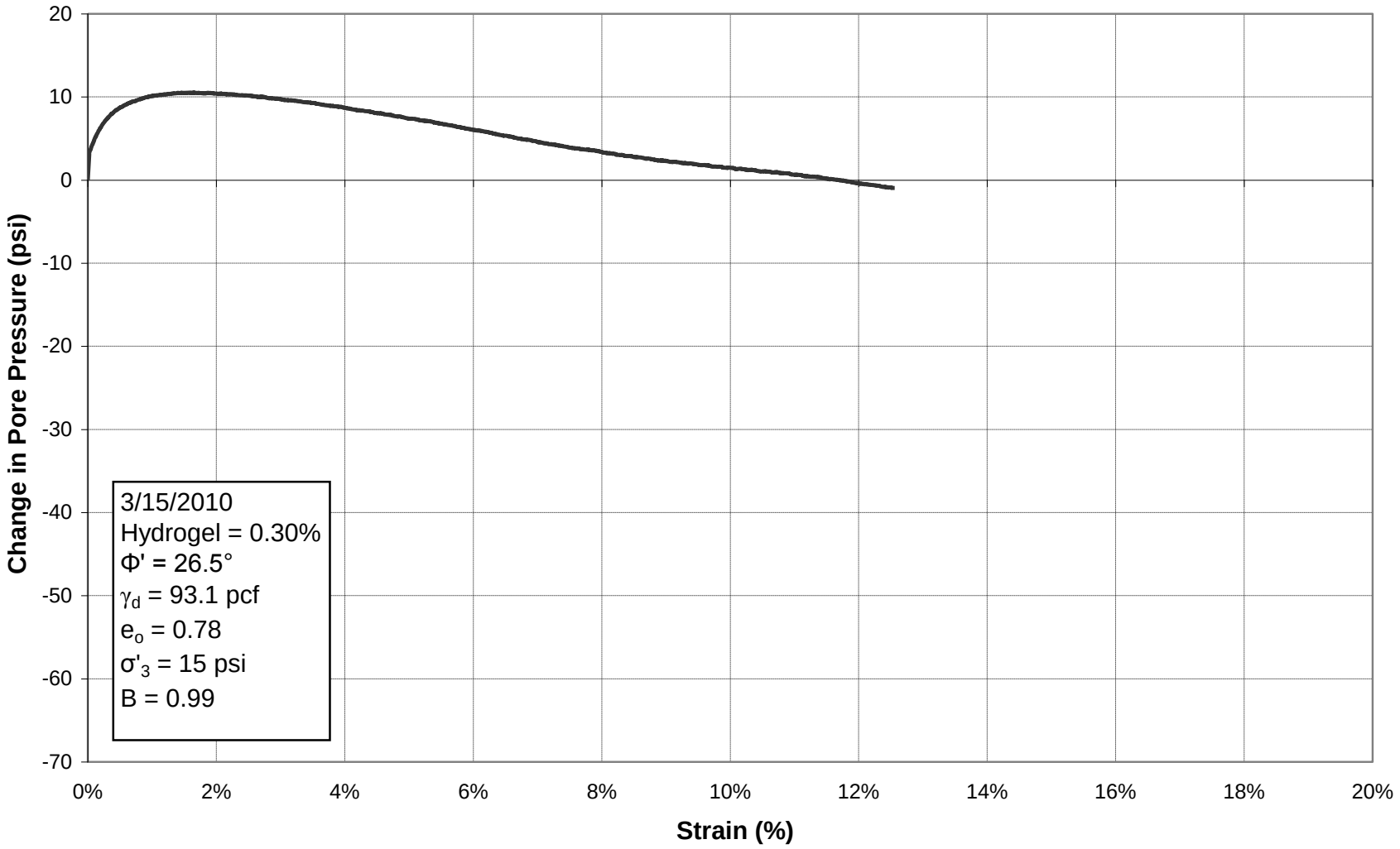

Figure E.108: Change in Pore Pressure vs. Strain for Triaxial Test 52, 0.30% Hydrogel

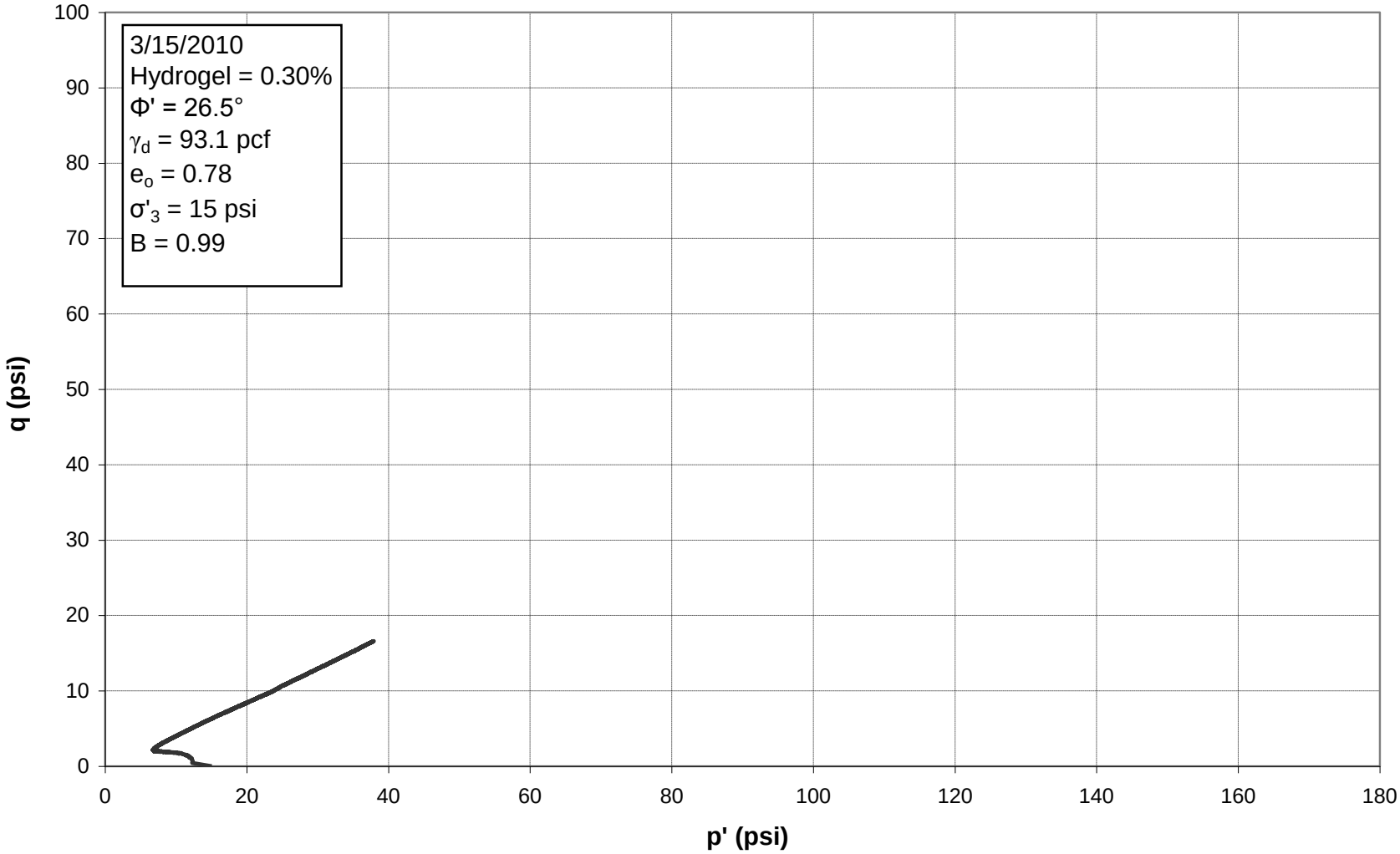

Figure E.109: p'-q Diagram for Triaxial Test 52, 0.30% Hydrogel

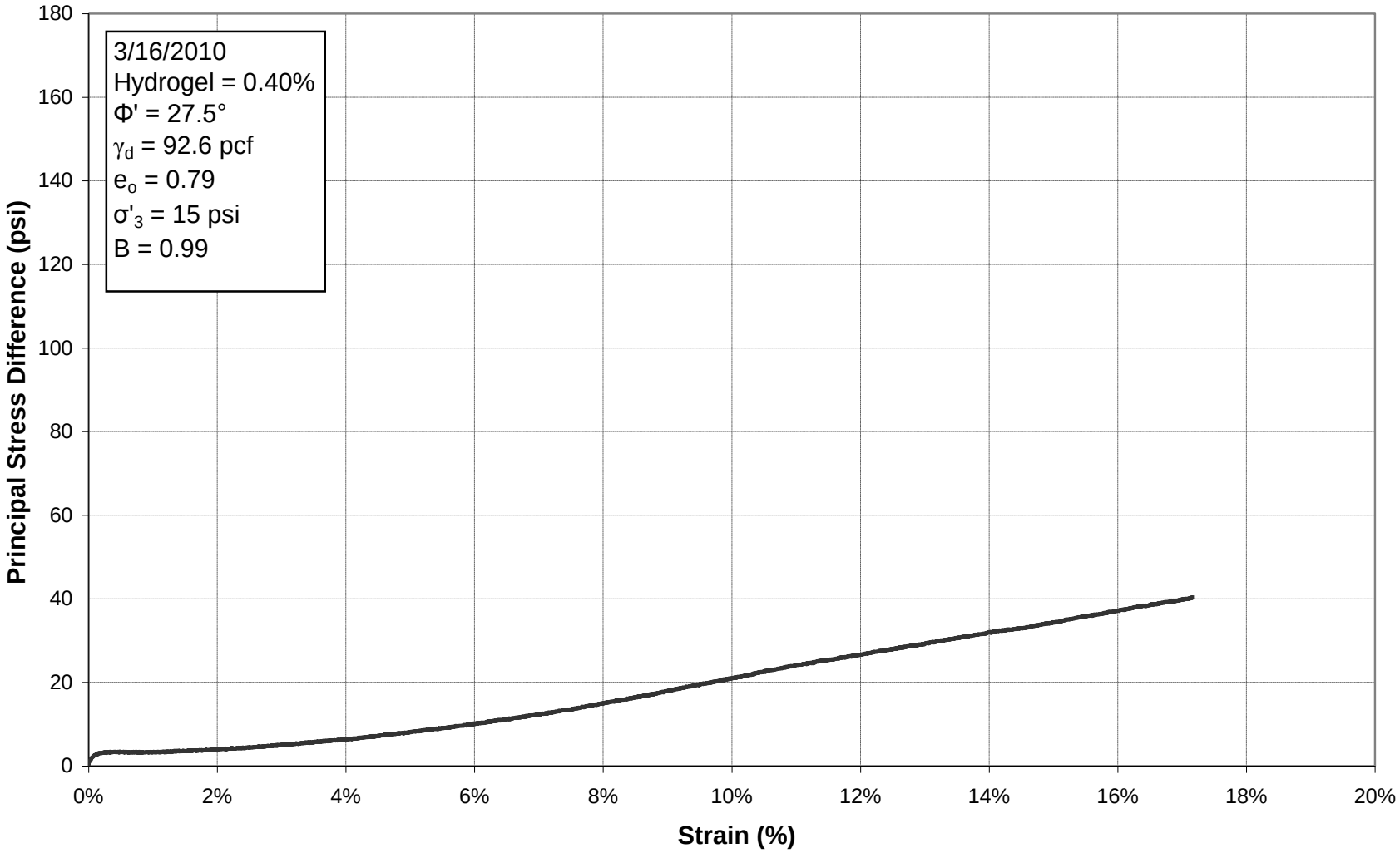

Figure E.110: Principal Stress Difference vs. Strain for Triaxial Test 53, 0.40% Hydrogel

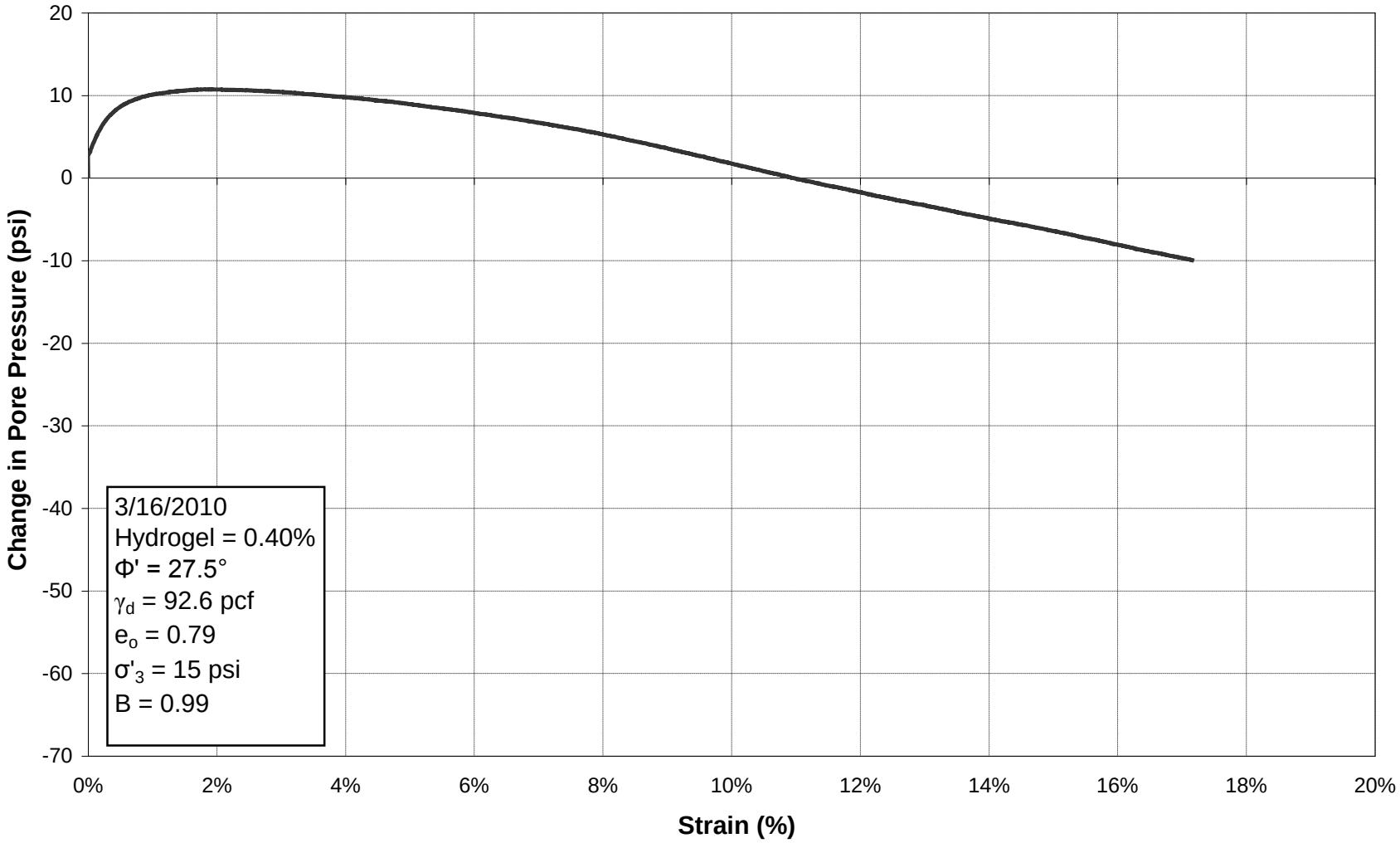

Figure E.111: Change in Pore Pressure vs. Strain for Triaxial Test 53, 0.40% Hydrogel

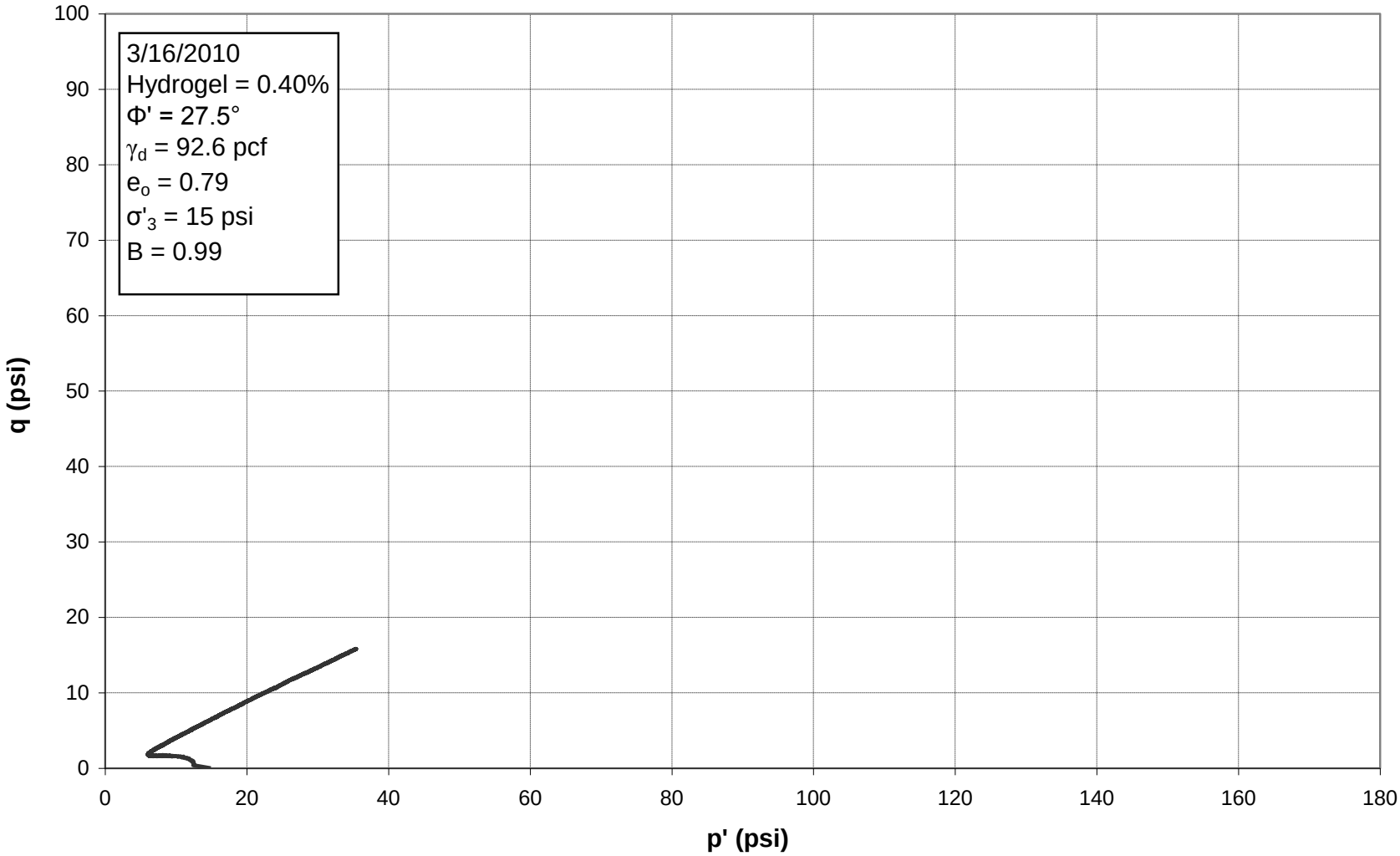

Figure E.112: p'-q Diagram for Triaxial Test 53, 0.40% Hydrogel

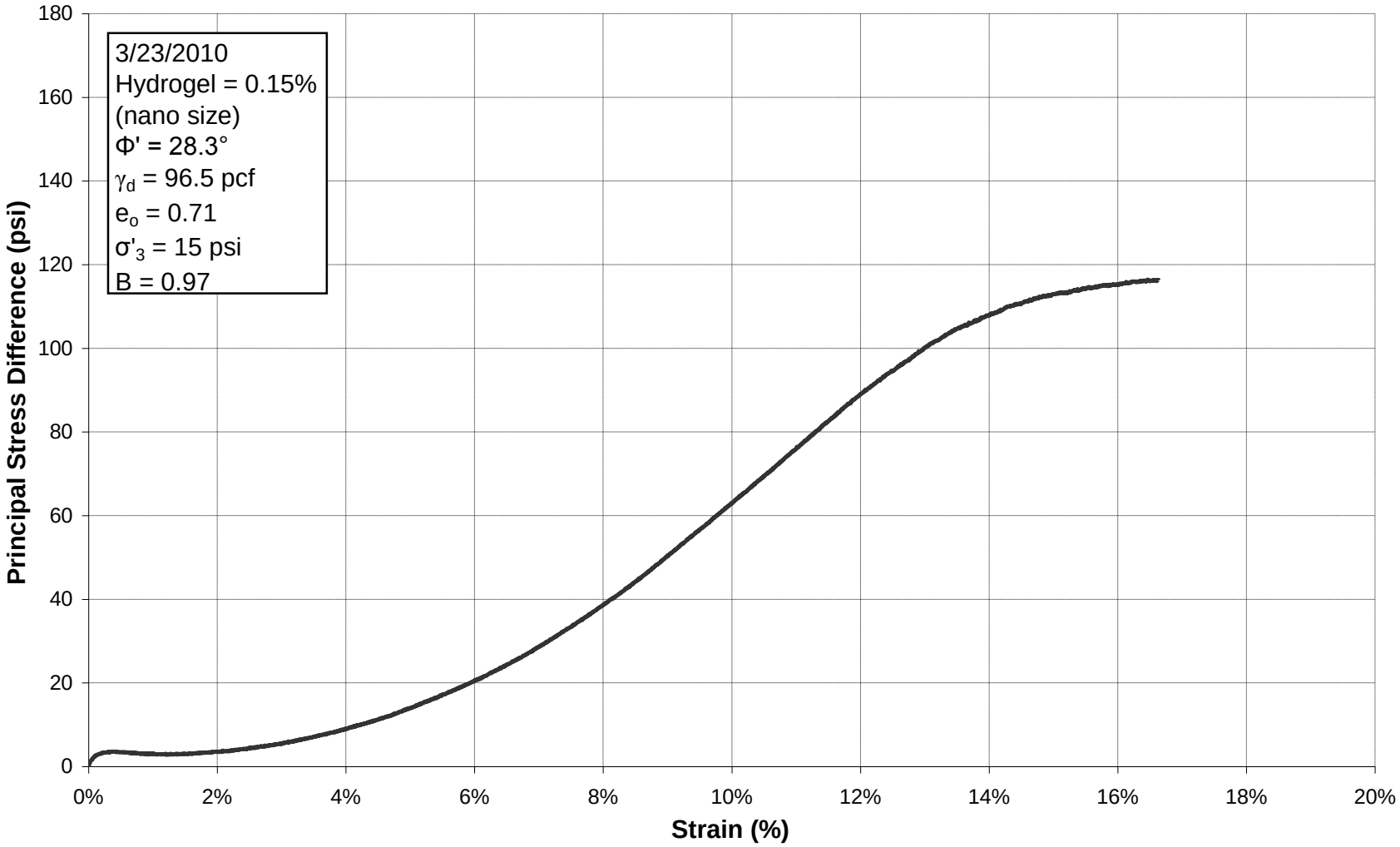

E.113: Principal Stress Difference vs. Strain for Triaxial Test 54, 0.15% Nanoparticle Hydrogel

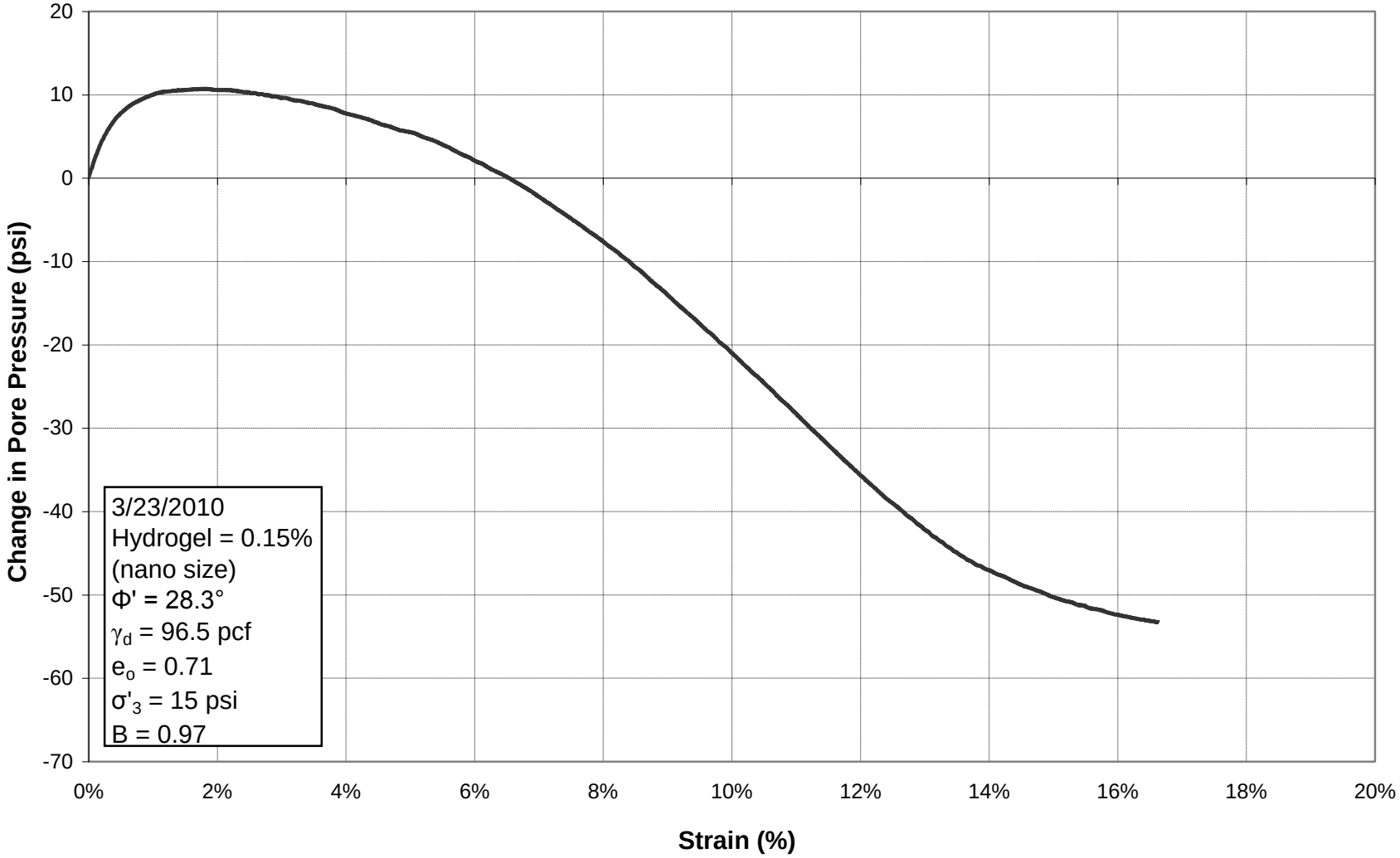

Figure E.114: Change in Pore Pressure vs. Strain for Triaxial Test 54, 0.15% Nanoparticle Hydrogel

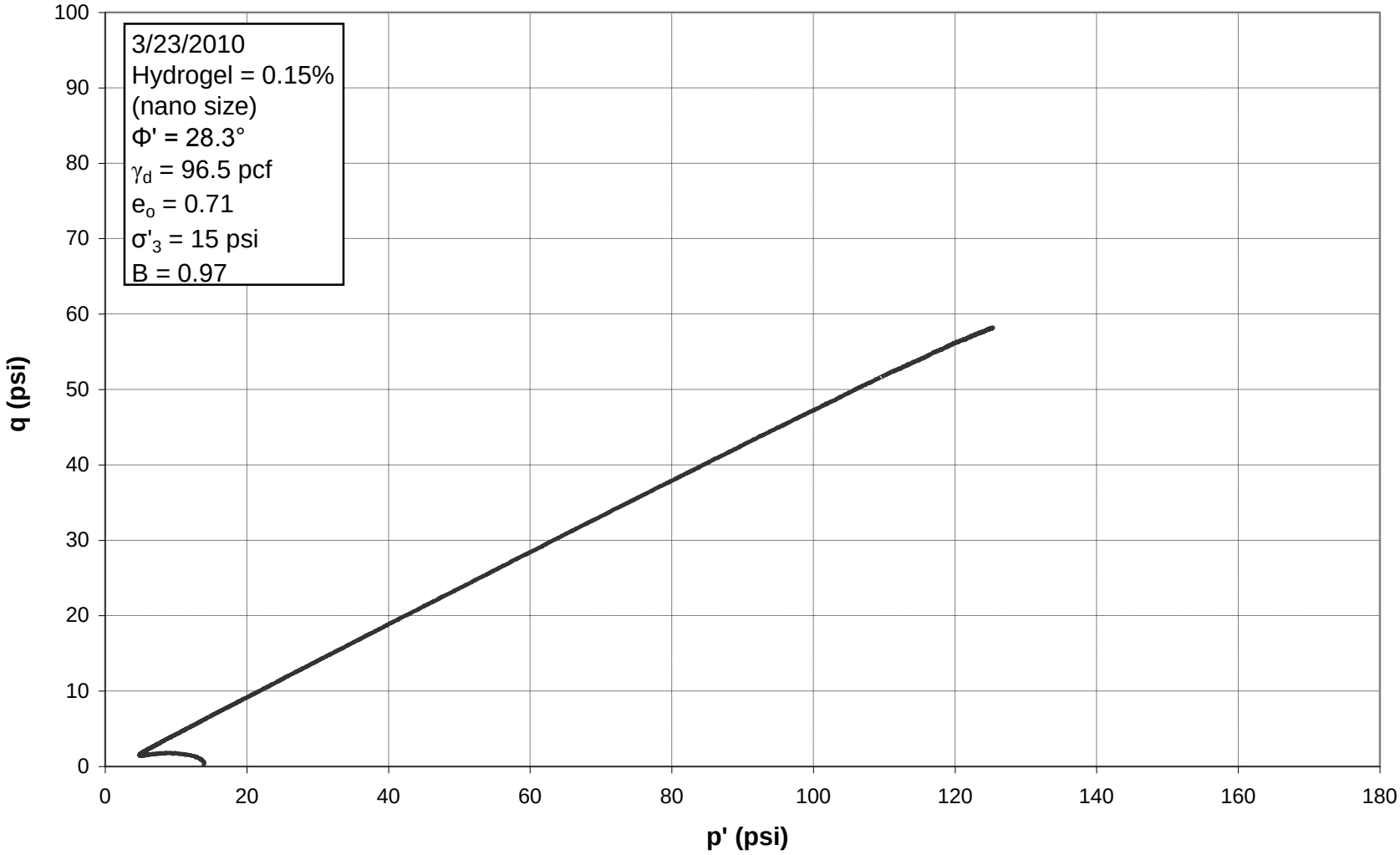

Figure E.115: p'-q Diagram for Triaxial Test 54, 0.15% Nanoparticle Hydrogel

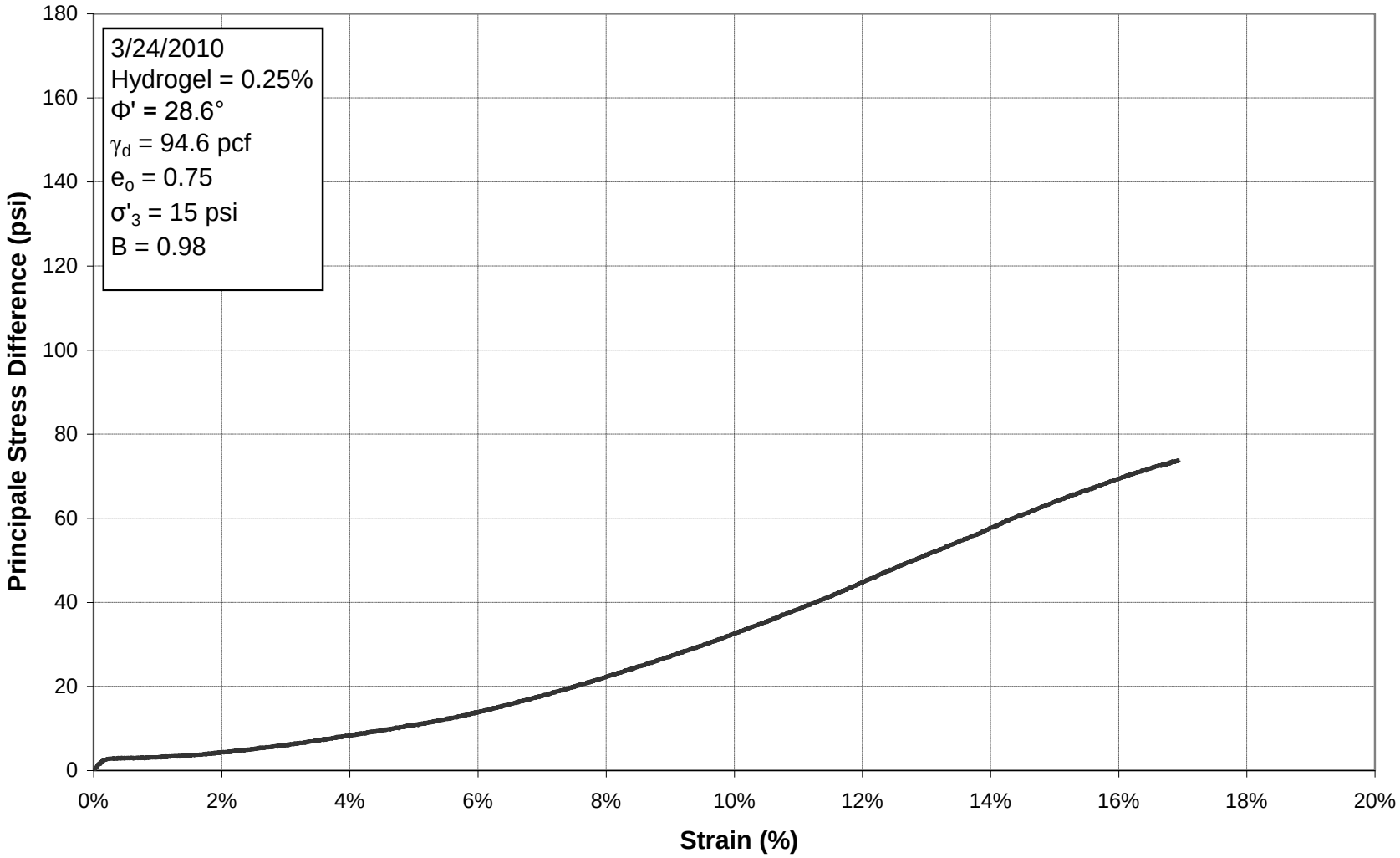

Figure E.116: Principal Stress Difference vs. Strain for Triaxial Test 55, 0.25% Hydrogel

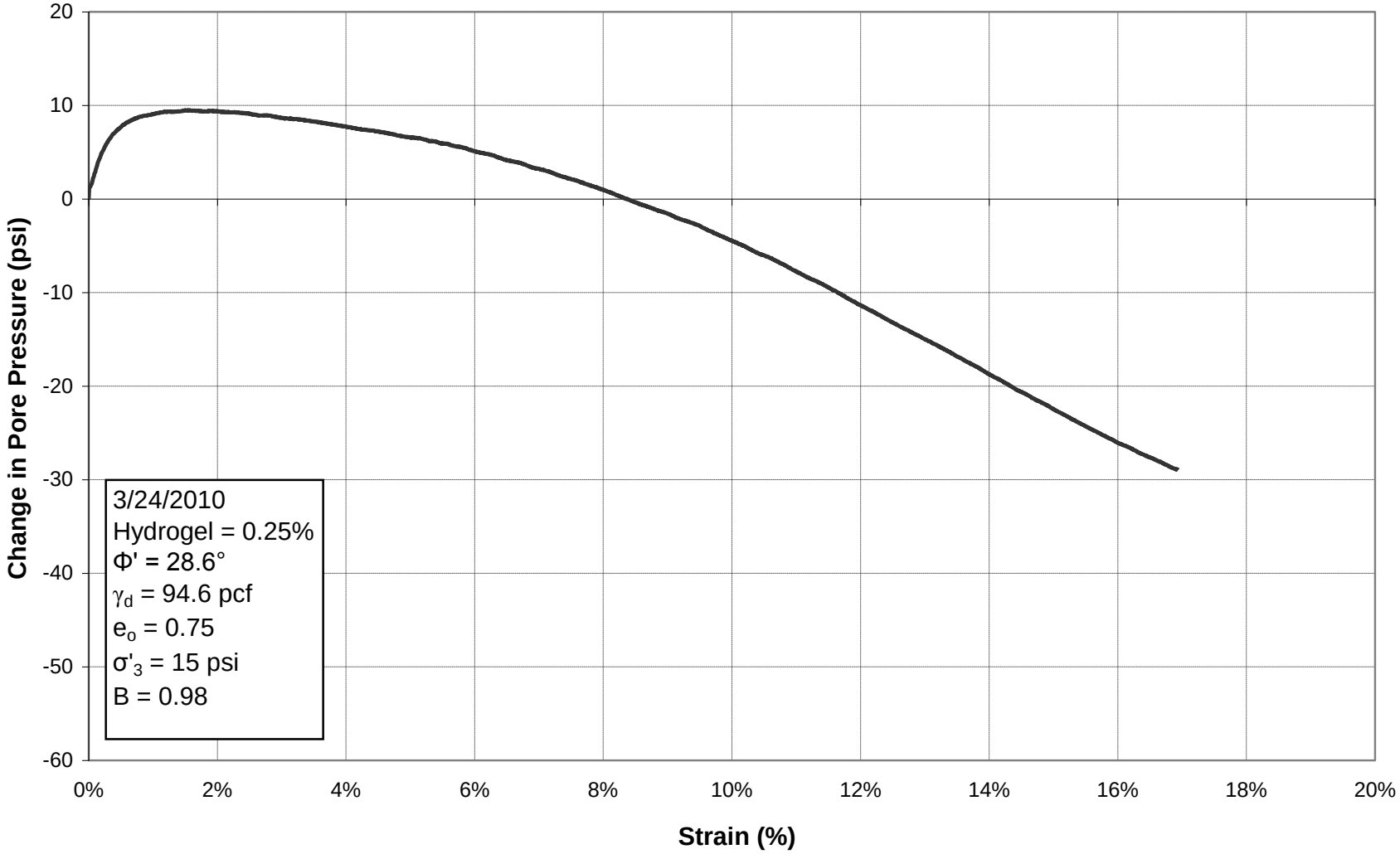

Figure E.117: Change in Pore Pressure vs. Strain for Triaxial Test 55, 0.25% Hydrogel

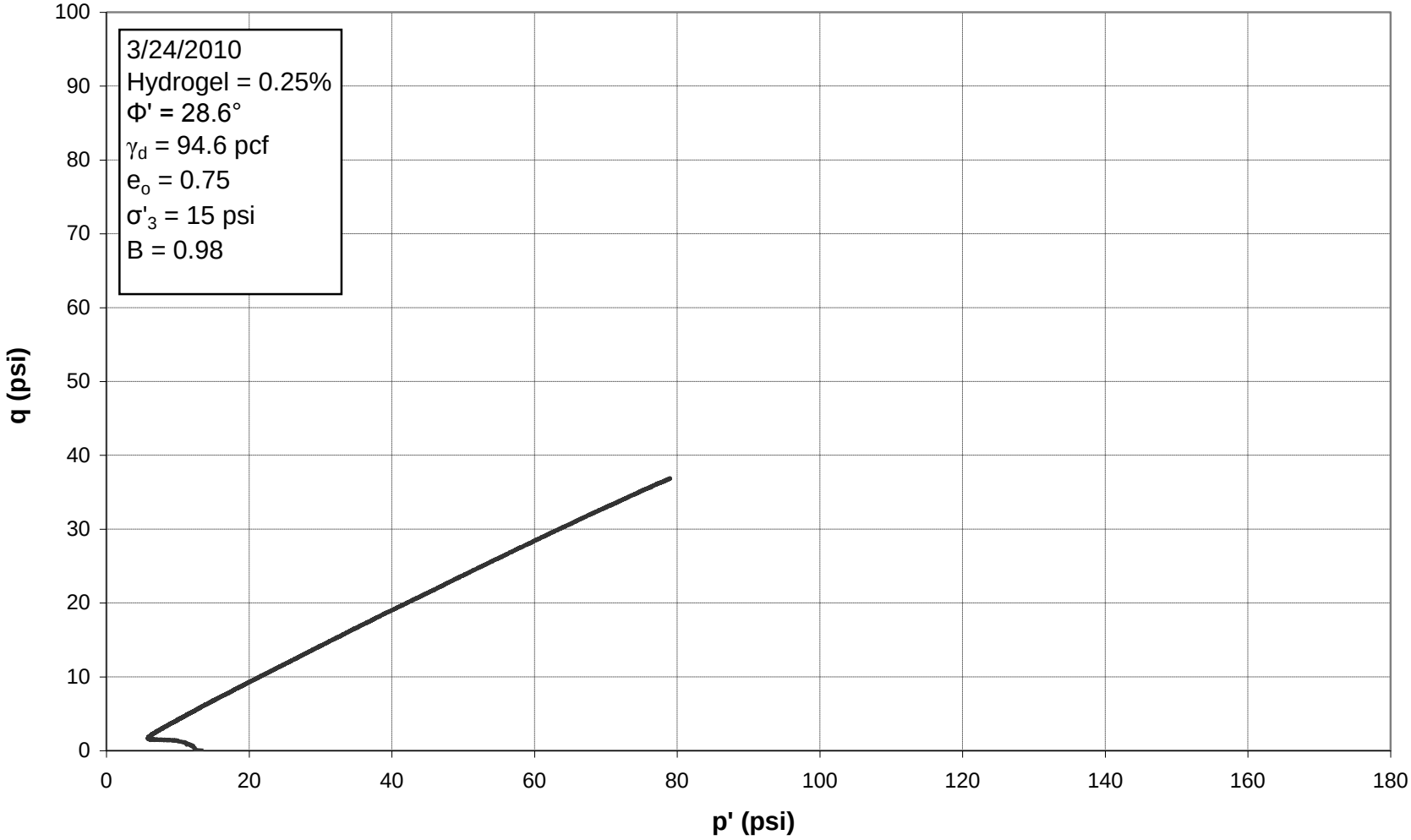

Figure E.118: p'-q Diagram for Triaxial Test 55, 0.25% Hydrogel

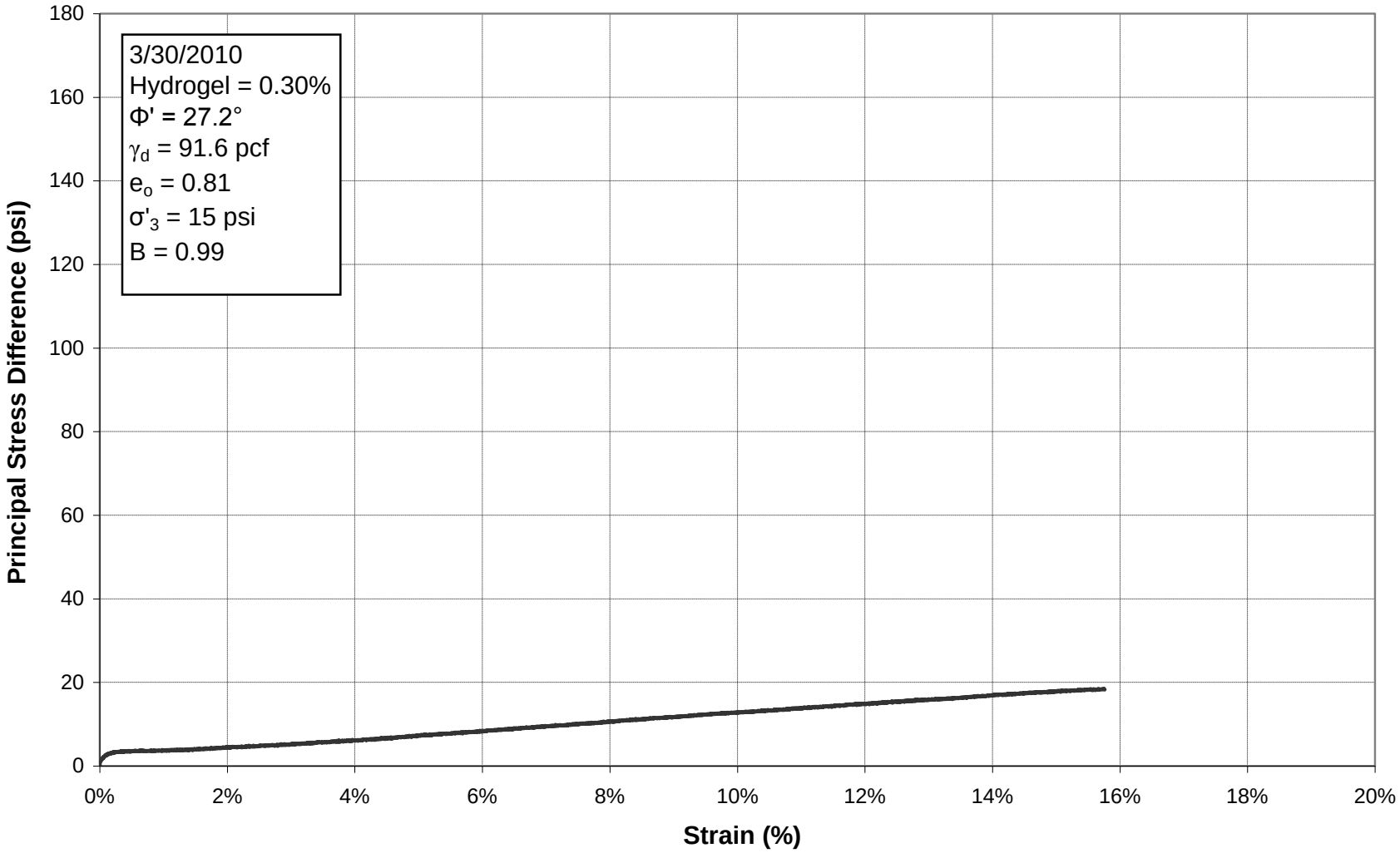

Figure E.119: Principal Stress Difference vs. Strain for Triaxial Test 56, 0.30% Hydrogel

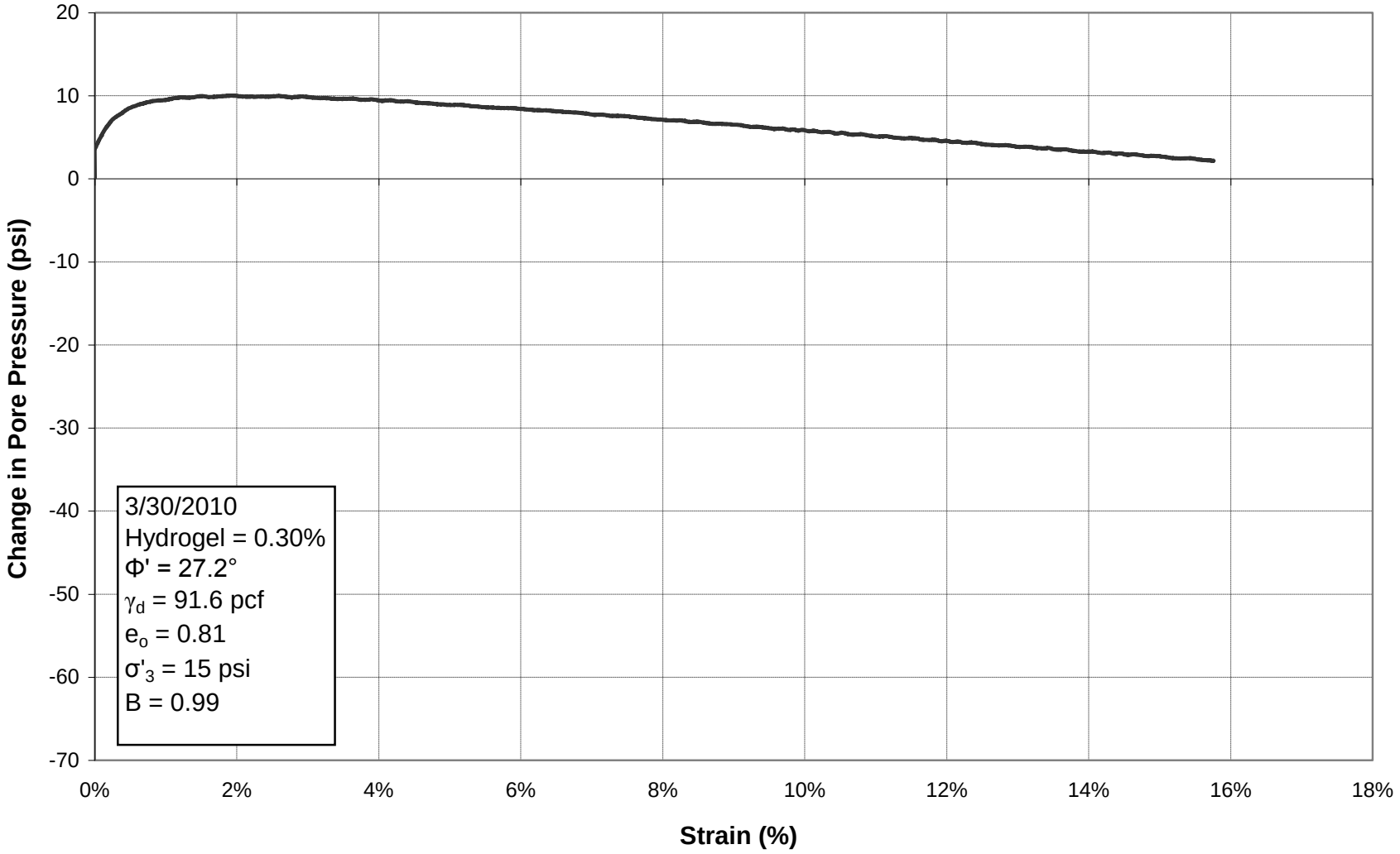

Figure E.120: Change in Pore Pressure vs. Strain for Triaxial Test 56, 0.30% Hydrogel

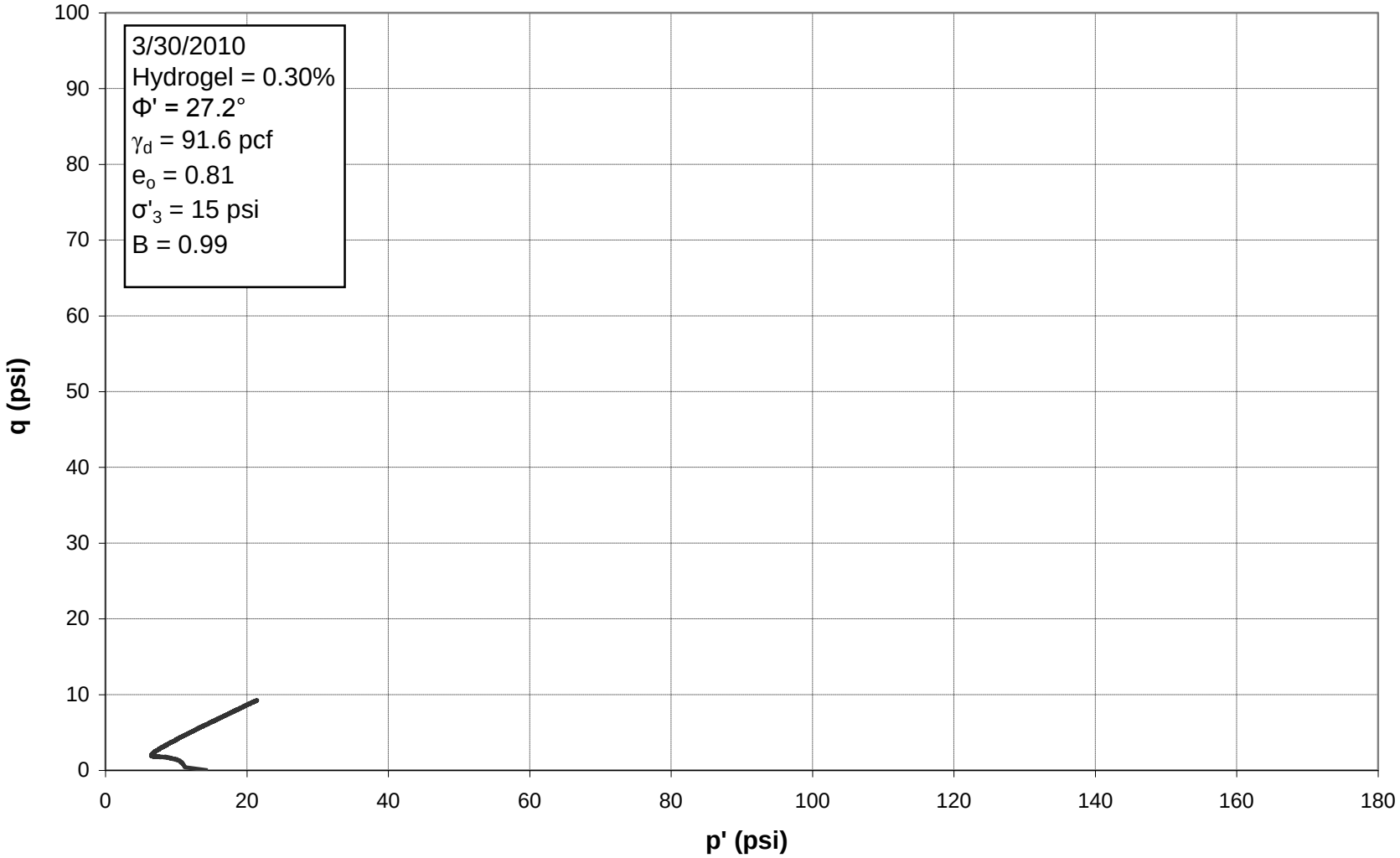

Figure E.121: p'-q Diagram for Triaxial Test 56, 0.30% Hydrogel

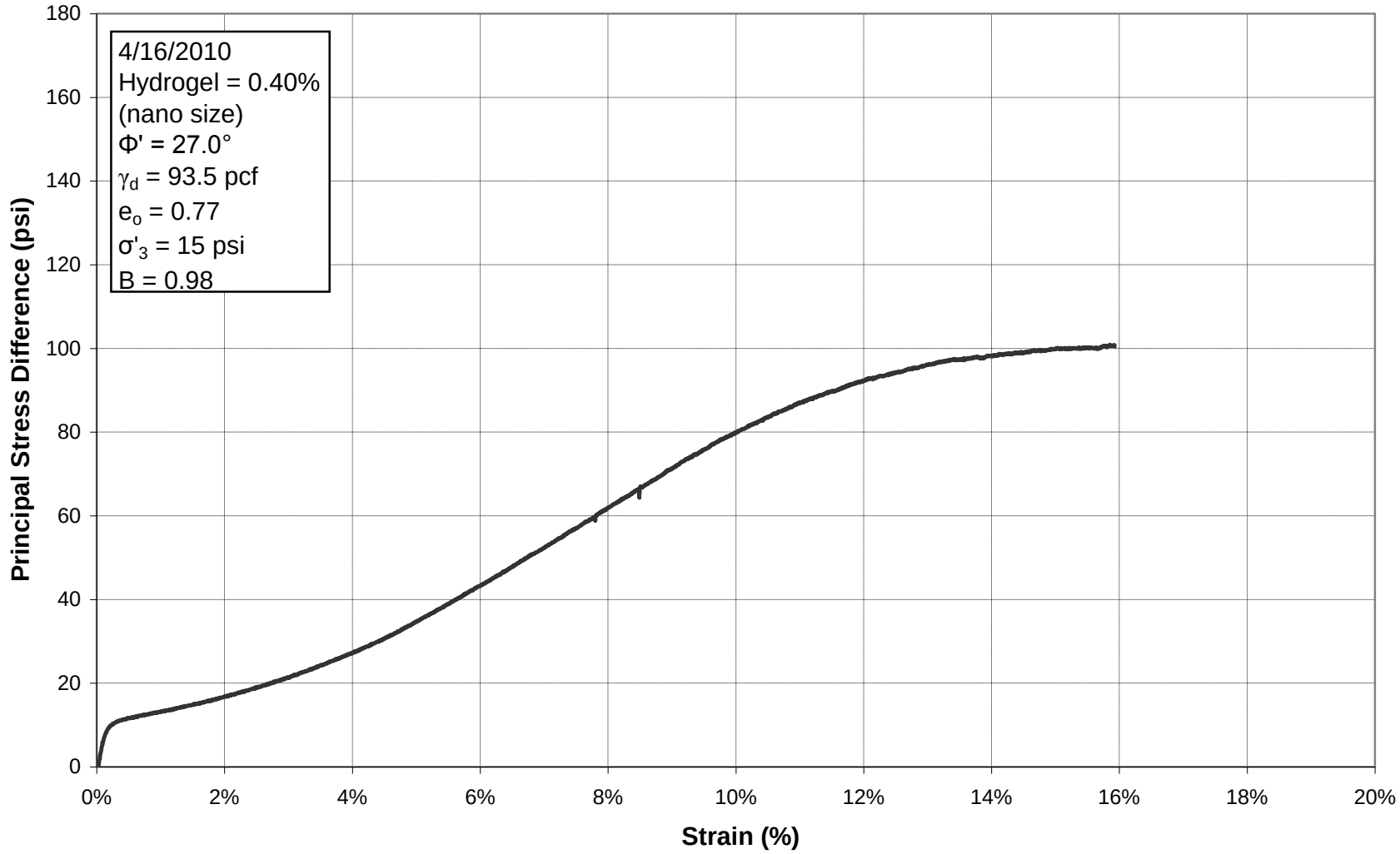

Figure E.122: Principal Stress Difference vs. Strain for Triaxial Test 57, 0.40% Nanoparticle Hydrogel

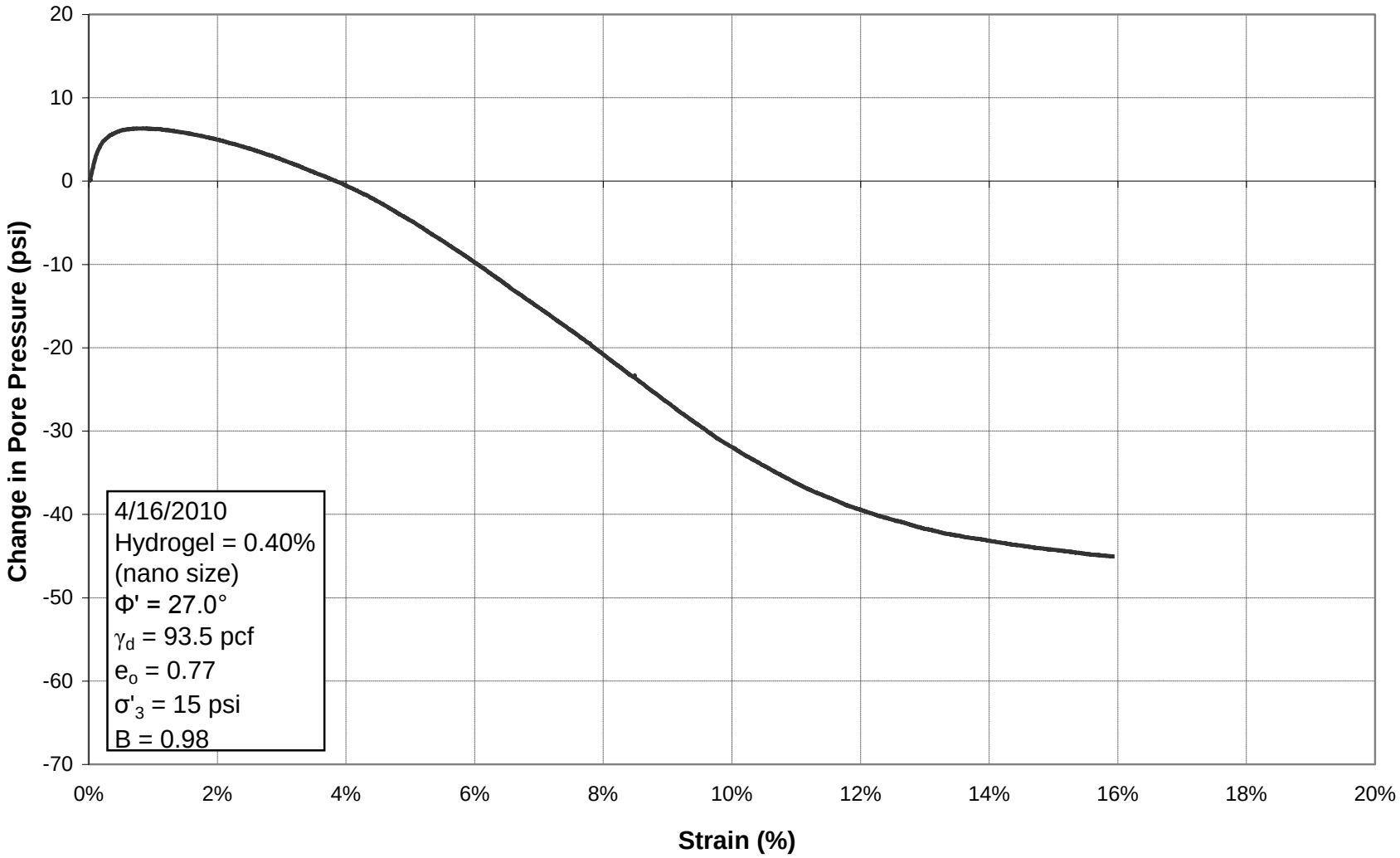

Figure E.123: Change in Pore Pressure vs. Strain for Triaxial Test 57, 0.40% Nanoparticle Hydrogel

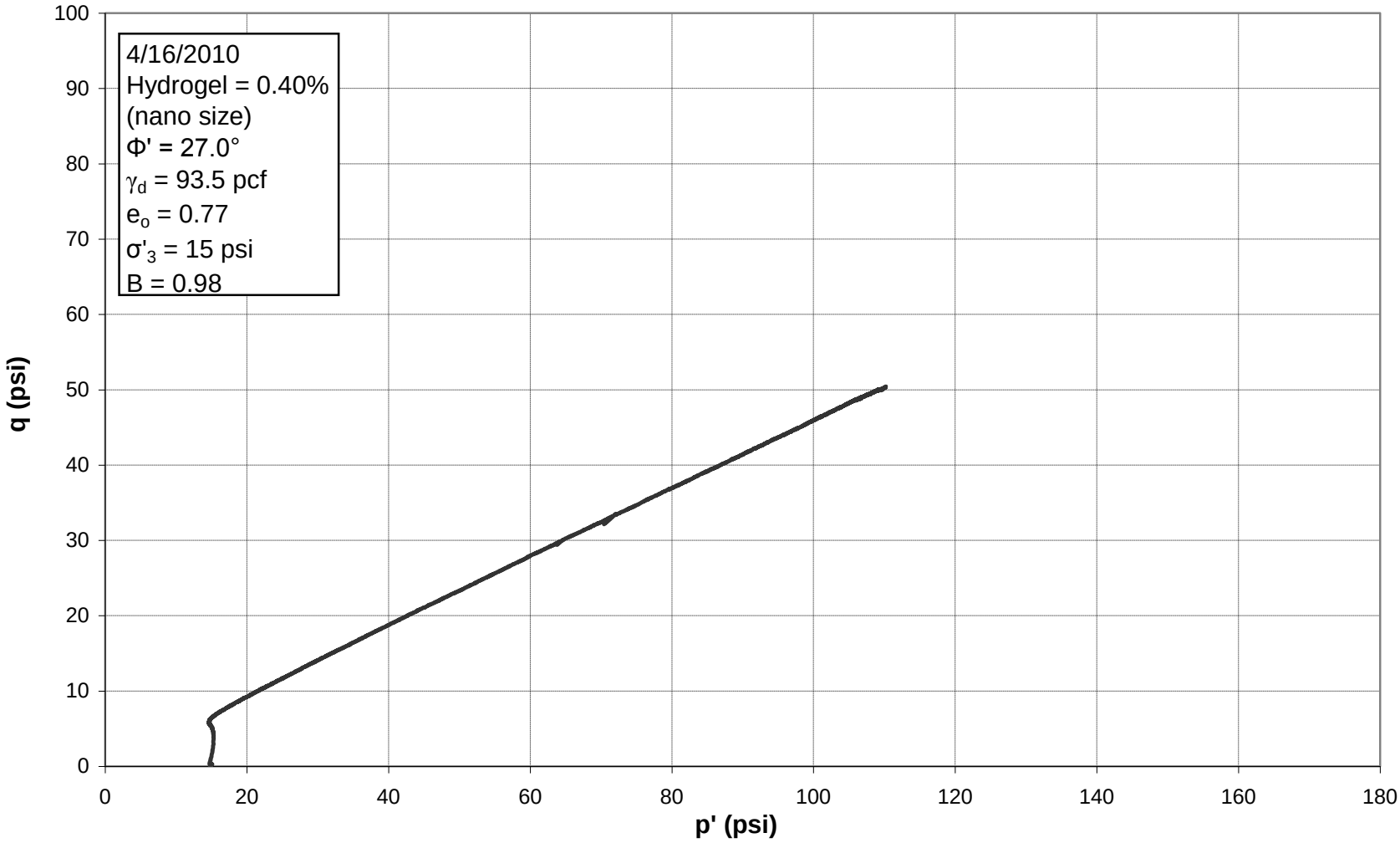

Figure E.124: p'-q Diagram for Triaxial Test 57, 0.40% Nanoparticle Hydrogel

Appendix F: Additional Cyclic Triaxial Data Plots

F.1 2004 Data Plots

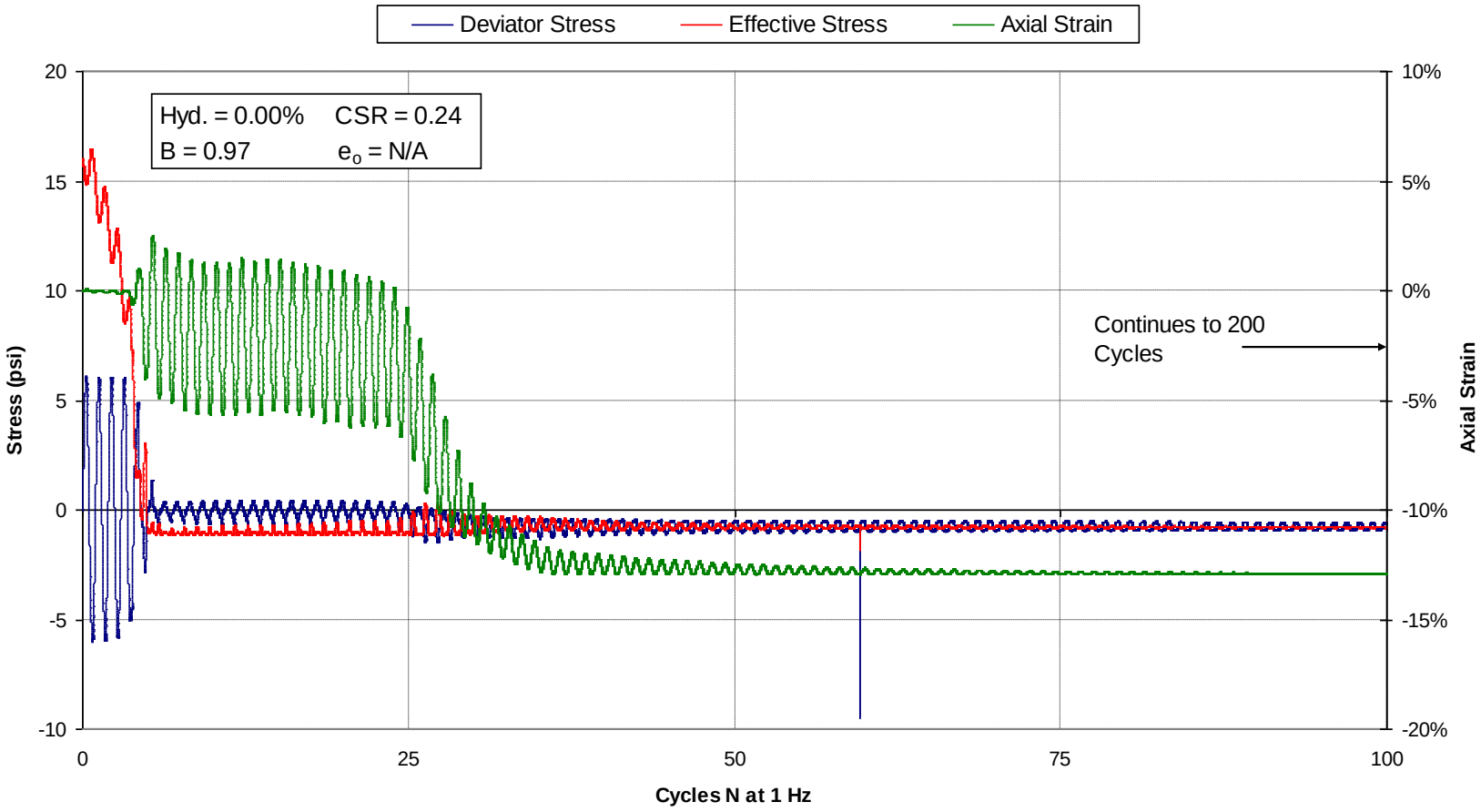

Figure F.1: Deviator Stress, Effective Stress, and Axial Strain vs. Cycles, for Ottawa sand Sample 0.00%n5 -Test 1 (0.00% Hydrogel); liquefaction occurred after 5 cycles; test was ended at 200 cycles

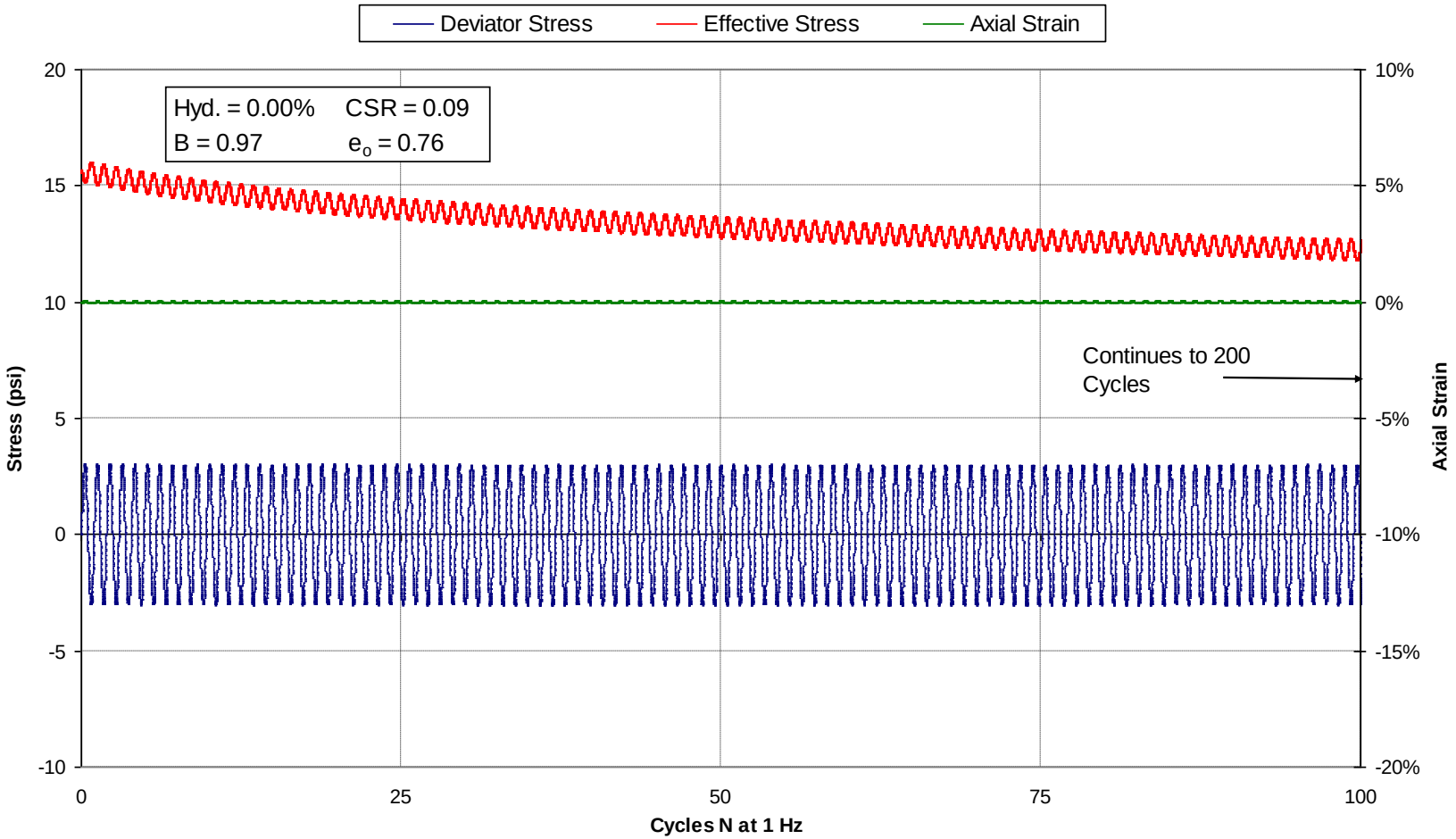

Figure F.2: Deviator Stress, Effective Stress, and Axial Strain vs. Cycles, for Ottawa sand Sample 0.00%n6 -Test 1 (0.00% Hydrogel); liquefaction did not occur; test was ended at 200 cycles

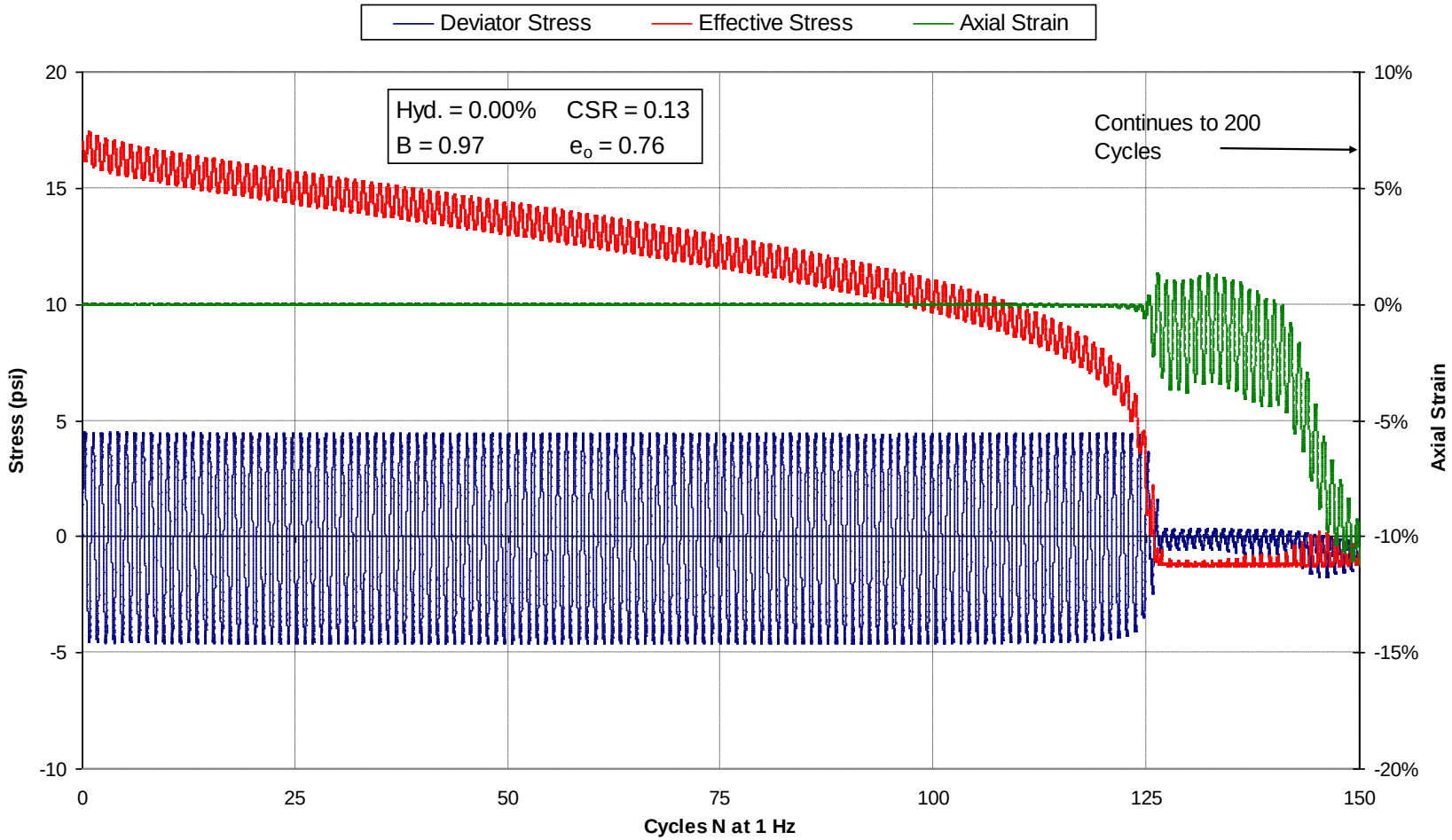

Figure F.3: Deviator Stress, Effective Stress, and Axial Strain vs. Cycles, for Ottawa sand Sample 0.00%n6 -Test 2 (0.00% Hydrogel); liquefaction occurred after 128 cycles; test was ended at 200 cycles (the horizontal scale is different from the other plots to show the point where liquefaction occurred)

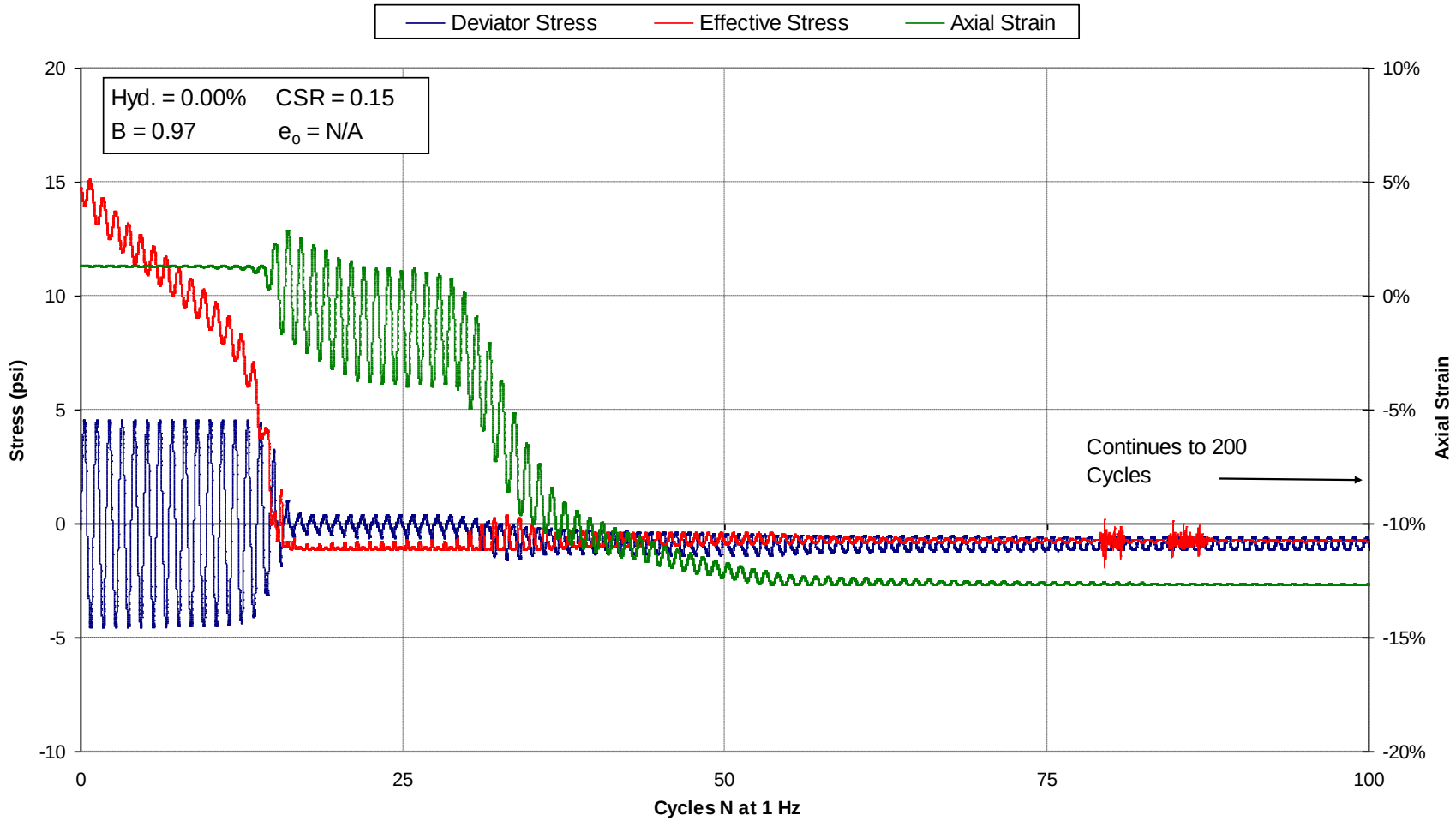

Figure F.4: Deviator Stress, Effective Stress, and Axial Strain vs. Cycles, for Ottawa sand Sample 0.00%n7 -Test 1 (0.00% Hydrogel); liquefaction occurred after 16 cycles; test was ended at 200 cycles

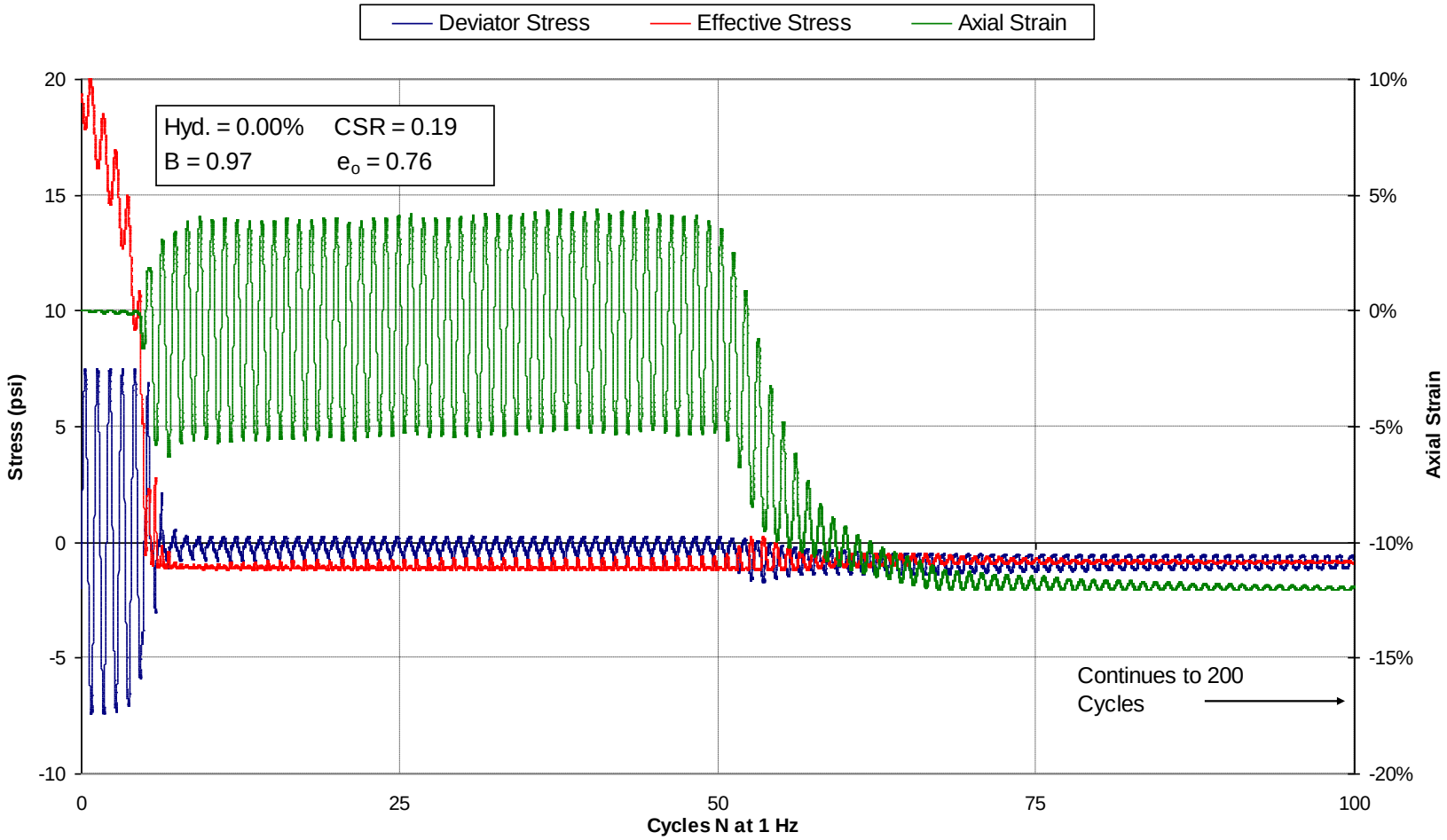

Figure F.5: Deviator Stress, Effective Stress, and Axial Strain vs. Cycles, for Ottawa sand Sample 0.00%n8 -Test 1 (0.00% Hydrogel); liquefaction occurred after 6 cycles; test was ended at 200 cycles

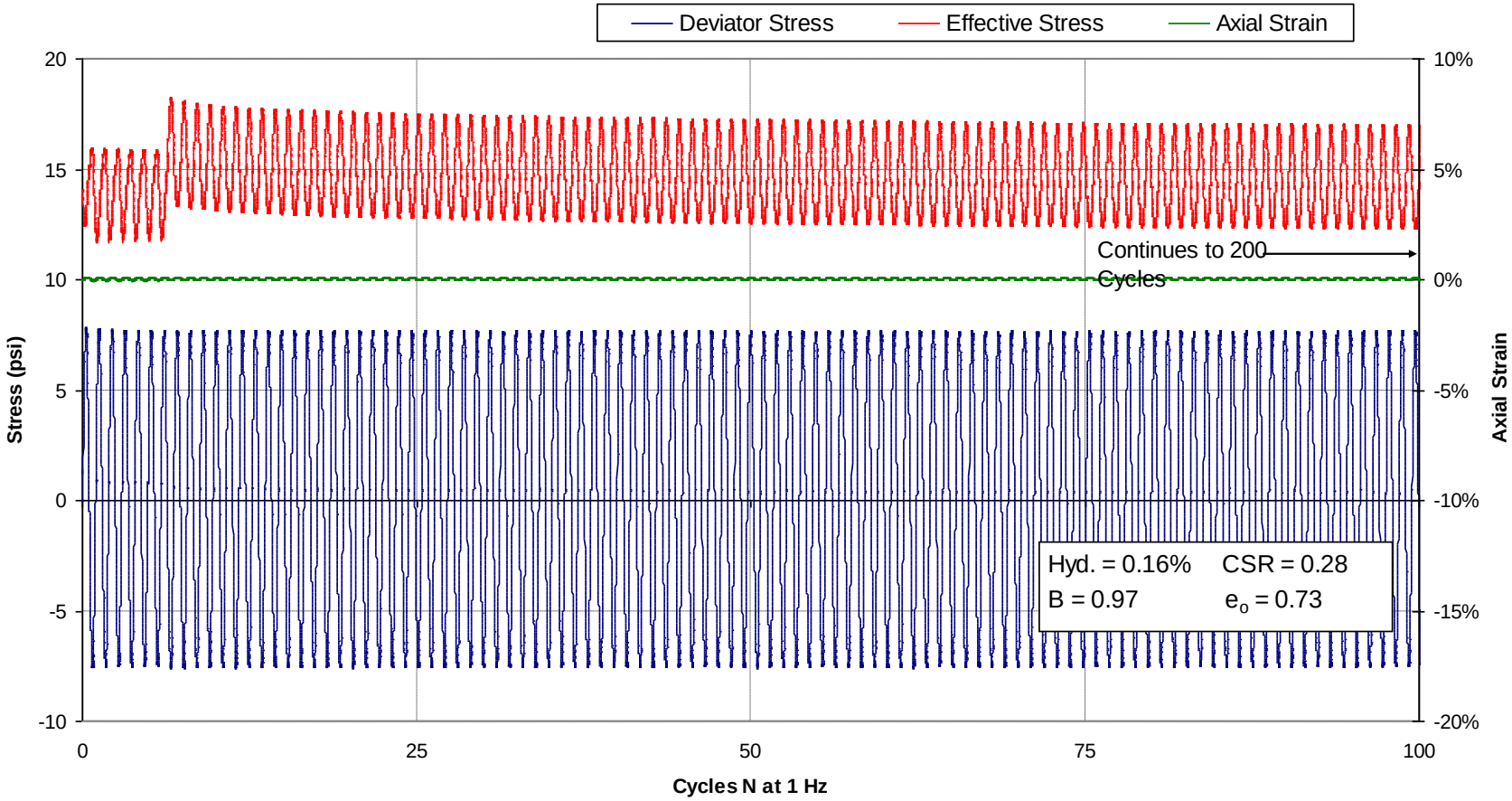

Figure F.6: Deviator Stress, Effective Stress, and Axial Strain vs. Cycles, for hydrogel treated Ottawa sand Sample 0.16%n1 -Test 1 (0.16% Hydrogel); liquefaction did not occur; test was ended at 200 cycles

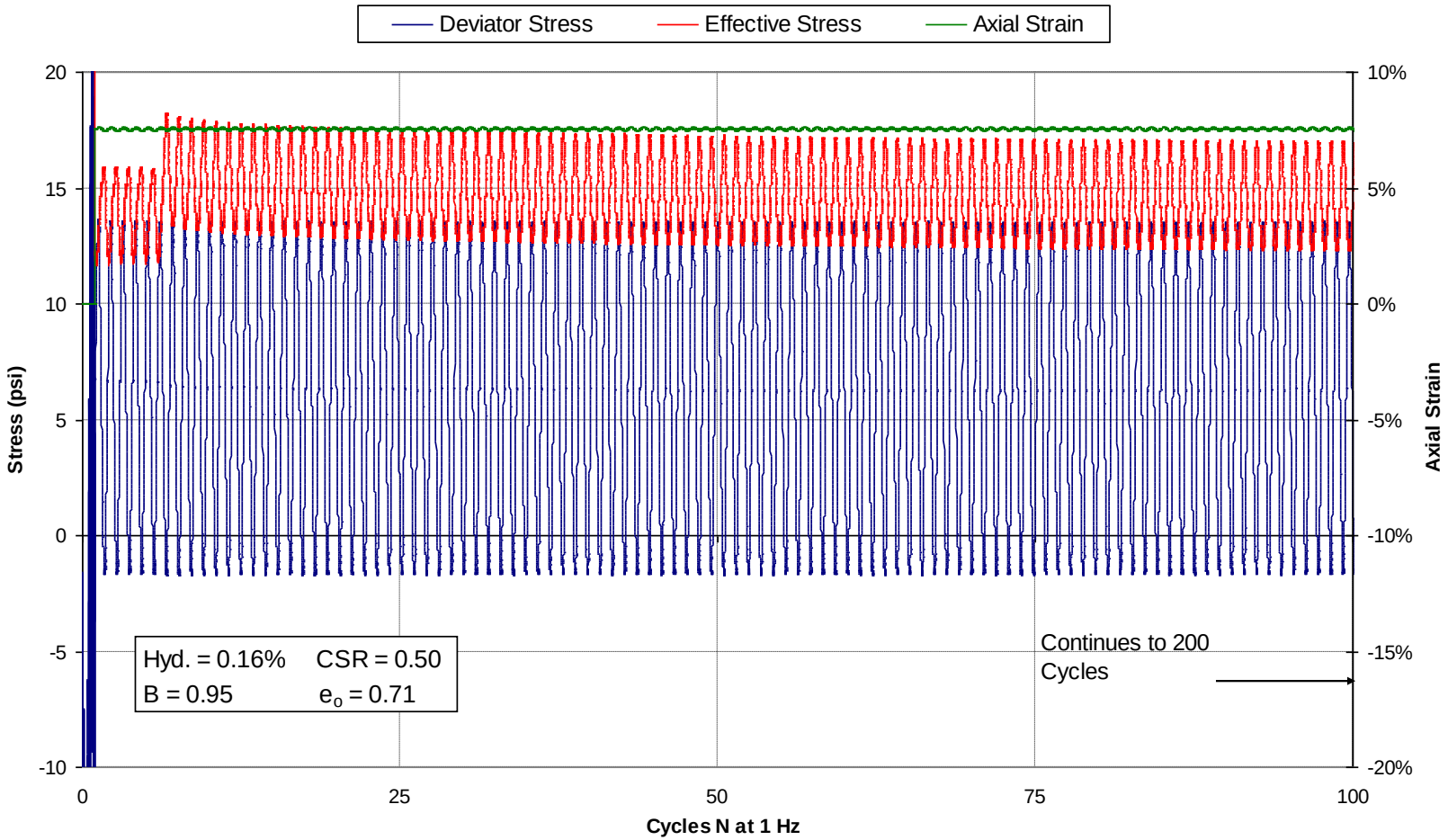

Figure F.7: Deviator Stress, Effective Stress, and Axial Strain vs. Cycles, for hydrogel treated Ottawa sand Sample 0.16%n2 -Test 1 (0.16% Hydrogel); liquefaction did not occur; test was ended at 200 cycles

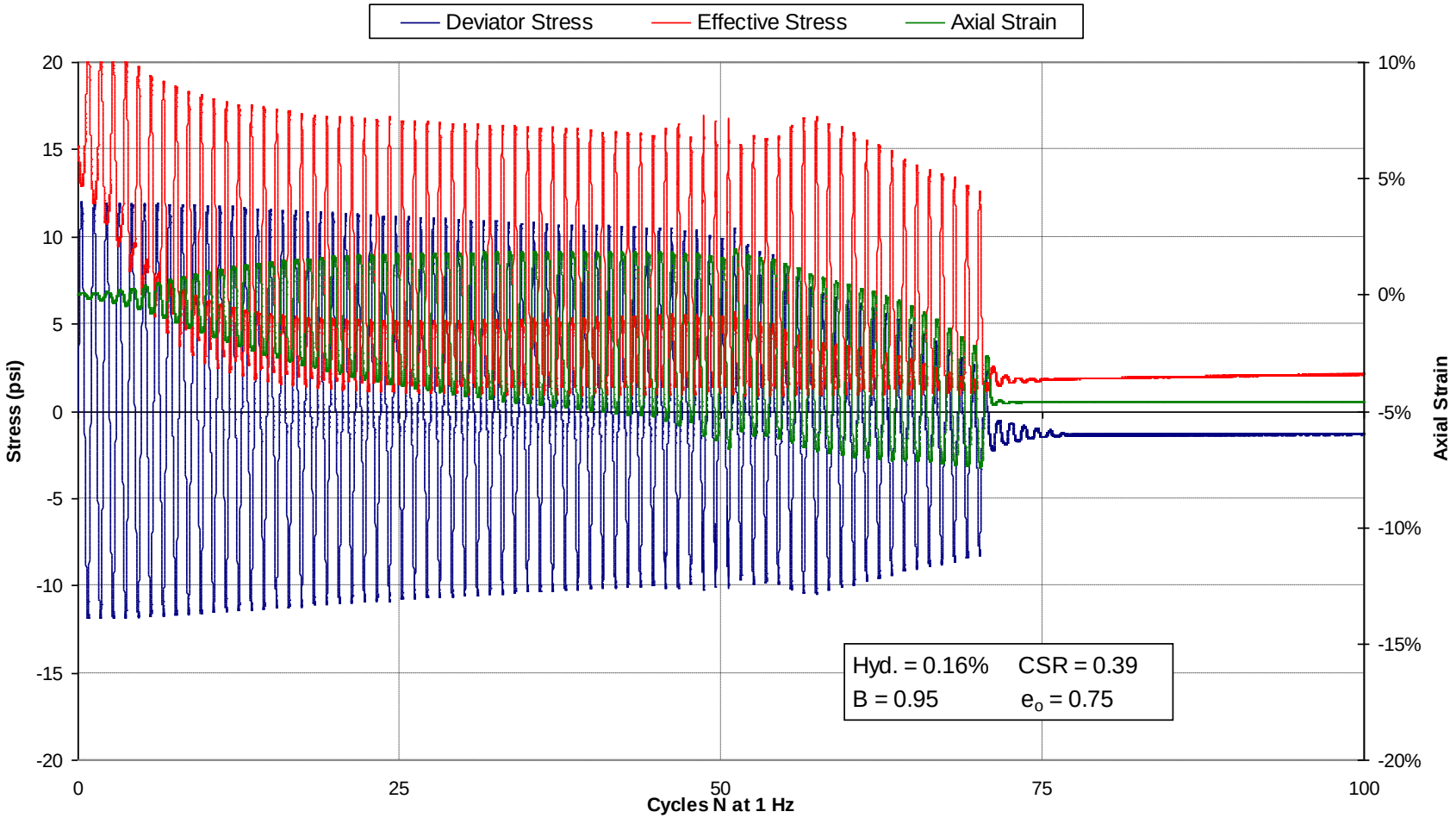

Figure F.8: Deviator Stress, Effective Stress, and Axial Strain vs. Cycles, for hydrogel treated Ottawa sand Sample 0.16%n3 - Test 1 (0.16% Hydrogel); liquefaction did not occur in the traditional sense, however strains were large; test was ended at 73 cycles (the vertical scale is different from the other plots in order to show all the data)

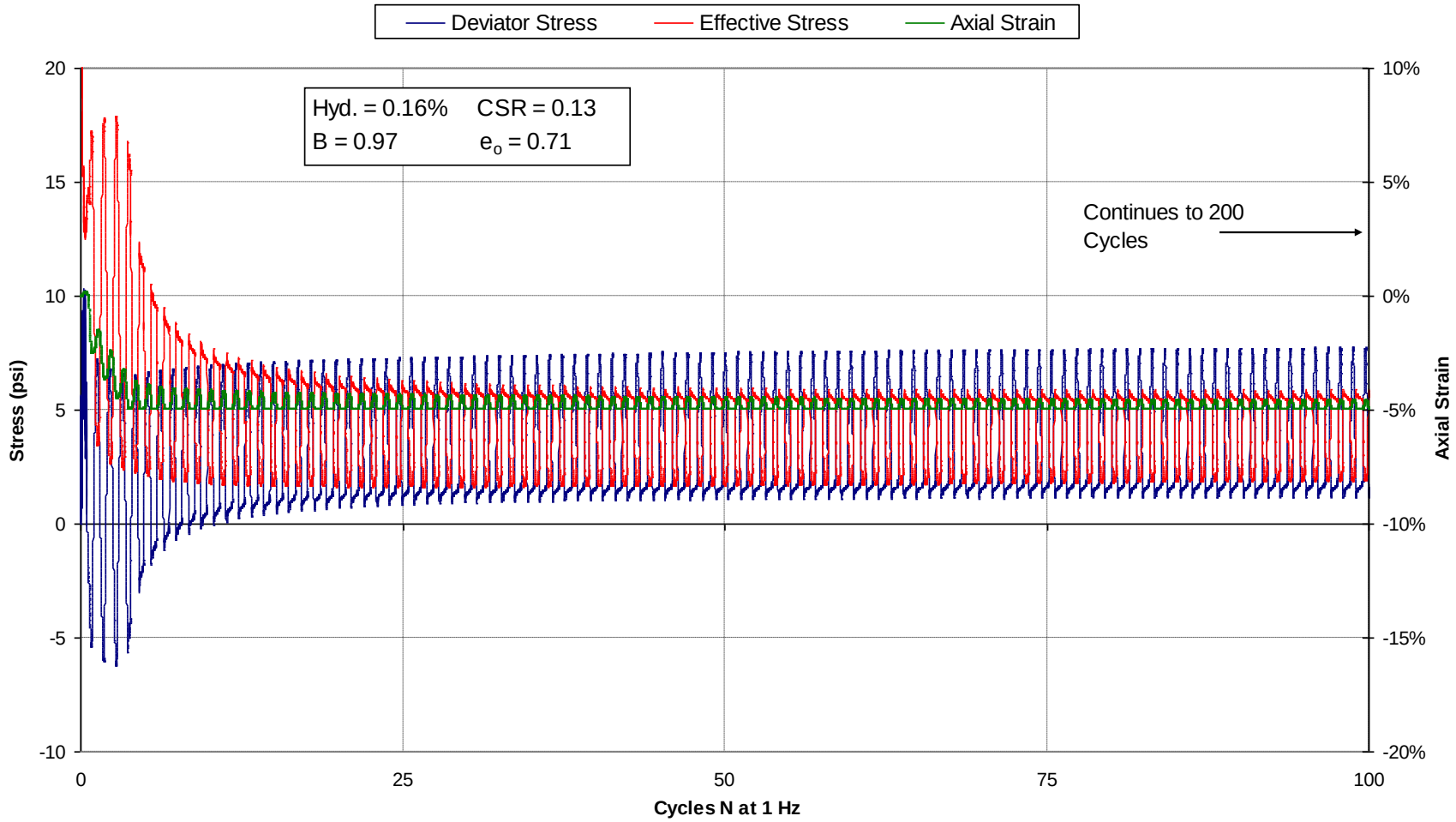

Figure F.9: Deviator Stress, Effective Stress, and Axial Strain vs. Cycles, for hydrogel treated Ottawa sand Sample 0.16%n4 - Test 1 (0.16% Hydrogel); liquefaction did not occur in the traditional sense, however strains were large; test was ended at 200 cycles

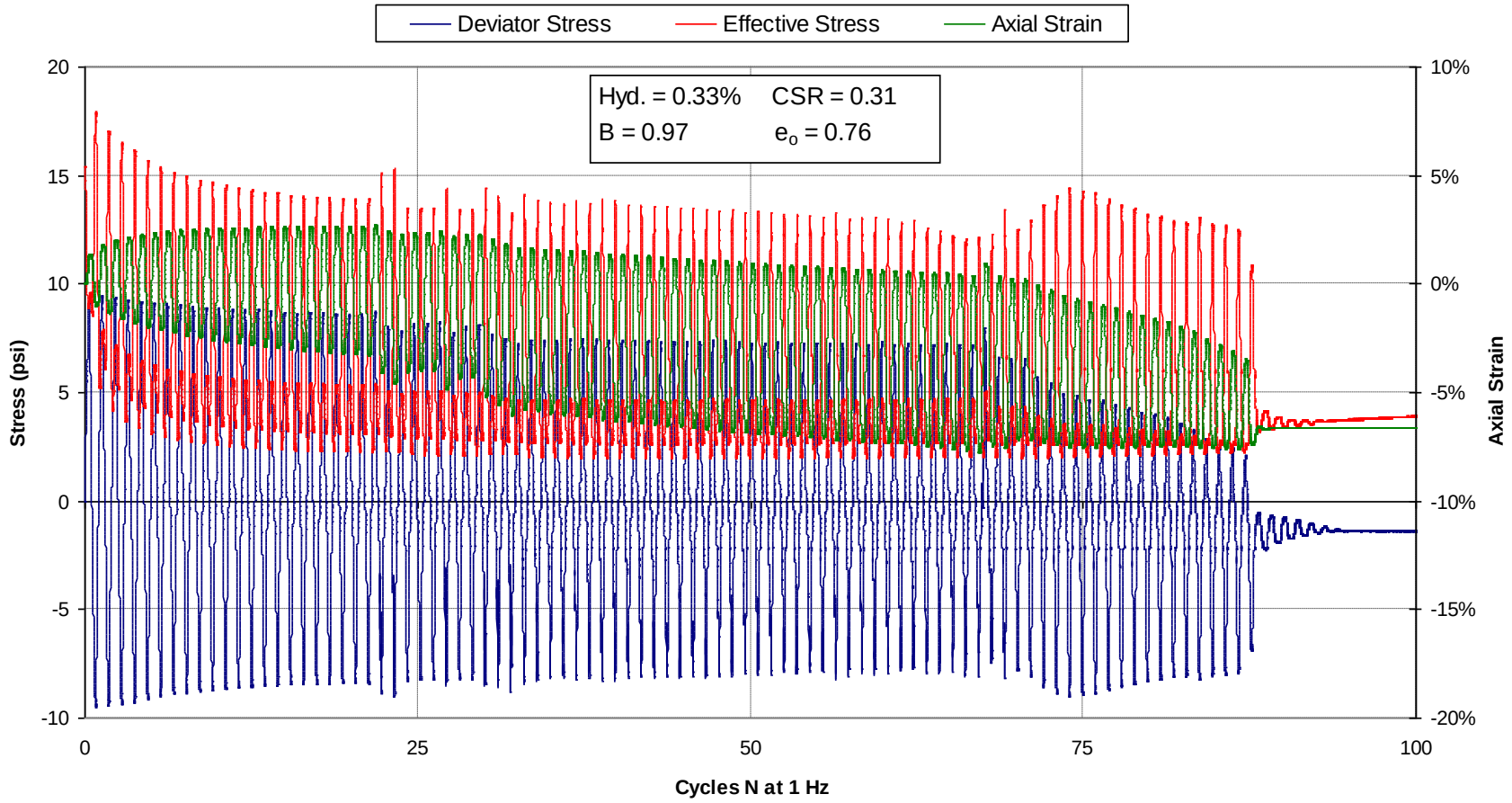

Figure F.10: Deviator Stress, Effective Stress, and Axial Strain vs. Cycles, for hydrogel treated Ottawa sand Sample 0.33%n1 -Test 1 (0.33% Hydrogel); liquefaction did not occur in the traditional sense, however strains were large; test was ended at 87 cycles

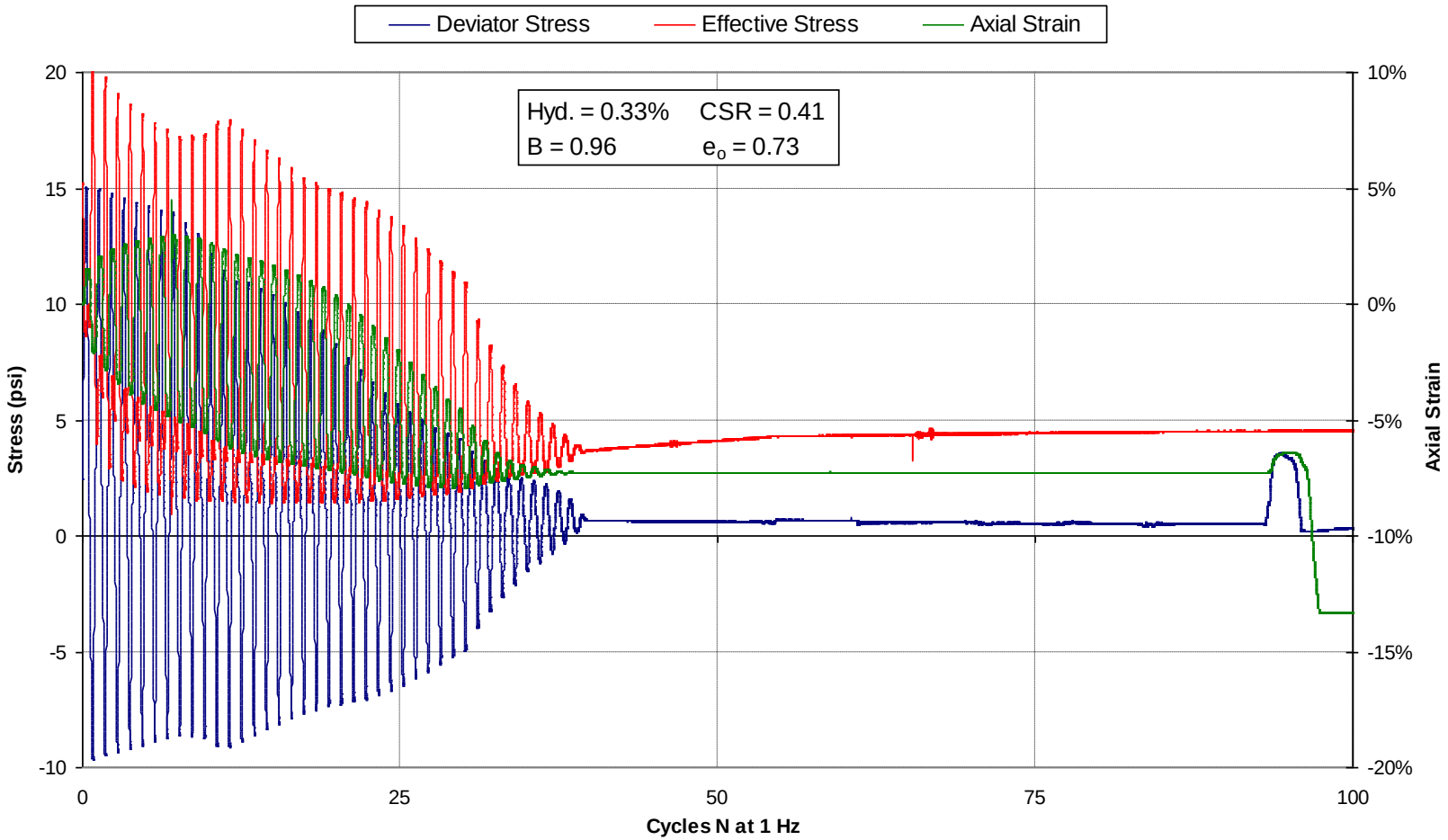

Figure F.11: Deviator Stress, Effective Stress, and Axial Strain vs. Cycles, for hydrogel treated Ottawa sand Sample 0.33%n3 -Test 1 (0.33% Hydrogel); liquefaction did not occur in the traditional sense, however strains were large; test was ended at 39 cycles

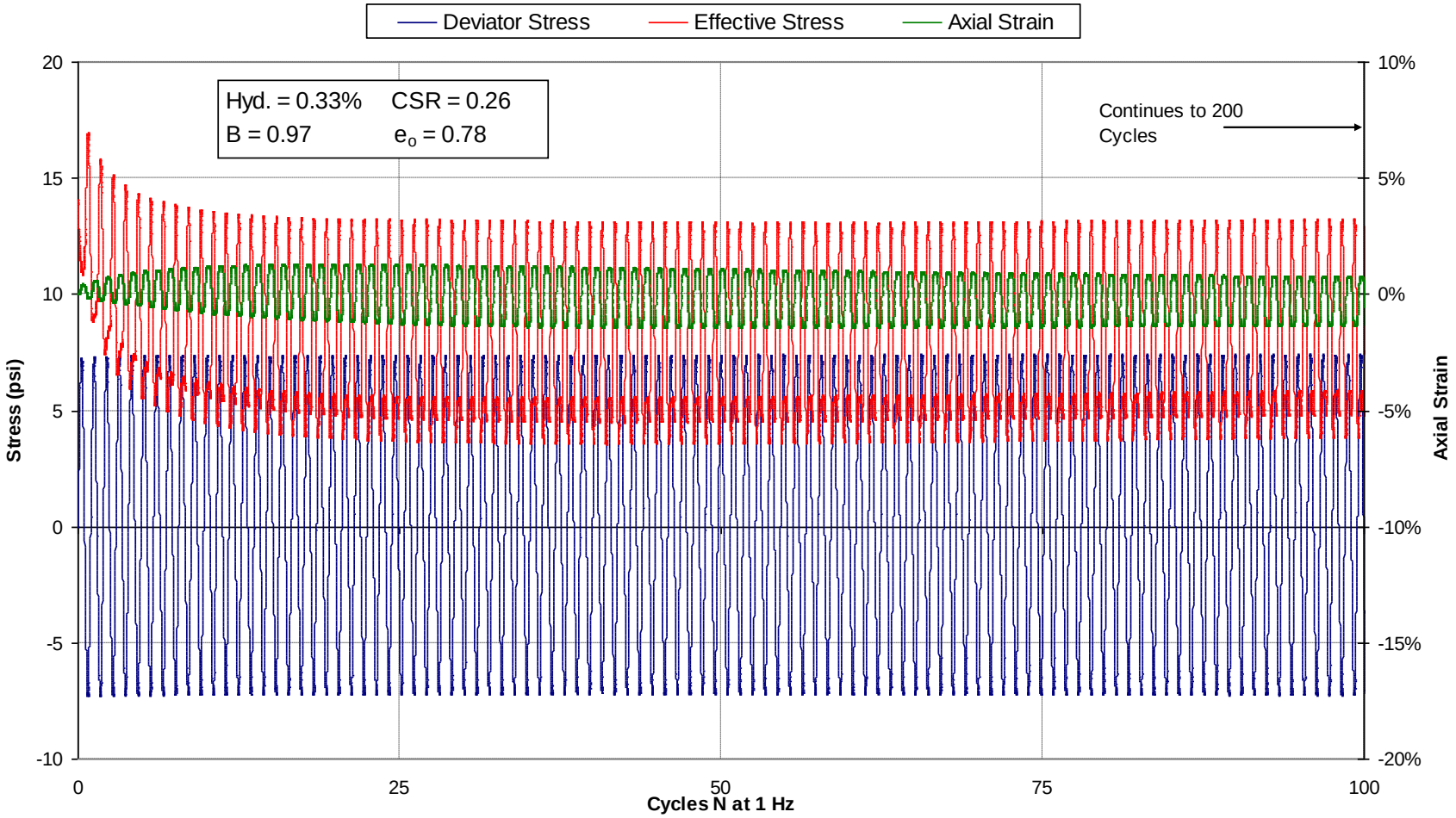

Figure F.12: Deviator Stress, Effective Stress, and Axial Strain vs. Cycles, for hydrogel treated Ottawa sand Sample 0.33%n4 -Test 1 (0.33% Hydrogel); liquefaction did not occur in the traditional sense, however strains were somewhat large; test was ended at 200 cycles

F.2 2008 Data Plots

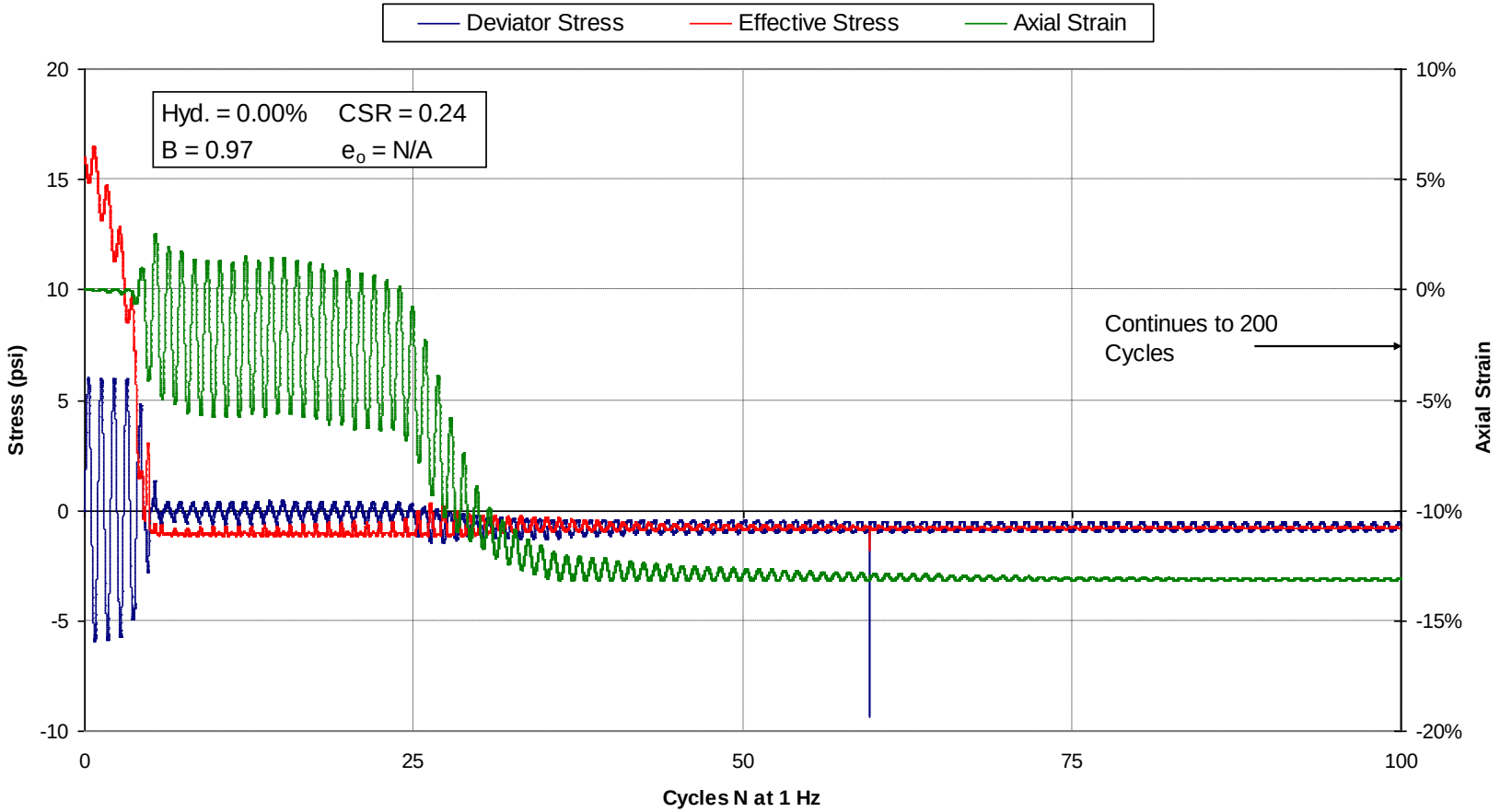

Figure F.13: Deviator Stress, Effective Stress, and Axial Strain vs. Cycles, for Ottawa sand Sample 0.00%A -Test 1 (0.00% Hydrogel); liquefaction occurred after 5 cycles; test was ended at 200 cycles

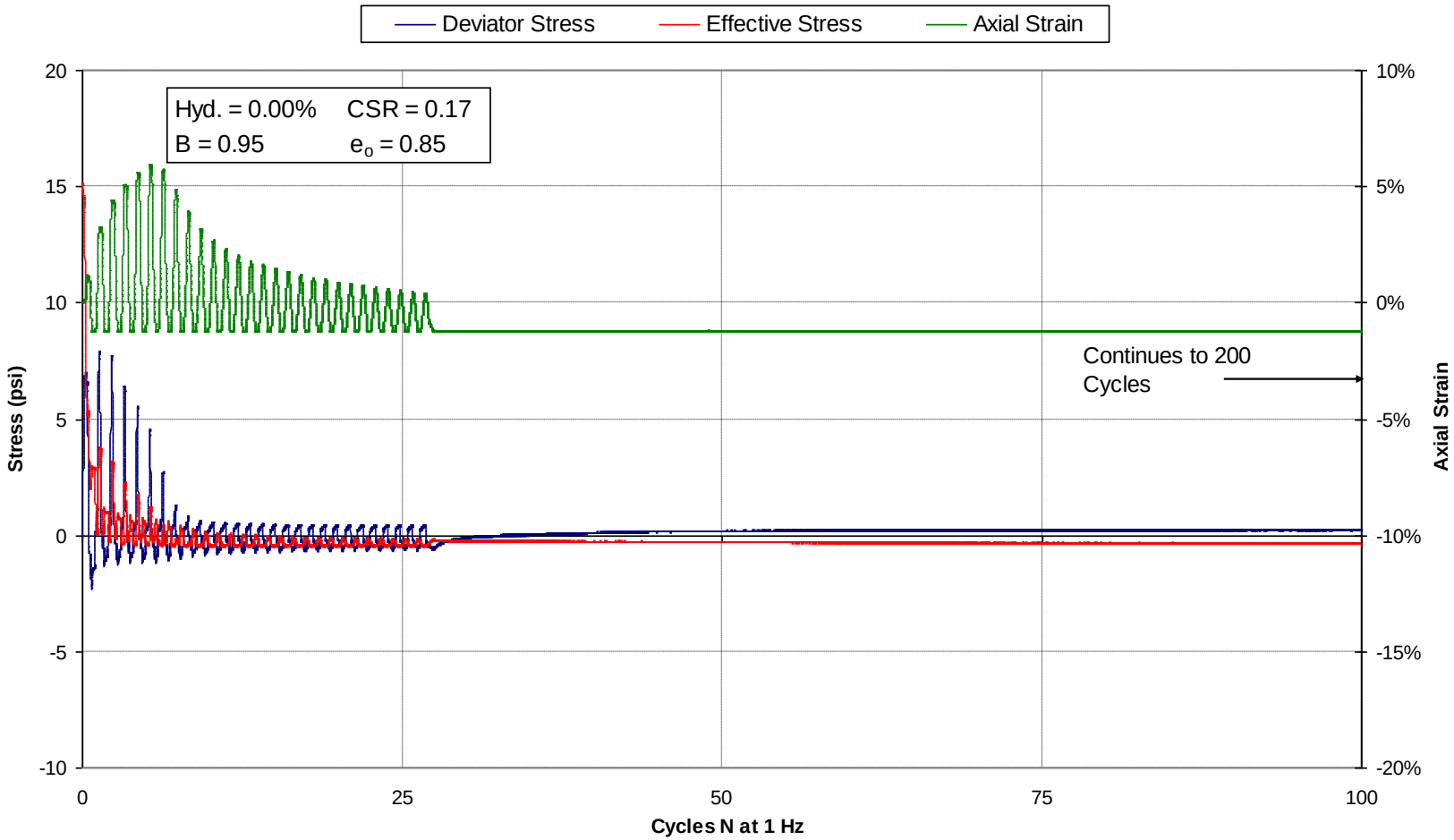

Figure F.14: Deviator Stress, Effective Stress, and Axial Strain vs. Cycles, for hydrogel treated Ottawa sand Sample 0.15%A -Test 1 (0.15% Hydrogel); liquefaction occurred immediately; test was ended at 200 cycles

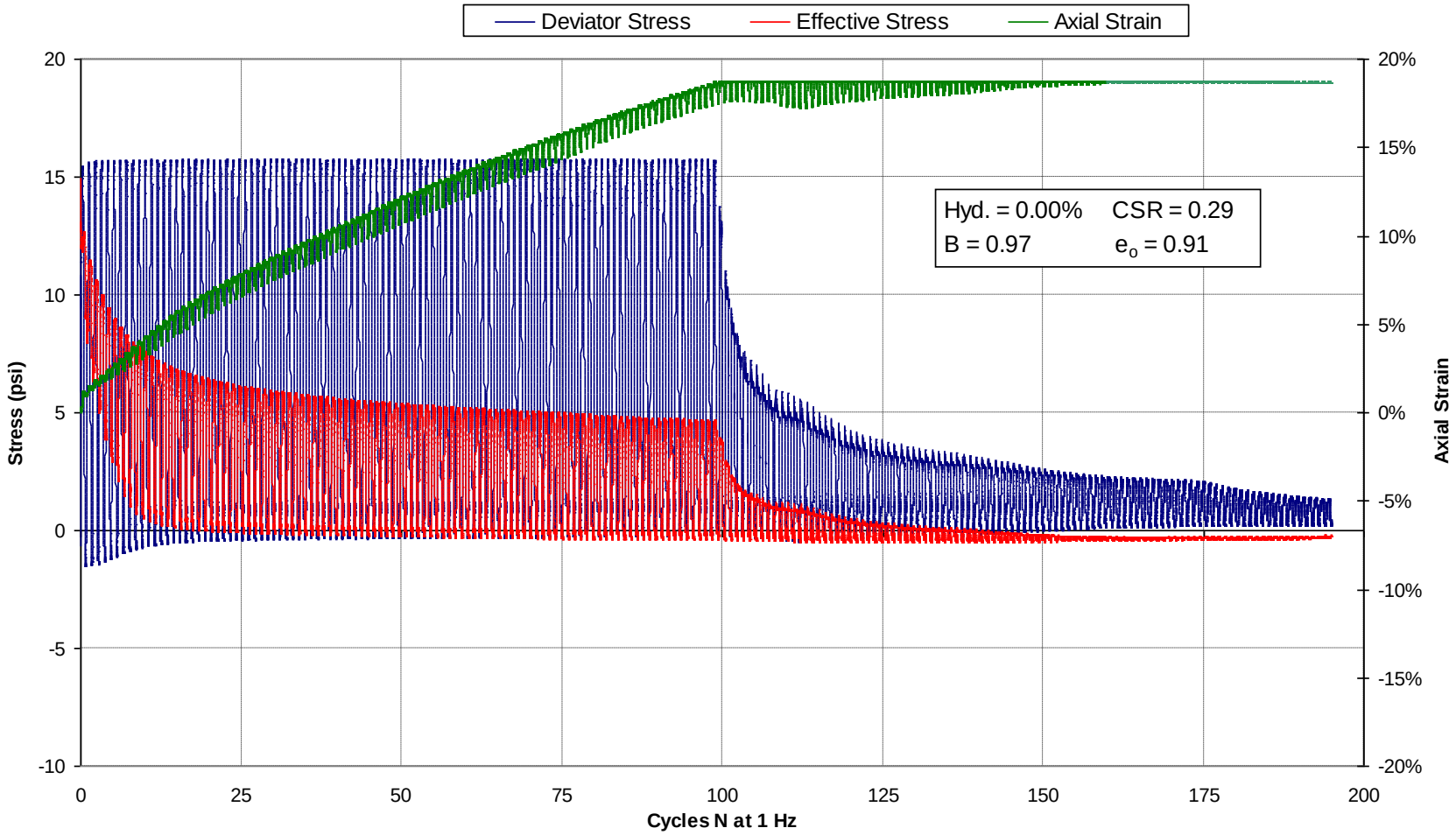

Figure F.15: Deviator Stress, Effective Stress, and Axial Strain vs. Cycles, for hydrogel treated Ottawa sand Sample 0.25%A -Test 1 (0.25% Hydrogel); liquefaction did not occur in the traditional sense; maximum strains were limited by the test machine to 18%; test was ended at 200 cycles (the scales are different from most of the other plots to better show changes in the data)

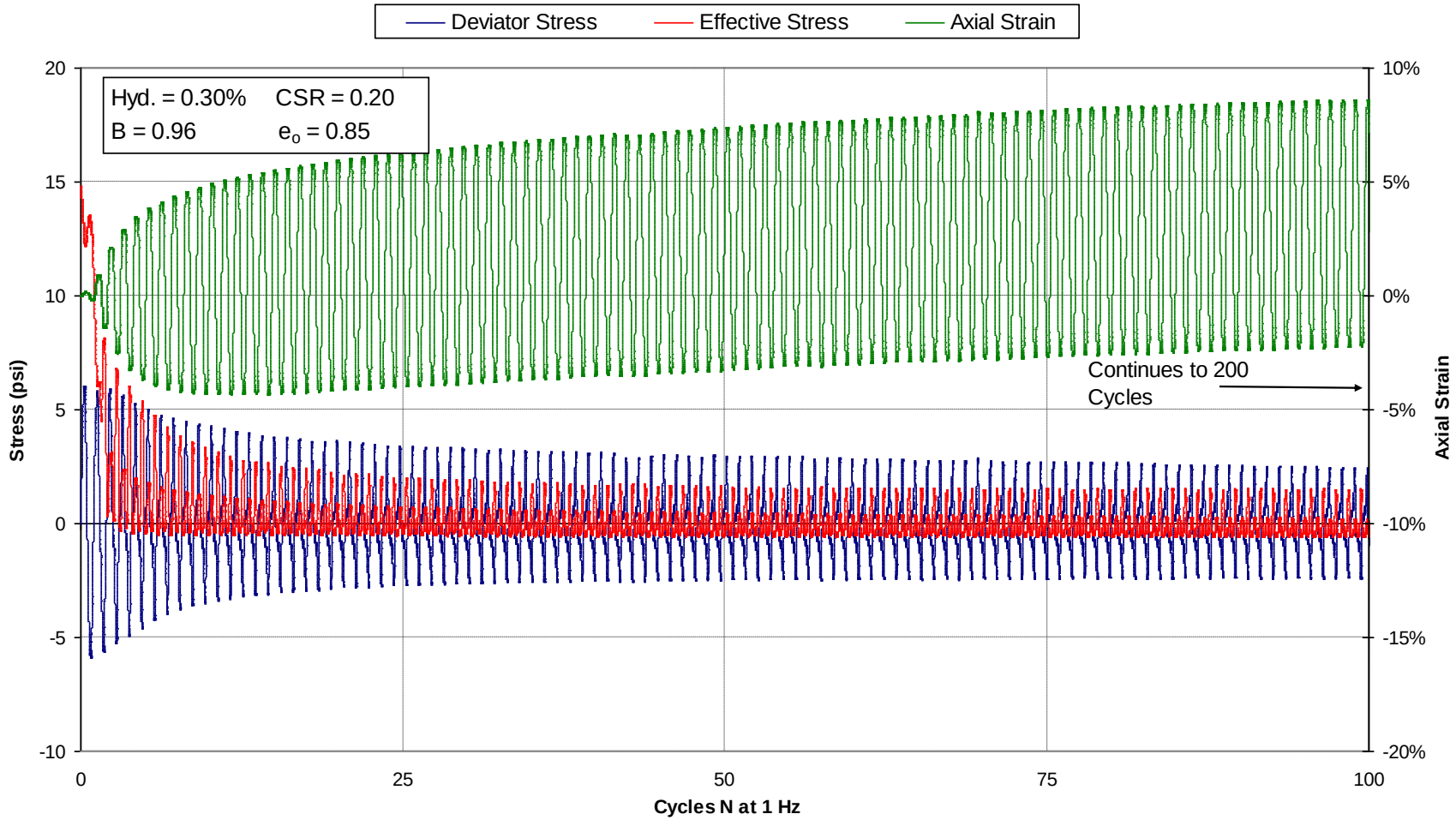

Figure F.16: Deviator Stress, Effective Stress, and Axial Strain vs. Cycles, for hydrogel treated Ottawa sand Sample 0.30%A -Test 1 (0.30% Hydrogel); liquefaction occurred after 3 cycles; test was ended at 200 cycles

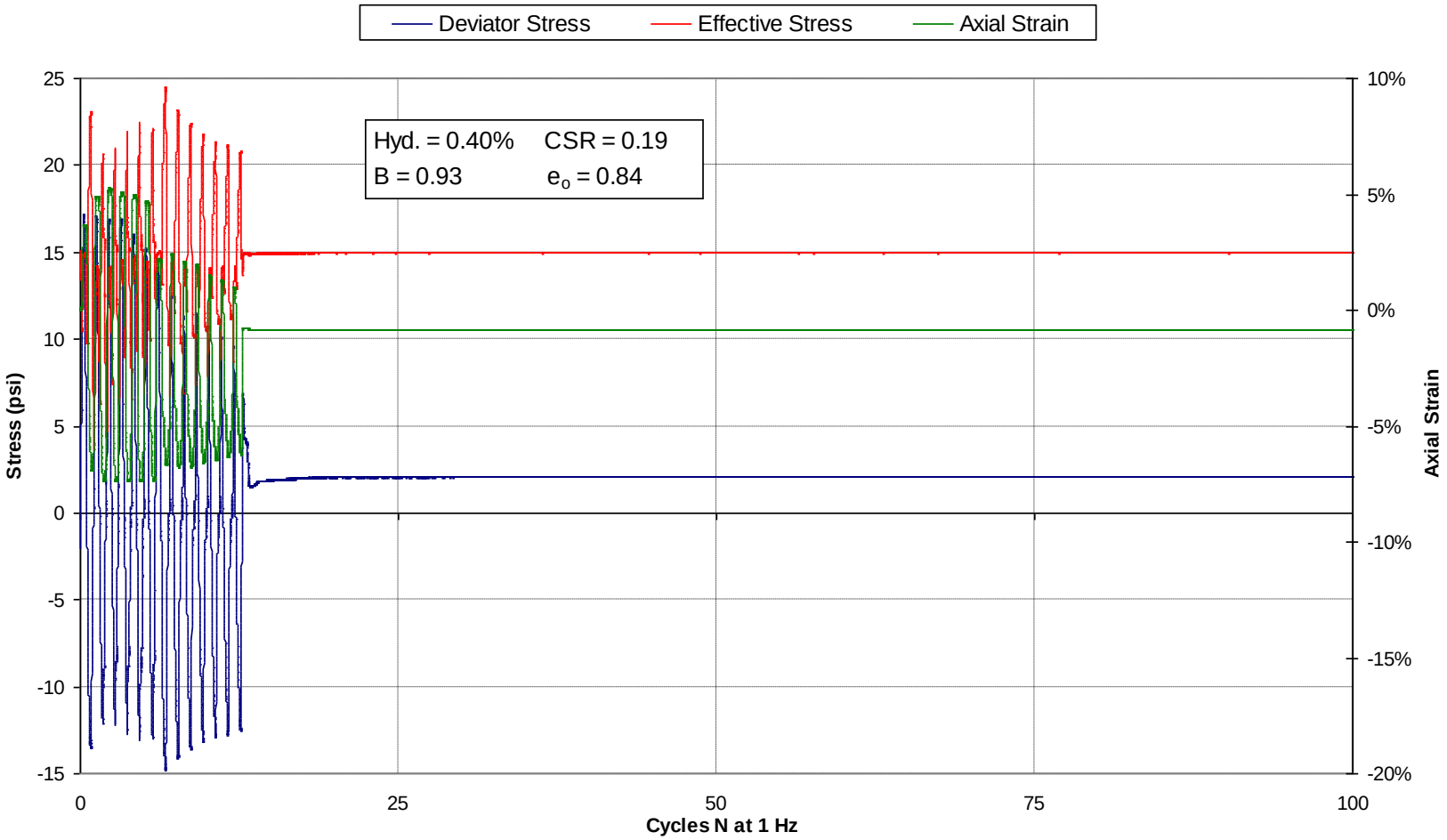

Figure F.17: Deviator Stress, Effective Stress, and Axial Strain vs. Cycles, for hydrogel treated Ottawa sand Sample 0.40%A -Test 1 (0.40% Hydrogel);, liquefaction did not occur, however strains were large; test was ended at 14 cycles (the vertical scale is different from other plots to better show the data)

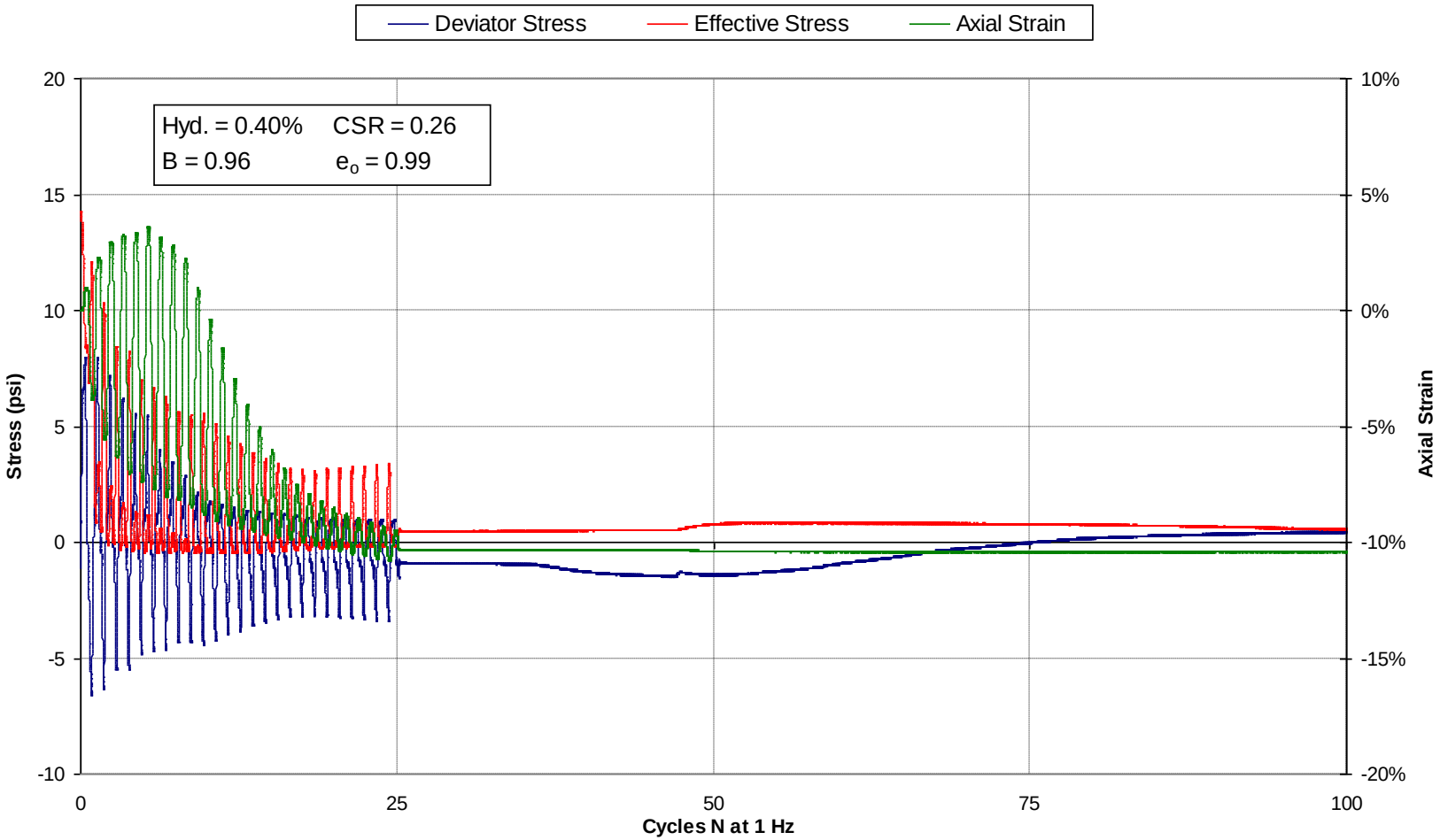

Figure F.18: Deviator Stress, Effective Stress, and Axial Strain vs. Cycles, for hydrogel treated Ottawa sand Sample 0.40%B -Test 1 (0.40% Hydrogel); liquefaction occurred after 3 cycles; test was ended at 25 cycles